PART I. A STUDY OF THE VELOCITY STRUCTURE OF THE EARTH BY THE USE OF CORE PHASES

PART II. THE 1971 SAN FERNANDO EARTHQUAKE SERIES FOCAL MECHANISMS AND TECTONICS

Thesis by

James Hall Whitcomb

In Partial Fulfillment of the Requirement

For the Degree of

Doctor of Philosophy

California Institute of Technology

Pasadena, California

1973

(Submitted April 12, 1973)

ACKNOWLEDGMENTS

Most of the work in Part I is due to the suggestions of Don L. Anderson and his advice and support throughout the study is gratefully acknowledged. The author benefited from many stimulating discussions with past and present staff and students of the Seismological Laboratory at the California Institute of Technology. J. Sclater and R. Fisher at the University of California, San Diego, and E. S. W. Simpson and E. Forder at the University of Captetown, Rondebosch, South Africa, kindly supplied unpublished bathymetry data for Chapter 4. The author is particularly indebted to Lincoln Laboratory at the Massachusetts Institute of Technology for making their array-processing facilities available and, in particular, David Davies and Bruce Julian for direct aid and discussions.

Part II has benefited greatly from the efforts of James A. Hileman who provided the seismicity plots, Jan D. Garmany who located most of the aftershocks, and Clarence R. Allen who located the large aftershocks and gave advice and support throughout, especially in the regional tectonics section. Leon T. Silver also provided helpful discussions on the tectonics of the San Fernando area. The author is indebted to many other organizations too numerous to mention for supplying their seismic data. John M. Nordquist and Mark Gapanoff read many of the records and ran many of the computer solutions. The author gives special thanks to the CIT technical personnel who installed and operated the portable stations during the aftershock series.

The manuscript was typed by Barbara Sloan and the figures were drafted by Laszlo Lenches.

This research was partially supported by the CIT Earthquake Research Affiliates, National Science Foundation Grant GA 29920, and the Advanced Research Projects Agency of the Department of Defense, and was partially monitored by the Air Force Office of Scientific Research under Contract No. F44620-72-C-0078. During part of this study, the author was supported by the California Institute of Technology Gutenberg Fellowship.

ABSTRACT

The initial objective of Part I was to determine the nature of upper mantle discontinuities, the average velocities through the mantle, and differences between mantle structure under continents and oceans by the use of P'dP', the seismic core phase P'P' (PKPPKP) that reflects at depth d in the mantle. In order to accomplish this, it was found necessary to also investigate core phases themselves and their inferences on core structure. P'dP' at both single stations and at the LASA array in Montana indicates that the following zones are candidates for discontinuities with varying degrees of confidence: 800-950 km, weak; 630-670 km, strongest; 500-600 km, strong but interpretation in doubt; 350-415 km, fair; 280-300 km, strong, varying in depth; 100-200 km, strong, varying in depth, may be the bottom of the low-velocity zone. It is estimated that a single station cannot easily discriminate between asymmetric P'P' and P'dP' for lead times of about 30 sec from the main P'P' phase, but the LASA array reduces this uncertainty range to less than 10 sec. The problems of scatter of P'P' main-phase times, mainly due to asymmetric P'P', incorrect identification of the branch, and lack of the proper velocity structure at the velocity point, are avoided and the analysis shows that one-way travel of P waves through oceanic mantle is delayed by 0.65 to 0.95 sec relative to United States mid-continental mantle.

A new P-wave velocity core model is constructed from observed

times, $dt/d\Delta$'s, and relative amplitudes of P'; the observed times of SKS, SKKS, and PKiKP; and a new mantle-velocity determination by Jordan and Anderson. The new core model is smooth except for a discontinuity at the inner-core boundary determined to be at a radius of 1215 km. Short-period amplitude data do not require the inner core Q to be significantly lower than that of the outer core. Several lines of evidence show that most, if not all, of the arrivals preceding the DF branch of P' at distances shorter than 143° are due to scattering as proposed by Haddon and not due to spherically symmetric discontinuities just above the inner core as previously believed. Calculation of the travel-time distribution of scattered phases and comparison with published data show that the strongest scattering takes place at or near the core-mantle boundary close to the seismic station.

In Part II, the largest events in the San Fernando earthquake series, initiated by the main shock at 14 00 41.8 GMT on February 9, 1971, were chosen for analysis from the first three months of activity, 87 events in all. The initial rupture location coincides with the lower, northernmost edge of the main north-dipping thrust fault and the aftershock distribution. The best focal mechanism fit to the main shock P-wave first motions constrains the fault plane parameters to: strike, N 67° ($\pm 6^{\circ}$) W; dip, 52° ($\pm 3^{\circ}$) NE; rake, 72° (67°-95°) left lateral. Focal mechanisms of the aftershocks clearly outline a downstep of the western edge of the main thrust fault surface along a northeast-trending flexure. Faulting on this

downstep is left-lateral strike-slip and dominates the strain release of the aftershock series, which indicates that the downstep limited the main event rupture on the west. The main thrust fault surface dips at about 35° to the northeast at shallow depths and probably steepens to 50° below a depth of 8 km. This steep dip at depth is a characteristic of other thrust faults in the Transverse Ranges and indicates the presence at depth of laterally-varying vertical forces that are probably due to buckling or overriding that causes some upward redirection of a dominant north-south horizontal compression. Two sets of events exhibit normal dip-slip motion with shallow hypocenters and correlate with areas of ground subsidence deduced from gravity data. Several lines of evidence indicate that a horizontal compressional stress in a north or north-northwest direction was added to the stresses in the aftershock area 12 days after the main shock. After this change, events were contained in bursts along the downstep and sequencing within the bursts provides evidence for an earthquake-triggering phenomenon that propagates with speeds of 5 to 15 km/day. Seismicity before the San Fernando series and the mapped structure of the area suggest that the downstep of the main fault surface is not a localized discontinuity but is part of a zone of weakness extending from Point Dume, near Malibu, to Palmdale on the San Andreas fault. This zone is interpreted as a decoupling boundary between crustal blocks that permits them to deform separately in the prevalent crustal-shortening mode of the Transverse Ranges region.

TABLE OF CONTENTS

Page

PART I.

A STUDY OF THE VELOCITY STRUCTURE OF THE EARTH BY THE USE OF CORE PHASES

1. INTRODUCTION

1.1 Development of the Study. Initially, the primary objective of this study was to determine the nature of upper mantle discontinuities, the average velocities through the mantle, and differences between mantle structure under continents and oceans by the use of the P'P' (PKPPKP) seismic core phase recorded at both single seismic stations and large-aperture arrays. It soon became apparent that the definition of the core phases was not sufficient to adequately accomplish the above goals. Thus, as an auxiliary to the study of the upper mantle, an investigation was made of core phases themselves and their determination of core velocity structure.

1.2 Motivation. The explosive increase of seismological data and research as a result of the VELA program during the last decade and the resulting jump in our knowledge of the earth's interior (as well as of seismic discrimination, the major goal of the program) is well documented. The establishment of a worldwide standard seismic station net (WWSS) and improvement of other seismic station nets has enabled the broad-frequency-band study of seismic phases from a single event over wide epicentral distance ranges; this has led to meaningful improvements in our definition of those phases. One of the most significant new techniques for seismological research that is a direct result of the VELA program is the use of large-aperture seismic arrays

to increase the signal-to-noise ratio and band-pass filter coherent energy in the wave-number domain. These developments have already led to a point in several areas of earth investigation too numerous to mention where improvement of earth-structure models can be confidently made over the classic investigations of Gutenberg, Richter, Jeffreys, Bullen, and Birch, which have withstood the test of time so well.

In the upper mantle, use of refracted body phases, surface waves, and normal modes of the earth to outline inhomogeneous velocity and density increases with depth has stimulated interest in investigation of the sharpness of these discontinuities. Reflections of seismic body waves, which have not been extensively used in the mantle, are well-suited to the study of sharp discontinuities because their steep incidence to the plane of the discontinuity gives them maximum sensitivity to the reflector depth and their mere existence puts fairly stringent limits on the reflector thickness. Possible reflections from the top of upper-mantle discontinuities were studied by Hoffman et al. (1961), Whitcomb and Anderson (1968), and Niazi (1969). A major difficulty with this type of phase is identification of a relatively low-amplitude reflection signal from other phases arriving after the first P wave on the seismogram. A convenient way around this problem is to use reflections from the underside of mantle discontinuities of the phase P'P' (PKPPKP); the deeper reflections arrive before the main surface reflection in a quiet part of the short-period

seismogram. This technique was first suggested by Gutenberg (1960) who noted arrivals up to 30 sec before P'P' and was later applied by Adams (1968), Whitcomb and Anderson (1968), Engdahl and Flinn (1969a), Whitcomb and Anderson (1970), and others. However, as with any newly discovered seismic phase, the uniqueness of its interpretation must be well-established and a possible source of misinterpretation was pointed out by Engdahl and Flinn (1969b) in their examples of the strong SKKKP phase as confirmed by Whitcomb and Anderson (1970). Another difficult challenge to uniqueness is posed by the maximum-time nature of the P'P' phase, which allows asymmetric reflections from the surface of the earth to arrive before the symmetric phase. It is therefore important to estimate the likelihood that asymmetric P'P' be misinterpreted as a deeper reflection.

Although the potential of P'P' as an accurate measure of earthquake depths and average velocity through the earth has long been recognized (Gutenberg and Richter, 1934), scatter of the P'P' readings has discouraged previous investigators from using the times for anything more than an approximate check on results. However, once the problem of core-phase branch identification and asymmetric P'P' are resolved, the major source of scatter can be attributed to multiple reflections from the ocean bottom and surface, and a meaningful analysis of P'P' times can be done.

Study of the upper-mantle velocity discontinuities, their nature and depths, is an important tool for inferring the chemical and physical

state of materials at those inaccessible depths (for example, Anderson, 1967). Lateral variations, or their absence, of both the discontinuity depths and average velocities in the upper mantle have direct application to the problems of the chemical and thermal state of the mantle and the dynamic configuration of convection in the mantle which is required by the observed gain (at oceanic rises) and loss (at trenches) of the oceanic lithosphere. However, lateral variations, especially in oceanic areas, are a difficult seismological problem because almost all stations are located on continental structures and the few island stations tend to have high noise levels. P'P' phases are one of the few seismological data types that can remotely sample under oceanic areas with continental stations.

The core has been subjected to more variable interpretations than perhaps any other region of the earth's interior. The reasons for this lie mostly in the inaccessibility of the core not only in terms of physical location but in terms of seismic observability due to the sharp and profound drop in seismic velocity as one passes from the mantle into the core. Complications that arise from looking through this extremely distorting "lens" have only recently begun to be unraveled through the improved observation capabilities of worldwide station nets and the large-aperature seismic arrays. As a result, models of core structure are now beginning to converge to a point where their details may shed some light on the physical properties of materials in the core and, thus, the composition,

physical state, and dynamics of those materials. In particular, details that are emerging from core studies are the high velocity gradient in the outermost core, the low gradient just above the inner-core boundary, the small velocity jump at the inner-core boundary, and high gradient at the top of the inner core. In addition, certain core phases suggest that there are strong lateral variations in material properties near the core-mantle boundary.

One might fairly inquire as to the potential usefulness of our improved knowledge of core phases and core structure other than the obvious desirability of increasing our general knowledge of this remote portion of the earth. Three relevant areas that are at the forefront of current scientific investigation are immediate candidates. One is related to the basic origins of our earth. The investigation of lunar mineral samples has led to theories involving the composition of the primary solar-system material, formation of the planetary bodies, including the earth, and finally to specific predictions that can be tested about the nature and composition of materials of the core as they relate to this process (for example, Anderson and Hanks, 1972). Second is the phenomenon of periodic reversal of the earth's magnetic field. This process is almost certainly related to dynamics within the outer core, and the velocity gradients in this region may be crucial parameters in discovering the mechanism and critical conditions necessary for reversal. The third

is related to the burgeoning field of plate tectonics and a recent proposal that narrow plumes extending from the core-mantle boundary to the surface of the earth are at least a partial driving mechanism and configuration control for lithospheric plates, which dominate the location and rate of major earthquake occurrence. The latter two, involving magnetic reversals and major earthquake occurrence, have clear social implications dealing with the quality of life on the earth's surface.

1.3 Scope. Chapter 2 is essentially a review and minor revision of the Whitcomb and Anderson (1970) study of the P'P' phase and its precursors at single stations for reflections under the Atlantic-Indian rise south of the tip of Africa and the Ninety-East ridge in the Indian Ocean; a new set of data is included for reflections under the rift zone of Southeast Africa. The revision of the previous paper takes into account the developments of core structure that culminate in Chapter 6. Conclusions from Chapter 2 are delayed in favor of the more complete investigation of P'P' in Chapter 3.

Chapter 3 investigates the $dt/d\Delta$ of the P'P' phase and its precursors for ten events recorded at the LASA array in Montana. The reflection areas are under the East Indian ocean, ocean areas near the Atlantic-Indian rise and East Indian rise (classic spreading

centers), and the Antarctic continent. The depth variation, continuity, strength, and an approximate limit on the thickness of the discontinuities are discussed.

Chapter 4 estimates the likelihood that asymmetric P'P' phases that reflect from dipping interfaces near the surface of the earth are misinterpreted at P'P' reflecting at depth.

Chapter 5 investigates the causes of the large scatter observed for the main P'P' phase and resolves the scatter by using relative amplitudes, bathymetry data, the ocean-surface reflection, and the results of Chapter 6. The results are analyzed with respect to ocean bottom reflectivity, the effect of P tables on hypocentral locations and calculated P'P' times, and the implications of the observed P'P' times on average mantle velocities under continents and oceans.

Chapter 6 makes a new determination of core structure using recent advancements in identification of core-phase branches with large-aperture arrays, the Jordan and Anderson (1973) B1 mantle model which has a different velocity structure and core radius than those previously used, and improved knowledge of core-phase amplitudes. The inversion takes observations of times, $dt/d\Delta$, and amplitudes of core phases and constructs a consistent $dt/d\Delta$ data set as a function of distance for the core phases P', SKS, and SKKS. The times of PmKP, where m is 2 or greater, are not used for the inversion because of the phase's maximum-time nature. The mantle times and distances

are stripped away using PcP and ScS (reflections from the core-mantle boundary) from the B1 model to get a $dt/d\Delta$ curve corresponding to the surface of the core. The classic Wiechert-Herglotz integration method is applied to the curve to obtain P-wave velocity with depth in the core and the resulting velocity model is then checked and modified by P' and PKiKP absolute times. Finally, oceanic and continental mantle velocity differences, Q structure of the core, and scattering of core phases are discussed in relation to the final core velocity model and observed data.

2. P'dP' OBSERVED AT SINGLE STATIONS

2.1 Introduction. Recent models of the structure of the upper mantle, such as those of Anderson and Toksöz (1963), Niazi and Anderson (1965), Archambeau et al. (1969), Johnson (1967), Ibrahim and Nuttli (1967), Green and Hales (1968), Julian and Anderson (1968), Anderson and Julian (1969), and Jordan and Anderson (1973) include regions of high velocity gradient in the upper mantle. The sharpness of these discontinuities has led to new interest in looking for reflections of seismic waves from structures in the upper mantle. Hoffman et al. (1961), Whitcomb and Anderson (1968), and Niazi (1969) studied possible reflections from the upper surfaces of discontinuities in the upper mantle.

Another reflection of interest is the reflection of P'P' (PKPPKP) from the underneath surface of discontinuities as shown in Figure 2.1. This reflection has the decided advantage of being in a quiet part of the seismic record before the main P'P' phase. Gutenberg (1960) noted arrivals up to 30 sec before P'P' and Adams (1968) interpreted P'P' precursors as reflections arriving up to 70 sec before the main phase. Because Adams was using isolated stations for reading the precursors, he could not recognize that some of his readings for the deep earthquakes were probably SKKKP which has a different $dt/d\Delta$ as noted by Engdahl and Flinn (1969b). The remaining

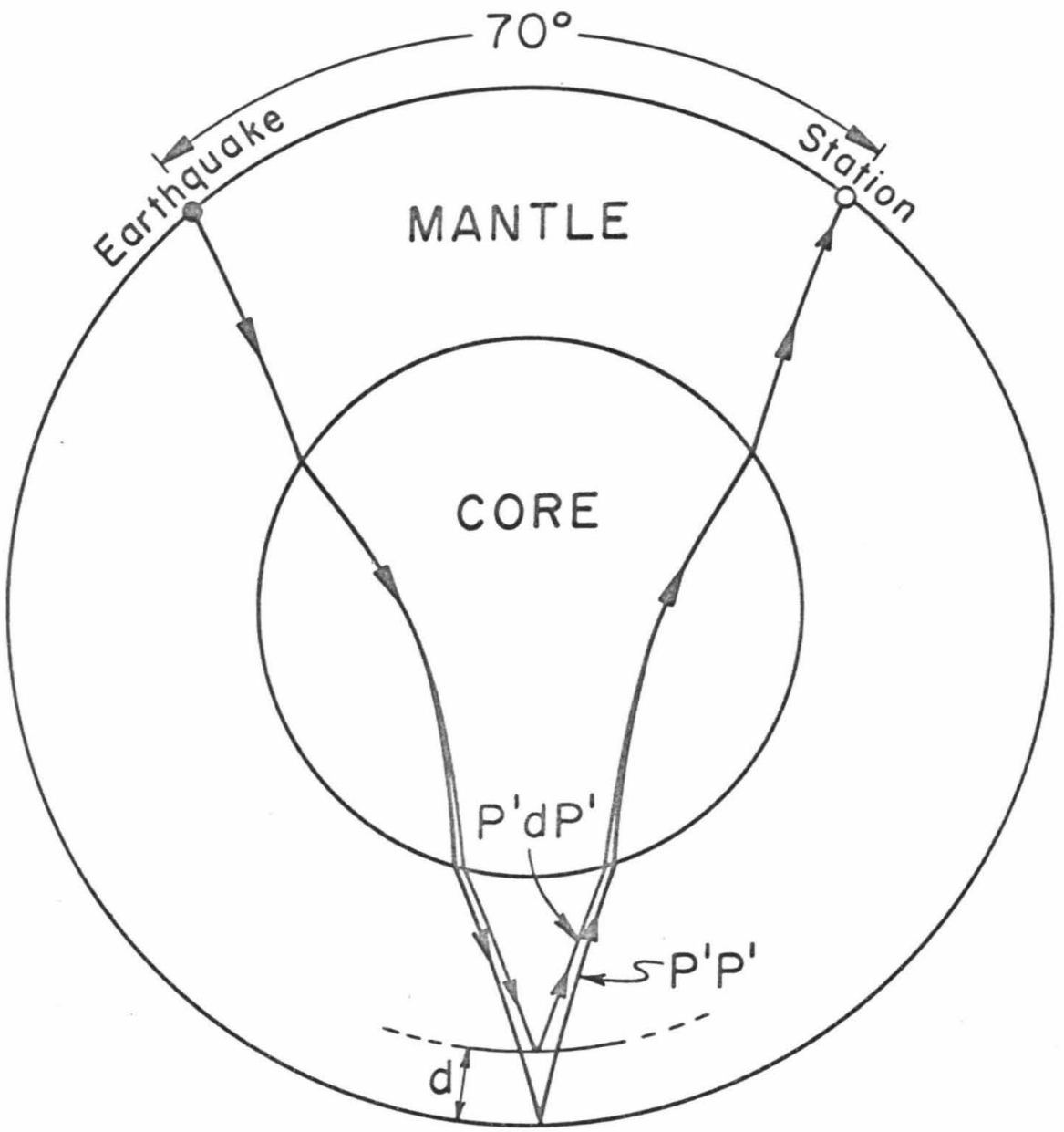

Figure 2.1

A schematic diagram of the P'P' and P'dP' phase ray paths through the earth.

readings of Adams indicated discontinuities near 65 to 70 km and 160 to 180 km in depth. However, as discussed in Chapter 4, all phases with lead times less than 30 sec from the main P'P' phase (an equivalent reflection depth of about 120 km) have an alternative explanation as asymmetric P'P' if only individual stations are used. Whitcomb and Anderson (1968) and Engdahl and Flinn (1969a) found a strong precursor with the proper $dt/d\Delta$ that they interpreted as P'P' reflecting at a depth near 650 km. These phases are called P'dP', as defined by Whitcomb and Anderson (1970), and indicate a reflection of the P'P' phase at a depth d in kilometers. Thus, a reflection at 650 km would be P'650P', and P'0P' is equivalent to P'P'. In this and succeeding chapters, all core-phase branch nomenclature and calculations are based on the development of core structure in Chapter 6.

Whitcomb and Anderson (1970) systematically searched seismic records of individual stations for P'P' precursors up to five minutes before the main phase, estimated depths and strengths of reflectors in the upper mantle, and discussed their correlation with possible phase changes. They investigated two geographic regions of reflection: one near the Atlantic-Indian rise south of the tip of Africa, and the second near the Ninety-East ridge in the Indian Ocean shown in Figure 2.2. This chapter reviews and somewhat modifies their P'dP' results to account for recent advances in the knowledge of

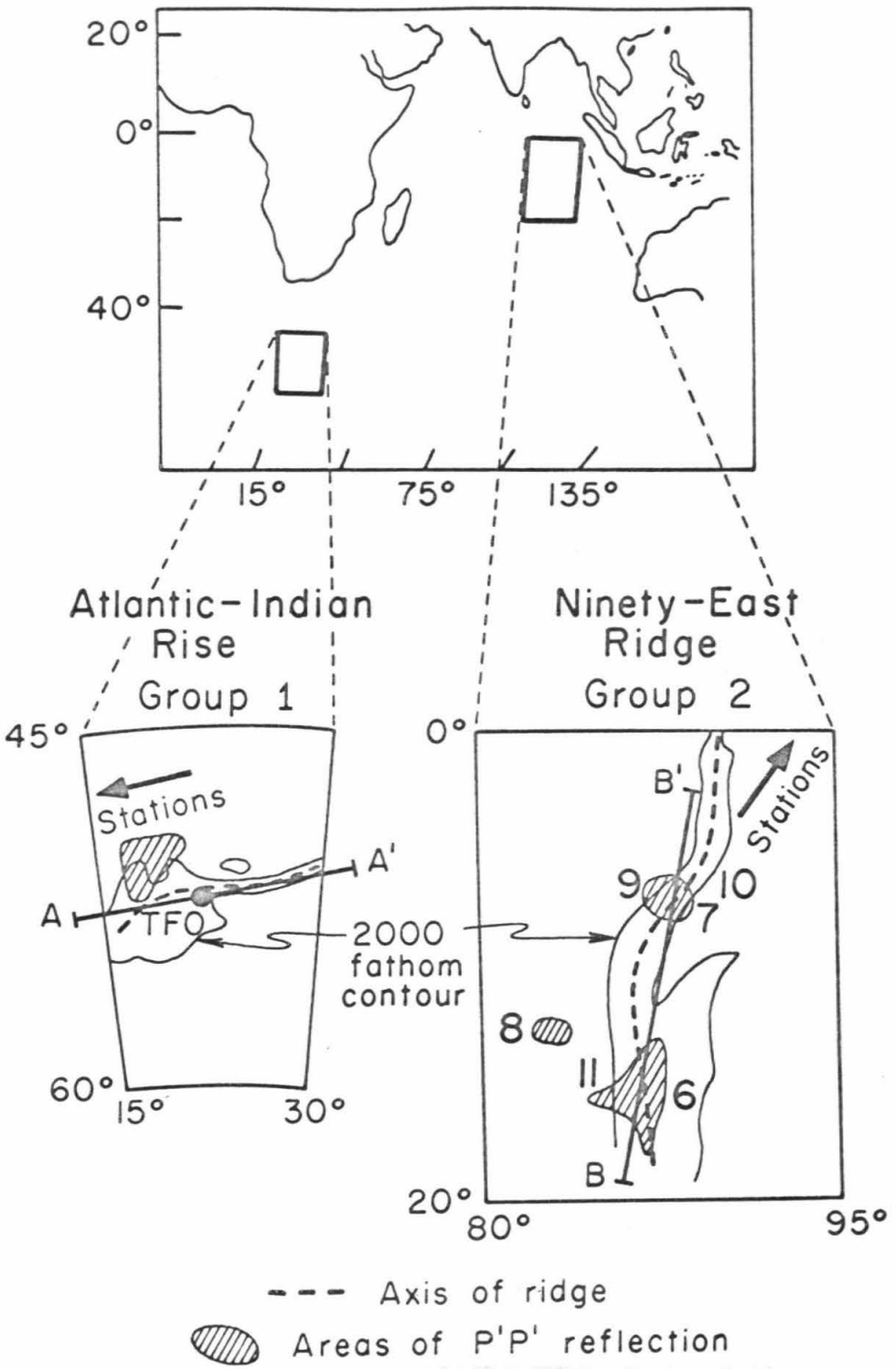

Figure 2.2

The regions of reflection of P'P' at the Atlantic-Indian rise and the Ninety-East ridge for the single-station data.

core structure that are developed in later chapters. The P'dP' single-station analysis is extended in this chapter to a new "continental" reflection area under the rift zone of Southeast Africa which allows us to compare results from oceanic mantle to continental mantle. Conclusions from the results of this chapter are deferred until they can be compared with the more complete analysis of P'dP' in the next chapter.

2.2 Data. The data were collected from short-period vertical seismometers located mainly at stations in Southern California as described in Whitcomb and Anderson (1970); some data were used from Central California and Arizona stations. Earthquakes from the Hokkaido region of the Japanese arc, reflecting under the Atlantic-Indian rise, and from South America, reflecting under the Ninety-East ridge, were used as seen in Figure 2.2; both areas are between 55° and 75° from Pasadena near the P'P' caustic where largest amplitudes are expected. The new events have reflection points under Southeast Africa for Southern California stations and are located at the northern Tonga trench. Table 2.1 shows the parameters for all events (from the USCGS bulletins) used for P'P' studies in this and succeeding chapters. The P-wave residuals at Southern California stations are less than one second.

The periods of the P'P' arrivals and precursors are generally

Table 2.1

Events used for P'P' studies.

No.	Date	Origin Time	Depth	Epicenter Lat.	Epicenter Long.	Mag.
1	05/31/64	0h 40m 36.4s	48 km	43.5°	146.8°	6.3
2	06/23/64	1h 26m 37.0s	77 km	43.3°	146.1°	6.2
3	06/11/65	3h 33m 44.9s	47 km	44.7°	148.7°	6.0
4	10/25/65	22h 34m 24.3s	180 km	44.2°	145.3°	6.2
5	01/29/68	10h 19m 5.6s	40 km	43.6°	146.7°	7.0
6	11/03/65	1h 39m 2.5s	583 km	-9.1°	-71.4°	6.2
7	05/11/67	15h 5m 16.8s	67 km	-20.3°	-68.5°	6.1
8	09/03/67	21h 7m 30.8s	38 km	-10.6°	-79.8°	6.5
9	12/21/67	2h 25m 21.6s	33 km	-21.8°	-70.0°	6.3
10	12/27/67	9h 17m 55.7s	135 km	-21.2°	-68.3°	6.4
11	06/19/68	8h 13m 35.0s	28 km	-5.6°	-77.2°	6.6
12	05/16/68	10h 39m 1.5s	33 km	41.5°	142.7°	7.0
14	11/09/63	21h 15m 30.4s	600 km	-9.0°	-71.5°	7.2
15	11/07/68	10h 2m 5.2s	0 km	73.4°	54.9°	6.0
16	10/14/69	7h 0m 6.2s	0 km	73.4°	54.8°	6.1
18	02/28/69	4h 25m 36.9s	33 km	36.2°	-10.5°	5.7
22	08/12/69	5h 3m 26.9s	33 km	43.6°	148.0°	6.5
23	10/09/67	17h 21m 49.5s	654 km	-21.1°	-179.3°	7.0

Table 2.1 (continued)

No.	Date	Origin Time	Depth	Epicenter Lat.	Epicenter Long.	Mag.
24	02/17/67	10h 10m 51.5s	19 km	-23.7°	-179.3°	7.0
25	01/19/67	12h 40m 12.6s	18 km	-14.8°	-178.8°	6.7
26	05/21/62	21h 15m 30.0s	342 km	-19.8°	-177.4°	7.0
27	04/14/57	19h 18m 2.0s	32 km	-15.4°	-173.4°	7.5
28	09/15/54	17h 56m 9.0s	542 km	-17.8°	-178.6°	7.0

in the 1.5 to 3.0 sec range on the Benioff short-period vertical seismometers. Waves with periods as short as one second and as long as five seconds are seen, however. No systematic difference in period is noted between the main branches of P'P' and the early arrivals, and all arrivals from the same earthquake tend to have similar periods in this distance range; this is discussed in more detail later.

Records from the various stations were read independently without reference to each other or to a travel-time scale, and all of the readings were made by the authors in an effort to be completely systematic. The readings of P'P' and precursors were read to the nearest second and were graded according to the following confidence scale:

3 - High; sharp pulse or a wave train with a sharp beginning.

2 - Medium; emergent beginning but a definite signal, usually a wave train.

1 - Low; small wave train with an emergent beginning; character (difference in period or amplitude) distinguishes it from the prevailing noise level.

Examples of seismograms with readings are shown in Figure 2.3.

In order to compare the P'P' data from different earthquakes, corrections were made for the earth's ellipticity and the focal depth of the earthquake in order to put the origin at the surface

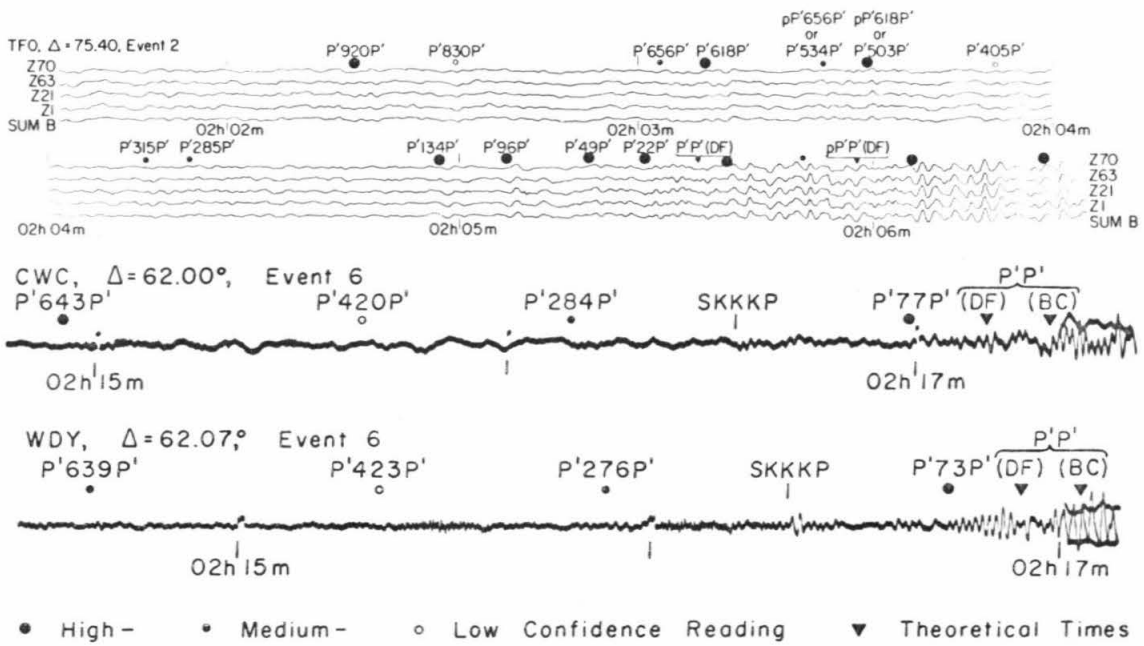

Figure 2.3

Short-period vertical records of P'P' and precursors from Events 2 (Tonto Forest Array) and 6 (stations CWC and WDY) with coded readings and theoretical main branch times.

of a standard spherical earth. The epicentral depth correction depends on which branch of P'P' is being considered because each branch has a different apparent slowness. Whitcomb and Anderson (1970) used the determination of the largest-relative-amplitude branch (the largest-amplitude branch on a single seismogram) from Adams and Randall (1964) as a function of distance. Subsequent investigations in Whitcomb (1971) and Chapters 5 and 6 have modified some conclusions about the relative amplitudes of the P' phases; and analysis of the original P'dP' data of Whitcomb and Anderson (1970), which is dependent on the relative amplitudes, will be altered slightly. They reasoned, as did Adams (1968), that the P'dP' phase observed on a single seismogram would be the same branch as the largest-relative-amplitude phase of P'P' for an equivalent core path. This assumption is based on the large and consistent amplitude differences observed for the branches of P' and P'P' (Adams and Randall, 1964; Whitcomb and Anderson, 1970; and Whitcomb, 1971) and is confirmed by the analysis of P'dP' using LASA in Chapter 3.

Once the determination of the proper branch for a reading is made, calculations can be done to correct the times and distances to a surface focus and calculate the depth d of the P'dP' phases as in Whitcomb and Anderson (1970). Due to the systematic reading of all phases on the record, it is necessary to identify as many

as possible of the phases other than P'P' and P'dP' and eliminate them from analysis. SKKKP, a phase identification by Engdahl and Flinn (1969b), is prominent in the recordings of Event 6 (Figure 2.2), and its $dt/d\Delta$ of 4.4 sec/deg easily separates it from the P'P' and precursor readings. pP'P', the near-source surface reflection of P'P', is seen and eliminated in a number of cases, and these are, except for Event 2, significantly smaller than the main phase P'P'. In Event 2 (a sample record is shown in Figure 2.2), the phase pP'P' is large with respect to the P'P' phase, and this leads to an ambiguity in identifying a precursor as pP'dP' or P'dP'. If both occur as reflections from a given depth, then the time difference between the pP'P' and P'P' phases should be the same as between pP'dP' and this possibility arises in Event 2. The Event 2 precursors in Figure 2.2 designated with a depth of 534 and 503 km could be the pP'P' reflections from 656 and 618 km which are seen approximately 23 sec earlier, the proper P'P'-pP'P' time interval for 77 km focal depth. This ambiguity is discussed later. Another phase that can be misinterpreted as P'dP' is asymmetric P'P' which, as discussed in Chapter 4, casts doubt on the interpretation of precursors less than 30 sec before the main phase for single-station analysis. Analysis of data in the 0 to 30 sec range is avoided in this chapter.

2.3 Ninety-East Ridge and Atlantic-Indian Rise Reflectors.

The Atlantic-Indian rise is a classical ocean-floor-spreading structure and is the continuation of the Mid-Atlantic rise into the Indian Ocean where it connects with the Mid-Indian rise. Study of the Ninety-East ridge (Francis and Raitt, 1967, and Le Pichon and Heirtzler, 1968) indicates that it is not a source of ocean-floor spreading but that it is some type of compressional feature with a thickening of the crust under the ridge. Distribution of the P'P' reflection points extends about 3° north of the Atlantic-Indian rise and about 5° west of the Ninety-East ridge as seen in Figure 2.2

Figure 2.4 from Whitcomb and Anderson (1970) shows the original zones of reflection proposed for the P'dP' data compared to velocity structures derived from various assumptions of mantle composition and phase changes. The revised interpretation of these data with the use of new core-phase information as developed in later chapters is represented in the histograms of Figure 2.5. The histogram is constructed by summing the weights of the readings at 20 km intervals and can be compared directly with the histograms in Whitcomb and Anderson (Figure 6, p. 5722). No significant change is made in the depths of the zones or their strengths as represented by the size of the sums. However, the data for the Ninety-East ridge have a somewhat larger scatter; also, the 20 km difference in depth originally proposed for reflection zones below 500 km and shown

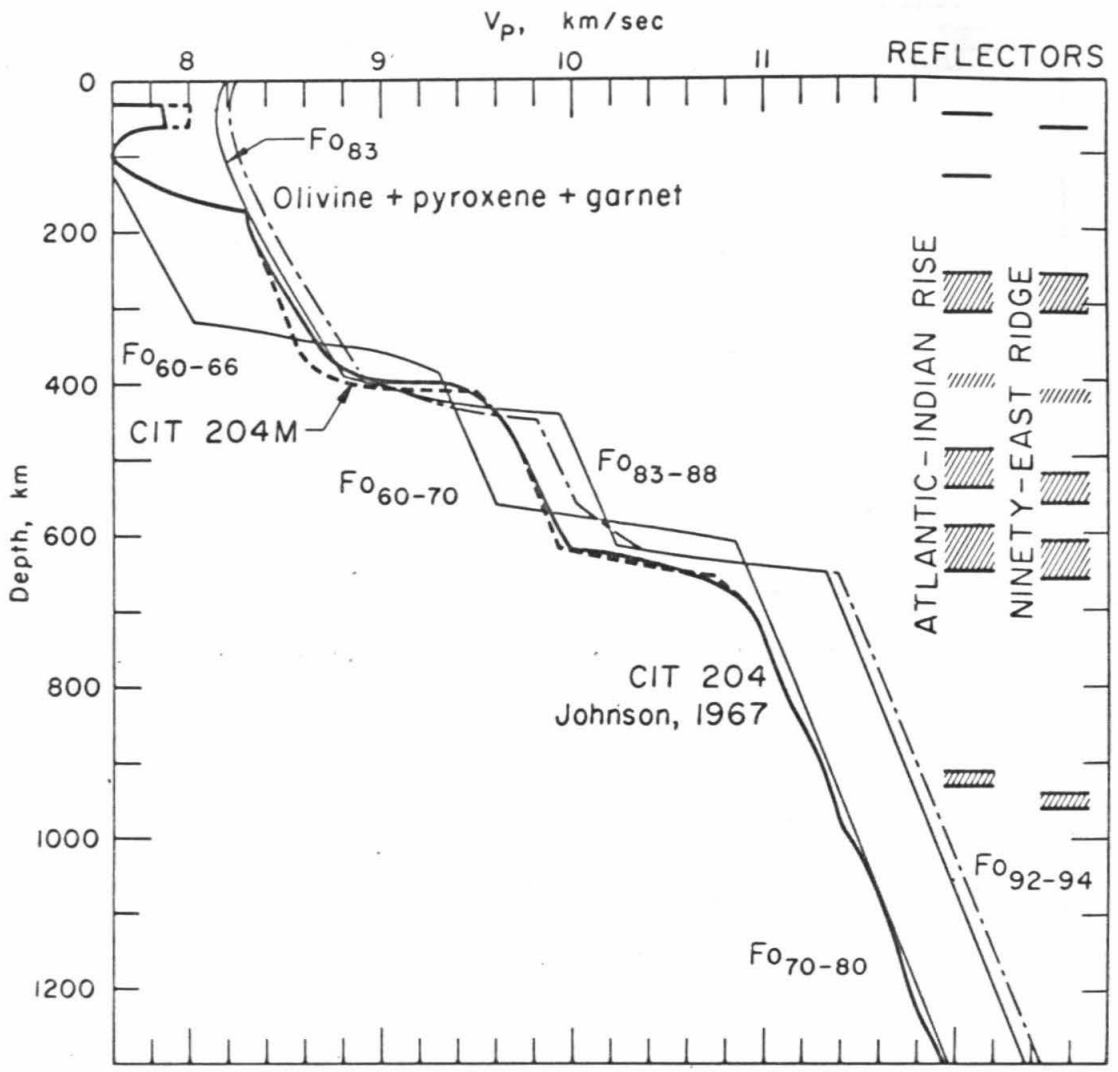

Figure 2.4

Comparison of reflecting zones with P-wave velocity models (CIT 204M and Johnson, 1967) and with calculated velocities of various mantle compositions (from Whitcomb and Anderson, 1970).

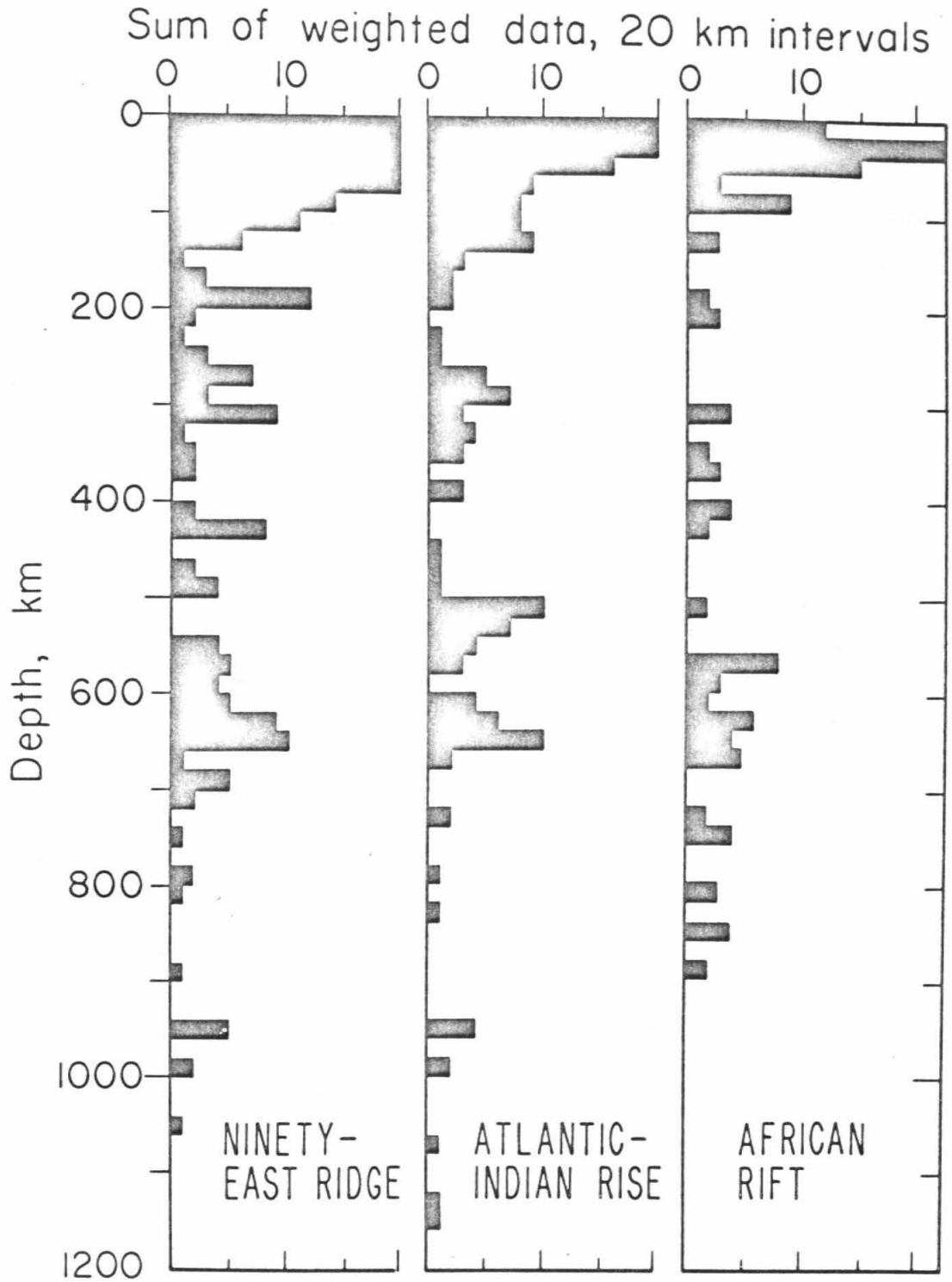

Figure 2.5

Histograms of the P'P' precursors interpreted as P'dP' as a function of depth for the Ninety-East ridge, Atlantic-Indian rise, and the African rift reflection areas. The summation interval is 20 km and the data are weighted by their confidence ratings as discussed in the text.

in Figure 2.4 is not as clear in the new data reduction of Figure 2.5. Figures 2.6 and 2.7 show the calculated depths of the precursor readings as a function of distance from the Atlantic-Indian rise and Ninety-East ridge (in Figure 2.2, perpendicular distance from lines A-A' and B-B', respectively). The Ninety-East ridge data extend over a greater distance and the reflectors appear to deepen to the west, especially in the depth ranges near 650 and 150 km. However, it is difficult to form any firm conclusions about the depth variation of these data in light of the possibility of asymmetric P'P' (Chapter 4). The possibility of depth differences is better evaluated in the following chapter where the use of array beam-forming methods resolves some of the uncertainties due to asymmetric phases.

The basic results from the Ninety-East ridge and Atlantic-Indian rise data are that arrivals strong enough to be read on single-station seismograms tend to group at specific depth zones when interpreted as P'dP'; the zones are near 950, 640, 520, and 820 km with marginal indications at 410 km as in Whitcomb and Anderson. The 630 zone is by far the strongest in terms of the number and strength of the phases. These zones have a one-to-one correspondence between the two areas which is significant when we consider that 1) the data are sampled from a narrow (Atlantic-Indian rise) and broad (Ninety-East ridge) range of epicentral distances, 2) the focal depths of the events vary widely, and 3) the P'P' phases for

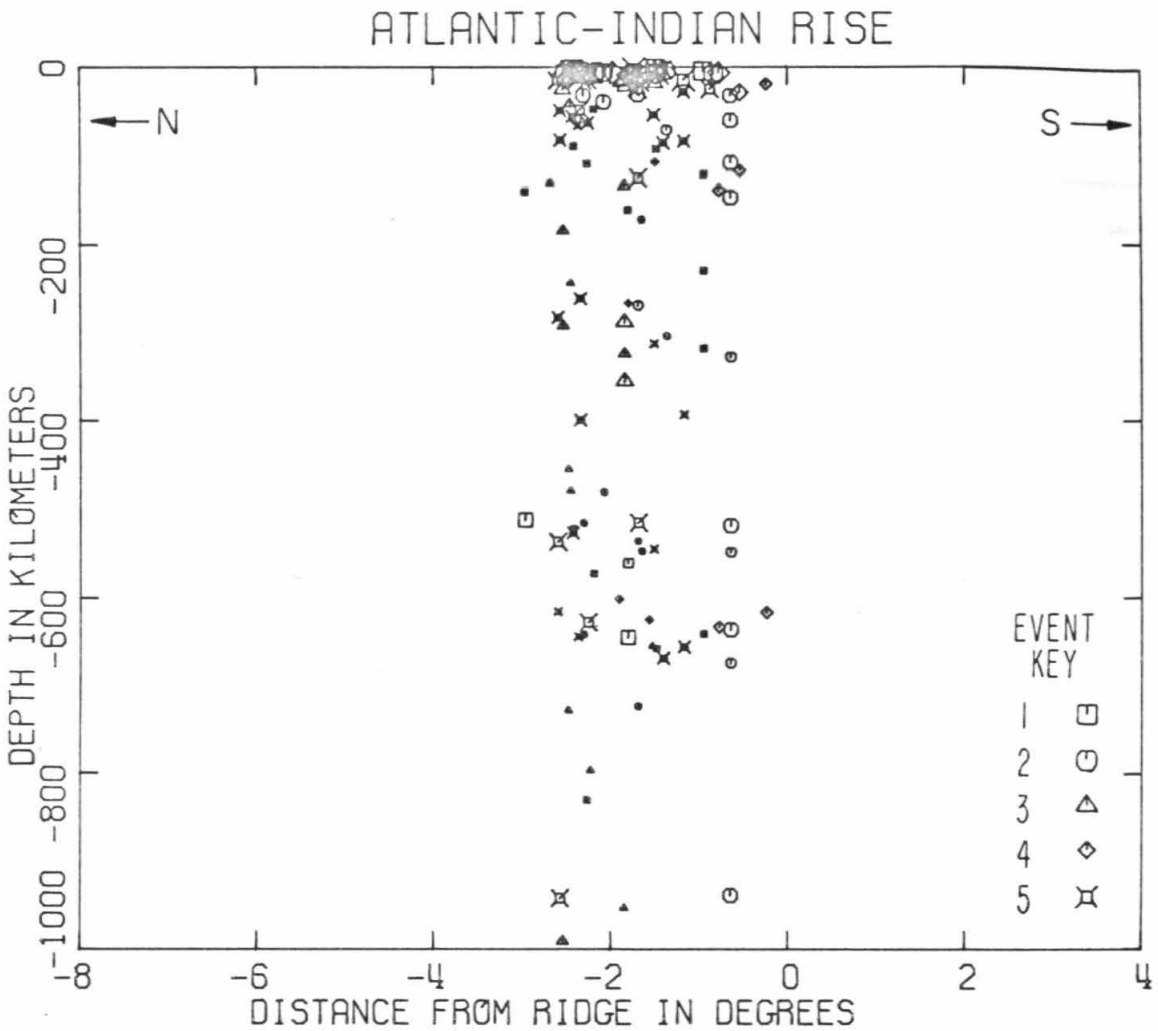

Figure 2.6

Atlantic-Indian rise P'dP' data plotted as a function of depth and distance from the rise (line A-A' in Figure 2.2). The size of the symbol indicates its confidence rating and the type of symbol indicates the event.

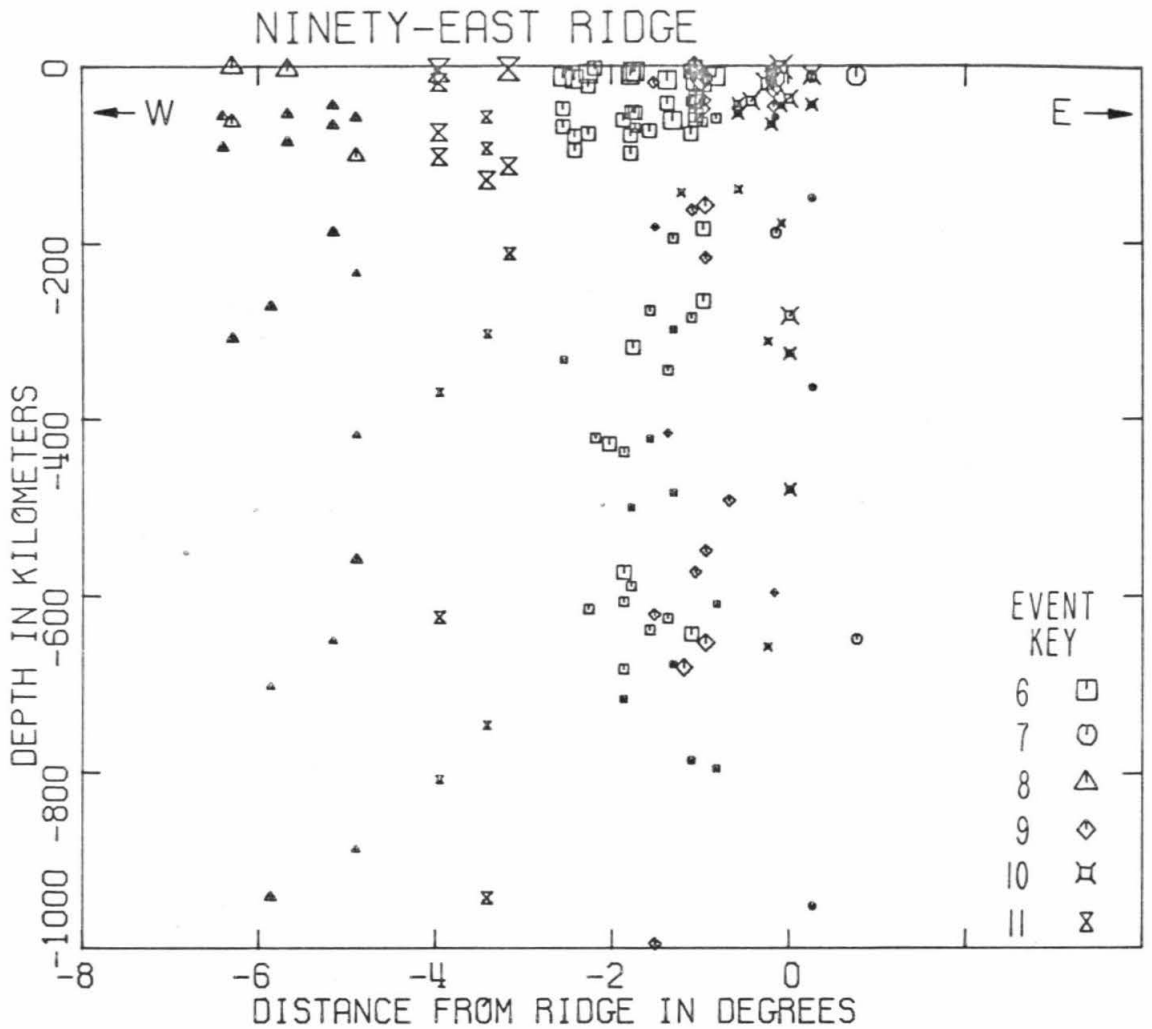

Figure 2.7

Ninety-East ridge P'dP' data plotted as a function of depth and distance from the ridge (line B-B' in Figure 2.2). The size of the symbol indicates its confidence rating and the type of symbol indicates the event.

each group reflect at widely separated locations on the earth. As mentioned previously, the interpretation of data corresponding to the 520 km zone is clouded by possibilities of their being reflections of secondary phases, such as pP'P', from the very large 640 km discontinuity. This problem has not been resolved as yet and may require another data type such as reflections from the top for a satisfactory answer. An outstanding exception to direct correspondence between the data of the two areas is the large histogram bar at about 190 km in the Ninety-East ridge data of Figure 2.5. It has no analogue in the Atlantic-Indian rise data and the difference may be significant in light of the results of Chapter 3.

2.4 Southeast Africa Reflectors. Figure 2.8 shows the South-east-Africa reflection area for P'P' from events at the northern trench. The epicenters of earthquakes in the African continent, shown for the time 1961-1969 (Anonymous, 1970), outline the African rift system, a broad and not too well defined seismic feature in the area of the reflections. Figure 2.5 shows the data interpreted as P'dP' in histogram form as a function of depth. The outstanding zone is again in the 630 km range as for the previous two areas shown in the same figure. There are some readings between 300 and 410 km that stand out principally because of the lack of data just above and below this range. Data deeper than 700 km are spread

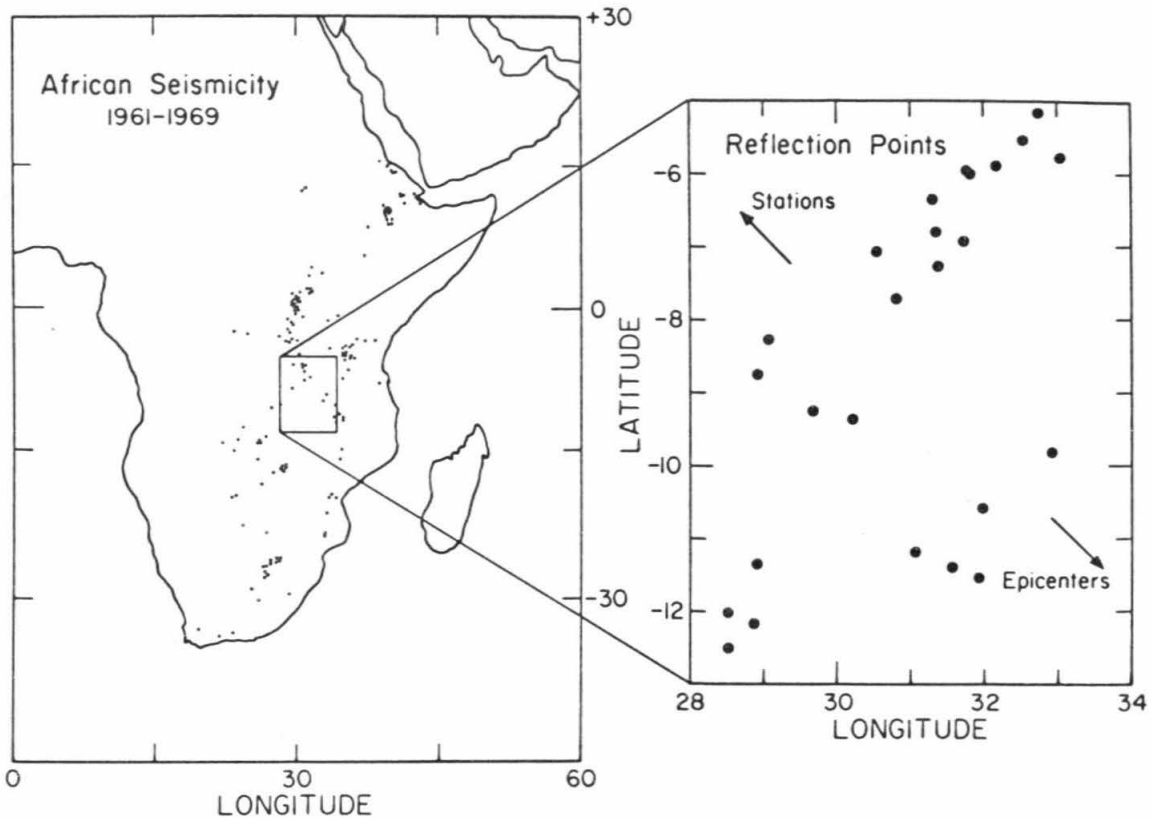

Figure 2.8

The regions of reflection of P'P' at the African rift zone in Southeast Africa for the single-station data.

between 720 and 900 km but no deeper points are seen similar to the 950 km zone of the previous data set. Readings also concentrate in the depths between 500 and 600 km but the same difficulties of interpretation are present as discussed previously. However, the depth distribution in this range is more like the Ninety-East ridge data than that of the Atlantic-Indian rise, an important consideration if the 520 km reflector can be shown to exist. Thus, the African rift data set, although it has fewer readings than the Atlantic-Indian rise or the Ninety-East ridge data sets, is more like the latter in its depth distribution.

3. P'dP' OBSERVED AT THE LASA ARRAY: REFLECTOR CONTINUITY AND SHARPNESS

3.1 Introduction. The previous studies of P'dP' (Adams, 1968; Whitcomb and Anderson, 1968; Engdahl and Flinn, 1969a; and Whitcomb and Anderson, 1970; and others) point out the need for direct and accurate $dt/d\Delta$ measurement of the phases with a large-aperture array such as LASA in Montana. Use of a large array enables one to greatly improve the signal-to-noise ratio of coherent arrivals by beam-forming and also to identify the proper branch of the arrival; the latter is an important consideration when calculating the depth d of P'dP'. Further, the observation of coherency across the array, which has an aperture of about 200 km, is some measure of continuity of the reflecting zones and this property is useful both here and in Chapter 6.

This chapter investigates the $dt/d\Delta$ of P'dP' phases from ten events recorded at LASA that pertain to the mantle under a wide range of surface-structure types. Four reflect under deep-oceanic structure near the Ninety-East ridge in the East Indian ocean; four reflect under oceanic structure that is near classic crustal-spreading rises; and two reflect under the Antarctic continent. The results confirm that the dominant P'dP' energy is from one branch which is the largest-amplitude P'dP' branch as assumed in Adams (1968),

Whitcomb and Anderson (1968 and 1970), and Chapter 2. The lateral continuity and strengths of the reflectors are estimated along with some approximate limits on their structures.

3.2 P'dP' Recorded at LASA. Figure 3.1 shows the P'dP' reflection areas with event numbers (parameters are given in Table 2.1) and symbols used in succeeding plots in this chapter. Events 5, 12, and 22 are 800 km south of the Atlantic-Indian rise (indicated by earthquake seismicity from Barazangi and Dorman, 1969) and Event 18 is in a corresponding position just 300 km south of the East Indian rise. Events 8, 9, 10, and 11 are all to the east of the Ninety-East ridge in the East Indian ocean which is an area of deep-oceanic structure. Events 15 and 16, which are from Novaya Zemlya explosions, reflect under the Antarctic continent.

The processing of the P'dP' phases at LASA is schematically illustrated in Figure 3.2. The P'dP' phase arrives at the array from a direction opposite from that of the event epicenter. The time series from the seismometers are filtered and summed for the direction of arrival at different slownesses or $dt/d\Delta$'s (the inverse of apparent velocity) to form beams. Each beam corresponds to a given value of $dt/d\Delta$. The power of each beam is then averaged over discrete time intervals (a one-second interval is used here) and the contours of equal power are constructed from several beams

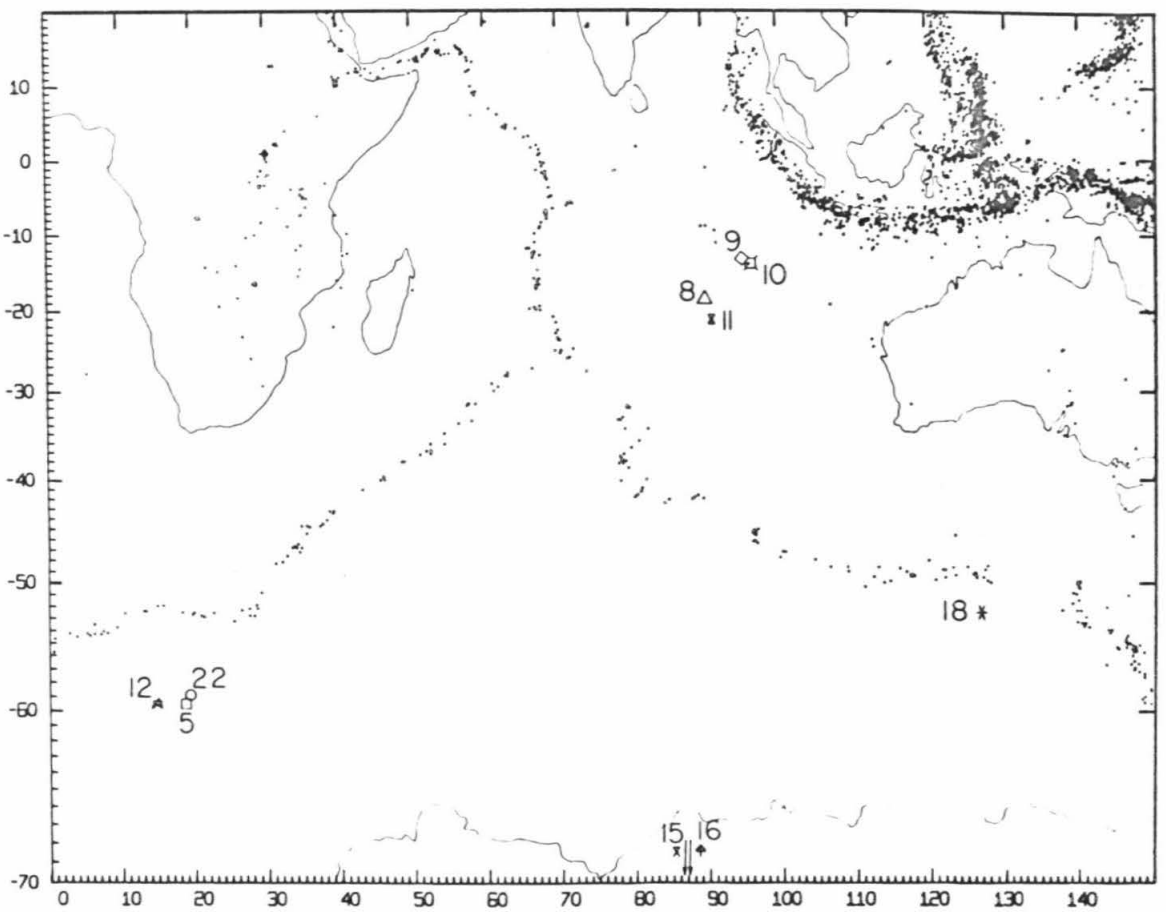

Figure 3.1

P'dP' reflection areas studied with the LASA array. Event numbers correspond to the event data in Table 2.1 and the associated symbols are used in succeeding plots in this chapter.

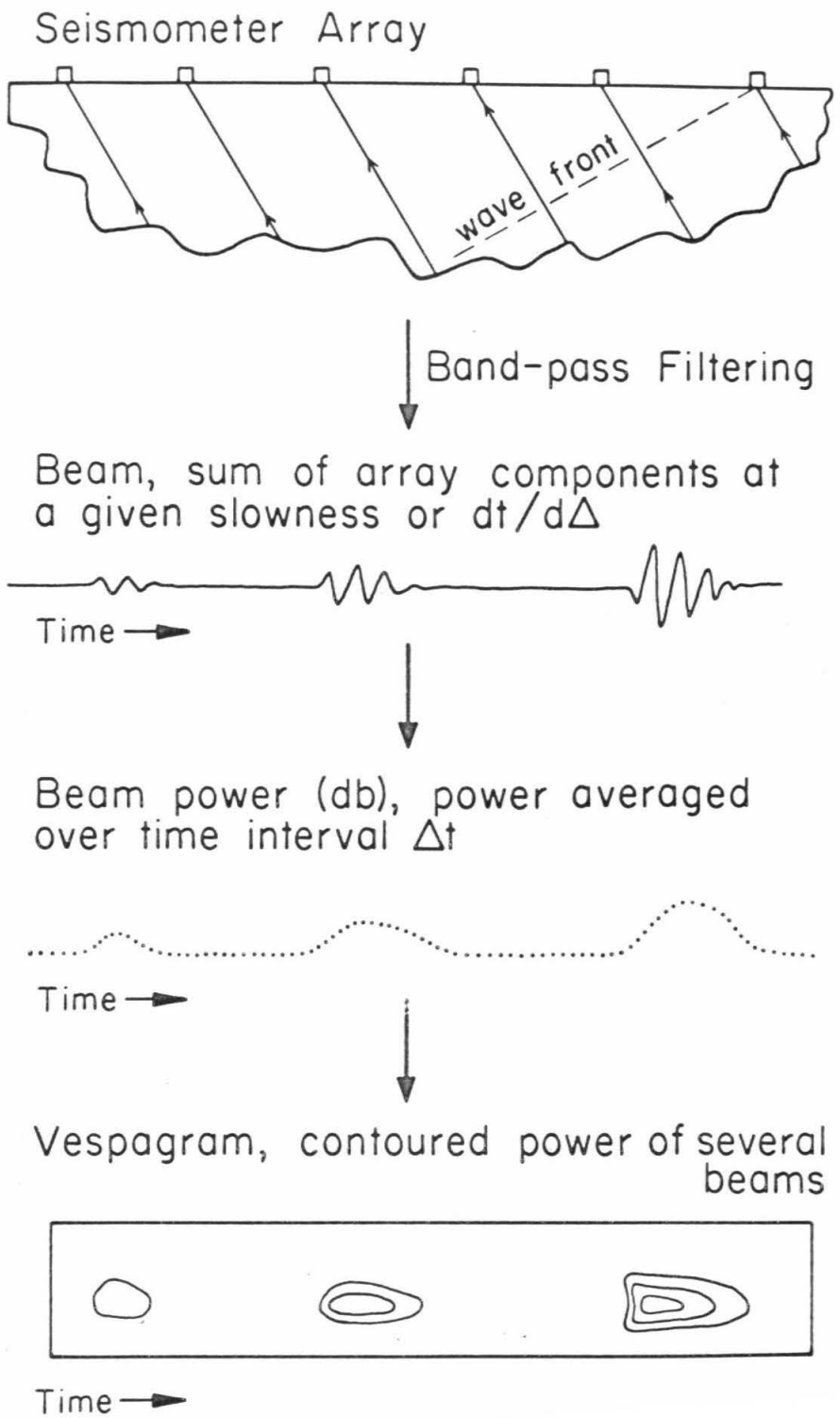

Figure 3.2

A schematic representation of the array processing involved in construction of a vespagram.

placed side by side. The result is a contour plot of coherent seismic-phase power as a function of $dt/d\Delta$ and time for a given azimuth of arrival; the procedure is termed a "vespa" process (velocity spectrum analysis) and the diagrams are called "vespagrams". Descriptions of the process and interpretations of vespagrams are in Kelly et al. (1968) and Davies et al. (1971). The problems of complex travel-time anomalies at the LASA sub-arrays have essentially been circumvented for beam-forming at the periods used here (about 1 to 3 sec) by extensive calibration of the relative sub-array travel-time anomalies such as the work of Engdahl and Felix (1971). Further, the results of Chapter 6 indicate that, except for arrivals from the south, calibration of LASA is quite adequate for core phases.

Figure 3.3 shows two examples of vespagrams for Events 8 and 5. Time increases to the right and $dt/d\Delta$ increases upwards. The power contours are at 2 db intervals with shading changes every 8 db or 4 contours. The heavy contour is a subjective judgment of the first contour above the noise level which is based on the early, quiet portion of the record; thus, power at or above the heavy contour level is considered to be signal of some type. The predicted times of the main P'P' phases are shown to the right above the vespagrams and the maximum power approximately corresponds to these times as expected. Event 8 is at an epicentral distance of 61.7° which predicts that the first branch should be DF at about 1.7 sec/deg, then the largest

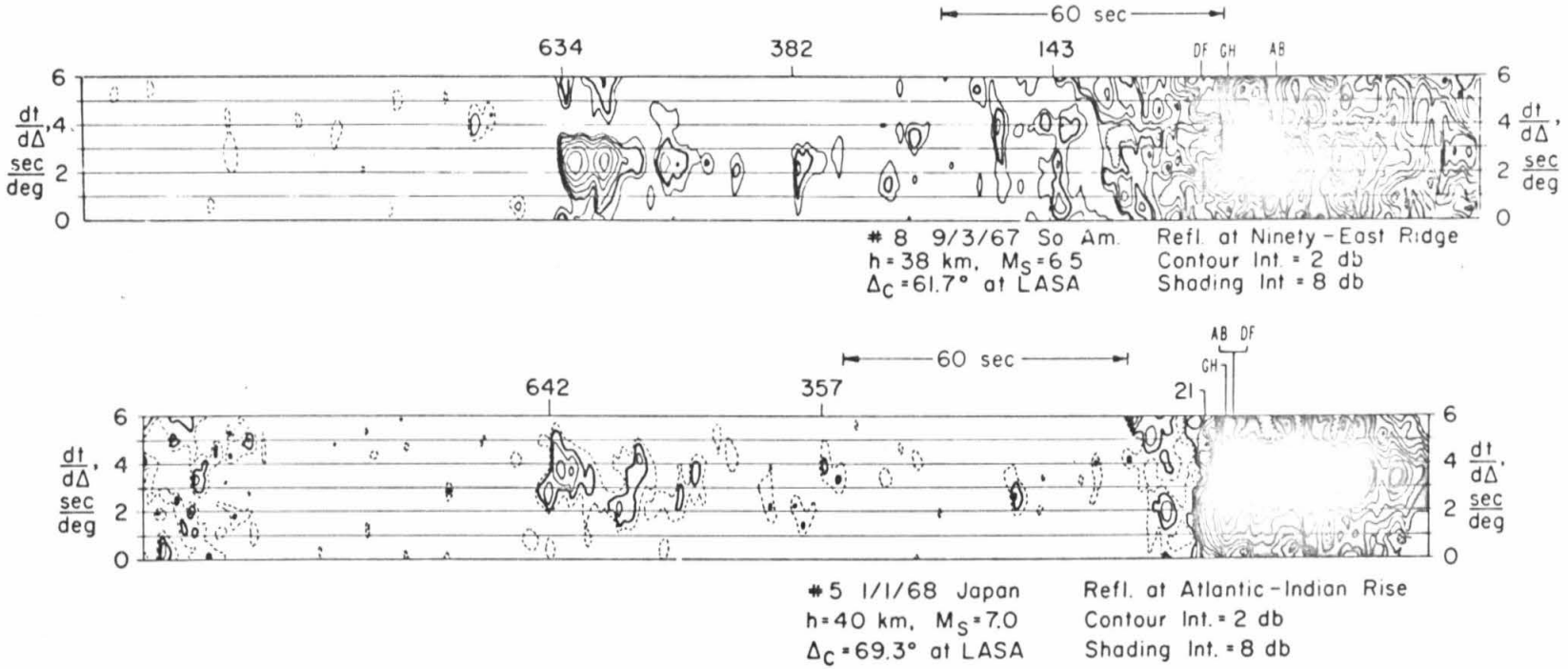

Figure 3.3

Vespagrams for Events 8 and 5. Theoretical main branch times and depths d of the P'dP' readings are shown.

branch BC at 2.7 sec/deg, and finally AB at 4.1 sec/deg as seen for the main phases in the travel time chart in Figure 3.4. These are all seen in the vespagram at their proper dt/dΔ's. Event 5 is at 69.3 where all three branches arrive within a few seconds of each other. Here the the dominant amplitude is that of the AB branch with its dt/dΔ near 3.5 sec/deg.

The outstanding phase at times earlier than the main P'P' phases stands out clearly for both events in Figure 3.3 about 2.5 min before the main phase. This is the P'640P' phase as interpreted by Whitcomb and Anderson (1968), Engdahl and Flinn (1969), Whitcomb and Anderson (1970), and others. It clearly has the most power of all the P'dP' phases studied thus far. The branch of the P'640P' phase is completely predictable on the basis of the maximum-amplitude ranges defined in Chapter 6. In Event 8, for example, only the BC branch of P'640P' is seen even though both the AB and DF branches are seen in the main P'P' phase. This is, of course, not precisely the case at distances where the maximum-amplitude change takes place from one branch to another but it is a good approximation between almost the entire range of 55° to 85° used in the interpretation of single-station data in Chapter 2. The dt/dΔ and, thus, bottoming depth in the core of a P'dP' phase is not the same as that of the main P'P' phase at a given station. However, for most cases they are nearly the same so that the branch with the maximum main phase amplitude is the branch with the maximum P'dP' amplitude with nearly the same dt/dΔ. Thus,

to pick the P'dP' phases usually means simply to follow the dt/dΔ of the maximum-amplitude main phase backwards in time until significant power peaks are seen.

Picks of the onset of peaks read in the above manner are shown in the travel-time plot of Figure 3.4. The symbols represent events used and are keyed in Figure 3.1 and Table 2.1. The symbol size represents the confidence of the reading as in Chapter 2, and the slopes through the data points indicate the measured dt/dΔ. The readings of P'dP' at a given station are all uniformly from a single branch with the exception of two readings near 76° that have dt/dΔ's more like that of the AB branch than that of the DF branch used for calculations in this range. This duality is a result of being on the border where the largest-amplitude branch is switched as discussed above. These two points were not used for depth calculations. The time range approximately 30 sec before the P'640P' phase is avoided in the readings due to the problems of identification mentioned in Chapter 2. Significant arrivals are noted here but their interpretation is difficult at present.

The depths of the P'dP' phases are calculated as in Chapter 2 and are shown in Figure 3.5 for the ten events. The P'640P' zone is the most consistent in terms of depth of onset and strength. Only two readings are deeper than this level. A reading near P'640P' was not picked for Event 10 (crossed-square symbol) but a second more objective

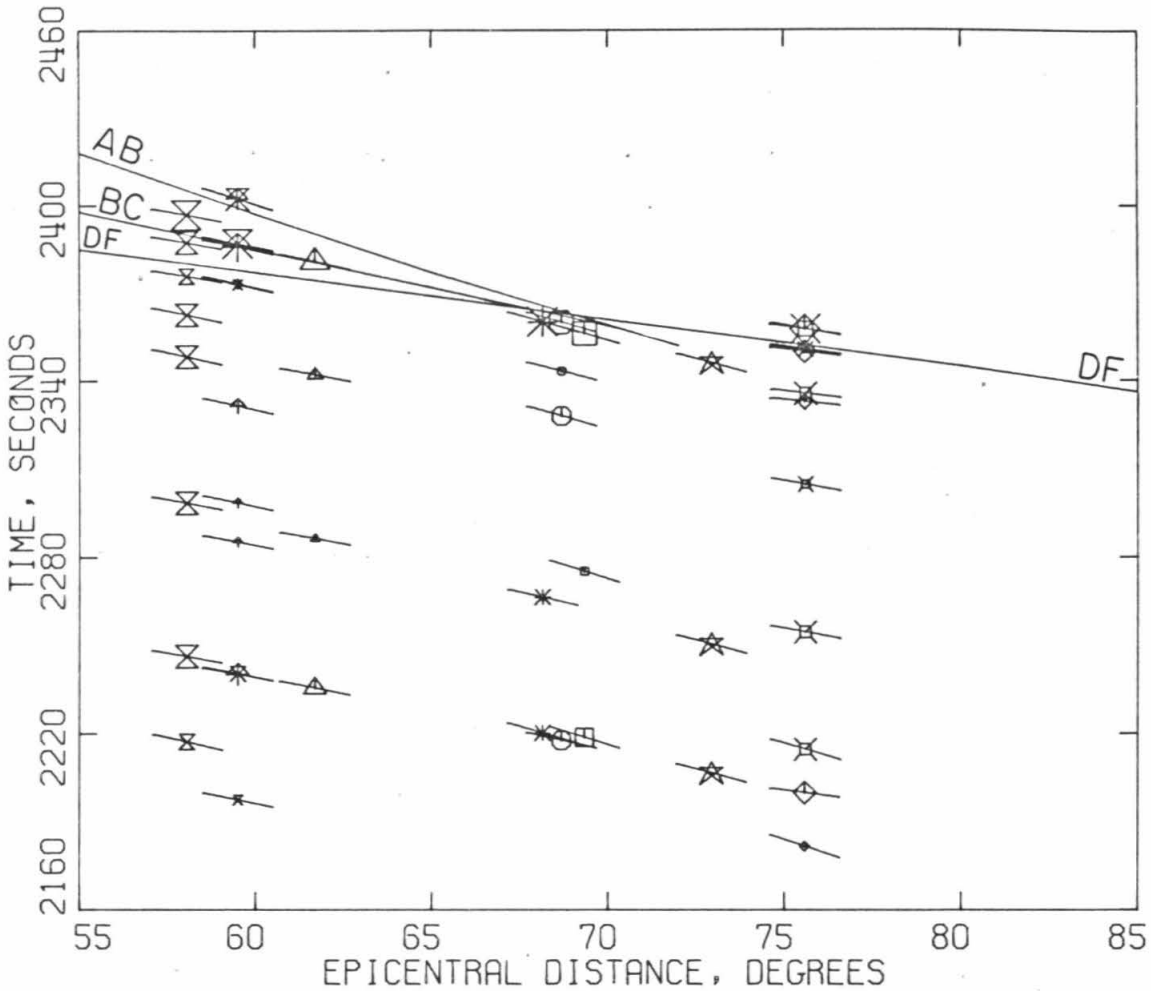

Figure 3.4

Travel-time plot of vespagram P'dP' readings with sloping lines to indicate measured $dt/d\Delta$. The size of the symbol indicates its assigned confidence rating. The theoretical main P'P' times are shown for reference.

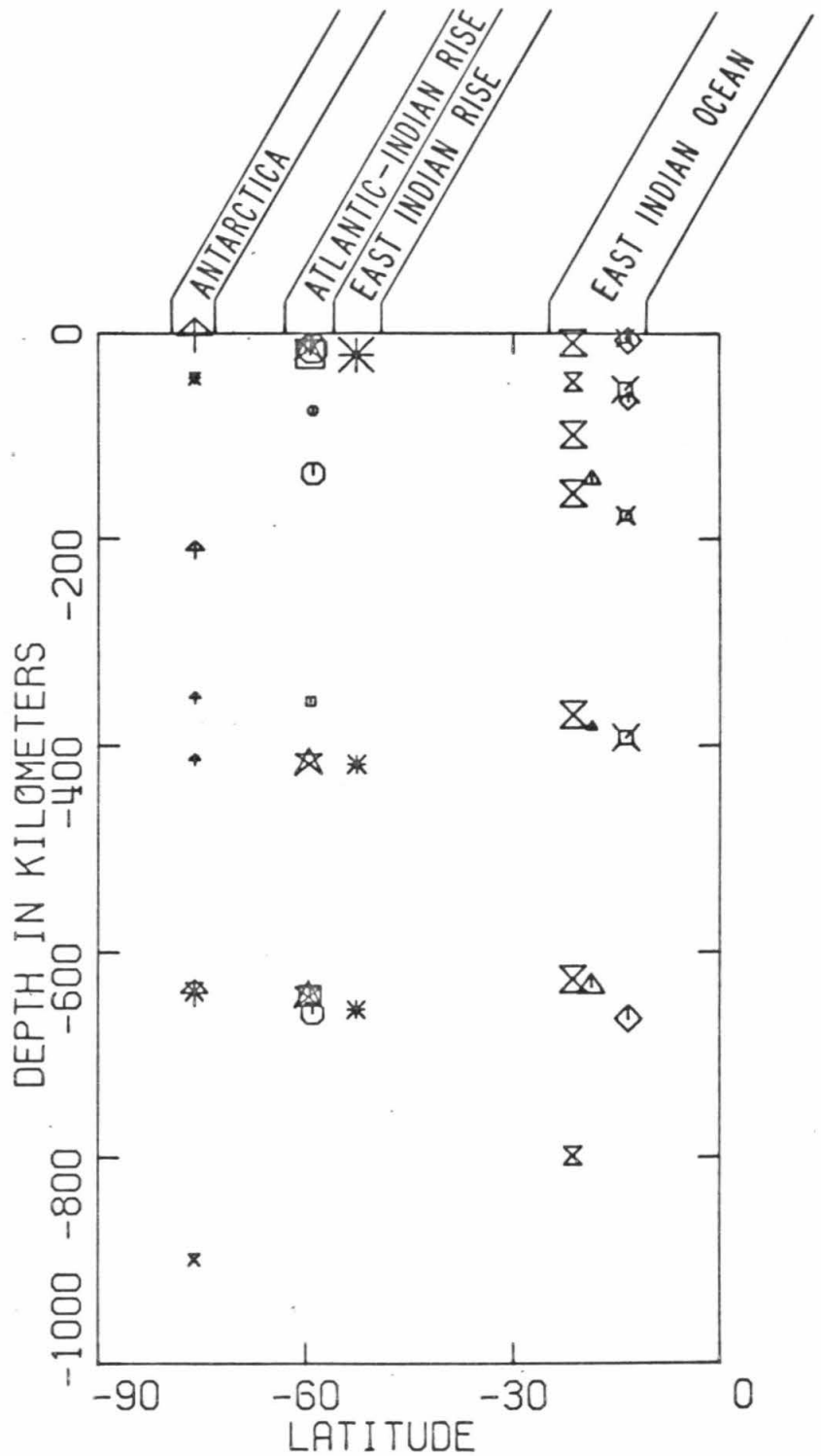

Figure 3.5

Calculated depths of the LASA-vespagram P'dP' readings from Figure 3.4 as a function of latitude (see the map of Figure 3.1).

method of phase identification outlined later does pick a phase in this zone. The onset of the P'640P' reflection is at 640 km for the two events reflecting under Antarctica, between 640 and 660 km for the four reflections near oceanic rises, and between 630 and 670 km for the four reflections under the East Indian ocean. All readings are omitted between the 640 km zone and about 500 km due to the problems of interpretation as discussed above. The next shallower level of readings is a zone between 360 and 410 km; under Antarctica and the rises, the readings are at the extreme depth ranges of this zone, and under the East Indian ocean they are in the middle of the range. Above 360 km, no readings are seen until about 200 km under Antarctica, 140 km near the Atlantic-Indian rise, and 140 to 180 km under the East Indian ocean.

Because of the subjective manner in which the significance of the power peaks is determined, a second method of picking phases is used. It was noted that all of the obviously significant arrivals have very sharp onsets, that is, the time derivative or onset slope of the proper power beam (see Figure 3.2) is large. Therefore, a criterion was developed whereby all onsets with a power slope or time derivative that exceeds a certain value are picked; the critical value was determined by the characteristics of the noise. Figure 3.6 shows the data points picked with this method plotted as a function of depth in the same manner as in Figure 3.5. The length

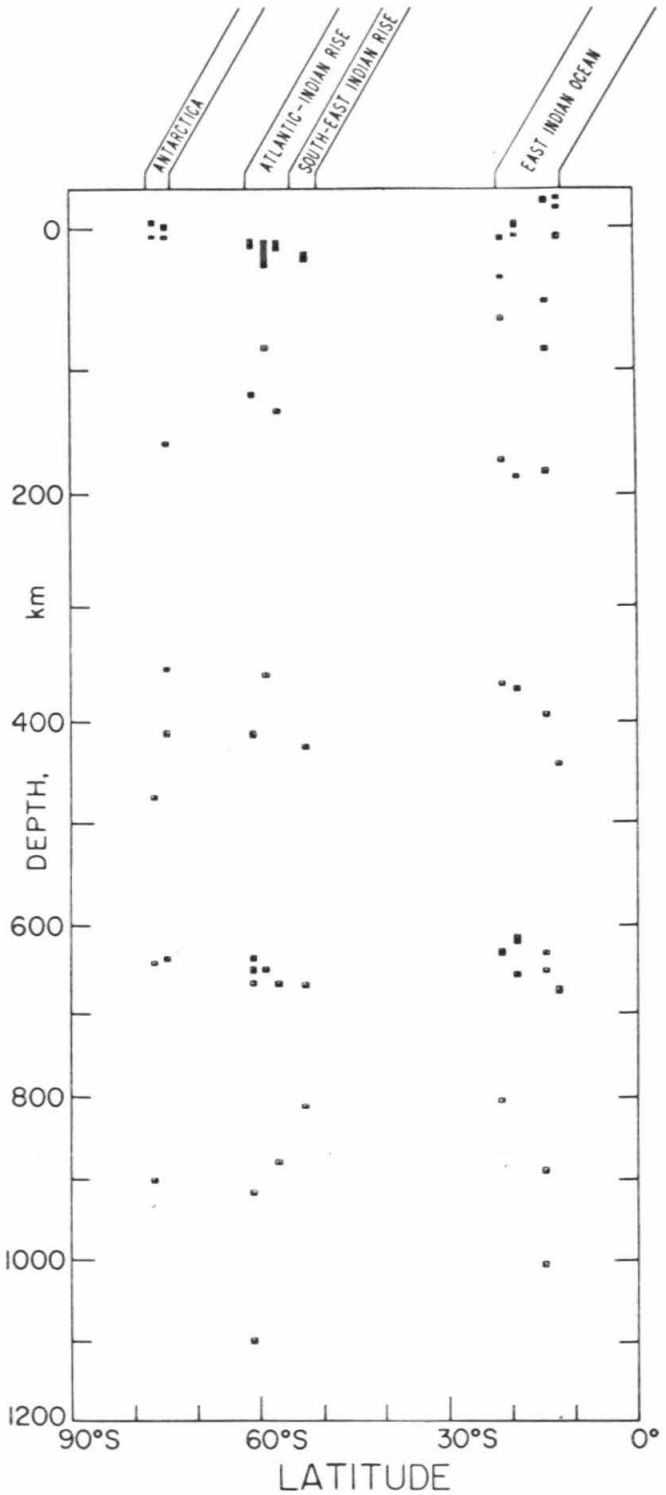

Figure 3.6

Calculated depths of the LASA-vespagram P'dP' phases read by the power-slope method described in the text. The event numbers are, from left to right; 15, 16, 12, 5, 22, 18, 11, 8, 10, and 9.

of the points is a measure of the time that the slope exceeds the critical value. Use of this method does not significantly alter the data for the 640 zone but adds a reading for Event 10 that was not picked with the previous method. The onset of the P'640P' reflection is at about 640 km for the two reflections under Antarctica, between 640 and 670 km for the four reflections near rises, and between 635 and 675 km for the four reflections under the East Indian ocean. The previous readings between the 360 and 410 km range are essentially unchanged but two new points are added for Events 15 and 9 near 470 and 450 km, respectively. Above 360 km, the depths of the readings are changed somewhat to about 160 km under Antarctica, 130 km near the Atlantic-Indian rise, and 180 km under the East Indian ocean; the rise points are still shallower than the other two areas. One significant difference in Figure 3.6 from the previous method of reading of Figure 3.5 is that more points are picked below the 640 km zone. All but two are approximately between 800 and 900 km deep.

3.3 Sharpness of the 640 km Discontinuity. The work of Richards (1971) and others have shown that a reflection amplitude more than about 3% requires a material property change that takes place over a distance that is less than one-half of a wavelength. Thus, the mere observation of a reflection with amplitudes larger

than 3% of the incident wave from a velocity discontinuity implies that the discontinuity is limited in thickness to less than one-half wavelength. Figure 3.7 shows an example of a P'601P' phase from the BC branch and the corresponding main phase. Both phases have a period very close to one second and the amplitude of the precursor is about 10% of the main phase, which is similar to the ratios reported by Engdahl and Flinn (1969), Whitcomb and Anderson (1970), and others. Although, amplitude comparisons with the main phase are difficult to interpret due to the generally unknown complexities of near-surface structure and asymmetric P'P' as discussed in Chapters 4 and 5, it is clear that the reflection from the P'640P' zone is larger than 3% of the incident wave. Thus, this single example implies that a velocity-density discontinuity of the order of 8% is required over a depth interval less than 5 km (for calculations, see Whitcomb and Anderson, 1970). A smaller jump in material properties would be required if the discontinuity were a series of alternating layers that caused constructive interference of the reflecting wave. However, this type of reflector would be strongly frequency dependent. Figure 3.8 shows power spectra of a LASA beam of the BC branch of P'P' and P'630P' from Event 8. The phases have a dominant period of about 2 sec and no significant difference is seen between the two between periods of 1 to 2 sec (1 to 0.5 hz). This result effectively rules out the constructive

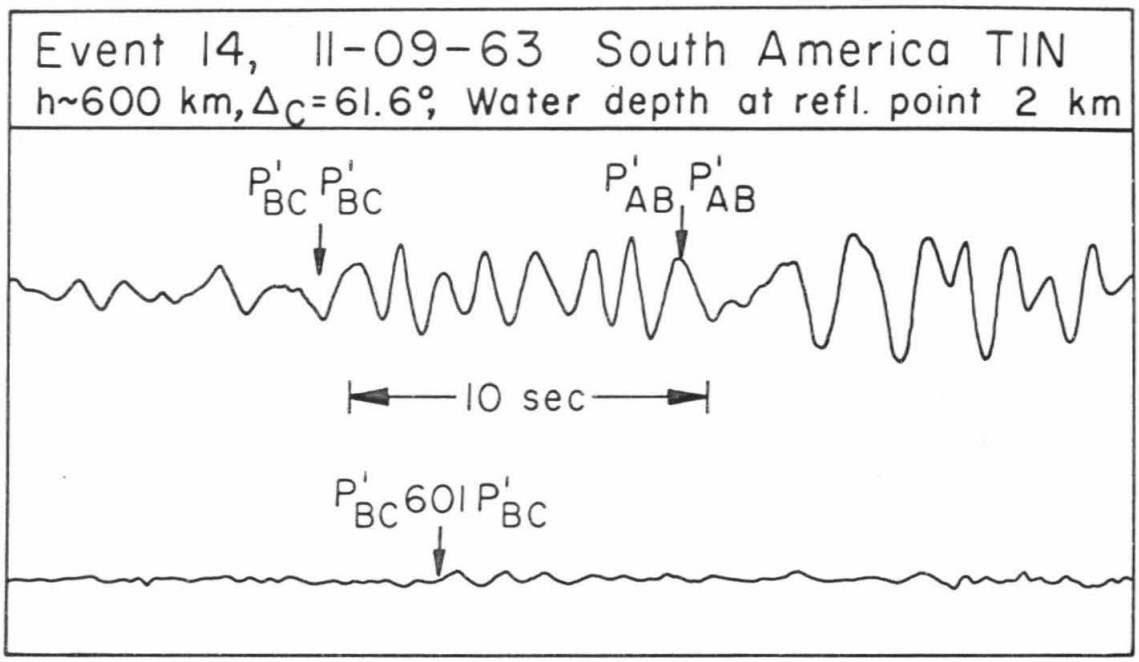

Figure 3.7

Comparison of the main P'P' phase with P'601P' at a single station. Both have nearly identical periods (about 1 sec) and the P'601P' amplitude is about 10% of that of the main phase.

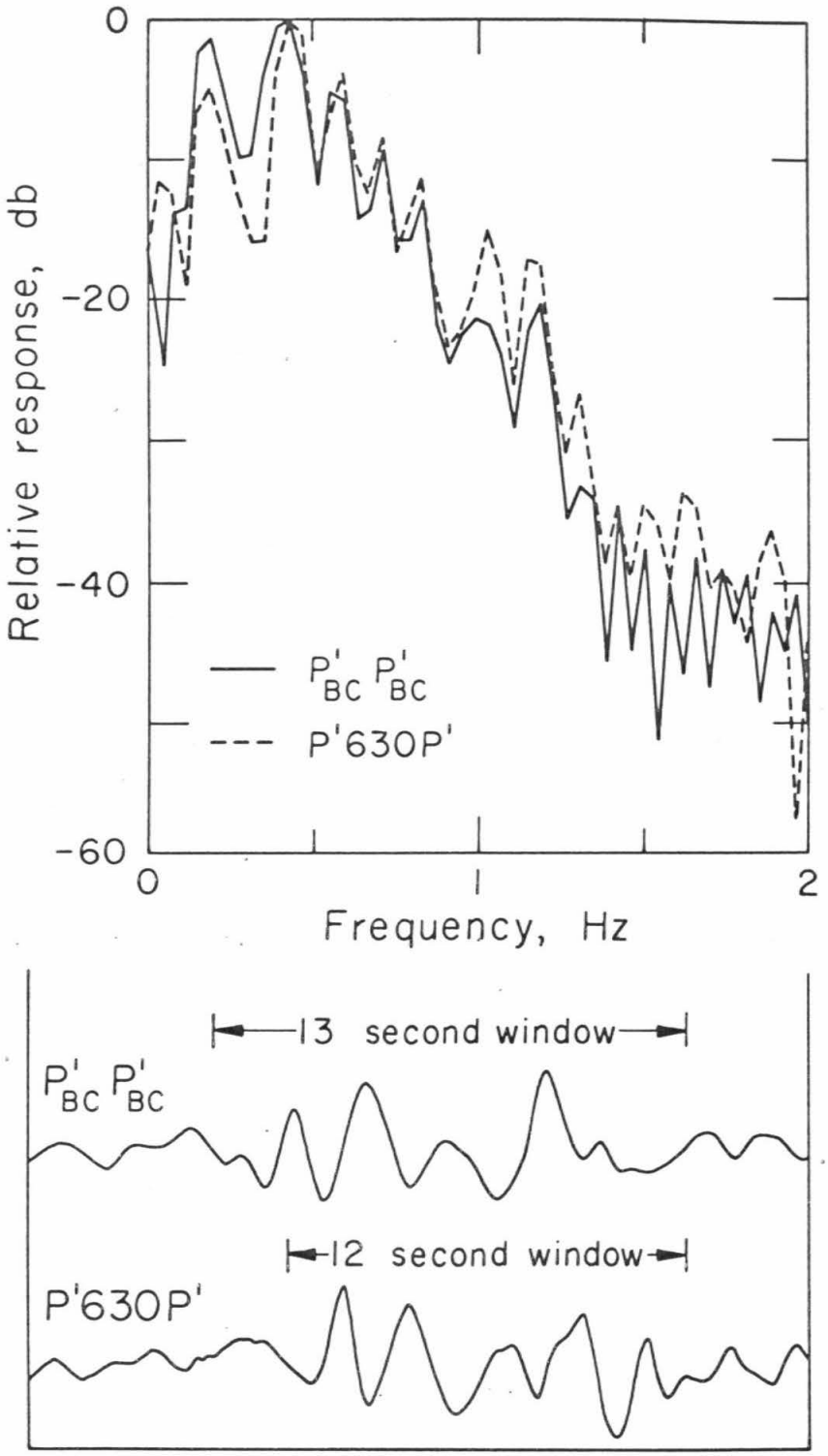

Figure 3.8

Comparison of the power spectrum of the main P'P' phase with that of P'630P' at LASA for Event 8. The dominant energy is at 2 sec (0.5 hz) and there is essentially no difference in relative spectral content between periods of 1 and 2 sec.

interference hypothesis because no difference is seen in reflectivity for a continuous range of wavelengths from 10 to 20 km.

3.4 Conclusions. Possible mantle discontinuities that reflect short-period seismic energy and produce P'dP' phases are reviewed in the order that they appear on the seismogram; that is, from the deepest to the shallowest zones.

800 to 950 km. Only scattered readings are present below 700 km and these tend to concentrate in the 800 to 950 km range. Single station data favor 950 km and the vespagram data interpreted by the power-slope method described above range between 800 and 900 km.

630 to 670 km. This is by far the strongest P'dP' phase at both single stations and in array beams and the reflection is present at every site studied thus far including normal deep oceans, oceanic and continental spreading centers, and continents. Evidence from comparison of the spectral contents of the reflection and the main P'P' phase from the same branch leads to the conclusion that the discontinuity must be a monotonic change in material properties of the order of 8% that occur over a depth range of 5 km or less. The maximum depth range of the onset (bottom edge) of the reflector is about 630 to 670 km as measured by the vespa process; this method is least susceptible to problems of asymmetric P'P' as discussed in Chapter 4. This 40 km depth range corresponds to a time range of 8 sec on the seismogram.

Reflections under the Antarctic appear to be 20 km shallower than those under the oceanic rise areas. The maximum scatter of depths is seen in the East Indian ocean region from vespagram data and this is supported by the scatter of data for the same region from single station data in Chapter 2 (Figures 2.5 and 2.7). Although the depth differences appear to be consistent at the different areas, it is probably premature to rule out the likelihood that the discontinuity is at the same depth everywhere and the ± 20 km (± 4 sec) variation is due to a combination of reading errors, lower-mantle velocity variations, and source complexity. The contribution due to reading errors should be no more than ± 1 sec and that due to different lower mantle velocities should be also no more than ± 1 sec.

500 to 600 km. A strong grouping of arrivals equivalent to P'dP' for this depth range is present in both the single station data for the Atlantic-Indian rise at 520 km in Chapter 2 (Figures 2.5 and 2.6). However, it is difficult to interpret these data as P'dP' because it is possible that the arrivals represent delayed near-source-related phases that are reflections from the strong 640 km discontinuity. The problem is not resolved here and its solution must be reserved for later investigations.

350 to 415 km. Data for this zone are more consistent in the vespagram analysis of this chapter than from the single station readings in Chapter 2. This may be evidence that the reflecting

discontinuities in this range are very close to horizontal but their reflection coefficients are small. Thus, their P'dP' phases across a large array such as LASA are very coherent which allows the beam-forming process to fully utilize its signal-to-noise improvement capabilities and bring out arrivals that are too weak to be regularly observed in the noise level of a single station.

280 to 300 km. Evidence for a discontinuity at this level comes solely from the single-station data of Chapter 2; a fact that somewhat weakens confidence in its existence. However, its absence in the vespagram readings may indicate that, although it is strong enough to give reflections, the discontinuity is not horizontal and varies in depth so that its P'dP' reflections are not coherent across a large array. Indeed, evidence for precisely this effect is seen in the vespagram for Event 8 in Figure 3.3. For times later than the indicated 382 km reading, energy peaks appear to diverge from the proper $dt/d\Delta$ for P'dP' (about 2.5 sec/deg) towards both higher and lower values of $dt/d\Delta$. This energy may represent asymmetric P'dP' phases reflecting from non-horizontal discontinuities and suggests that spherical symmetry is absent above a depth of about 350 km.

100 to 200 km. Further evidence for lack of spherical symmetry in the mantle above 350 km comes from depth variations of reflections in the range of 100 to 200 km, especially from the vespagram data which have no readings from 350 km until this level. East Indian Ocean and Atlantic-Indian rise data indicate strong reflections

at 190 km and 130 km, respectively, in both the single-station readings (Figure 2.5) and the vespagram readings (Figures 3.5 and 3.6). The Antarctic continent data show a reflection from 160 to 200 km depending on the method of reading the vespagrams. If these reflections are from the same discontinuity, a conclusion that has some support from the observation that they are the first vespagram readings above 350 km, then a strong candidate for the cause of the discontinuity is the bottom of the low-velocity zone. Anderson and Sammis (1970) have shown that partial melting is the most likely cause of the low-velocity zone and this puts some limitations on conditions between 100 and 200 km for the different areas by the nature of the discontinuity depth variation. The depth of the lower boundary of partial melting is strongly dependent on both rock temperature and content of volatiles such as water; both an increase of temperature or an increase of volatile content will increase the depth of the lower partial-melt boundary. The boundary appears shallowest near oceanic rise areas which, if the temperature hypothesis were adopted, would imply that temperatures near 150 km are colder beneath rises than elsewhere. A model that produces this situation is unlikely, especially in the framework of plate tectonics concepts. Thus, the most attractive hypothesis is that volatiles are depleted in the upper-most mantle near the Atlantic-Indian rise relative to that under continental or older oceanic crustal areas. An alternative explanation for a

discontinuity depth that is shallower near oceanic spreading centers is a solid-solid phase change. If the phase-change depth dependence is entirely due to temperature differences and temperatures under the rise are higher, then a negative-phase-equilibrium slope is required.

4. ASYMMETRIC P'P'

4.1 Introduction. Precursors up to 30 seconds before P'P' (PKPPKP) were first noted by Gutenberg (1960) and were interpreted as sub-surface reflections. Later authors including Adams (1968), Engdahl and Flinn (1969a), Whitcomb and Anderson (1970), Whitcomb (1971), Adams (1971), and Richards (1972) have made studies of these and earlier precursors based on the same interpretation that they are reflections within the upper mantle, i.e., P'dP' (as defined by Whitcomb and Anderson, 1970) where d is the depth of reflection.

This new data type is important because it can give details of upper mantle structure heretofore unavailable, and provides one of the few means at hand for comparison of mantle structure under different lithospheric regions such as continents and oceans. However, as with any newly discovered seismic phase, the uniqueness of its interpretation must be well established. A violation of this uniqueness was pointed out by Engdahl and Flinn (1969b), who showed that the phase SKKKP for deep earthquakes occurs in the same part of the travel-time curve and could be mistaken for P'dP'. This problem is eliminated by avoiding readings at the time of SKKKP at a single station, or by using the difference in $dt/d\Delta$ between SKKKP and P'dP' at an array of stations.

A much more difficult problem is posed by the maximum-time nature

of P'P' phases discussed by Jeffreys and Lapwood (1957) and later by Richards (1972) and Wright (1972). Asymmetric P'P' phases reflecting from dipping interfaces at or near the earth's surface would arrive earlier than the main phase for all branches except for a special path of the AB branch. This chapter deals with the estimation of asymmetric P'P' amplitudes and, therefore, the likelihood that these phases be misinterpreted as P'dP'.

4.2 Asymmetric Reflections of P'P'. P'P' is a true maximum-time phase with the exception of the receding AB branch. Specifically, if P'P' reflects from any non-horizontal surface of the earth at a non-symmetrical point, it will arrive earlier than its symmetrical counterpart. This is not true for the receding AB branch reflecting on the station-epicenter great circle; the AB branch is thus a "mini-max" phase (in the reverse sense of the phase PP for which symmetric reflections on the great circle arrive earlier). It will be seen, however, that asymmetric reflections off the great circle are most important and for our purposes the AB branch is effectively a maximum-time phase.

For convenience of calculation, asymmetric P'P' reflections are divided into two types as shown in Figure 4.1: those in the great circle plane and those out of the great circle plane reflecting at points on a line that is perpendicular to the great circle and passes through the symmetrical reflection point. Of course, any

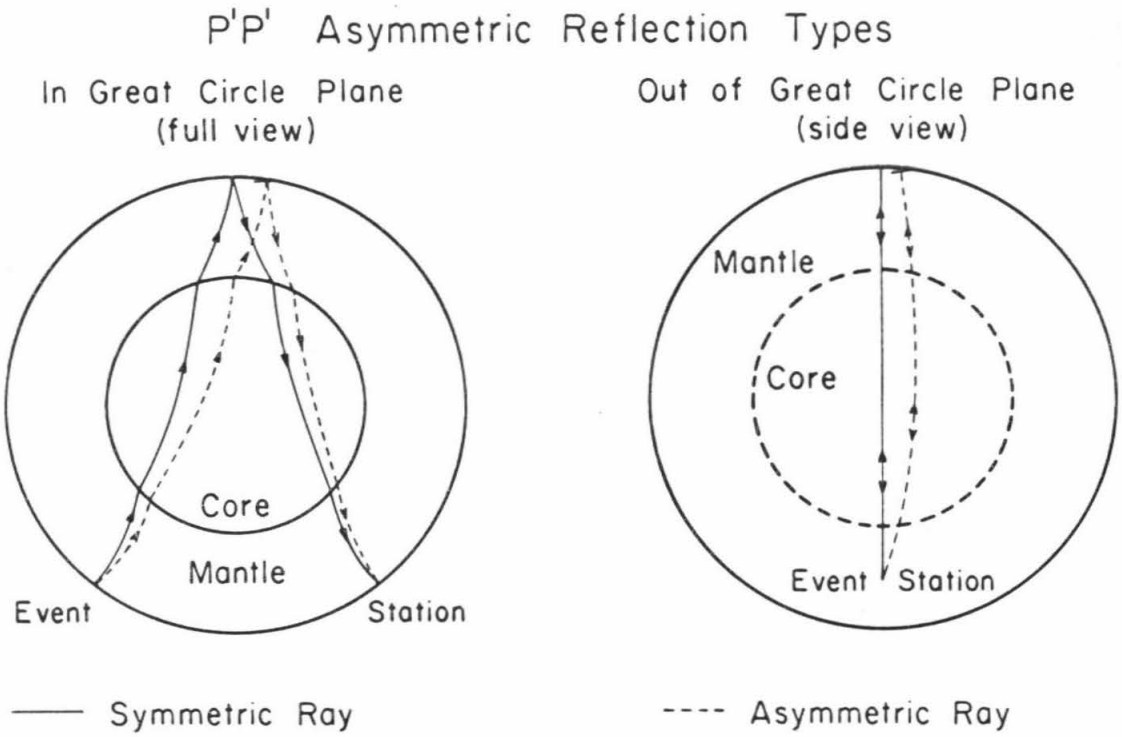

Figure 4.1

Asymmetric reflection types: in the great circle plane, and out of the great circle plane. Symmetric rays are shown for reference.

combination of these two types is permitted. The symmetric ray is shown in each case in Figure 4.1. In all of the calculations, the non-horizontal reflector is assumed to be at or very near the earth's surface where the largest reflection amplitudes are expected. The reflectivity coefficient of the Moho (Mohorovičić discontinuity) is about 0.14 (Whitcomb and Anderson, 1970). This reduces the amplitude almost to the 10% cutoff used below and the asymmetric reflection from this interface is probably not important. The most likely candidates for asymmetric reflectors are a non-horizontal ocean bottom or land surface; the former's reflectivity can be as high as 0.8 and the latter's is 1.0. Therefore, no reduction in amplitude is made for asymmetric phase reflectivity coefficients because they may be equal to that of the symmetric phase.

Another possibility for the generation of asymmetric P'P' phases lies in the distortions of $dt/d\Delta$ produced by inhomogeneities in the upper mantle. A good example is a cold lithospheric slab sinking into the mantle at trench areas. However, the calculations of Julian (1970, Figure 4.2) show that, for such a complex structure, the anisotropy scatters the rays too severely to reflect from the surface a second core phase of significant amplitude. Broader anisotropic structures in the upper mantle might be more effective in evenly distorting a large cone of P'P' energy, but calculations of this effect must await a better understanding of broad lateral variations

in upper mantle structure.

4.3 Observed Amplitudes. Figure 4.2 shows schematic travel-time curves of the branches of P'P' and P'dP. The relative amplitudes (amplitudes relative to the DF branch) of the P' branches have been calculated from the results of Chapter 6 with a mantle Q of 2000 and a core Q of 2200 and are shown in Figure 4.3. The actual amplitude data scatter by as much as ± 50% from these curves. However, the P' amplitudes contrast so markedly as a function of distance and the branch, that useful predictions can be made of relative amplitudes (that is, amplitude ratios on the same seismogram) of specified rays.

The P'P' precursor amplitudes are 30% to 50% of the main P'P' phase at lead times of 0 to 30 seconds and 10% to 20% of the main phase at lead times greater than 30 seconds (Whitcomb and Anderson, 1970). We initially assume, and later justify, that only the 0- to 30-second precursors are candidates for asymmetric P'P'. Therefore, we can define a likelihood criterion as follows: when the asymmetric P'P' amplitudes fall below 10% of the theoretical symmetric phase, they are too small to be identified as readings. That is, when the calculated asymmetric P'P' amplitudes fall below one-third of the smallest actual readings in that time-window, we conclude that the readings are not asymmetric P'P'.

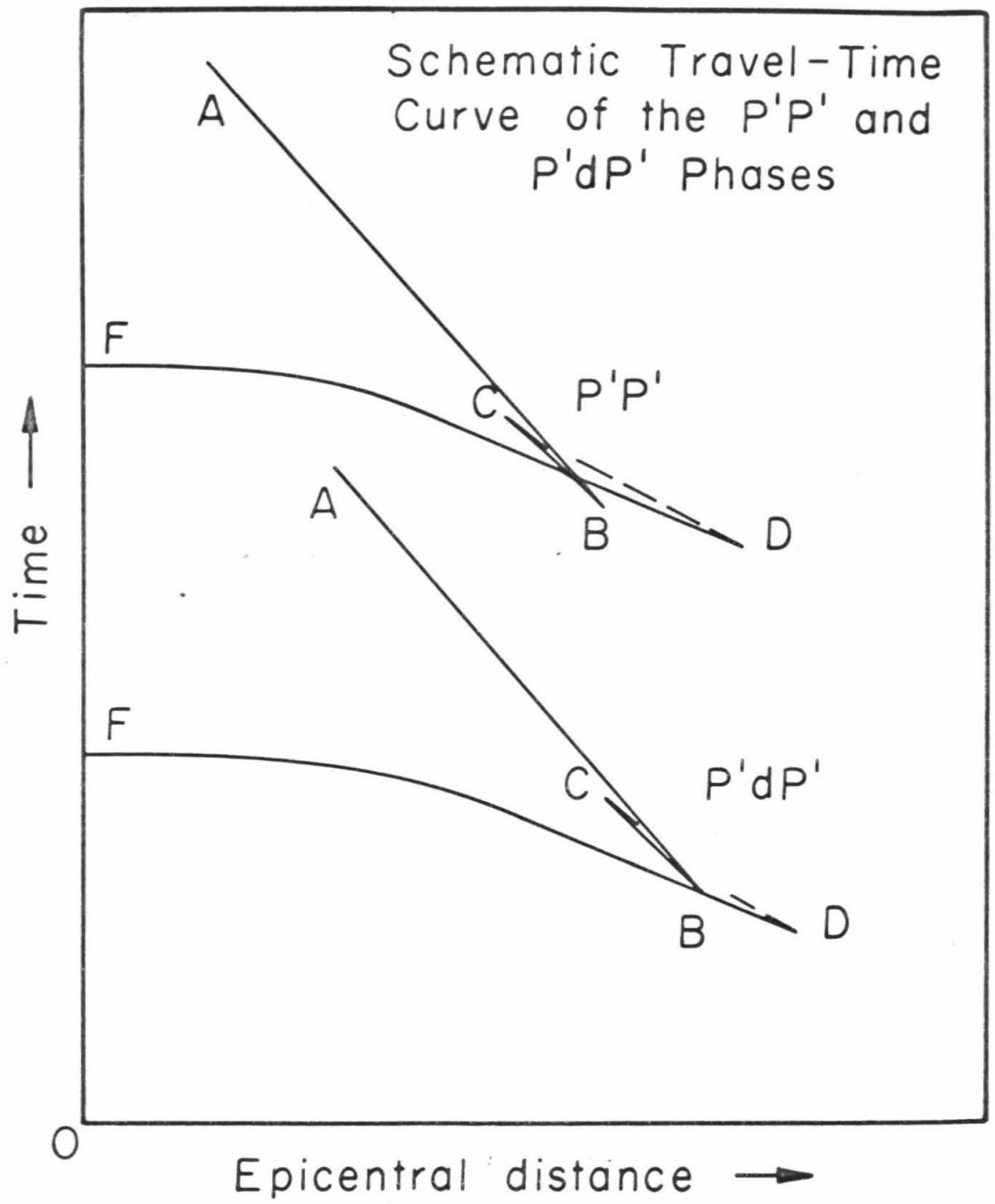

Figure 4.2

Schematic travel-time curves of the branches of P'P' and P'dP'.

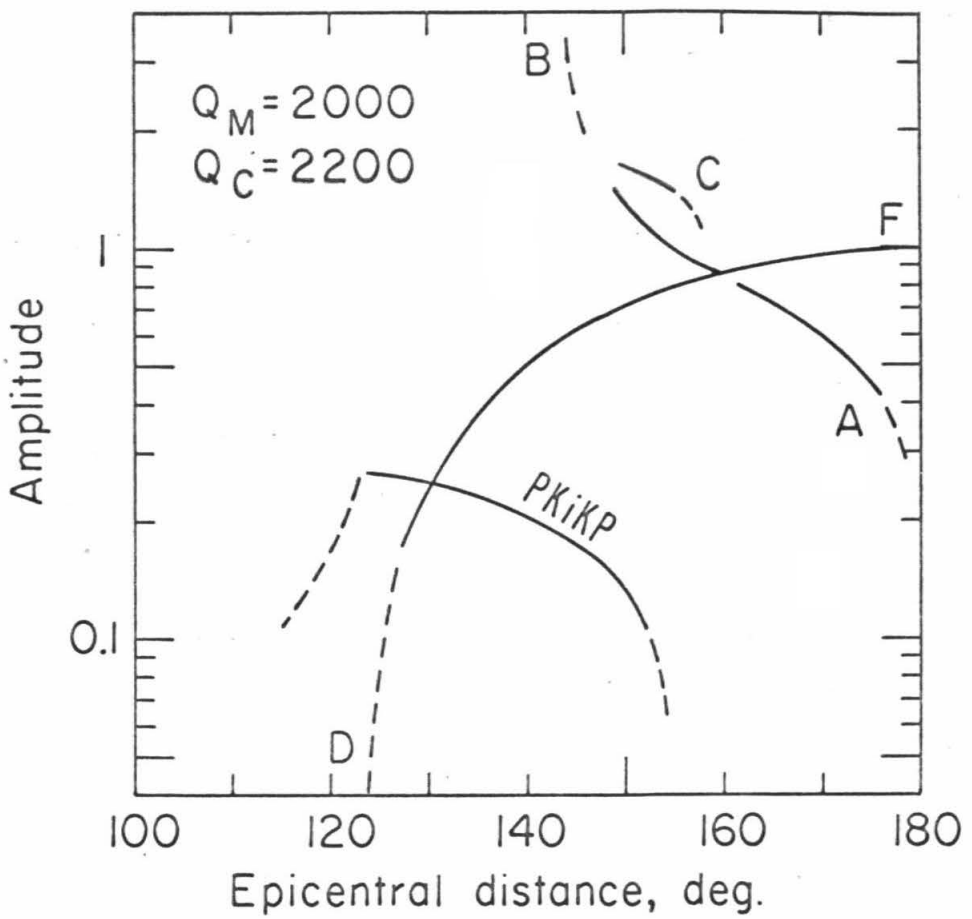

Figure 4.3.

Amplitudes of the branches of P' calculated from the model of Chapter 6 and normalized by the DF branch at 180° epicentral distance. A Q of 2000 was used for the mantle and 2200 for the core.

4.4 Theoretical Amplitudes of Symmetric P'P'. Because the amplitudes of P'P' are not as well known as those of P', we translate P' into symmetric P'P' amplitudes for use as comparisons. From Bullen (1963, p. 127), the energy density due to geometrical spreading of a seismic ray at the earth's surface can be written in the form

$$E(\Delta) = \frac{Bf}{\sin \Delta} \left| \frac{d^2T(\Delta)}{d\Delta^2} \right| \tag{4.1}$$

where B is a constant, f is a function depending mainly on emergence angle, T is the travel time, and Δ is epicentral distance.

Suppose now that $T_1(\Delta)$ corresponds to P' of the DF branch; for a surface focus $T_{11}(2\Delta)$ corresponds to P'P' of the same branch. From symmetry we can write

$$T_{11}(2\Delta) = 2T_1(\Delta) \tag{4.2}$$

or, defining $\Delta' = 2\Delta$, (2) becomes

$$T_{11}(\Delta') = 2T_1(\Delta) \tag{4.3}$$

Then, differentiating twice with respect to Δ', we have

$$\left| \frac{d^2T_{11}(\Delta')}{d(\Delta')^2} \right| = \frac{1}{2} \left| \frac{d^2T_1(\Delta)}{d\Delta^2} \right| \tag{4.4}$$

The energies for the P' and P'P' phases, DF branch, are then, from equation (4.1),

$$E_1(\Delta) = \frac{B_1 f_1}{\sin \Delta} \left| \frac{d^2 T_1(\Delta)}{d\Delta^2} \right| \tag{4.5}$$

and

$$E_{11}(\Delta') = \frac{B_1 f_{11}}{\sin (2\Delta)} \frac{1}{2} \left| \frac{d^2 T_1(\Delta)}{d\Delta^2} \right| \tag{4.6}$$

respectively; where again Δ corresponds to the P' epicentral distance and Δ' to the P'P' distance for the same part of the branch.

The energy expression (4.5) and (4.6) can be related to amplitude by (Bullen, 1963, p. 128)

$$E = \frac{2\pi^2 \rho \lambda a^2}{\tau^2} \tag{4.7}$$

where ρ is density of the medium, λ is wave-length, τ is wave period, and a is amplitude. All of our observations are in the period range 1 to 2 seconds so that, for our purposes, amplitude is directly proportional to the square root of energy. Thus, from (4.5), (4.6), and (4.7) we can form amplitude functions for P' and P'P'

$$a_1(\Delta) = \frac{BF_1(\Delta)}{\sqrt{\sin \Delta}} \tag{4.8}$$

$$a_{11}(\Delta') = \frac{BF_1(\Delta)}{\sqrt{2 \sin (2\Delta)}} \tag{4.9}$$

where B is a new constant, and $F_1(\Delta)$ is a ray parameter containing emergence angle and some spreading information. Now we can see that the ratio of the symmetric P'P' amplitude to the corresponding P' amplitude from (4.8) and (4.9) is

$$\frac{a_{11}(\Delta')}{a_1(\Delta)} = \sqrt{\frac{\sin (\Delta)}{2 \sin (2\Delta)}}$$

$$= \frac{1}{\sqrt{4 \cos \Delta}} \tag{4.10}$$

This function is shown in Figure 4.4.

We can now transform the amplitude data for P' in Figure 4.3 to amplitudes of P'P' using equation (4.10), which involves only geometrical spreading. Figure 4.5 shows the P'P' amplitudes from this calculation with the amplitudes normalized by that of the DF branch at 0° epicentral distance.

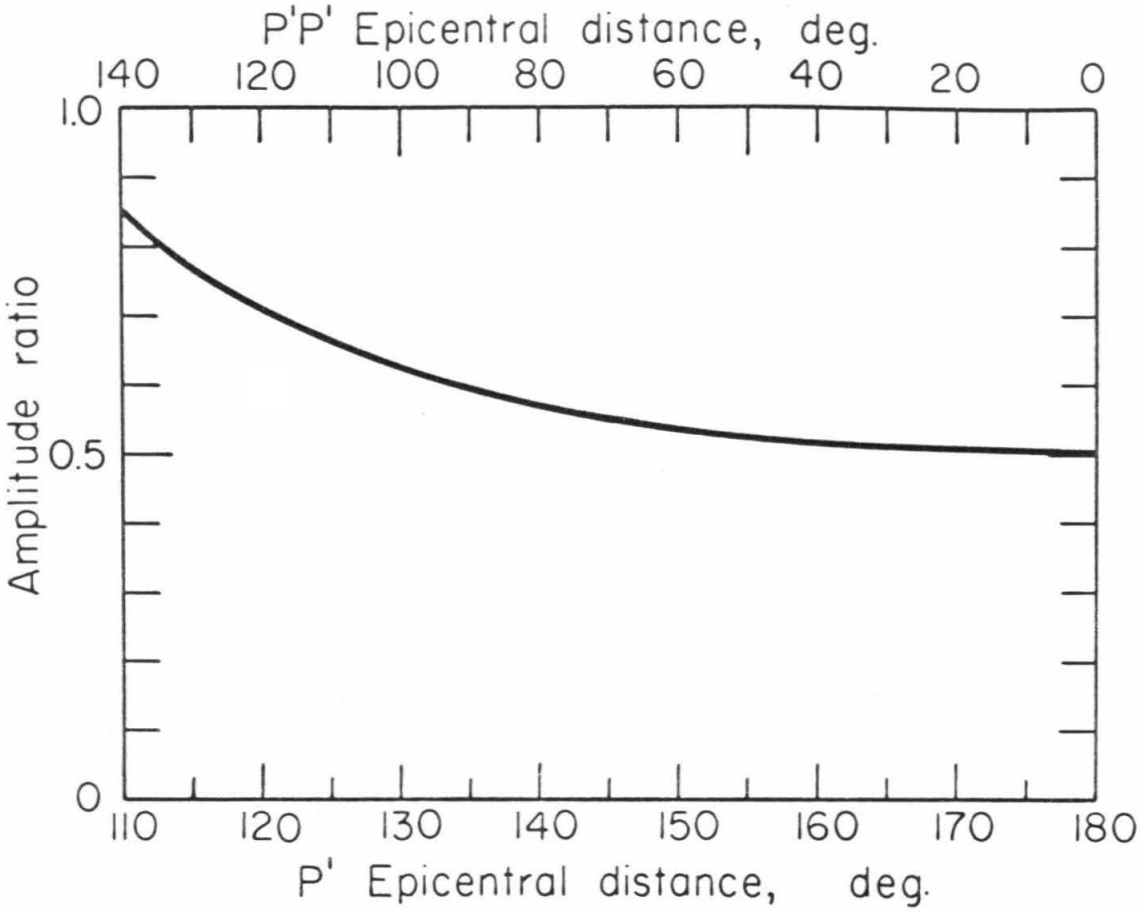

Figure 4.4

Amplitude ratio of P'P'/P' from geometrical spreading.

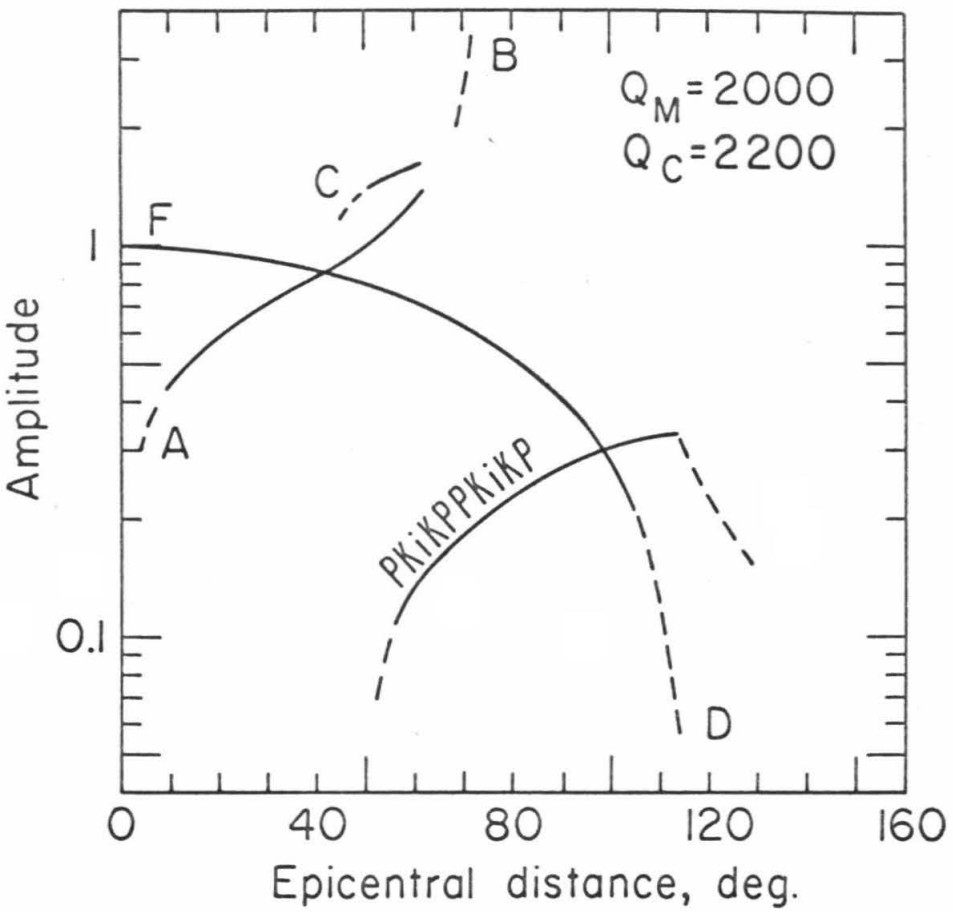

Figure 4.5

Amplitudes of the branches of symmetric P'P' calculated from the P' amplitudes of Figure 4.3. Amplitudes are normalized by the amplitude of DF at 0° epicentral distance.

4.5 Estimated Amplitudes of Asymmetric P'P' from Extensive Dipping Reflectors. In this section, we assume that the reflecting surface is large enough so that a small change in its size does not change the reflection amplitude. The geometrical spreading of an asymmetric P'P' phase is a function of the particular P' branch travelled on each leg and is also a strong function of the reflecting surface shape, which may focus or defocus the energy. The latter phenomenon is not easily resolvable and, for now, we assume that neither focusing nor defocusing takes place at the reflecting point. Spreading due to the particular P' branch is easily handled because the equivalent distance for each leg of an asymmetric P'P' phase can be calculated and the corresponding rays and relative amplitudes for each of those distances are known. Each P' leg travelled can be used to estimate the asymmetric P'P' amplitude. But because we are trying to set an upper limit on the amplitudes, we will simply use the largest-amplitude P' leg for our calculations unless one of the legs falls below 1% of the largest-amplitude symmetric phase. Use of the largest-amplitude P' leg will compensate somewhat for any focusing effects.

The P'dP' studies have been done in the epicentral distance range of 55° to 80° with the largest-amplitude branches being BC between 55° and 62.5°, AB between 62.5° and 73°, and DF between 73° and 80° (Whitcomb, 1971). We want to calculate for each of

these distance ranges the earliest precursor time for an asymmetric P'P' reflection with an amplitude that is 10% of the largest-amplitude phase. For time calculations, the velocity model developed in Chapter 6 was used.

First we direct our attention to reflections in the great circle plane as shown in Figure 4.1. Table 4.1 shows the asymmetric phases that give the earliest 10%-amplitude arrivals. The lead time shown is calculated from the time of the largest-amplitude symmetric P'P' branch at that distance. The dip of the reflector for all of the reflections in the great circle plane is less than 2°. The earliest lead times of 41.9 and 32.5 sec are at distances where BC or AB is the largest-amplitude branch and one leg of asymmetric P'P' is P'_{DF} at 120°. Although the amplitude criterion that was established is satisfied by these phases, their amplitudes should never be significantly above the 10% cutoff due to the P'_{DF} leg near 120°, and they are not as important at these distances as phases out of the great circle plane as seen below. The remaining asymmetric phases in the great circle plane have lead times less than 21 sec.

Next we calculate the times of asymmetric P'P' out of the great circle plane reflecting on a line that is perpendicular to the great circle and which intersects the symmetrical reflection point as seen in Figure 4.1. Table 4.1 shows that the asymmetric phases out of the great circle plane with each leg composed of the same branch are significantly earlier than the phases in the preceding

Table 4.1

Earliest Asymmetric P'P' Phases

with 10% Amplitudes at a Single Station

Largest Amplitude Branch of P'P'	Δ	1st P' Leg Branch-Δ	2nd P' Leg Branch-Δ	Reflector Dip	Lead Time (sec)	Azimuth Deviation at Station
In Great Circle Plane						
BC (55°-62.5°)	61.5°	BC 155°	BC 143.5°	< 2°	2.9	0°
	62.5	DF 177.5°	DF 120°	< 2°	32.5	0°
	55°	DF 161.5°	BC 143.5°	< 2°	21.0	0°
AB (62.5°-73°)	62.5°	BC 154°	BC 143.5°	< 2°	11.8	0°
	62.5°	DF 177.5°	DF 120°	< 2°	41.9	0°
	62.5°	DF 154.0°	BC 143.5°	< 2°	19.9	0°
DF (73°-80°)	73°	DF 167°	DF 120°	< 2°	13.5	0°

Table 4.1 (continued)

Largest Amplitude Branch of P'P'	Δ	1st P' Leg Branch-Δ	2nd P' Leg Branch-Δ	Reflector Dip	Lead Time (sec)	Azimuth Deviation at Station
Out of Great Circle Plane						
BC (55°-62.5°)	55°	BC 143.5°	BC 143.5°	5.1°	48.8	50°
AB (62.5°-73°)	62.5°	AB 143.5°	AB 143.5°	5.2°	39.5	35°
DF (73-80°)	73°	DF 120°	DF 120°	3.0°	89.1	63°

paragraph: up to 48.8 seconds in the BC range, 39.5 seconds in the AB range, and 89.1 seconds in the DF range. The reflector dips range from 3° to 5.2°. The DF branch is left out of the BC and AB range calculations due to the same amplitude arguments put forth in the preceding paragraph. Because the asymmetric P'P' out of the great circle plane can be constructed of nearly the same rays as the symmetric P'P', the asymmetric amplitudes are relatively large. Thus, P'P' out of the great circle plane is the most likely asymmetric phase to be seen as a precursor to the main phase at lead times greater than a few seconds.

4.6 Effect of the Finite Size of the Reflecting Surface. The previous calculations assumed an extensive, nearly plane reflecting surface. Because the boundaries of major physical property changes in the earth are, or have been controlled in a rough sense by equal pressure and temperature surfaces that are approximately spherically symmetric, the boundaries themselves tend to be spherically symmetric or "horizontal". Deviations from spherical symmetry are readily observed, especially at major boundaries at or near the earth's surface: the land-surface, ocean-bottom, and Moho discontinuity for example. But, because we need nearly plane surfaces with which to reflect P'P' waves, it is important to observe that the more a typical boundary deviates from spherical symmetry, the less extensive are its nearly planar surfaces; that is, it is rougher. For example, the

ocean surface is horizontal over extensive areas, whereas steep slopes of mountains have almost no planar surfaces of dimensions larger than a few kilometers. We must therefore estimate what surface extent is adequate for appreciable reflection of P'P' energy. This can be approximated by a calculation of the Fresnel diffraction pattern of a wave that is reflected from a semi-infinite plane with a straight edge (Born and Wolf, 1965, p. 433). A wavelength of 10 km and an observer distance of 12,000 km are used. The calculated amplitude at the observer begins to be affected appreciably when the reflector edge is within 170 km of the optical reflection point. Thus, for reflection surfaces of radii less than 170 km or diameters less than 340 km, the amplitude will begin to be reduced because of the size of the reflection surface, and reflections from surfaces significantly smaller, say 100 km in dimension, will probably not be seen.

The results of Table 4.1 show that the earliest asymmetric P'P' phases, based on a 10% amplitude cut-off, reflect from surfaces dipping from 3° to 5.2°. It is a difficult task to find a 3°-dipping surface at the ocean bottom or land surface that is nearly planar over dimensions of 100 km. Thus the cases in Table 1 are too extreme because of the finiteness of the asymmetric P'P' reflector, and the earliest lead times for the rays out of the great circle plane are probably too large. If the reflector dip were set at an upper limit of 3°, then the phases travelling out of the great circle

plane would be limited to lead times of 30 seconds or less for the GH and AB branches and 80 seconds for the DF branch. If a more reasonable dip limit of 2° is set, then all branches would have asymmetric P'P' lead times less than about 20 seconds.

4.7 Effect of Array Processing. Seismic arrays, through beam-forming, have the ability to band-pass filter coherent energy in both $dt/d\Delta$ and azimuth. When this is done, considerable improvement over recording at a single station can be made by elimination of the undesired asymmetric P'P' phases. Bandpass of a particular $dt/d\Delta$ eliminates all asymmetric P'P' phases whose last P' leg has a different $dt/d\Delta$ than the largest-amplitude branch for that epicentral-distance range. More importantly, bandpass of arrivals from a certain azimuth eliminates those asymmetric phases travelling out of the great circle plane, which are the most bothersome type. However, because the band-pass is not a delta function and has some width, arrivals that deviate only a little from the desired azimuth will be passed. A typical beam azimuth response is shown in Figure 4.6 for the LASA array in Montana for the outer three rings: D, E, and F. A $dt/d\Delta$ of 2.0 sec/deg. and frequency of 1.0 hz was used. The curve shows that the amplitude response falls to 10% at an azimuth of 16° off the great circle path. If this 16° azimuth limit is used for the phases in Table 4.1, then all of the asymmetric P'P' phases are limited to lead times less than 10 seconds.

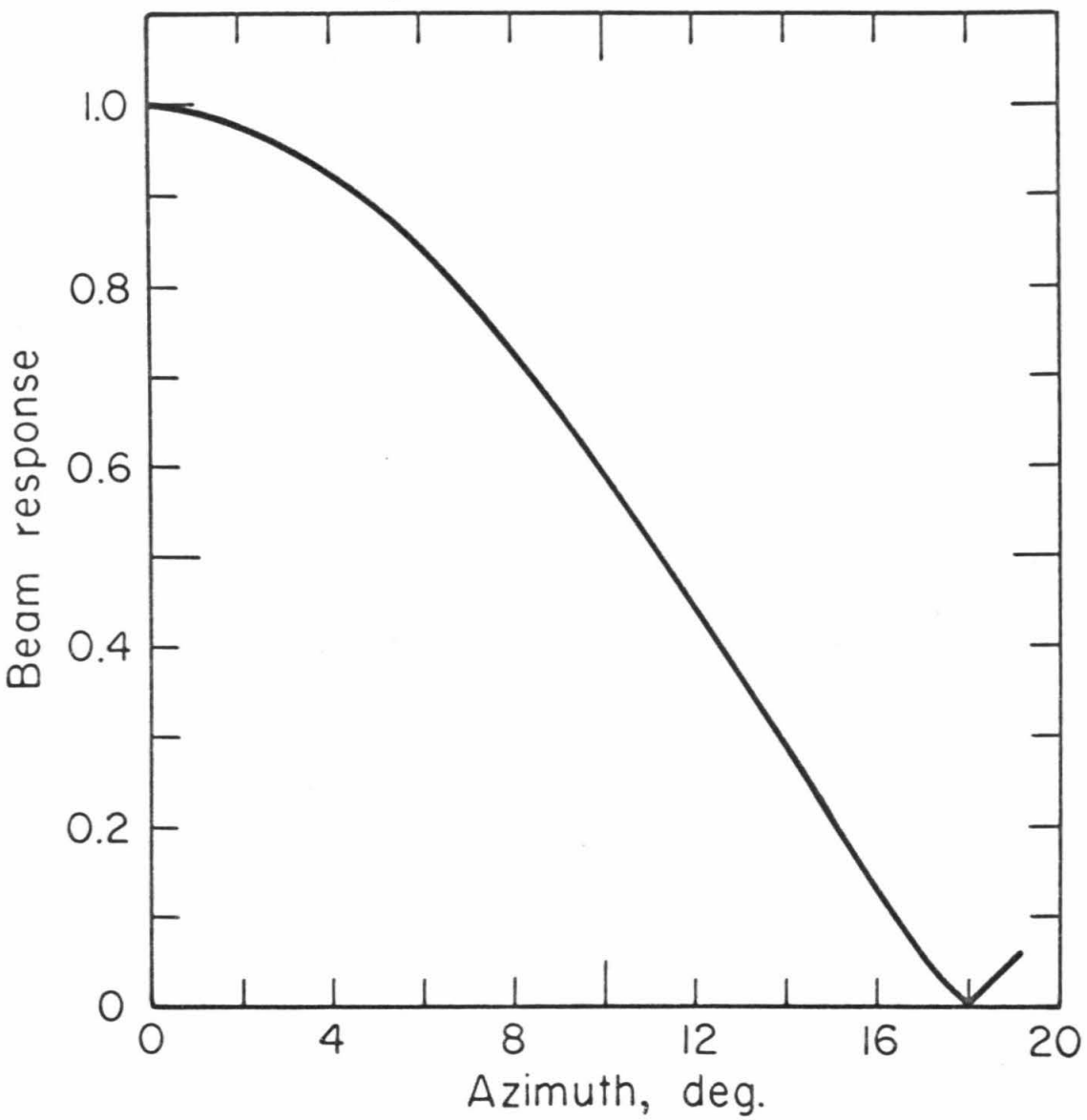

Figure 4.6

LASA beam azimuth response for rings D, E, and F. A dt/dΔ of 2.0 seconds/degree and frequency of 1.0 hz was used.

4.8 Conclusions and Summary. The possible ranges where asymmetric P'P' might be observed are summarized in Figure 4.7. The ranges are relative to the largest-amplitude symmetric P'P' branches that are used for the study of P'dP' phases. Three ranges corresponding to recording at a single station with 2° and 3° reflector dips and recording at a LASA-type array are shown. The calculations have been considerably simplified on the conservative side and should represent lead-time maximums that include consideration of the relative amplitudes of P' phases, the finiteness of the reflecting surfaces of dipping interfaces, and the beam-forming capabilities of a seismic array.

From Figure 4.7, we conclude that for lead times much less than 30 seconds, equivalent to a P'dP' with d at about 110 km, a single station cannot easily discriminate between asymmetric P'P' and P'dP'. The DF range between 75° and 85° may be worse depending on the reflector dip. However, use of a beam-forming array such as LASA in Montana reduces the possible asymmetric P'P' lead times to less than 10 seconds.

Examination of P'P' precursors at single stations in both the seismic recordings and data summaries in Whitcomb and Anderson (1970), Whitcomb (1971), and Chapter 2 reveals that there is a significant build-up of energy starting at around 30 seconds lead time. The vespagram of the array data shown in Chapter 3 further indicates that much of this energy within a 30-second lead time is arriving at $dt/d\Delta$'s different from those of the largest-amplitude branch and

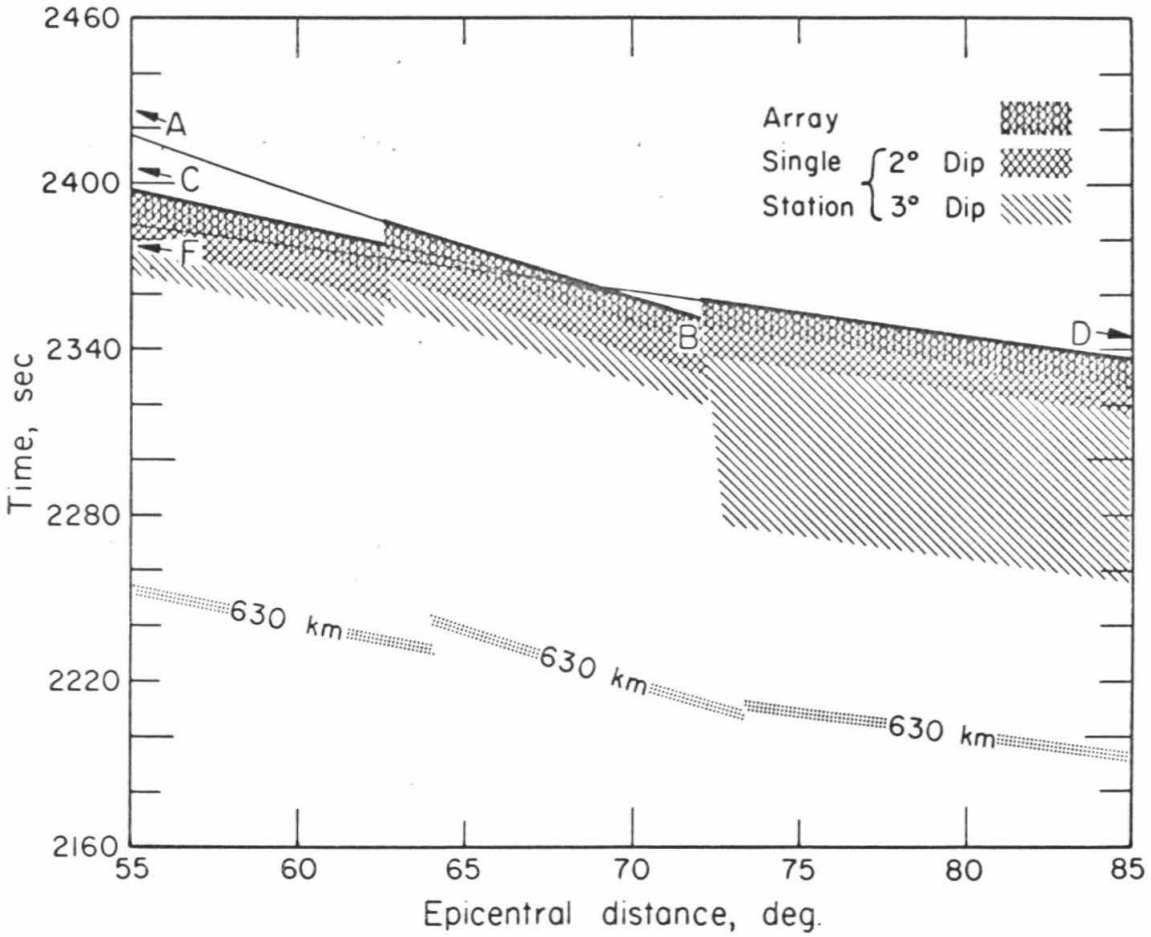

Figure 4.7

A schematic summary of possible asymmetric P'P'-phase lead times recorded at a single station with 2° and 3° reflector dips and at a LASA-type array. The largest-amplitude branches are indicated by heavy lines and the time of a P'630P' phase is shown for reference.

other symmetric branches. This would imply that asymmetric P'P' is indeed present. However, there are arrivals in the same figure with lead times between 10 and 30 seconds recorded at LASA with the proper $dt/d\Delta$ that indicate the presence of P'dP' phases. Thus, we must conclude that both asymmetric P'P' and P'dP' are seen on the seismic record from 0 to 30 seconds lead time. The interpretation of these phases as solely P'dP' by studies such as Gutenberg (1960), Adams (1968), Whitcomb and Anderson (1968), Engdahl and Flinn (1969a), Whitcomb (1971), and Adams (1971) is therefore in question because single stations were used for interpretation. Precursors with 0- to 30-second lead times should be studied using seismic arrays.

Deeper reflections, such as the strong P'640P' phase, can also show leading, emergent arrivals of asymmetric phases if the reflection is strong enough. This is indeed seen on good single-station recordings of the deep reflector such as the excellent example of Adams (1971, Figure 6), but the emergent arrivals are not seen in array-formed beams such as those in Chapter 3.

A further effect that is apparent from the analysis of asymmetric P'P' is that the geographical reflection point of a P'P' phase is poorly determined. An example of this is seen in the first entry in Table 4.1. An asymmetric surface reflection 6° away from the symmetric reflection point differs in time from the symmetric reflection by only 3.0 seconds. It is apparent that, unless the

orientation of the reflector is known, one can determine the reflection point of a P'P'-type phase to within only a few degrees.

5. THE TIMES AND LARGEST RELATIVE AMPLITUDES OF P'P' AND AVERAGE MANTLE VELOCITIES UNDER CONTINENTS AND OCEANS

5.1 Introduction. Gutenberg and Richter (1934), upon their discovery of the P'P' phase, recognized its potential for accurate measurement of travel-time through the earth and the resulting benefits to hypocentral-depth location and earth-velocity determination. However, scatter of the P'P' readings has discouraged investigators from using the main P'P' phase for anything but an approximate check on times (for example, Gutenberg, 1951; Subiza and Bâth, 1964; Engdahl, 1968; Whitcomb and Anderson, 1970; and others). A partial explanation for the scatter is asymmetric P'P' which arrives earlier than the symmetrically reflected phases as discussed in Chapter 4 and in Whitcomb (1973). But, at least some of the difficulty lies in assignment of the incorrect P'P' branch to a reading and in assumption of the incorrect velocity structure at the reflection point. Before a meaningful analysis of P'P' times can be performed, these problems must be resolved, and that is the objective of this chapter.

The problems of asymmetric P'P' are avoided by isolation of the P'P' reflection from the ocean surface, which is perfectly horizontal for purposes here. The identification of the proper P'P' branch is done using the LASA array in Montana to measure the $dt/d\Delta$ of a phase and by the determination of the largest-relative-amplitude branch

of P'P' at a given distance. This is shown to be very consistent and is an important aid in identification of a P'P' branch at single stations which provide most of the data used here. The bathymetry and crustal structure is well-known at most of the oceanic reflection points studied and, when the data are analyzed as a function of their crustal structure, the ocean-bottom and ocean-surface reflections and their times are easily identified. The reflections are then analyzed with respect to ocean-bottom reflectivity, the effect of P tables on hypocentral locations and calculated P'P' times, and the implications of the observed P'P' times on average mantle velocities under continents and oceans.

5.2 Data. Earthquakes from the northern part of the Japanese Arc and South America are used (except for one event, they are the same as those used in Chapter 2) and their parameters are given in Table 2.1. The corresponding oceanic reflection areas are near the Ninety-East Ridge, Indian Ocean, and the Atlantic-Indian Rise, south of Cape Good Hope shown in Figures 5.1 and 5.2, respectively. Seismic recordings were used from several stations in California and from the Tonto Forest Array in Arizona (in one case). In addition, the $dt/d\Delta$ or apparent wave slowness of some of the phases was determined using the LASA installation in Montana as a beam-forming array as in Chapter 3. An example of P'P' on a vespagram plot is shown for two events in Figure 5.3. However, the majority of the data was

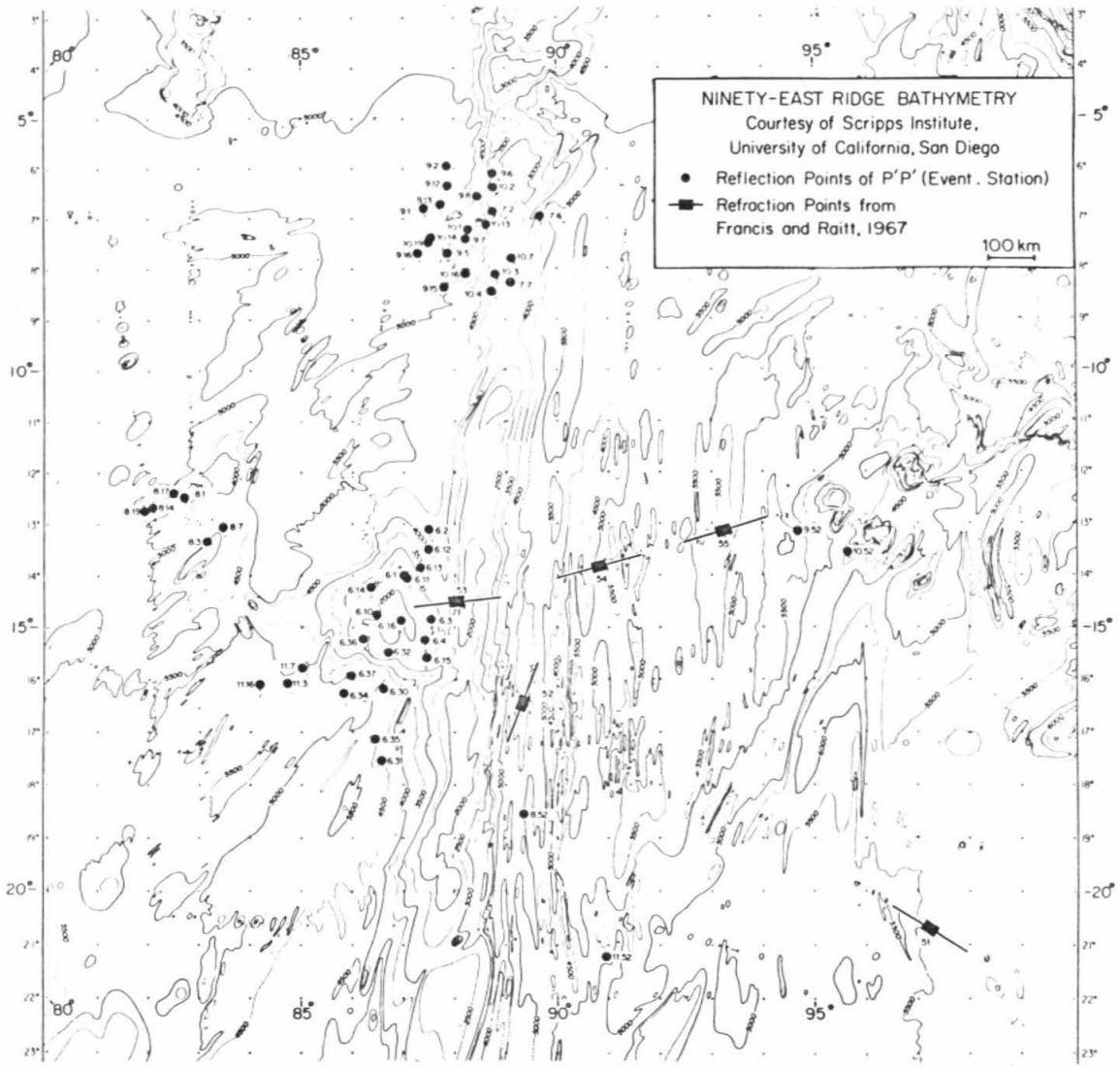

Figure 5.1

Map of the reflection points at the Ninety-East ridge, events 6,8,11 (southern group) and events, 7,9,10 (northern group). Bathymetry was provided by the University of California, San Diego. Contour interval is 500 meters.

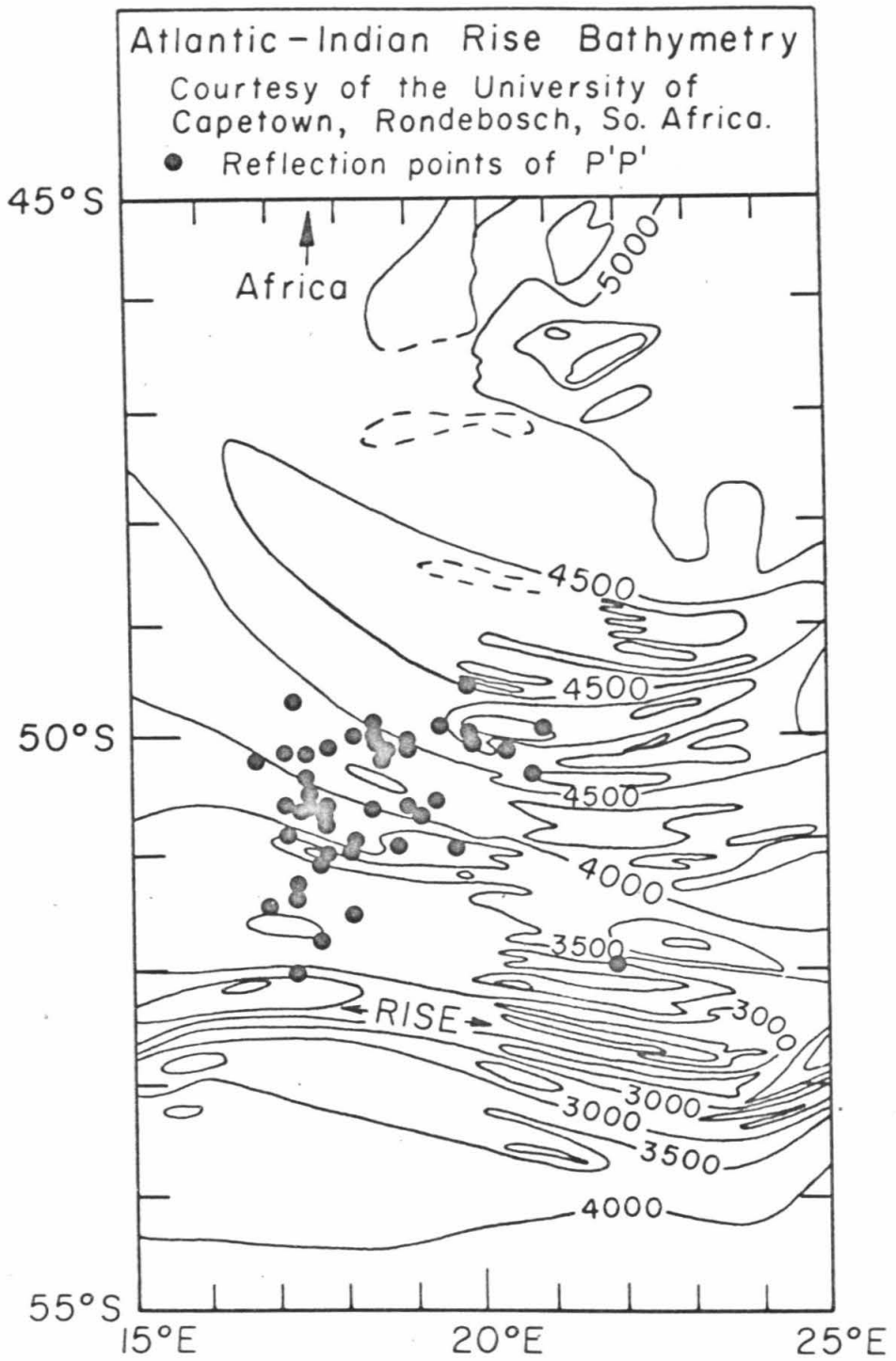

Figure 5.2

Map of the reflection points at the Atlantic-Indian rise, events 1,2,3,4,5,12. Bathymetry is from unpublished data of E.S.W. Simpson and Erica Forder, University of Capetown, Rondebosch, South Africa. Contour interval is 500 meters.

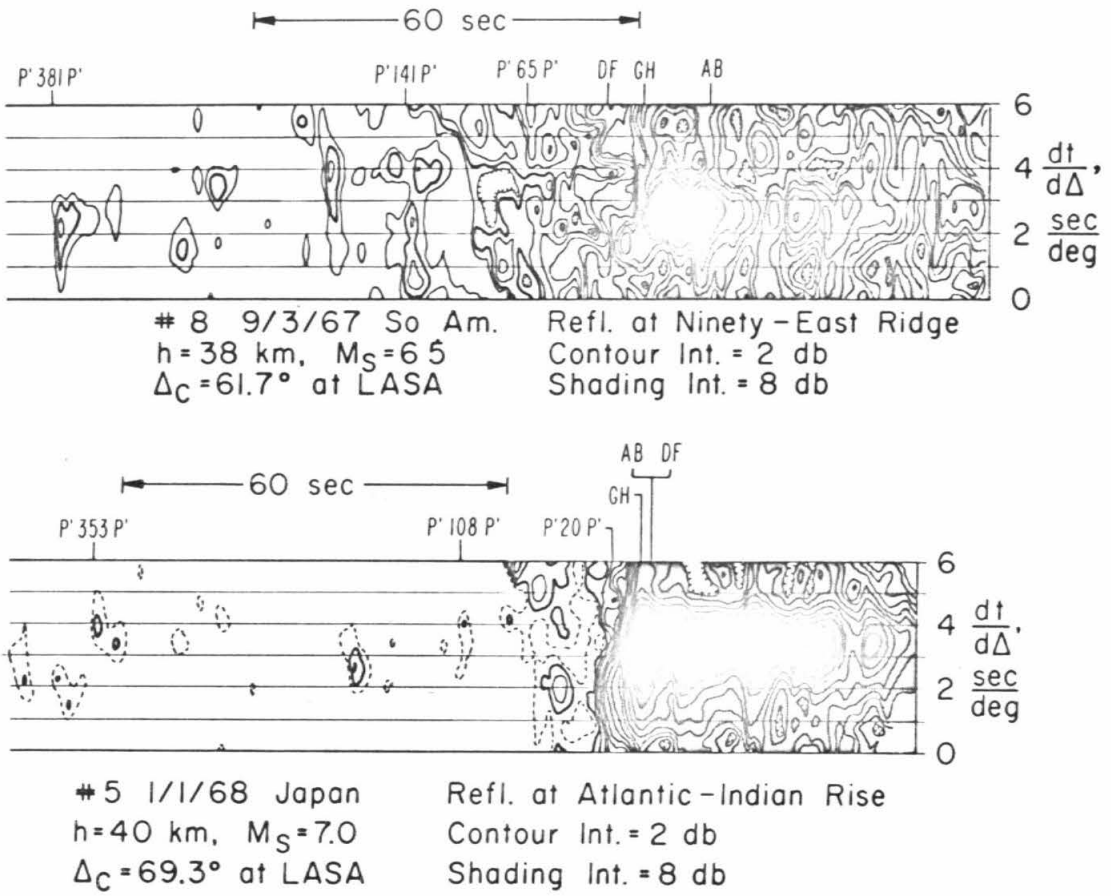

Figure 5.3

Vespagrams (velocity spectra) or contour plots of beam signal power in db as a function of time and dt/dΔ for Events 8 and 5. Depths of reflection and theoretical main branch times are shown; main branch times are from Chapter 6. Note the double arrival at the dt/dΔ for the BC branch in Event 8. The first is interpreted as the ocean-bottom reflection and the second is the ocean-surface reflection.

picked as signal onsets on individual seismograms as in Chapter 2. The times were read to the nearest second and were graded according to the following scale:

4 - Beginning of the largest-amplitude P'P' phase on the record.

3 - Sharp pulse or a wave train with a sharp beginning.

2 - Emergent beginning but a definite signal, usually a wave train.

1 - Small wave train with an emergent beginning; character (difference in period or amplitudes) distinguishes it from the prevailing noise level.

The data were reduced to surface-focus on a spherically symmetric earth in the same manner as in Chapter 2.

Knowledge of the largest-amplitude branch at a given distance is useful because 1) it is unambiguous, 2) it is nearly independent of amplitude variations caused by local structure from station to station, 3) it is a constraint on core velocity structure (as seen in Chapter 6), and 4) it is a simple way to identify the branch of the largest-amplitude P'P' phase on the record. The latter property is most helpful when direct measurement of $dt/d\Delta$ is not possible such as at a single station. P'P' largest amplitudes are shown as solid points in the travel-time plot of Figure 5.4. In all of the time plots, the solid points represent grade 4, and the open points represent grade 3 (largest points) through grade 1 (smallest points).

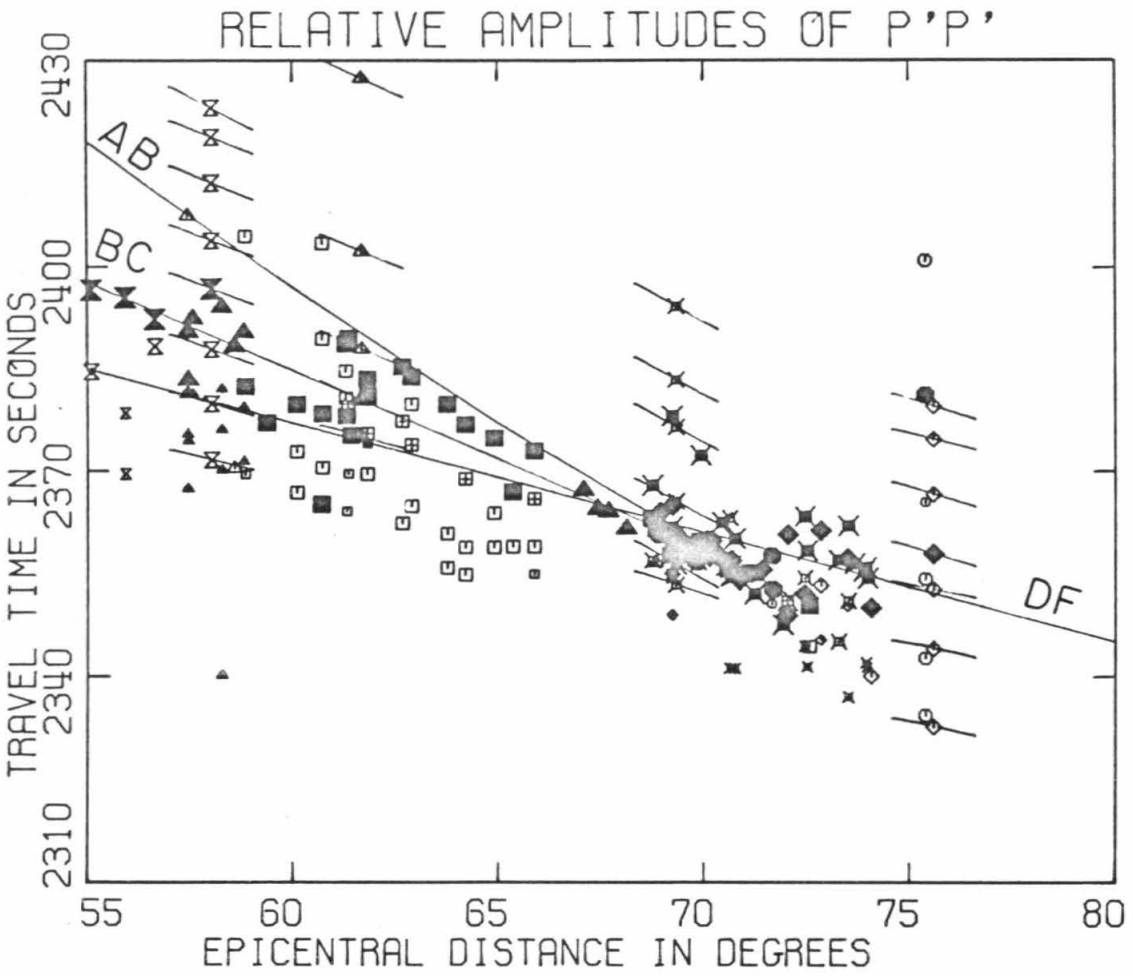

Figure 5.4

Main P'P' phase travel times and largest amplitudes (shown as solid points) as a function of epicentral distance. Sloping lines through points indicate the $dt/d\Delta$ measured at LASA. Largest amplitude branches are BC between 55° and 62.5°, AB between 62.5° and 72°, and DF between 72° and 80°. Points close to a branch which is not the largest-amplitude branch are not used as P'dP' data. The symbols are the same as those in Figures 2.6 and 2.7.

The type of symbol identifies the event for which the key is given in Table 5.1. Several stations were used for each event so that the same symbol is seen at different distances. Adams and Randall (1964) stated that the largest-amplitude P'P' branches are $P'_{DF}P'_{DF}$ at distances greater than 70°, $P'_{GH}P'_{GH}$ between 70° and 54°, and $P'_{AB}P'_{AB}$ at distances less than 54°. As discussed in Chapter 6, the P'_{GH} phase between P'_{AB} and P'_{DF} is identified as P'_{BC}. However, the phase and its $dt/d\Delta$ are well-determined and the analysis here is independent of the terminology. For consistency with Chapter 6, it will always be called P'_{BC} in the remainder of this chapter. Figure 5.4 indicates that Adams and Randall's largest-amplitude determinations are correct except in the range of 62.5° to 72°. In this range, it is apparent that the largest amplitudes follow the AB branch from 62.5° to the end of the B caustic at about 72°. Measurement of $dt/d\Delta$ from LASA are indicated by sloping lines through the data and they show that the largest amplitude branch is BC at 58° and 62°, AB at 69°, and DF at 76° as predicted.

5.3 Analysis and Discussion. The predicted times of P'P' arrivals shown in Figure 5.4 are based on P' studies by Adams and Randall (1964), Bolt (1968), and Cleary and Hales (1971) as discussed in Chapter 6. It can be seen that the largest amplitudes sometimes miss the predicted times for that branch by several seconds, such as

the LASA data at 58°, 69°, and 76° (points pierced by short lines indicating $dt/d\Delta$). Figure 5.5 shows the same data divided into three groups based on their reflection location: Ninety-East Ridge, Events 6, 8, 11 (southern group in Figure 5.1); Ninety-East Ridge, Events 7, 9, 10 (northern group in Figure 5.1); and the Atlantic-Indian Rise (Figure 5.2). In order to compare all largest-amplitude P'P' data with each other, irrespective of the branch they represent, all of the times are reduced by subtracting the predicted time of the largest-amplitude P'P' branch at the distance (BC between 55° and 62.5°, AB between 62.5° and 72°, and DF between 72° and 80°). It is to be remembered that these predicted times correspond to continents, since that is where most of the P' data is gathered.

If one initially assumes that the average mantle velocities seen by P' phases do not vary, then the main variation of the reduced P'P' times will be due to differences at the reflection point of crustal structure, water depth, and of course depth and dip of the reflector. Three crustal velocity models shown in Figure 5.6 that differ only in the upper 56 km are used to estimate the time variations. The model used for continental crust is from the CIT 208 model of Johnson (1969). For oceanic models, two types of crust were chosen based on seismic refraction work done by Francis and Raitt (1967) in the deep ocean (5.3 km water depth) and on the Ninety-East Ridge (2.0 km water depth), here called models Oc and 90°E, respectively. Since, as

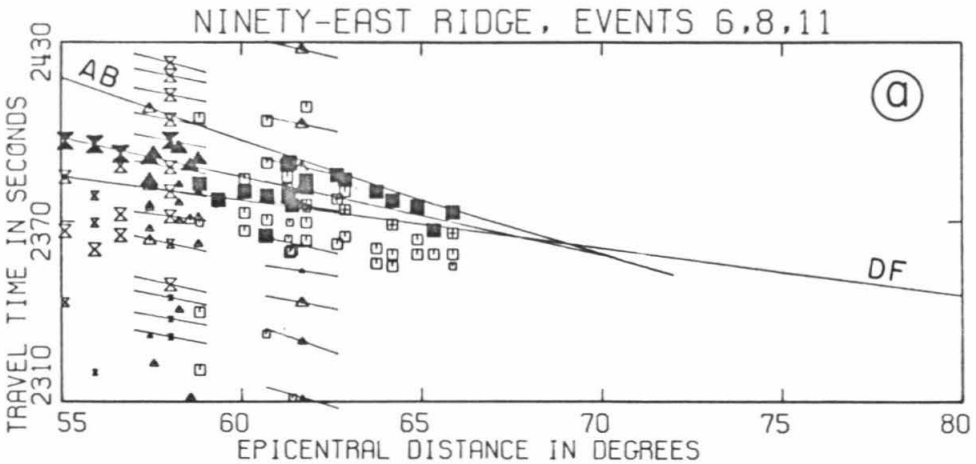

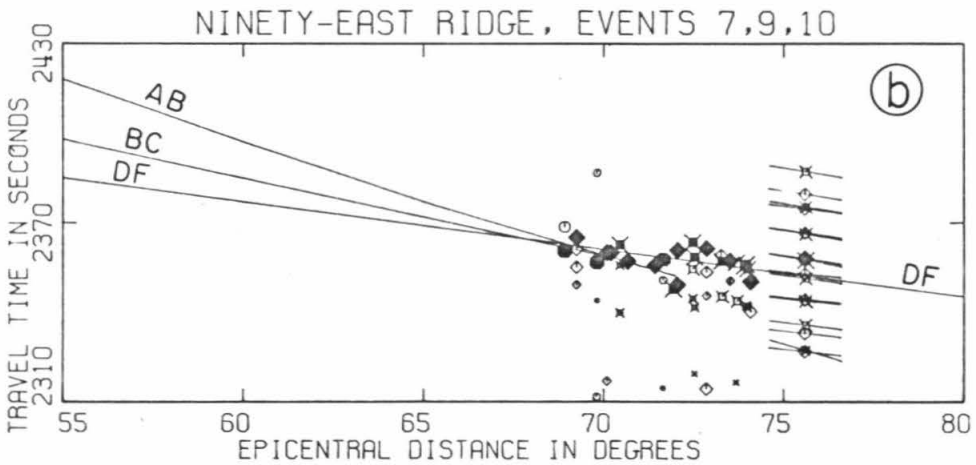

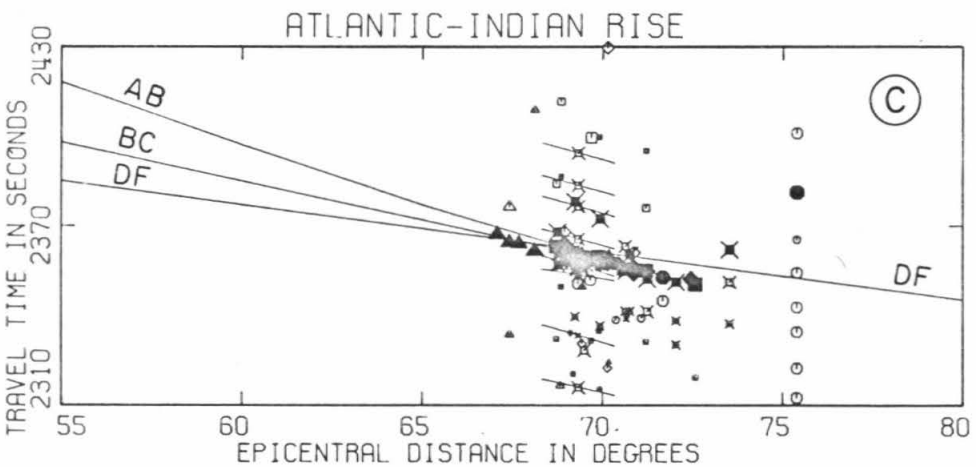

Figure 5.5

Travel times as a function of spicentral distance for each reflection area. Points with a cross in the center and points with the wrong $dt/d\Delta$ compared to the largest-amplitude branch for that range are not used. The symbols are the same as those used in Figures 2.6 and 2.7.

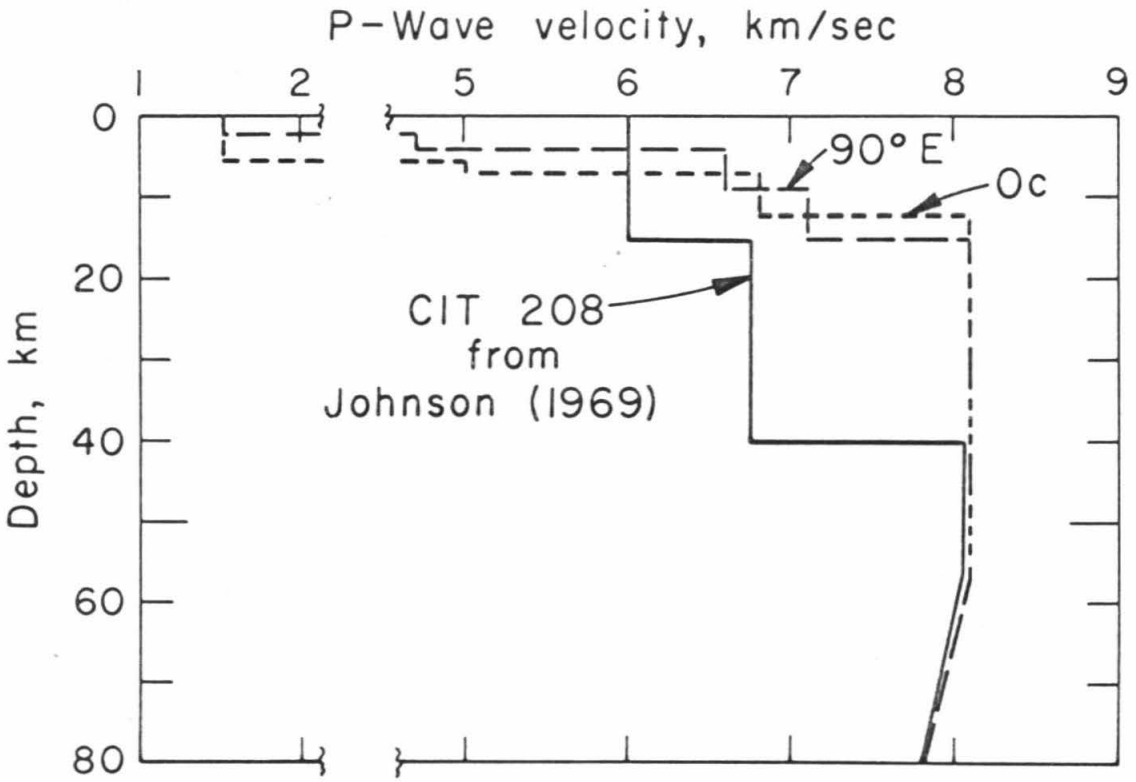

Figure 5.6

P-wave crustal-velocity models CIT208 [from Johnson, 1969], 0c, 90°E.

stated above, the P'P' branch times used to reduce the P'P' observations are based on continentally-observed P', then a reduced time of zero corresponds to a reflection of P'P' from the surface of the continental crust of Figure 5.6. Because the lowest velocity in the models is that of the ocean water, variations of ocean depth dominate the variations of time for surface reflections of the models and the data are best presented as a function of water depth at the reflection point.

Bathymetry charts for the reflection areas vary in coverage (Figures 5.1 and 5.2). The best data are from the Ninety-East Ridge, Events 6, 8, and 11, and Figure 5.7 shows the reduced times as a function of water depth (again, zero time corresponds to a surface reflection under a continent). The dashed lines in Figure 5.7 indicate interpolated times calculated for a reflection from the ocean surface and ocean bottom between model Oc, with a 5.3 km water depth and model 90°E with a 2 km depth. A fairly good fit of largest amplitude arrivals can be made to surface and bottom reflection times if the predicted times are increased by 2.5 sec. This fit, shown as the solid lines in Figure 5.7, is made mainly on the basis of ocean surface reflections, which should have the least scatter. The implications of this time shift are evaluated later. The three late points near 2 km ocean depth are probably due to using the wrong branch to reduce their times; they are near the right time for AB but are at a distance less than 62.5° so that the BC branch was used for reduction. With the adjustment of 2.5

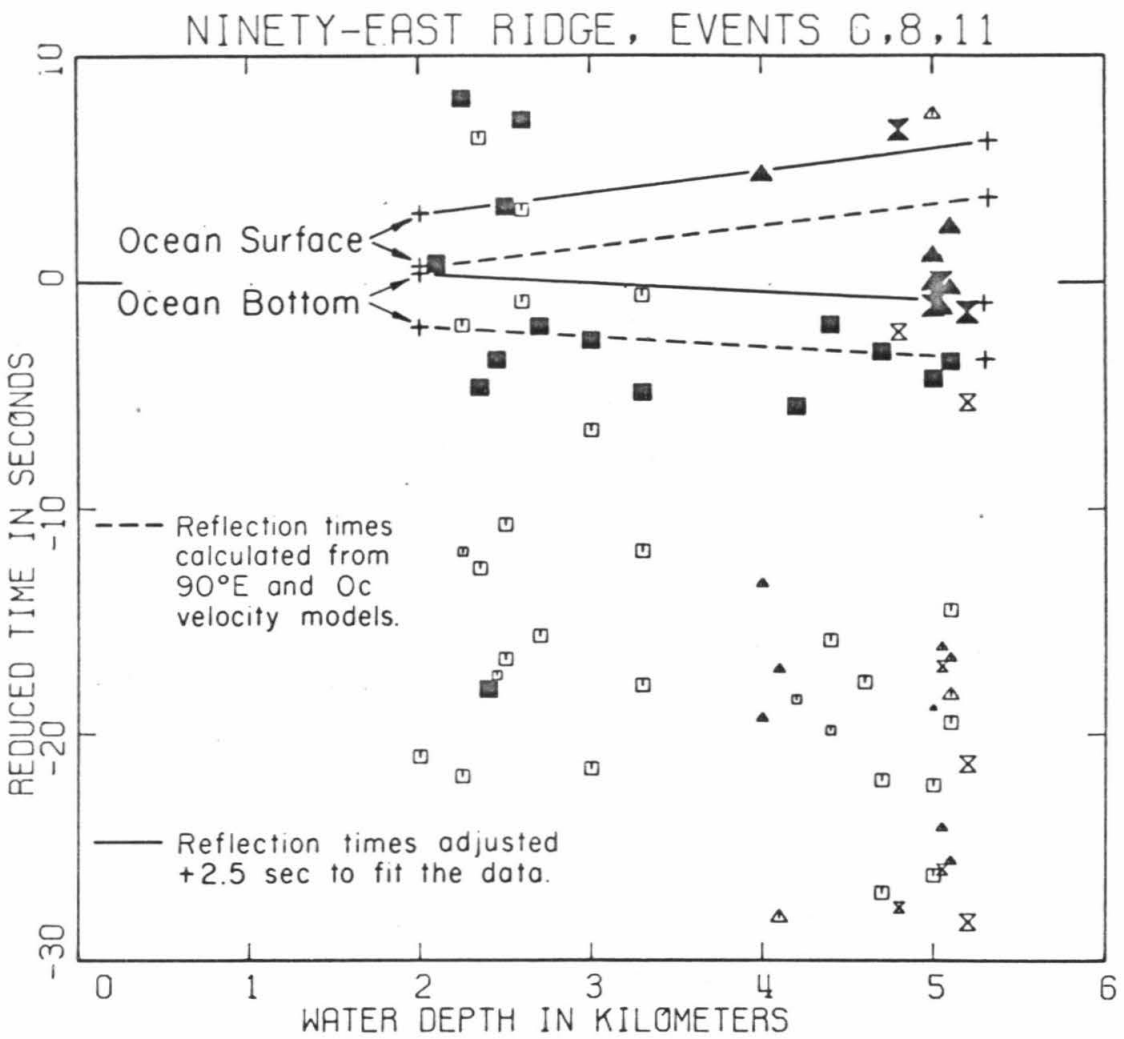

Figure 5.7

Reduced times as a function of water depth for Ninety-East ridge, Events 6, 8, 11 data. The dashed lines represent times for ocean-surface and ocean-bottom reflections which are extrapolated between velocity models 90°E (2.0 km water depth) and Oc (5.3 km water depth). The solid lines represent the same times adjusted to fit the data. The symbols are the same as those used in Figure 2.7.

sec to fit the water surface reflection times, it is seen that most of the largest-amplitude data are earlier than the ocean bottom time; some are close to the ocean surface time. But, most importantly, there is a gap between the ocean-bottom and ocean-surface times as would be expected; that is, no reflection should occur within the water.

Reduced-time data from Events 7, 9, and 10 on the Ninety-East Ridge (not shown) show no systematic distribution, probably because the reflections are too closely spaced (Figures 5.1 and 5.5) and the bathymetry data in that area are too sparse to provide a useful comparison of reduced times with water depth.

The Atlantic-Indian Rise plot of reduced time as a function of water depth is shown in Figure 5.8. The dashed lines again correspond to predicted times from the Oc and 90°E velocity models (Figure 5.6), and the solid lines correspond to the adjusted times just as in Figure 5.7. The largest-amplitude data do not fit the slope of the calculated ocean surface reflection as well. However, the bathymetry data are based on very few ship tracks and the shallower water depths can be systematically plotted too deep, since any smoothing caused by lack of data will wipe out the high bottom features. Thus, shallow water points would tend to be displaced towards too great a water depth, as they appear in Figure 5.8. Nonetheless, the important trend of a widening gap with deeper water is easily seen in the data

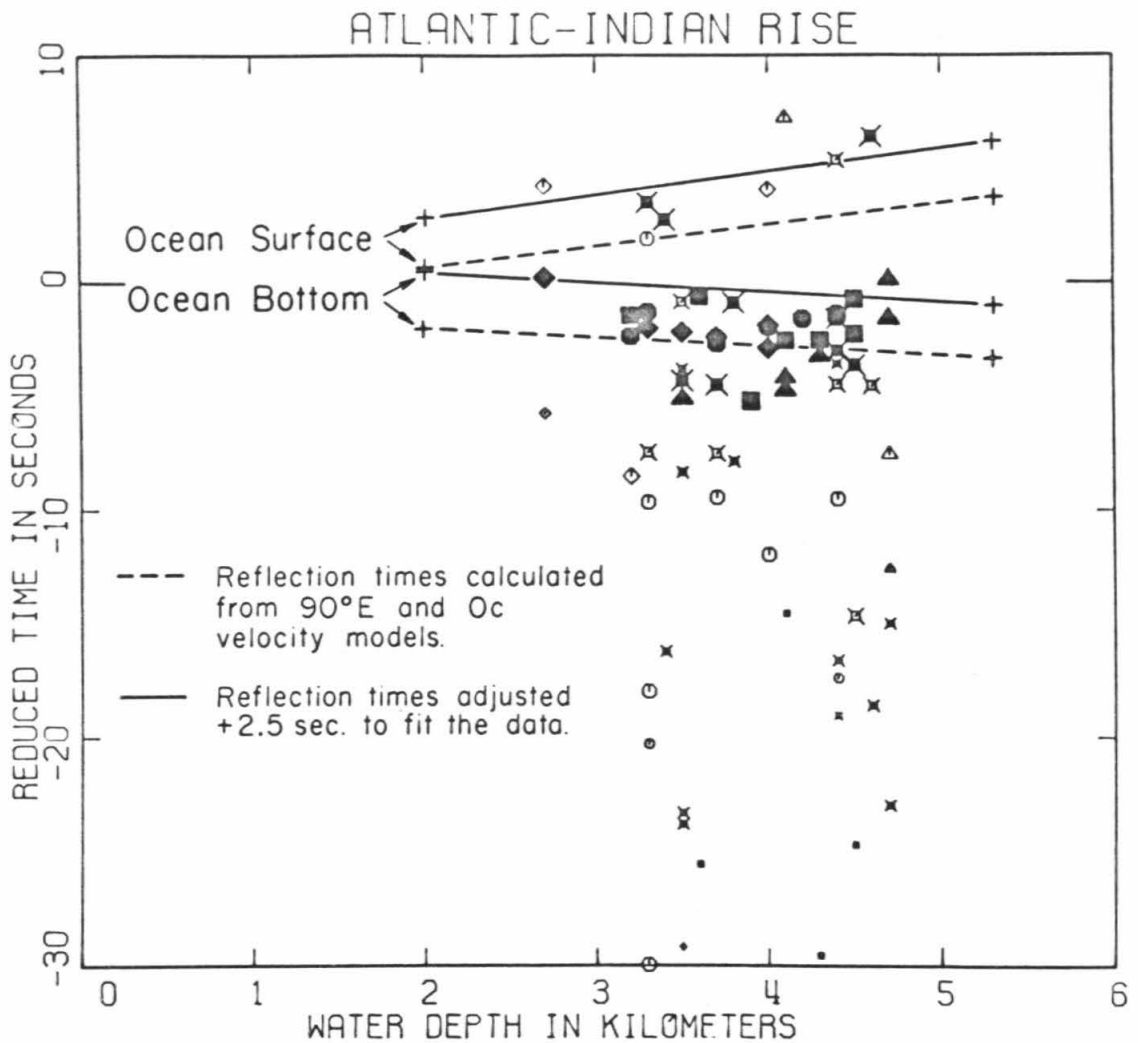

Figure 5.8

Reduced times as a function of water depth for Atlantic-Indian rise data. The dashed lines represent times for ocean-surface and ocean-bottom reflections which are extrapolated between velocity models 90°E (2.0 km water depth) and Oc (5.3 km water depth). The solid lines represent the same times adjusted to fit the data. The symbols are the same as those used in Figure 2.6.

and the 2.5 sec time shift is again required to agree with the surface reflection for the deep-ocean points.

In both Figures 5.7 and 5.8, the largest-amplitude points tend to scatter to earlier times than that predicted for the ocean-bottom reflection. This effect can be explained by two possible phenomena. Due to the technique for reading the phases as described in a previous section, it is expected that if two signals arrive within one or two periods of each other (for P'P' this is within about three seconds) then they are read as one arrival with the earlier arrival time. The second arrival may be missed even if it is larger because both phases may appear as a single emergent wave train. This effect is important but presently unavoidable when calculating the time of the largest-amplitude P'P' phase. Thus, if there is a strong reflector in the crust as much as 20 km deeper than the largest-amplitude reflector, the two phases may merge and the deeper interface will be erroneously designated as the strongest reflector. The second possibility is an earlier arrival of asymmetric P'P' as discussed in Chapter 4. The combination of these two effects predicts that reflections from the earth-air or earth-water interface will always tend to be scattered between the predicted time and earlier times. But the reflection from the water-air interface of an ocean, because it is horizontal (for our purposes), does not suffer the asymmetric P'P' complication. Neither is there an intermediate reflection between the times of the ocean-bottom and ocean-surface reflection,

as the data of Figure 5.7 and 5.8 clearly indicate.

The data of Figures 5.7 and 5.8 show that the largest-amplitude reflector can be associated with either the ocean-bottom or ocean-surface reflection. Simple reflectivity calculations indicate that, if there is a fairly hard ocean bottom with P-wave velocity greater than about 3.5 km/sec (density about 1.8 gm/cc), the bottom reflection will be larger than the ocean-surface reflection. Conversely, the amplitude of the bottom reflection is easily reduced below that from the surface reflection by an appreciable sediment layer; sediment velocities are usually much less than 3.5 km/sec. Interference effects can also be effective in reducing the ocean-bottom reflection amplitude. For example, a sediment layer that is one-fourth wavelength thick, about 0.2 to 0.5 km, overlying a crystalline-rock strata will cause destructive interference of the ocean-bottom reflection. The detailed sediment data needed to test this hypothesis are not available. However, studies of Ewing et al. (1969) show that sediment thicknesses in the Ninety-East Ridge's northern group area can be up to 0.5 km thick adjacent to the ridge, and in the southern group up to 0.3 km adjacent to the ridge. Sediment thicknesses in the vicinity of the Atlantic-Indian Rise can be up to 0.5 km. A further and perhaps very effective mode of reducing the amplitude of ocean-bottom reflections is scattering due to large bathymetric relief. A non-horizontal reflecting surface

changes the $dt/d\Delta$ of an incoming ray and prevents the ray from continuing on its second P' leg through the same level of the earth's core. This effect, discussed in Chapter 4, tends to scatter the reflecting energy. Thus, the ocean-bottom character may be expected to have a large effect on reflection amplitudes. Relative to the ocean-surface reflection, reduced ocean-bottom-reflection amplitudes can be expected with thick sediments, sediments of one-quarter wave length (about 0.2 to 0.5 km thick), or strong bottom relief. For bottoms that are flat with thin sediment cover, the ocean-bottom reflection should be the largest-amplitude P'P' phase. Most of the data of Figures 5.7 and 5.8 fall into the latter category.

It is important to assess the validity of the 2.5 sec time shift required to fit P'P' observed times because of the implications to average mantle velocities under continents, from which the predicted times were derived, and under oceans, from which a large part of the observed times were derived. Because the predicted P'P' times are based on tables of P' for a surface focus, the assumptions that go into the development of P' tables are of prime importance. A typical study of the times of P' generally avoids the uncertainties of focal-depth and origin-time determinations by adjusting the origin time until the P residuals are minimized at epicentral distances near 90°. The adjustment is based on the assumption that near-source time anomalies for P' will be approximately the same as those for P at

its steepest emergent angle, and effectively makes the total travel-time of P' dependent on the P table used to locate the earthquake. Of course, when the origin time and focal depth of an event are accurately resolved, such as for explosions, dependence on a P table is not necessary. However, most of the P' studies are of the former type.

It is clear that one must estimate the effects of the dependence of P' time on P tables for the calculation of predicted P'P' times. From the discussion above, the measurement of P' times is effectively the differential time of the P' phase relative to P at 90°, $[t_{P'}(\Delta') - t_P(90°)]$, to which the P-table time at 90°, $t_P^M(90°)$, is added to construct the P' table:

$$t_{P'}^M(\Delta') = [t_{P'}(\Delta') - t_P(90°)] + t_P^M(90°) \quad . \tag{5.1}$$

In all of these calculations, a superscript denotes reference to a particular table and lack of a superscript denotes actual (and generally unknown) travel times for a surface focus. Calculation of P'P' times from (5.1) is then simply a matter of doubling the time and distance:

$$t^{C}_{P'P'}(2\Delta') = 2\ t^{M}_{P'}(\Delta')$$

$$= 2\ t_{P'}(\Delta') + 2\ [t^{M}_{P}(90°) - t_{P}(90°)] \qquad (5.2)$$

$$= t_{P'P'}(2\Delta') + 2\ [t^{M}_{P}(90°) - t_{P}(90°)]$$

or

$$t^{C}_{P'P'}(\Delta) = t_{P'P'}(\Delta) + 2\ [t^{M}_{P}(90°) - t_{P}(90°)] \qquad (5.3)$$

where $\Delta = 360° - 2\Delta'$.

Direct observations of P'P' times are similarly tied to focal depths and origin times, and differential times are also used to avoid their uncertainties. But, because the distances for P and P'P' coincide, the differential times can be measured directly at the same station, which avoids some problems of station anomalies. Thus, the total travel time of the observed P'P' phase is

$$t^{O}_{P'P'}(\Delta) = [t_{P'P'}(\Delta) - t_{P}(\Delta)] - t^{M}_{P}(\Delta)$$

$$= t_{P'P'}(\Delta) + [t^{M}_{P}(\Delta) - t_{P}(\Delta)] \qquad (5.4)$$

The difference between observed and calculated P'P' that is due to assumptions of a P table is therefore

$$\delta t = t^{O}_{P'P'}(\Delta) - t^{C}_{P'P'}(\Delta)$$

$$= [t^{M}_{P}(\Delta) - t_{P}(\Delta)] - 2\,[t^{M}_{P}(90°) - t_{P}(90°)] \qquad (5.5)$$

The size of the model-related terms in equation (5.5) depend on how well the P-wave model represents the "real" earth. Unfortunately, the "real" earth velocities can only be estimated and one must choose what he feels is the best approximation. Figure 5.9 (from Jordan and Anderson, 1973) shows that recent P tables are generally bracketed by the B1 model of Jordan and Anderson and the 1968 tables in the epicentral distances range of 65° to 90°, the range of applicability here. Therefore the "real" earth values, that is the $t_P(\Delta)$ and $t_P(90°)$ terms in equation (5.5), are assumed to fall somewhere between these two tables. All of the events used for P'P' readings were located with Jeffreys-Bullen tables and all of the P' tables have been correspondingly normalized to the same tables, which are then used for the $t^{M}_{P}(\Delta)$ and $t^{M}_{P}(90°)$ terms in equation (5.5). If we let $\Delta = 70°$, a typical distance for P'P', and use the time differences in Figure 5.9 of the B1 and 1968 tables from the Jeffreys-Bullen values, then δt in equation (5.5) is between -0.6 and -1.2 sec. This correction reduces the previous required adjustment of 2.5 sec in Figures 5.7 and 5.8 to between 1.9 and 1.3 sec, with the observed times still later than those predicted.

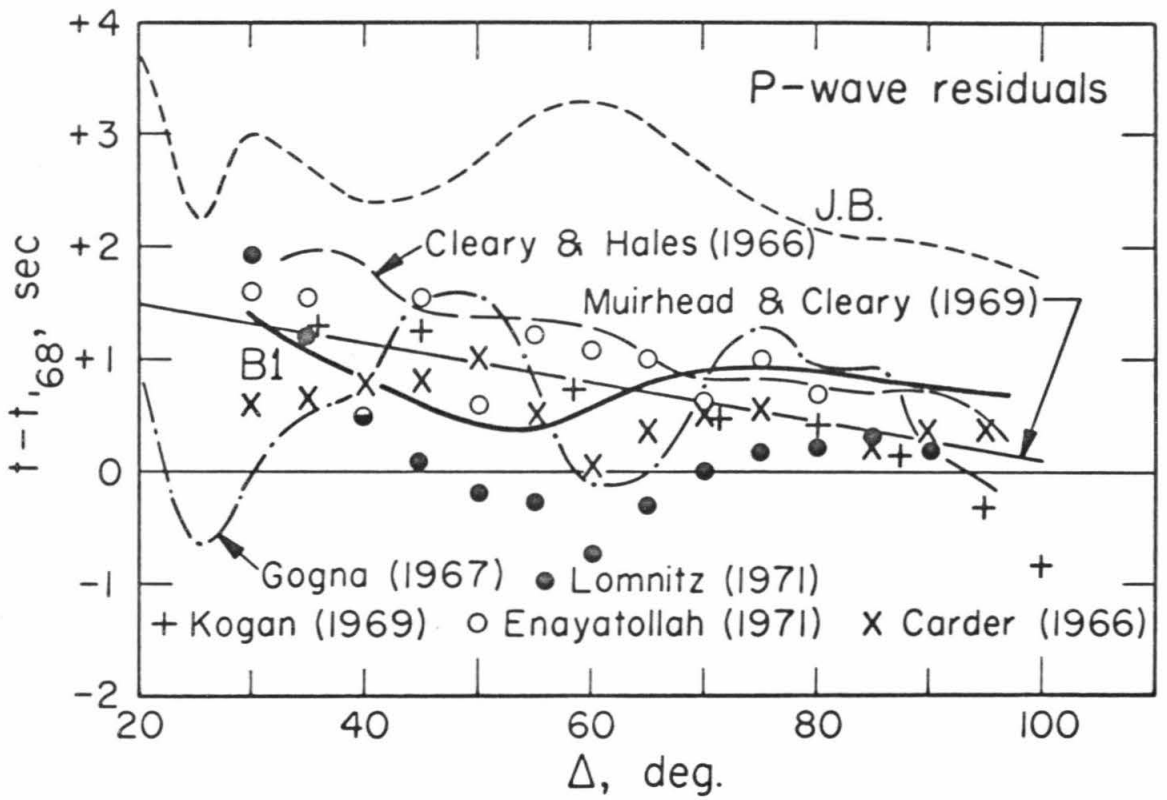

Figure 5.9

Comparison of P-wave travel times relative to the 1968 P tables as a function of epicentral distance for several investigators (from Jordan and Anderson, 1973).

Because differential times were used, near-source and near-station time anomalies should be minimal and the 1.3 to 1.9 sec adjustment is undoubtedly from lateral differences in mantle velocity structure. The nature of the mantle at the two source regions is unclear; both sets of events are associated with trench structures which represent the down-going lithospheric slab in plate tectonic theory. However, anomalous times from these regions are generally believed to be early (for example see Davies and MacKenzie, 1969) which is in the opposite direction of our anomaly. The mantle at the stations is continental and should correspond to the P' tables used to derive predicted P'P' times. Therefore the mantle under the oceanic reflection points is the remaining candidate for an average mantle velocity that will delay times relative to those predicted. Because P'P' traverses the mantle under the reflection twice, the anomaly corresponds to a one-way delay of 0.65 to 0.95 sec (the uncertainty due to reading arrivals to the nearest second is ± 0.25 sec). This is not a large delay and is of the same size as station delays observed in the Basin and Range Province relative to the Central United States (Cleary and Hales, 1966). There appears to be no difference between the time anomaly under a typical oceanic basin, that near the Ninety-East Ridge which is not considered a spreading center, and the time anomaly under a classic spreading center, the Atlantic-Indian Rise.

Although P'P' reflections from the surface of continents is not as dependable because a horizontal surface is not assured there as with the ocean surface, it is interesting to note that the LASA largest amplitudes from Antarctic reflections in Chapter 3 are within a second of zero reduced time as seen in Figure 5.10. This supports the assumption that zero reduced time corresponds to a P'P' reflection under a continent, but there is always the possibility that the arrivals are too early by a few seconds due to asymmetric P'P'. The largest-amplitude reflections are clearly at the ocean bottom for the LASA data near the rises and at the ocean surface for that in the East Indian ocean; the ocean-bottom to ocean-surface 8 sec gap shows up nicely in the latter case. As can be seen in Figure 3.2, the reflection points near -60° latitude are on somewhat younger and sediment-isolated ocean floors compared to the East-Indian ocean points. Thus, varying sediment thickness is an attractive explanation for the largest-amplitude reflection seen from the ocean bottom near the rises (thinner sediments) and from the ocean surface in the East Indian ocean (thicker sediments that reduce the ocean bottom reflection).

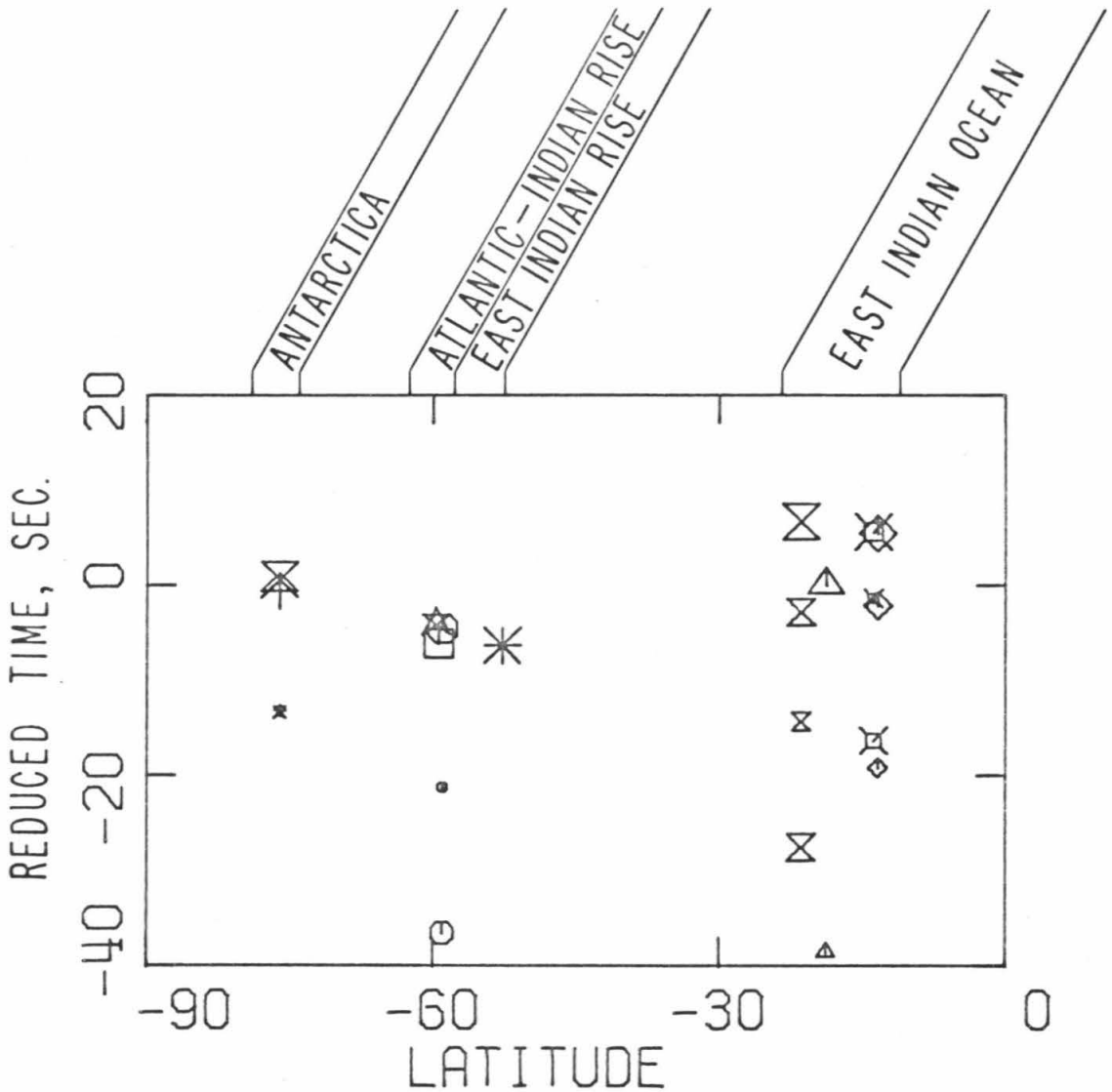

Figure 5.10

Reduced times of the LASA data from Chapter 3. The symbols are the same as those in Figure 3.1.

5.4 Summary. The times of the P'P' phase have previously been thought to scatter too severely to be useful for investigation of earth structure. The problems appear to be due to asymmetric P'P', incorrect identification of the branch, and lack of the proper velocity structure at the reflection point. They are solved by use of the horizontal ocean surface as a reflector, use of the LASA array and largest-relative amplitudes as branch identification tools, and use of detailed bathymetry maps at the reflection points of P'P'. The ocean-bottom reflection is generally the largest-amplitude phase of P'P' but occasionally the ocean-surface reflection is seen to be larger; calculations show that reasonable variations of ocean-bottom type permit either case. The ocean-surface reflection is easily identifiable by its strong time dependence on water depth. When corrected by recent determinations of P velocity in the mantle and core, the predicted times of P'P' agree with observations only if they are delayed by 1.3 to 1.9 sec. This time anomaly is attributed to a delay in the oceanic mantle under the reflection points relative to continental mantle on which the predicted times are based. The anomaly corresponds to a one-way time delay of 0.65 to 0.95 sec which is not exceedingly large. It corresponds in size to time delays observed at stations in the Basin and Range Province relative to the Central United States.

6. CORE STRUCTURE

6.1 Introduction. A multitude of compressional-wave velocity models for the earth's core exist in the literature. Some of these are shown in Figure 6.1 taken from Kovach (1971), who gives a review of core studies. The problems in determining core velocity lie in three main observational difficulties of core phases: 1) structure in different parts of the core must be gleaned from widely different types of core phases, some of which are easier to observe than others; 2) all core phases are observed through the "lens" of the mantle whose effects, which are only partially known, must be removed from the data; and 3) simple identification of certain core phases and their end points has often proved difficult.

The motivation for making a new determination of the core velocity structure arises from some major improvements in core data in the areas outlined above. Use of large seismic arrays enables the direct measurement of $dt/d\Delta$ or wave slowness of core phases which, in addition to being a new independent data set, greatly aids in the identification of core phases. A major modification in the mantle "lens" through which we see the core has been made by Jordan (1972) and Jordan and Anderson (1973); their favored mantle model, called the B1 model in the remainder of this chapter, is significantly different in velocity structure and core radius from those previously used for core studies. Finally, amplitudes of the PKP branches

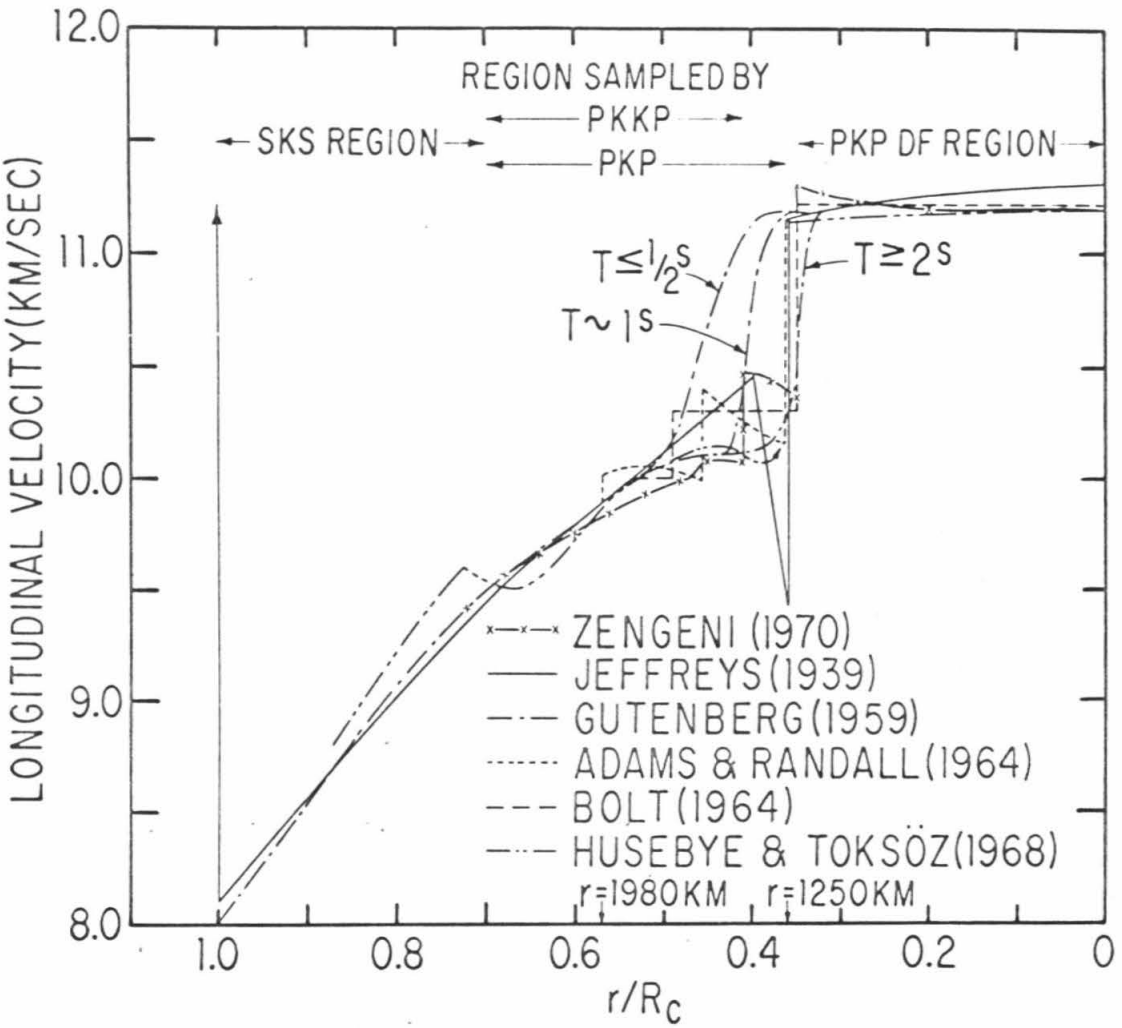

Figure 6.1

A sample of compressional-wave velocity models of the earth's core from Kovach (1971).

are better known and provide additional constraints on core models.

The nomenclature of core phases has a rather complicated history largely due to the problems of phase identification. The notation of PKP, SKS, PKS, etc., is well established. P or S denotes ray travel in the mantle and K is the ray segment in the core; P' is the accepted shorthand for PKP. Discovery of the inner core by Lehmann (1936) led to the definitions PKIKP and PKiKP(Jeffreys, 1939a) where travel through the inner core is denoted by I and reflection from the inner core boundary by i, respectively. In anticipation of the results of this paper, the labeling of the end-points of the PKP or P' branches by Jeffreys (1939b) is adopted as shown in Figure 6.2. With the use of these end-points and the notation of Adams and Randall (1964), the abbreviated form is adopted where P'_{AB} identifies the branch of the P' curve from points A to point B and P'_{DF} is used in place of PKIKP. P'_{CD} is the same as the reflection PKiKP but since the inner core reflection exists at distances shorter than point D, the notation PKiKP is retained. Figure 6.3 shows the ray paths followed by the P' phases of Figure 6.2; each ray is emitted from the surface source at take-off angles spaced by 0.2° intervals. For the ray tracing, the P-wave velocities in model B1 are used for the mantle and the final velocity model of this paper is used for the core. The shallowest ray to enter the core defines point A and steeper rays follow the P' curve of Figure 6.2 through

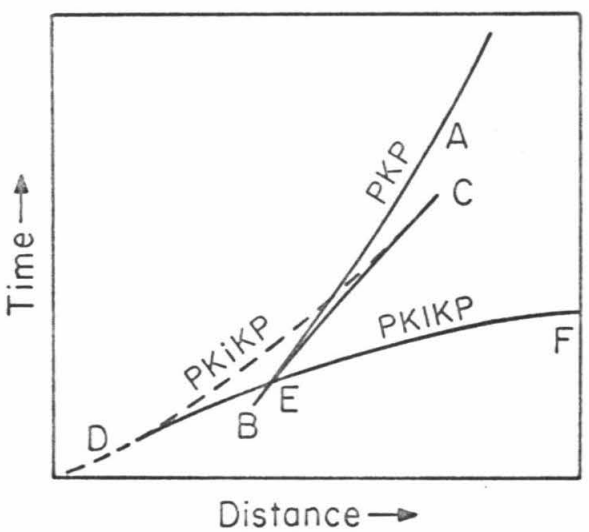

Figure 6.2

P' branches and end-point designations after Jeffreys (1939).

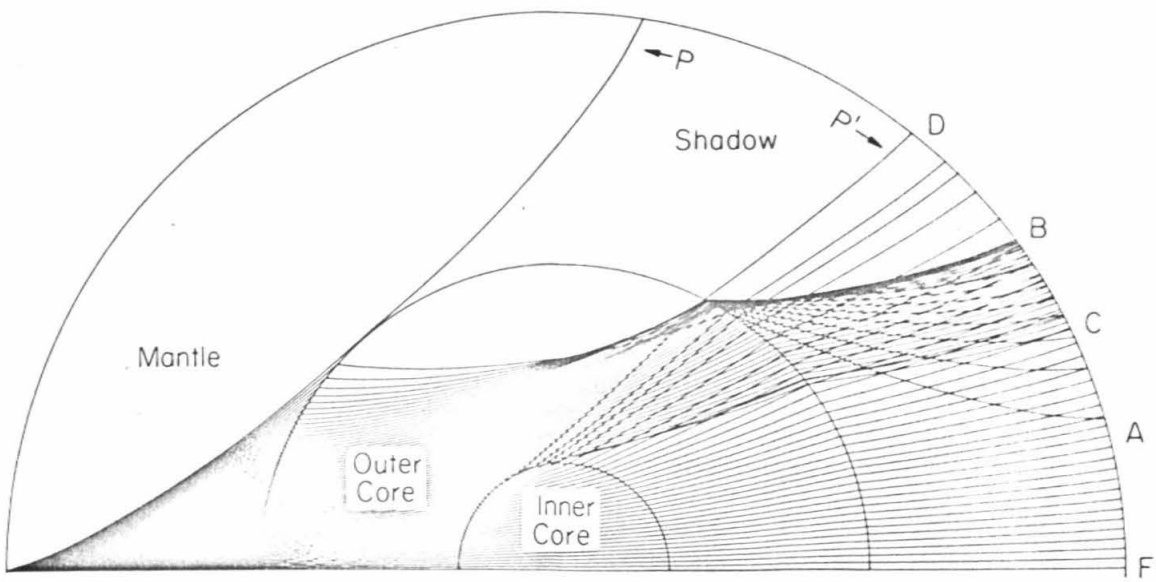

Figure 6.3

P' ray tracing from a surface source at take-off angles spaced by 0.2 deg intervals. The Jordan (1972) model is used for the mantle and the final model of this paper is used for the core.

points B, C, D, and finally F, which is the ray that points straight down from the source.

The plan of this study is to use observations of times, $dt/d\Delta$, and amplitudes of core phases to construct a consistent $dt/d\Delta$ data set as a function of distance for the core phases, P', SKS, and SKKS. The times of PmKP, where m is 2 or greater, are not used for the inversion because of the phase's maximum time nature. The mantle times and distances are stripped away using PcP and ScS (reflections from the core-mantle boundary) from the Bl model to get a $dt/d\Delta$ curve corresponding to the surface of the core. The classic Wiechert-Herglotz integration method is applied to the curve to obtain P-wave velocity with depth in the core and the resulting velocity model is then checked and modified by P' and PKiKP absolute times. Finally, oceanic and continental mantle velocity differences, Q structure of the core, and scattering of core phases are discussed in relation to the final core velocity model and observed data.

6.2 Method. P' is easily observed on short-period instruments and is in a relatively clear part of the travel-time chart. It therefore has the best-determined times, $dt/d\Delta$'s, and amplitudes of the core phases and it would be desirable to use this phase for determining velocity throughout the core. Unfortunately, the outer

part of the core is a low-velocity zone for P' because of the high-velocity mantle which prevents those rays from bottoming above a radius of 2400 km. P', therefore, can be used only to obtain an average velocity above that level. The phases SKS and SKKS, while not as well-determined as P' due to their long-period character and the fact that earlier arrivals may obscure their beginnings, do bottom in the outer core and are the best phases available for velocity inversion at those levels. In order to strip away the effects of the mantle from the different core phases and put them on a common basis, the classic method developed by Wadati and Masuda (1934) is employed. It consists of the use of PcP or ScS data with a specified $dt/d\Delta$ and subtraction of the time and distance from the corresponding core phase with the same $dt/d\Delta$. This process effectively removes the times and distances of the P legs from PKP and the S legs from SKS and SKKS to leave only the time and distance traveled in the core, denoted t_K and Δ_K, respectively. The $dt/d\Delta$ for a given ray is left unchanged in the process. At this point, all the different types of core data are reduced to a common base, that is, the core-mantle boundary, and analysis can proceed as if the mantle were absent.

With Δ_K and $dt/d\Delta$ data for a family of rays that start and end at the core-mantle boundary, the standard Wiechert-Herglotz

method can be applied to obtain the radial velocity distribution in the core (Bullen, 1963). Inherent in the Wiechert-Herglotz method is the assumption that the ratio r/v, where r is radius and v is P-wave velocity, is a continuously decreasing or constant function as r decreases. If this requirement is not fulfilled, then a level exists where rays do not bottom which is defined as a "low-velocity zone". Note that v may drop with decreasing r without a low-velocity zone being present as defined above as long as r/v is constant or decreasing at the same time. Proof of the existence or absence of a low-velocity zone is one of the most difficult tasks in seismological inversion, but in this study, all of the data are found to be satisfied with no low-velocity zone in the core.

6.3 Data. The gathering and reduction of core phase data, including corrections for ellipticity for possible errors in source locations and origin times, is a significant undertaking. Because of this, most core studies tend to concentrate on specific phases or branches. One of the major problems in attempting to combine several sets of core data is to account for the varying assumptions and models that are implicit in the data reduction process; these are generally referred to in the literature as baseline corrections. There are two general types of baseline corrections: those that use a certain time table or velocity model as a reference, termed

here as a model baseline, and those that use a specific group of stations as a reference, termed here a station baseline. Combinations of these types are often used. In this study, when a data set includes the model baseline correction, the correction is adjusted to correspond to the mantle model B1 which is the reference mantle used throughout. When a data set includes the station baseline correction, which uses a group of stations as a reference, no adjustment is made to the data. However, we should recognize that, if there is a difference between oceanic and continental mantle, the data are biased towards the continents which are the base for almost all stations. Some of the results of this paper bear on the station baseline problem.

Model B1 satisfies a large number of normal mode and differential travel time data, in addition to the mass and moment of inertia of the earth. Because of the averaging nature of this data, the model more nearly represents a earth-wide average of the mantle velocities than earlier determinations. Jordan and Anderson (1973) made an estimate of the core radius using differential times of PcP-P and obtained a value of 3485 km. This is somewhat larger than that attributed to Jeffreys (1939c) of 3473 km and Taggert and Engdahl (1968) of 3477 km. However, the recent results of Hales and Roberts (1970b) and Engdahl and Johnson (1972) support the larger value.

The P'_{DF} times used here are those of Cleary and Hales (1971) who estimated the times, station anomalies and source anomalies for

18 events over the entire range of the phase, 110° to 180°. Cleary and Hales adjusted their data to a model baseline by making the times relative to their P travel-time curve between 94° and 100°. Thus, the times for P'_{DF} depend on the times for P at 100° and they are not the same for other models. In order to make their data set compatible with the B1 mantle, 0.4 sec was added. Cleary and Hales also adjusted their data to a station baseline by specifying that stations in shield areas have anomalies of about -1.0 sec and stations in the Basin and Range Province of the United States have anomalies of about +1.0 sec. Because of the ease with which P'_{DF} is observed, it is considered the most dependable of the core-phase data sets and no further modifications are made to the Cleary and Hales data. However, the results of this paper do suggest some minor changes near point D of the branch.

Theory requires that P'_{DF} be concave downward along its entire length while PKiKP, the reflection from the inner core, is concave upward; the two phases are tangent to each other at point D. As Cleary and Hales point out, their fit of an eighth-order polynomial to the data has an upward curvature near 110°. The reversal of curvature occurs at 121°, although they believe that the reversal is not significant and that a straight line can be just as readily fit to the data between 110° and 135°. Upward curvature or at least a stright-line fit between 110° and 135° has been found in

previous studies of the P'_{DF} branch (Gogna, 1968; and Bolt, 1968) and indicates that we are not forced to bring the point D to as short a distance as 110°, as done by Jeffreys (1939a). At distances shorter than point D, PKiKP is a partial reflection. Therefore, we expect a sharp dropoff in amplitude of the P'_{DF}-PKiKP arrival as the observer passes through D towards shorter distances (see, for example, the calculations of Buchbinder, 1971). Use of this criterion with the P'_{DF} amplitude studies of Denson (1952, Figure 8), Hai (1963, Figures 15 and 16), and Buchbinder (1971, Figures 6-10) places the point D in the range of 120° to 125°. Point F is of course at 180° with a $dt/d\Delta$ of zero.

The times for the branch P'_{AB} are constructed initially from P'_{AB}-P'_{DF} differential times, a measurement which requires no assumption of baselines, which are then added to the P'_{DF} times already tabulated. The P'_{AB}-P'_{DF} differential times are taken from the tables of Bolt (1968) and are in substantial agreement (except for a difference of 1.0 sec near 158°) with those measured by Jordan (1972) as seen in Figure 6.4. Point B is a caustic which results from the outer core appearing as a low velocity zone to the P' phase. There is no equivalent caustic for the phases of the type SKS. Diffraction from the ray theoretical position of the caustic by one-second-period energy should be limited to less than 3° according to calculations by Jeffreys (1939b). As discussed below,

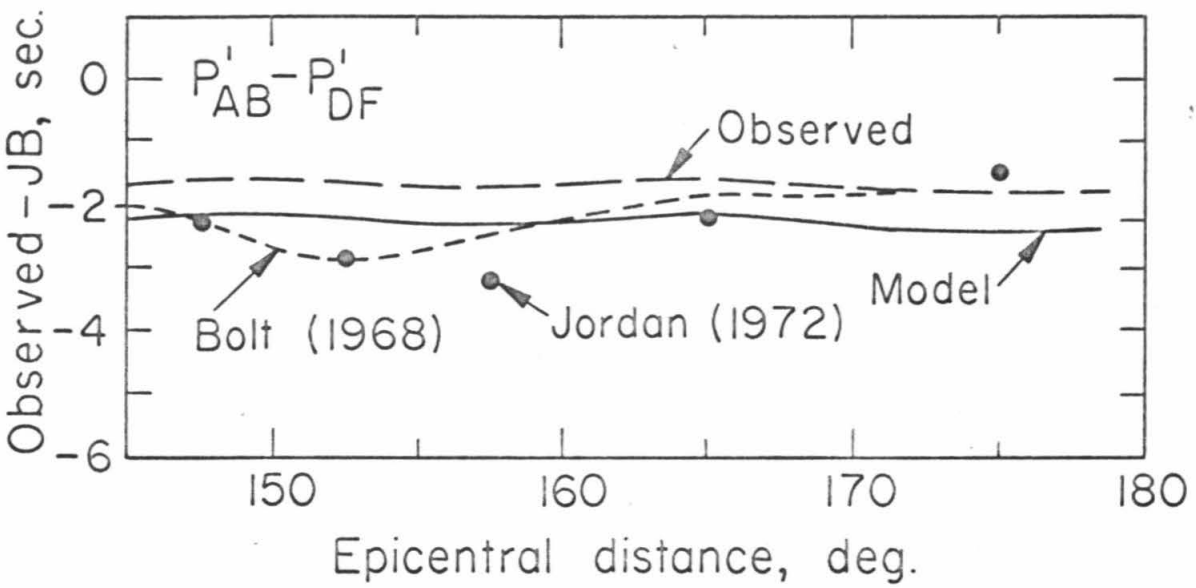

Figure 6.4

$P'_{AB}-P'_{DF}$ differential times of Bolt (1968) and Jordan (1972) relative to the Jeffreys-Bullen tables. The observed data for model inversion and the final model are also shown.

evidence suggests that asymmetries of the earth cause arrival of scattered energy at much shorter distances, but this should not greatly affect the location of the caustic because the amplitudes at point B dominate all other P' energy. Shahidi (1968) gives a good review of efforts to locate the B caustic and, by fitting his amplitude data to the expected distribution calculated from the Airy integral, he places the ray theoretical caustic at 144.2°, the initial value used here. The point A is difficult to fix precisely from available data. The curvature of the P'_{AB} travel-time curve becomes small towards A which requires that the amplitudes also become small. This effect, combined with diffraction into the shadow zone beyond A by finite-wave-length energy (discussed by Richards, 1973, and others) means that A is not marked by a sharp dropoff in amplitudes. Bolt (1968) measured what he believed to be weak P'_{AB} phases at 185° and the P' records of Jordan (1972, Figures 4.7 and 4.8) show P'_{AB} to be clear arrivals at 176°. The position of A is not as sensitive to core velocity structure as it is to the velocity at the base of the mantle (as pointed out by Buchbinder, 1972) and deviations from spherical symmetry at the core mantle boundary. Thus, because its precise position does not greatly affect derivation of the core model, point A is loosely constrained to be between 175° and 185°.

Gutenberg (1957, 1958, and 1959) reported short period arrivals

preceding P'_{DF} in the range 110° to 143° which he attributed to a dispersive layer in the earth just above the inner core. Bolt (1962), Adams and Randall (1964), Ergin (1967), Engdahl (1968), Zengeni (1970), Buchbinder (1971) and others explained these arrivals as due to one or more separate branches of P' that derive from spherically symmetric discontinuities just above the inner core. The scattered nature of these arrivals has more recently led Haddon (1972) to postulate that they are due to irregularities on or near the core-mantle boundary, not to structure deep within the core. Supporting Haddon's hypothesis, Müller (1973) computed theoretical seismograms from the Bolt (1964) core model and found that the phases predicted by the model's discontinuity just above the inner core were not observed on long-period seismograms. The recent measurements of Doornbos and Husebye (1972) at the NORSAR array in Norway suggest that the P'_{DF} precursors have $dt/d\Delta$'s near 3.3 sec/deg in the range 136° to 143°, just before the B caustic. But, no energy with $dt/d\Delta$ near that of P'_{GH} of the Bolt (1968) tables is seen. This agrees with the scattering hypothesis as discussed below, but it does not rule out the P'_{IJ} branch hypothesis of Adams and Randall (1964).

If the P'_{DF} precursors are indeed P' branches from spherically symmetric discontinuities within the core, they should have coherency equivalent to that of P'_{DF}. Their amplitudes on short-period seismograms have been shown by Buchbinder (1971, Figures 6-10) to be

largest near 140°, just before the B caustic, where they are approximately equal to the amplitudes of P'_{DF}. Beam-forming at the LASA array in Montana has demonstrated that the main core phases are coherent across that array (Whitcomb, 1971; and Davies et al., 1971) which is about twice the aperture of the NORSAR array. Therefore, the branches in question should always be seen at the proper $dt/d\Delta$ in the range near 140° just as the other core phases are always seen at their respective $dt/d\Delta$'s and distances. Davies et al. (1971) investigated P' phases for one event at distances shorter than the B caustic at 143.2° and found no coherent energy other than that for the P'_{DF} phase. The same results were seen by Whitcomb (1971) for the P'P' phase of two events at 75.6° and 75.8°; these distances are equivalent to P' at 142.2° and 142.1°, respectively. In order to confirm these results, beam-forming was performed at LASA for 4 events in the distance range 130° to 142°. Figure 6.5 shows two examples of the resulting vespagrams (contour plots of beam power as a function of time and $dt/d\Delta$ in the direction of the event) for events near 135.4° and 139.5°. No coherent energy is seen at the $dt/d\Delta$'s other than that of P'_{DF} in the two examples shown or in the remaining two events, which are at distances of 137.8° and 140.1°. Thus, the precursors to P'_{DF} are definitely not coherent across an array that is the size of LASA as the established P' and P'P' branches have proven to be. This conclusion strongly supports

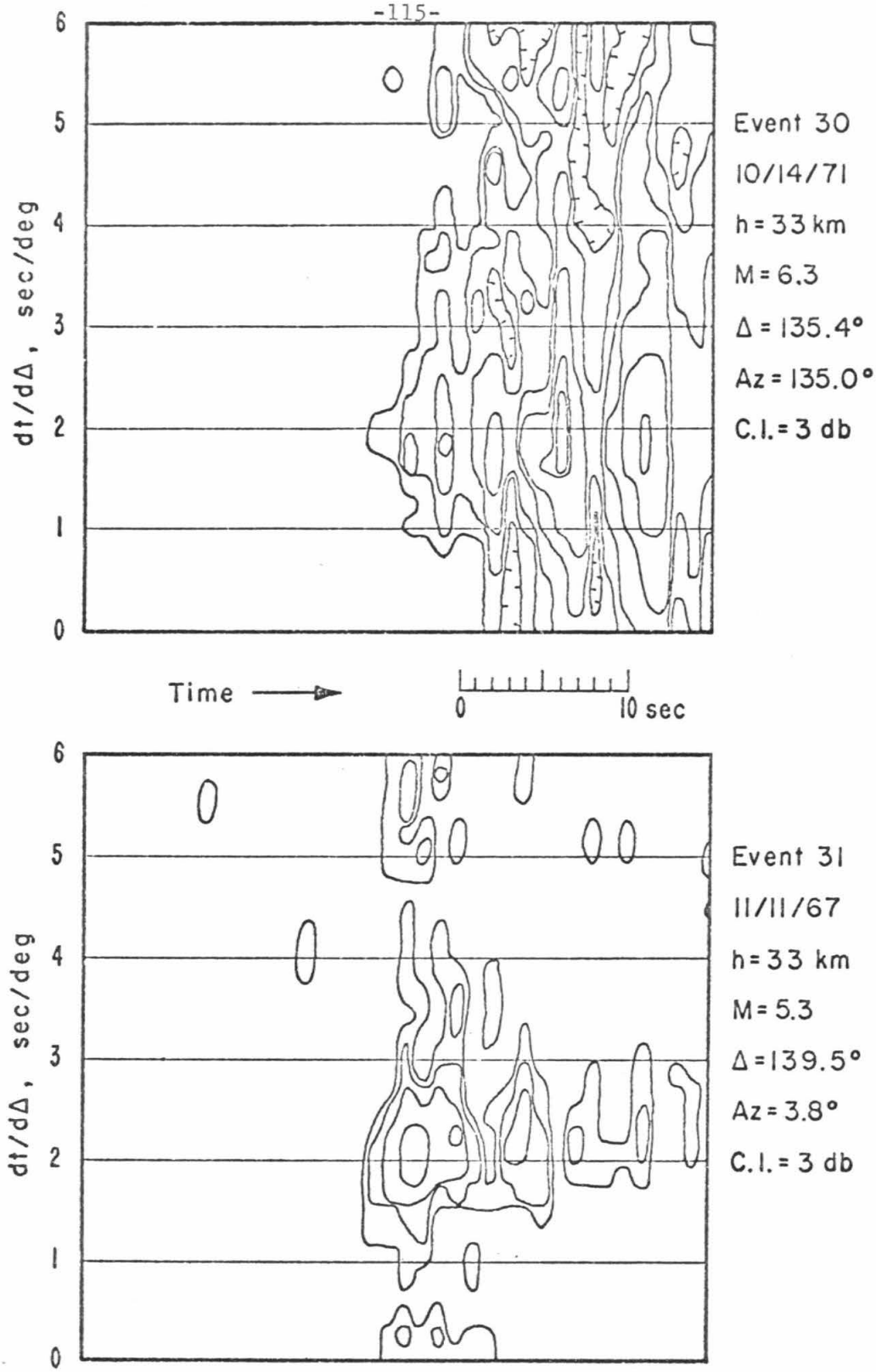

Figure 6.5. Vespagrams (contour plots of beam power as a function of time and $dt/d\Delta$ in the direction of the event) of P' in the epicentral distance ranges 135.4° and 139.5°.

Table 6.1

dt/dΔ Measured at LASA

Event No.	Date	Origin Time Lat. Long. Depth Magn.	Surface-Focus Δ(deg)	Azimuth of Arrival (deg)	Equiv. P' Δ(deg)	dt/dΔ (sec/deg)	Phase
8	09/03/67	21 07 30.8	61.7	330.2	149.2	4.3	P'P'
		10.6 S 79.8 W			149.2	2.6	P'P'
		38 6.5			149.2	1.7	P'P'
					150.4	2.5	P'640P'
9	12/21/67	02 25 21.6	75.6	325.5	142.2	1.8	P'P'
		21.8 S 70.0 W			143.1	1.8	P'640P'
		33 6.3					
10	12/27/67	09 17 55.7	75.6	323.7	142.1	2.0	P'P'
		21.2 S 61.3 W			144.1	3.6	P'640P'
		135 6.4					

Table 6.1 (continued)

Event No.	Date	Origin Time / Lat. / Depth	Long. / Magn.	Surface-Focus Δ(deg)	Azimuth of Arrival (deg)	Equiv. P' Δ(deg)	dt/dΔ (sec/deg)	Phase
11	06/19/68	08 13	35.0	58.0	325.3	151.0	4.3	P'P'
		5.6 S	77.2 W			151.0	2.3	P'P'
		28	6.6			151.0	1.5	P'P'
						152.2	2.3	P'640P'
5	01/29/68	10 19	05.6	69.3	132.1	145.3	3.4	P'P'
		43.6 N	146.7 E			147.4	3.8	P'640P'
		40	7.0					
12	05/16/68	10 39	01.5	72.9	132.9	143.5	3.3	P'P'
		41.5 N	142.7 E			143.5	2.0	P'P'
		33	6.5					
22	08/12/69	05 03	26.9	68.7	131.4	145.7	3.5	P'P'
		43.6 N	148.0 E			147.0	2.7	P'640P'
		33	6.5					

Table 6.1 (continued)

Event No.	Date	Origin Time Lat. Long. Depth Magn.	Surface-Focus Δ(deg)	Azimuth of Arrival (deg)	Equiv. P' Δ(deg)	dt/dΔ (sec/deg)	Phase
15	11/07/68	10 02 05.2	59.5	186.2	150.3	4.1*	P'P'
		73.4 N 54.9 E			150.3	2.7*	P'P'
		0 6.0			150.3	1.6*	P'P'
					151.5	2.6*	P'640P'
16	10/14/69	07 00 06.2	59.5	186.2	150.3	4.1*	P'P'
		73.4 N 54.8 E			150.3	2.7*	P'P'
		0 6.1			150.3	1.6*	P'P'
					151.5	2.4*	P'640P'
18	02/28/69	04 25 36.9	68.2	240.1	145.9	3.1	P'P'
		36.2 N 10.5 W			148.0	3.2	P'640P'
		33 5.7					

Table 6.1 (continued)

Event No.	Date	Origin Time Lat. Long. Dept. Magn.	Surface-Focus Δ(deg)	Azimuth of Arrival (deg)	Equiv. P' Δ(deg)	dt/dΔ (sec/deg)	Phase
30	10/14/71	22 36 28.6 54.3 S 1.8 E 33 6.3	135.4	135.0	135.4	1.6	P'
31	11/11/67	15 05 10.3 6.1 S 71.3 E 33 53.3	139.5	3.8	139.5	2.0	P'

*0.6 sec/day added

the hypothesis that these phases are not normal P' branches but are scattered energy due to asymmetries somewhere in the earth.

A strong P' arrival is present in the distance range 146° to about 155° at times between the P'_{AB} and P'_{DF} phases. The simplest explanation of this phase is a continuation from the caustic B to point C as shown in Figure 6.2. Adams and Randall (1964) made a special study of arrivals between P'_{AB} and P'_{DF} and their data are shown in Figure 6.6 in the form of a reduced time plot (reduced by 2.6 sec/deg). Adams and Randall did not adjust their data to a model baseline but instead used several explosions and deep earthquakes for which the hypocenters were specially studied. Their data, reduced to a surface focus, are somewhat dependent on the Jeffreys-Bullen tables used for locating the events, but they did not specifically use a model baseline and no baseline adjustments were made. The P' branches shown in Figure 6.6 are discussed below.

The $dt/d\Delta$'s for P' have been measured directly using the LASA seismic array. Data from Whitcomb (1971) with some new measurements for P', P'P', and P'640P' (the P'P' phase reflecting at 640 km) are given in Table 6.1. Distances in the table for the latter two wave types are for the corresponding P' phase distance for ease of comparison. These data plus data for P' from Davies et al. (1971) measured at LASA and Doornbos and Husebye (1972) measured at NORSAR are plotted as a function of epicentral distance in Figure 6.7. As

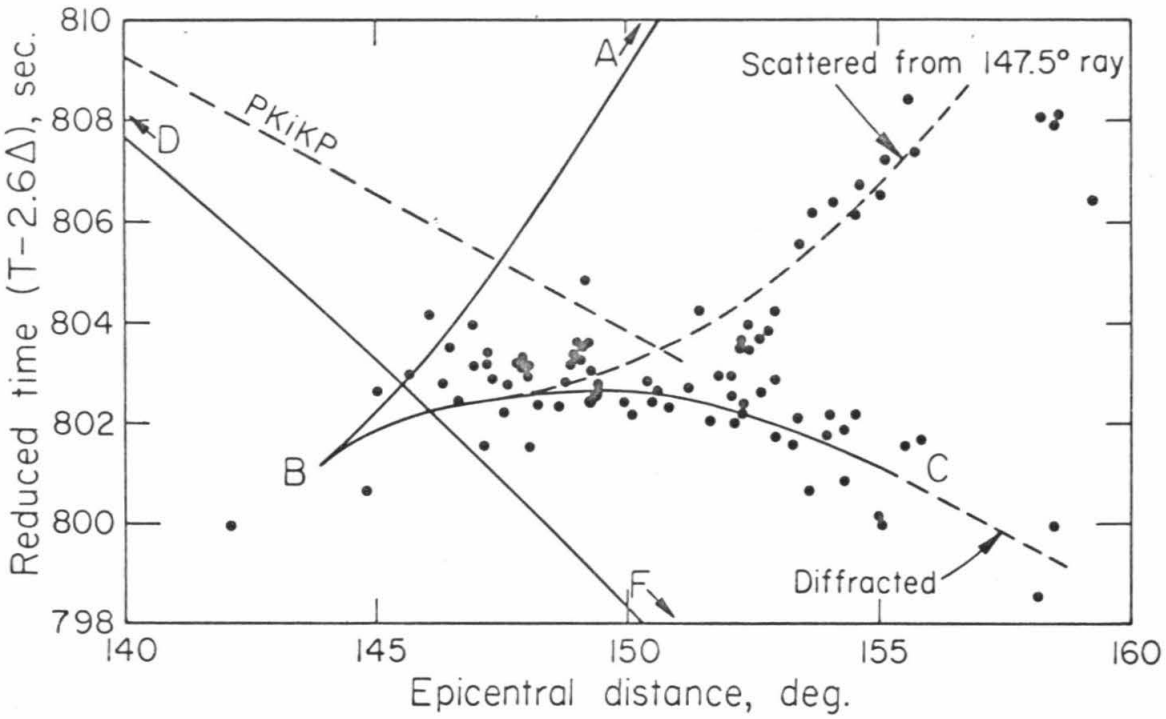

Figure 6.6

Arrivals between P'_{AB} and P'_{DF} shown in a reduced time plot (reduced by 2.6 sec/deg) from Adams and Randall (1964). The branches P'_{AB}, P'_{DF}, and the final fit of P'_{BC} to the data are shown.

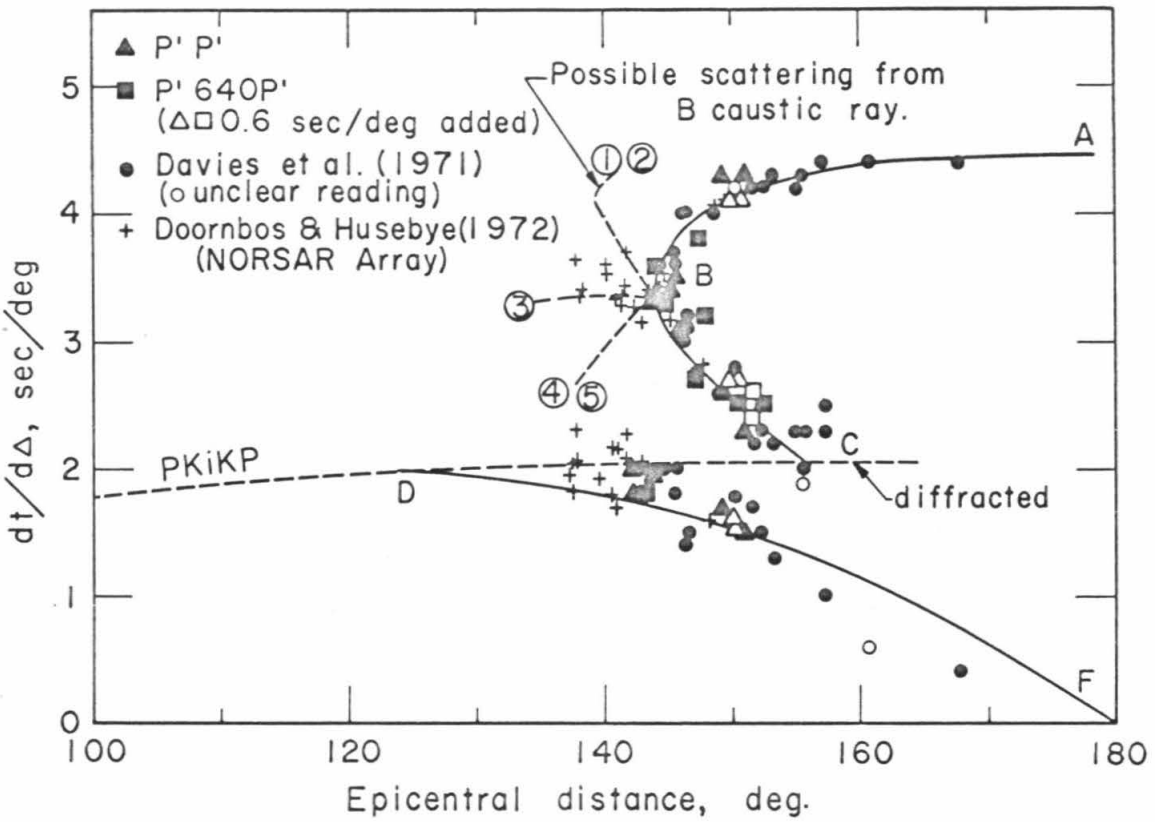

Figure 6.7

dt/dΔ measured at LASA as a function of distance for P', P'P', and P'640P' phases; distances for the latter two phases have been adjusted to the corresponding P' phase distance.

can be seen, the A-B-C part of P' is very well defined by the $dt/d\Delta$ data. P'_{DF} is not as well defined, partly because there are few data beyond 155° and because most of the data are in a distance range where P'_{DF} is complicated by the other P' phases arriving near the same time (see Figure 6.2). The data from NORSAR between 3 and 4 sec/deg at distances shorter than B will be discussed later. There is no obvious dependence in Figure 6.7 on azimuth of arrival for most of the LASA data, which is a measure of how well the individual station anomalies within the array are determined. There is an exception however in Events 15 and 16 in Table 1, which arrive from the south at an azimuth of 186.2°. Three different branches are present on the vespagrams for both events and their data fit that of Figures 6.7 only if 0.6 sec/deg is added to the measured $dt/d\Delta$'s. The points, which have been adjusted by this amount, are marked with parentheses in Table 6.1 and as open triangles and squares in Figure 6.7. These events indicate that the LASA station anomalies need revision for steeply incident arrivals from the south.

Amplitudes at a given distance are required by ray theory to be proportional to $\sqrt{|d^2t/d\Delta^2|}$ ignoring Q effects (Bullen, 1963). Thus, the amplitudes are a function of the slope of the $dt/d\Delta$ curve or the curvature of the travel-time curve. In practice, measured amplitudes scatter considerably (see for example Buchbinder, 1971; Figures 6-10; and Jordan, 1972, Figures 4.7 and 4.8). However,

for multiple core phases arriving at the same distance, Adams and Randall (1964), Whitcomb and Anderson (1970) and Whitcomb (1971) have shown that one phase is usually the largest and this simple information over the P' range is found to be an extremely useful constraint when used in conjunction with the independently determined times and $dt/d\Delta$'s. Table 6.2 summarizes the approximate ranges and corresponding largest relative amplitudes for the P' phases. The ranges from 154° to 180° where the largest amplitudes are either P'_{AB} or P'_{DF} are determined from data of Hai (1963), Engdahl (1968), Buchbinder (1971), and Jordan (1972) that are shown as P'_{AB}/P'_{DF} amplitude ratios in Figure 6.8. A large amount of scatter allows only an approximate estimation of the distance where P'_{AB}/P'_{DF} drops below one, taken as 61° ± 7° epicentral distance. The large scatter of P'_{AB}/P'_{DF} may be an indication of lower mantle or core asymmetries; for example small corrugations of the core-mantle boundary cause large variations of the P'_{AB} and P'_{DF} amplitudes as illustrated by the simplified calculation of Jordan (1972, Figure 4.10).

The amplitudes and $dt/d\Delta$'s are especially useful in determining the travel-time curve of P'_{BC}, which has been subjected to the most variable interpretation in the past because of interference in the region of the B caustic. The determination procedure began with an

Table 6.2

Ranges of the Largest-Relative-Amplitude P' Phases

Epicentral Distance	P' Branch
< 143.8°	P'_{DF} or PKiKP
143.8° - 148.7°	P'_{AB}
148.7° - 153.5°	P'_{BC}
153.5° - 161° (±7°)	P'_{AB}
161° (±7°) - 180°	P'_{DF}

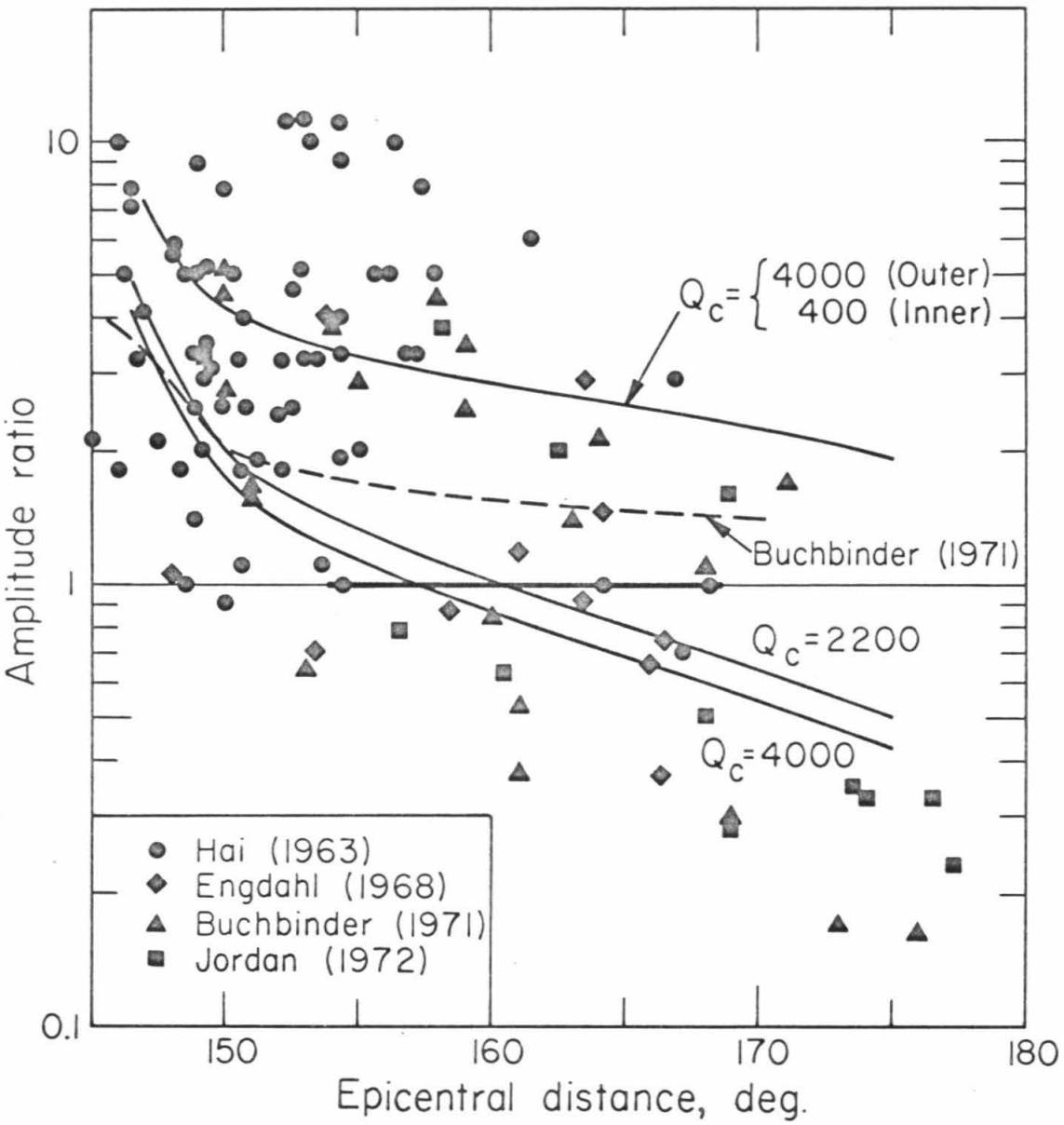

Figure 6.8

Observed and calculated amplitude ratios of P'_{AB}/P'_{DF}. Various Q structures are used with the final model and periods of one second for the calculations. The result of Buchbinder (1971) is also shown.

initial fit of a curve to the travel-time data of Figure 6.6. Point C was initially set at 154° because both the travel-time data of Figure 6.6 and the $dt/d\Delta$ data of Figure 6.7 appear to scatter beyond that distance. The scatter is taken as an indication of amplitude drop due to entry into the ray shadow, and arrivals at greater distances would therefore be diffracted around the inner core. The expected diffracted phase is shown in Figures 6.6 and 6.7. An initial $dt/d\Delta$ curve was derived from a curve fit to the time data of Figure 6.6. The $dt/d\Delta$ curve was then adjusted to agree with the $dt/d\Delta$ data of Figure 6.7 while maintaining constant the quantity

$$\int_B^C \left(\frac{dt}{d\Delta}\right) d\Delta \qquad (6.1)$$

which is equivalent to fixing the ends of the travel-time curve at points B and C. The same procedure of combining time and $dt/d\Delta$ data was applied to constructing a $dt/d\Delta$ curve for P'_{AB}. A $dt/d\Delta$ curve for P'_{DF} was calculated directly from the times without further modification because of the paucity and scatter of $dt/d\Delta$ data as seen in Figure 6.4, and the assumed dependability of the time readings due to the clarity of that phase. At this point, the maximum relative amplitude determinations were used by requiring that $|d^2t/d\Delta^2|$, or the derivative of the calculated $dt/d\Delta$ curves, be largest for the

largest amplitude phase in each range defined in Table 6.2. During the adjustments, the integral properties of the time and dt/dΔ curves defined by quantities similar to (6.1) and

$$\int_B^C \left(\frac{d^2t}{d\Delta^2}\right) d\Delta \qquad (6.2)$$

were maintained constant, which effectively fixes the ends of the curves. $d^2t/d\Delta^2$ was smoothed on all data sets. As a result of the dt/dΔ and amplitude adjustments, the original times for P'_{BC} that were determiend from the data of Figure 6.6 were shifted by no more than 0.3 sec. However, P'_{AB} times were shifted by + 1.2 sec in the region near 152°. This was mainly due to the large values of dt/dΔ between about 148° and 155° seen in Figure 6.7. Possible reasons for this are discussed later. The dt/dΔ of point C is fixed at 4.50 sec/deg by the P-wave velocity and depth at the base of the mantle model used. At point B, it was initially fixed at 3.30 sec/deg from the travel-time data and partly from comparison with the data in Figure 6.7; the final model has 3.36 sec/deg. The dt/dΔ at point C is important because the difference between it and the dt/dΔ at point D, which is well determined at 1.98 sec/deg (1.95-1.99), determine the velocity jump at the inner core boundary. Unfortunately, the scatter of both the time data of Figure 6.6 and the dt/dΔ data

of Figure 6.7 allow only loose limits to be put on the $dt/d\Delta$ of C, 2.0 to 2.3 sec/deg. Thus, the time and $dt/d\Delta$ data appear to loosely constrain the velocity jump at the inner core boundary to be between 0.11 and 1.49 km/sec. However, as discussed below, the introduction of PKiKP data provides additional constraints that allow a better determination of the velocity jump.

The initial data for SKS and SKKS were taken from Hales and Roberts (1970 and 1971) who fit polynomials to their data after calculating station anomalies and source anomalies. They adjusted the times to a station baseline which would give stations in the central United States a zero station anomaly. Their data for SKS range from 85° to 126° and those for SKKS range from 90° to 126°, and are given by the polynomials

$$t_{SKS} = 1493.96 + 4.61\ (\Delta - 105.0) - 0.0440\ (\Delta - 105.0)^2 \qquad (6.3)$$

$$t_{SKS} = 1539.18 + 7.02\ (\Delta - 105.0) - 0.0161\ (\Delta - 105.0)^2 \quad . \qquad (6.4)$$

6.4 Inversion and Discussion of Results. Appendix 1 gives Δ, t and $dt/d\Delta$ data for the core phases P', SKS, and SKKS in one-degree intervals of Δ along with the corresponding Δ_k and t_k values obtained by stripping the B1 mantle from the data. The resulting $dt/d\Delta$ data as a function of Δ_k used for the initial Wiechert-Herglotz inversion

are shown in Figure 6.9. The separation of the points in the figure corresponds to one degree spacing of the indicated phase on the earth's surface. As can be seen, rays arriving in a one degree interval at the earth's surface near the B caustic of P' sample a broad depth range of the core, whereas rays in a one-degree interval near point A sample an extremely narrow depth range of the core. This effectively constrains the shape of the P'_{AB} travel-time curve near point A much more than near point B, and also implies that changing the Δ of point A a few degrees will affect the velocity in only a small region of the core.

Because the parameters of the P', SKS, and SKKS phases are measured independently, the agreement of $dt/d\Delta$ where they overlap in Figure 6.9 is a measure of the consistency of the data. It is seen that SKS and SKKS agree where they overlap (as noted by Hales and Roberts, 1971), and that SKS agrees with the $dt/d\Delta$ of P' at point A. However, SKS increasingly deviates from P' at greater Δ_k ranges and the deviation reaches a significant amount past the data from point B of P'. The P' $dt/d\Delta$'s are believed to be more reliable in this range because they were derived both from direct measurements and observed times, whereas those for SKS were obtained from a second-order polynomial fit to the data; the polynomial-fitting process allows the largest errors of the first derivative near the ends of the fit. The connecting points of the $dt/d\Delta$ data for P', SKS, and

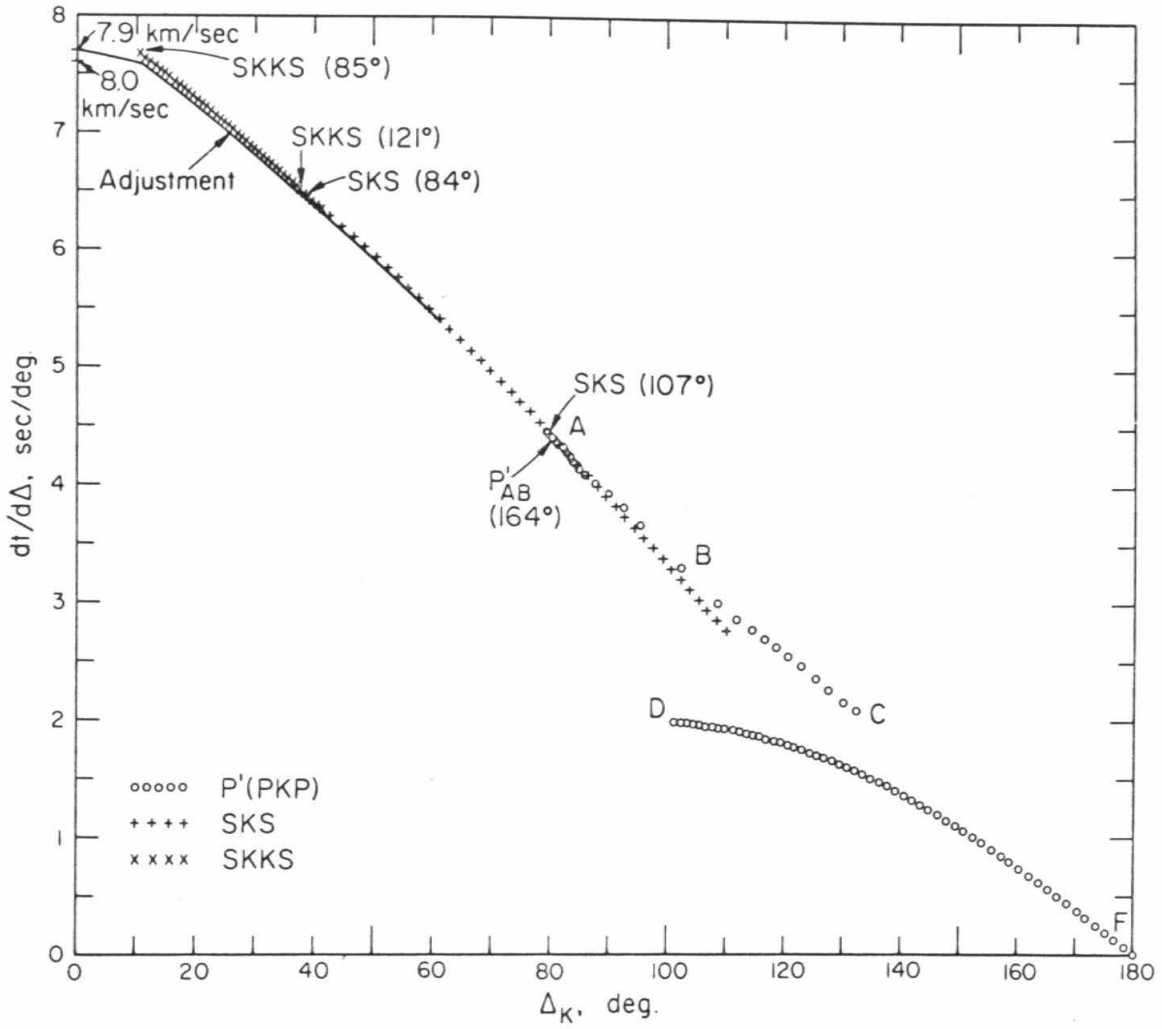

Figure 6.9

dt/dΔ as a function of Δ_k for the core phases used in the Wiechert-Herglotz inversion. The ranges where the different phases were joined are indicated. An adjustment was made to the SKS and SKKS data as shown for the final model.

SKKS are shown in Figure 6.9. It is seen from the figure that coverage is still not complete in the first 10° of Δ_k, which corresponds to about the outermost 24 km of the core. Velocities in this interval will have little effect on the average velocity through the core, but they are important for an initial starting value in the Wiechert-Herglotz inversion. Once the radius of the core is fixed, the velocity at the surface of the core is determined by the $dt/d\Delta$ value at $\Delta_k = 0°$. It will be seen that, although $dt/d\Delta$ and therefore velocities in this range must be assumed, an upper limit of 8.0 km/sec can be put on the velocity at the surface of the core if a low velocity zone is not present.

When an initial inversion of the $dt/d\Delta$ data is done, with an assumption of the starting velocity at the core surface, it is readily apparent that the data set thus far developed is relatively insensitive to the radius of the inner core. Without a precise determination of the inner core radius several other variations in the model are permitted involving tradeoffs between the velocity jump at the inner core, the positions of the points C and D of P'. and the relative times of the P' branches. The radius of the inner core boundary is most sensitive to the times of the phase PKiKP at short epicentral distances (0° to 50°), and this phase has been identified for explosions and earthquakes by Engdahl et al. (1970) and others. A one second shift in the time of PKiKP (or in the

travel time through the outer core) gives only a 5 km shift of the inner core radius. But, to shift the time of P'_{DF} by one second with a change in radius would take an adjustment of more than 100 km. The final inversion produces an inner core radius of 1215 km when constrained to fit the PKiKP data to within 0.2 sec. The value is essentially the same as the 1216 km found by Engdahl *et al.* and exactly the same as the 1215 km found by Jordan and Anderson (1973) from the same data, which illustrates the insensitivity of the determination to different mantle and outer core velocity models. This radius is not too different from the results of Bolt (1964) who proposed a "mean radius" of 1220 km but is considerably less than the 1257 km of Jeffreys (1939a).

For the velocity model to be compatible with an inner core radius of 1215 km, the $dt/d\Delta$ data of P'_{BC}, and the requirement that point C be at a Δ less than 155° as determined above, the velocity at the base of the outer core must be 10.27 km/sec or greater, which requires that the $dt/d\Delta$ at point C must be about 2.07 sec/deg or less. At point D, 1.98 sec/deg is the value adopted for the $dt/d\Delta$ and that gives a velocity at the top of the inner core of 10.73 km/sec; values between 1.95 and 1.99 sec/deg are possible, however, which would give a velocity range of 10.68 to 10.89 km/sec. Thus, the velocity jump at the inner core boundary is calculated from short-period data to be 0.46 km/sec with an uncertainty range of 0.41 to 0.62 km/sec.

The jump is small but is in agreement with the recent determinations of 0.58 km/sec by Buchbinder (1971) and 0.6 to 0.7 km/sec by Müller (1973) who used long-period amplitude data. 0.46 km/sec is in agreement with Müller's jump because the final velocity model has a rapid velocity increase just below the inner core boundary which would cause the velocity jump to appear larger to long-period energy. The above parameters for rays grazing the inner core boundary result in placement of point C at 155.4° and point D at 123.6° epicentral distance.

The velocity model derived from the original $dt/d\Delta$ data and determination of the inner core boundary parameters produces absolute P'_{DF} times that are late by about 2 sec, even when the $dt/d\Delta$ at $t_k = 0$ is assumed to be its minimum possible value (the value of the first SKKS data point; see Figure 6.9). In order to fit the absolute times, the velocity in the outer core must be increased. Based on the previous judgment that P' data are the most accurate, an adjustment is made to SKS and SKKS $dt/d\Delta$ values in the ranges that are used for the inversion. The values are reduced by adding the cosine-taper function

$$\delta = (-0.78 \text{ sec/deg}) \quad \cos\left[\frac{\pi}{2}\,\frac{(\Delta'_k-\Delta_k)}{(\Delta'_k-\Delta''_k)}\right] \qquad (6.5)$$

where $\Delta'_k = 79.9°$ and $\Delta''_k = 10.7°$. This adjustment retains the smoothness of the $dt/d\Delta$ curve and keeps the maximum change of the observed

$dt/d\Delta$ data to less than 0.8% for SKS and 0.9% for SKKS (accounting for the derivation of SKKS from SKKS-SKS times). This is a minor $dt/d\Delta$ change which translates into time shifts of the SKS and SKKS curves of about a second. The adjustment is shown in Figure 6.9. The $dt/d\Delta$ assumed at $\Delta_k = 0°$ is 7.70 sec/deg and gives a velocity at the top of the core of 7.90 km/sec. The lowest $dt/d\Delta$ possible without a low velocity zone at the top of the core is 7.60 sec/deg which results in a velocity of 8.00 km/sec; this velocity is considered an upper bound for the top of the core. The seismological data do not provide a reasonable lower bound; it will have to be determined from new data or from physical principles. This range of velocities agrees with the recent determinations of Hales and Roberts (1971) of 7.91 km/sec from the same SKS and SKKS data as used here and of Jordan and Anderson (1973) of 8.02 km/sec from normal mode and differential travel-time data.

The final P-wave velocity model for the core is tabulated in Table 6.3 and shown in Figure 6.10. The core models of Jeffreys (1939a), Gutenberg (1958, $T \geq 2$ sec), Bolt (1964), and Hales and Roberts (1971) are shown for comparison. The outstanding characteristic of the Jeffreys model is the sharp low velocity zone just above the inner core. This derived mainly from his locations of points C and D of the P' curve. Gutenberg's model is smooth but has different radii for the inner core as a function of seismic-wave frequency in an attempt

Table 6.3

P-wave velocity model of the core.

R(km)	d(km)	V(km/sec)
0	6371	11.17
100	6271	11.17
200	6171	11.17
300	6071	11.17
400	5971	11.17
500	5871	11.17
600	5771	11.16
700	5671	11.16
800	5571	11.15
900	5471	11.14
1000	5371	11.11
1100	5271	11.05
1215	5156	10.73
1215	5156	10.27
1300	5071	10.25
1400	4971	10.22
1500	4871	10.18
1600	4771	10.15
1700	4671	10.09
1800	4571	10.01

Table 6.3 (continued)

R(km)	d(km)	V(km/sec)
1900	4471	9.93
2000	4371	9.84
2100	4271	9.75
2200	4171	9.67
2300	4071	9.57
2400	3971	9.47
2500	3871	9.37
2600	3771	9.27
2700	3671	9.16
2800	3571	9.05
2900	3471	8.94
3000	3371	8.81
3100	3271	8.68
3200	3171	8.52
3300	3071	8.34
3400	2971	8.11
3485	2886	7.90

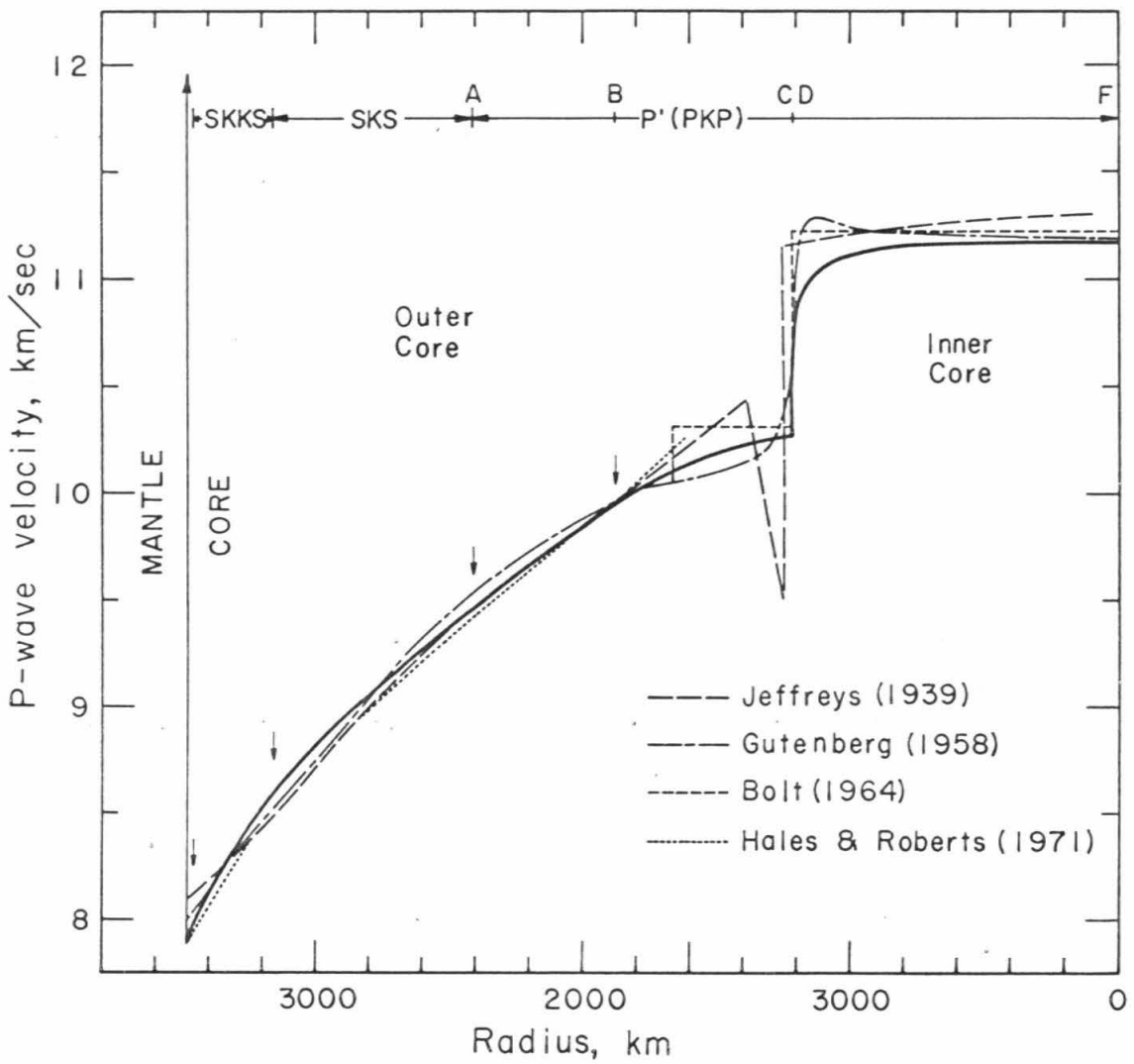

Figure 6.10

The final P-wave velocity model (heavy line). The ranges corresponding to the core phases used for velocity inversion at that depth are indicated at the top of the figure and marked with arrows along the velocity profile. Some earlier core models are shown for comparison.

to explain precursors to the P'_{DF} phase; only the smallest radius corresponding to $T \geq 2$ sec is shown which would be the model if no precursors were present. The Bolt model, which is the same as that of Jeffreys except just above and within the inner core, is an example of the class of models with discontinuities that generate extra branches to explain the P'_{DF} precursors. The model of Hales and Roberts relates only to the outer core because it was derived only from the SKS and SKKS data. Their data were used here for radii of 2411 to 3461 km and the differences between their curve and that of this paper for the same range is due to a different core radius and mantle S-velocity structure, and a minor adjustment of their $dt/d\Delta$'s.

The core model of Jordan and Anderson (1973), which was derived from the normal mode and differential travel-time data, is dependent on the starting model of the inversion in that the initial model is perturbed until all data are satisfied within specified limits. When comparing models, the important factors are the sensitivity of the data to velocity at specific levels in the core and the direction of perturbation from the starting model. Figure 6.11 shows both the model of Table 3 and the B1 core model; the starting velocities have been subtracted from both models. The direction of perturbation of the B1 model is in the direction of the Table 6.3 model at the

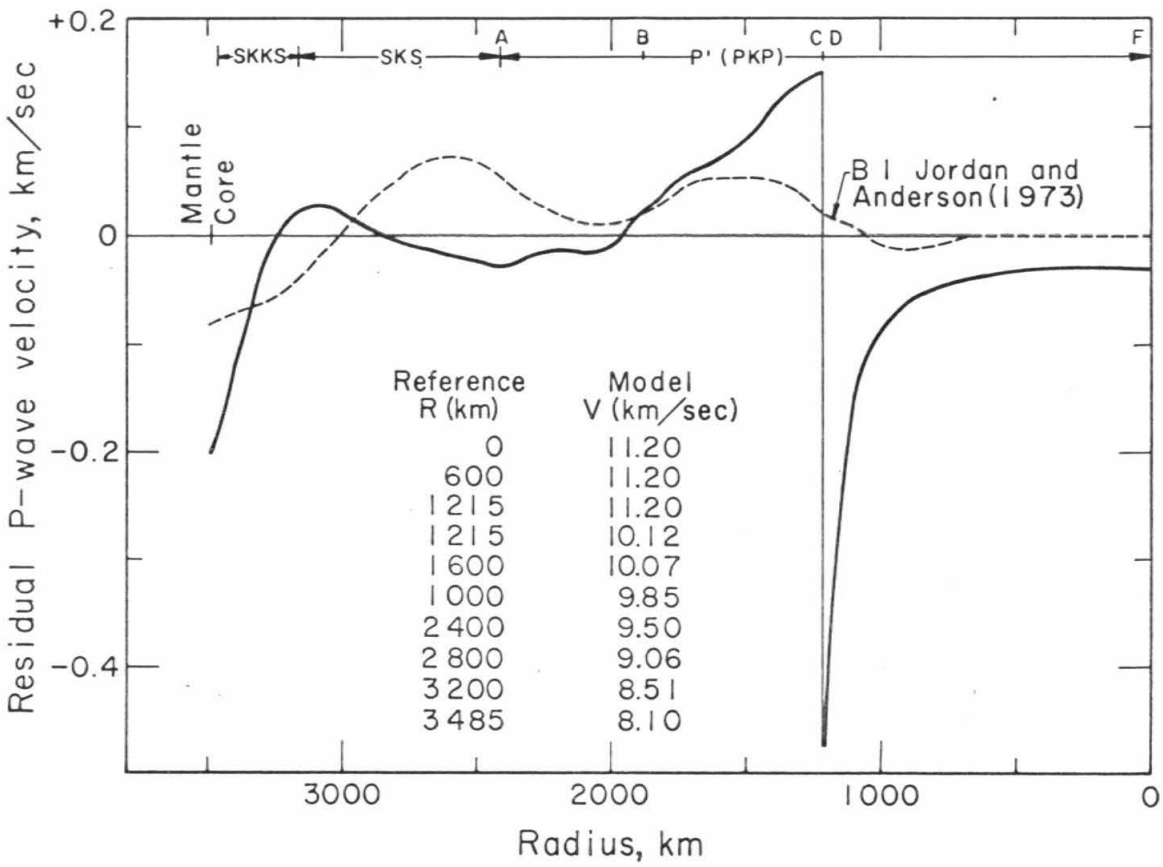

Figure 6.11

The final P-wave velocity model compared with the B1 model of Jordan (1972). The models have been reduced by the subtraction of Jordan's starting model tabulated in the figure. The ranges corresponding to the core phases used for velocity inversion at that depth are indicated at the top of the figure.

mantle-core boundary, the region above the inner core, and within the inner core except that no perturbation is made below a radius of 700 km. The large difference at the inner core boundary is due to the larger velocity jump used by Jordan and Anderson and the remainder of the inner core is not significantly different. The outstanding discrepancy between the two models is in the outer core at a radius of about 2600 km. The B1 perturbation is relatively large (0.07 km/sec) and positive whereas the velocities of Table 6.3 are somewhat less than the starting model. This discrepancy occurs mainly in the SKKS depth range which cannot be considered as well-determined as that of P', but the averaging kernels published by Jordan (1973) for this region are quite broad with side lobes extending into other depth ranges. Therefore, it is difficult to say at the present which model is most reliable. Resolution of the discrepancy will be reserved for future work.

The fit of the model of Table 6.3 to the $dt/d\Delta$ data of P' is shown in Figure 6.7. The $dt/d\Delta$ data plot to the inside of the model curve at the B caustic because the P'_{AB} and P'_{BC} phases arrive at almost the same time (see Figure 6.6). Thus, the beam power peaks of the vespagram merge to a single peak with the center point at some intermediate value between the $dt/d\Delta$'s for the separate phases. A similar effect can be expected at distances shorter than 144° where P'_{DF} and PKiKP arrive at nearly the same time. The fit of

the model to Adams and Randall (1964) time data between P'_{AB} and P'_{DF} is shown in Figure 6.6. P'_{BC} follows quite well the curvature of the main branch of data and plots about 0.3 sec behind the leading edge of the points, which have a scatter of about 1.0 sec. A dashed line is continued from point C to indicate the expected time of arrival of a high frequency phase that has been diffracted around the inner core. The two points observed near 158° may be related to this phase.

Table 6.4 shows the fit of the model to the observed time data set for the core phases as modified above by $dt/d\Delta$ and amplitude data. The times are listed in 5° intervals and the endpoints calculated from the model of Table 6.3 are also given. The residuals (observed - calculated) are positive for P'_{AB} and are less than 0.3 sec. The residuals for P'_{DF} are negative and their magnitudes are less than 0.4 sec. Calculated PKiKP times fit the curve of Engdahl et al. (1970) to within 0.2 sec.

It is interesting to note that the P'_{AB}-P'_{DF} differential times of the final model shown in Figure 6.4 generally parallel the Jeffreys-Bullen times and approximately average the Bolt (1964) and Jordan (1972) values. However, the differential time observed-model residuals given in Table 6.4 are + 0.6 sec. The observed times are different from the Bolt values mainly due to the high $dt/d\Delta$ of P'_{AB} in the distance range of 145° to 165°. The differential times for the model cannot be greatly modified by changing the parameters

Table 6.4

Fit of the Model to Observed Times

Phase		Δ	Observed	Model	O-M
P'(PKP) (surface focus)	A	178.2		1322.0	
		175	(1308.1)[1]	1307.8	0.3
		170	(1285.8)	1285.6	0.2
		165	1263.7	1263.5	0.2
		160	1241.8	1241.6	0.2
		155	1220.2	1220.0	0.2
		150	1199.2	1199.0	0.2
		145	1179.4	1179.3	0.1
	B	143.8	1175.1	1175.1	0.0
		145	1178.9	1178.8	0.1
		150	1192.6	1192.6	0.0
	C	155.4	1205.0	1204.9	0.1
	D	123.6	1139.9[2]	1140.3	-0.4
		125	1142.7	1143.0	-0.3
		130	1152.5	1152.9	-0.4
		135	1162.0	1162.4	-0.4
		140	1171.2	1171.5	-0.4
		145	1179.9	1180.3	-0.4
		150	1188.0	1188.3	-0.3

Table 6.4 (continued)

Phase	Δ	Observed	Model	O-M
P'(PKP) (surface focus)	155	1195.2	1195.6	-0.4
	160	1201.5	1201.9	-0.4
	165	1206.6	1207.0	-0.4
	170	1210.4	1210.8	-0.4
	175	1212.8	1213.1	-0.3
	F 180	1213.6	1213.9	-0.3
PKiKP	150		1193.9	
	140		1173.3	
	130		1153.0	
	120		1133.2	
	110	1113.8[3]	1114.0	-0.2
	100	1095.5	1095.6	-0.1
	90	1078.2	1078.3	-0.1
	80	1062.2	1062.1	0.1
	70	1047.4	1047.3	0.1
	60	1034.2	1034.2	0.0
	50	1022.8	1022.7	0.1
	40	1013.2	1013.1	0.1
	30	1005.7	1005.5	0.2
	20	1000.1	1000.0	0.1
	10	996.9	996.7	0.2
	0	995.8	995.6	0.2

Table 6.4 (continued)

Phase	Δ	Observed	Model	O-M
P'_{AB}-P'_{DF}	145	-0.5	-1.0	0.5
	150	11.2	10.7	0.5
	155	25.0	24.4	0.6
	160	40.3	39.7	0.6
	165	57.1	56.5	0.6
	170	75.4	74.8	0.6
	175	95.3	94.7	0.6
SKS	85	1384.1[4]	1387.9	-3.8
	90	1414.9	1418.2	-3.3
	95	1443.4	1446.3	-2.9
	100	1469.8	1472.5	-2.7
	105	1494.0	1496.6	-2.6
	110	(1515.9)	1518.5	-2.6
	115	(1535.7)	1538.4	-2.7
	120	(1553.2)	1556.6	-3.4
	125	(1568.6)	1572.8	-4.2
SKKS	85	1392.3[4]	1394.9	-2.6
	90	1430.3	1432.6	-2.3
	95	1467.4	1469.4	-2.0
	100	1503.7	1505.4	-1.7
	105	1539.2	1540.6	-1.4

Table 6.4 (continued)

Phase	Δ	Observed	Model	O-M
SKKS	110	1573.9	1575.1	-1.2
	115	1607.8	1608.8	-1.0
	120	1640.9	1641.6	-0.7
	125	(1673.1)	1673.8	-0.7
SKKS-SKS	85	8.2[4]	7.0	1.2
	90	15.4	14.4	1.0
	95	24.0	23.1	0.9
	100	33.9	32.9	1.0
	105	45.2	44.0	1.2
	110	(58.0)	56.6	1.4
	115	(72.1)	70.4	1.7
	120	(57.7)	85.0	2.7
	125	(104.5)	101.0	3.5

[1]Bracketed times not used in inversion

[2]Cleary and Hales (1970)

[3]Engdahl *et al*. (1970)

[4]Hales and Roberts (1970 and 1971)

at the inner core boundary. In order to reduce the observed-model residual, we must either decrease the velocity in the outer core or increase the velocity in the inner core. As discussed below, a reduction of the outer core velocities is undesirable because of residuals of the P4KP phase and the preferred solution would be an increase in the inner core by an average of about 0.03 km/sec, which would then agree with the model B1 value of 11.20 km/sec. The velocity increase would require minor decreases of the P'_{DF} $dt/d\Delta$ curve of the order of 0.03 sec/deg near point D, and a corresponding shift of the branch times reaching a maximum of -0.6 sec at D. A further implication of this velocity change and reduction of the residual would be to confirm the disagreement approaching 1.5 sec with the Bolt and Jordan P'_{AB}-P'_{DF} differential times near 150° to 155° as seen in Figure 6.3. However, this apparent conflict may be explained by a scattered phase arriving in this range just before P'_{AB} as discussed below.

The residuals of SKS (observed-model) are between -2.6 and -4.2 sec as seen in Table 6.4. Gutenberg and Richter (1939, p. 99) pointed out that possible errors in reading S-type waves may derive from conversions to or from P-wave energy either near the source or near the receiver, resulting in times a few seconds too early. Observations confirming the phenomenon of S-to-P conversion at the base of the crust in Fennoscandia have been published by Båth and Stefansson (1966),

Whitcomb (1969), and others and are readily observed in seismograms from many stations in the United States (author, unpublished data). Further, the recent trend of observed S travel-time curves towards later times (for example, the results of Hales and Roberts, 1970) compared to the Jeffreys-Bullen tables indicate that the older S-wave tables may have been affected by converted phases. However, this affect must be kept separate from the previously mentioned problem of station baselines and associated implications of differences in average mantle velocities under continents and oceans. The SKS phase should be the least affected by conversions near the earth's crust because of its steep angle of incidence. Thus, the final model residuals of SKS are mainly due to 1) the S station baseline assumed, 2) the mantle model used to derive the $dt/d\Delta$ versus Δ_k curve, and 3) the P' station baseline to which all of the absolute core phase times have been anchored. Adjustment of the baseline of the SKS times observed by Hales and Roberts (1970) by + 3.4 sec would bring the observed times within 0.8 sec of the final model (see Table 6.4), which is considered a satisfactory fit. Assuming that the B1 model is a good worldwide average of mantle S-wave velocities, and that P'_{DF} station baselines are the same for continents and oceans, we would conclude that S waves arrive at continental stations about 3.4 sec earlier than a hypothetical worldwide average arrival time. However,

P'_{DF} station baselines are probably not the same. An estimate of the difference between P'_{DF} station baselines between oceanic and continental mantle structures is made in Chapter 5 from P'P' phases reflecting under oceans. P waves travelling through continental mantle arrive about 0.7 to 1.0 sec earlier than those through oceanic mantle (a P'P' anomaly of 1.3 to 1.9 sec). Using the surface areas of continents and oceans to average this value over the earth produces about a 0.6 (0.5 to 0.7) sec difference between the P'_{DF} world-average and continental station baselines. Adjustment for this P-wave station baseline determines that S waves arrive at continental stations about 4.0 sec earlier than a hypothetical worldwide average arrival time. This station baseline correction would considerably reduce the large differences (-3.0 to -7.5 sec) between the B1 model S times and the observations of Hales and Roberts (1970) to be between + 1.0 and -3.5 sec. The difference between S station baselines for continents and oceans is predicted to be 5.7 sec. with the oceanic mantle slower.

Multiple core reflections of the type PmKP have been studied by Engdahl (1968), Buchbinder (1971 and 1972), Adams (1972) and others. Comparison of the P4KP times from the model of Table 6.3 with those from Adams, who made ellipticity and first-order station corrections to Novaya Zemlya explosion data, shows that the model is apparently too late by 3.4 sec, or 0.85 sec per K leg. An increase of the velocity in the outer core to remove the disagreement would

cause the P'_{AB} residuals to be about + 0.85 sec in Table 6.4, which is a relatively large residual for that phase. However, the time of the PmKP phase is not only sensitive to velocity in the core, but it is very sensitive to the radius of the core. To agree with the P4KP times would require only a 4 km decrease of the core radius, that is, the inner reflecting surface of the core. Because the radius was fixed by reflection from the upper surface of PcP, the PmKP discrepancy raises the possibility that the core-mantle boundary is a transition region of the order of 4 km thick. Thus, short period reflections from the upper surface would effectively reflect from a boundary slightly shallower than reflections from underneath. An alternative to a transition region is provided by recent evidence such as that of Mitchell and Helmberger (1973) that there is a 0.3 to 0.5 km/sec high-velocity zone up to 70 km thick immediately above the core-mantle boundary. Adjustment for this zone to fit PcP-P data would decrease the core radius by up to 2.5 km, which would remove most of the discrepancy between P' and PmKP. However, conclusions based on the use of PmKP times, where m is 2 or larger, are seriously compromised by their maximum time nature (Jeffreys and Lapwood, 1957). Reflections from non-spherically symmetric surfaces give rise to phases arriving earlier than the calculated symmetric-phase time. The effect is greatest for reflections out of the great circle plane (Whitcomb, 1973). Thus, if the PcP-determined core radius and the

P'_{AB} times are correct, the PmKP data indicate either that the core-mantle boundary is a transition region approximately 4 km thick or that the boundary is not spherically symmetric.

Up to this point, no account for Q structure in the core has been made. It is clear that the Q in the outer core is relatively high from the studies of the PmKP phase such as those of Buchbinder (1971), who determined a Q of 4000, and Adams (1972), who put a lower limit on Q of 2200. The Q of the inner core through which P'_{DF} travels is a much more difficult determination. No phase with multiple travel paths bottoming at the same depth, such as PmKP, is available. Amplitudes of P'_{DF} between 123° and 143° affect only the outer 134 km of the core and are difficult to separate from the PKiKP phase which arrives just after P'_{DF}. Thus, P'_{DF} beyond 146° is the best candidate for determining the inner-core Q. It is well known that short-period amplitudes of core phases scatter by an order of magnitude. Attempts to reduce this scatter by taking the amplitude ratio P'_{AB}/P'_{DF} to remove near-station effects do not significantly reduce this scatter as seen in the data of Figure 6.8. Buchbinder (1971) found that his velocity model required a Q of 400 in the inner core to agree with the relative amplitudes of P'_{AB} and P'_{DF}. His calculation of P'_{AB}/P'_{DF} is shown in Figure 6.8. The Q model of Buchbinder was applied to the model of Table 6.3 and the resulting amplitude ratio calculated from ray theory is shown in the figure. All calculations

are done at a frequency of 1 hz with a mantle Q of 2000. The P'_{AB}/P'_{DF} values are above one out to at least 170°, which is also a characteristic of Buchbinder's curve. However, the observed ratios, even though scattered, seem to require a drop below one at least by distances of 170° because no data point beyond 172° is above 0.4. The amplitude ratio is now calculated for the model in Table 6.3 using a constant Q in the core of 4000 and shown in the figure. This curve is more satisfactory at the larger distances and is well within the data scatter elsewhere. The same calculation shown for a constant Q of 2200 appears to be a slightly, but not significantly, better fit. While the data scatter prevents us from ruling out the possibility of a low Q in the inner core, the calculations show that there is certainly no requirement from short-period P' data that the inner core Q be significantly lower than that of the outer core.

A conclusion was reached earlier that the precursors to P'_{DF} at distances shorter than 143° are due to scattering either at the core-mantle boundary or within the core. Scattering is most likely from rays in or near point B because the P'_{DF} precursors appear to converge at that point, and the amplitudes of P' are largest there. Times and distances for point scattering of up to ± 20° from the point B ray is calculated at five regions in the earth as shown in Figure 6.12. Regions 1 and 2 are just above and below the core-mantle

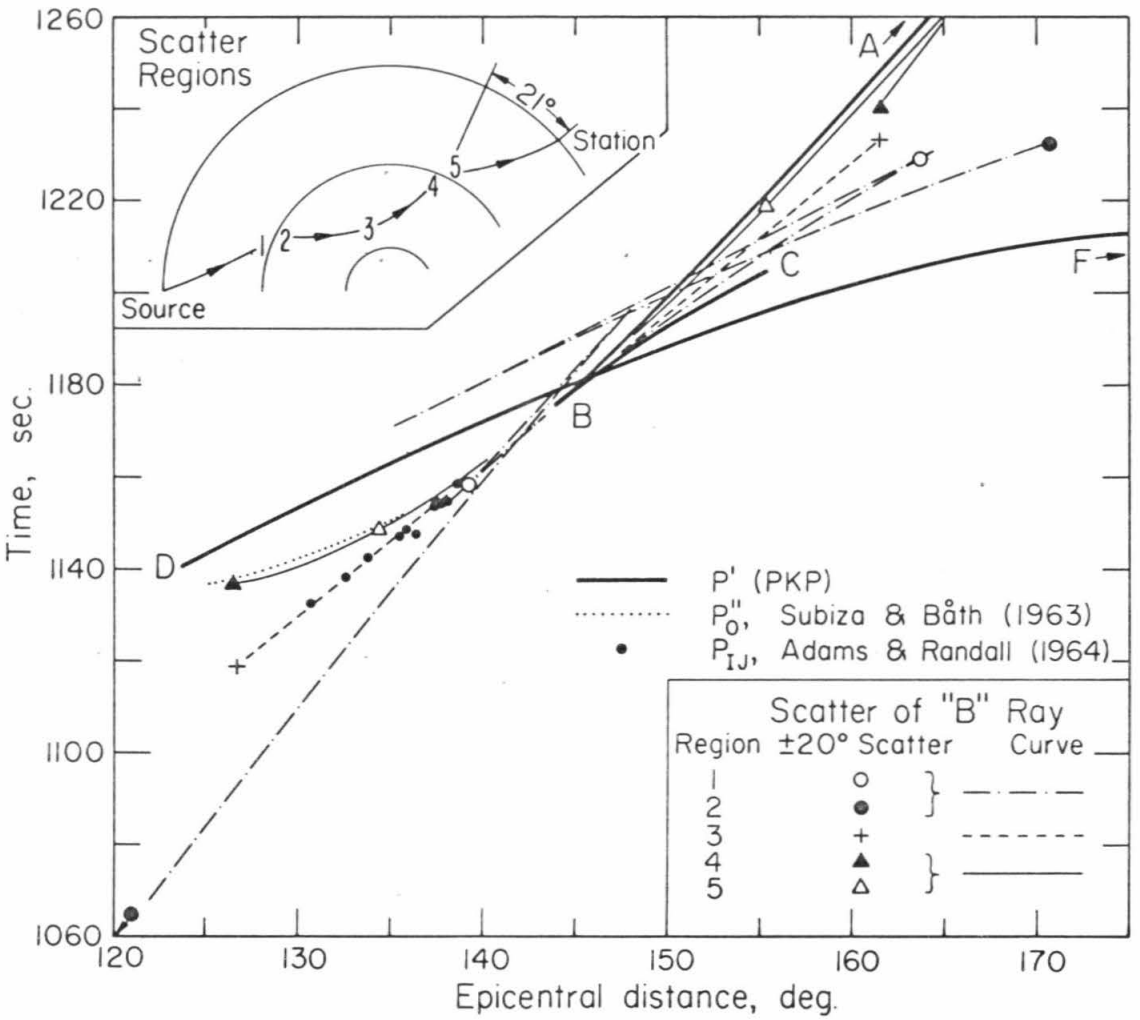

Figure 6.12

Scattering travel-time curves from the point B ray of P'. Five point scatterers are located along the ray as shown in the inset and the symbols indicate a maximum scatter angle of ± 20°. P' from the final model and some observed data are also shown.

boundary near the source; Region 3 is at the bottoming point of the ray; and Regions 4 and 5 are just below and above the core-mantle boundary near the station. The travel-time curves for scattered energy from each region are shown in the figure with symbols indicating maximum (20°) scatter. The curves for Regions 1 and 2 near the source and those of Regions 4 and 5 near the station coincide except that their 20° scatter points are at different distances. The 20° scatter points clearly illustrate that scattering just below the boundary in the low-velocity media is much more effective (Regions 2 and 4) than just above (Regions 1 and 5). In order to produce the same scatter distances as those for Regions 2 and 4 by a dipping core-mantle boundary, dips of at least the same order as the scattering angles are required.

For distances shorter than about 140° in Figure 6.12, the times and $dt/d\Delta$'s of the scattered arrivals vary markedly with the scatter location. Subiza and Båth (1964) made a comprehensive study of the P'_{DF} precursor times and periods and found that the first arrivals fit a curve that was strongly concave upwards, which they labeled P''_o. Their determination of P''_o is shown in Figure 6.12 and it agrees remarkably well with the scatter curve from the near-station core-mantle boundary (Regions 4 and 5). The later arrivals of Subiza and Båth, called P''_1 (not shown), would easily fit scattering from the same region of rays near point B. The periods of P''_o and P''_1 are between 0.5 and 1.0 sec. The phase "X" of Hai (1963) closely agrees

with the P''_o phase. Arrivals earlier than P''_o were read by Adams and Randall (1964) and were interpreted as an extra branch labeled P'_{IJ}; their readings for distances shorter than 139° are shown in Figure 6.12. These readings could be explained by either scattering within the core (which is not significantly different from Adams and Randall's proposed discontinuity) or scattering of another ray near point B from the core boundary near the source. However, only six readings of Adams and Randall precede the Region 4 and 5 curve by more than 3 sec which weakens any conclusions about the data's origin. The travel-time data of the P'_{DF} precursors from Buchbinder (1971, Figure 3) scatter between the Adams and Randall and Subiza and Båth values, but the data show a clear concave upwards curvature as indicated by the curve fit to the data by Buchbinder. Doornbos and Husebye (1972), who analyzed the P'_{DF} precursor times and $dt/d\Delta$'s at the NORSAR array in Norway, did not cover epicentral distances shorter than 136°. As seen in Figure 6.12, the Regions 3 and 4 scatter curves are not well-separated beyond 136° but the measurements of $dt/d\Delta$ of 3.3 to 3.6 sec/deg at 138° by Doornbos and Husebye tend to favor the curve of Regions 1 and 2 or that of Region 3. However, as Doornbos and Husebye state, strong corrections to their data were necessary and the calibration of the array is not complete, which makes their $dt/d\Delta$ data subject to future revision.

The scatter curves in Figure 6.12 beyond 145° fall in the time space between the P'_{AB} and P'_{BC} branches. Their dt/dΔ's are quite different and this characteristic may be useful in determining the origin of scattered energy in this distance range. The Adams and Randall (1964) arrivals after P'_{BC} shown in Figure 6.6 were the basis of their extension of P'_{IJ} beyond 145°. The points later than P'_{BC} at distances between 153° and 156° appear to have a slope or dt/dΔ larger than that proposed for P'_{IJ} in this range (see also, Adams and Randall, 1964, Figure 5). The scattered phase that fits these points best is from the ray of P'_{BC} at 147.5° scattered from the core boundary near the station; the phase is shown in Figure 6.6.

Scatter of the point B ray from core boundary near the station precedes the P'_{AB} branch by 1 to 3 sec between 150° and 165° as seen in Figure 6.12. As the scatter curve approaches 165°, the scatter angle increases and the likelihood of scattering decreases. This mechanism gives an attractive explanation of the apparent discrepancy between the observed P'_{AB}-P'_{DF} differential times and the values of Bolt (1968) and Jordan (1972) centered at about 150° to 155° as seen in Figure 6.4. Increased use of short-period high-gain instruments since the publication of the Jeffreys-Bullen table may have led to a more frequent reading of the scattered phases whose periods are generally shorter than a second. Thus, more recent readings of P'_{AB} tend to be the earlier scattered phase instead, resulting in a dip of

the P'_{AB}-P'_{DF} curve relative to the Jeffreys-Bullen values near 150° to 155°. Extension of the Bolt and Jordan values at 175°, where the earlier scattered phase is absent, backwards and in parallel with the Jeffreys-Bullen values would coincide with the observed curve in Figure 6.4, which was constructed with times, $dt/d\Delta$'s, and relative amplitudes.

Comparison of the observations to the scatter curves leads to the conclusion that the strongest scattering of P' appears to take place near the core-mantle boundary closest to the observing station. The angular distance from the station of the scattering point on the boundary is about 21° as shown in Figure 6.12. Inspection of the ray plot of Figure 6.3 supports this conclusion because adjacent rays are more concentrated at this location on the core-mantle boundary than at any other; in fact, all rays of P'_{AB} must pass through an internal caustic as seen in the figure. The most effective scattering location that agrees with the data is just below the core-mantle boundary near the station. Scattering of up to 20° is required for the P'_{DF} precursors and a much larger angle is needed if the scattering takes place above the boundary. The P'_{IJ} times of Adams and Randall (1964) at distances shorter than 143° and the $dt/d\Delta$ data of Doornbos and Husebye (1972) may be evidence for scattering within the core or at the core-mantle boundary near the source. However, the data do not permit a more definite conclusion about scattering from these regions at present.

6.5 Summary. A core P-wave velocity model is constructed from observed times, $dt/d\Delta$'s, and relative amplitudes of P'; the observed times of SKS, SKKS, and PKiKP; and a new mantle-velocity determination model B1 by Jordan and Anderson (1973) which represents a spherically-symmetric average over the earth. The resultant velocity structure fits the P' absolute times to within 0.4 sec and the P'_{AB}-P'_{DF} differential times to within 0.6 sec. These residuals could be reduced to less than 0.1 sec by a small velocity increase in the inner core if some adjustment were made to the P'_{DF} curve of Cleary and Hales (1971) near point D up to a maximum of 0.6 sec. The $dt/d\Delta$'s observed at the LASA array in Montana and the maximum-relative amplitudes of the P'-type phases provide important constraints on the data used for inversion and the final velocity model, especially the P'_{AB} and P'_{BC} branches. The PKiKP times of Engdahl et al. (1970) are fit to within 0.2 sec which results in an inner core radius of 1215 km; this is essentially the same as the 1216 km derived by Engdahl et al. The model's ray-theoretical end-points of the P' refraction branches for a surface focus are at 123.6° for D, 155.4° for C, 143.8° for B, and 178.2° for A; all of these values are within observational limits.

Care is taken in the use of the time data to keep assumptions of a model baseline and a station baseline separate. The final core velocity model is mainly dependent on the $dt/d\Delta$'s of the core phases,

the absolute times of the P' branch, and the absolute PKiKP times. The absolute SKS time residuals are then a function of the P station baseline and the mantle S-velocity structure that is stripped from the observed times. After correction for the oceanic P baseline from Chapter 5, the SKS continental station baseline is calculated to be 4.0 sec earlier than that for the earth average. The model's baseline-adjusted SKS and SKKS residuals are within 0.8 sec and 2.7 sec, respectively, of Hales and Roberts' (1970 and 1971) observations. Use of this same baseline reduces the disagreement between the S times of Jordan and Anderson (1973) and those of Hales and Roberts (1970) to between + 1.0 and - 3.5 sec. The agreement suggests that contamination of the Hales and Roberts' S readings with earlier converted phases from near the station is not much greater than about 3 sec from that of SKS, and contamination of the latter should be small due to its steep angle of emergence. The baseline analysis leads to the conclusion that mantle velocities, presumably in the upper mantle, are slower under oceans that those under continents. The travel-time differences are of the order of 0.8 sec for P waves and 5.7 sec for S waves.

The core velocity model is smooth except for a discontinuity at the inner-core boundary. The velocity jump at the inner-core boundary is determined to be between 0.41 and 0.62 km/sec from the inner-core

boundary radius (fixed by PKiKP times), the $dt/d\Delta$ at point D of P', and constraints on the position of point C of P'. Velocity at the top of the core has an upper bound of 8.0 km/sec. Very steep velocity gradients are required by SKKS data in the outer 400 km of the core and the gradient smoothly decreases to a low, but not negative, value just above the inner-core boundary. The velocity gradient is again very steep at the top of the inner core but rapidly levels out to between 11.17 and 11.20 km/sec over most of the inner core.

Q in the outer core has been shown to be high, 2200 to 4000, from PmKP studies of previous investigators (Buchbinder, 1971; Adams, 1972; and others). However, because no similar phase has been observed for the inner core, the Q at that depth is much more difficult to estimate. The determination of an inner-core Q of 400 by Buchbinder (1971) is not required by the highly scattered short-period P' amplitude data, and an improved fit can be easily made with Q constant in the core.

Most, if not all, of the arrivals preceding P'_{DF} at distances shorter than 143° appear to be due to scattering as proposed by Haddon (1972) and not due to spherically symmetric discontinuities just above the inner core. Doornbos and Husebye (1972) measured a $dt/d\Delta$ of about 3.3 sec/deg for the precursors between 136° and 143° at the NORSAR array in Norway. This is the same $dt/d\Delta$ as that of the B caustic and effectively rules out the P'_{GH} branch of Bolt (1964), but

the P'_{IJ} branch of Adams and Randall (1964) does not disagree with this measurement. However, investigation of the precursors just short of the B caustic at the LASA array in Montana, a larger array, shows no coherent energy other than P'_{DF} even though the amplitudes of the precursors should be maximum and nearly the same as P'_{DF} at this range. The precursors clearly do not have the coherency of the P' main branches which is a finding that strongly supports the scattering hypothesis.

Calculation of the travel-time distribution of scattered phases and comparison with published data show that the strongest scattering takes place at or near the core-mantle boundary close to the receiving station. Scattering is from rays of, or near, the B caustic, of P'. The scattering angles are up to at least 20° for energy of 0.5 to 1.0 sec periods and scattering at a given angle is more effective just below the core-mantle boundary than above. Arrivals previously identified as P'_{IJ} beyond 145° and possible early readings of the P'_{AB} branch between about 150° and 160° can also be attributed to scattering from this region. Placement of the scatterer close to core-mantle boundary near the station is the most reasonable location because adjacent rays leaving the source are more concentrated at this point on the core-mantle boundary than at any other, thus providing the maximum energy density available for scattering. There are a few observed arrivals that cannot be explained by scattering from the

core-mantle boundary near the station and, if the readings are actually core-phase energy, they must be interpreted as scattering either within the core or close to the core-mantle boundary near the source. Until more complete evidence is available, the latter explanation is preferred because only one scattering level is required.

REFERENCES

Adams, R. D., Multiple inner core reflections from a Novaya Zemlya explosion, Bull. Seism. Soc. Am., 62, 1063 1972.

Adams, R. D., Reflections from discontinuities beneath Antarctica, Bull. Seism. Soc. Am., 61, 1441, 1971.

Adams, R. D., Early reflections of P'P' as an indication of upper mantle structure, Bull. Seism. Soc. Am., 58, 1933, 1968.

Adams, R. D., and M. J. Randall, The fine structure of the earth's core, Bull. Seism. Soc. Am., 54, 1299, 1964.

Anderson, D. L., Phase changes in the upper mantle, Science, 157, 1165, 1967.

Anderson, D. L., and T. C. Hanks, Formation of the earth's core, Nature, 237, 387, 1972.

Anderson, D. L., and B. R. Julian, Shear velocities and elastic parameters of the mantle, J. Geophys. Res., 74, 3281, 1969.

Anderson, D. L., and C. Sammis, Partial melting in the upper mantle, Phys. Earh Planet. Interiors, 3, 41, 1970.

Anderson, D. L., and M. N. Toksöz, Surface waves on a spherical earth, 1. Upper mantle structure from Love waves, J. Geophys. Res., 68, 3483, 1963.

Anonymous, World Seismicity 1961-1969, map published by National Earthquake Information Center, U. S. Dept. of Commerce, Washington, D. C., 1970.

Archambeau, C. B., E. A. Flinn, and D. G. Lambert, Fine structure of the upper mantle, J. Geophys. Res., 74, 5825, 1969.

Barazangi, M. and J. Dorman, World seismicity maps compiled from ESSA, Coast and Geodetic Survey, Epicenter data, 1961-1967, Bull. Seism. Soc. Am., 59, 369, 1969.

Båth, M., and R. Stefansson, S-P conversion at the base of the crust, Ann. Geofis. (Rome), 19, 119, 1966.

Bolt, B. A., Estimation of PKP travel times, Bull. Seism. Soc. Am., 58, 1305, 1968.

Bolt, B. A., The velocity of seismic waves near the earth's center, Bull. Seism. Soc. Am., 54, 191, 1964.

Bolt, B. A., Gutenberg' early PKP observations, Nature, 196, 122, 1962.

Born, M., and E. Wolf, Principles of Optics, 3rd ed., Pergamon Press, New York, 808 p., 1965.

Buchbinder, G.G.R., Travel times and velocities in the outer core from PmKP, Earth Planet. Sci. Letters, 14, 161, 1972.

Buchbinder, G.G.R., A velocity structure of the earth's core, Bull. Seism. Soc. Am., 61, 429, 1971.

Bullen, K. E., Introduction to the Theory of Seismology, 3rd ed., University Press, Cambridge, 1963.

Cleary, J. R., and A. L. Hales, PKIKP times and S station anomalies, J. Geophys. Res., 76, 7249, 1971.

Davies, D., E. J. Kelly, and J. R. Filson, Vespa process for analysis of seismic signals, Nature Phys. Sci., 232, 8, 1971.

Davies, D., and D. P. McKenzie, Seismic travel-time residuals and plates, Geophys. J. R. Astr. Soc., 18, 51, 1969.

Denson, M. E., Jr., Longitudinal waves through the earth's core, Bull. Seism. Soc. Am., 42, 119, 1952.

Doornbos, D. J., and E. S. Husebye, Array analysis of PKP phases and their precursors, Phys. Earth Planet. Int., 5, 387, 1972.

Engdahl, E. R., Core phases and the earth's core, Ph.D. thesis, Saint Louis University, 1968.

Engdahl, E. R., and C. P. Felix, Nature of travel-time anomalies at LASA, J. Geophys. Res., 76, 2706, 1971.

Engdahl, E. R., and E. A. Flinn, Seismic waves reflected from discontinuities within the upper mantle, Science, 163, 177, 1969a.

Engdahl, E. R., and E. A. Flinn, Remarks on the paper 'Early reflections of P'P' as an indication of upper mantle structure' by R. D. Adams Bull. Seism. Soc. Am., 59, 1415, 1969b.

Engdahl, E. R., E. A. Flinn, and C. F. Romney, Seismic waves reflected from the Earth's inner core, Nature, 228, 852, 1970.

Engdahl, E. R., and L. E. Johnson, A new PcP data set from nuclear explosions on Amchitka island, EOS, Trans. Am. Geophys. Un., 53, 1045, 1972.

Ergin, K., Seismic evidence for a new layered structure of the earth's core, J. Geophys. Res., 72, 3669, 1967.

Ewing, M., S. Eittreim, M. Truchan, and J. I. Ewing, Sediment distribution in the Indian Ocean, Deep-Sea Res., 16, 231, 1969.

Francis, T. J. G., and R. W. Raitt, Seismic refraction measurements in the southern Indian Ocean, J. Geophys. Res., 72, 3015, 1967.

Gogna, M. L., Travel times of PKP from Pacific earthquakes, Geophys. J., 16, 489, 1968.

Green, R. W. E., and A. L. Hales, The travel times of P waves to 30° in the central United States and upper mantle structure, Bull. Seism. Soc. Am., 58, 267, 1968.

Gutenberg, B., Waves reflected at the "surface" of the earth: P'P'P'P', Bull. Seism. Soc. Am., 50, 71, 1960.

Gutenberg, Beno, Physics of the Earth's Interior, Academic Press, New York, 240 p., 1959.

Gutenberg, B., Caustics produced by waves through the earth's core, Geophys. J., 3, 238, 1958.

Gutenberg, B., The boundary of the Earth's inner core, Trans. Am. Geophys. U., 38, 750, 1957.

Gutenberg, B., PKKP, P'P', and the earth's core, Trans. Am. Geophys. U., 32, 373, 1951.

Gutenberg, B., and C. F. Richter, On seismic waves (fourth paper), Gerlands Beitrage zur Geophysik, 54, 94, 1939.

Gutenberg, B. and C. F. Richter, On P'P' and related waves, Gerlands Beitrage zur Geophysik, 41, 149, 1934.

Haddon, R. A. W., Corrugations on the mantle-core coundary or transition layers between inner and outer cores?, EOS Trans. Am. Geophys. U., 53, 600, 1972.

Hai, N., Propagation des ondes longitudinales dans le neyau terrestre, Annales de Geophysique, 19, 285, 1963.

Hales, A. L., and J. L. Roberts, The velocities in the outer core, Bull. Seism. Soc. Am., 61, 1051, 1971.

Hales, A. L., and J. L. Roberts, The travel times of S and SKS, Bull. Seism. Soc. Am., 60, 461, 1970.

Hales, A. L., and J. L. Roberts, Shear velocities in the lower mantle and the radius of the core, Bull. Seism. Soc. Am., 60, 1427, 1970b.

Hoffmann, J. P., J. W. Berg, Jr., and K. L. Cook, Discontinuities in the earth's upper mantle as indicated by reflected seismic energy, Bull. Seism. Soc. Am., 51, 17, 1961.

Ibrahim, A. K., and O. W. Nuttli, Travel-time curves and upper mantle structure from long-period S waves, Bull. Seism. Soc. Am., 57, 1063, 1967.

Jeffreys, H., The times of the core waves (second paper), M.N.R.A.S., Geophys. Suppl., 4, 594, 1939a.

Jeffreys, H., The times of the core waves, M.N.R.A.S., Geophys. Suppl., 4, 548, 1939b.

Jeffreys, H., The times of P, S, and SKS, and the velocities of P and S, Mon. Not. Roy. Astro. Soc., Geophys. Suppl., 7, 498, 1939c.

Jeffreys, H., and E. R. Lapwood, The reflection of a pulse within a sphere, Proc. Roy. Soc. Lon., Series A, 241, 455, 1957.

Johnson, L. R., Array measurements of P velocities in the lower mantle, Bull. Seism. Soc. Am., 59, 973, 1969.

Johnson, L. R., Array measurements of P velocities in the upper mantle, J. Geophys. Res., 72, 6309, 1967.

Jordan, T. H., Estimation of the Radial Variation of Seismic Velocities and Density in the Earth, Ph.D. Thesis, California Institute of Technology, 199 p., 1972.

Jordan, T. H., and D. L. Anderson, Earth structure from free oscillations and travel times, submitted to Geophys. J., 1973.

Julian, B. R., Ray tracing in arbitrarily heterogeneous media, Mass. Inst. of Tech. Lincoln Lab. Technical Note 1970-45, 1, 1970.

Julian, B. R., and D. L. Anderson, Travel times, apparent velocities and amplitude of body waves, Bull. Seism. Soc. Am., 58, 339, 1968.

Kelly, E. J., L. T. Fleck, and P. E. Green, Special methods for detailed analysis of individual events, in Seismic Discrimination Semi-annual Technical Summary, 30 June 1968, Lincoln Laboratory, Massachusetts Institute of Technology, Lexington, 1968.

Kovach, R. L., Comments on the fine structure of the earth's core, Comm. on Earth Sci.: Geophys., 2, 31, 1971.

Lehmann, I., P', Publications du Bureau central seismologique international, Serie A: Travaux scientifiques, fasc. 14, 87, 1936.

LePichon, X., and J. R. Heirtzler, Magnetic anomalies in the Indian Ocean and sea-floor spreading, J. Geophys. Res., 73, 2101, 1968.

Mitchell, B. J., and D. V. Helmberger, Shear velocities at the base of the mantle from observations of S and ScS, submitted to J. Geophys. Res., 1973.

Muller, G., Amplitude studies of core phases, J. Geophys. Res., in press, 1973.

Niazi, M., Use of source arrays in studies of regional structure, Bull. Seism. Soc. Am., 59, 1631, 1969.

Niazi, M., and D. L. Anderson, Upper mantle structure of western North America from apparent velocities of P waves, J. Geophys. Res., 70, 4033, 1965.

Richards, P. G., Calculation of body waves, for caustics and tunnelling in core phases, unpublished manuscript, 1973.

Richards, P. G., Seismic waves reflected from velocity gradient anomalies within the earth's upper mantle, Zeitschrift fur Geophysik, 38, 517, 1972.

Shahidi, M., Variation of amplitude of PKP across the caustic, Phys. Earth Planet. Int., 1, 97, 1968.

Subiza, G. P., and M. Båth, Core phases and the inner core boundary, Geophys. J., 8, 496, 1964.

Taggert, J., and E. R. Engdahl, Estimation of PcP travel times and the depth to the core, Bull. Seism. Soc. Am., 58, 1293, 1968.

Wadati, K., and Masuda, K., On the travel time of earthquake waves, Part VI, The Geophys. Magazine, Tokyo, 8, 187, 1934.

Whitcomb, J. H., Asymmetric P'P'--an alternative to P'dP' reflections in the upper-most mantle (0-110 km), Bull. Seism. Soc. Am.,

Whitcomb, J. H., Reflections of P'P' seismic waves from 0 to 150 km depth under the Ninety East Ridge, Indian Ocean, and the Atlantic-Indian Rise, Am. Geophys. U., Monograph 14, 211, 1971.

Whitcomb, J. H., Array data processing techniques applied to long-period shear waves at Fennoscandian seismograph stations, Bull. Seism. Soc. Am., 59, 1863, 1969.

Whitcomb, J. H., and D. L. Anderson, Reflection of P'P' seismic waves from discontinuities in the mantle, J. Geophys. Res., 75, 5713, 1970.

Whitcomb, J. H., and D. L. Anderson, Reflections from upper mantle discontinuities (Abstract), Trans. Am. Geophys. Union, 49, 716, 1968.

Wright, C., Array studies of seismic waves arriving between P and PP in the distance range 90° to 115°, Bull. Seism. Soc. Am., 62, 385, 1972.

Zengeni, T. G., PKKP and the fine structure of the earth's core, Ph.D. thesis, Stanford University, 1970.

APPENDICES

1. Δ, t, $dt/d\Delta$, Δ_k, and t_k for the core phases used in the initial Wiechert-Herglotz inversion.

PHASE	DELTA (DEG)	T (SEC)	DT/DD (SEC/DEG)	DELTA(K) (DEG)	T(K) (SEC)
P'(F)	180	1213.56	0.0	180.00	702.76
	179	1213.53	0.065	178.33	702.71
	178	1213.43	0.130	176.65	702.54
	177	1213.27	0.190	175.03	702.28
	176	1213.05	0.250	173.41	701.92
	175	1212.77	0.310	171.78	701.47
	174	1212.43	0.370	170.15	700.92
	173	1212.02	0.440	168.42	700.21
	172	1211.55	0.500	166.80	699.45
	171	1211.02	0.560	165.17	698.58
	170	1210.43	0.615	163.59	697.66
	169	1209.79	0.670	162.01	696.64
	168	1209.09	0.730	160.38	695.49
	167	1208.33	0.790	158.74	694.25
	166	1207.51	0.845	157.15	692.95
	165	1206.64	0.895	155.62	691.62
	164	1205.72	0.955	153.97	690.10
	163	1204.74	1.005	152.43	688.59
	162	1203.71	1.055	150.88	687.00
	161	1202.63	1.100	149.39	685.39
	160	1201.51	1.145	147.91	683.72
	159	1200.34	1.195	146.36	681.91
	158	1199.12	1.240	144.86	680.08
	157	1197.86	1.280	143.41	678.25
	156	1196.56	1.320	141.97	676.38
	155	1195.22	1.360	140.51	674.43
	154	1193.84	1.400	139.07	672.44
	153	1192.42	1.440	137.61	670.36
	152	1190.96	1.475	136.22	668.34
	151	1189.47	1.505	134.87	666.33
	150	1187.95	1.540	133.47	664.19
	149	1186.39	1.575	132.06	662.01
	148	1184.80	1.600	130.77	659.96
	147	1183.19	1.625	129.48	657.88
	146	1181.55	1.655	128.13	655.66
	145	1179.88	1.680	126.84	653.50
	144	1178.19	1.700	125.60	651.41
	143	1176.48	1.725	124.30	649.20
	142	1174.74	1.750	123.01	646.94
	141	1172.98	1.770	121.77	644.77

PHASE	DELTA (DEG)	T (SEC)	DT/DD (SEC/DEG)	DELTA(K) (DEG)	T(K) (SEC)
	140	1171.20	1.790	120.54	642.56
	139	1169.40	1.810	119.29	640.32
	138	1167.58	1.825	118.11	638.18
	137	1165.75	1.840	116.92	636.00
	136	1163.90	1.860	115.69	633.71
	135	1162.03	1.875	114.51	631.51
	134	1160.15	1.885	113.38	629.39
	133	1158.26	1.900	112.20	627.16
	132	1156.35	1.915	111.10	624.89
	131	1154.43	1.925	109.89	622.74
	130	1152.50	1.935	108.71	620.58
	129	1150.56	1.940	107.71	618.51
	128	1148.60	1.945	106.64	616.43
	127	1146.65	1.955	105.52	614.24
	126	1144.69	1.965	104.40	612.04
	125	1142.72	1.975	103.27	609.82
	124	1140.74	1.980	102.21	607.72
	123	1138.76	1.985	101.16	605.63
	122	1136.78	1.989	100.09	603.52
P'(D)	121	1134.79	1.990	99.09	601.53
P'(C)	155	1204.12	2.070	132.44	669.68
	154	1202.01	2.150	130.06	664.54
	153	1199.81	2.253	127.72	659.40
	152	1197.51	2.357	125.32	653.87
	151	1195.10	2.458	122.94	648.14
	150	1192.59	2.549	120.66	642.42
	149	1190.00	2.625	118.55	636.99
	148	1187.34	2.694	116.53	631.58
	147	1184.61	2.771	114.37	625.68
	146	1181.80	2.865	111.89	618.69
	145	1178.88	3.000	108.68	609.30
P'(B)	144	1175.79	3.300	102.27	589.14
	145	1179.38	3.664	95.30	564.93
	146	1183.12	3.807	92.51	554.52
	147	1186.99	3.929	89.91	544.45
	148	1190.97	4.017	87.80	536.09
	149	1195.03	4.090	85.97	528.65
	150	1199.15	4.138	84.91	524.46
	151	1203.30	4.171	84.35	521.96
	152	1207.49	4.200	83.92	520.18

PHASE	DELTA (DEG)	T (SEC)	DT/DD (SEC/DEG)	DELTA(K) (DEG)	T(K) (SEC)
	153	1211.70	4.226	83.51	518.43
	154	1215.94	4.249	83.20	517.15
	155	1220.20	4.269	82.98	516.00
	156	1224.48	4.288	82.71	515.03
	157	1228.78	4.307	82.34	513.46
	158	1233.10	4.326	81.94	511.73
	159	1237.43	4.344	81.41	509.41
	160	1241.79	4.359	81.00	507.64
	161	1246.15	4.370	80.87	507.09
	162	1250.53	4.380	80.76	506.61
	163	1254.91	4.390	80.56	505.71
	164	1259.31	4.399	80.21	504.19
	165	1263.71	4.406		
	166	1268.13	4.413		
	167	1272.55	4.420		
P'(A)	168	1276.98	4.425		
SKS	107	1503.00	4.435	79.86	499.87
	106	1498.52	4.525	78.16	492.39
	105	1493.95	4.615	76.53	484.75
	104	1489.29	4.700	74.88	477.08
	103	1484.55	4.785	73.22	469.23
	102	1479.72	4.875	71.52	461.00
	101	1474.80	4.965	69.81	452.61
	100	1469.79	5.055	68.09	443.95
	99	1464.69	5.140	66.39	435.31
	98	1459.51	5.225	64.69	426.47
	97	1454.24	5.315	62.93	417.20
	96	1488.88	5.405	61.15	407.69
	95	1443.43	5.495	59.37	397.95
	94	1437.89	5.580	57.61	388.20
	93	1432.27	5.665	55.84	378.26
	92	1426.56	5.755	54.00	367.80
	91	1420.76	5.845	52.15	357.04
	90	1414.87	5.930	50.32	346.26
	89	1408.90	6.015	48.48	335.29
	88	1402.84	6.105	46.57	323.72
	87	1396.69	6.195	44.64	311.84
	86	1390.45	6.285	42.68	299.61
	85	1384.12	6.375	40.69	287.02
SKS	84	1377.70	6.460	38.74	274.48

PHASE	DELTA (DEG)	T (SEC)	DT/DD (SEC/DEG)	DELTA(K) (DEG)	T(K) (SEC)
SKKS	121	1647.38	6.505	37.61	270.38
	120	1640.86	6.535	36.94	265.99
	119	1634.30	6.565	36.26	261.54
	118	1627.72	6.600	35.55	256.89
	117	1621.10	6.635	34.83	252.51
	116	1614.45	6.665	34.15	247.64
	115	1607.77	6.695	33.47	243.05
	114	1601.06	6.730	32.75	238.23
	113	1594.31	6.765	32.03	233.33
	112	1587.53	6.795	31.33	228.66
	111	1580.72	6.825	30.64	223.90
	110	1573.88	6.860	29.91	218.93
	109	1567.00	6.895	29.27	213.87
	108	1560.09	6.925	28.47	209.02
	107	1553.15	6.955	27.76	204.09
	106	1546.18	6.985	27.06	199.18
	105	1539.18	7.020	26.31	193.92
	104	1532.14	7.055	25.55	188.60
	103	1525.07	7.085	24.83	183.55
	102	1517.97	7.115	24.11	178.39
	101	1510.84	7.145	23.39	173.25
	100	1503.68	7.180	22.62	167.72
	99	1496.48	7.215	21.85	162.16
	98	1489.25	7.245	21.10	156.82
	97	1481.99	7.275	20.36	151.41
	96	1474.70	7.310	19.58	145.69
	95	1467.37	7.345	18.78	139.84
	94	1460.01	7.375	18.02	134.24
	93	1452.62	7.405	17.26	128.64
	92	1445.20	7.435	16.49	122.92
	91	1437.75	7.470	15.66	116.84
	90	1430.26	7.505	14.84	110.83
	89	1422.74	7.535	14.05	104.68
	88	1415.19	7.565	13.25	98.65
	87	1407.60	7.600	12.40	92.23
	86	1399.99	7.635	11.54	85.64
SKKS	85	1392.34	7.665	10.72	79.35
ASSUMED	0	0.0	7.700	0.0	0.0

PART II.

THE 1971 SAN FERNANDO EARTHQUAKE SERIES FOCAL MECHANISMS AND TECTONICS

1. INTRODUCTION

The main shock of the San Fernando earthquake series occurred on February 9, 1971, in the tectonically active Transverse Ranges structural province of Southern California. Immediately following the main shock, the aftershock region was inundated with portable instrumentation from many agencies including the California Institute of Technology (CIT) to make this the most extensively monitored aftershock sequence to date and provide a unique data set for aftershock studies. Allen et al.(1972) assigned the main shock parameter as: 34° 24.7' N, 118° 24.0 W, h = 8.4 km, and M_L = 6.4. The main fault motion, as inferred from observed surface faulting (Kamb et al., 1971, and U. S. Geological Survey Staff, 1971), static displacement of the ground surface (Jungels and Anderson, 1971; Jungels and Frazier, 1973; and Alewine and Jordan, 1973), and from the initial focal mechanisms (Division of Geological and Planetary Sciences, California Institute of Technology, 1971; Whitcomb, 1971; Wesson et al., 1971; Dillinger and Espinosa, 1971, and Canitez and Toksoz, 1972), was of the thrust type on a north-northeast-dipping fault plane with some left-lateral strike-slip. The general type and orientation of the main fault plane agree with mapped north-dipping thrust faults which bound many of the southern edges of the Transverse Ranges.

From the lunate-shaped distribution of the M_L = 3.0 or larger aftershock epicenters shown in Figure 1 and the relatively low seismicity near the surface break (Allen et al., 1971; Hanks et al.,

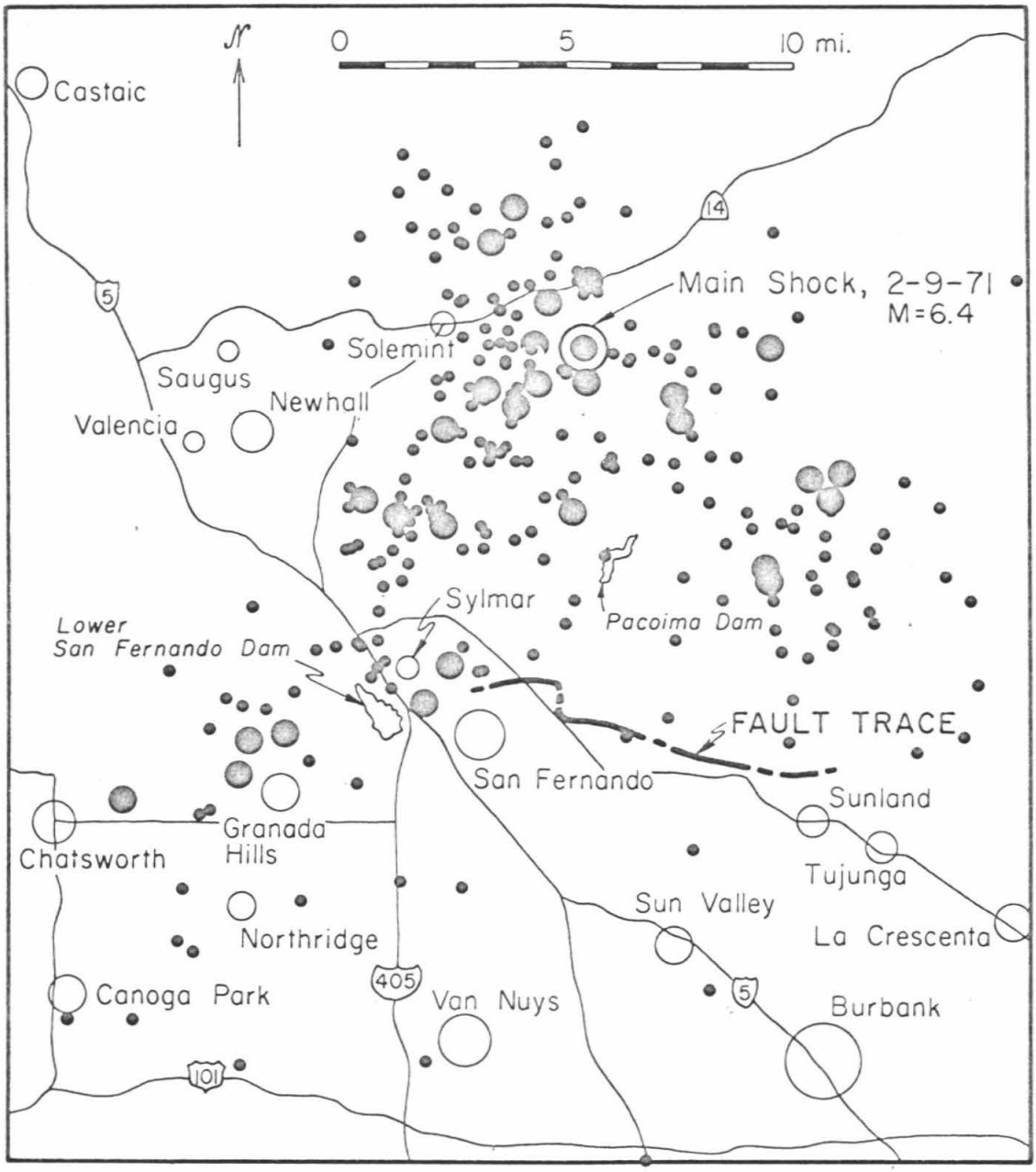

Figure 1.

Epicentral locations of the main San Fernando event of February 9, 1971, and aftershocks through December 31, 1971. All events of M_L = 3.0 or larger, including those not specially studied, are shown. The larger points indicate events of M_L = 4.0 or larger.

1971; Wesson et al., 1971; and Allen et al., 1972), it appears that the stresses were completely relieved on the main fault surface and the larger aftershocks were mainly limited to the edges where stress was concentrated. However, Whitcomb (1971), using focal mechanisms, showed that the apparent lunate symmetry is misleading in that the tectonic pattern along each limb of the distribution is totally different.

Allen et al. (1972) used the largest aftershocks, mainly those with M_L = 4.0 or greater, to formulate a tectonic model of the associated faulting. The focal mechanisms which substantiate that development are presented first with a review of the model's construction. We then investigate a more extensive set of 87 aftershocks chosen in a uniform manner from the three months between the onset of the series and May 7, 1971. The cutoff date is the time when many of the CIT portable seismometer trailers were removed and the aftershock rate had decreased to less than one per four days. This second set confirms the general features of the fault surface model. Some of the individual focal mechanisms and their locations are obviously not compatible with the model, but this might have been predicted for a region with such large tectonic movement of up to two meters (see for example Burford et al., 1971), and complex geological structure and seismicity (Wentworth et al., 1971). The deviations of the focal mechanisms from the model-predicted norm are shown to provide additional insight into the time and spatial

variations of the tectonics in the aftershock region. We then investigate isolated bursts of activity occurring later in the series which suggest a propagating phenomenon that triggers events. Last, we relate the pre-1971 seismicity and the mapped structure in the region to the tectonic features of the San Fernando earthquake series.

2. DATA SET

A major goal of aftershock studies is to outline the associated tectonics of the region. It is therefore desirable to chose the set of aftershocks that is most representative of the major tectonic stress release. This means that the aftershock set must contain the largest events. A practical limit is set at the lower end of the magnitude scale due to a limit on the size of the data set and the signal strengths that the stations record. From this reasoning, the aftershock set that is most representative of the regional tectonic activity includes all events above a certain size.

Two definitions of cutoff size are used. The first set is defined as all aftershocks of M_L = 4.0 or larger. P-wave first motions that are immersed in the coda of previous shocks are not used, and this unfortunately precludes the use of events during the first hour of the aftershock series. But the set is complete after the first hour, giving a total of 20 events. A histogram of all aftershocks of M_L = 4.0 or larger is shown in Figure 2a. The dark portions

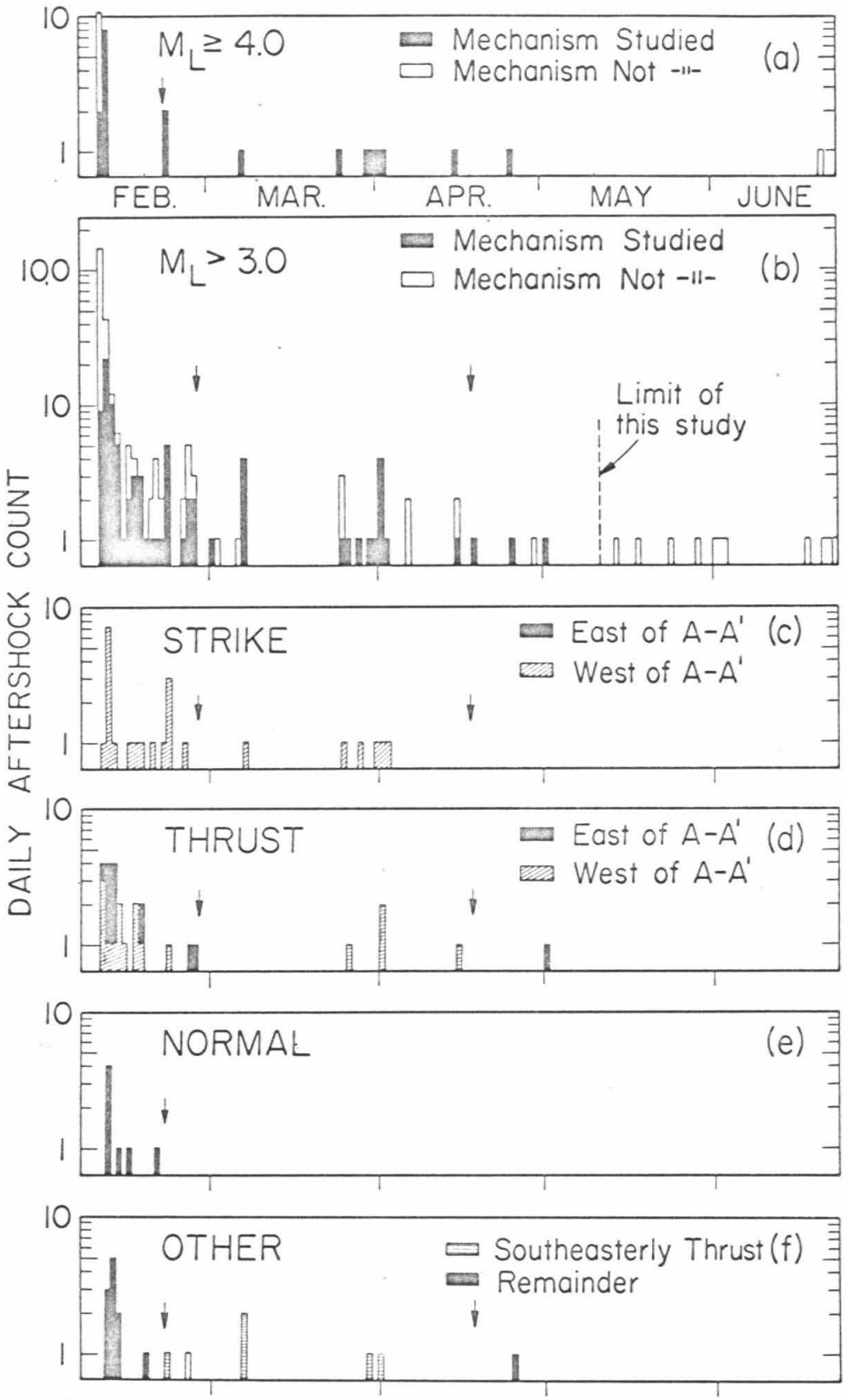

Figure 2. Histograms of the aftershock groups: (a) M_L of 4.0 or greater, (b) M_L greater than 3.0, (c) strike-slip events that fit the model, (d) thrust events that fit the model, (e) events with normal dip slip, (f) others.

indicate the events in the first set.

The second set is defined as those shocks whose P-wave first motions are clear on most of the CIT permanent stations, most of which are between 90 and 300 km from the epicenters. The rationale for this definition is that the data from the more distant stations are much less sensitive to hypocentral location and velocity errors than the close-in portable stations when their first motions are mapped onto the focal hemisphere. Again, the homogeneity of the aftershock set is compromised by the occasional immersion of first motions in the coda of a previous shock. This occurs most often during the first few hours of the aftershock series, and its effect on the conclusions cannot be estimated. One can only assume that the masking is distributed randomly with aftershock type, and that the stress release during the first few hours is not basically different except in rate from the remainder of the series. Some of the conclusions reached below deal with the latter assumption. A histogram of the aftershocks with M_L's larger than 3.0 is shown in Figure 2b. The dark portions indicate the events included in the second set.

Table 1 lists all of the events of the second set, which of course includes the first set, along with M_L, location, location quality, focal mechanism quality, and number of stations used for first motion determinations (most of these parameters are discussed below). The smallest shock that fulfills the criterion of first-motion

Table 1

No.	Date	Time (h:m)	M_L	Epicenter 34°N Lat.	Epicenter 118°W Lon.	Depth	Location Quality	Focal Mechanism Quality	First Motion Stations
Main	2/09	14:00	6.4	24.7'	24.0'	8.4	B*	B	101
1		15:10	3.9	24.8	24.7	8.	C@	C	7
2		15:38	3.9	24.4	28.0	8.	C@	B	12
3		15:58	4.8	22.46	20.10	9.0	B*	C	12
4		16:19	4.2	27.44	25.62	-1.	C*	B	12
5		17:03	3.9	22.2	29.5	8.	C@	B	10
6		17:19	3.6	24.7	26.8	8.	C@	B	12
7		18:29	3.8	23.7	28.9	8.	C@	C	13
8		20:53	3.4	26.1	23.7	8.	C@	A	15
9		20:56	3.7	18.5	21.3	8.	C@	B	11
10	/10	01:38	3.9	19.3	32.0	8.	C@	B	17
11		03:12	4.0	22.20	18.12	0.8	B*	A	18
12		05:06	4.3	24.67	19.76	4.7	B*	C	19
13		05:18	4.5	25.55	24.85	5.8	B*	C	20
14		05:41	3.7	21.6	17.8	8.	C@	A	16
15		06:24	3.4	24.4	19.5	8.	C@	A	12
16		06:54	3.4	23.7	27.0	8.	C@	C	13

Table 1 (continued)

No.	Date	Time (h:m)	M_L	Epicenter 34°N Lat.	Epicenter 118°W Lon.	Depth	Location Quality	Focal Mechanism Quality	First Motion Stations
17	2/10	07:00	3.5	18.1	18.5	8.	C@	A	14
18		07:14	3.4	21.4	26.5	8.	C@	A	18
19		07:27	3.8	24.1	26.1	8.	C@	C	17
20		09:33	3.2	19.6	15.2	8.	C@	A	16
21		10:00	3.4	26.8	27.7	8.	C@	B	19
22		11:29	3.2	27.2	25.6	8.	C@	B	20
23		11:31	4.2	23.06	27.30	6.0	B*	A	20
24		11:45	3.5	23.4	28.5	8.	C@	A	20
25		12:42	3.4	20.7	16.9	8.	C@	A	18
26		13:49	4.3	23.94	25.12	9.7	A*	B	21
27		14:35	4.2	21.69	29.20	4.4	A*	A	22
28		17:38	4.2	23.74	21.98	6.2	A*	B	20
29		18:54	4.2	26.75	26.16	4.2	A*	B	21
30		19:06	3.5	22.51	18.07	11.3	B	A	21
31		23:42	3.5	23.14	21.41	8.1	B	C	22
32	/11	00:30	3.5	24.50	16.63	5.0	B+	B	24
33		03:43	3.2	25.05	26.32	8.0	A	B	25

Table 1 (continued)

No.	Date	Time (h:m)	M_L	Epicenter 34°N Lat.	Epicenter 118°W Lon.	Depth	Location Quality	Focal Mechanism Quality	First Motion Stations
34	2/11	04:07	3.4	18.39	32.13	11.3	B+	B	22
35		07:33	3.3	27.41	26.50	12.4	A	A	22
36		09:24	3.3	24.91	20.34	5.0	B+	B	26
37		11:32	3.5	20.20	18.83	0.5	A+	B	26
38		14:21	3.5	17.78	19.28	2.4	B	B	26
39		16:43	3.6	22.07	27.70	2.3	A	A	23
40		19:35	3.7	24.00	26.87	6.4	A	B	26
41		23:35	3.7	21.11	20.21	4.6	A	B	25
42	/12	08:09	3.2	21.56	21.28	1.8	B	B	24
43		09:20	3.3	25.56	25.73	8.1	A	A	27
44		09:52	3.4	21.55	27.18	2.0	A	A	26
45		15:02	3.4	24.41	25.86	9.5	B	A	25
46		16:22	3.9	24.77	25.50	9.2	A	A	26
47	/13	06:44	3.2	19.64	32.80	1.6	B	A	28
48	/14	03:38	3.3	23.86	23.03	9.4	A	A	23
49		13:44	3.8	17.97	30.67	1.1	B	A	30
50	/15	08:04	3.9	28.27	24.63	12.9	A	A	27
51		08:46	3.4	24.42	26.48	7.9	A	A	23
52		13:03	3.4	25.65	26.12	9.7	A	A	22
53	/16	04:37	3.5	17.25	32.61	0.6	B	A	25

Table 1 (continued)

No.	Date	Time (h:m)	M_L	Epicenter 34°N Lat.	Epicenter 118°W Lon.	Depth	Location Quality	Focal Mechanism Quality	First Motion Stations
54	2/16	07:08	3.3	24:40	26.86	9.3	A	B	22
55		14:39	3.1	20.07	17.87	10.0	A	A	23
56	/17	10:15	3.5	21.46	18.38	5.3	A	B	20
57	/18	22:09	3.2	23.18	25.85	4.4	A	A	17
58	/19	02:45	3.5	21.45	27.58	-1.5	B	B	22
59	/20	08:09	3.6	27.24	24.38	15.2	A	B	21
60	/21	02:42	3.6	17.69	31.86	6.8	B	A	20
61		05:50	4.7	23.85	26.32	6.9	A*	A	27
62		07:15	4.5	23.52	25.65	7.2	A*	A	26
63		07:43	3.5	23.87	25.58	4.9	A	A	21
64		14:06	3.5	23.89	26.70	6.2	A	A	19
65	/24	16:04	3.7	26.48	24.64	10.8	A	A	21
66	/25	11:27	3.2	25.23	26.51	7.5	A	B	17
67		20:27	3.5	20.17	21.79	-2.0	B	A	20
68	/26	03:33	3.5	25.13	22.95	7.5	A	A	20
69		21:22	3.3	27.25	27.21	10.0	A	C	18
70	3/01	04:28	3.4	24.05	26.00	4.4	A	C	19
71	/07	01:33	4.5	21.19	27.35	3.2	A*	A	33
72		06:56	3.9	22.59	26.00	4.9	A	C	27
73		07:11	3.3	22.65	26.22	0.8	A	B	23

Table 1 (continued)

No.	Date	Time (h:m)	M_L	Epicenter 34°N Lat.	Epicenter 118°W Lon.	Depth	Location Quality	Focal Mechanism Quality	First Motion Stations
74	3/25	21:36	3.3	24.83	22.85	3.8	A	B	25
75	3/25	22:54	4.2	21.38	28.47	4.6	A*	A	28
76	/26	20:55	3.3	28.09	27.68	11.3	A	A	19
77	/28	17:16	3.7	21.28	28.39	5.7	A	A	28
78	/30	08:54	4.1	17.74	27.84	2.6	A*	A	29
79	/31	14:52	4.6	17.15	30.89	2.1	A*	A	30
80	4/01	01:54	3.4	15.94	35.34	6.3	B	B	23
81		15:03	4.2	24.72	25.19	7.1	A*	A	31
82		21:15	3.2	24.32	25.85	7.9	A	A	21
83		21:18	3.5	23.73	25.73	7.3	A	B	28
84	/02	05:40	4.0	17.03	31.70	3.0	A*	A	30
85	/15	11:14	4.2	15.88	34.62	4.2	A*	A	28
86	/25	14:48	4.0	22.09	18.86	-2.0	B*	A	20
87	5/01	04:25	3.6	26.00	24.15	4.8	A	A	22

@Location modified from Allen et al. [1971]

+Location from Hanks et al. [1971]

*Location from Allen et al. [1972]

clarity at most of the CIT telemetry stations has an M_L of 3.1. Essentially all shocks with an M_L of 3.5 or larger fulfill the criterion and are included unless masked by a previous shock. The histogram of Figure 2b shows that most of the aftershocks above M_L = 3.0 after the first two days have first motions that are clear enough to be included in the second set, and it can be considered to have an approximate magnitude cutoff of M_L = 3.3.

The stations used for P-wave first motions in this study with their operating agencies, coordinates, and periods of operation are given in Table 2. The station locations in relation to the approximate epicentral distribution of aftershocks (Allen et al., 1972) are shown in Figure 3. All readings were made from short-period vertical seismometers. Although 47 stations were used for first motion studies, varying periods of operation for the portable stations and the weakness of the first arrival of smaller shocks at distant stations reduced the actual number of first motions read per event. The number of readings for most events ranged from 10-20 for the first twenty hours of the aftershock series and 20-30 for the remainder of the study time period. Some instrument polarity reversals did appear, usually in instrumentation that was temporary or involved complex electronics such as a telemetry link from seismometer to recorder. However, the station coverage and the number of events were sufficient to reveal the reversal. Also, in almost every case, a reversal could be confirmed by polarity checks with teleseismic events.

Table 2

Station	Agency	Lat. N.	Long. W.	Period of Operation
AGM	EML	34 29.5	118 19.3	2/10-4/24
ANM	EML	34 27.2	118 30.6	3/15-4/24
BAR	CIT	32 40.8	116 40.3	permanent
BHR	USC	34 00.5	118 21.7	2/27-present
BLA	CIT	34 14.8	118 26.7	3/02-present
BQR	CIT	34 17.6	118 35.4	2/09-5/07
BRC	CIT	34 17.6	118 35.4	2/09-5/07
BRCL	LGO	34 23.0	117 46.3	2/12-2/14
CLC	CIT	35 49.0	117 35.8	permanent
CSP	DWR	34 17.9	117 21.5	permanent
CWC	CIT	36 26.4	118 04.7	permanent
ENG	CIT	34 08.4	118 05.2	semi-permanent
GLA	CIT	33 03.1	114 49.6	permanent
GOK	CIT	34 23.1	118 28.3	2/10-5/06
GOR	LGO	34 46.9	118 48.0	2/10-2/14
GSC	CIT	35 18.1	116 48.3	permanent
HAY	CIT	33 42.4	115 38.2	permanent
HCC	USC	33 59.6	118 23.0	2/28-present
IND	CIT	34 25.2	118 16.2	2/10-4/22
IPC	USC	33 58.2	118 20.4	3/04-present
IRC	CIT	34 23.3	118 23.9	2/09-5/07
ISA	CIT	35 38.6	118 28.6	permanent
JBF	USC	33 59.6	118 20.7	3/25-present
LSV	LGO	34 36.4	118 19.5	2/10-2/12
MER	LGO	34 29.8	118 02.4	2/12-2/14
MLM	EML	34 23.4	118 04.8	2/10-4/24
MWC	CIT	34 13.4	118 03.5	permanent

Table 2 (continued)

Station	Agency	Lat. N.	Long. W.	Period of Operation
OMM	EML	34 19.8	118 36.0	2/25-4/24
PAS	CIT	34 08.9	118 10.3	permanent
PLM	CIT	33 21.2	116 51.7	permanent
PYR	DWR	34 34.1	118 44.5	permanent
RTM	EML	34 35.8	118 14.8	2/10-3/15
RTR	CIT	34 11.9	118 09.4	semi-permanent
RVR	CIT	33 59.6	117 22.5	permanent
SBC	CIT	34 26.5	119 42.8	permanent
SCF	NOS	34 26.3	118 17.3	2/10-2/17
SGM	NOS	34 23.1	118 24.8	2/10-2/17
SHC	NOS	34 30.5	118 21.8	2/10-2/17
SOC	CIT	34 26.1	118 21.7	2/10-5/06
SWM	CIT	34 43.0	118 35.0	permanent
SWML	LGO	34 42.1	118 32.1	2/10-2/14
SYP	CIT	34 31.6	119 58.7	permanent
TIN	CIT	37 03.3	118 13.7	permanent
USC	USC	34 00.8	118 17.3	2/06-2/28
USCB	USC	34 00.1	118 20.5	2/12-2/14
USCP	USC	34 02.7	118 32.1	2/12-2/14
WSM	EML	34 36.4	118 33.5	2/10-4/24

CIT: California Institute of Technology
DWA: California Department of Water Resources
EML: Earthquake Mechanisms Laboratory, NOS
LGO: Lamont-Doherty Geological Observatory
NOS: Las Vegas Branch of NOS
USC: University of Southern California

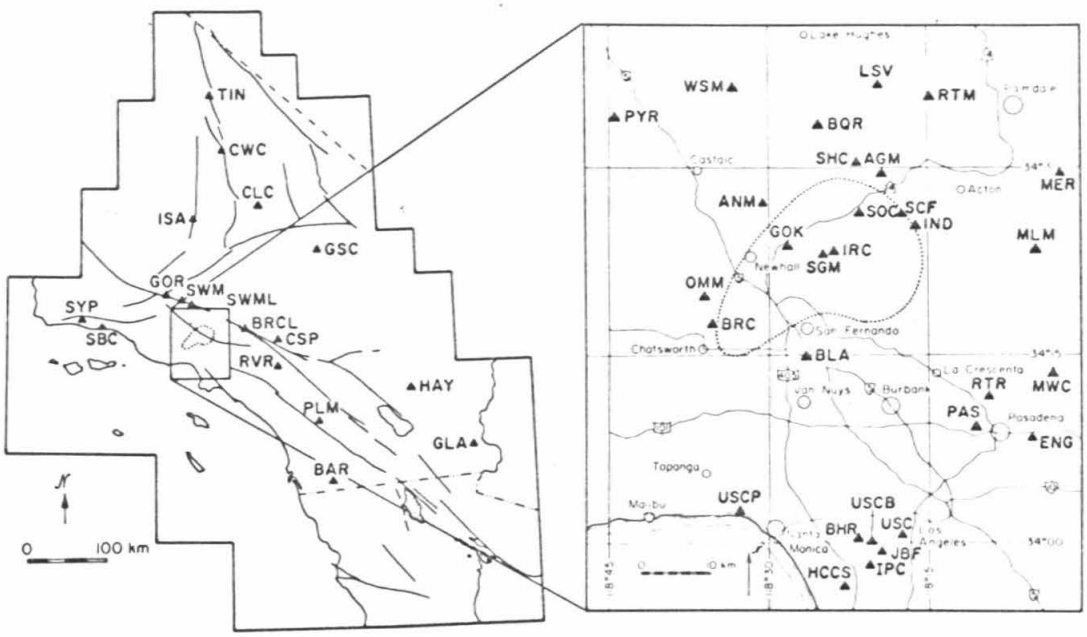

Figure 3.

Location map of stations used for first motion studies; station data are listed in Table 2. The approximate aftershock zone is shown for reference.

3. HYPOCENTRAL LOCATIONS

The hypocentral locations done by us are computed with the same method as that used by Allen et al. (1972) except that the closer stations are weighted more heavily, especially for shallow hypocenters. The stations used for locations are those of CIT and the Earthquake Mechanisms Laboratory (EML) shown in Figure 3 and Table 2, and in some cases SUS, which is a station of the United States Geological Survey's National Center for Earthquake Research (see Wesson et al., 1971). For shocks in the western extremity of the aftershock region, the westerly stations BRC, OMM, and SUS are given large weights to offset the bias introduced by the fact that most of the close stations lie to the east. Because the aftershocks in the set are all larger than M_L = 3.0, S-wave arrival times are difficult to measure on the high-gain film records of the CIT portable stations. These S-wave arrival times that are read from the CIT stations and those listed in the EML data reports are given half the weight of their associated P-wave arrival times.

In the earlier part of the aftershock sequence, approximately the first twenty-four hours, not enough portable stations were in place for precise hypocentral locations. Allen et al. (1972) recomputed the locations of the events with M_L = 4.0 or larger in this early period by applying time correction factors to arrival times from the permanent southern California stations. The corrections were computed from precise locations of later shocks by use of the

portable stations. The locations taken from Allen et al (1972) are indicated with stars in Table 1. The remainder of the locations in this early period are from Allen et al. (1971) with some modification to account for systematic epicentral shifts which are present when comparing locations from only the permanent station data to those from the closer portable station data. The modified locations are indicated in Table 1 with @ symbols. Four of the event hypocenters have been computed by Hanks et al. (1971) and are indicated by crosses in Table 1. The remaining locations were computed by us.

The accuracy of the hypocenters in this study is estimated following the definitions of Allen et al. (1972). Depending on the number and location of the stations and the standard error of the computer solution, the quality of the hypocentral locations is divided into three categories: "A" locations are generally accurate to within 2 km horizontally and 4 km vertically; "B" locations are felt to be accurate to within 4 km horizontally and 8 km vertically; and "C" locations include all those that are considered less accurate. The location qualities are given in Table 1. As can be seen by the definitions, the accuracy of the epicentral determination is much better than that of the depth; this is especially true for those events with shallow depths. Direct confirmation of the location accuracies is extremely difficult short of drilling down and firing a large explosive at hypocentral depths. However, the accuracies estimated for the different qualities are considered conservative

based on variations of the hypocenter as a function of reasonable changes of velocities, station corrections, station combination, and station weighting. Because all of the "A" and "B" quality events are located in essentially the same manner, hypocenters in the same region should be located more accurately relative to each other than is implied by the above estimates of absolute location accuracy.

4. FOCAL MECHANISM DETERMINATIONS

P-wave first motions are used exclusively for the focal-mechanism determinations. The first motion reading is classified as good or fair depending on a subjective estimate of the onset clarity and how confident we are that the motion is truly the first arrival; doubts in the latter situation occur most often at distances where P_n is the first arrival. A record is also kept of arrivals that have emergent character when, by a subjective judgment involving the epicentral distance and size of the aftershock, one would expect the first motion to be sharp; these arrivals are designated as having nodal character implying that they map on the focal sphere near one of the nodal planes of the double couple. While this character is not used in the fit of the double-couple mechanism to the data, it is found that these points indeed tend to map near the nodal planes. It is therefore believed that, with proper precautions, they can be

used in future studies as additional information in a focal mechanism fit.

The source takeoff angle is calculated by ray tracing as a function of the aftershock's epicentral distance and depth using the P-wave velocity model shown in Figure 4. The model is based mainly on the results of Healy (1963), who analyzed a reversed refraction profile between Santa Monica Bay and Camp Roberts, California, that passes very close to the epicentral area. Takeoff angles were calculated also for the velocity model shown as a dashed line in Figure 4, which includes a 7.2 km/sec layer at the base of the crust. However, the rays refracted along the top of this layer were first arrivals for only a very small epicentral distance range, which made the difference between the two velocity models insignificant. This is especially true in light of the large lateral variations in shallow crustal structure demonstrated by Wesson and Gibbs (1971). These variations probably have much greater effect on the ray takeoff angles and azimuths, and if one were to use a more sophisticated velocity model, lateral variations should be included. The use of the more distant stations helps to minimize these effects because the rays leaving the hypocenter in a downward direction presumably encounter less drastic lateral changes in velocity. Wesson and Gibbs' results generally confirmed the shallow part of Healy's (1963) model with crystalline basement rock velocities of around 6 km/sec. Although they obtained near-surface sediment velocites in the Santa Susana

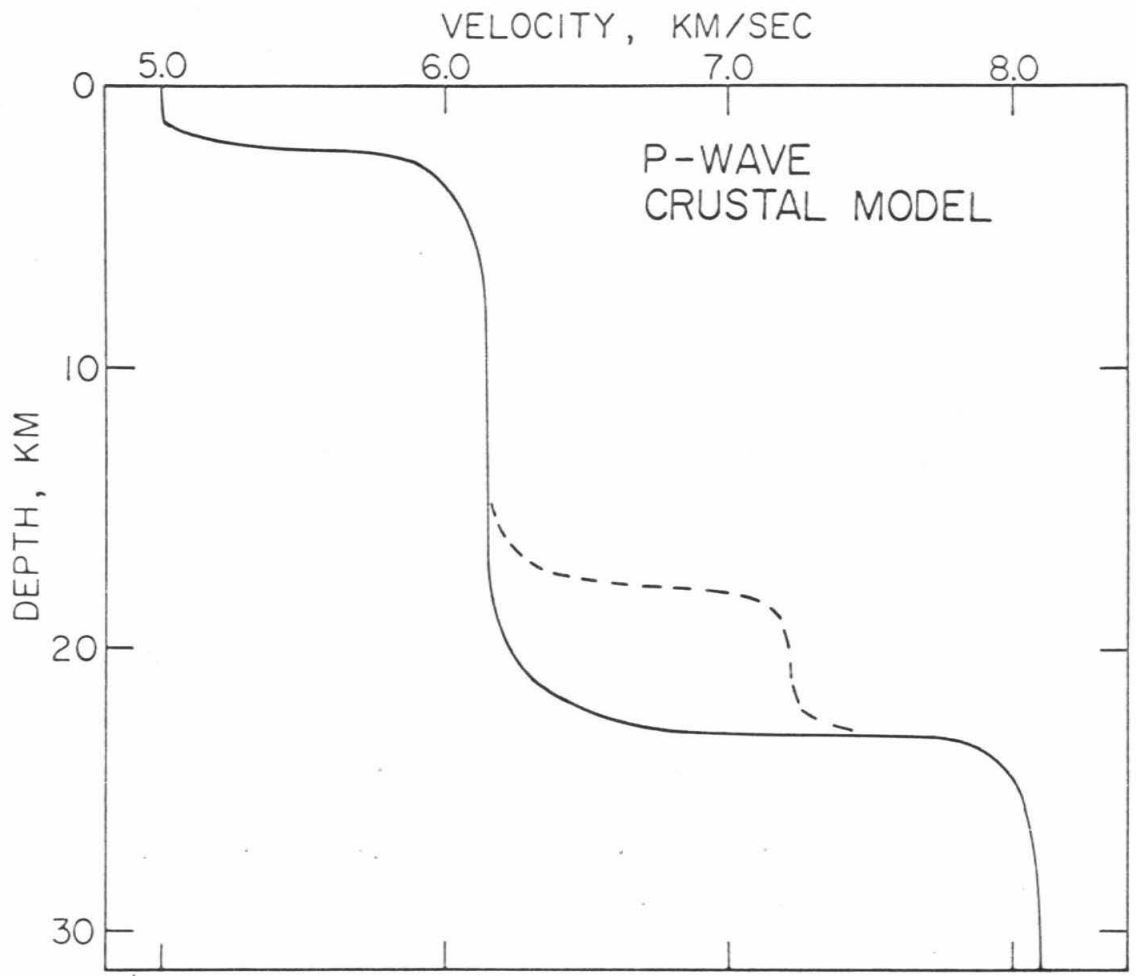

Figure 4.

P-wave velocity distribution used to map the first motion data onto the focal sphere. The dashed line indicates a variation of the velocity that produced no significant changes in the mapping.

Mountains as low as 3.4 km/sec, this velocity is not used here in the focal mechanism computations for shallow hypocenters in the southwest aftershock region. The initial ruptures of the larger aftershocks would be in the stronger, and therefore higher-velocity, rocks because they support most of the stress. Thus, the shallow hypocenters, which are always the most inaccurate, are assumed to be deep enough to be in higher-velocity sedimentary or crystalline rock.

The focal mechanism of the main shock has been recomputed using some new close-in station data and estimates of the P_g-P_n breakover distance based on the aftershock data at stations near this range. The best fit to the P-wave first motion data constrains the fault plane parameters to: strike, N 67° (±6°) W; dip 52° (±3°) NE; and rake 72° (67°-95°) left lateral. Choice of the northeast-dipping plane as the fault plane rather than the auxiliary plane is based upon its close correspondence to the observed surface faulting, the hypocentral locations of aftershocks, and the regional geology. The best fit is determined by minimizing the reading misfits to a double couple with an algorithm that is described in Appendix 1. The fit to the data is shown in Figure 5. Circles are compressions and crosses are dilatations. It is interesting to note that the fault plane is very well determined but the rake angle, which is tied to the auxiliary plane, is much less so; this illustrates that station distributions can selectively constrain some focal mechanism parameters much better than others.

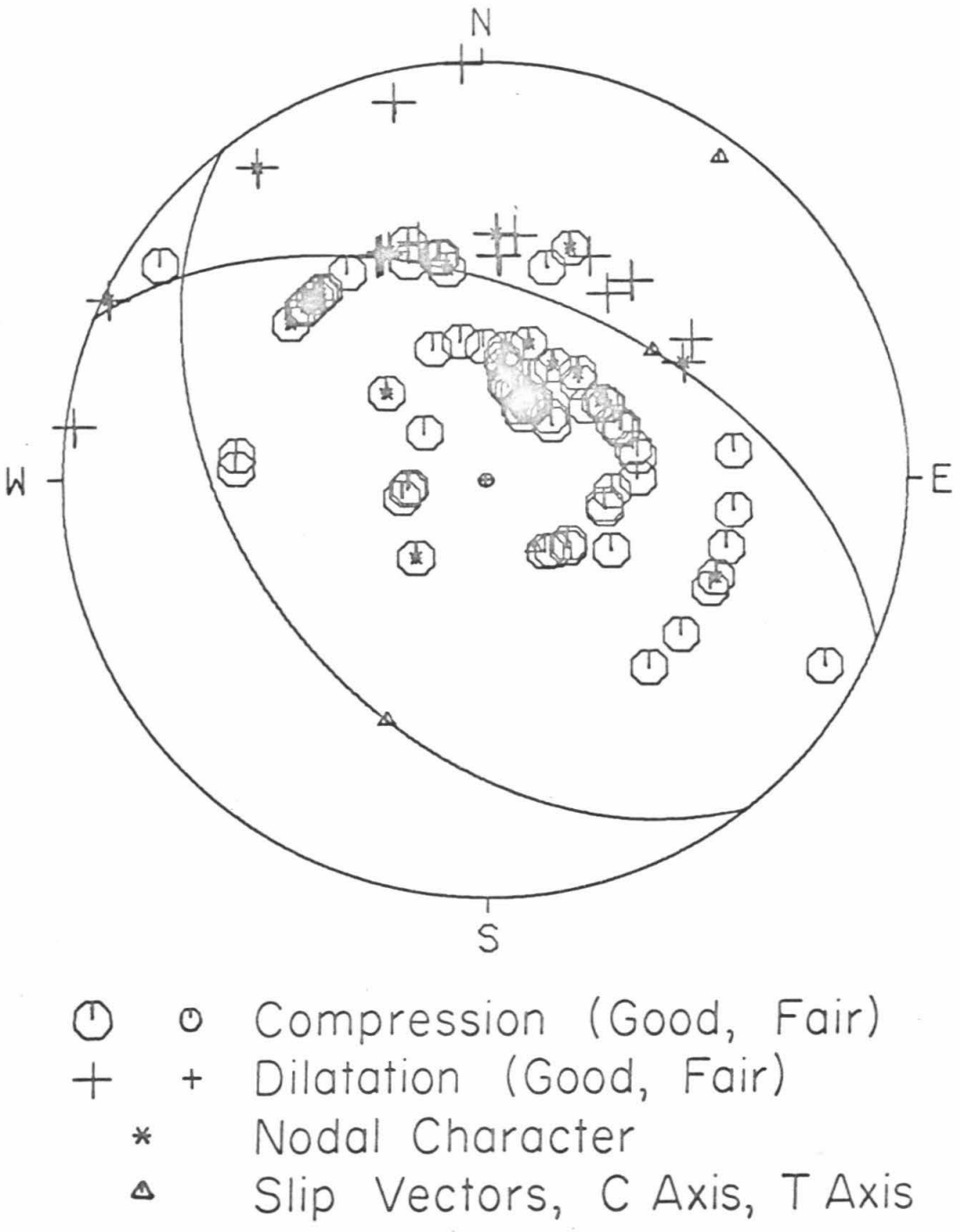

Figure 5.

The main February 9, 1971, San Fernando shock first motion data and the best fit of the double-couple mechanism. The data are shown on an equal-area projection of the lower focal hemisphere.

Canitez and Toksöz (1972) have estimated the rake angle from surface waves to be 45°, which would indicate a much greater average strike-slip over the fault plane than that of the initial rupture and, as seen later, the aftershocks. However, the determination was made using only six stations covering one quadrant at the source, and the effects of varying crustal structures were not calculated for the surface-wave paths. Thus, while their rake is interesting and has important implications, we prefer to withhold an attempt to explain this deviation pending a more complete confirmation of the value.

The double-couple focal mechanisms of the aftershocks are fit to the data by eye under the influence of the reading qualities, good or fair. An estimate of the quality of the solution is made based on the degree to which data constrain the orientation of the solution. "A" solution parameters are felt to be within 10° of the actual values, "B" solution parameters are felt to be within 20°, and "C" events are all others and are not assigned a solution. These definitions are intended to apply to the worst-constrained parameters of the solution.

Figure 6 shows data for all aftershocks with M_L = 4.0 or larger and Appendix 2 shows first motion data and focal mechanism solutions for all the aftershocks investigated; the plots include first motion data and the focal-mechanism solutions mapped on equal-area stereo plots of the lower focal hemisphere. The event numbers correspond

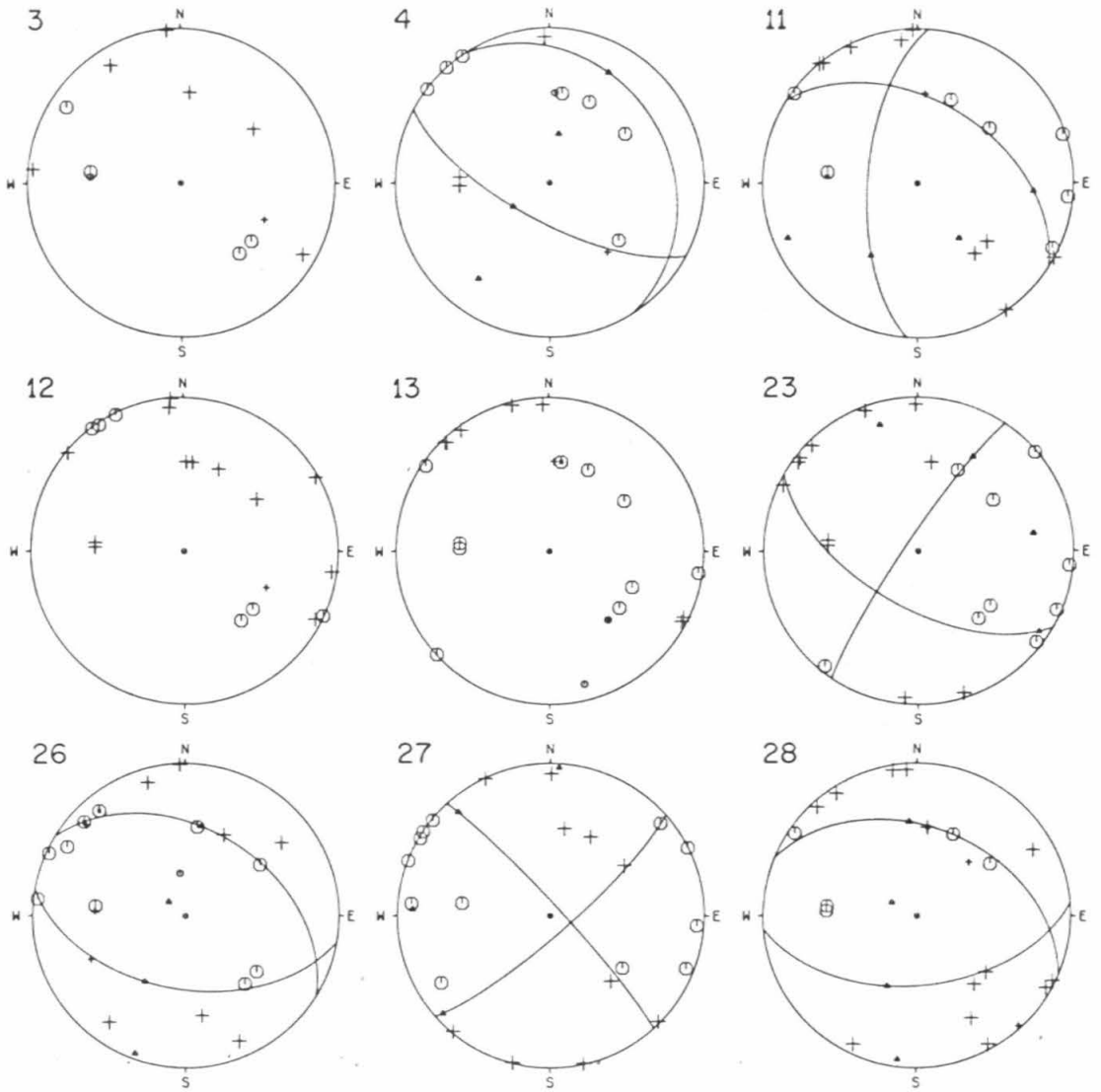

Figure 6.

M_L of 4.0 or greater aftershock first motion data and their focal mechanism fits. The numbers correspond to the events in Table 1. The data are shown on an equal-area projection of the lower focal hemisphere.

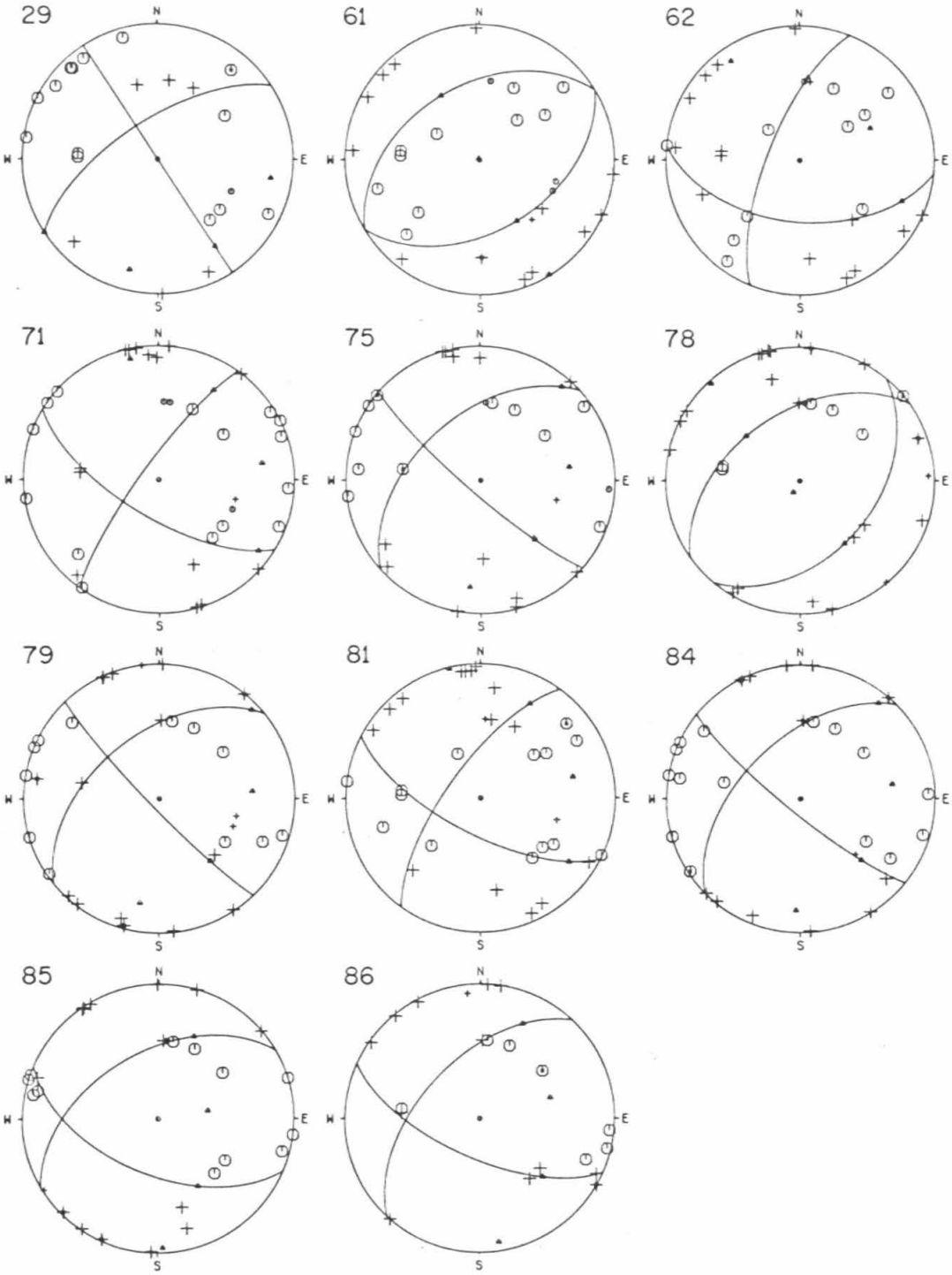
29
61
62
71
75
78
79
81
84
85
86
N
S
E
W

to those in Table 1.

5. TECTONIC INTERPRETATION

5.1 Magnitude 4.0 or larger shocks and development of a fault model. As defined above, the first set of aftershocks consists of those with an M_L = 4.0 or larger. The fit of focal planes to the first-motion data shown in Figure 6 is transformed to schematic diagrams of the quadrants in the lower focal hemisphere delineating the areas of compressional (dark) and dilatational (light) first motions and are shown at their epicentral locations in Figure 7. The larger diagrams denote "A" quality focal mechanisms, and the smaller are of "B" quality. Three of the twenty events have "C" quality focal mechanisms with no determination of the planes, but their epicentral locations are included in the figure. This set is complete after the first hour of the series and Figure 7 shows that most of the activity of these largest shocks is on the western limb, which is separated approximately from the rest of the aftershock sequence by the line A-A'. It is also apparent that over half of the focal mechanisms along the western limb have a steeply-dipping plane striking northeast parallel to the limb direction with left-lateral strike-slip fault motion. If these strike-slip mechanisms are connected to a single surface that is related to the tectonic motion of the main shock, then the strike-slip surface must be below the main thrust

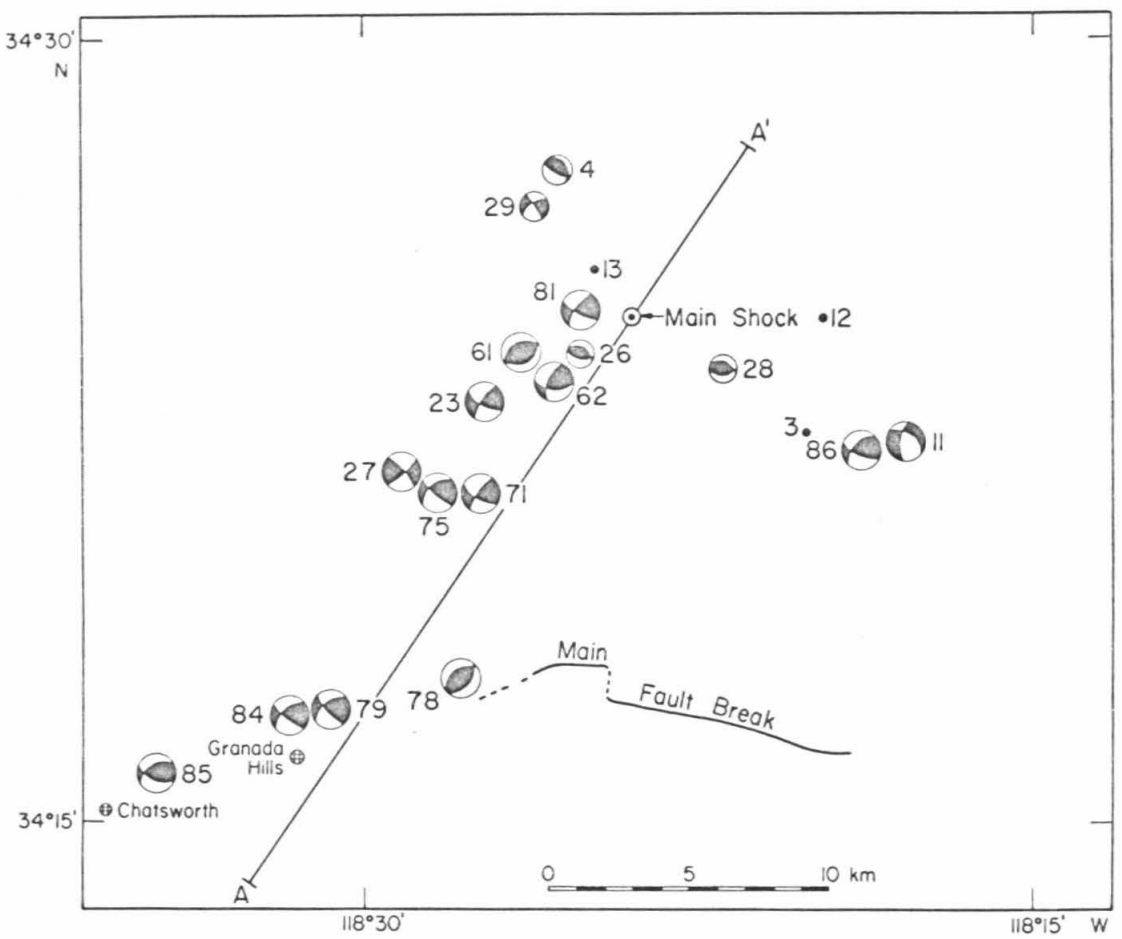

Figure 7.

M_L = 4.0 or greater aftershocks as schematic diagrams of the compressional (dark) and dilatational (light) first-motion quadrants in the lower hemisphere. The diagrams are at the event's epicenters and the numbers refer to those in Table 1. The size of the diagram refers to its focal mechanism quality of "A" (larger) or "B" (smaller, see text). All events with "A" and "B" quality focal mechanisms are included and the locations of three "C" quality mechanisms are indicated by points (Events 3, 12, and 13).

fault plane defined by the surface rupture, focal mechanism and hypocenter of the main shock. If the strike-slip surface were above the main fault plane, the motion would be right lateral for northeast striking faults, contrary to the observed motion. This distribution of focal mechanisms can be explained by the fault surface model first presented in Allen et al. (1972) and shown in Figure 8. It was based on many of these same data. The figure is a schematic structural contour map showing simplified contours, in kilometers, on the fault plane. The fault surface associated with the main thrust rupture is in the eastern portion of the map. In the vicinity of the western limb of aftershocks, the surface has a steep flexure that is down-stepped to the west and is associated with left-lateral strike slip motion. This flexure tended to limit the initial rupture to the west and, because of the resulting stress concentration in this zone, it was responsible for most of the aftershock activity. Two events, numbers 4 and 85 in Figure 7, are on the western edge of the western limb of aftershocks but their mechanisms are mainly thrust, similar to the main shock. These events can be explained by the flattening of the surface to the west as shown in Figure 8. However, the model requires that the thrusts west of the flexure be deeper than those to the east; this is one of the important hypothesis to be tested with the second aftershock set.

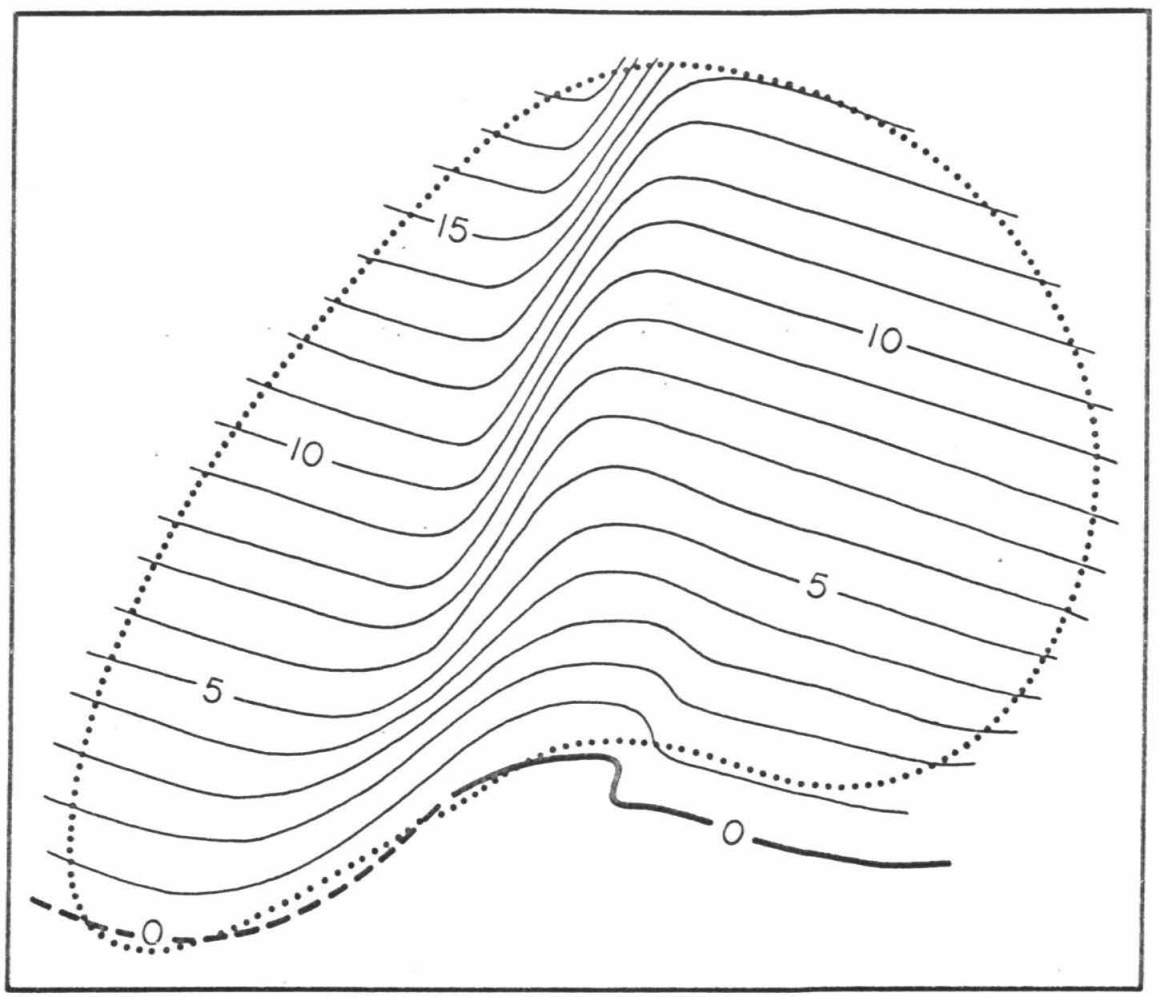

Figure 8.

San Fernando fault surface model showing the surface as simplified contours, in km, with a downstep to the west that explains the strike-slip events along the west limb of the aftershock zone (Allen et al., 1972).

5.2 Test of the model with the second aftershock set. The fault model developed for the twenty M_L = 4.0 or larger shocks should be representative of the major strain release of the aftershock series. The second and larger set of 87 aftershocks including smaller events can now be analyzed with the model as a test framework.

Figure 9 presents all of the "A" and "B" quality focal mechanisms that agree with the model of Figure 8. As before, they are shown as a map of schematic diagrams of the compressional (dark) and dilatational (light) first-motion quadrants in the lower focal hemisphere. The epicentral locations may be slightly in error due to crowding in the figure. Two-thirds (50/75) of the "A" and "B" focal mechanisms are included in Figure 9; certainly this represents strong support for the fault model of Figure 8. Certain characteristic features noted in Figure 6 are preserved here in Figure 9. Most of the activity is in the well-defined western limb of the aftershock sequence. Half of these events in the western limb have a plane dipping steeply to the northwest and striking to the northeast roughly parallel to the limb, and the motion on the planes is predominantly left-lateral strike-slip. The criterion for designating these aftershock focal mechanisms as mostly strike-slip or thrust is simply whether the rate (the angle in the fault plane between horizontal and the slip vector) is less than or greater than 45° respectively. While it appears that some thrust events appear to map within the western limb, a more complete location analysis done below shows that the thrusts in this area

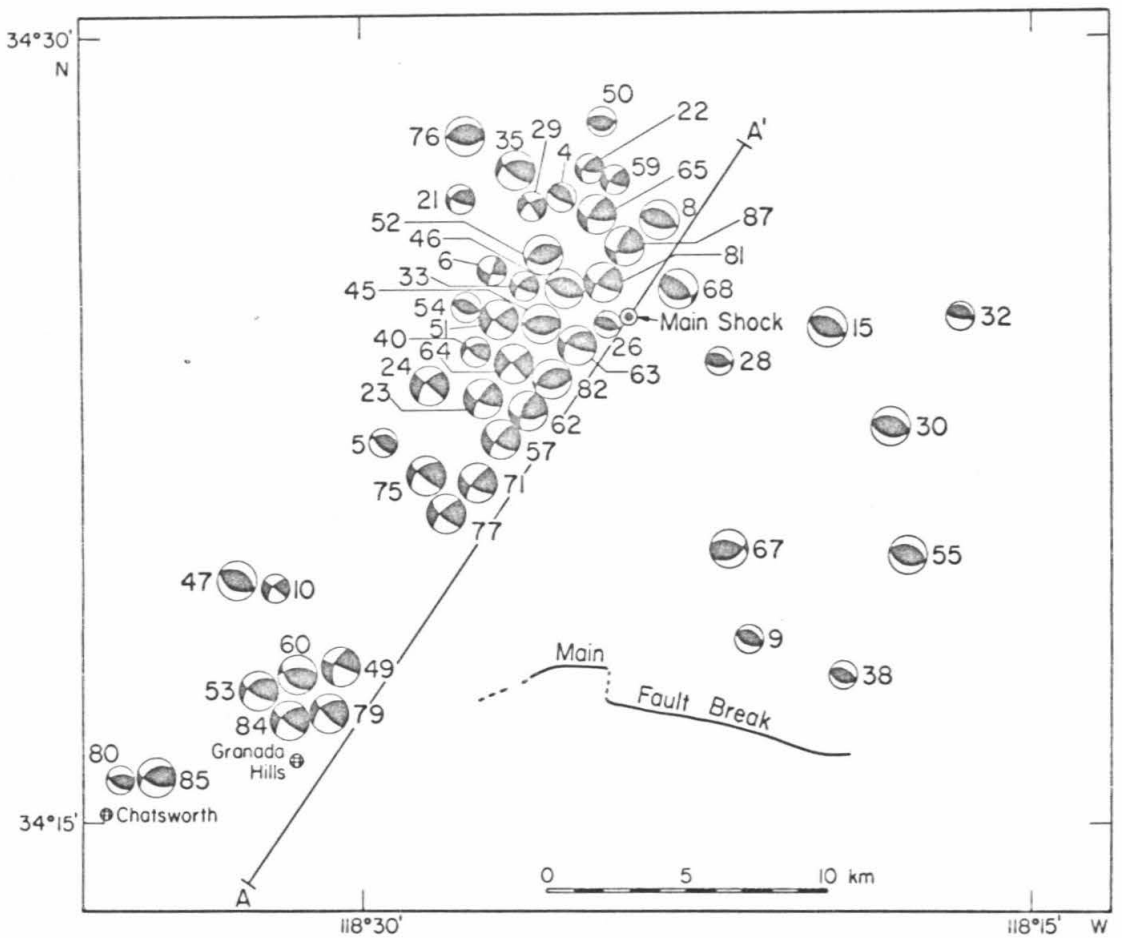

Figure 9.

Map of all "A" and "B" quality focal mechanisms that fit the model of Figure 8 (see caption of Figure 7). The epicenters may be slightly in error where the diagrams are crowded.

clearly tend to occur deeper and to the west of the strike-slip events.

The histograms of the thrust and strike-slip events that agree with the model are shown in Figures 2c and 2d. There is little difference in their overall time distribution, but if they are separated into east and west regions by A-A' (as indicated by different shading in the figure), they show that the model-related events east of A-A' larger than M_L = 3.0 are absent after the first 18 days of the series for two months. Thus, at least two and perhaps three preliminary stages in the aftershock sequence (separated by the arrows in Figures 1c and 1d) are defined by the events that fit the fault model of Figure 8: the first 18 days during which thrusting activity extended east of A-A'; February 27 to about April 17 when activity was mostly confined to the west of A-A'; (this stage, from evidence presented below, may have started 6 days earlier); and perhaps a third stage beyond April 17 when model-related activity east of A-A' is presented again. This division also coincides with the overall distribution of aftershocks with time in Figure 2a. The first stage contains the initial surge of aftershocks defined by a rather sharp cutoff on February 26; the second stage is characterized by a burst of aftershock activity initiated by M_L = 4.0 or larger shocks (these series are discussed below); and the third stage is characterized by a low aftershock rate with few M_L = 4.0 or larger events.

It is difficult to compare the whole set of focal mechanisms with the model of Figure 8 by placing them all on a single map because they are too numerous. A more compact method of comparison is provided by the classic parameters of the double-couple focal mechanism: the two slip vectors, the compression axis, and the tension axis. The model predicts certain ranges of these parameters which are shown in Figure 10; the approximate deviations from the ranges corresponding to the "A" (10° variation, shaded region) and "B" (20° variation, open region) quality focal mechanisms indicate the regions of expected scatter. The slip vector in the auxiliary plane, the compression axis, and the tension axis all sweep out extensive paths. The only fixed parameter is the north-northeast slip vector in the fault plane. This results from the requirements that the medium through which the fault surface passes be perfectly rigid and that no voids be created along the surface. The data for all of the "A" and "B" quality focal mechanisms are shown in Figure 10 with symbols representing strike-slip (squares) and thrust (circles) that agree with the model, and normal (N) and other (X) that do not agree with the model; the last two classifications are discussed below. "A" quality focal mechanisms are indicated by either solid points or circled letters. Most of the aftershocks fit the fault-surface model of Figure 8 very closely. The compression axes point generally north-south and nearly horizontally, and the tension axes point between vertical

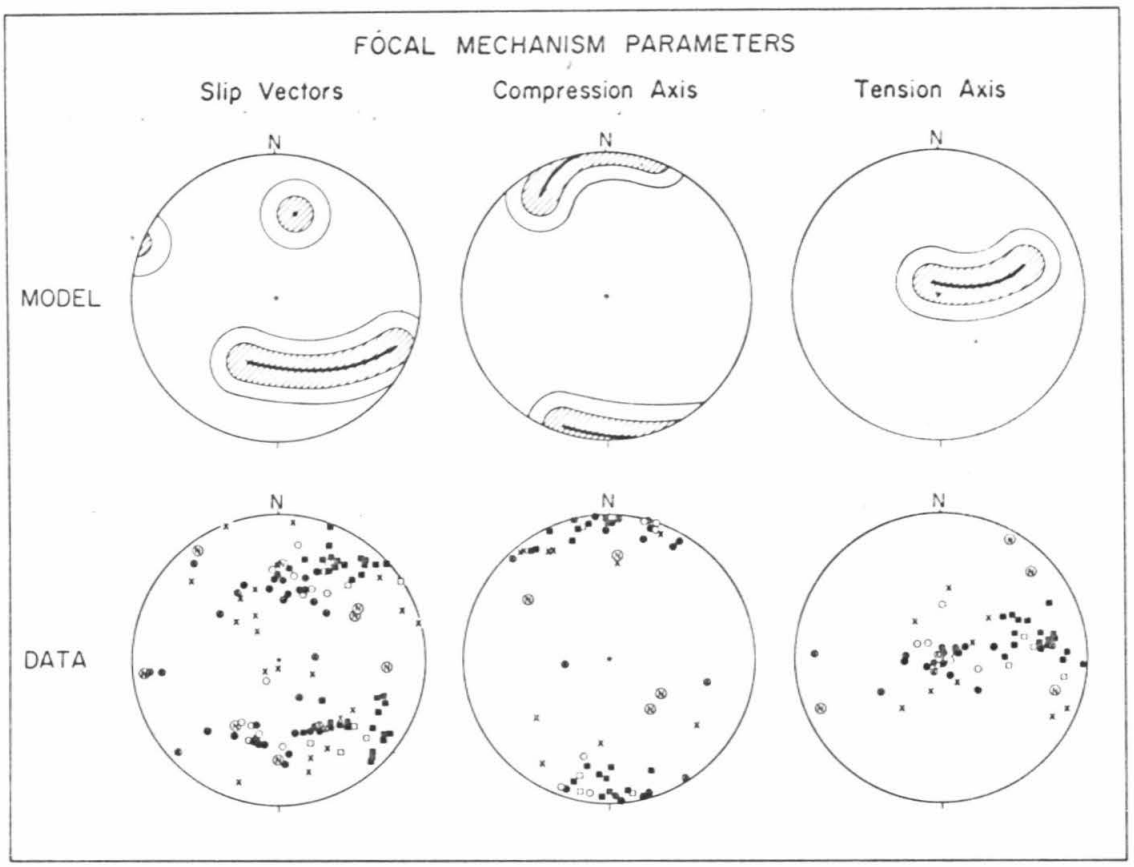

Figure 10.

The classic focal mechanism parameters (slip vectors, compression axis, and tension axis) on the lower focal hemisphere for the model of Figure 8 and for the data consisting of all "A" and "B" quality focal mechanisms. The symbol explanation is given in the text and in Figure 11.

and east depending on whether the mechanism is thrust or strike slip, respectively. The slip vectors in the fault plane scatter a little more than expected; the strike-slip data dip shallower and point more easterly than those of the thrust mechanisms. While it is difficult to completely rule out some systematic bias introduced by the station distribution or the focal-mechanism fitting technique, this consistent deviation between the thrust and strike-slip fault-plane slip vectors is considered real. As will be seen below, it has some bearing on the idealistic assumptions of rigidity and volume conservation used to formulate the initial model.

Precise locations of the aftershock hypocenters provide an important means of testing the three-dimensional fault surface model, especially because of the fault's complex non-planar nature. Only "A" and "B" quality locations in conjunction with "A" and "B" quality focal mechanisms are used, and these are presented in map view in Figure 11. The symbols represent strike-slip and thrust mechanisms that agree with the model, and normal and other mechanisms as in Figure 10. As identified earlier, there is a well-defined linear zone along the west of the line A-A' containing a majority of the events. We now project all of the points west of A-A' in Figure 11 onto a vertical plane along A-A' and present the resulting cross-section in Figure 12a. All of the strike-slip events south of the main event in this plot are limited to a shallow-dipping zone indicated by shading in the figure. Further, all but one thrust event,

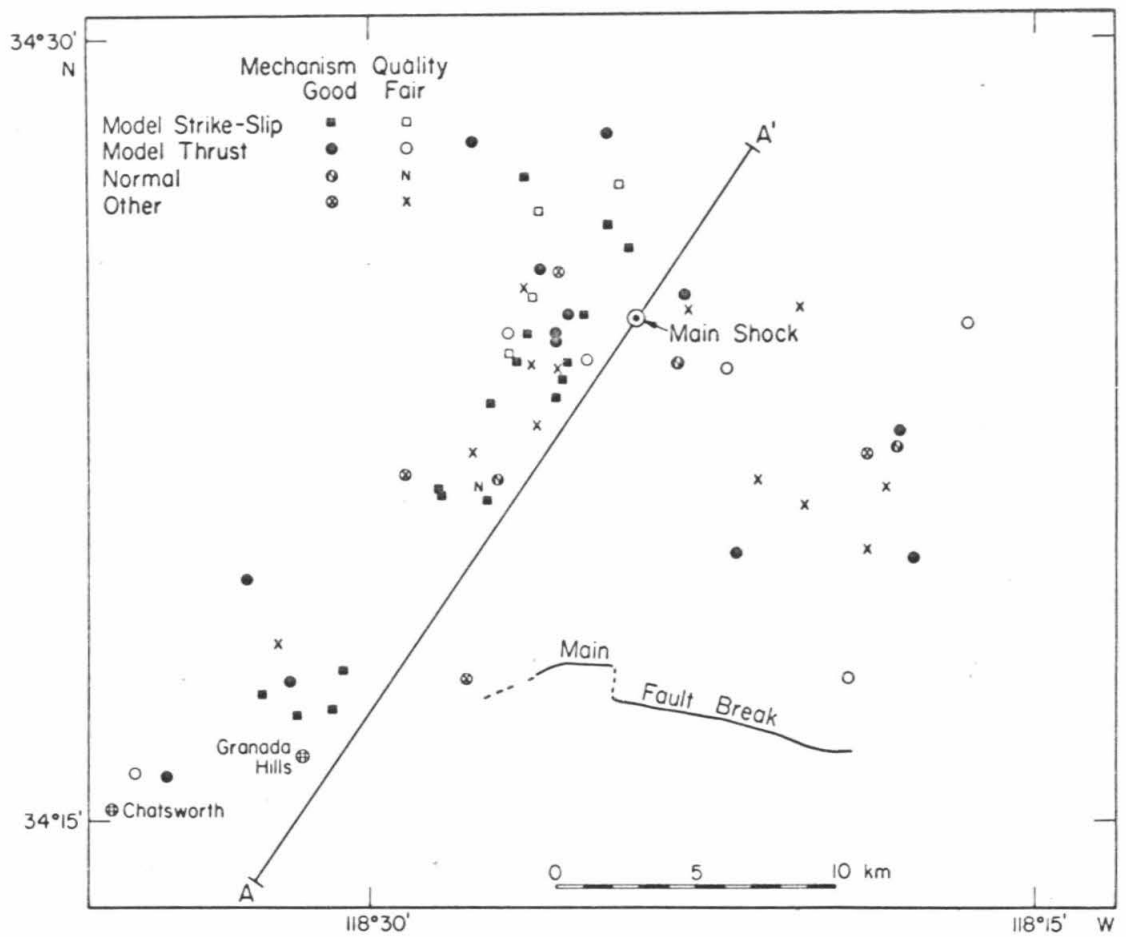

Figure 11.

Epicentral location of shocks with "B" or better quality for both locations and focal mechanisms.

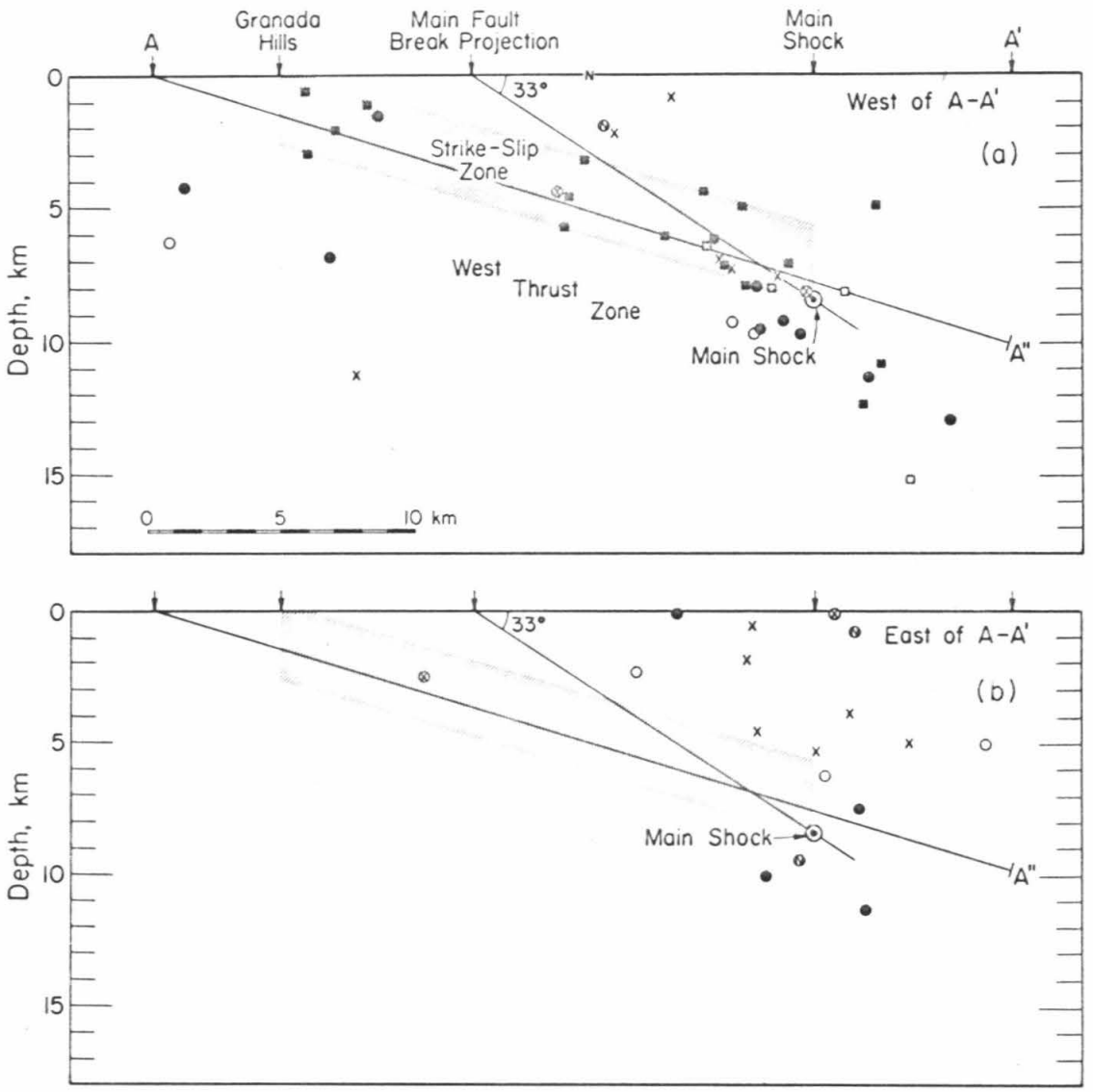

Figure 12.

Projection of hypocenters from Figure 11 onto the cross-section A-A' for (a) aftershocks west of A-A' and (b) aftershocks east of A-A'. The west thrust zone and strike-slip zone shown in (a) correspond to the structure in the westerly part of the model in Figure 8.

which is towards A and is fairly distant from A-A' (see Figure 11), plots below the strike-slip zone. This is strong confirmation of the downstep in the western portion of the fault surface model in Figure 8. The same cross-section for those events east of A-A' is shown in Figure 12b. The depths of these events are scattered but tend to plot above or in the upper part of the strike-slip zone with only three exceptions, Events 30, 48, and 55 (locations are shown in Figures 9 and 11). A further characteristic of the fault surface model is that the thrust mechanisms in the western limb of aftershocks should be not only deeper but further west compared to the strike-slip mechanisms. In Figure 13, we project all of the points of Figure 10 onto a plane perpendicular to the line A-A" (shown in Figure 12a); this corresponds to viewing the fault surface nearly edge-on but at a somewhat shallower angle. It is immediately apparent that the thrust events to the left (northwest) of the main shock and A-A' tend to be below and to the northwest of the strike-slip zone as the model predicts.

As noted previously, half of the focal mechanisms along the western limb have a steeply-dipping plane striking northeast nearly parallel to the limb direction with left-lateral strike-slip motion (Figure 9). The model shown in Figure 8 predicts that the strike of this plane should vary from a direction exactly parallel to the limb direction (the direction of A-A') for a perfectly vertical fault surface to a direction somewhat east of the A-A' azimuth for

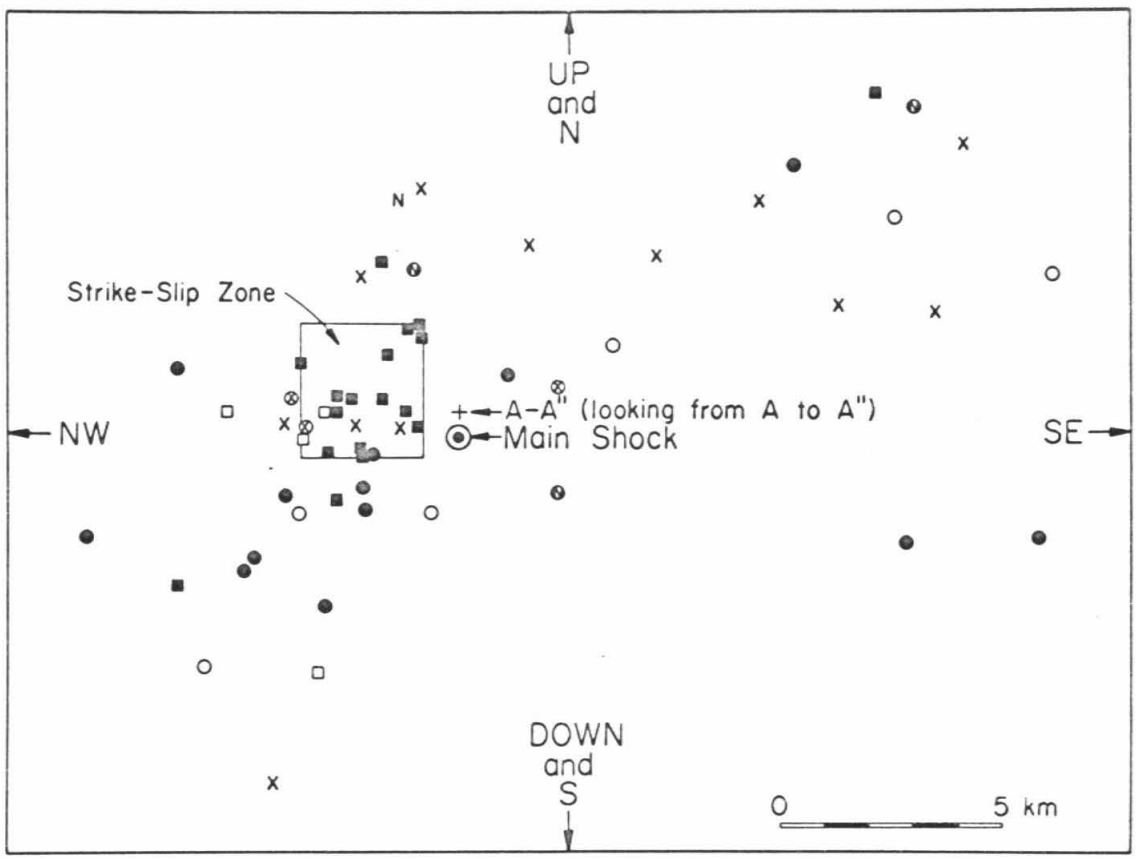

Figure 13.

Projection of hypocenters from Figure 11 onto a plane perpendicular to A-A" (see Figure 12). Here, the strike-slip zone of Figure 12 is given a third dimension.

a fault surface dipping steeply to the northwest. Northeast strikes of all of the strike-slip events in the western limb are plotted in the azimuthal histogram of Figure 14. The histogram interval is 5° and the direction of A-A' is shown for reference. The data have a well-defined peak just east of the direction of A-A' and thus indicate consistency with the model.

The hypocentral location of the main shock (Figure 12) is surprisingly close to the aftershock distribution in light of its estimated location accuracy (within 4 km horizontally and 8 km vertically). Hanks (1972), based on his analysis of the Pacoima Dam accelerogram and distant recordings of the main shock, suggested a hypocentral depth of 12 to 15 km. But, this would be in the range of both the aftershock distribution and the calculated main shock hypocenter if the latter is shifted down and to the northeast about 4 km, an adjustment within the stated location accuracy. Thus, the main shock depths estimated by Allen et al. (1972) and Hanks (1972) generally agree with the aftershock distribution and clearly show that the initial rupture of the main thrust fault was near its lower, northern-most edge.

5.3 Events that deviate from the model. One-third (25/75) of the "A" and "B" quality focal mechanisms do not fit the fault-surface model of Figure 8. An important subset of this group is composed of

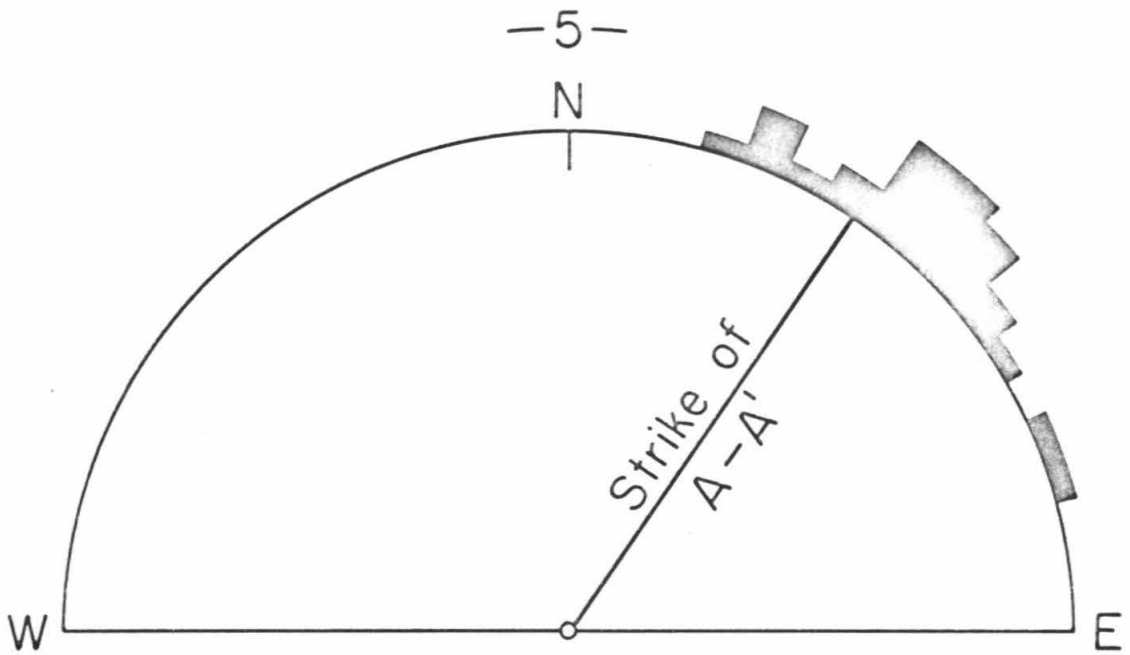

Figure 14.

Radial histogram in five degree intervals of fault-plane strikes for all strike-slip events in the western aftershock limb. The model of Figure 8 predicts that the strikes would group slightly to the east of the direction of A-A', as the data confirm.

focal mechanisms that have normal fault motion, that is, those for which the center of the equal-area projection falls in the dilatational quadrant. Figure 15 presents all seven of the "A" and "B" quality focal mechanisms that have normal fault motion. They are shown as a map of schematic diagrams of the double-couple mechanisms. For these events, the tension axis is nearly horizontal and the compression axis is shifted significantly from its usual north-south, nearly horizontal configuration. This is seen in the data for the normal mechanisms designated as "N" in Figure 10. Three of the normal events are scattered in the eastern aftershock region, one is near the main shock epicenter, and a clustered group of three centers on the line A-A' in the central portion of the west aftershock limb. The cross-sections in Figure 12a and 12b (again, these include only "A" and "B" locations) show that the scattered normal events in the eastern region are shallow; the one near the main shock epicenter is deep, possibly a bad location; and the group straddling A-A' is shallow. The shallow depth and association with the upper thrust block of all but perhaps the normal event near the main shock agree with effects due to curvature of the main fault surface as discussed below. However, the tight clustering of normal events along the edge A-A' of the strike-slip zone indicates that other stress disturbances may play a role in these three events. A clue for such an inhomogeneous stress in this region has already been provided by the discrepancy of fault-plane slip vectors in Figure 10 between strike-slip and thrust

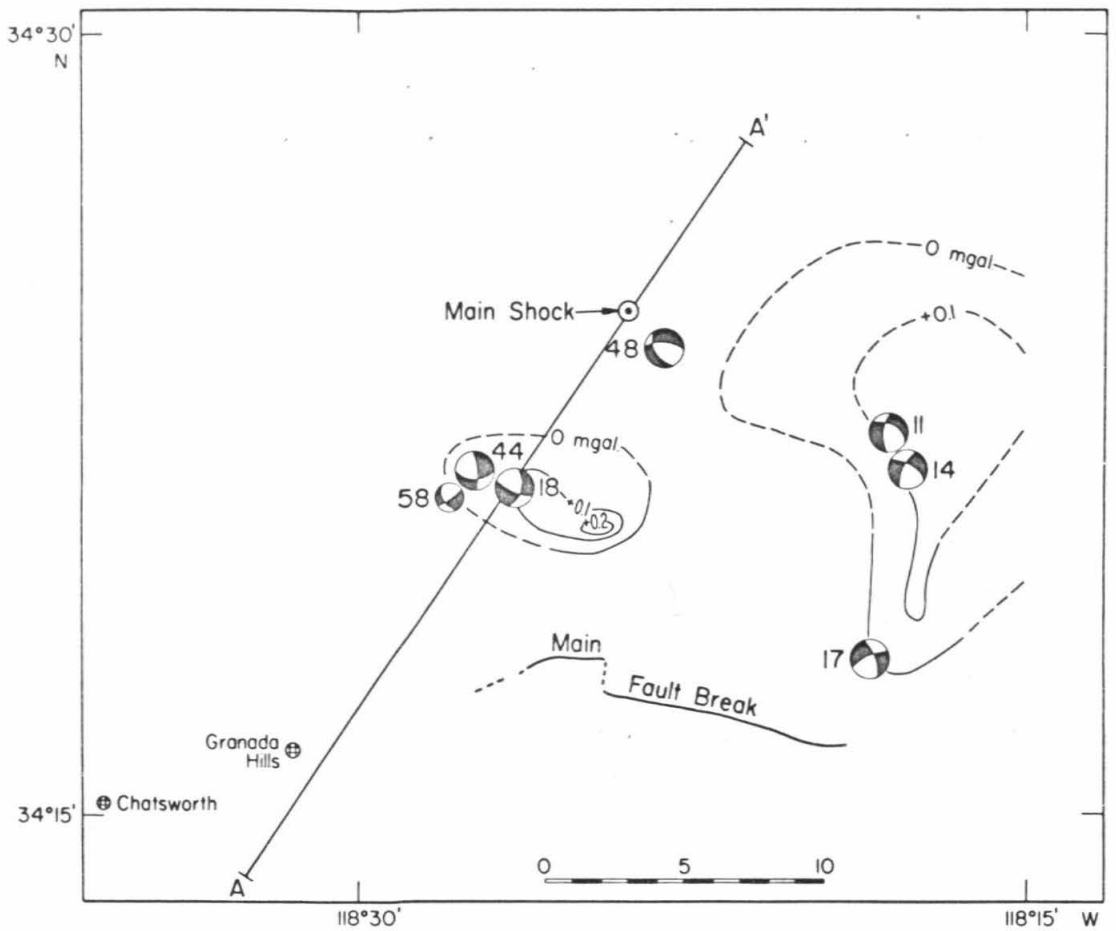

Figure 15.

Map of focal mechanisms of the normal group (see the caption of Figure 7). Their locations correspond well with areas of shallow tensional stress associated with ground subsidence that is indicated by the outlined areas of positive gravitational acceleration change (Oliver et al., 1972). Negative changes are not shown.

events. If, as the slip vector data indicate, the upper block's southerly motion is more to the west in the strike-slip zone than that to the east of A-A', then the motion would tend to create a void along the main fault's downstep which would manifest itself as extension in an elastic material.

Exceptionally good confirmation of the areas of compressional release is seen in Oliver et al. (1972), Figure 3). Their data, which show the change in gravitational acceleration due to the tectonic motions of the San Fernando series, outline two areas of acceleration increase; this implies a decrease in the ground elevation that results from local compressional release. The areas of positive acceleration change (after Oliver et al, 1972) are outlined in the map of the normal events in Figure 15. One area, relatively confined in lateral extent, coincides with the location of the three normal events along the central west aftershock limb. A second much broader area coincides with the normal events in the eastern aftershock area.

A histogram showing the time sequence of the normal events is shown in Figure 2e. If the larger set of aftershocks is a fair representation of the aftershock activity, then we must conclude that events with normal faulting cease after only ten days (February 29) into the aftershock sequence. One might fairly inquire as to the statistical significance of this distribution. This can be easily estimated by assuming that the normal events are randomly distributed throughout the set and calculating the joint probability that they

would all occur before February 19. The probability is 4%, which indicates that the observed lack of normal events after February 19 is significant. Thus, no matter what their source, the tensional stresses causing the normal events seem to be compensated within a time period of about ten days. This falls within and further characterizes the first stage of the series defined earlier.

The remaining 18 events which do not fit the fault surface model are shown in the map of schematic focal mechanisms in Figure 16. A commonly occurring focal mechanism type in this set can be classified as northeast striking thrust faults. The events of this type which fall near the strike-slip zone, Events 61, 66, 76, 73, 74, 78, and 83, can be explained by southeasterly thrust motion on the fault surface model of Figure 8. This motion is consistent with the idea of compensation for the deviatory tectonic movements causing tension and normal events along A-A'. Support for this hypothesis comes from the fact that the last normal event occurred in the central west limb vicinity along A-A' on February 19 (Event 58) and the first compensatory thrust event described above occurred on February 21 (Event 61), less than three days later. Thus, this time would mark the initiation of a north or northwest compressional addition to the local stress in the strike-slip zone which stops the shallow normal events and even causes a series of compensatory southeasterly thrust movements on the main downstepped fault surface. As can be seen in

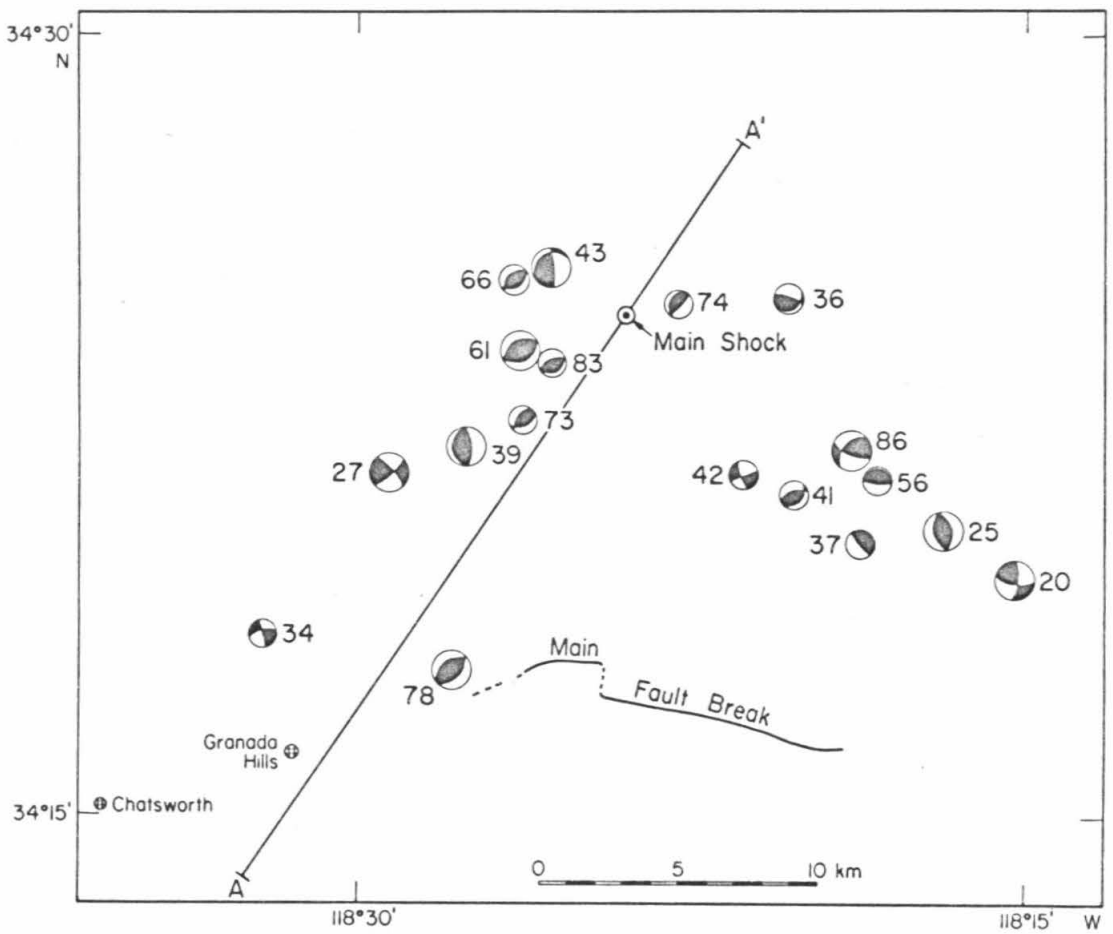

Figure 16.

Map of focal mechanisms of the other group (see the caption of Figure 7).

Figure 2a, February 21 also stands out as the first day after February 10 that had events of M_L = 4.0 or larger, initiating the series 61-64 which closely concentrate in the northern part of the west limb.

If the compensatory thrust events, which begin on February 21, are separated from the events on Figure 16, we find that, remarkably, all but one of the remaining events occur in the first stage between the 9th and 17th of February as shown in the histogram of Figure 2f. The exception occurred late in this set on April 25 during the possible third stage, which was indicated above. Most of these events are in the upper thrust block east of A-A' (see Figures 16 and 12b). From these considerations, we conclude that these remaining events represent complex fracturing in the upper thrust block resulting from the main tectonic motion. Their activity ceased at the same time, and probably for the same reason, as that of the normal events near February 19-21, and may have been reinitiated near the latter part of April.

5.4 The dip of the main thrust fault. As seen from the P-wave first motions of the main shock shown in Figure 5, the dip of the fault at the initial rupture point is well-determined at about 52°. But a line from the main surface rupture to the hypocenter of the main shock computed at 8.4 km depth by Allen et al.(1972) dips at

only about 33° (Figure 12a shows an approximation of the dip line). Also, the fault plane slip vector data in Figure 10 indicate an average plunge of around 40°, although the strike-slip event slip vectors plunge shallower and trend more to the east than those of the thrust events.

Additional evidence for steepening of the fault plane to the north is presented by the cross-section of Figure 12a. There is a notable steepening of the hypocentral distribution of strike-slip events to the north in the zone of the main shock's hypocenter. Because of the seismometer station distribution, this region gives the best control for hypocentral determinations and therefore the steepening is probably real. Note that the thrust hypocenters in this zone can be accounted for in the existing model of Figure 8 without modification, and only the three deep strike-slip events to the north indicate steepening.

Most of the events that are near the hypocenter of the main shock are west of A-A' (see Figure 11). Thus, the slip vectors of the model-compatible events along the west limb should provide a good test to show a systematic steepening to the north. Figure 17 is a plot of the slip-vector plunge as a function of distance along A-A' for these events. Some increase of plunge to the north can be seen, especially if only the strike-slip events (square symbols) are considered. But the slip plunge of vectors from the thrust events in the southwest area (towards A) conflict with this interpretation, unless the fault-surface also includes a steepening in the extreme

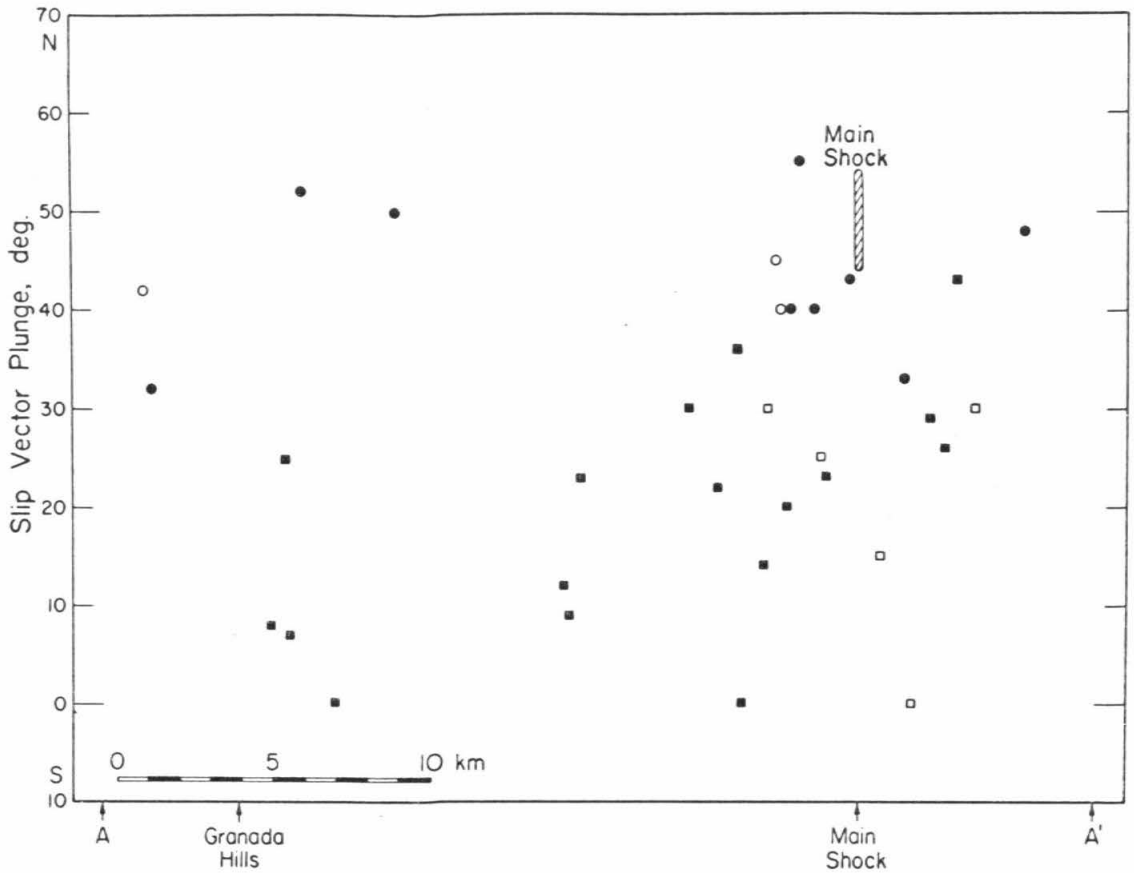

Figure 17.

Slip-vector plunges for all events west of A-A' (see Figure 11) as a function of distance along A-A'. Squares are strike-slip events and circles are thrust events. Steepening to the north is indicated if the thrust events near A can be ignored.

southwestern portion. The main characteristic of the data in Figure 17 is that the slip vectors of strike-slip events plunge less than those of the thrust events. The thrust events in turn have plunges that are not significantly different from the range of the main shock (a range is shown because of the uncertainty of the main shock's auxiliary plane determinations). East of A-A', the fault-plane slip vectors of thrust events are also not significantly different from that of the main shock and show no systematic steepening to the north (see Figure 9). One possibility that would reduce the steep thrust-fault dips is a change of the hypocentral velocity used to calculate the focal mechanisms, especially that of the main shock. An increase in P-wave velocity of about 0.8 km/sec (from 6.1 to 6.9) would have the effect of shallowing the thrust plane dip of the main shock focal mechanism (from about 50° to about 40°). This velocity is not totally unrealistic for certain crustal rocks but no evidence exists for a velocity this high at the main shock's hypocenter.

While it is apparent from the discussion above that the evidence is not conclusive, we believe that the arguments in favor of the fault steepening with depth are stronger. Thus, we support the early results of many investigators (Hanks et al., 1971; Wesson et al., 1971; Wesson and Wilson, 1972; and Allen et al., 1972) that the main thrust fault surface dips at 35°-40° near the surface and steepens to 52° at the main shock hypocentral depth, 8-12 km. Wesson and Wilson (1972) used this conclusion in their proposal that the

San Gabriel fault was the main rupture surface at depth; we discuss this possibility in a later section.

5.5 Early March and March-April series. During what is defined as the second stage of the overall aftershock series, at least two significant bursts of activity occurred in the set of events larger than M_L = 3.0. The first series began on March 7 with an M_L = 4.5 event in the central portion of the west limb. Three events followed on the same day and all were in or near (within 1.5 km) the west limb. The activity for several days both before and after the series was less than an event per day as seen in Figure 2b. The second series began 18 days later on March 25 with an M_L = 4.2 event at nearly the identical hypocenter as the initial event of the first series. Eleven events followed over the next 8 days and all were also in or near (within 2.0 km) the west limb. Five of the aftershocks in this series had M_L's of 4.0 or larger and one, on March 31, caused some further damage in the Granada Hills area. No intervening events above M_L = 3.0 occurred in the time between the two series and the average activity of events this size was less than one per day after the end of the March 25 series.

The parallelism between the two series is striking: initiation at the same location by shocks of M_L = 4.0 or larger, relative quiescence both before and after each series, and a limitation

of epicenters to the west limb. But even more significant is the time sequence of the series' events along the west limb. Figure 18 is a plot of the event times as a function of distance along A-A' (see Figure 11). The symbols again represent the focal-mechanism types, and the adjacent set of numbers indicates the event numbers and M_L value. Blank numbers indicate aftershocks larger than $M_L = 3.0$ that are not in Table 1 and whose hypocentral locations should be considered as of "C" quality. Lines connect events that are adjacent in time, and are dashed where one of the events is not in Table 1. The data show a systematic sequencing of aftershocks along the west limb, especially when several events occur advancing in one direction along the limb, such as the sequences 71-74 and 76-80. Based on this sequencing in two separate aftershock series that have other strong similarities, we conclude that the time-space distribution of both series is not random and therefore a causal relationship must exist between the events within each series. This causal relationship may not be as simple as that implied by connecting successive events with lines as in Figure 18. However, where several events occur sequentially in one direction of advance as in the previously mentioned sequences 71-74 and 76-80, a propagating phenomenon that triggers events with an apparent horizontal velocity of 4 to 15 km/day is suggested. It is interesting to compare these rates with those observed for propagating creep events in Central California of 0.5 to 10 km/day (Robert Nason, personal communication, 1972). The slopes

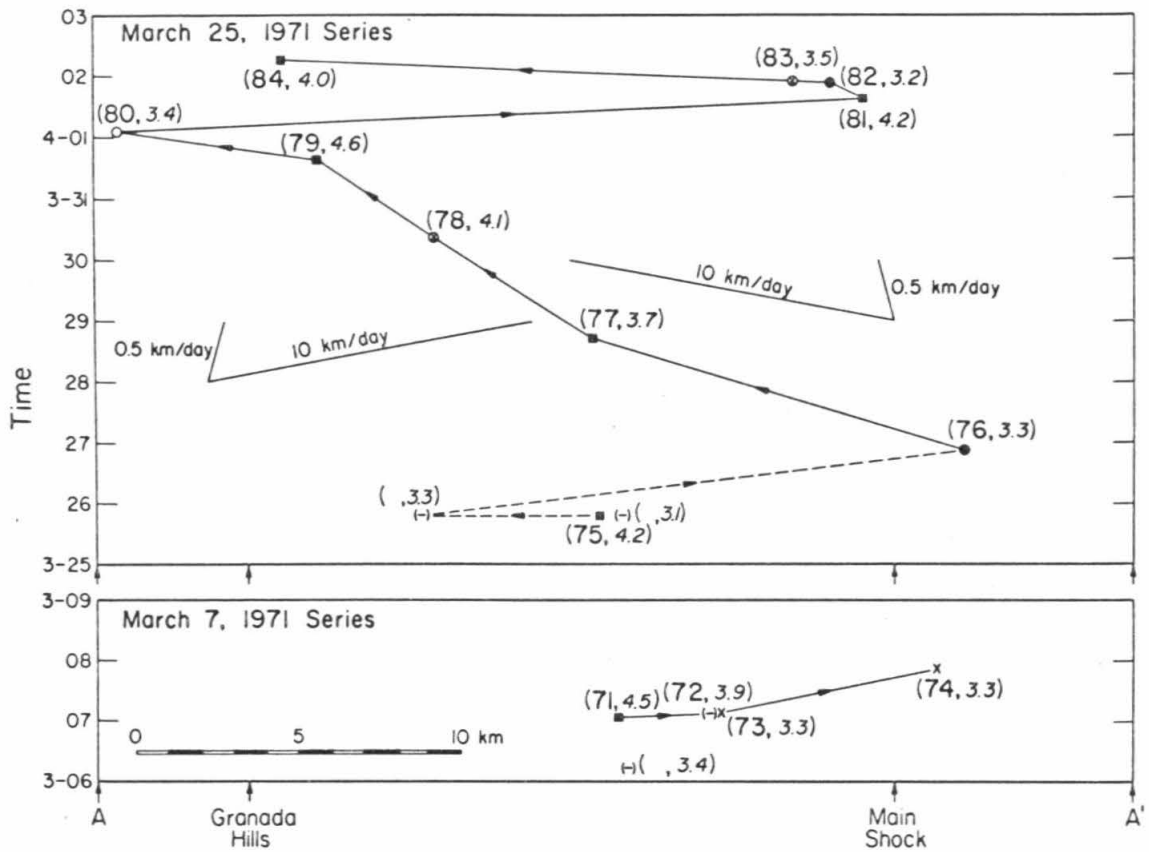

Figure 18.

Aftershock origin time as function of distance along A-A' (see Figure 10) for all events larger than M_L = 3.0 during March 7-8, 1971, and March 25-April 2, 1971. The larger numbers correspond to those of the events in Table 1 (events not in the table have no numbers) and the smaller to the magnitudes. The symbols are described in Figure 11 except for events with no focal mechanism, indicated by a dash.

corresponding to these velocities are shown in Figure 18. The propagation rates of the aftershocks in Figure 18 are at the higher range of the rates observed by Nason, but they are certainly comparable.

5.6 Regional tectonics and seismicity. Figure 19 outlines most of the major faults in an area from Santa Monica Bay on the southwest to the Mojave desert on the northeast (modified from Jennings and Strand, 1969). The approximate area of the aftershock epicenters is shown for reference. The San Fernando fault trace occurs in the southeastern edge of the Ventura basin, a highly folded synclinorium within the Transverse Range province that contains remarkably thick sections of Tertiary and Quaternary strata (up to 6 km in the Santa Susana mountains area, Wesson and Gibbs, 1971). The basin contains many thrust faults on which much of the uplift of the adjacent mountains has taken place. Of these thrusts, the Santa Susana fault, which shows evidence of late Quaternary movements (Wentworth et al., 1971), is the closest to the San Fernando fault and lies immediately to the west, as seen in Figure 19. Oil field data on the western and eastern part of the Santa Susana thrust show that it has a shallow north dip at the surface and steepens to about 50° when it reaches 0.7 km depth (Hall et al., 1958, and Roth and Sullwold, 1958). Similar oil field data on the San Cayetano thrust further to the west (not shown in Figure 19) indicate a 30° to 35° north dip at the surface steepening to about 50° as it reaches depths near 4 km shown in Figure 20

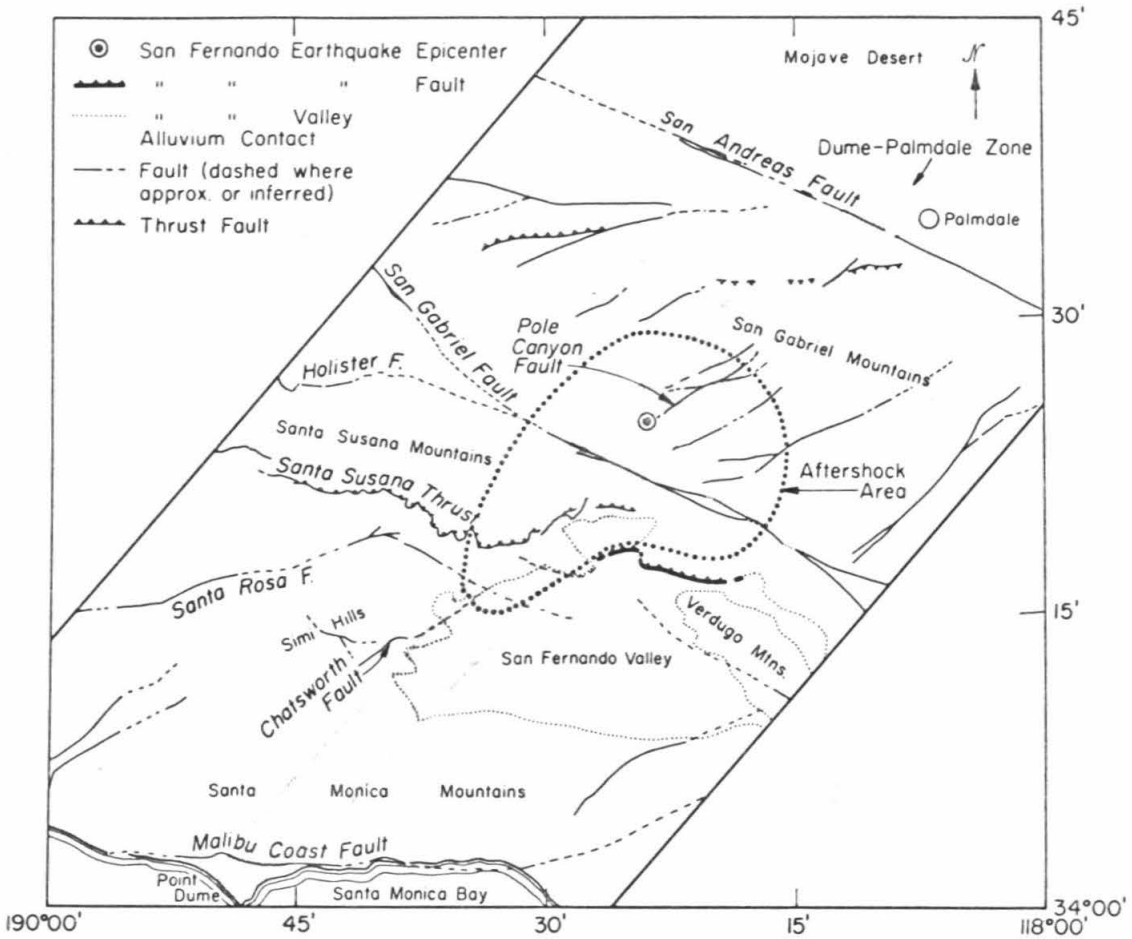

Figure 19.

Major tectonic features in the area around San Fernando.

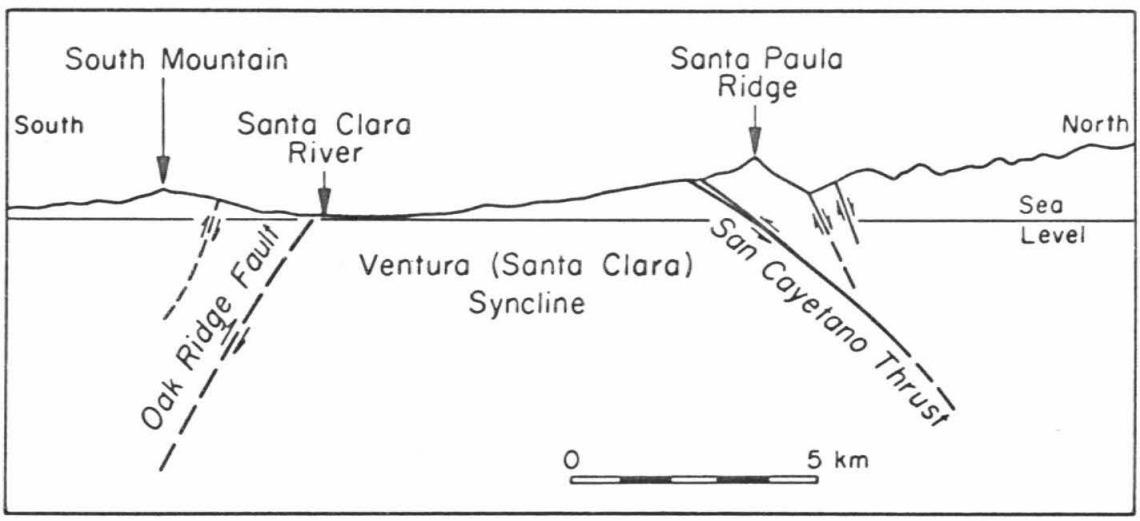

Figure 20.

Cross-section of the Ventura syncline showing the San Cayetano thrust fault (modified from Bailey and Jahns, 1954, Figure 8). Note the steepening with depth and the normal faulting to the north.

(Bailey and Jahns, 1954). This is precisely the dip behavior proposed for the San Fernando thrust fault, which is part of the same fault system.

Of further interest in the San Cayetano thrust area are the mapped normal dip-slip faults dipping to the north in the up-thrust block just north of the San Cayetano fault trace. This faulting is also in agreement with the San Fernando fault tectonics, specifically the focal mechanisms and gravity data in the northeast aftershock zone which indicate shallow normal faults (Figure 15).

The theoretical and experimental work of Sanford (1959) directly bears on the phenomena of thrust faults steepening to dips greater than 45° with depth and the occurrence of shallow normal dip-slip faults in the up-thrown block. He showed that the normal faulting is a result of the steepening of the thrust fault and that the steepening itself is directly related to laterally varying vertical forces at depth. The steepening can be simply explained by the fact that all vertical forces at depth must converge to zero at the earth's surface. Thus, while laterally-varying vertical forces can be supported by rock strength at depth and cause fractures dipping steeper than 45°, the only possible stresses at the earth's surface are horizontal, and fracture criteria require a thrust fault that dips shallower than 45°. Sanford's results are shown in Figure 21.

The implications of these laterally varying vertical forces are important to the regional stress picture. Emphasis in the vicinity

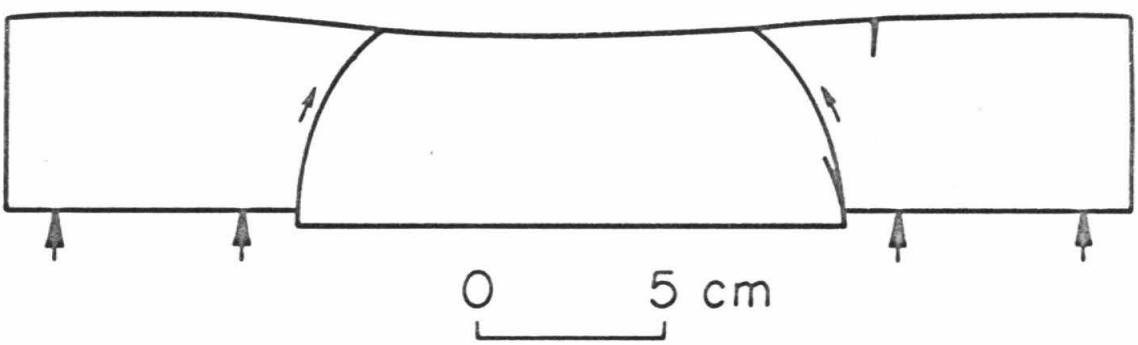

Figure 21.

Results of an experimental fracturing experiment by Sanford (1959, Figure 17) that shows a thrust fault steepening with depth and tensional fractures in the up-thrust block.

of the San Andreas fault is commonly placed on horizontal movements and stresses dominating the tectonics, especially since the emergence of concepts of plate tectonics. However, it is clear from the above that significant vertical stresses other than overburden pressure are also acting at depth in the Ventura basin. The question naturally arises as to the relative magnitude and origin of these stresses. First, the horizontal stresses must be a substantial part of the regional stress field because the extensive folding in the Ventura basin is due to north-south compression (Bailey and Jahns, 1954) which is still active. Isostatic imbalance is not the cause for the vertical stresses because it is apparent that the mountains north of the Ventura basin have been moving up, and this would require a mass deficiency under the mountains. But seismic and gravity evidence for the San Gabriel mountains, which were uplifted in the San Fernando earthquake, indicate no mass deficiency and perhaps even an excess (Mellman, 1972). It appears that the most likely cause for the vertical stresses is a partial upward redirection of the horizontal stress either by a deep obstruction over which the surface blocks are forced or by complex distortion due to buckling at depth as the crust is shortened. Indeed, the great bend in the San Andreas fault zone as it crosses the Transverse Ranges of southern California virtually demands vertical adjustments in the adjacent regions if lateral movements are to be continuous along the San Andreas fault. The stress at depth in the Ventura basin area is most likely a combination of a dominant horizontal stress and

laterally-varying vertical stress as in Sanford's model that would result in the major compressional stress axis dipping 10° or more at depth.

The existence of the left lateral strike-slip zone, which is the downstep in the fault surface model of Figure 8, is well established from the focal mechanisms and the southerly curvature of the aftershock zone and main fault break in this region. As pointed out by Allen et al. (1972), further support for the existence of the downstep comes from the mapped geology of the area (Wentworth et al., 1971, Figure 2). The trace of the Santa Susana thrust makes a sharp bend to the north when it enters the zone from the west (Figure 19) in exactly the manner postulated for the San Fernando fault. Further, basement rocks are widely exposed in the San Gabriel Mountains east of this zone, whereas only younger sedimentary rocks are exposed to the west. The latter strongly supports the concept of a flexural or faulted downstep to the west in this area. However, it is not clear that the thrust faulting to the west of the zone is associated with a single downstepped thrust fault as depicted in the model of Figure 8 or as two or more parallel thrust faults for which there are several candidates in the mapped geology of the area (Jennings and Strand, 1969). The western thrust mechanisms occur mainly in the extreme northwest or southwest corners of the aftershock zone with only one intervening thrust event (Event 5) in the central part of the zone

(Figure 9). Also, the steep slip vector plunges of thrust events near Granada Hills (Figure 17) and deeper hypocenters (Figure 12a) deviate from the model and the hypothesis of a shallow fault dip at the surface; however, these effects may be related to the greater hypocentral location inaccuracies in this region. Although these are not serious objections to this feature of the model, they point out the possibility of more than one thrust surface extending to the west of the established main fault downstep.

The San Gabriel fault is a major structural feature in the San Fernando area and its trace cuts through the center of the aftershock zone (Figure 19). Although it has some evidence of dip-slip, its main motion has been right-lateral strike slip with no evidence of late Quaternary displacements (Wentworth et al., 1971). Dip measurements of the San Gabriel fault in the aftershock region are complicated in many locations by nearby parallel thrust faulting that cuts across the San Gabriel fault plane. But where the fault is uncomplicated and clearly exposed, it is steeply north-dipping at 70° to 80° (Oakeshott, 1954, Oakeshott, personal communication, 1972). This steep dip agrees with the extreme linearity of the fault trace as it cuts through the varying topography of the western San Gabriel mountains. Wesson and Wilson (1972) have proposed that the San Gabriel fault was the initial rupture surface of the San Fernando earthquake. They based this on the steepening with depth of the San Fernando fault surface and on ground elevation changes in the

vicinity of the San Gabriel fault trace. As discussed above, evidence seems to favor a steepening of the San Fernando thrust fault surface with depth, but this is a characteristic of all of the north-dipping thrust faults along the Ventura basin. It is more likely that the steepening of the San Fernando fault is due to the same cause and not to its special geometrical relationship with the San Gabriel fault, which appears to have a very different geologic history. Also, as stated above, the dip of the San Gabriel fault is probably steeper than 52°, the dip of the initial San Fernando rupture surface. The positive gravity changes in the northeast aftershock zone shown in Figure 15 indicate that the ground surface just north of the San Gabriel fault experienced a decrease in elevation. If any shallow displacements took place on the San Gabriel fault, this evidence indicates that it was normal dip-slip instead of thrust.

Seismicity in the region of Figure 19 before 1971 shows some interesting earthquake distributions. Figure 22 is a map of epicenters for all events located by CIT for the time periods 1961-1962 (Figure 22a), 1969 (Figure 22b), and 1960-1970 (Figure 22c). The locations are believed to be accurate to within about 9 km. The San Fernando aftershock zone and some of the major faults are shown for reference. During 1961-1962 (Figure 22a), the earthquakes clearly define a zone that coincides with the location and direction of the west limb of San Fernando aftershocks but extends from Point Dume near Malibu on the southwest to the San Andreas fault near Palmdale on the northeast.

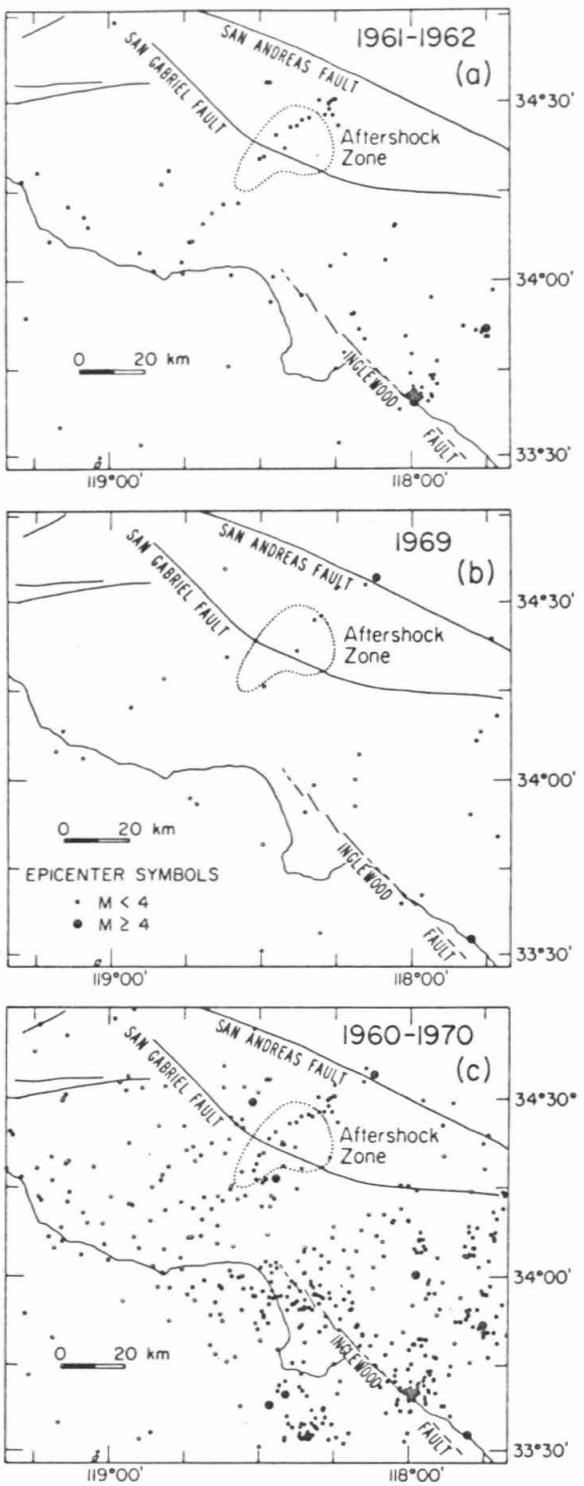

Figure 22.

Seismicity around the San Fernando region for the time periods (a) 1961-1962, (b) 1969, and (c) 1960-1970. The epicentral locations are believed to be accurate to within 9 km. The San Fernando aftershock zone and some of the major faults are shown for reference.

For discussion purposes it will be designated the Dume-Palmdale zone and is outlined in Figure 19. Figure 22b shows that the northeastern part of this zone was active in 1969 including an M_L = 4.0 event on the San Andreas fault. Figure 22c confirms that the Dume-Palmdale zone is suggestively outlined even when compared with the total seismicity over the ten-year period before the main shock, 1960-1970. No similar pattern in the zone is seen in the years prior to this interval back through 1935, although this may be because the earlier epicentral locations are considerably less accurate. There is a possible indication of activity along the zone from the M_L = 5.2 earthquake of August 30, 1930 (Wentworth et al., 1971). The original epicentral assignment, which was not well constrained, was in the Santa Monica Bay. But, minor damage at both the Chatsworth Dam and Lower Van Norman Dam, which lie along the western edge of the San Fernando valley, suggests that the epicenter was on or near the Dume-Palmdale zone. Other lineations that are outlined by seismicity but do not coincide with any obvious surface structure in Southern California are reported by Ryall et al. (1966) and Richter (1969). These lineations often strike in the direction nearly perpendicular to the major northwest-southeast strike-slip faults of the region; this is approximately the conjugate shear direction in association with a dominant horizontal compression.

The significance of activity on the Dume-Palmdale zone is that

it precedes the San Fernando series and exactly coincides with the west aftershock limb and the main shock epicenter as seen in Figure 19. While the zone is not obviously outlined by continuous geologic features of the area, there are some mapped structures that appear to be related. The sharp bend in the trace of the Santa Susana thrust has already been mentioned. The western edge of the San Fernando Valley also lies along this trend and is fault controlled with the east side down (Corbato, 1963). One of the members of this family of faults is the Chatsworth fault, which shows some evidence of Quaternary displacements (Wentworth et al., 1971). Although some maps show the northwest-trending Northridge Hills fault as cutting continuously across this zone, geologic relationships in the area of intersection are obscure. Still farther south, however, the Santa Monica Mountains and the Malibu Coast fault are clearly continuous across the Dume-Palmdale trend, and the zone must terminate in this area.

North of the San Gabriel fault, parallel to and within the Dume-Palmdale zone, are a number of northeast-trending faults that have had a history of left-lateral displacement. For example, Oakeshott (1958) points out that the east-trending Soledad fault is clearly offset by the northeast-trending Pole Canyon fault, which passes virtually through the epicenter of the San Fernando earthquake. However, most of these faults seem to have been active primarily in Miocene time, with no major displacements since that time (L. T. Silver,

personal communication, 1972). This represents a major problem, because the San Gabriel fault itself appears to have had about 50 km of right-lateral displacement in Plio-Pleistocene time (Crowell, 1954, 1962), and thus it should have displaced these earlier northeast-trending faults. If one accepts the large movement on the San Gabriel fault, he cannot argue for a continuous Dume-Palmdale zone that has been active since Miocene time. There are, however, many northeast-trending faults within the Transverse Ranges north of the San Gabriel fault, and it is not necessary to assume that the faults currently delineating the Dume-Palmdale zone have always been in their same relative positions.

Regardless of the complex geologic history of the region, the Dume-Palmdale zone appears to be an active zone at the present time, perhaps taking advantage of previously existing lines of weakness. The location of the San Fernando main shock, the strike-slip zone of the main fault surface, and the seismicity represented in Figure 22 currently show the zone to be a linear region of weakness where stress can be concentrated. This leads us to believe that the zone represents a decoupling boundary between crustal blocks that permits them to deform separately in the prevalent crustal shortening mode of the region. The fact that this zone of weakness does not extend northeast across the San Andreas fault is evidence that it is being carried along in the crust or lithosphere as displacement takes place along the San Andreas. Apparently, most of the crustal shortening is done

south of the San Andreas in this area as reflected in the aseismicity of the Mojave block to the north (Allen et al., 1965). The aseismicity is probably related to greater strength in the Mojave block due to its thicker crust (Mellman, 1972).

6. SUMMARY AND CONCLUSIONS

The main shock of the San Fernando earthquake occurred at 14 00 41.8 GMT on February 9, 1971. Allen et al. (1972) assigned it a magnitude (M_L) of 6.4 and a location at 34° 24.7' N, 118° 24.0 W, h = 8.4 km; they estimated the hypocenter to be within 4 km horizontally and 8 km vertically. Hanks (1972), based on his analysis of the Pacoima Dam accelerogram and distant recordings of the main shock, suggested a hypocentral depth of 12 to 15 km, which is within the range given by Allen et al. A main shock depth of 12 km is compatible with the location of the aftershocks of Figure 12 if the epicenter is shifted northwest about 4 km, again within the range given by Allen et al. Thus, within the constraints of the data, the location of the main shock's initial rupture coincides with the lower, northernmost edge of the aftershock distribution.

The best focal mechanism fit to the P-wave first motions of the main shock gives the initial thrust plane parameters of: Strike, N 67° (± 6°) W; Dip, 52° (± 3°) NE; Rake, 72° (67°-95°) left lateral. Evidence from the slip vectors of the aftershocks suggests that the

rake is closer to 80°, but this assumes that the main shock and aftershock motions were the same. The evidence of fault-surface displacement from Kamb et al. (1971, Figure 2) scatters between the extremes of the rake angle.

In order to have as homogeneous a representation of the aftershock tectonics during the first three months as possible, the aftershocks were chosen for analysis on the basis of size. The first set of events were defined as all those of M_L = 4.0 or larger; twenty of these had onsets clear enough for anlaysis during the first three months of the series. The second set was defined as those with clear onsets at most of the CIT telemetered stations; this essentially corresponds to a magnitude cutoff at about M_L = 3.3 and a total of 87 aftershocks fulfilled the requirement. The second set, of course, contains the first. Of the second set of 87, only 12 focal mechanism solutions were poorly constrained, and most of these occurred during the first few hours of the series when the portable stations were not yet in operation.

In both sets of aftershocks, most of the activity was along a linear northeast striking region encompassing the main shock epicenter and bounding the aftershock region to the west. This region, the west aftershock limb, is dominated in both aftershock sets by focal mechanisms in which one plane strikes along the limb and dips steeply to the northwest with left-lateral strike-slip motion. Thrust mechanisms resembling that of the main shock occurred both to the west

and to the east of the west limb. From these considerations it is clear that the west limb outlines a major discontinuity in the main thrust fault surface. These data require a single non-planar fault surface that incorporates a downstep to the west in the north-dipping thrust fault plane as shown in Figure 8. Two-thirds of the focal mechanisms are either strike-slip or thrust with orientations and epicentral locations in agreement with the fault surface model and provide strong support for its validity. An interesting way of illustrating this is the comparison (shown in Figure 10) of slip vectors, tension axes, and compression axes of the focal mechanisms with the distribution of these parameters predicted by the fault surface model. Except for some scatter and minor deviations (which correlate with other phenomena in the series), the data clearly have the same distribution. Further confirmation for the model is provided by the agreement of fault-plane strikes for shocks with strike-slip mechanisms with that predicted from the orientation of the west aftershock limb. The hypocentral locations bear out the model's characteristics that the strike-slip events along the west aftershock limb are limited to a narrow zone, at least south of the main shock epicenter, and that the thrusts in and to the west of the west limb tend to be deeper.

While the dip of the main shock initial rupture surface is 51° (± 3°), evidence from the main shock hypocenter relative to the

surface faulting and the distribution of the aftershock hypocenters south of the main shock indicates a dip of around 35° at shallower depths on the main fault surface. There is also some indication of steepening with depth of the aftershock slip vectors although this is not as clear. The complication arises from the thrust event slip vectors west of the west aftershock limb, and may indicate that the thrusting to the west is not on a single downstepped surface but is on two or more unconnected thrust planes. However, within and to the east of the west aftershock limb, the data favor a fault surface whose slip vector starts with a 50° plunge at the initial rupture at depth, and curves to a 35° plunge as it extends to shallower depths.

A series of north-dipping thrust faults to the west of the San Fernando area exhibit steepening with depth in precisely the same manner as that proposed for the San Fernando fault. These faults strike along the trend of the Ventura basin and have late Quaternary movements that form mountains to the north, in the same tectonic setting as the San Fernando fault. Sanford (1959) showed that this steepening to dips greater than 45° may be related to laterally-varying vertical forces at depth, which has important implications to the regional stress picture. The most likely cause for the vertical stresses is a partial upward redirection of the horizontal compressive stress, which from the time of extensive folding in the Ventura basin to the present has been the dominant stress in the region.

The San Gabriel fault, a major structural feature cutting through the aftershock region, apparently played no significant role in the displacements of the main San Fernando event. There is no evidence for late Quaternary displacements of the main San Fernando event. There is no evidence for late Quaternary displacements on the fault and no direct evidence that it slipped in the main event. At depth, it is probably much steeper than the 52° dip of the initial rupture surface. Gravity data, which reflect ground surface displacements, indicate that, if any shallow displacements took place on the San Gabriel fault, they had a normal dip-slip component.

One-third of the focal mechanisms do not fit the fault surface model of Figure 8. This is not surprising because the strain release due to the aftershocks is minor compared to that of the main shock, and some of the aftershocks should represent a relief of complex stress concentrations due to motions of the main shock. According to the theoretical and experimental work of Sanford (1959), one of these stress concentrations should be a tension field in the shallow upper thrust block resulting from the steepening of the thrust fault with depth. Ground surface elevation decreases and shallow normal focal mechanisms north of the main fault break confirm the existence of this tension field after the main event. A close concentration of shallow focal mechanisms and localized ground subsidence on the west aftershock limb near the western projection of the main fault break indicates further complexity. The consistent deviation between the

strike-slip and thrust event slip-vector azimuths (Figure 10) predicts a divergence of motion along the downstep of the west aftershock limb. This divergence, which would produce a local tension field, would be most pronounced as the downstep of the main fault surface approaches the ground surface, which is the precise location of the observed concentration of shallow normal events and ground subsidence.

Another class of focal mechanisms can be separated from the events that do not fit the model. They are defined as those events which occur along the west aftershock limb with a thrust plane striking in the same direction as the limb. The motion of the these events is consistent with the idea of compensation (on the downstep fault surface) for the divergence that caused local tension along the west limb. These compensatory thrust events did not begin until February 21, 12 days after the main shock. All of the remaining focal mechanisms in this set were located in the upper thrust block east of the west aftershock limb and were confined with only one exception to the time period of February 9-17, before the onset of the compensatory thrust events. They are presumably related to localized stress concentrations due to displacements of the main shock.

Other evidence points to this time as one of significant change in the stress field of the aftershock area. The last normal focal mechanism in the set occurred on February 19, three days before the first compensatory thrust event. February 21 was the first day since February 10 that an event with M_L = 4.0 or larger occurred in the

series; this initiated a series of aftershocks that closely concentrated in the northern part of the west aftershock limb. After this time, at least until April 17, the aftershock activity was characterized by isolated bursts of events starting with M_L = 4.0 or larger events. These bursts were essentially confined to the west aftershock limb until April 17 when the bursts ceased and minor activity continued throughout the aftershock area. The time-space distribution of these events indicate that some time near February 21, 12 days after the main shock, a horizontal compressional stress in a north or north-northwest direction was added to the stress in the aftershock area. As a result, events related to stress release of the main shock ceased and activity was concentrated in bursts of events along the downstep of the main fault surface. Effects due to this change of stress appear to have stopped by April 17, about two months later.

While the aftershock activity was by no means finished after May 7, 1971, the end of this investigation, the aftershock rate for M_L's larger than 3.0 by that time had dropped to about one every four days. Thus, this study covers the time period of most of the aftershocks. The question of whether the tectonic activity changes in character after this period even though the aftershock activity is very low is an important subject for future investigation.

The bursts of aftershocks along the west limb during the period between February 21 and April 17 show systematic time-space relationships in themselves. The events within two of the bursts have a

systematic sequencing north and south along the west aftershock limb that is not random and must be explained by a causal relationship. While the relationship may not be as simple as a unidirectional front that triggers events, there is some evidence for a triggering phenomenon that propagates with speeds of 4 to 15 km/day. These speeds are somewhat high but comparable to those observed for wave fronts defined by the onset of creep events on the San Andreas fault.

Seismicity in 1961, 1962, and 1969 before the San Fernando series outlines a linear region extending from Point Dume, near Malibu, in the southwest to Palmdale, on the San Andreas fault, in the northeast. This region exactly coincides with the west aftershock limb and the main shock epicenter. While the zone is not obviously outlined by mapped geologic structures along its extent, it coincides with some major structural discontinuities such as the fault-controlled west edge of the San Fernando Valley, the sharp north bend of the Santa Susana fault, the downstep of the San Fernando fault, and the general trend of left-lateral strike-slip faulting in the San Gabriel mountains. The history of this zone of weakness is not clear but it was probably active in the San Gabriel mountain block during Miocene and lower Pliocene and is recently active along the western edge of the San Fernando Valley. It is interpreted as a decoupling boundary between crustal blocks that permits them to deform separately in the prevalent crustal-shortening mode of the Transverse Ranges region.

REFERENCES

Alewine, R. W., III, and T. H. Jordan, Generalized inversion of earthquake static displacement fields, in press, Geophys. J. Roy. Astr. Soc., 9th Geophysical Symposium Issue, 1973.

Allen, C. R., G. R. Engen, T. C. Hanks, J. M. Nordquist, and W. R. Thatcher, Main shock and larger aftershocks of the San Fernando earthquake, February 9, through March 1, 1971, U. S. Geol. Survey Prof. Paper 733, 17, 1971.

Allen, C. R., T. C. Hanks, and J. H. Whitcomb, San Fernando earthquake: seismological studies and their tectonic implications, Calif. Div. of Mines and Geology Bulletin on the San Fernando Earthquake. in press, 1972.

Allen, C. R., St. Amand, P., Richter, C. F., and Nordquist, J. M., Relationship between seismicity and geologic structure in the southern California region, Bull. Seism. Soc. Am., 55, 753, 1965.

Bailey, T. L., and R. H. Jahns, Geology of the transverse range province, Southern California, in Geology of Southern California, Calif. Div. of Mines, Bull. 170, Chapter II, 83, 1954.

Burford, R. O., R. O. Castle, J. P. Church, W. T. Kinoshita, S. H. Kirby, R. T. Ruthven, and J. C. Savage, Preliminary measurements of tectonic movements, U. S. Geol. Survey Prof. Paper 733, 80, 1971.

Canitez, N., and M. N. Toksőz, Static and dynamic study of earthquake source mechanism: San Fernando Earthquake, J. Geophys. Res., 77, 2583, 1972.

Corbato, C. E., Bouguer gravity anomalies of the San Fernando Valley, California, California Univ. Pubs. Geol. Sci., 46, 1, 1963.

Dillinger, W., and A. F. Espinosa, Preliminary fault-plane solution for the San Fernando earthquake, U. S. Geol. Survey Prof. Paper 733, 142, 1971.

Division of Geological and Planetary Sciences, California Institute of Technology, Preliminary seismological and geological studies of the San Fernando, California, earthquake of February 9, 1971, Bull. Seism. Soc. Am., 61, 491, 1971.

Hall, E. A., G. G. Rickels, and W. O. Plant, Oakridge oil field, in A guide to the geology and oil fields of the Los Angeles and Ventura regions, ed. J. W. Higgins, Pacific Section of the Am. Assoc. Petro. Geol., 204 P, 1958.

Hanks, T. C., A Contribution to the Determination and Interpretation of Seismic Source Parameters, Ph.D. Thesis, Calif. Inst. Tech., 184 p., 1972.

Hanks, T. C., T. H. Jordan, and J. B. Minster, Precise locations of aftershocks of the San Fernando earthquake, 2300 (GMT) February 10 - 1700 February 11, 1971, U.S. Geol. Survey Prof. Paper 733, 21, 1971.

Healy, J. H., Crustal structure along the coast of California from seismic-refraction measurements, J. Geophys. Res., 68, 5777, 1963.

Jennings, C. W., and R. G. Strand, Geologic Map of California, Los Angeles Sheet, Calif. Div. of Mines and Geol., 1969.

Jungels, P., and D. L. Anderson, Strains and tilts associated with the San Fernando earthquake, U. S. Geol. Survey Prof. Paper 733, 77, 1971.

Jungels, P. H., and G. A. Frazier, Finite element analysis of the residual displacements for an earthquake rupture: source parameters for the San Fernando earthquake, in press, J. Geophys. Res., 1973.

Kamb, W. B., L. T. Silver, M. J. Abrams, B. A. Carter, T. H. Jordan, and J. B. Minster, Pattern of faulting and nature of fault movement in the San Fernando earthquake, U. S. Geol. Survey Prof. Paper 733, 1971.

Mellman, G. R., Seismic observations and their tectonic implications for the Pacific-North American plate boundary (abstract), Geo. Soc. Am. Abs., 4, 198, 1972.

Oakeshott, G. B., Geology and mineral deposits of the San Fernando Quadrangle, Los Angeles, County, California, Calif. Div. of Mines Bull. 172, 147 p., 1958.

Oakeshott, G. B., Geology of the Placerita oil field, Los Angeles County, in, Geology of Southern California, Calif. Div. of Mines Bull. 170, map sheet no. 31, 1954.

Oliver, H. W., S. L. Robbins, R. B. Grannell, R. W. Alewine, and S. Biehler, Surface and subsurface movements determined by remeasuring gravity, Calif. Div. of Mines and Geology Bulletin on the San Fernando Earthquake, in press, 1972.

Richter, C. F., Transversely aligned seismicity and concealed structures, Science, 166, 173, 1969.

Roth, G. H., and H. H. Sullwold, Jr., Cascade oil field, in A guide to the geology and oil fields of the Los Angeles and Ventura regions, ed. J. W. Higgins, Pacific Section of Am. Assoc. Petro. Geologists, 204 p., 1958.

Ryall, A., D. B. Slemmons, and L. D. Gedney, Seismicity, tectonism, and surface faulting in the western United States during historic time, Bull. Seism. Soc. Am., 56, 1105, 1966.

Sanford, A. R., Analytical and experimental study of simple geologic structures, Bull. Geol. Soc. Am., 70, 19, 1959.

U. S. Geological Survey Staff, Surface faulting, U. S. Geol. Survey Prof. Paper 733, 55, 1971.

Wentworth, C. M., R. F. Yerkes, and C. R. Allen, Geologic setting and activity of faults in the San Fernando area, California, U. S. Geol. Survey Prof. Paper 733, 6, 1971.

Wesson, R. L., and D. H. Wilson, Faulting in the San Fernando earthquake of February 9, 1971 (abstract), EOS Am. Geophys. Union Trans., 53, 449, 1972.

Wesson, R. L., and J. F. Gibbs, Crustal structure in the vicinity of the San Fernando, California earthquake of 9 February 1971 (abstract), EOS Am. Geophys. Union Trans., 52, 804, 1971.

Wesson, R. L., W. H. K. Lee, and J. F. Gibbs, Aftershocks of the earthquake, U. S. Geol. Survey Prof. Paper 733, 1971.

Whitcomb, J. H., Fault-plane solutions of the February 9, 1971 San Fernando earthquake and some aftershocks, U. S. Geol. Survey Prof. Paper 733, 1971.

Appendix 1

FOCPLT Program Description.

A computer program has been developed to easily reduce and plot P-wave first motion data, plot nodal planes, and, if desired, compute the constraints of the data on the program's choice of a double-couple focal mechanism solution. It was written to provide an efficient means of estimating the quality of a focal mechanism, a difficult task for even those workers experienced in the art of fitting mechanisms, and a nearly impossible task for those who are not.

The fitting of a double-couple mechanism to first-motion data is a rather unusual minimization problem because of the yes-no nature of each station's agreement with a particular solution orientation; we desire to minimize the number of no's. This characteristic produces stair-step slopes leading down to flat-bottomed minima. The problem's extreme non-linearity and the fact that multiple minima in the solution space are common prohibit use of any simple linear technique to find the minima and require that the entire solution space be investigated, which makes an efficient method of search desirable.

When estimating the constraints on the solution, we find that some data are obviously bad, that is they are clearly in the middle of a quadrant with which they disagree. Thus, only data that are

near the nodes of the solution are meaningful constraints. As in fitting a line to a set of data, it may be desirable to define a norm related to the distance of the misfit to the nodal line so that a minimization criterion such as least-squares can be used to minimize the misfit; a procedure like this removes the flat bottom of the minimum unless there are no misfits. This criterion should only be applied to misfits close to the nodes because obviously bad data as mentioned above should not be used in the solution. The norm used in this program (as an option) is the smallest angular distance of the misfit from the node and the smallest linear sum of these distances out to a specified limit is the minimization criterion.

In order to evenly sample the solution space in the most efficient manner, the intrinsic character of the equal-area plot is used. The location of points on a computer printing plot, the mode of data presentation, is used to determine the orientation of the nodal-plane poles (slip vectors); this minimizes wasted computations. In the present configuration the program gives resolution of the focal mechanism solution to within the nearest 3 1/2 deg. This can be made finer but the need for greater resolution is questionable in light of uncertainties in near-focus velocities. In addition, efficiency is enhanced through the use of symmetries and anti-symmetries of the double-couple focal mechanism; these halve the number of computations over a straight sweep through the range of the Eulerian angles.

The following diagrams show solution-constraint plots (equal-area of the lower focal hemisphere) for the slip vectors (in one plot), the compression axis, and tension axis for the San Fernando main shock. A plus sign marks the minimum-misfit solution and the numbers indicate the number of misfits above the minimum. The range of ones for example indicates the range of possible solutions if the most critical station in any direction were to be reversed. A weight of 1/2 for fair readings (as opposed to a weight of 1 for good) and the use of the taper as described above allow numbers between the integers; the fractional parts are dropped for plotting. The first set of diagrams have a taper width of 0° and the second set has a width of ± 3.5° (0.06) from the nodal lines.

Following each set is a diagram of the focal mechanism quadrants of the chosen solution (an example of the program's ink plot is in Figure 5). It must be emphasized that this computed best solution is significant only if the constraint, measured by the steepness of the minima wells in the constraint plots, is tight. The program choses the best solution by fixing the pole in the center of the most constrained slip-vector minimum and finding the other pole closest to the center of the other minimum.

The time for the program on an IBM 370-55, if the solution constraint calculation is chosen, is approximately

$$\text{time (sec)} = 42 + 1.64 \text{ (No. of Stations)}$$

Instructions for the program's use follow the diagrams.

SLIP VECTOR PLOT

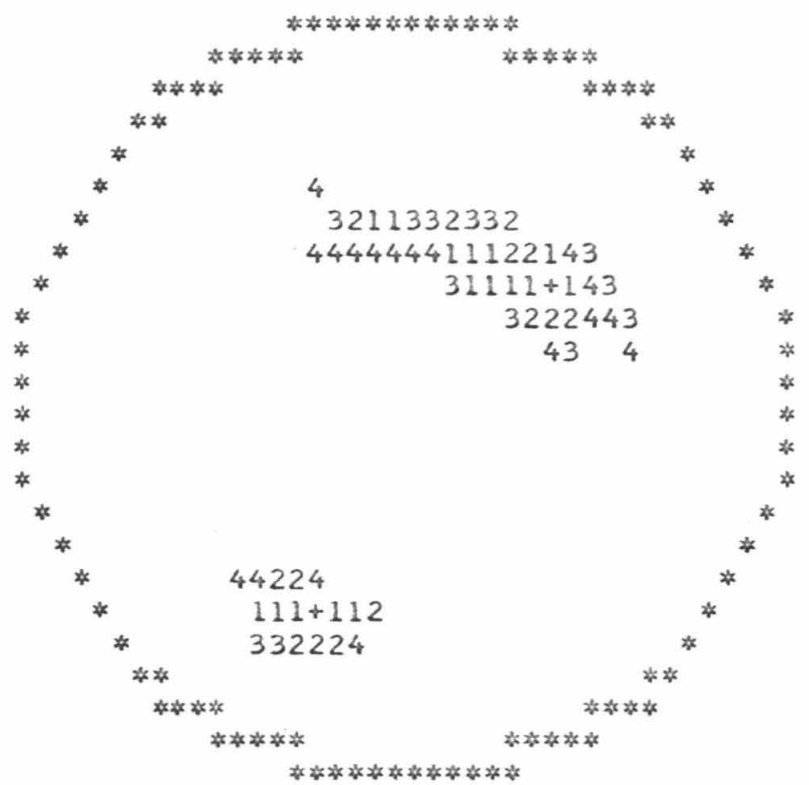

EVENT DATA
MAIN 0 02 09 71 14 0 41.6
8.4 34.000 24.70 -118.000 24.00 6.4

NUMBER OF STATIONS=101 STATIONS IN ERROR= 8
MINIMUM SCORE= 8.00 TAPER= 0.0

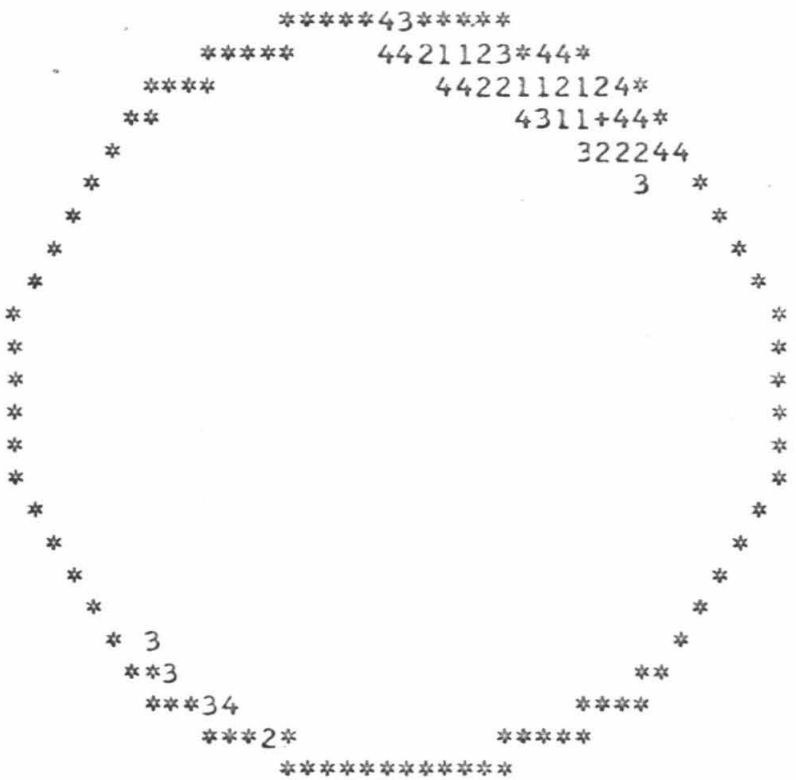

COMPRESSION AXIS

```
              *****43*****
          *****    4421123*44*
       ****           4422112124*
      **                  4311+44*
     *                       322244
    *                           3  *
   *                                *
  *                                  *
 *                                    *
*                                      *
*                                      *
*                                      *
*                                      *
*                                      *
*                                      *
 *                                    *
  *                                  *
   *                                *
    *                              *
     * 3                          *
      **3                       **
       ***34                 ****
          ***2*          *****
              ************
```

```
EVENT DATA
     MAIN     0  02 09 71  14  0 41.6
            8.4   34.000 24.70 -118.000 24.00  6.4

NUMBER OF STATIONS=101      STATIONS IN ERROR=  8
MINIMUM SCORE= 8.00         TAPER= 0.0
```

TENSION AXIS

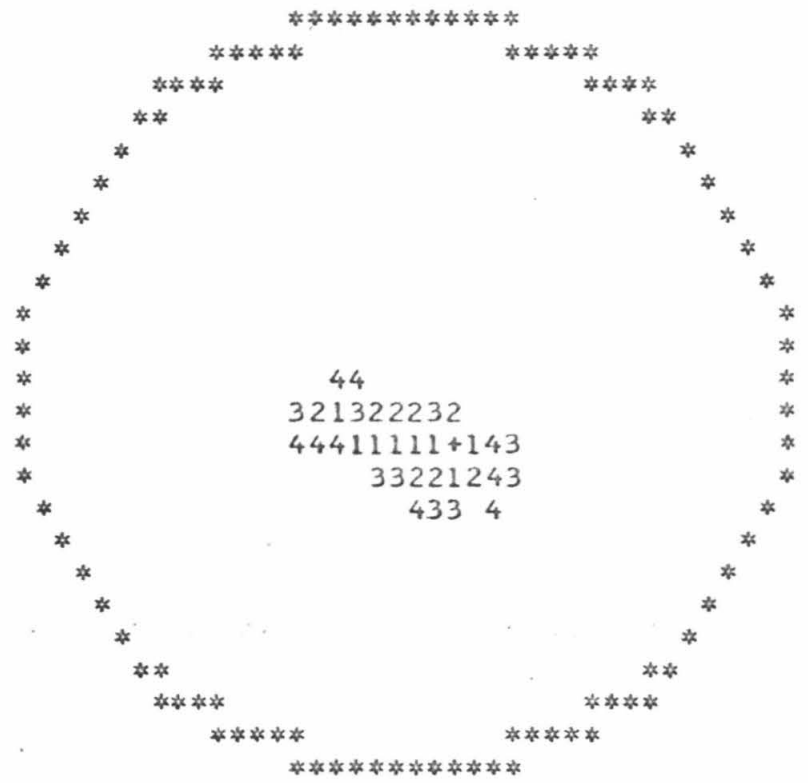

EVENT DATA
MAIN 0 02 09 71 14 0 41.6
8.4 34.000 24.70 -118.000 24.00 6.4

NUMBER OF STATIONS=101 STATIONS IN ERROR= 8
MINIMUM SCORE= 8.00 TAPER= 0.0

COMPRESSIONAL AND DILATATIONAL QUADRANTS

SHADED QUADRANTS ARE COMPRESSIONAL

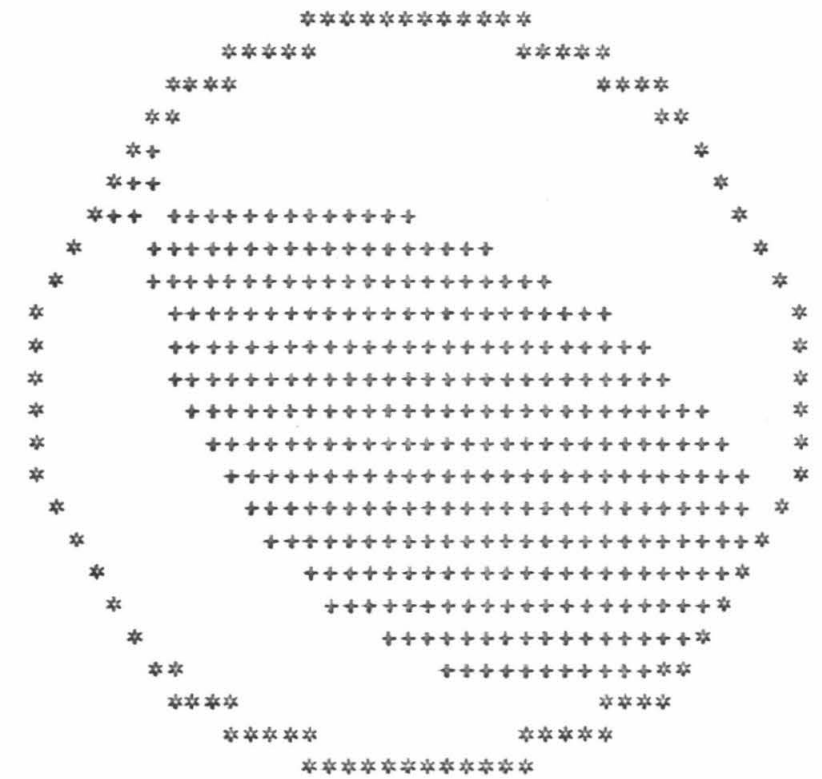

EVENT DATA
MAIN 0 02 09 71 14 0 41.6
8.4 34.000 24.70 -118.000 24.00 6.4

AZ1=142.1 DIP1= 41.6 AZ2=292.7 DIP2= 52.3

SLIP VECTOR PLOT

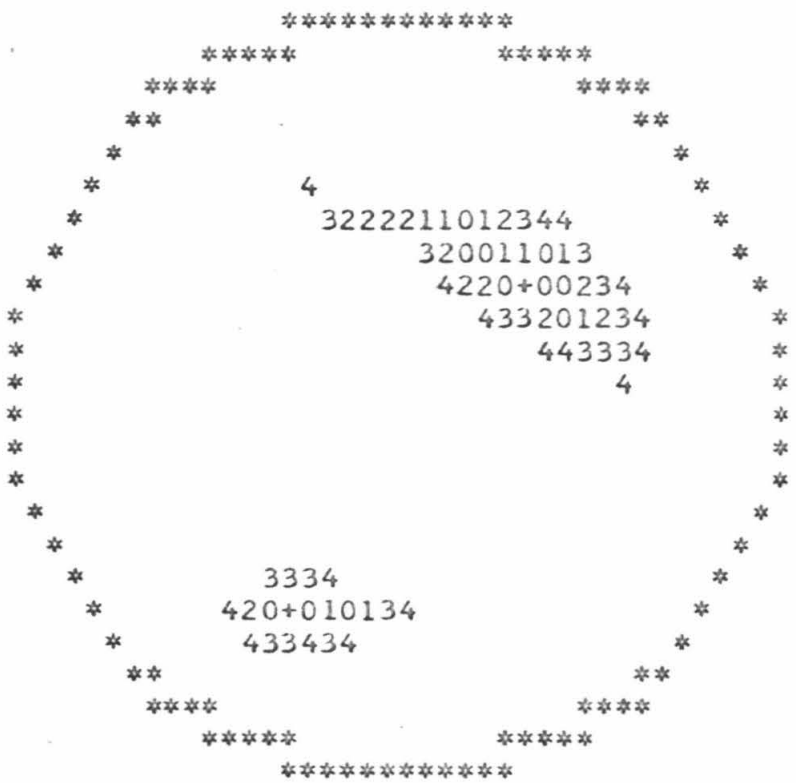

EVENT DATA
MAIN 0 02 09 71 14 0 41.6
8.4 34.000 24.70 -118.000 24.00 6.4

NUMBER OF STATIONS=101 STATIONS IN ERROR= 11
MINIMUM SCORE= 5.47 TAPER= 0.060

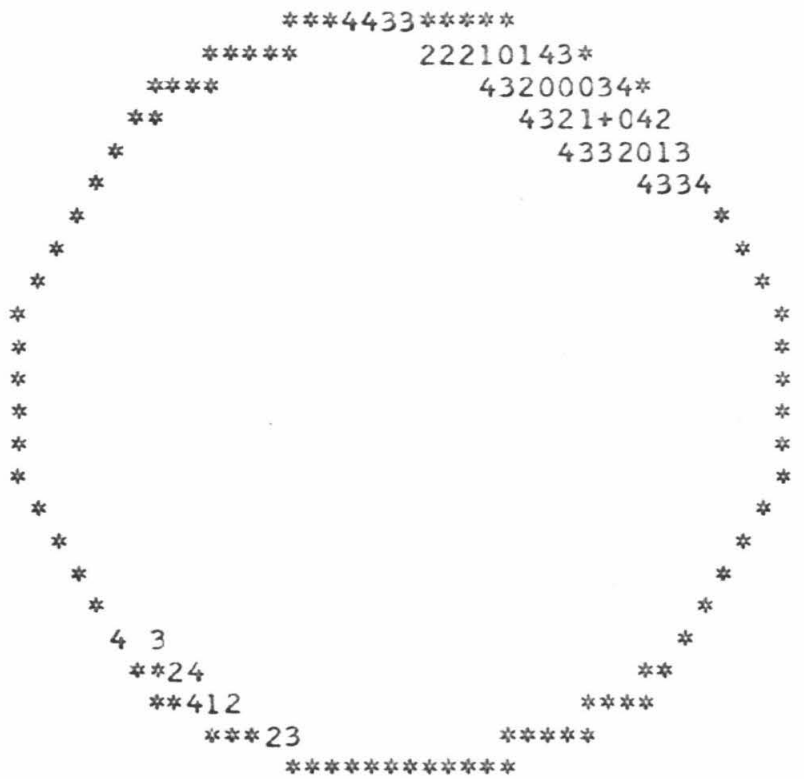

COMPRESSION AXIS

```
              ***4433*****
          *****      22210143*
       ****              43200034*
      **                   4321+042
     *                       4332013
    *                            4334
   *                                 *
  *                                   *
 *                                     *
*                                       *
*                                       *
*                                       *
*                                       *
*                                       *
*                                       *
 *                                     *
  *                                   *
   *                                 *
    *                               *
     4 3                           *
      **24                       **
       **412                  ****
          ***23          *****
              ************


 EVENT DATA
      MAIN     0  02 09 71  14  0 41.6
           8.4   34.000 24.70 -118.000 24.00  6.4

NUMBER OF STATIONS=101      STATIONS IN ERROR= 11
MINIMUM SCORE= 5.47         TAPER= 0.060
```

TENSION AXIS

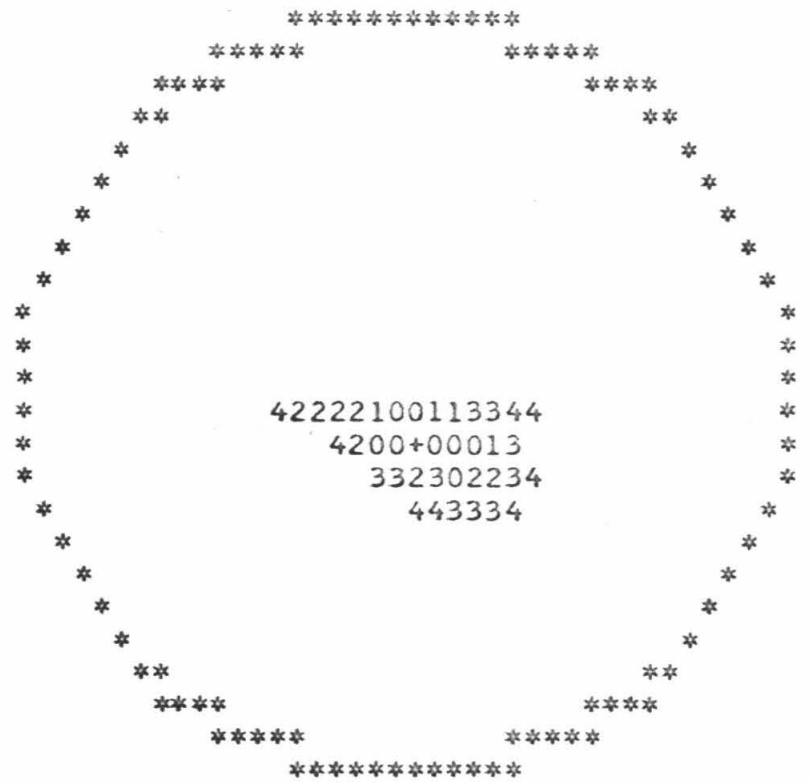

EVENT DATA
MAIN 0 02 09 71 14 0 41.6
8.4 34.000 24.70 -118.000 24.00 6.4

NUMBER OF STATIONS=101 STATIONS IN ERROR= 11
MINIMUM SCORE= 5.47 TAPER= 0.060

COMPRESSIONAL AND DILATATIONAL QUADRANTS

SHADED QUADRANTS ARE COMPRESSIONAL

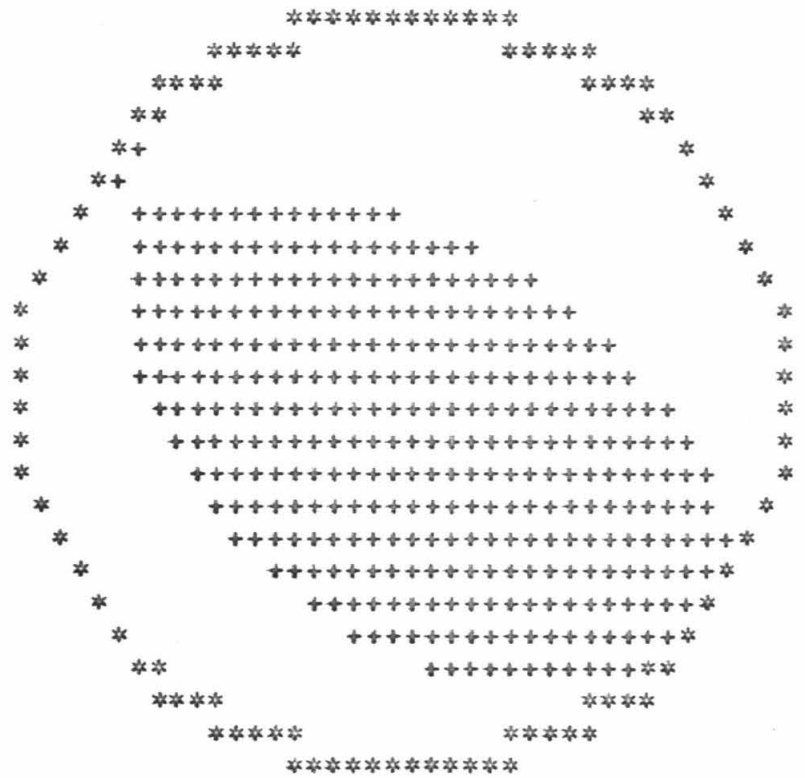

EVENT DATA

MAIN 0 02 09 71 14 0 41.6

8.4 34.000 24.70 -118.000 24.00 6.4

AZ1=138.1 DIP1= 38.1 AZ2=296.9 DIP2= 53.8

```
CCCCCCCCCCCCCCCCCCCCCCCCCCCCCCCCCCCCCCCCCCCCCCCCCCCCCCCCCCCCCCCCCCCCCCCCCCC
C
C      THIS PROGRAM PLOTS P-WAVE FIRST MOTION DATA ON THE LOWER FOCAL
C HEMISPHERE IN AN EQUAL-AREA PROJECTION. A TAKEOFF ANGLE TABLE(VS. DEL)
C AND STATION PARAMETER TABLE ARE READ IN FIRST.  THEN, READINGS FOR
C EACH EVENT ARE READ, REDUCED, AND PLOTTED (OPTIONAL) WITH STATION
C NAMES (OPTIONAL).
C     OPTIONS ARE AVAILABLE TO PLOT THE NODAL PLANES FOR A GIVEN FOCAL
C MECHANISM OR TO CALCULATE THE 'BEST' FOCAL MECHANISM FOR THE GIVEN
C DATA DISTRIBUTION.  CARE MUST BE TAKEN IN USING THE CALCULATED FOCAL
C MECHANISM TO SEE THAT THE SOLUTION IS WELL-CONSTRAINED IN THE SLIP-
C VECTOR PLOTS.  IF NOT WELL-CONSTRAINED, THE SOLUTION SHOULD BE IGNORED
C AND THE DISTRIBUTION OF EQUAL MISFIT AREAS IN THE SLIP-VECTOR PLOT
C SHOULD BE USED TO DETERMINE THE POSSIBLE ORIENTATIONS OF THE NODAL
C PLANES.
C
CCCCCCCCCCCCCCCCCCCCCCCCCCCCCCCCCCCCCCCCCCCCCCCCCCCCCCCCCCCCCCCCCCCCCCCCCCC
C INPUT DATA
C
C   CARD
C   1-5  I5         NDEPTH=NUMBER OF DEPTHS IN TABLE
C   6-77 18A4       TIDEN =IDENTITY OF VELOCITY MODEL USED TO GET TABLE.
C   DO FOLLOWING NDEPTH TIMES
C       CARD
C       1-10 F10.3      TDEPTH=DEPTH(KM) FOR THIS TABLE
C      11-15  I5        NENTRY=NUMBER OF ENTRIES IN THIS TABLE
C       CARDS
C       1-8   5(2F8.3)  TDEL=DISTANCE(DEG)
C       8-16            TEANG=EMERGENCE ANGLE(DEG)
C       ETC.               (FIVE ENTRIES OR PAIRS PER CARD NENTRY TIMES)
C
C   CARD
C   1-5  I5         NS=NUMBER OF STATIONS WITH COORDINATES
C   DO FOLLOWING NS TIMES
C       CARDS
C       7-10  A4        STA  =STATION NAME(RIGHT JUSTIFIED)
C      11-20  F10.3     SLAT1=LATITUDE(DEG)
C      21-25  F5.2      SLAT2=LATITUDE(MIN)
C      26-30  F5.2      SLAT3=LATITUDE(SEC)
C      31-40  F10.3     SLON1=LONGITUDE(DEG)
C      41-45  F5.2      SLON2=LONGITUDE(MIN)
C      46-50  F5.2      SLON3=LONGITUDE(SEC)
C
C   CARD
C   1-5  I5         NC=NUMBER OF STATION DISTANCE CORRECTONS
C   DO FOLLOWING NC TIMES
C       CARDS
C       2-5  A4         SNAM=STATION NAME (RIGHT JUSTIFIED)
C       6-10 F5.3       COR=EPICENTRAL DISTANCE CORRECTION TO BE ADDED
C                           TO ACCOUNT FOR VARIATION IN CRITICAL DIST.
C                                   (DEGREES)
```

```
C
C
C __THE FOLLOWING GROUP MAY BE REPEATED AS OFTEN AS NECESSARY
C|      CARD OF EVENT PARAMETERS
C|       1-8  A8           ENAM=NAME
C|       9-13 I5           IEVN =NUMBER
C|      15-22 A8           DATE =DATE
C|      26-27 I2           IEHR =HOUR
C|      29-30 I2           IEMI =MINUTE
C|      32-35 F4.1         ESEC =SECOND
C|      36-40 F5.0         DEPTH=DEPTH(KM)
C|      41-49 F9.3         ELAT1=LAT(DEG)
C|      50-55 F6.2         ELAT2=LAT(MIN)
C|      56-64 F9.3         ELON1=LONG(DEG)
C|      65-70 F6.2         ELON2=LONG(MIN)
C|      71-75 F5.1         EMAG =MAGNITUDE
C|      CARD OF FOCAL MECHANISM PLOT AND CALCULATION PARAMETERS
C|       1-10 F10.3        R90  RADIUS OF PLOT CIRCLE
C|      11-15 I5           NSPAR  IF 1, PLOT STATION NAMES
C|      16-20 I5           NOPLT  IF 1, NO PLOTS MADE
C|      21-25 I5           NOMEC   EQUALS 0 IF FAULT PLANE SOLUTION DESIRED
C|                         EQUALS 1 IF FAULT PLANE SOLUTION NOT DESIRED
C|                         OTHER PARAMETERS MAY BE OMITTED IF NOMEC = 1
C|      26-30 I5           MAXSCR   SPECIFIES HIGHEST NUMBER OF DISAGREE -
C|                         MENTS THAT WILL BE PLOTTED BY FLTPLN. HIGHEST
C|                         NUMBER THAT WILL BE PLOTTED IS MAXSCR-1. MAXSCR
C|                         MAY HAVE VALUES FROM 1 TO 6.
C|      31-35 I5           NSKIP   CONTROLS RESOLUTION OF SEARCH FOR BEST
C|                         SOLUTION. NSKIP=1 YIELDS HIGHEST RESOLUTION.
C|                         NSKIP MAY HAVE VALUES OF 1,2, OR 3.
C|      36-40 I5           NPRNT   SMALL PLOTS ONLY IF NPRNT = 1
C|                         LARGE PLOTS ONLY IF NPRNT = 2
C|                         BOTH SIZES FOR ANY OTHER VALUE OF NPRNT
C|      41-45 F5.3         TAPER    APPLIES WEIGHTING FUNCTION WHICH
C|                         TAPERS TO 0 FROM UNITY WITHIN A DISTANCE
C|                         ARSIN(TAPER) FROM THE NODAL PLANES.
C|      CARDS OF READING DATA
C|       2-5  A4           RSTA =STATION NAME (RIGHT JUSTIFIED)
C|       7-8  I2           IRHR =EVENT HOUR
C|       9-10 I2           IRMI =EVENT MINUTE
C|      13-20 A8           RDATE=EVENT DATE
C|      25    A1           RCODE=C(COMPRESSION), D(DILITATION)," "(NEITHER)
C|      26-30 I5           IQUAL=2(GOOD), 1(POOR); MINUS=NODAL CHARACTER
C|      CARD OF FOCAL MECHANISM PARAMETERS IF GIVEN
C|                         (IF PLOTTING OF NODAL PLANES NOT DESIRED,
C|                         LEAVE BLANK; IGNORED IF NOMEC=0)
C|       1-30              BLANK
C|       31-40 F10.0       AZ1 =AZIMUTH OF FIRST PLANE STRIKE (DEG),MUST BE
C|                                COUNTER CLOCKWISE FROM DIP DIRECTION
C|       41-50 F10.0       DIP1=DIP OF FIRST PLANE (CANNOT BE 90 UNLESS
C|                                BOTH PLANES ARE 90)
C|       51-60 F10.0       AZ2 =AZIMUTH OF SECOND PLANE STRIKE (DEG), MUST
C|____________                   BE COUNTER CLOCKWISE FROM DIP DIRECTION
C
C  THE LAST CARD SHOULD HAVE NINES IN COLUMNS 9-13 FOR A NORMAL STOP.
CCCCCCCCCCCCCCCCCCCCCCCCCCCCCCCCCCCCCCCCCCCCCCCCCCCCCCCCCCCCCCCCCCCCCCCC
```

Appendix 2.

P-wave First Motion Data and Focal-mechanism Diagrams

This appendix is intended as a supplement to the thesis of Whitcomb (Part II, California Institute of Technology, 1973) entitled "The 1971 San Fernando Earthquake Series Focal Mechanisms and Tectonics" referred to here as the main paper. It contains the P-wave first-motion data, focal mechanism diagrams, and associated parameters for 87 aftershocks of the series discussed in the main paper.

The stations used for P-wave first motions in this study are described in the main paper. All first-motion readings were made personally by the author in order to insure consistency; short-period seismometers were used exclusively. Although seismograms from a total of 47 stations were read, varying periods of operation for the portable stations and the weakness of the first arrival of smaller shocks at distant stations reduced the actual number of first motions read per event. The number of readings for most events ranged from 10-20 for the first twenty hours of the aftershock series and 20-30 for the remainder of the study time period (February 9 to May 7, 1971). Some instrument polarity reversals did occur, usually in instrumentation that was temporary or involved complex electronics such as a telemetry link from seismometer to recorder. However, the station coverage and the number of events were sufficient to reveal the reversals. Also

in almost every case, a reversal could be confirmed by polarity checks with teleseismic events.

The first-motion readings are designated as compressional (C, circles) or dilatational (D, plus signs) with a quality assignment of good (weight 2, large symbols) or fair (weight 1, small symbols). A further classification of nodal character (minus in the tables, stars in the diagrams) was given if the arrival had emergent character when, by a subjective judgment involving the epicentral distance and size of the aftershock, one would expect the first motion to be sharp.

The readings are mapped onto the lower focal hemisphere of an equal-area stereographic projection by ray tracing through a smooth 23 km-thick crustal velocity model described in the main paper.

The double-couple focal mechanisms of the aftershocks are fit to the data by eye under the influence of the reading qualities, good or fair. An estimate of the quality of the solution is made, A, B, or C, as described in the main paper; the C quality rating implies that the parameters are not constrained within 20° and no solution is given.

The table format begins with the event parameters: event number, origin time (hr, min), date, depth, epicentral location, and local magnitude. If the focal mechanism is of quality A or B, its parameters are given in terms of the nodal planes' orientations (azimuth, dip), the slip vectors in those planes (azimuth, take-off angle measured from vertical), and the directions of the principal

stress axes (azimuth, take-off angle measured from vertical). The locations of the slip vectors and the principal stress axes are shown as small triangles in the plots. The next parameters in the table are epicentral distance (deg), azimuth at the event (deg), take-off angle measured from vertical, and the x and y coordinates (inches) of the data in the plot. Rays that pierce the upper-focal hemisphere are projected backwards onto the lower hemisphere, a procedure permitted by the symmetry of the double-couple.

EVENT DATA

1,1510 0 02/09/71 15 10 0.0

8.0 34.000 24.80 -118.000 24.70 3.9

STA	DIR	QUAL	DIST	EVAZ	TOA	X	Y
CSP	C	2	0.880	97.391	92.332	-2.428	0.315
GSC	C	2	1.591	55.691	49.400	1.220	0.833
ISA	D	1	1.098	357.530	89.636	-0.107	2.490
MWC	C	2	0.350	123.215	98.866	-1.924	1.260
PLM	C	2	1.668	128.925	49.400	1.149	-0.928
PYR	C	2	0.314	299.872	99.309	1.985	-1.140
SYP	C	1	1.299	275.549	49.400	-1.470	0.143

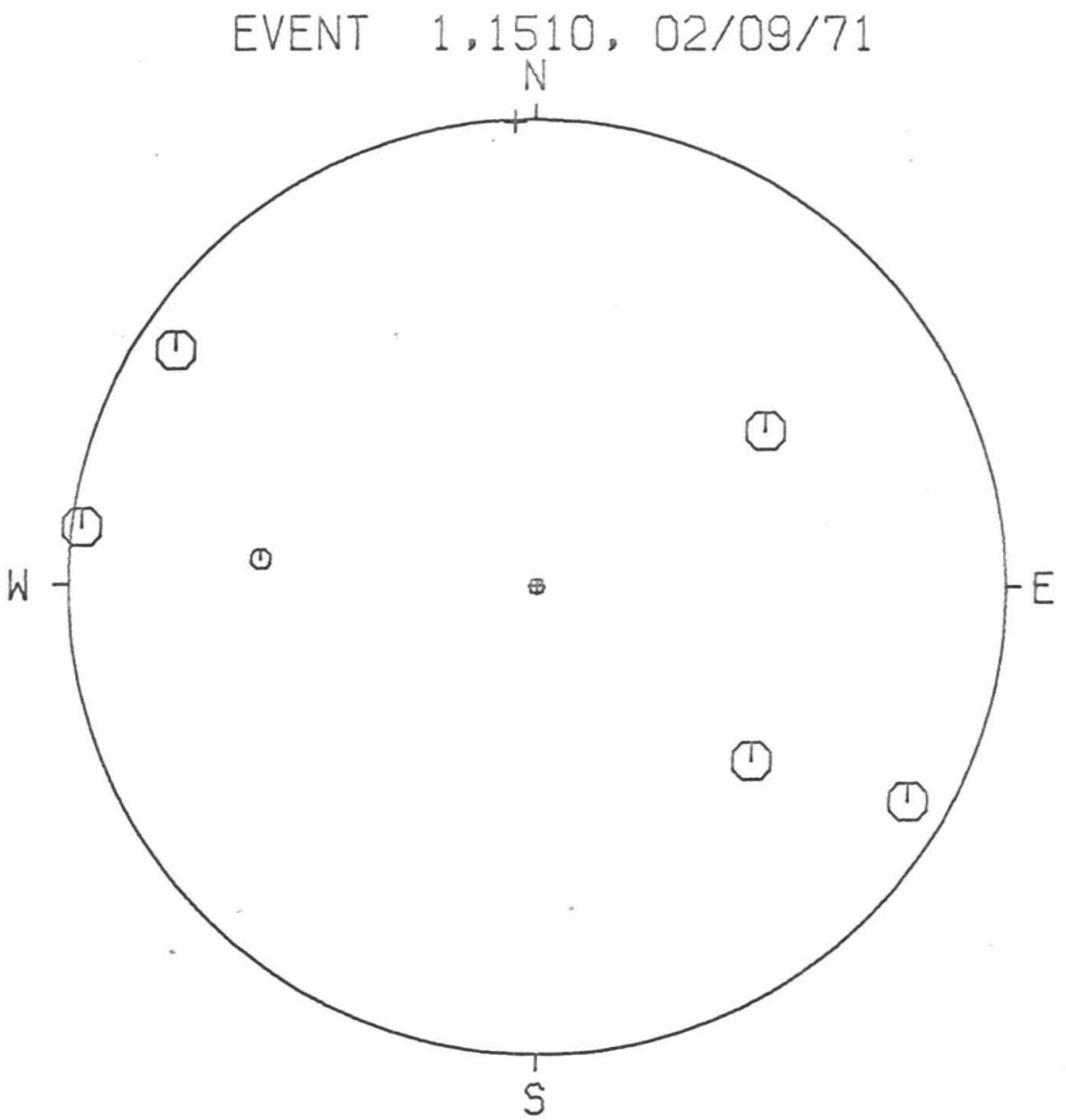
EVENT 1,1510, 02/09/71
N
W
E
S

EVENT DATA

2,1538 0 02/09/71 15 38 0.0

8.0 34.000 24.40 -118.000 28.00 3.9

STA	DIR	QUAL	DIST	EVAZ	TOA	X	Y
BAR	D	2	2.283	138.468	49.400	0.980	-1.106
CSP	C	2	0.924	96.679	91.783	-2.444	0.286
GSC	C	2	1.633	56.355	49.400	1.230	0.819
HFD	C	1	2.452	105.775	49.400	1.422	-0.402
ISA	D	2	1.104	359.621	89.565	-0.016	2.490
MWC	C	2	0.386	118.670	98.426	-2.026	1.108
PAS	C	2	0.357	136.682	98.784	-1.579	1.674
PLM	D	1	1.699	127.767	49.400	1.168	-0.905
PYR	D	2	0.280	305.785	99.732	1.849	-1.333
SBC	D	1	1.199	272.818	49.400	-1.476	0.073
SYP	C	2	1.255	276.065	49.400	-1.469	0.156
RCTR	C	2	0.330	129.075	99.107	-1.781	1.446

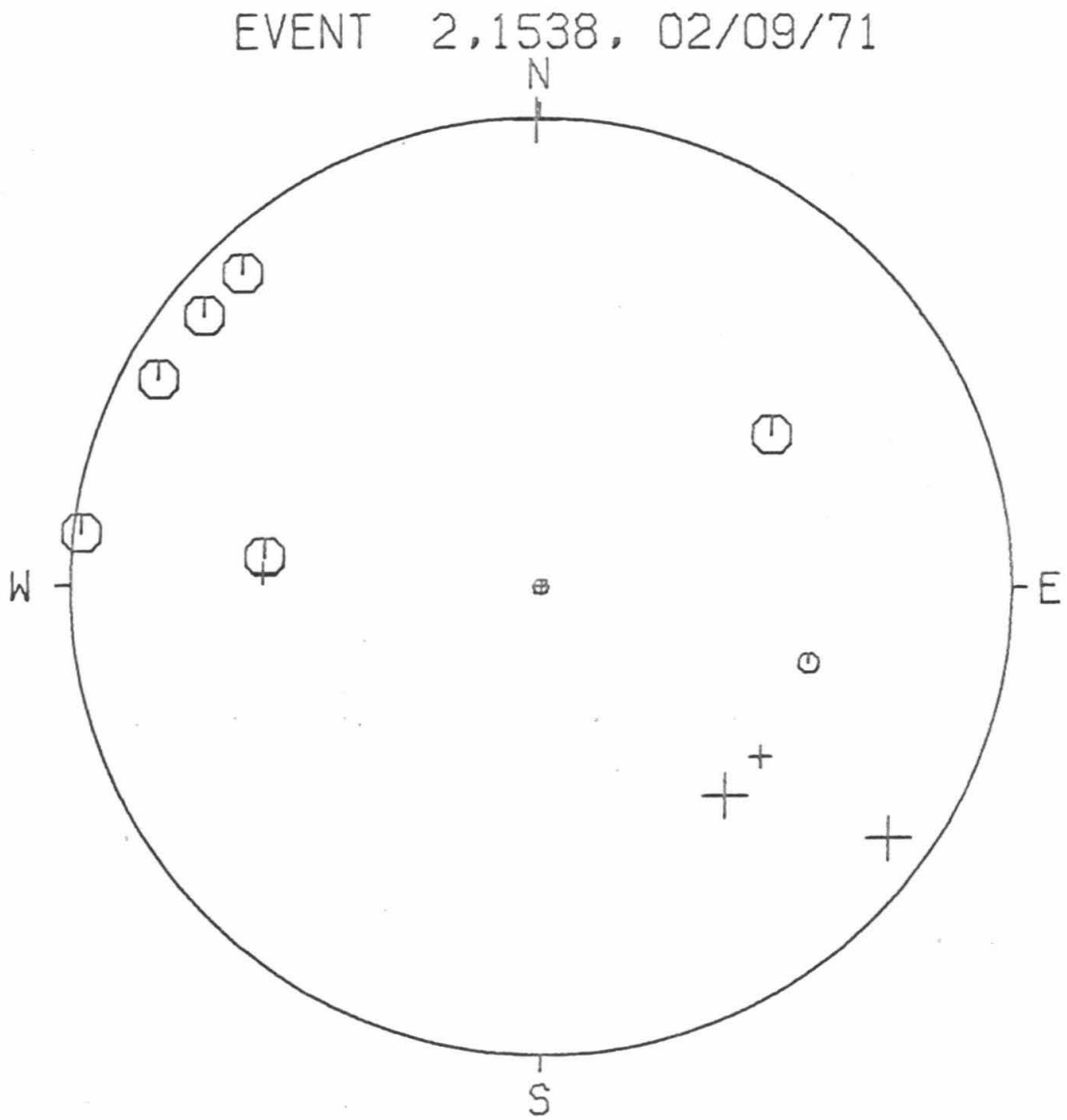
EVENT 2,1538, 02/09/71
N
W
E
S

EVENT DATA

3,1558 0 02/09/71 15 58 0.0

9.0 34.000 22.46 -118.000 20.10 4.8

STA	DIR	QUAL	DIST	EVAZ	TOA	X	Y
BAR	C	2	2.188	140.118	49.400	0.947	-1.134
CSP	D	2	0.813	95.485	93.688	-2.407	0.231
CWC	D	2	2.071	5.744	49.400	0.148	1.470
GLA	D	1	3.208	113.308	49.400	1.357	-0.585
GSC	D	2	1.562	53.242	49.400	1.184	0.884
ISA	D	2	1.142	354.794	89.103	-0.225	2.470
MWC	C	2	0.276	123.682	102.009	-1.851	1.234
PAS	D	2	0.265	149.206	102.249	-1.136	1.906
PLM	C	2	1.594	129.315	49.400	1.143	-0.936
PYR	D	2	0.389	300.297	99.505	1.972	-1.152
SBC	C	1	1.309	273.922	49.400	-1.474	0.101
SYP	C	2	1.366	277.003	49.400	-1.466	0.180

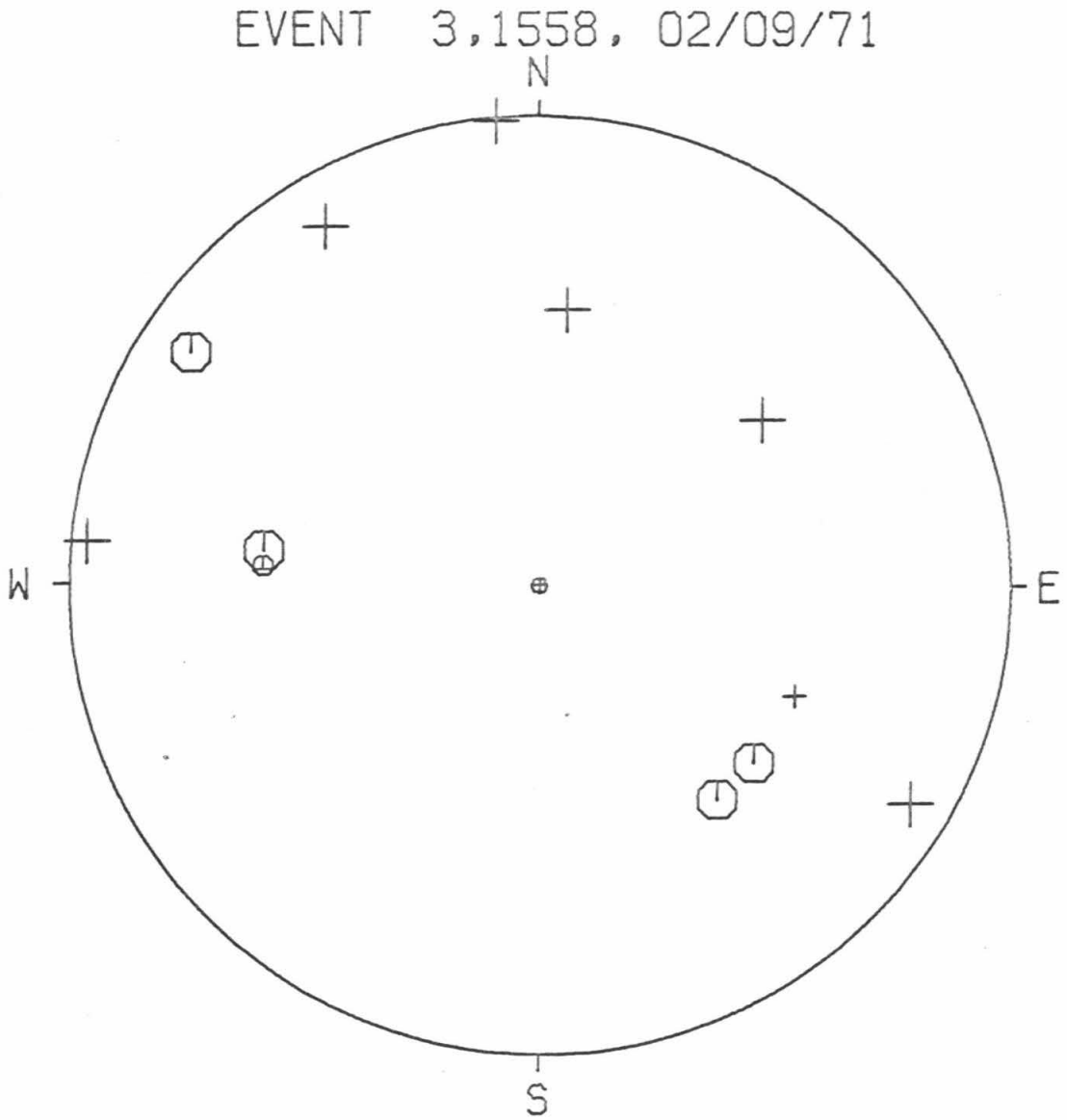
EVENT 3,1558, 02/09/71
N
W
E
S

EVENT DATA

4,1619 0 02/09/71 16 19 0.0

3.0 34.000 27.44 -118.000 25.62 4.2

AZ1= 327.000
DIP1= 23.000
AZ2= 118.300
DIP2= 69.578

SLIP VECTORS= 28.300 69.578 237.000 23.000

PRIN AXES = 10.780 26.154 216.640 66.161

STA	DIR	QUAL	DIST	EVAZ	TOA	X	Y
BAR	D	1	2.300	139.934	44.933	0.870	-1.034
CLC	C	2	1.518	26.405	44.933	0.601	1.210
CWC	C	2	1.998	8.098	44.933	0.190	1.338
GSC	C	2	1.578	57.252	44.933	1.136	0.731
ISA	D	2	1.054	358.042	81.397	-0.079	2.304
MWC	C	2	0.386	127.612	87.808	1.942	-1.496
PAS	C	2	0.375	145.599	87.912	1.386	-2.025
PLM	C	2	1.705	129.801	44.933	1.038	-0.865
SBC	D	2	1.230	268.413	50.437	-1.506	-0.042
SYP	D	2	1.283	273.789	44.933	-1.348	0.089
TIN	C	1	2.597	3.510	44.933	0.083	1.349
ENGN	C	2	0.425	138.353	87.433	1.624	-1.826

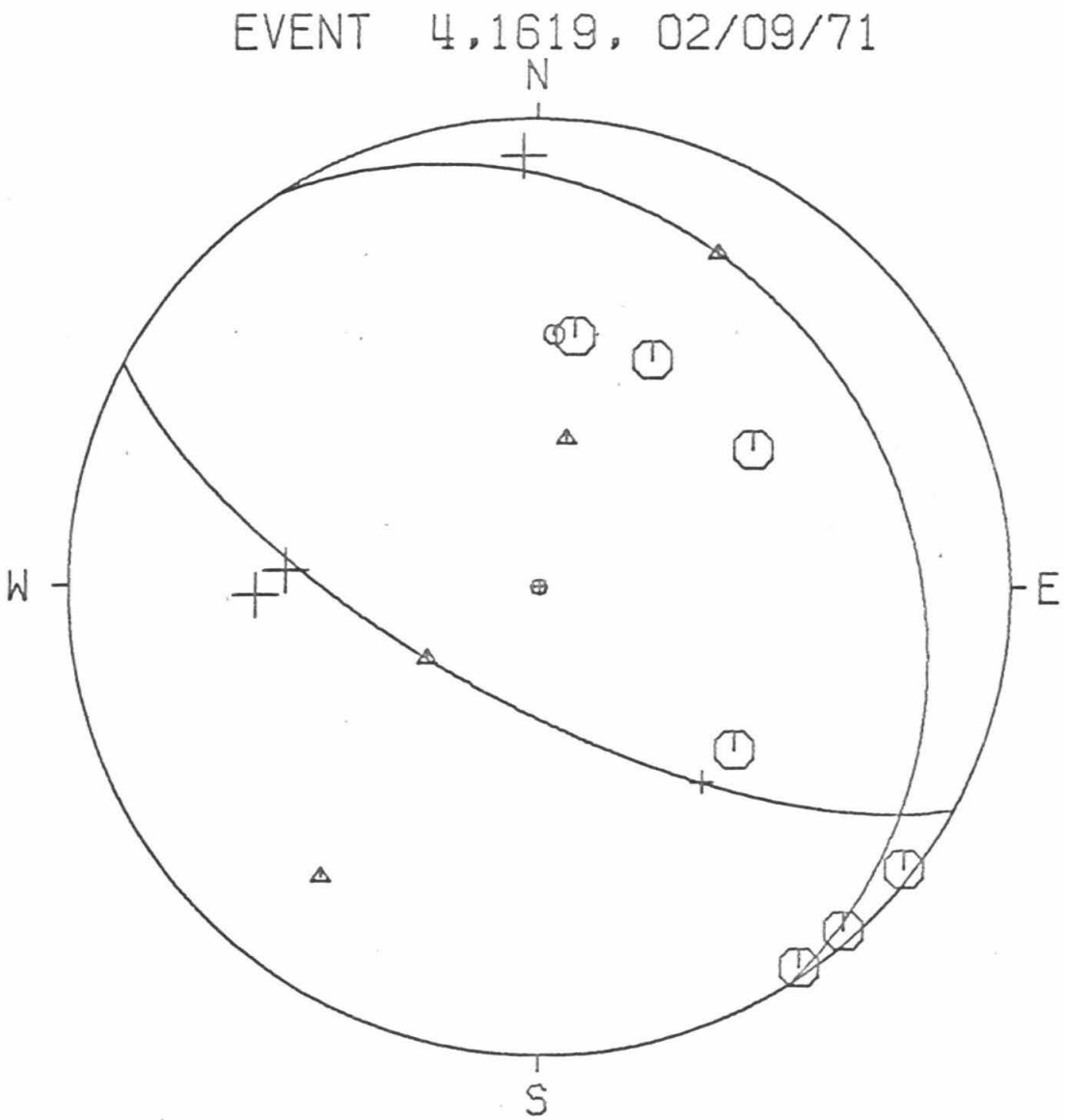
EVENT 4,1619, 02/09/71
N
W
E
S

EVENT DATA

5,1703 0 02/09/71 17 3 0.0

8.0 34.000 22.20 -118.000 29.50 3.9

AZ1= 280.000
DIP1= 40.000
AZ2= 136.000
DIP2= 55.830

SLIP VECTORS= 46.000 55.830 190.000 40.000

PRIN AXES = 96.913 20.146 210.335 81.690

STA	DIR	QUAL	DIST	EVAZ	TOA	X	Y
BAR	C	1	2.270	137.449	49.400	0.999	-1.088
CSP	D	2	0.941	94.385	91.571	-2.458	0.189
CWC	C	1	2.092	9.176	49.400	0.236	1.458
GSC	C	2	1.670	55.698	49.400	1.220	0.833
ISA	D	1	1.141	0.552	89.116	0.024	2.481
MWC	C	2	0.388	112.316	98.395	-2.137	0.877
PAS	D	2	0.346	129.915	98.914	-1.763	1.475
SBC	D	2	1.180	274.668	49.400	-1.472	0.120
SYP	D	1	1.238	277.818	49.400	-1.464	0.201
TIN	C	1	2.688	4.498	49.400	0.116	1.473

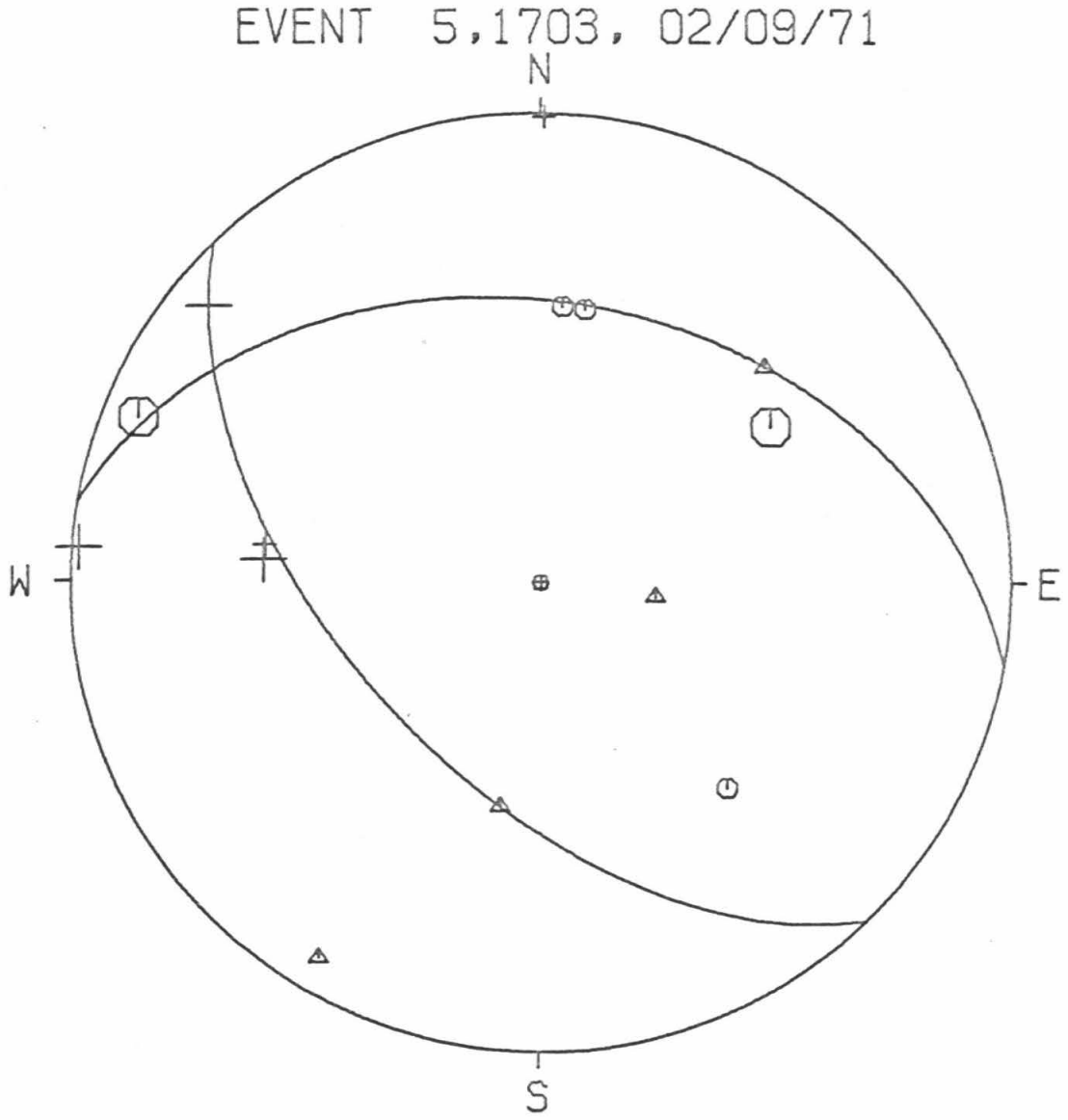
EVENT 5,1703, 02/09/71
N
W
E
S

EVENT DATA

6,1719 0 02/09/71 17 19 0.0

8.0 34.000 24.70 -118.000 26.80 3.6

AZ1= 108.000
DIP1= 70.000
AZ2= 198.000
DIP2= 90.000

SLIP VECTORS= 108.000 90.000 18.000 70.000

PRIN AXES = 64.779 76.005 331.219 76.005

STA	DIR	QUAL	DIST	EVAZ	TOA	X	Y
CSP	C	2	0.908	97.131	91.978	-2.437	0.305
CWC	D	1	2.045	8.358	49.400	0.215	1.462
GSC	C	2	1.616	56.194	49.400	1.228	0.822
ISA	D	2	1.099	358.860	89.626	-0.050	2.491
MWC	D	2	0.373	120.447	98.579	-1.988	1.169
PAS	D	2	0.349	139.173	98.879	-1.503	1.740
PLM	D	1	1.689	128.246	49.400	1.160	-0.915
PYR	D	2	0.290	302.933	99.605	1.915	-1.241
SBC	D	1	1.215	272.384	49.400	-1.476	0.061
SYP	D	2	1.270	275.718	49.400	-1.470	0.147
ENGN	D	2	0.403	132.269	98.206	-1.713	1.557
RCTR	D	2	0.321	131.590	99.225	-1.713	1.521

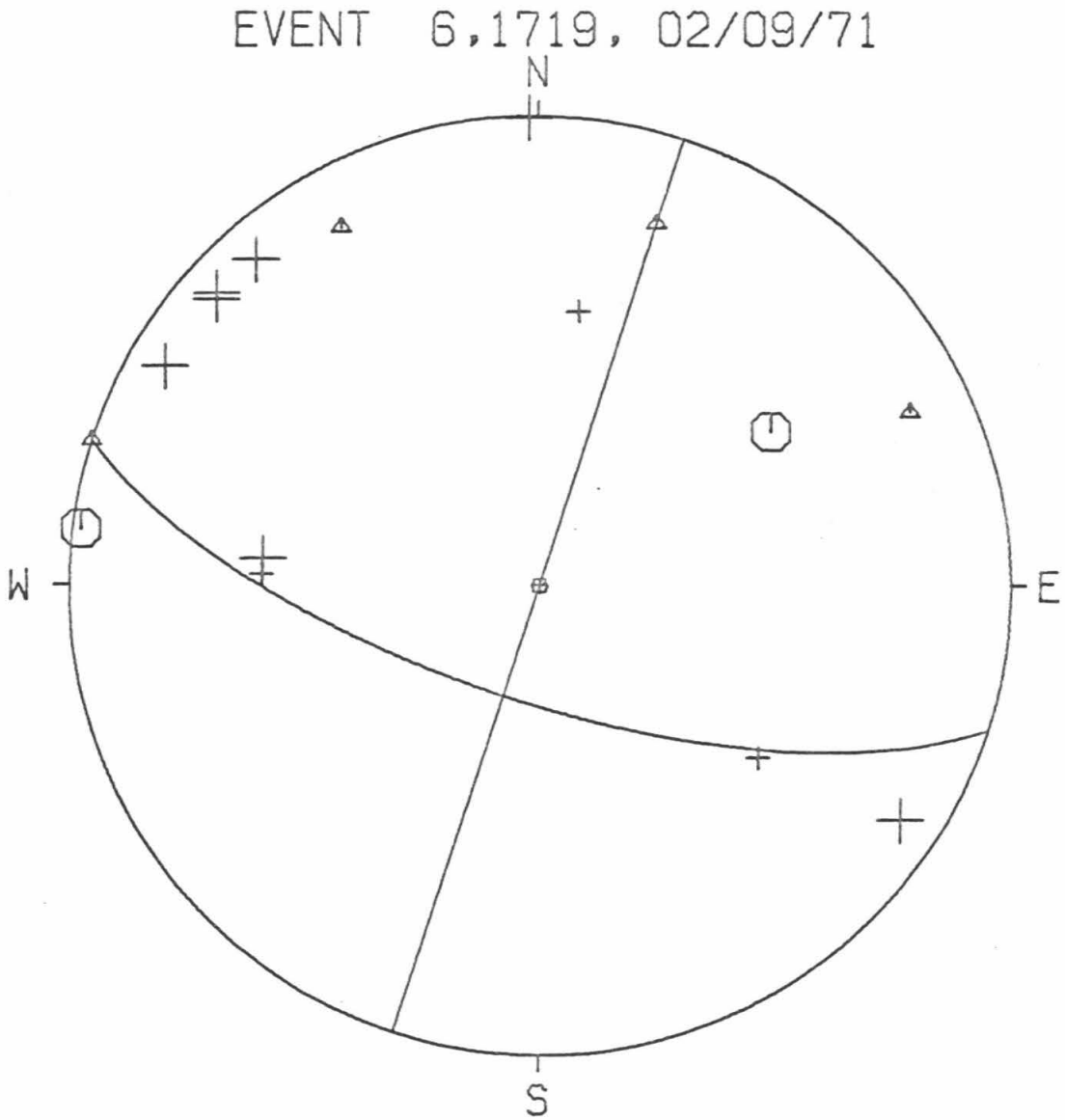
EVENT 6,1719, 02/09/71
N
W
E
S

EVENT DATA

7,1829 0 02/09/71 I8 29 0.0

8.0 34.000 23.70 -118.000 28.90 3.8

STA	DIR	QUAL	DIST	EVAZ	TOA	X	Y
BAR	D	2	2.283	138.032	49.400	0.988	-1.098
CSP	C	2	0.935	95.919	91.646	-2.451	0.254
ISA	C	2	1.116	0.188	89.423	0.008	2.487
MWC	C	2	0.391	116.259	98.358	-2.073	1.023
PAS	C	2	0.357	133.955	98.777	-1.657	1.597
PLM	C	1	1.702	127.187	49.400	1.177	-0.893
PYR	D	2	0.276	309.044	99.775	1.769	-1.435
SBC	C	2	1.187	273.439	49.400	-1.475	0.089
SYP	C	2	1.243	276.625	49.400	-1.468	0.170
TIN	D	2	2.662	4.368	49.400	0.113	1.473
RVR	C	2	1.001	113.298	90.836	-2.279	0.982
ENGN	C	2	0.414	127.774	98.070	-1.832	1.420
RCTR	C	2	0.333	126.214	99.070	-1.851	1.356

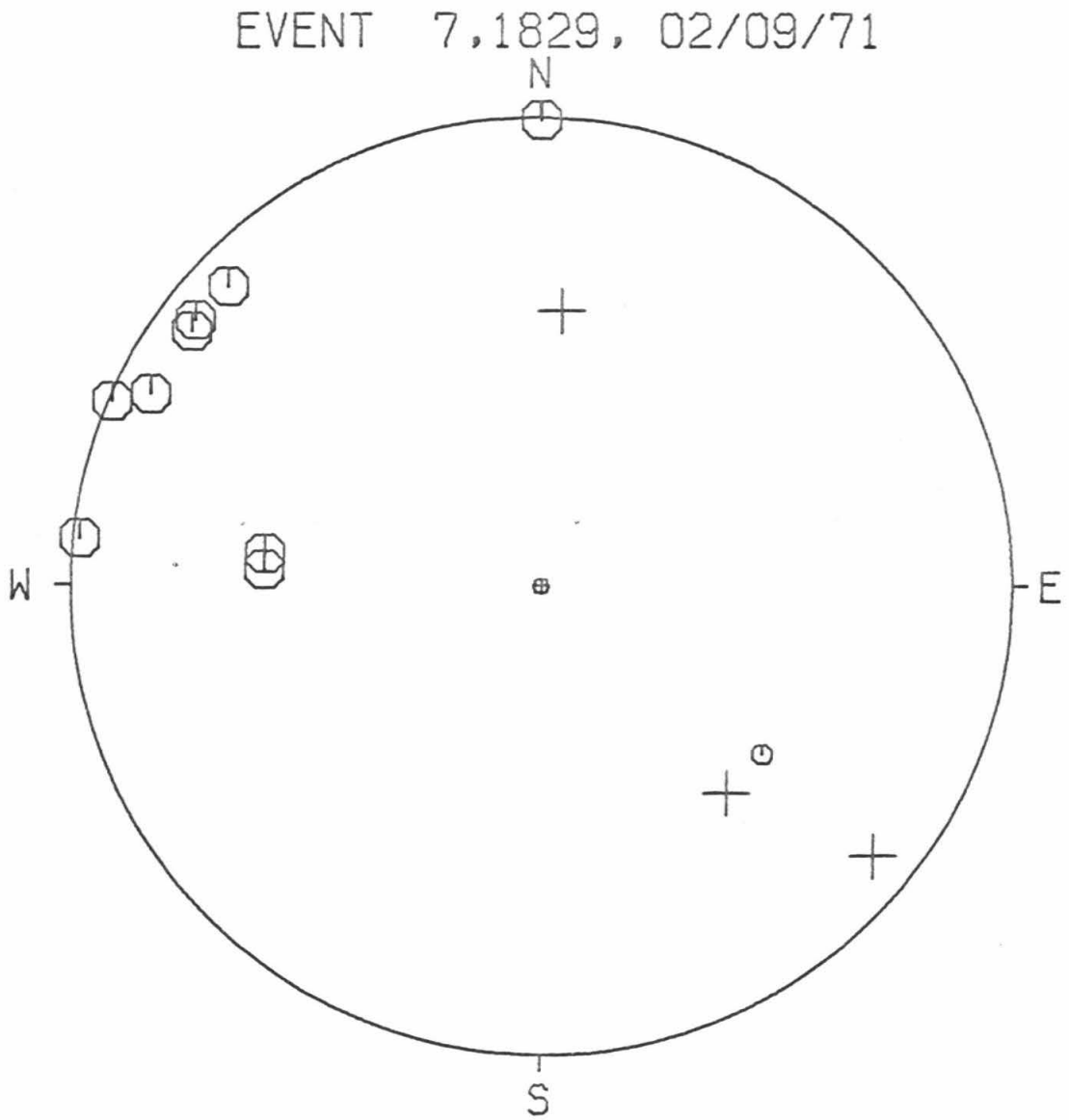
EVENT 7,1829, 02/09/71
N
W
E
S

EVENT DATA

8,2053 0 02/09/71 20 53 0.0
8.0 34.000 26.12 -118.000 23.70 3.4

AZ1= 298.000
DIP1= 48.000
AZ2= 105.800
DIP2= 42.652

SLIP VECTORS= 15.800 42.652 208.000 48.000

PRIN AXES = 267.355 6.683 22.182 87.311

STA	DIR	QUAL	DIST	EVAZ	TOA	X	Y
CLC	D	2	1.526	25.167	49.400	0.628	1.337
CSP	D	2	0.870	99.139	92.456	-2.415	0.388
CWC	C	1	2.016	7.285	49.400	0.187	1.465
GSC	D	-2	1.568	56.063	49.400	1.226	0.825
ISA	D	2	1.078	356.843	89.893	-0.138	2.494
MWC	D	2	0.352	127.499	98.845	-1.825	1.400
PAS	D	2	0.343	147.271	98.956	-1.242	1.932
PLM	C	2	1.671	129.827	49.400	1.135	-0.946
PYR	C	2	0.318	295.805	99.263	2.062	-0.997
SYP	C	2	1.311	274.656	49.400	-1.473	0.120
TIN	C	1	2.618	2.922	49.400	0.075	1.475
RVR	C	1	0.954	117.318	91.419	-2.194	1.133
BOUQ	D	2	0.088	334.533	125.844	0.692	-1.453
BRWN	D	2	0.219	227.993	103.835	1.620	1.459
ENGN	D	2	0.390	139.044	98.370	-1.515	1.745

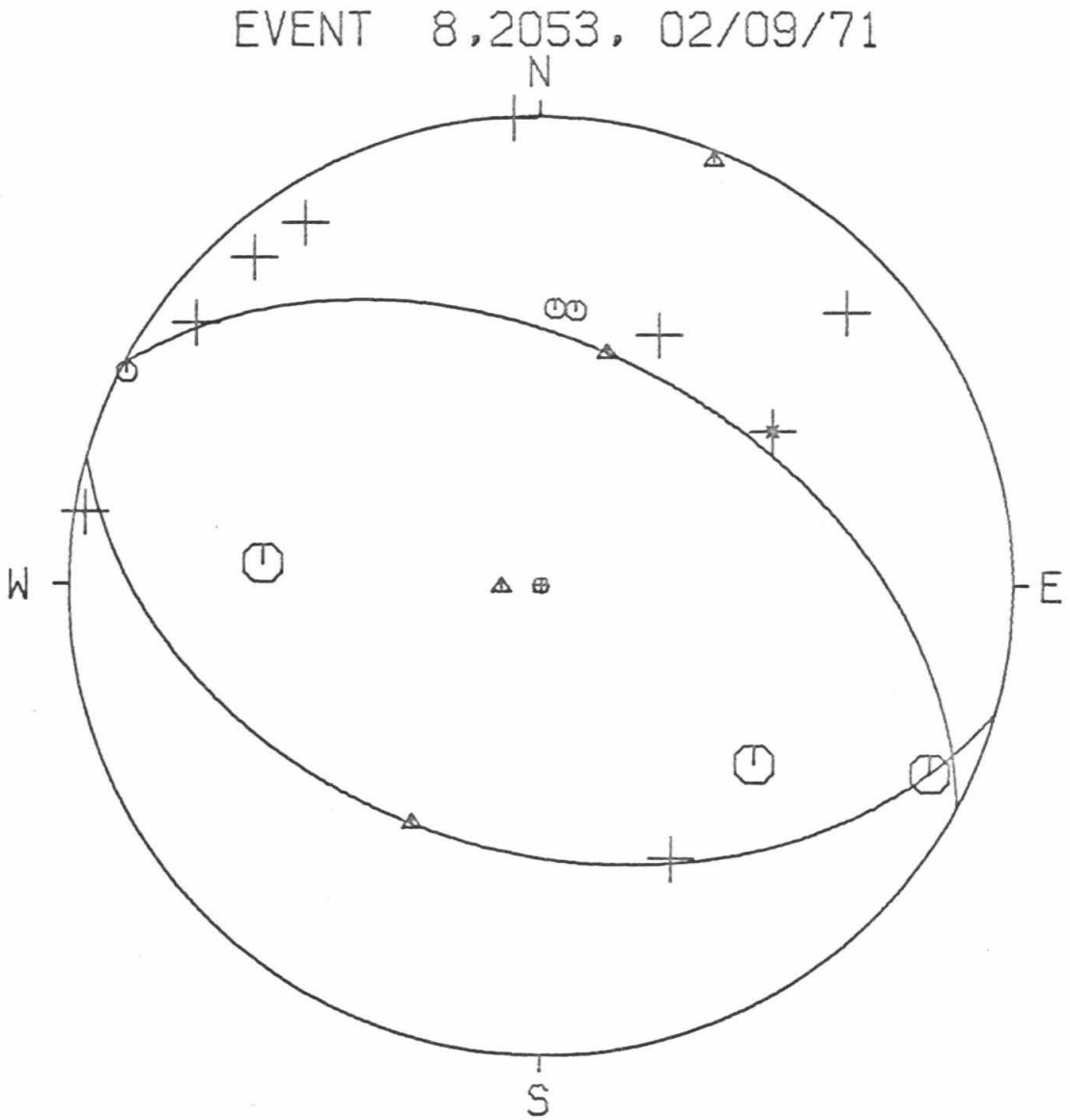
EVENT 8,2053, 02/09/71
N
W
E
S

EVENT DATA

9,2056 0 02/09/71 20 56 0.0

8.0 34.000 18.50 -118.000 21.30 3.7

AZ1= 119.000
DIP1= 50.000
AZ2= 299.000
DIP2= 40.000

SLIP VECTORS= 209.000 40.000 29.000 50.000

PRIN AXES = 28.958 5.007 208.999 85.000

STA	DIR	QUAL	DIST	EVAZ	TOA	X	Y
CSP	D	1	0.826	92.068	92.994	-2.432	0.088
GSC	C	2	1.616	51.713	49.400	1.160	0.915
ISA	C	2	1.206	355.746	49.400	-0.110	1.473
MWC	C	2	0.261	109.584	99.964	-2.142	0.762
PAS	C	2	0.222	136.774	103.490	-1.499	1.595
PLM	C	1	1.566	127.061	49.400	1.179	-0.890
PYR	C	2	0.412	309.265	98.099	1.794	-1.467
SYP	D	2	1.360	279.793	49.400	-1.456	0.251
RVR	C	2	0.872	110.929	92.431	-2.285	0.874
BOUQ	D	2	0.213	340.514	104.363	0.723	-2.044
ENGN	D	2	0.280	127.292	99.732	-1.813	1.381

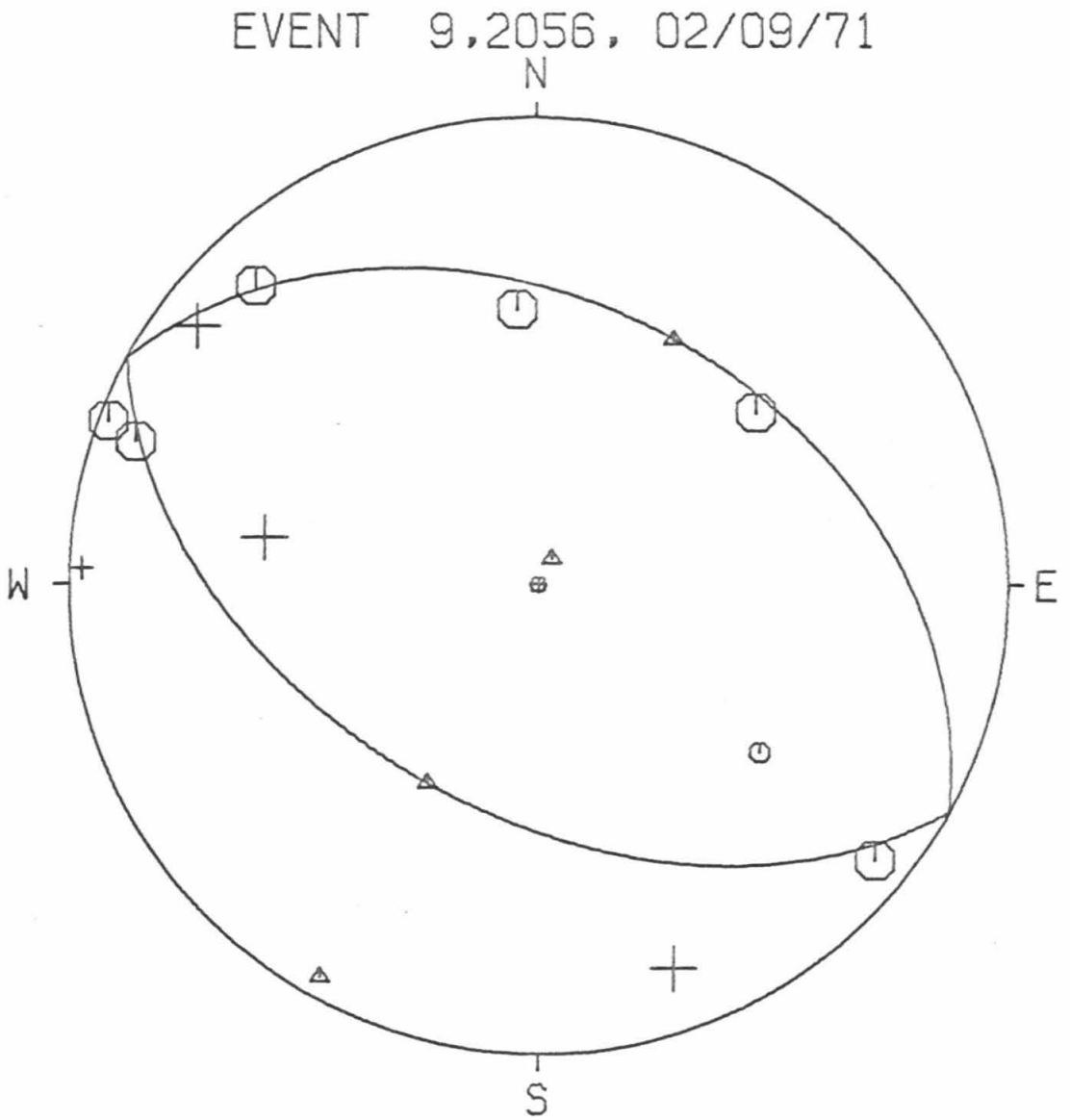
EVENT 9,2056, 02/09/71
N
W
E
S

EVENT DATA

10,0138 0 02/10/71 1 38 0.0

8.0 34.000 19.30 -118.000 32.00 3.9

AZ1= 217.500
DIP1= 70.000
AZ2= 307.500
DIP2= 90.000

SLIP VECTORS= 217.500 90.000 127.500 70.000

PRIN AXES = 174.281 76.005 80.715 76.005

STA	DIR	QUAL	DIST	EVAZ	TOA	X	Y
BAR	D	1	2.259	135.959	49.400	1.027	-1.062
CLC	C	2	1.678	26.982	49.400	0.670	1.317
CSP	C	2	0.974	92.286	91.171	-2.472	0.099
CWC	D	2	2.146	9.855	49.400	0.253	1.456
GSC	C	2	1.726	54.991	49.400	1.210	0.848
ISA	D	2	1.190	2.004	49.400	0.052	1.476
MWC	C	2	0.407	104.677	98.164	-2.240	0.587
PAS	C	2	0.348	120.394	98.893	-1.983	1.163
PLM	C	-2	1.694	124.324	49.400	1.220	-0.833
PYR	D	2	0.301	325.206	99.466	1.304	-1.877
SBC	C	2	1.151	277.653	50.496	-1.495	0.201
SYP	C	2	1.212	280.258	49.400	-1.454	0.263
RVR	C	2	1.015	108.610	90.659	-2.356	0.793
BOUQ	D	2	0.204	21.961	105.275	-0.802	-1.990
BRWN	C	2	0.069	224.302	133.558	0.974	0.998
ENGN	C	2	0.413	116.256	98.088	-2.078	1.025
RCTR	C	2	0.336	112.018	99.034	-2.128	0.861

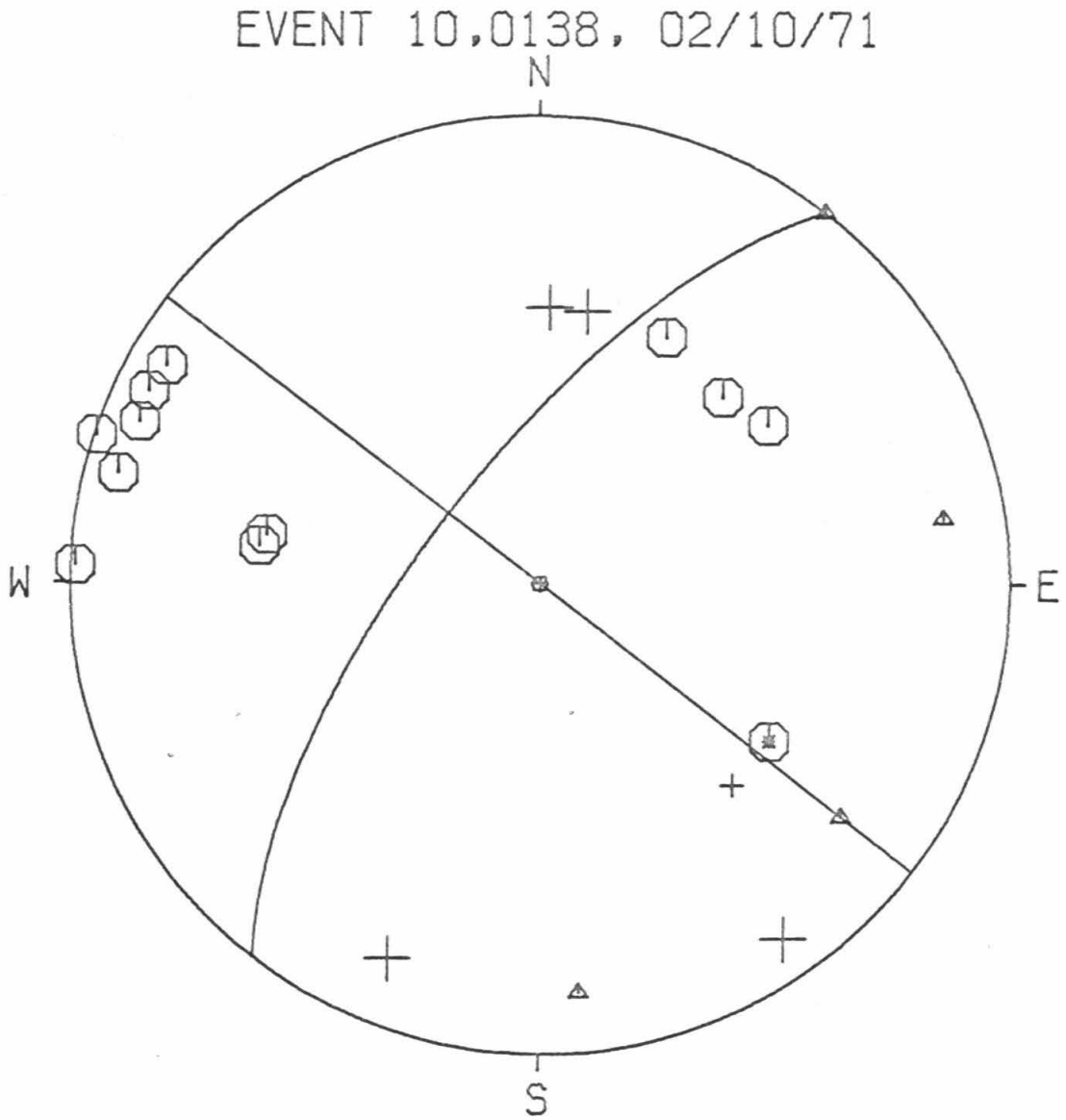
EVENT 10,0138, 02/10/71
N
W
E
S

EVENT DATA
11,0312 0 02/10/71 3 12 0.0
3.0 34.000 22.20 -118.000 18.12 4.0

AZ1= 302.500
DIP1= 46.000
AZ2= 184.000
DIP2= 63.706

SLIP VECTORS= 94.000 63.706 212.500 46.000

PRIN AXES = 142.808 36.445 246.981 79.749

STA	DIR	QUAL	DIST	EVAZ	TOA	X	Y
BAR	D	2	2.167	140.614	44.933	0.857	-1.044
CLC	C	2	1.555	21.635	44.933	0.498	1.256
CSP	C	2	0.785	95.308	83.978	2.355	-0.219
CWC	D	1	2.073	5.000	44.933	0.118	1.346
GSC	C	2	1.543	52.526	44.933	1.072	0.822
ISA	D	2	1.149	353.611	80.493	-0.254	2.270
MWC	C	2	0.250	126.197	89.106	2.002	-1.465
PAS	D	2	0.247	154.048	89.136	1.086	-2.231
PLM	D	2	1.570	129.845	44.933	1.037	-0.866
PYR	D	2	0.414	298.797	87.536	-2.143	1.178
SBC		-1	1.337	274.219	44.933	-1.347	0.099
SYP	C	2	1.394	277.069	44.933	-1.341	0.166
RVR	C	2	0.856	115.857	83.299	2.114	-1.025
USC	D	2	0.357	178.249	88.086	0.075	-2.457
BOUQ	D	2	0.181	320.698	89.937	-1.583	1.933
BRWN	C	2	0.253	251.391	89.084	-2.350	-0.791
ENGN	D	2	0.291	142.097	88.718	1.519	-1.950
RCTR	D	2	0.210	145.184	89.489	1.421	-2.043

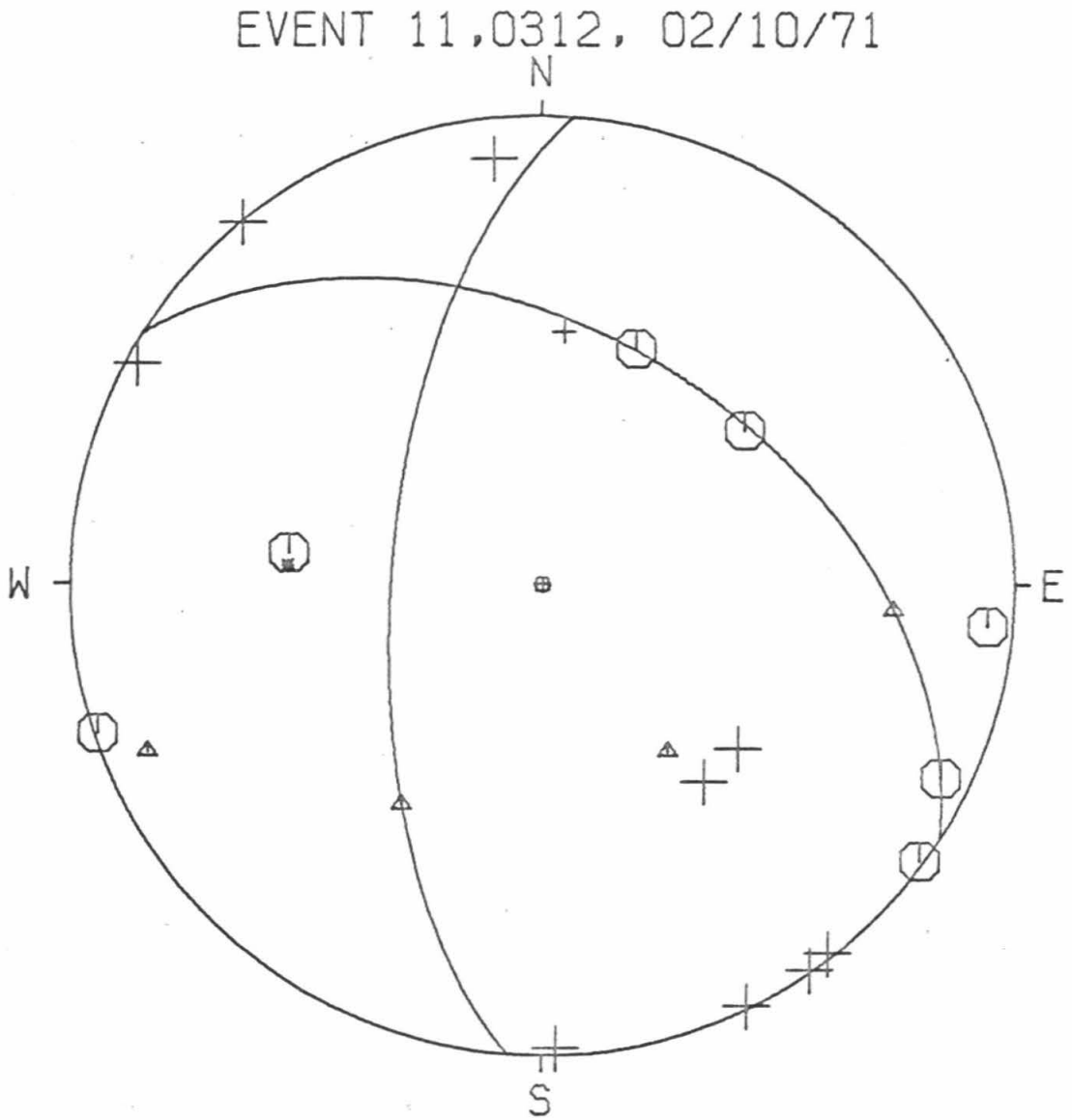
EVENT 11,0312, 02/10/71
N
W
E
S

EVENT DATA

12,0506 0 02/10/71 5 6 0.0

5.0 34.000 24.67 -118.000 19.76 4.3

STA	DIR	QUAL	DIST	EVAZ	TCA	X	Y
BAR	C	2	2.213	140.824	48.650	0.920	-1.129
CLC	D	2	1.526	22.974	48.650	0.568	1.341
CSP	D	2	0.812	98.020	86.079	2.389	-0.337
CWC	D	2	2.034	5.719	48.650	0.145	1.449
GLA	D	1	3.218	113.944	48.650	1.331	-0.591
GSC	D	2	1.537	54.231	48.650	1.182	0.851
ISA	D	2	1.106	354.427	83.064	-0.228	2.333
MWC	D	2	0.295	130.367	91.396	-1.881	1.599
PAS	C	2	0.295	153.659	91.396	-1.096	2.213
PLM	C	2	1.614	130.435	48.650	1.108	-0.945
PYR	C	2	0.376	295.138	90.563	2.252	-1.057
SBC	D	2	1.312	272.656	48.650	-1.455	0.067
SYP	D	2	1.367	275.468	48.650	-1.450	0.139
TIN	D	2	2.640	1.755	48.650	0.045	1.456
RVR	D	2	0.895	117.582	85.233	2.122	-1.108
USC	D	2	0.399	175.172	90.324	-0.210	2.484
BRWN	D	2	0.249	240.649	92.068	2.139	1.203
ENGN	C	2	0.337	143.386	90.957	-1.479	1.990
RCTR	C	2	0.257	146.295	91.800	-1.365	2.047

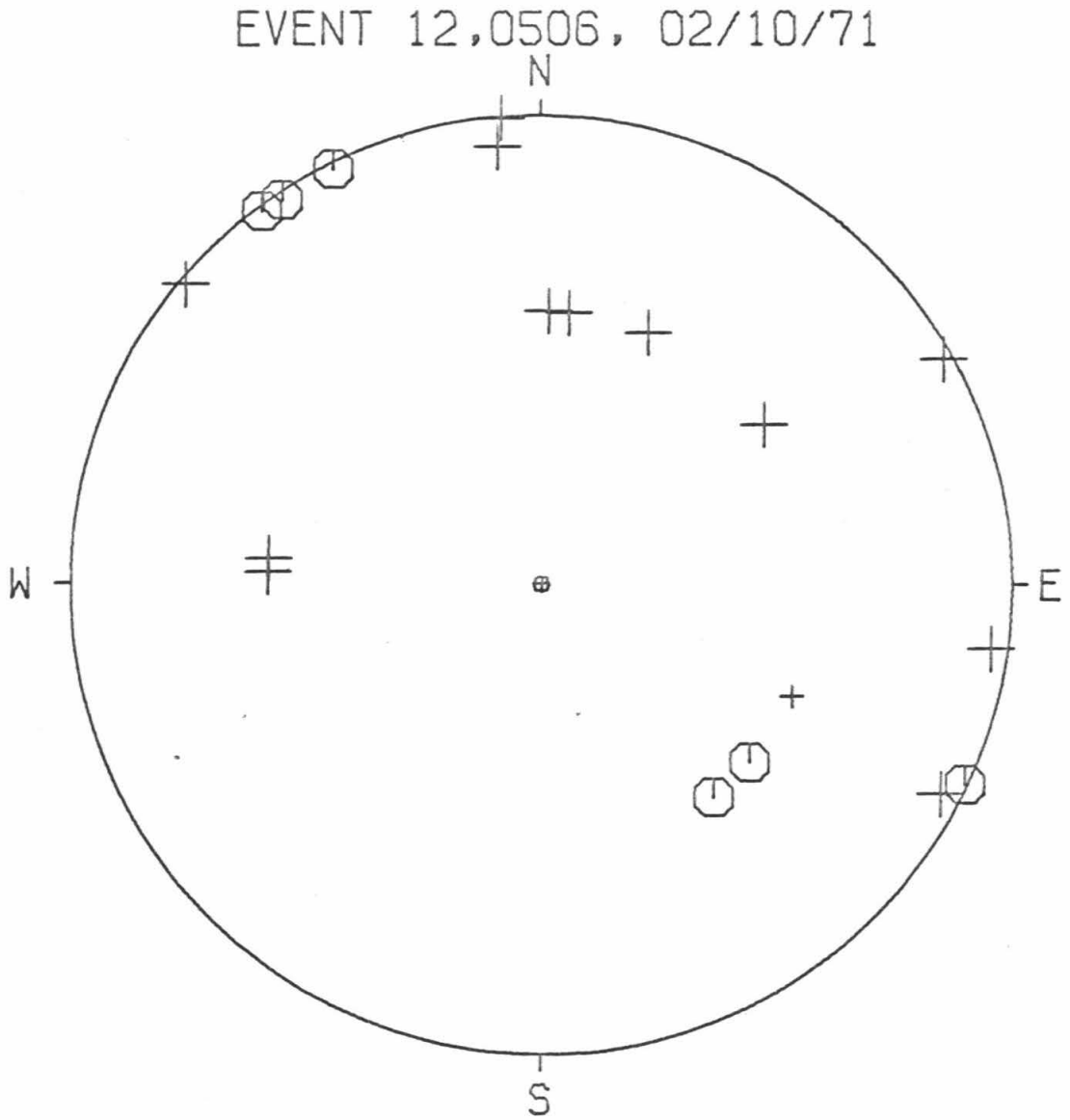
EVENT 12,0506, 02/10/71
N
W
E
S

EVENT DATA

13,0518 0 02/10/71 5 18 0.0

5.8 34.000 25.55 -118.000 24.85 4.5

STA	DIR	QUAL	DIST	EVAZ	TOA	X	Y
BAR	C	-1	2.269	139.634	48.850	0.947	-1.114
CLC	C	2	1.541	25.541	48.850	0.630	1.319
CSP	C	2	0.884	98.305	87.194	2.412	-0.352
CWC	C	-2	2.028	7.683	48.850	0.195	1.449
GLA	C	2	3.288	113.634	48.850	1.339	-0.586
GSC	C	2	1.586	56.103	48.850	1.213	0.815
ISA	D	2	1.086	357.600	85.005	-0.100	2.387
MWC	C	2	0.359	124.745	92.876	-2.002	1.389
PAS	D	2	0.343	144.059	93.051	-1.428	1.969
PLM	C	2	1.677	129.213	48.850	1.133	-0.924
PYR	D	2	0.306	298.123	93.443	2.138	-1.142
SBC	C	2	1.241	271.910	48.850	-1.461	0.049
SYP	C	2	1.296	275.085	48.850	-1.456	0.130
TIN	D	1	2.628	3.244	48.850	0.083	1.460
RVR	D	2	0.963	116.348	86.332	2.167	-1.073
USC	D	2	0.425	165.838	92.158	-0.600	2.378
BOUQ	C	1	0.088	345.436	101.562	0.562	-2.164
BRWN	C	2	0.199	227.479	89.599	-1.836	-1.684
ENGN	D	2	0.394	136.443	92.494	-1.685	1.772
RCTR	D	2	0.312	136.866	93.388	-1.658	1.770

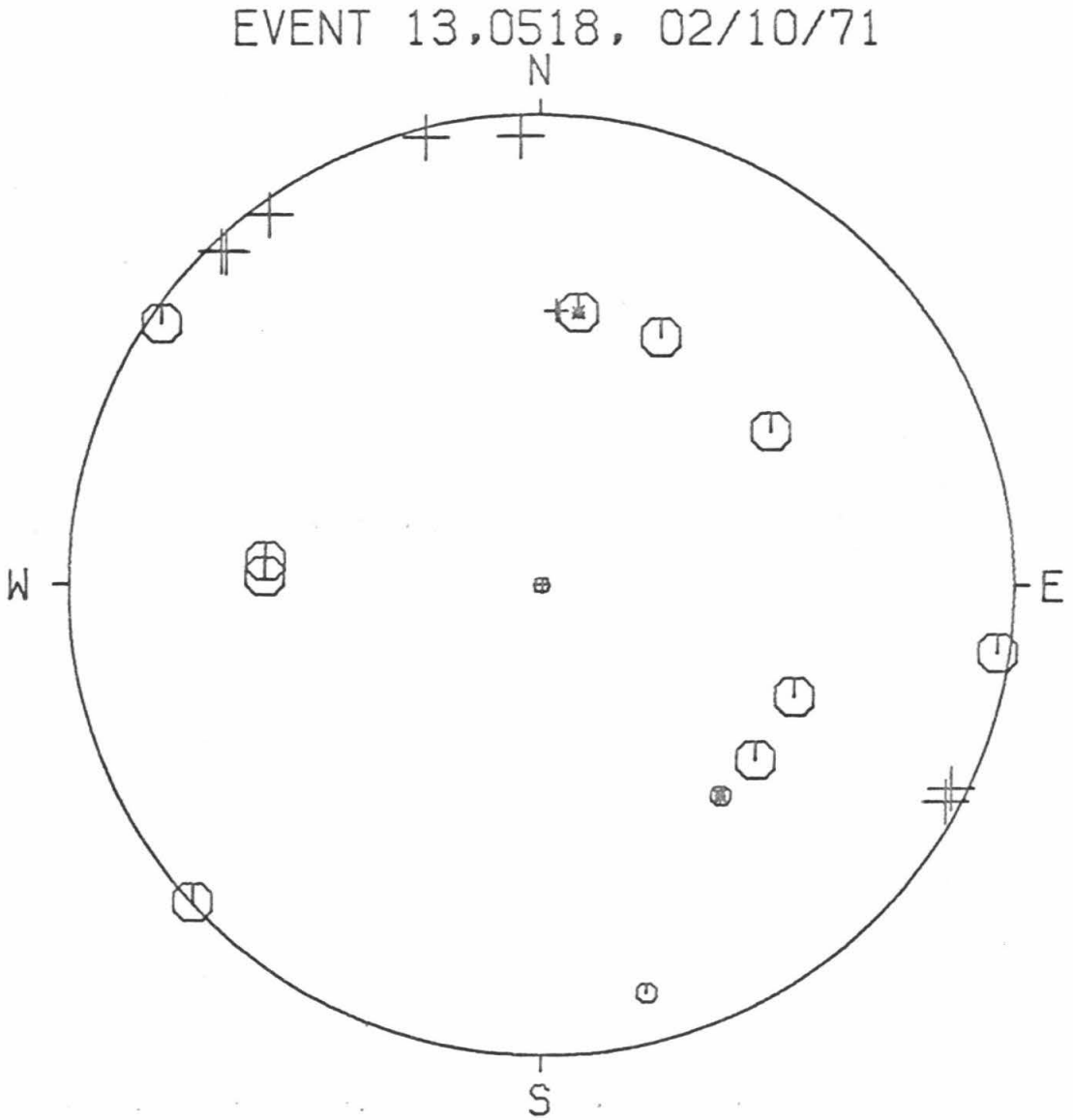
EVENT 13,0518, 02/10/71
N
W
E
S

EVENT DATA

14,0541 0 02/10/71 5 41 0.0

8.0 34.000 21.60 -118.000 17.80 3.7

AZ1= 300.500
DIP1= 66.000
AZ2= 203.000
DIP2= 73.661

SLIP VECTORS= 113.000 73.661 210.500 66.000

PRIN AXES = 160.144 60.887 252.983 84.912

STA	DIR	QUAL	DIST	EVAZ	TCA	X	Y
BAR	D	2	2.157	140.543	49.400	0.939	-1.141
CLC	C	2	1.563	21.351	49.400	0.538	1.376
CSP	C	2	0.780	94.855	93.562	-2.412	0.205
GLA	C	1	3.173	113.322	49.400	1.357	-0.585
GSC	C	2	1.546	52.126	49.400	1.166	0.907
ISA	D	2	1.159	353.469	49.400	-0.168	1.468
MWC	C	2	0.242	125.398	101.526	-1.823	1.295
PAS	D	2	0.237	154.102	102.001	-0.972	2.002
PLM	D	-2	1.560	129.672	49.400	1.137	-0.943
PYR	D	2	0.423	299.840	97.961	2.013	-1.155
SBC	C	2	1.342	274.582	49.400	-1.473	0.118
SYP	C	2	1.400	277.438	49.400	-1.465	0.191
USC	D	2	0.347	178.934	98.907	-0.043	2.298
BOUQ	D	2	0.193	321.790	106.329	1.311	-1.665
ENGN	D	2	0.281	141.723	99.714	-1.412	1.789
RCTR	D	2	0.200	144.639	105.651	-1.236	1.742

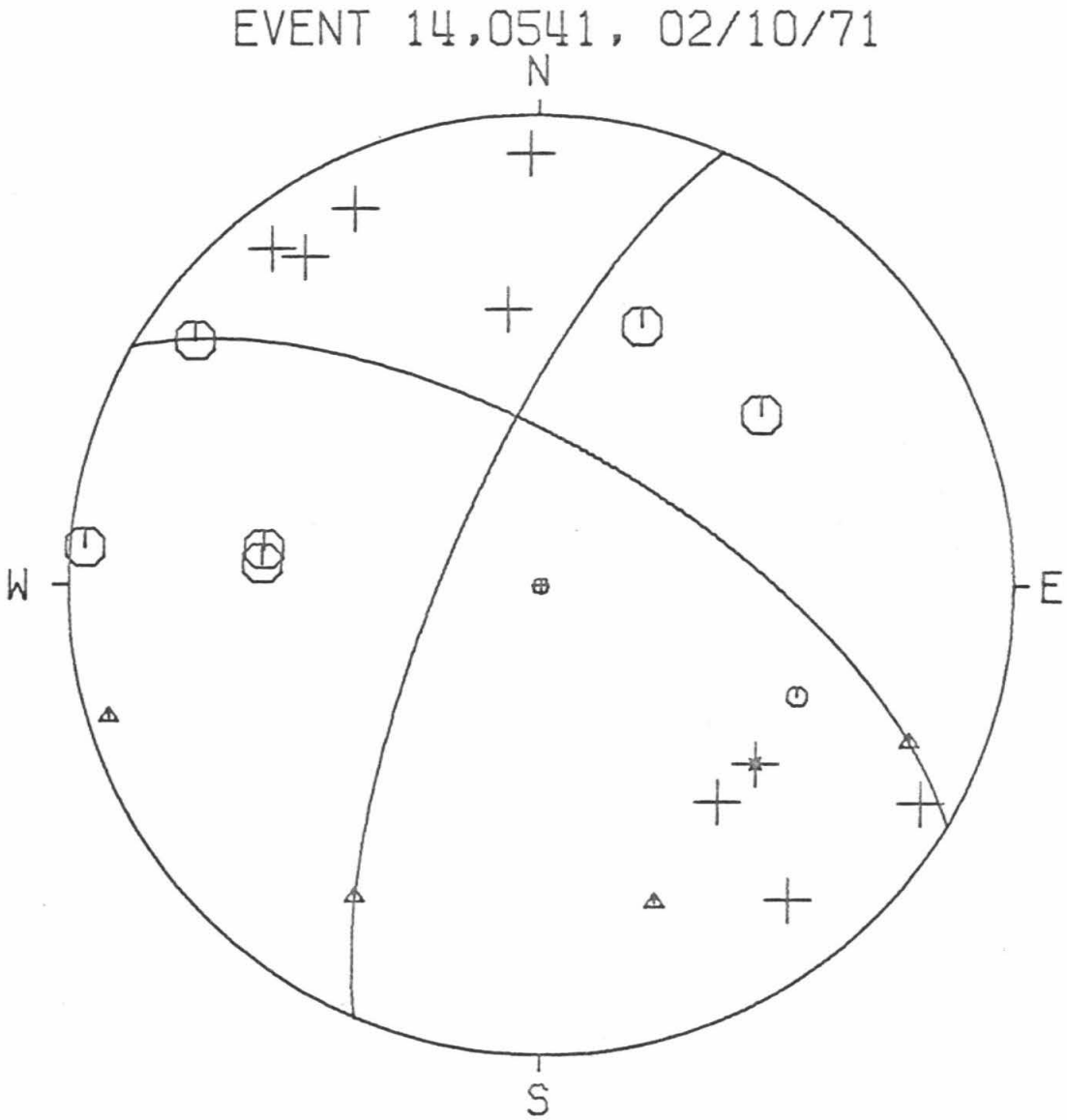
EVENT 14,0541, 02/10/71
N
W
E
S

EVENT DATA

15,0624 0 02/10/71 6 24 0.0

8.0 34.000 24.40 -118.000 19.50 3.4

AZ1= 300.000
DIP1= 45.000
AZ2= 114.000
DIP2= 45.157

SLIP VECTORS= 24.000 45.157 210.000 45.000

PRIN AXES = 298.875 3.016 206.995 89.921

STA	DIR	QUAL	DIST	EVAZ	TOA	X	Y
CLC	D	2	1.529	22.788	49.400	0.572	1.362
CSP	C	1	0.808	97.639	93.218	-2.407	0.323
GSC	D	2	1.537	54.019	49.400	1.196	0.868
ISA	C	-2	1.110	354.285	89.487	-0.248	2.476
MWC	C	2	0.289	130.053	99.621	-1.746	1.468
PAS	D	2	0.289	153.924	99.613	-1.003	2.049
PLM	C	2	1.609	130.405	49.400	1.125	-0.958
PYR	C	2	0.381	295.531	98.483	2.083	-0.995
SYP	C	2	1.371	275.649	49.400	-1.470	0.145
USC	D	2	0.395	175.640	98.315	-0.176	2.305
BOUQ	D	1	0.143	317.788	112.520	1.319	-1.454
ENGN	D	2	0.332	143.481	99.085	-1.365	1.844

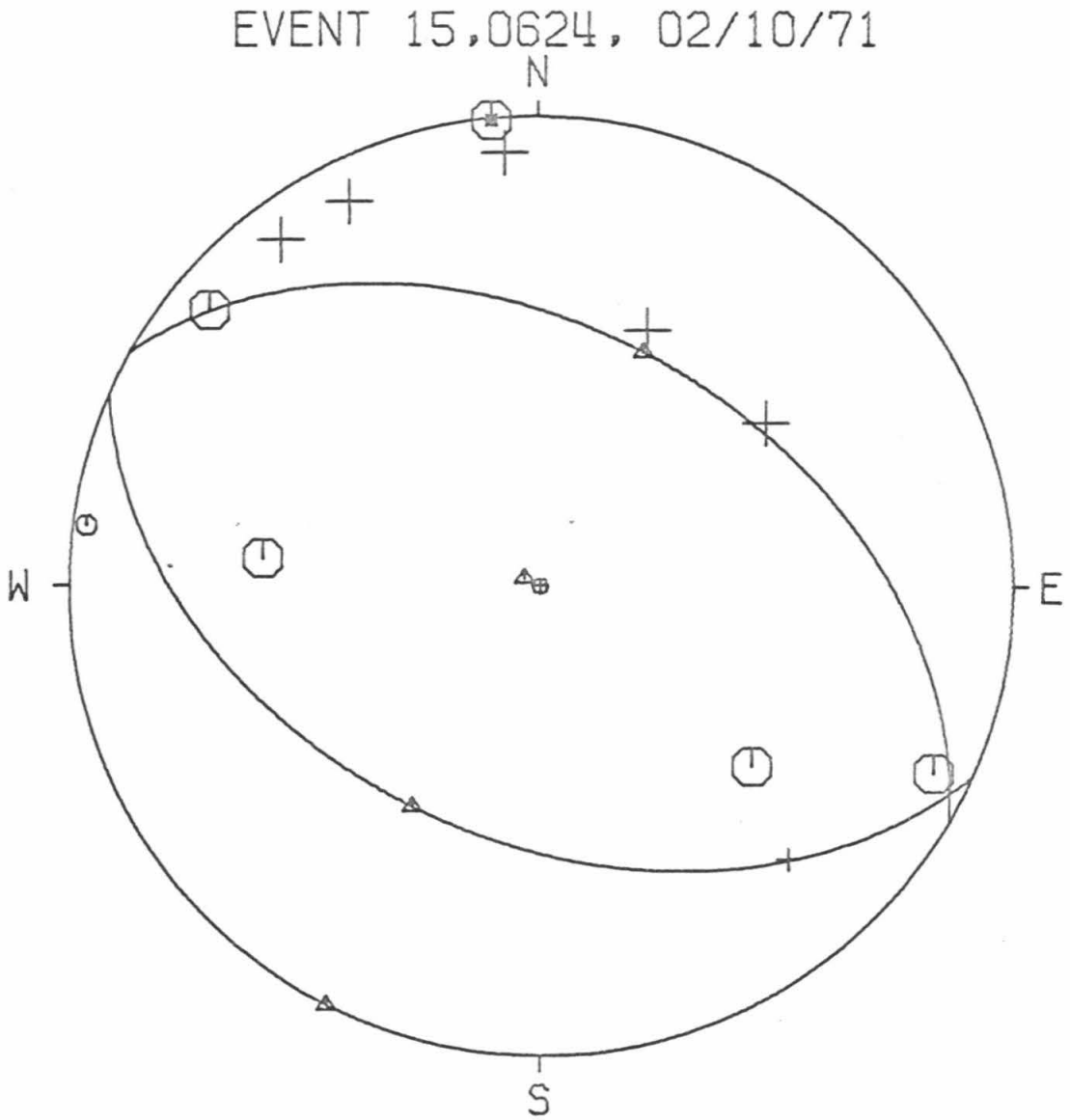
EVENT 15,0624, 02/10/71
N
W
E
S

EVENT DATA

16,0654 0 02/10/71 6 54 0.0

8.0 34.000 23.70 -118.000 27.00 3.4

STA	DIR	QUAL	DIST	EVAZ	TCA	X	Y
GSC	C	2	1.628	55.760	49.400	1.221	0.831
ISA	D	2	1.116	359.000	89.421	-0.043	2.487
MWC	C	2	0.367	117.963	98.650	-2.035	1.081
PAS	D	2	0.339	137.022	99.006	-1.565	1.680
PLM	D	1	1.681	127.748	49.400	1.168	-0.904
PYR	D	2	0.297	305.965	99.514	1.849	-1.341
SBC	D	1	1.213	273.525	49.400	-1.475	0.091
SYP	C	2	1.269	276.495	49.400	-1.468	0.167
RVR	C	2	0.977	113.934	91.131	-2.262	1.004
USC	D	1	0.404	160.657	98.200	-0.767	2.184
BOUQ	D	2	0.115	3.656	118.092	-0.116	-1.815
BRWN	C	2	0.157	228.090	109.804	1.513	1.358
ENGN	D	-2	0.395	130.222	98.315	-1.765	1.493

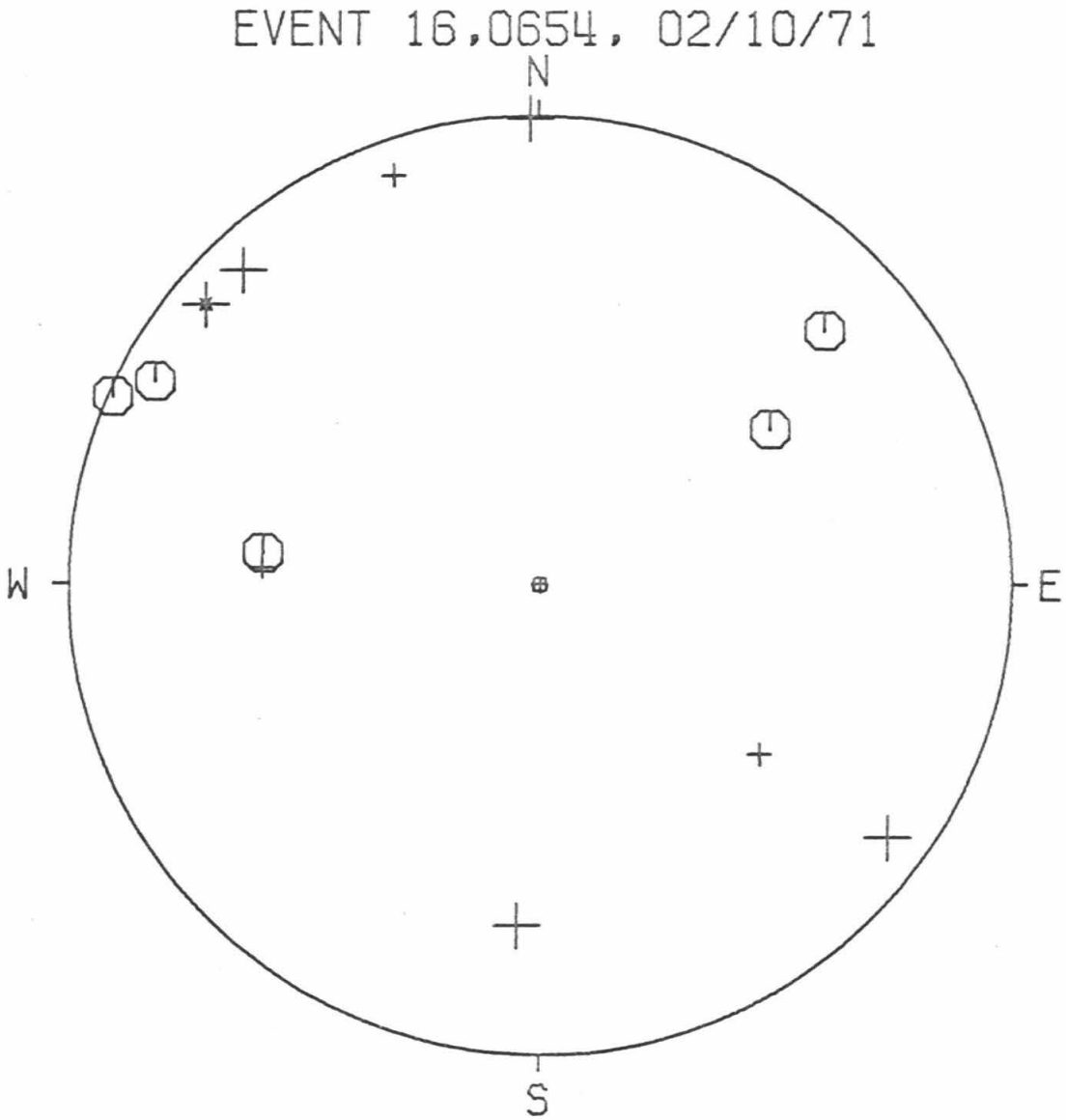
EVENT 16,0654, 02/10/71
N
W
E
S

EVENT DATA

17,0700 0 02/10/71 7 0 0.0

8.0 34.000 18.10 -118.000 18.50 3.5

AZ1= 340.000
DIP1= 73.000
AZ2= 246.000
DIP2= 77.148

SLIP VECTORS= 156.000 77.148 250.000 73.000

PRIN AXES = 202.406 68.652 293.517 87.166

STA	DIR	QUAL	DIST	EVAZ	TOA	X	Y
CSP	C	2	0.788	92.335	93.469	-2.421	0.099
GSC	D	2	1.590	50.678	49.400	1.143	0.936
ISA	C	1	1.216	354.152	49.400	-0.151	1.470
MWC	C	2	0.225	112.792	103.235	-2.024	0.850
PAS	C	2	0.193	143.999	106.329	-1.246	1.715
PLM	C	2	1.532	127.768	49.400	1.168	-0.905
PYR	C	2	0.447	306.821	97.672	1.863	-1.395
SYP	C	2	1.399	279.799	49.400	-1.456	0.251
TIN	D	1	2.748	1.335	49.400	0.034	1.477
RVR	C	2	0.833	111.502	92.904	-2.266	0.893
USC	D	2	0.289	176.801	99.621	-0.127	2.278
BOUQ	C	2	0.236	332.280	102.162	1.033	-1.966
BRWN	C	2	0.237	261.822	102.081	2.200	0.316
ENGN	C	2	0.245	131.515	101.214	-1.680	1.487

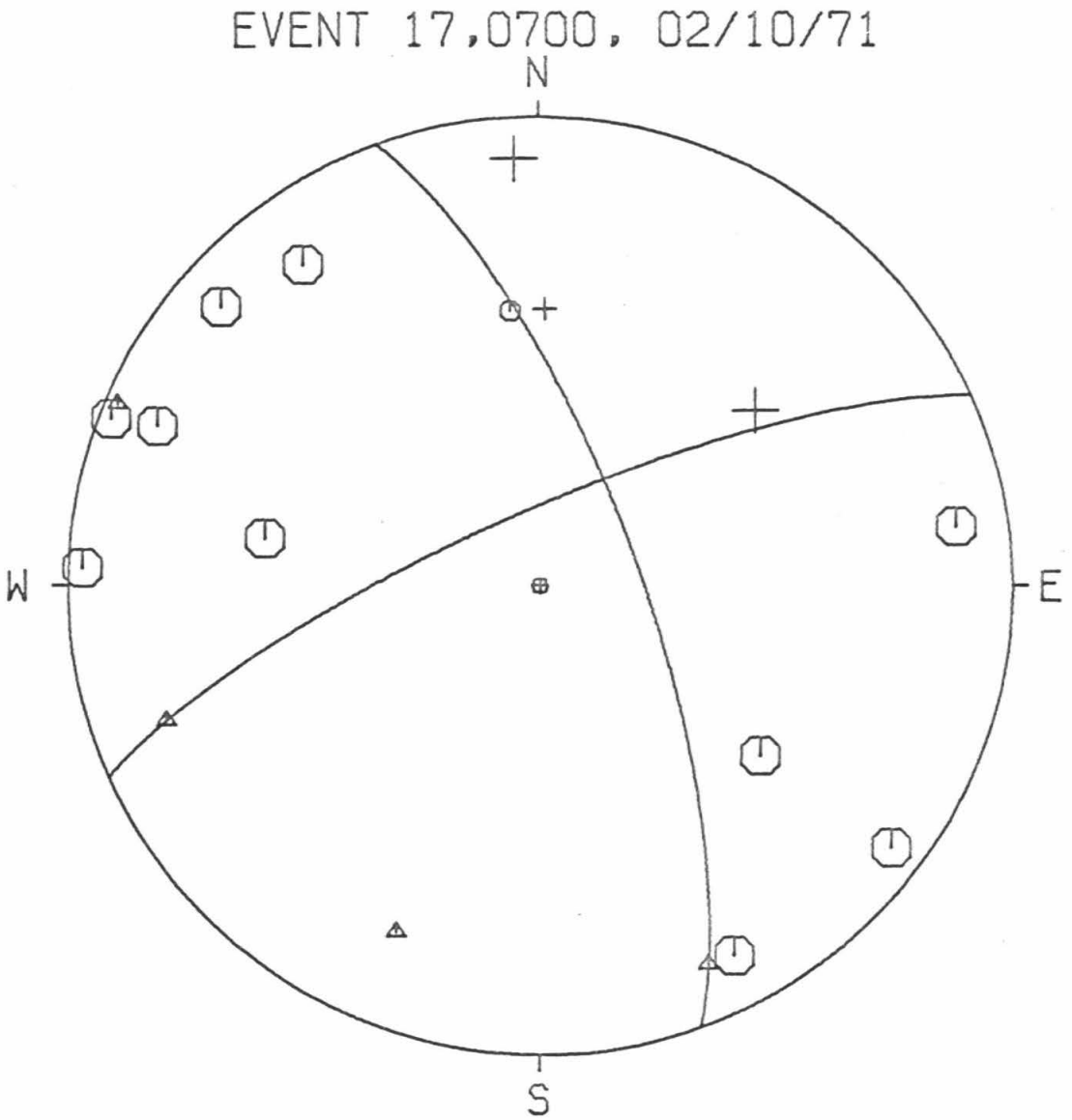
EVENT 17,0700, 02/10/71
N
W
E
S

EVENT DATA

18,0714 0 02/10/71 7 14 0.0

8.0 34.000 21.40 -118.000 26.50 3.4

AZ1= 14.000
DIP1= 58.000
AZ2= 113.000
DIP2= 75.945

SLIP VECTORS= 23.000 75.945 283.999 58.000

PRIN AXES = 337.992 56.877 240.218 78.289

STA	DIR	QUAL	DIST	EVAZ	TOA	X	Y
BAR	D	2	2.232	138.031	49.400	0.988	-1.098
CLC	D	2	1.613	25.197	49.400	0.629	1.337
CSP	C	1	0.900	94.262	92.085	-2.447	0.182
GSC	D	1	1.644	54.526	49.400	1.203	0.857
ISA	D	1	1.155	358.729	49.400	-0.033	1.477
MWC	D	2	0.346	113.370	98.914	-2.110	0.912
PAS	D	2	0.307	133.177	99.394	-1.668	1.565
PLM	C	1	1.653	126.856	49.400	1.182	-0.886
PYR	D	2	0.327	310.766	99.151	1.736	-1.497
SBC	C	2	1.222	275.250	49.400	-1.471	0.135
SYP	C	2	1.281	278.202	49.400	-1.462	0.211
TIN	D	1	2.698	3.629	49.400	0.094	1.474
RVR	D	2	0.956	112.070	91.388	-2.289	0.928
USC	D	2	0.366	159.703	98.670	-0.799	2.161
BOUQ	D	2	0.155	0.184	110.101	-0.007	-2.025
BRWN	C	2	0.144	239.218	112.241	1.693	1.009
ENGN	D	2	0.366	126.517	98.664	-1.852	1.371
RCTR	D	2	0.285	124.049	99.672	-1.889	1.277

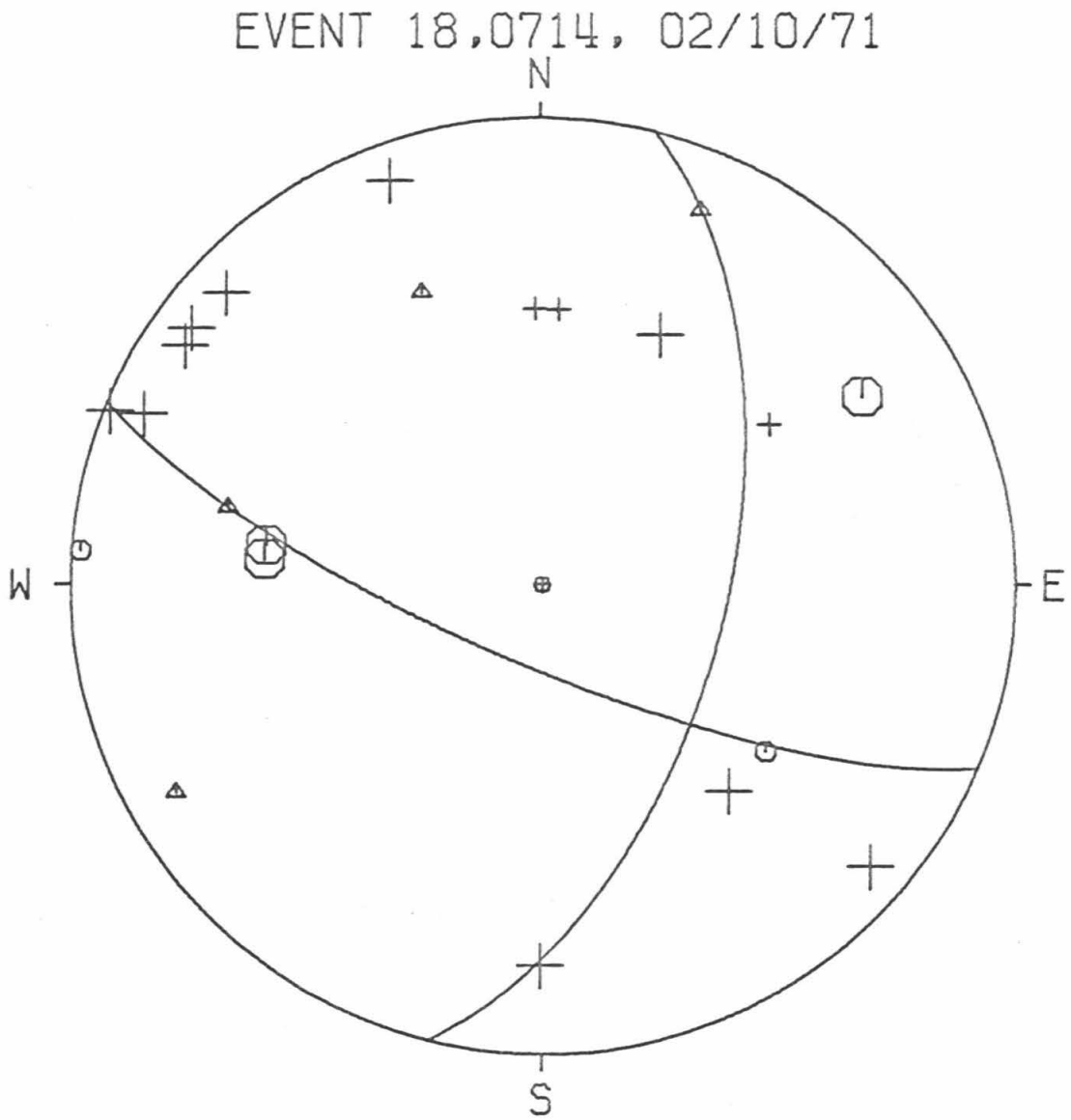
EVENT 18,0714, 02/10/71
N
W
E
S

EVENT DATA

19,0727 0 02/10/71 7 27 0.0

8.0 34.000 24.10 -118.000 26.10 3.8

STA	DIR	QUAL	DIST	EVAZ	TCA	X	Y
BAR	D	2	2.262	138.898	49.400	0.971	-1.113
CLC	C	2	1.570	25.716	49.400	0.641	1.331
CWC	C	2	2.054	8.058	49.400	0.207	1.463
GLA	C	2	3.295	113.120	49.400	1.359	-0.580
GSC	C	2	1.614	55.712	49.400	1.221	0.832
ISA	D	2	1.110	358.432	89.497	-0.068	2.488
MWC	D	2	0.360	120.008	98.737	-1.994	1.151
PAS	D	1	0.336	139.411	99.042	-1.493	1.743
PLM	C	2	1.676	128.199	49.400	1.161	-0.914
PYR	D	2	0.304	303.623	99.434	1.904	-1.266
SBC	C	2	1.225	273.244	49.400	-1.475	0.084
SYP	C	2	1.281	276.182	49.400	-1.469	0.159
RVR	D	2	0.969	114.638	91.233	-2.248	1.031
USC	D	2	0.407	162.644	98.164	-0.691	2.210
BRWN	C	2	0.172	228.542	108.305	1.552	1.371
ENGN	D	2	0.390	132.226	98.370	-1.711	1.553
RCTR	D	2	0.308	131.686	99.379	-1.708	1.521

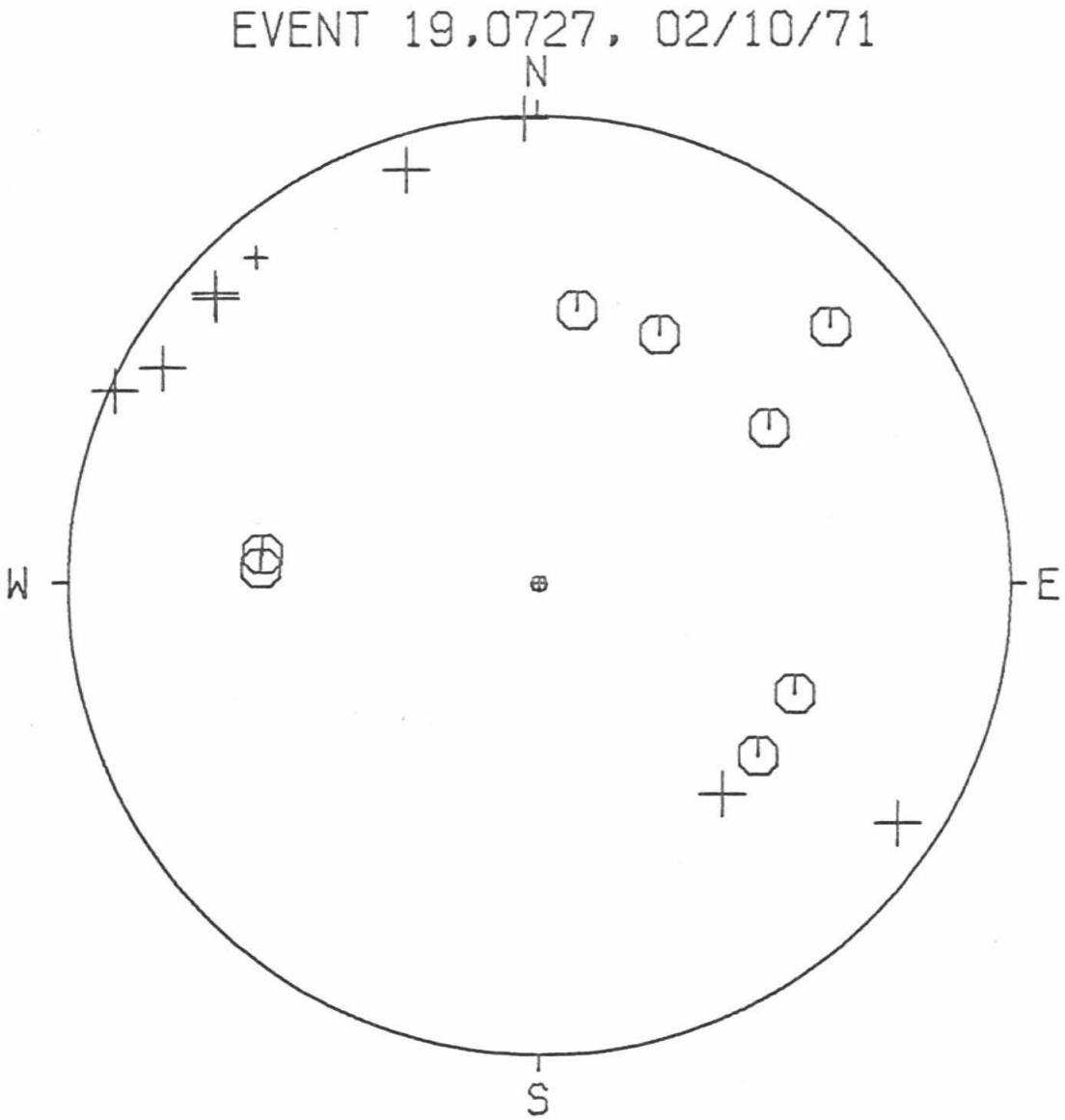
EVENT 19,0727, 02/10/71
N
W
E
S

EVENT DATA

20,0933 0 02/10/71 9 33 0.0

8.0 34.000 19.60 -118.000 15.20 3.2

AZ1= 4.000
DIP1= 74.000
AZ2= 100.000
DIP2= 69.971

SLIP VECTORS= 10.000 69.971 273.999 74.000

PRIN AXES = 321.272 64.082 52.589 87.290

STA	DIR	QUAL	DIST	EVAZ	TOA	X	Y
BAR	C	1	2.108	140.747	49.400	0.935	-1.144
CLC	D	2	1.581	19.727	49.400	0.499	1.391
CSP	D	2	0.743	93.184	94.024	-2.407	0.134
ISA	C	2	1.197	352.118	49.400	-0.203	1.463
MWC	C	2	0.195	123.964	106.133	-1.762	1.187
PAS	C	2	0.193	159.429	106.329	-0.745	1.984
PLM	C	2	1.512	129.596	49.400	1.138	-0.942
PYR	C	2	0.471	301.100	97.378	1.999	-1.206
SYP	C	1	1.440	278.545	49.400	-1.461	0.220
RVR	C	2	0.801	114.365	93.302	-2.211	1.001
USC	C	2	0.315	185.377	99.294	0.215	2.279
BOUQ	C	2	0.241	319.890	101.683	1.438	-1.707
BRWN	D	2	0.284	260.058	99.680	2.246	0.394
NRTM	D	2	0.271	1.162	99.837	-0.046	-2.276
ENGN	C	2	0.233	143.653	102.405	-1.313	1.784
RCTR	C	2	0.153	148.655	110.361	-1.050	1.724

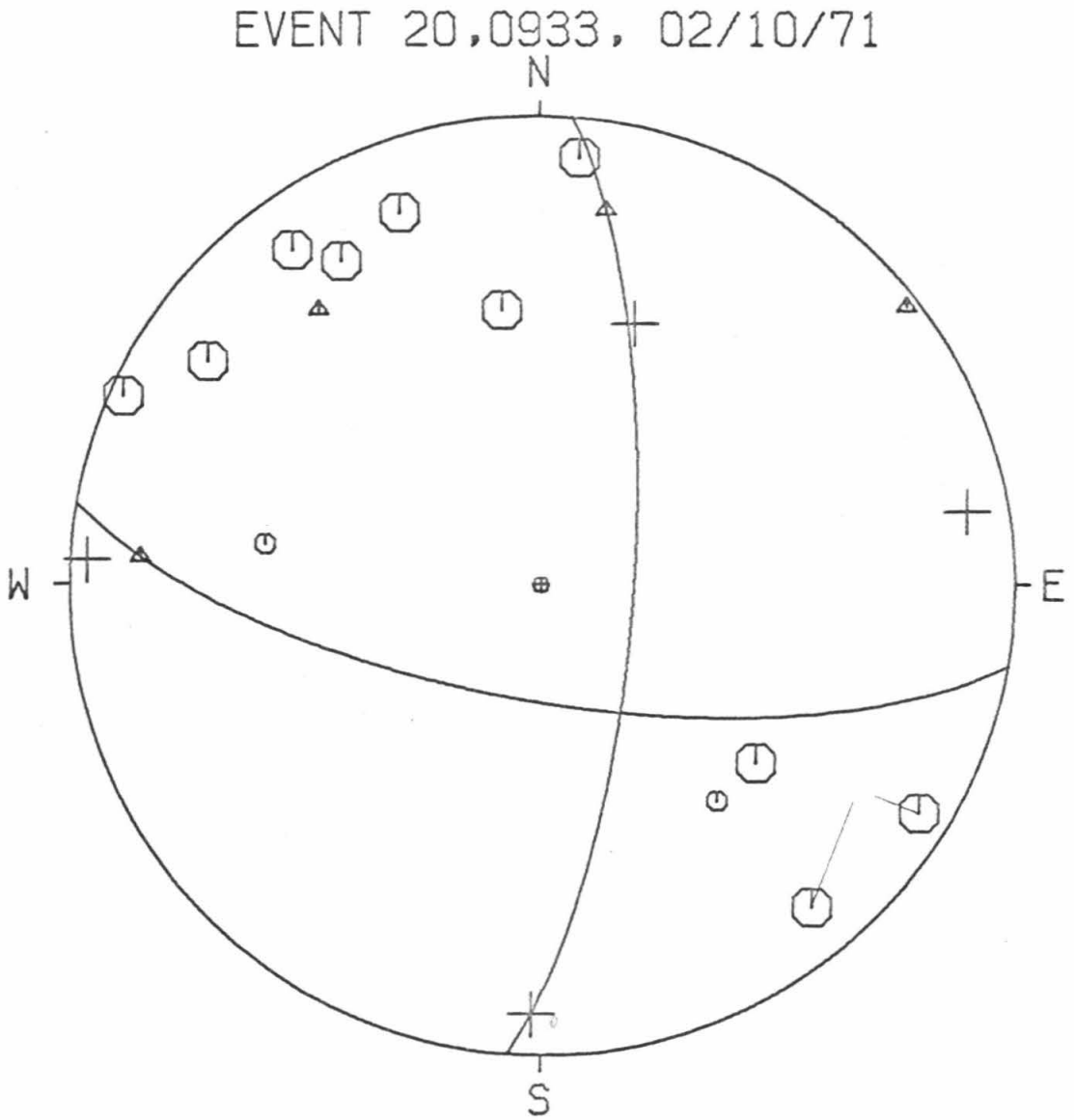
EVENT 20,0933, 02/10/71
N
W
E
S

EVENT DATA

21,1000 0 02/10/71 10 0 0.0

8.0 34.000 26.80 -118.000 27.70 3.4

AZ1= 224.000
DIP1= 34.000
AZ2= 111.500
DIP2= 75.527

SLIP VECTORS= 21.500 75.527 134.000 34.000

PRIN AXES = 55.906 40.276 177.895 65.827

STA	DIR	QUAL	DIST	EVAZ	TOA	X	Y
BAR	D	1	2.311	139.202	49.400	0.965	-1.118
CLC	C	2	1.540	27.166	49.400	0.675	1.314
CSP	C	2	0.925	99.022	91.770	-2.431	0.386
GSC	C	2	1.608	57.467	49.400	1.246	0.795
ISA	D	2	1.064	359.414	90.058	0.026	-2.499
MWC	D	2	0.403	123.864	98.218	-1.922	1.290
PAS	D	2	0.383	141.104	98.457	-1.450	1.797
PLM	D	2	1.721	128.898	49.400	1.150	-0.928
PYR	D	2	0.262	298.310	99.945	2.002	-1.078
SBC	D	2	1.202	271.036	49.400	-1.477	0.027
SYP	D	2	1.255	274.305	49.400	-1.473	0.111
RVR	D	2	1.008	116.371	90.754	-2.225	1.103
USC	D	2	0.456	161.649	97.560	-0.733	2.211
BOUQ	D	2	0.069	14.374	133.558	-0.346	-1.350
BRWN	C	2	0.188	214.824	106.828	1.203	1.730
NRTM	D	2	0.234	49.270	102.323	-1.680	-1.447
ENGN	D	2	0.437	134.564	97.798	-1.656	1.631
SWM	D	2	0.289	339.693	99.621	0.792	-2.140
RCTR	D	2	0.353	134.410	98.824	-1.643	1.610

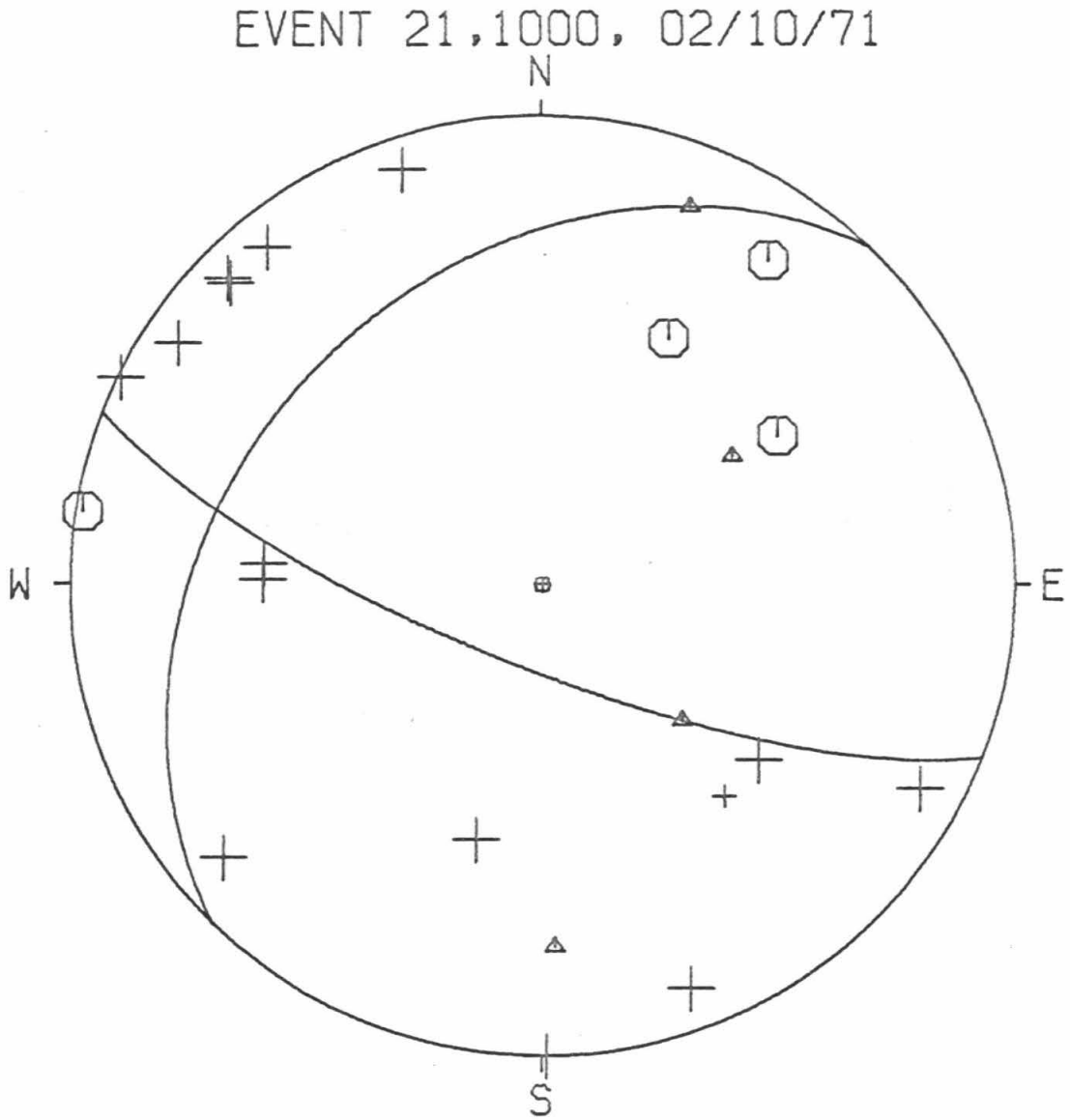
EVENT 21,1000, 02/10/71
N
W
E
S

EVENT DATA

22,1129 0 02/10/71 11 29 0.0

8.0 34.000 27.20 -118.000 25.60 3.2

AZ1= 211.500
DIP1= 58.000
AZ2= 108.000
DIP2= 69.515

SLIP VECTORS= 18.000 69.515 121.500 58.000

PRIN AXES = 66.140 51.526 161.994 82.689

STA	DIR	QUAL	DIST	EVAZ	TCA	X	Y
CLC	D	1	1.521	26.327	49.400	0.655	1.324
CSP	C	2	0.898	99.830	92.106	-2.418	0.419
CWC	D	2	2.002	8.074	49.400	0.208	1.463
GSC	C	2	1.580	57.122	49.400	1.241	0.802
ISA	D	2	1.058	358.036	90.129	0.086	-2.496
MWC	D	2	0.383	127.081	98.464	-1.842	1.392
PAS	D	2	0.372	145.318	98.598	-1.312	1.896
PLM	D	-2	1.703	129.708	49.400	1.137	-0.944
PYR	D	2	0.286	294.636	99.655	2.073	-0.951
SBC	C	2	1.231	268.235	49.400	-1.477	-0.046
SYP	D	2	1.284	273.912	49.400	-1.474	0.101
RVR	D	2	0.985	117.531	91.030	-2.197	1.145
USC	D	2	0.454	165.406	97.581	-0.587	2.254
BOUQ	D	2	0.063	349.021	136.401	0.250	-1.289
BRWN		-1	0.213	219.725	104.363	1.385	1.667
NRTM	D	2	0.208	45.432	104.814	-1.537	-1.514
ENGN	D	2	0.422	138.067	97.978	-1.550	1.726
SWM	D	2	0.295	334.034	99.547	1.000	-2.053
NSCF	D	2	0.119	105.631	117.409	-1.769	0.495
RCTR	D	2	0.339	138.813	98.999	-1.512	1.728

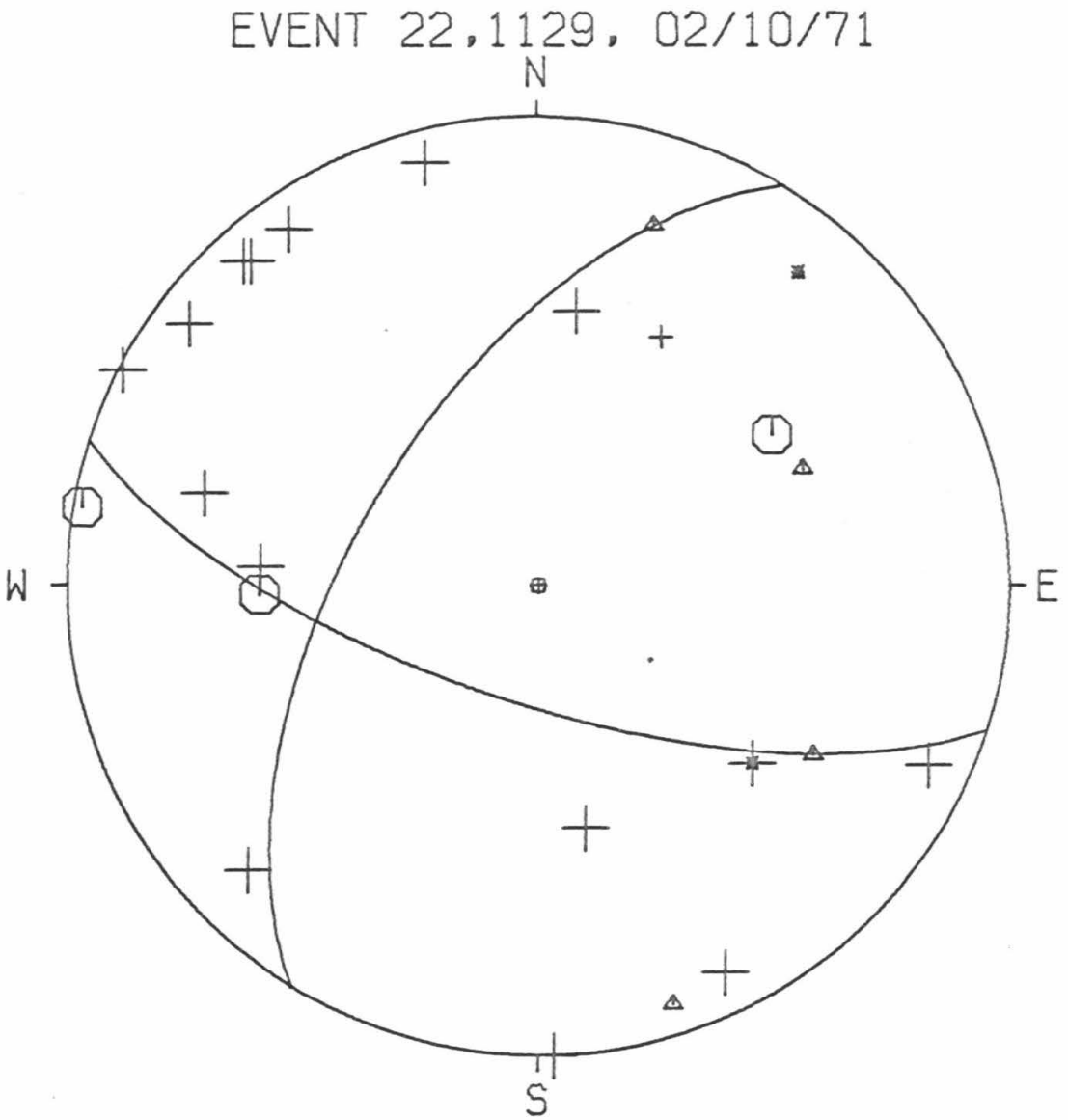
EVENT 22,1129, 02/10/71
N
W
E
S

EVENT DATA

23,1131 0 02/10/71 11 31 0.0

6.0 34.000 23.06 -118.000 27.30 4.2

AZ1= 120.000
DIP1= 60.000
AZ2= 214.000
DIP2= 83.110

SLIP VECTORS= 124.000 83.110 30.000 60.000

PRIN AXES = 81.178 64.000 343.361 74.411

STA	DIR	QUAL	DIST	EVAZ	TOA	X	Y
BAR	C	2	2.260	138.282	48.900	0.974	-1.092
CLC	C	2	1.593	25.971	48.900	0.641	1.316
CSP	C	2	0.913	95.493	87.342	2.430	-0.234
CWC	D	2	2.073	8.433	48.900	0.215	1.448
GSC	C	2	1.637	55.536	48.900	1.207	0.828
ISA	D	2	1.126	359.196	84.997	-0.034	2.388
MWC	D	2	0.366	116.209	93.328	-2.177	1.072
PAS	D	2	0.333	135.175	93.690	-1.705	1.715
PLM	C	2	1.678	127.363	48.900	1.163	-0.888
PYR	C	2	0.300	307.956	94.055	1.900	-1.482
SBC	D	2	1.209	273.722	48.900	-1.460	0.095
SYP	D	2	1.267	277.029	48.900	-1.452	0.179
RVR	C	2	0.977	113.268	86.638	2.228	-0.958
USC	D	2	0.395	159.563	93.013	-0.850	2.280
BOUQ	D	2	0.127	5.212	94.739	-0.218	-2.385
BRWN	C	2	0.148	229.572	91.400	1.880	1.601
NRTM	C	2	0.274	38.831	94.339	-1.507	-1.872
ENGN	D	2	0.391	128.555	93.062	-1.902	1.516
SWM	D	2	0.349	342.394	93.514	0.733	-2.309
RCTR	D	2	0.308	126.817	93.964	-1.931	1.445

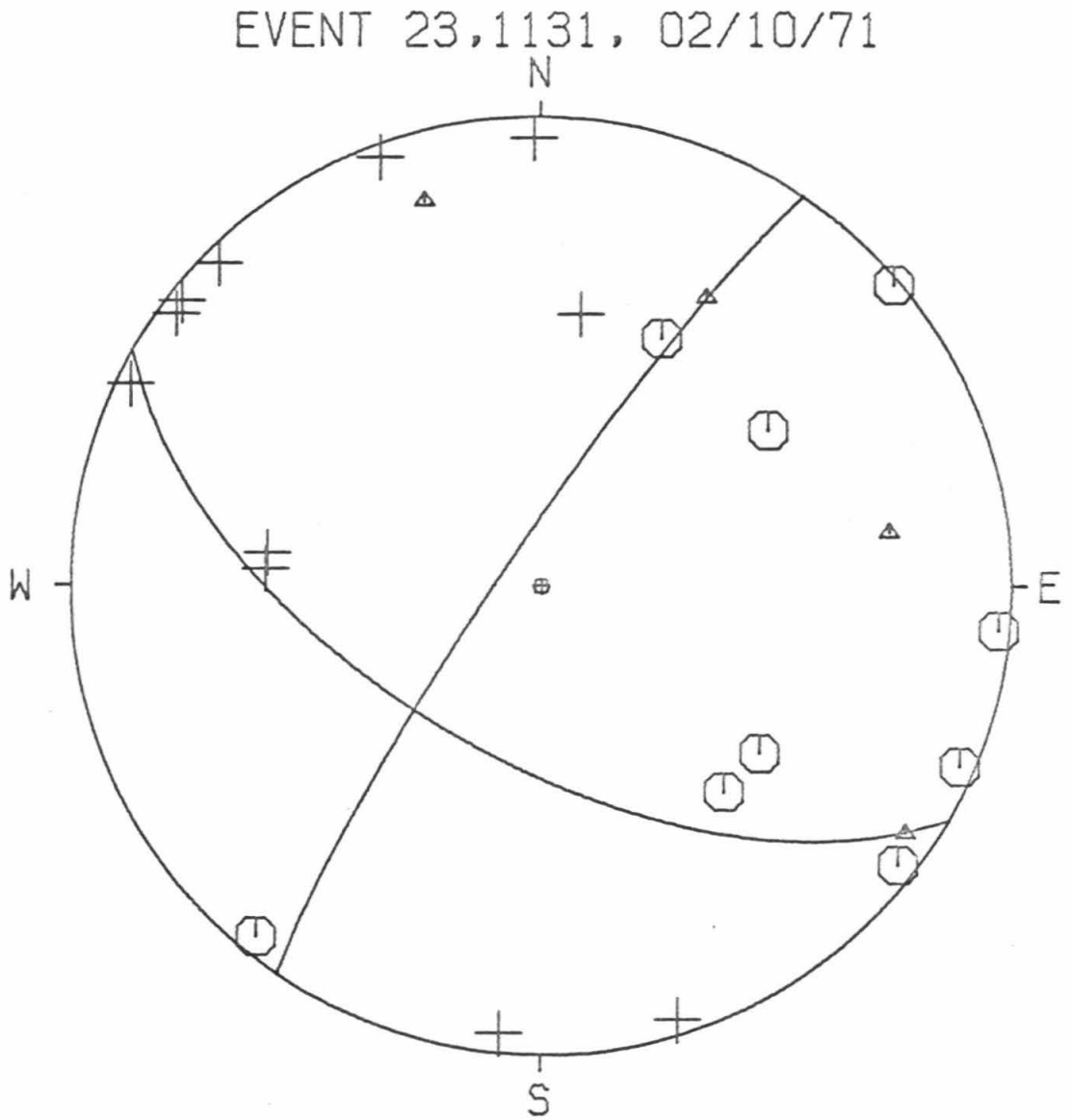
EVENT 23,1131, 02/10/71
N
W
E
S

EVENT DATA
24,1145 0 02/10/71 11 45 0.0
8.0 34.000 23.40 -118.000 28.50 3.5

AZ1= 219.500
DIP1= 66.000
AZ2= 129.500
DIP2= 90.000

SLIP VECTORS= 39.500 90.000 129.500 66.000

PRIN AXES = 81.909 73.286 177.087 73.285

STA	DIR	QUAL	DIST	EVAZ	TCA	X	Y
BAR	D	1	2.276	138.056	49.400	0.987	-1.099
CLC	C	2	1.595	26.583	49.400	0.661	1.321
CSP	C	2	0.930	95.721	91.718	-2.450	0.245
CWC	D	2	2.070	8.896	49.400	0.228	1.460
GSC	C	2	1.648	56.006	49.400	1.225	0.826
ISA	D	2	1.121	359.938	89.359	-0.003	2.486
MWC	C	2	0.384	115.984	98.445	-2.076	1.012
PAS	D	-2	0.350	134.038	98.866	-1.653	1.598
PLM	D	2	1.695	127.170	49.400	1.177	-0.893
PYR	D	2	0.285	309.363	99.672	1.763	-1.446
SBC	C	1	1.192	273.639	49.400	-1.474	0.094
SYP	C	2	1.250	276.851	49.400	-1.467	0.176
RVR	C	2	0.994	113.212	90.918	-2.279	0.977
USC	D	2	0.407	157.669	98.164	-0.880	2.142
BOUQ	D	2	0.125	12.942	116.099	-0.419	-1.823
BRWN	C	2	0.140	223.412	113.085	1.340	1.416
NRTM	D	2	0.281	42.066	99.714	-1.527	-1.692
ENGN		-1	0.408	127.834	98.152	-1.829	1.421
SWM	D	2	0.339	344.750	98.999	0.604	-2.215
RCTR		-1	0.326	126.149	99.158	-1.851	1.352

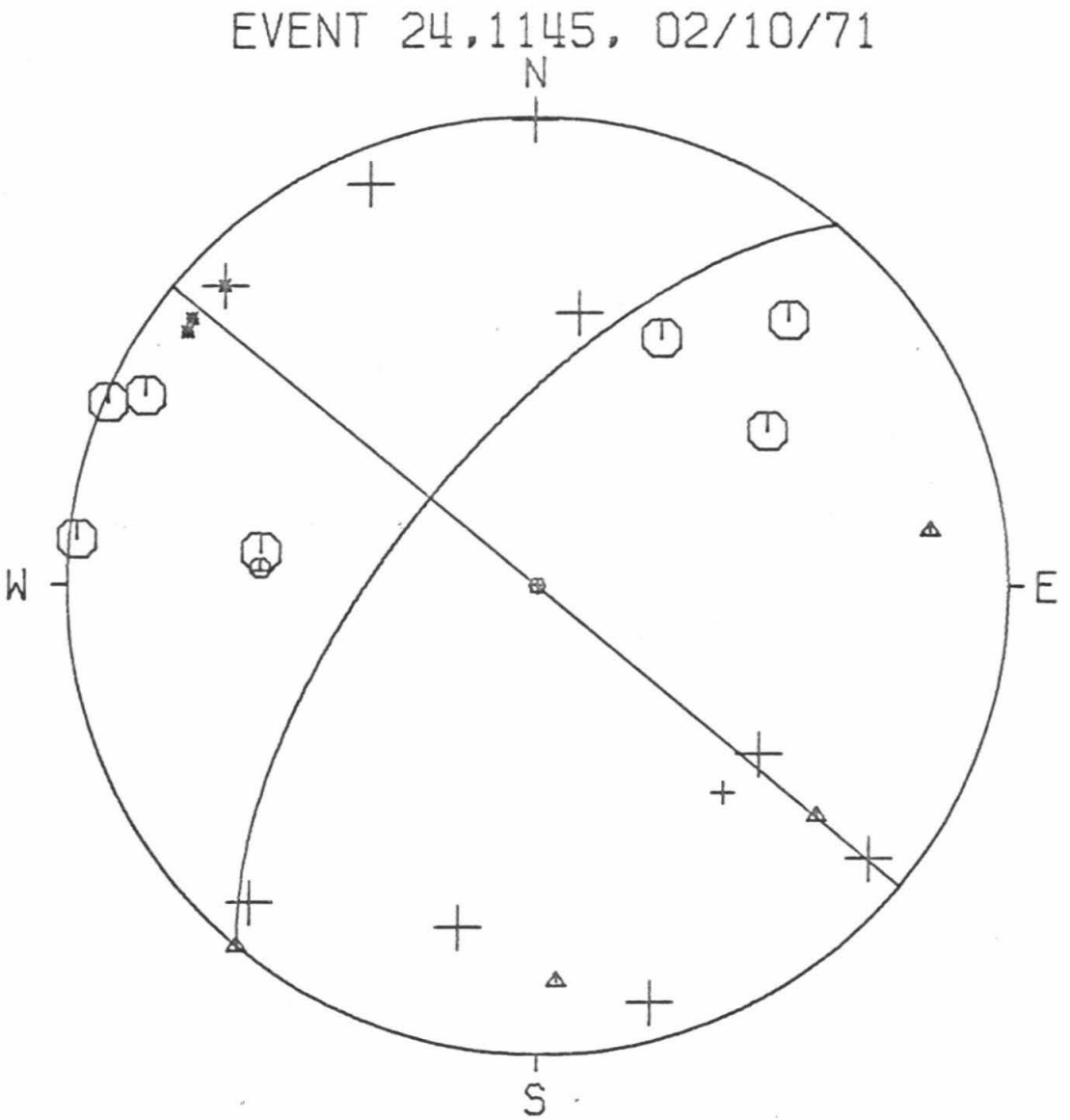
EVENT 24,1145, 02/10/71
N
W
E
S

EVENT DATA

25,1242 0 02/10/71 12 42 0.0

8.0 34.000 20.70 -118.000 16.90 3.4

AZ1= 165.000
DIP1= 45.000
AZ2= 345.000
DIP2= 45.000

SLIP VECTORS= 255.000 45.000 75.000 45.000

PRIN AXES = 0.000 0.256 254.998 90.000

STA	DIR	QUAL	DIST	EVAZ	TOA	X	Y
CLC	C	2	1.572	20.739	49.400	0.523	1.382
CSP	D	2	0.767	94.179	93.724	-2.411	0.176
GSC	C	2	1.545	51.422	49.400	1.155	0.921
ISA	D	-2	1.176	353.012	49.400	-0.180	1.466
MWC	D	2	0.225	124.535	103.235	-1.808	1.245
PAS	C	2	0.219	155.311	103.835	-0.911	1.981
PLM	C	2	1.542	129.554	49.400	1.139	-0.941
PYR		-1	0.441	300.701	97.738	2.000	-1.187
SBC		-1	1.355	275.239	49.400	-1.471	0.135
RVR	D	2	0.830	114.807	92.947	-2.210	1.022
USC	D	2	0.332	181.033	99.085	0.041	2.294
BOUQ	D	2	0.211	321.450	104.542	1.348	-1.692
BRWN	D	2	0.264	256.088	99.927	2.208	0.547
NRTM	D	2	0.255	6.509	100.303	-0.257	-2.251
ENGN	C	2	0.262	141.824	99.954	-1.405	1.787
NSCF	C	2	0.097	356.740	123.029	0.096	-1.683
NSGM	D	2	0.122	296.783	116.746	1.655	-0.835
RCTR	C	2	0.180	145.061	107.551	-1.197	1.713

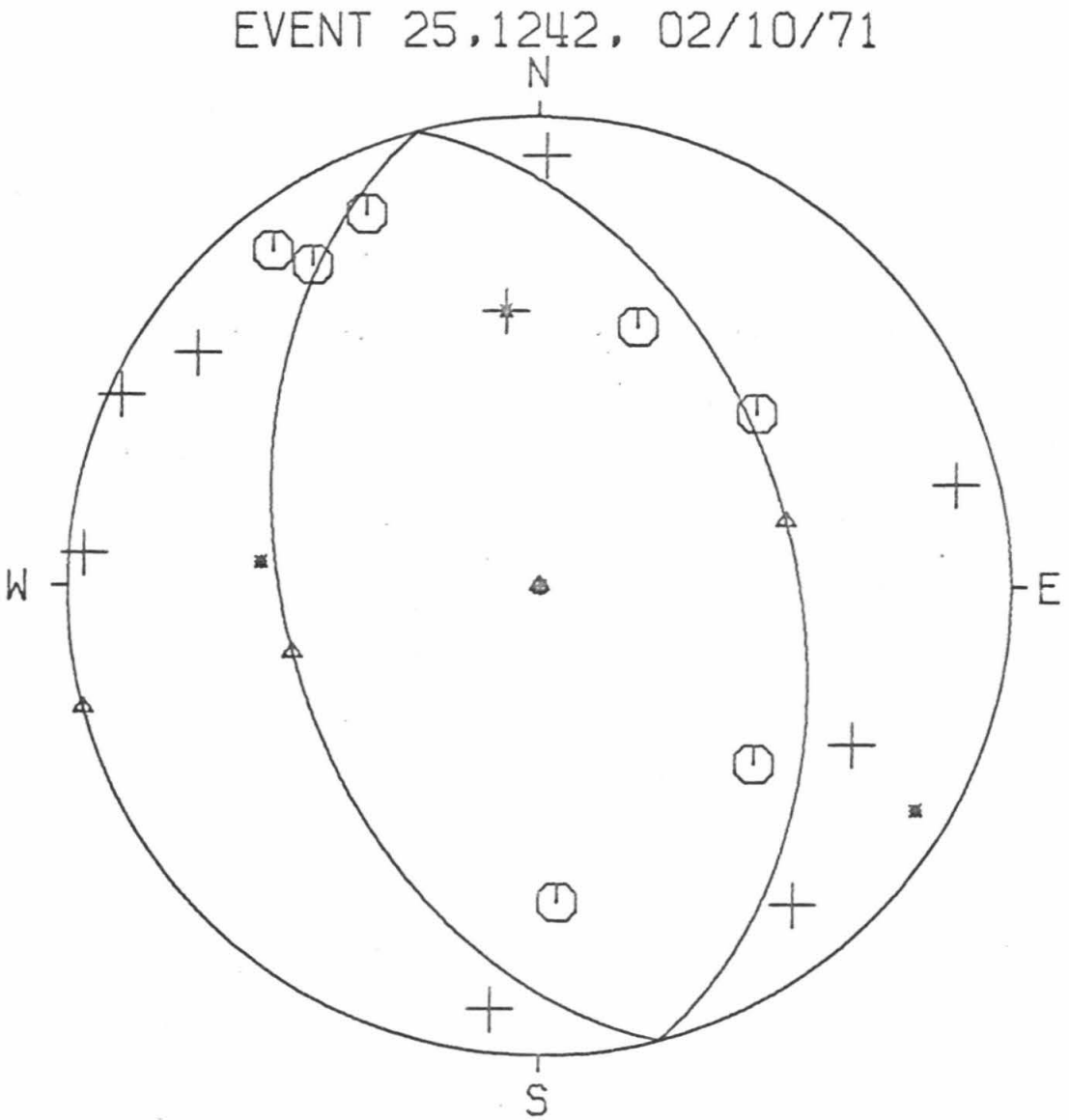
EVENT 25,1242, 02/10/71
N
W
E
S

EVENT DATA

26,1349 0 02/10/71 13 49 0.0

9.7 34.000 23.94 -118.000 25.12 4.3

AZ1= 100.000
DIP1= 50.000
AZ2= 301.500
DIP2= 42.046

SLIP VECTORS= 211.500 42.046 10.000 50.000

PRIN AXES = 310.227 11.589 200.020 85.952

STA	DIR	QUAL	DIST	EVAZ	TOA	X	Y
BAR	C	2	2.252	139.123	49.400	0.967	-1.117
CLC	D	2	1.567	25.240	49.400	0.630	1.336
CSP	C	2	0.884	96.530	93.166	-2.414	0.276
CWC	C	2	2.055	7.684	49.400	0.198	1.464
GSC	C	2	1.604	55.376	49.400	1.216	0.839
ISA	D	2	1.113	357.822	89.460	-0.095	2.486
MWC	C	2	0.347	120.518	101.505	-1.927	1.136
PAS	C	-2	0.324	140.843	102.148	-1.403	1.723
PLM	C	2	1.663	128.416	49.400	1.158	-0.918
SBC	D	1	1.239	273.140	49.400	-1.475	0.081
SYP	C	2	1.295	276.226	49.400	-1.469	0.160
RVR	C	2	0.955	114.809	92.273	-2.224	1.028
USC	D	2	0.400	164.369	99.955	-0.613	2.190
BOUQ	D	2	0.114	350.630	124.023	0.270	-1.637
BRWN	D	2	0.180	232.391	112.165	1.563	1.204
NRTM	D	2	0.245	35.444	105.264	-1.244	-1.748
ENGN	C	-2	0.377	133.147	100.612	-1.648	1.544
SWM	D	2	0.346	336.926	101.521	0.877	-2.058
NSCF	D	1	0.119	65.157	122.799	-1.536	-0.711
NSGM	C	1	0.034	172.573	156.917	-0.091	0.701
RCTR	D	1	0.295	132.799	102.990	-1.615	1.496

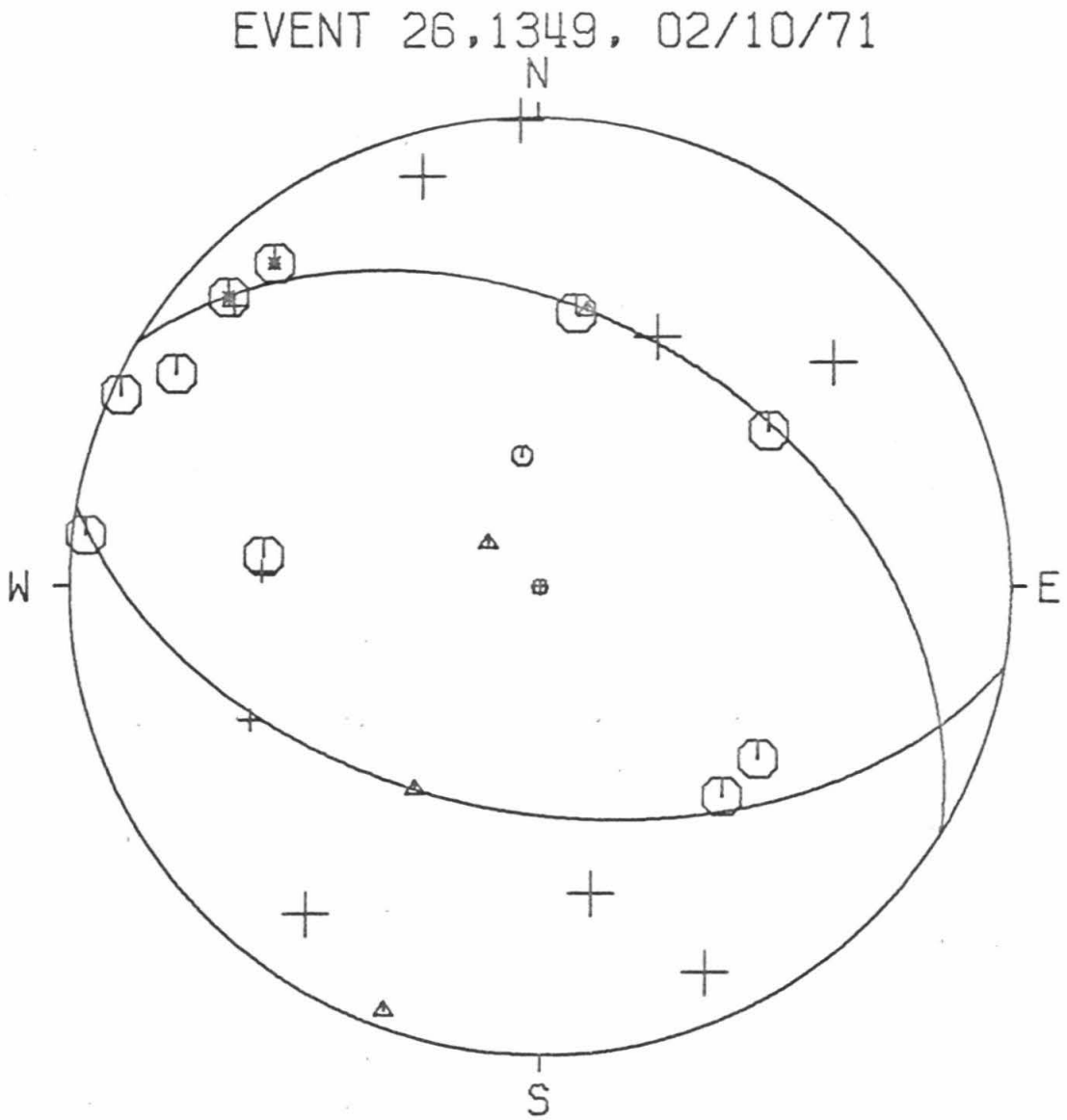
EVENT 26,1349, 02/10/71
N
W
E
S

EVENT DATA
27,1435 0 02/10/71 14 35 0.0
4.4 34.000 21.69 -118.000 29.20 4.2

AZ1= 48.500
DIP1= 80.000
AZ2= 317.500
DIP2= 84.349

SLIP VECTORS= 227.500 84.349 318.499 80.000

PRIN AXES = 272.707 78.906 3.293 86.953

STA	DIR	QUAL	DIST	EVAZ	TOA	X	Y
BAR	D	2	2.261	137.384	48.500	0.983	-1.069
CLC	D	2	1.625	26.433	48.500	0.646	1.300
CSP	C	2	0.937	93.861	83.435	2.347	-0.158
CWC	D	2	2.100	9.030	48.500	0.228	1.434
GSC	D	2	1.672	55.379	48.500	1.195	0.825
ISA	D	2	1.149	0.365	81.340	0.015	2.304
MWC	C	2	0.381	111.335	88.915	2.307	-0.901
PAS	C	2	0.337	129.271	89.345	1.924	-1.573
PLM	C	2	1.686	126.201	48.500	1.172	-0.858
PYR	D	2	0.295	314.571	89.759	-1.777	1.751
SBC	C	2	1.185	275.097	80.146	-2.267	0.202
SYP	C	2	1.244	278.202	48.500	-1.437	0.207
RVR	C	2	0.992	111.440	82.887	2.178	-0.855
USC	D	2	0.385	154.718	88.880	1.057	-2.238
BOUQ	D	2	0.153	14.217	90.589	-0.611	-2.411
BRWN	C	2	0.114	229.565	96.775	1.787	1.523
NRTM	D	2	0.309	39.842	89.625	1.596	1.913
ENGN	C	2	0.399	123.667	88.742	2.058	-1.371
SWM	D	2	0.364	347.372	89.081	-0.542	2.420
NSCF	C	2	0.183	63.299	89.746	2.228	1.121
NSGM	C	2	0.071	58.239	107.474	-1.778	-1.101
RCTR	C	2	0.318	120.930	89.533	2.136	-1.280

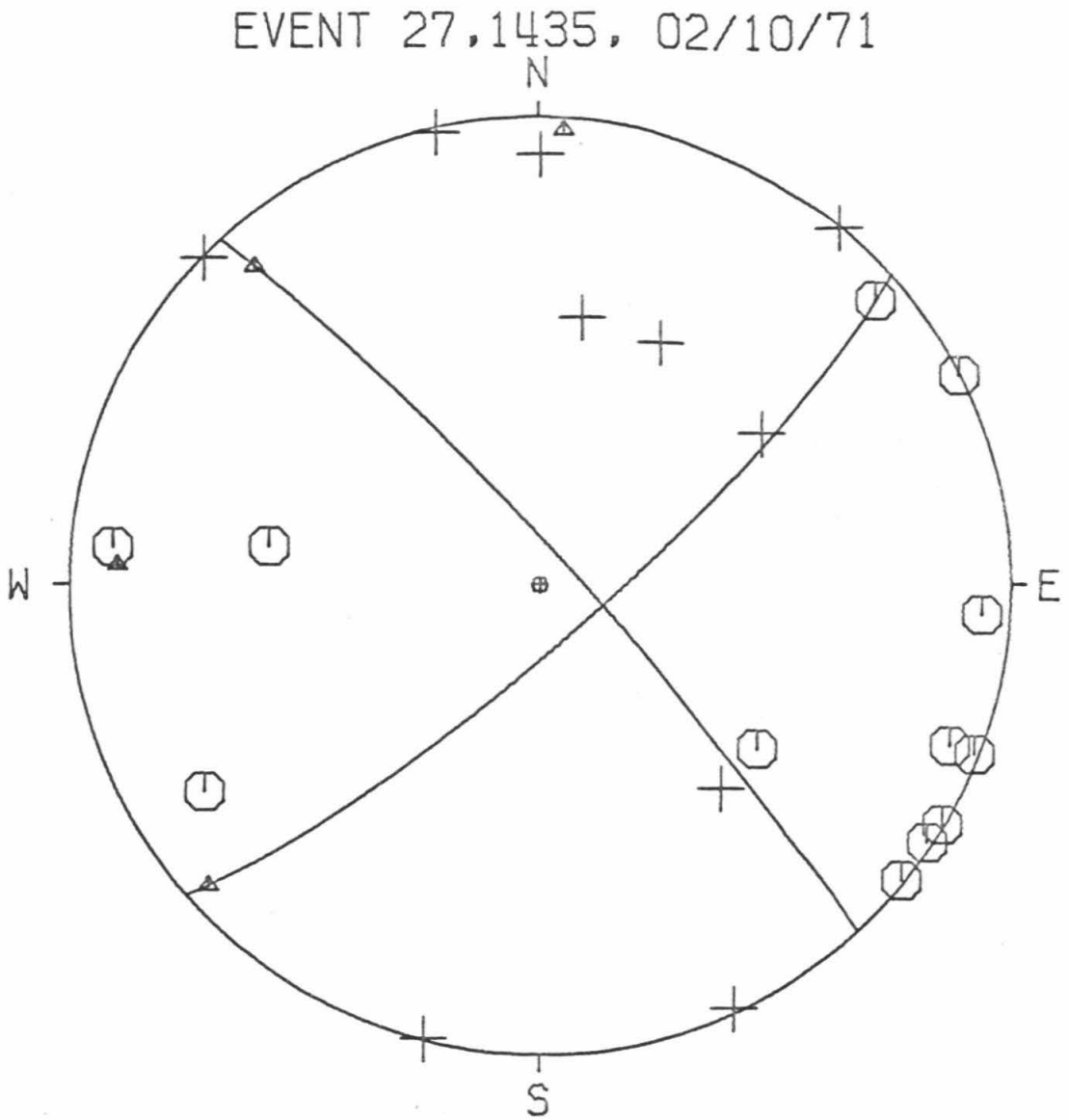
EVENT 27,1435, 02/10/71
N
W
E
S

EVENT DATA
28,1738 0 02/10/71 17 38 0.0
6.2 34.000 23.74 -118.000 21.98 4.2

AZ1= 85.000
DIP1= 52.000
AZ2= 292.500
DIP2= 41.374

SLIP VECTORS= 202.500 41.374 354.999 52.000

PRIN AXES = 298.478 14.995 187.520 84.532

STA	DIR	QUAL	DIST	EVAZ	TOA	X	Y
BAR	D	2	2.221	139.938	48.950	0.943	-1.121
CLC	C	2	1.552	23.772	48.950	0.590	1.340
CWC	D	-2	2.053	6.504	48.950	0.166	1.455
GSC	C	2	1.571	54.410	48.950	1.191	0.852
ISA	D	2	1.118	355.871	85.517	-0.173	2.394
MWC	C	2	0.309	124.316	94.498	-1.982	1.353
PAS	D	2	0.296	146.952	94.642	-1.307	2.009
PLM	D	2	1.628	129.311	48.950	1.133	-0.928
PYR	D	2	0.355	299.244	93.988	2.104	-1.178
SBC	C	2	1.282	273.134	48.950	-1.463	0.080
SYP	C	2	1.338	276.199	48.950	-1.456	0.158
RVR	D	2	0.915	115.837	87.772	2.206	-1.068
USC	D	2	0.388	170.450	93.625	-0.401	2.386
BOUQ	D	2	0.131	331.938	114.853	0.895	-1.680
BRWN	D	2	0.215	240.006	104.185	1.881	1.086
NRTM	D	2	0.226	25.955	96.937	-1.026	-2.108
ENGN	D	2	0.345	137.826	94.093	-1.617	1.785
SWM	D	2	0.369	330.984	93.838	1.171	-2.112
LGOR	D	1	0.527	317.334	92.082	1.663	-1.805
NSGM	D	1	0.056	223.993	139.546	0.849	0.879

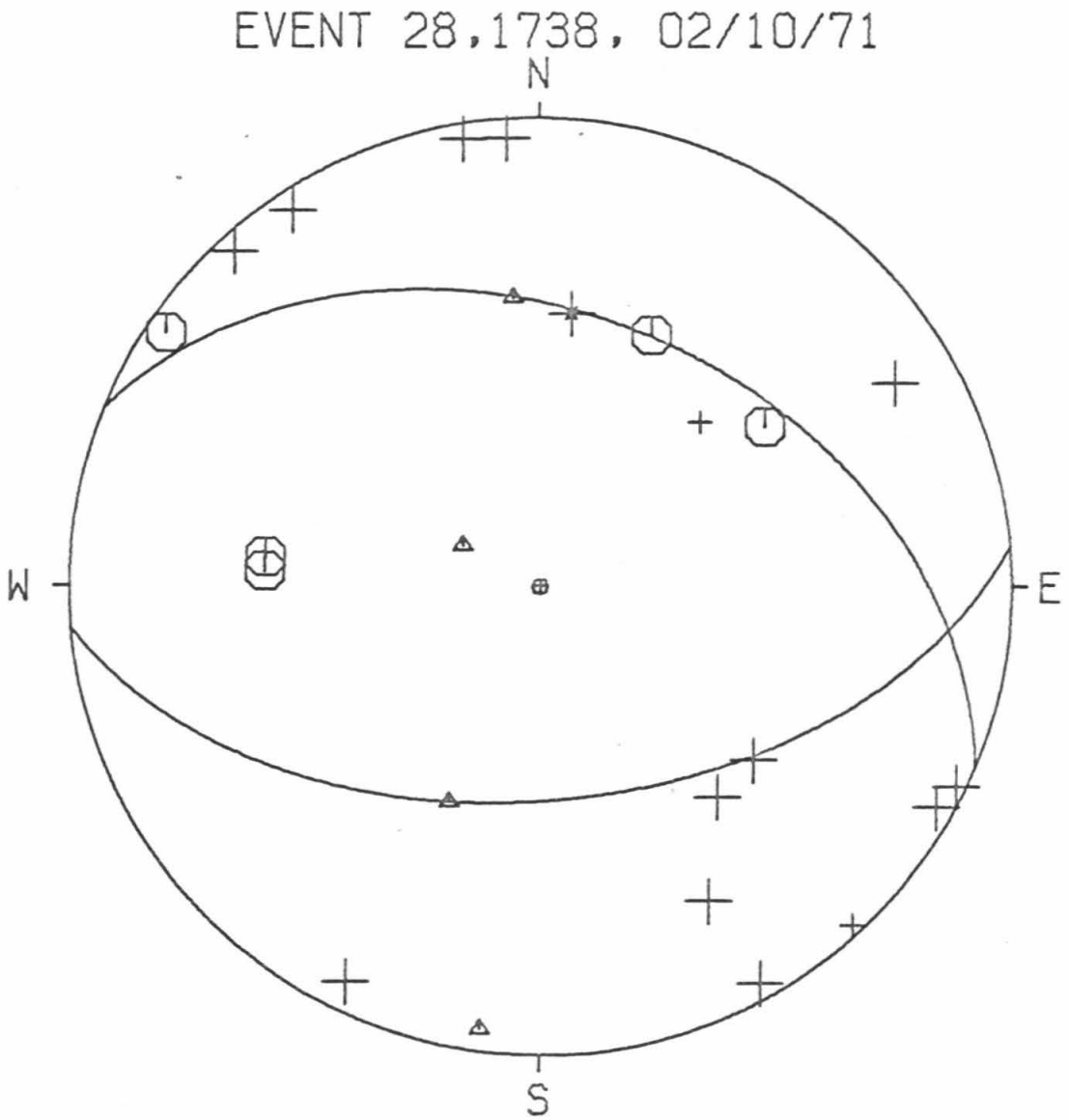
EVENT 28,1738, 02/10/71
N
W
E
S

EVENT DATA

29,1854 C 02/10/71 18 54 0.0

8.1 34.000 26.75 -118.000 26.16 4.2

AZ1= 237.000
DIP1= 66.000
AZ2= 147.000
DIP2= 90.000

SLIP VECTORS= 57.000 90.000 147.000 66.000

PRIN AXES = 99.417 73.286 194.586 73.285

STA	DIR	QUAL	DIST	EVAZ	TOA	X	Y
BAR	C	2	2.296	139.605	49.400	0.957	-1.125
CLC	D	2	1.531	26.456	49.400	0.658	1.323
CSP	C	2	0.905	99.328	92.078	-2.422	0.398
CWC	D	2	2.010	8.257	49.400	0.212	1.462
GLA	C	1	3.313	113.815	49.400	1.352	-0.597
GSC	C	2	1.590	57.037	49.400	1.240	0.804
ISA	D	2	1.066	358.412	90.090	0.069	-2.497
MWC	C	2	0.385	125.649	98.547	-1.874	1.344
PAS	C	2	0.371	143.733	98.740	-1.362	1.856
PLM	C	2	1.704	129.337	49.400	1.143	-0.936
PYR	C	2	0.282	296.498	99.922	2.036	-1.015
SBC	C	2	1.223	271.714	49.400	-1.477	0.044
SYP	C	2	1.276	274.256	49.400	-1.473	0.110
RVR	C	2	0.989	116.926	91.040	-2.209	1.122
USC	C	2	0.449	164.207	97.703	-0.633	2.239
BRWN	C	-2	0.202	219.540	105.721	1.359	1.646
NRTM	D	2	0.219	45.390	103.996	-1.550	-1.529
ENGN	C	2	0.421	136.517	98.069	-1.595	1.682
SWM	D	2	0.299	336.029	99.698	0.926	-2.083
NSGM	D	2	0.071	164.756	132.551	-0.374	1.372
RCTR	C	2	0.339	136.960	99.166	-1.564	1.675

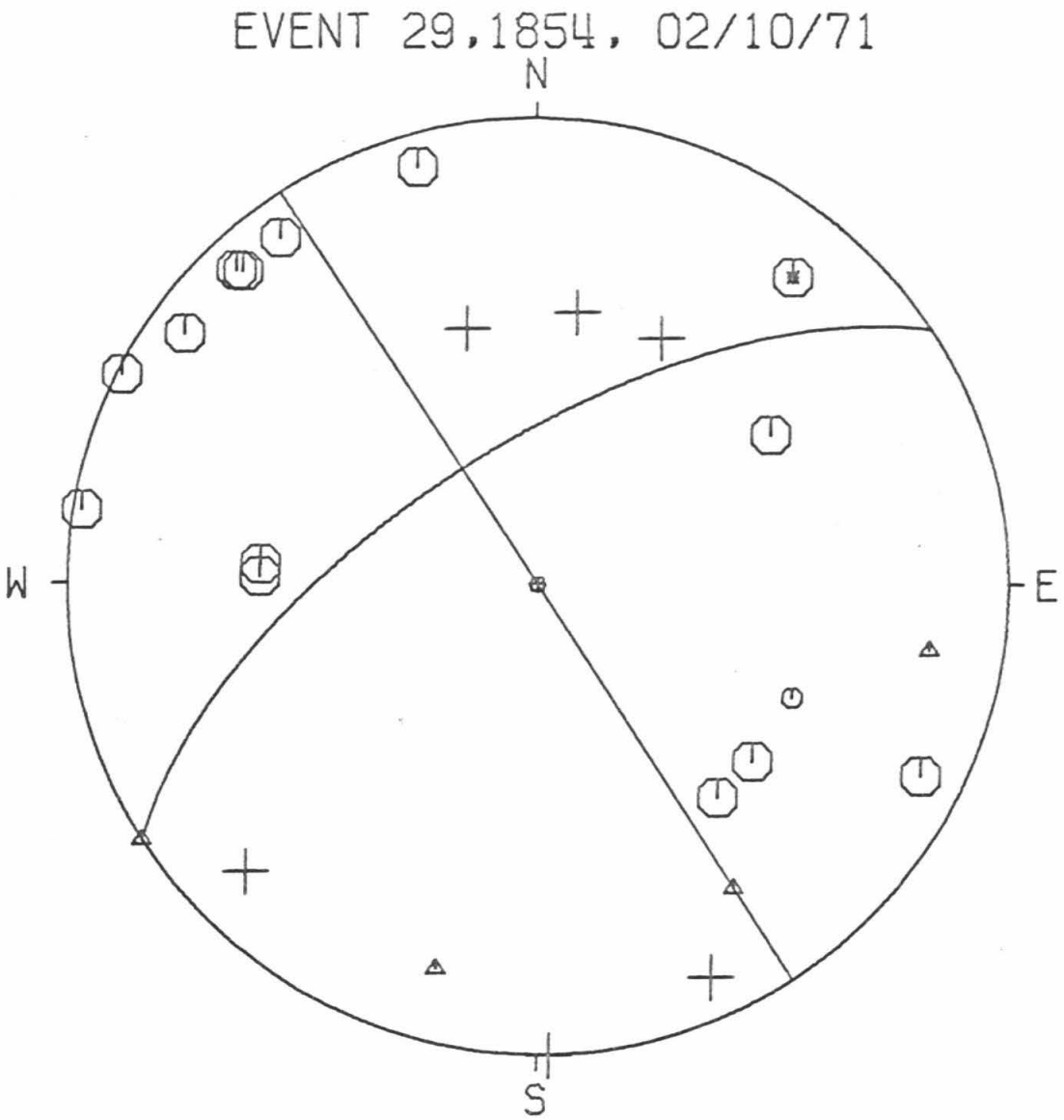
EVENT 29,1854, 02/10/71
N
W
E
S

EVENT DATA

30,1906 0 02/10/71 19 6 0.0

11.3 34.000 22.51 -118.000 18.07 3.5

AZ1= 286.000
DIP1= 48.000
AZ2= 106.000
DIP2= 42.000

SLIP VECTORS= 16.000 42.000 196.000 48.000

PRIN AXES = 195.941 3.011 16.000 87.000

STA	DIR	QUAL	DIST	EVAZ	TCA	X	Y
BAR	C	1	2.171	140.718	49.400	0.935	-1.144
CLC	D	2	1.550	21.677	49.400	0.546	1.373
CSP	D	2	0.785	95.851	95.259	-2.370	0.243
GSC	D	2	1.540	52.655	49.400	1.175	0.896
ISA	D	2	1.144	353.555	49.400	-0.166	1.468
MWC	D	2	0.253	127.417	108.187	-1.647	1.260
PAS	D	2	0.253	154.834	108.233	-0.881	1.876
PLM	D	1	1.573	130.016	49.400	1.131	-0.950
PYR	D	2	0.413	298.225	101.002	1.981	-1.064
SBC	C	2	1.337	273.952	49.400	-1.474	0.102
SYP	C	2	1.394	276.823	49.400	-1.467	0.176
RVR	D	2	0.858	116.187	94.338	-2.157	1.061
USC	D	2	0.362	178.391	103.259	-0.062	2.194
BOUQ	D	2	0.179	319.825	116.634	1.198	-1.419
BRWN	D	1	0.256	249.906	108.050	1.950	0.714
NAGM	D	2	0.124	352.231	126.843	0.214	-1.567
NRTM	D	2	0.227	11.404	111.030	-0.396	-1.962
ENGN	D	2	0.296	143.072	106.208	-1.275	1.697
NSCF	C	2	0.071	8.520	142.978	-0.166	-1.110
NSGM	C	1	0.099	290.287	133.538	1.308	-0.484
RCTR	D	2	0.215	146.266	112.472	-1.091	1.634

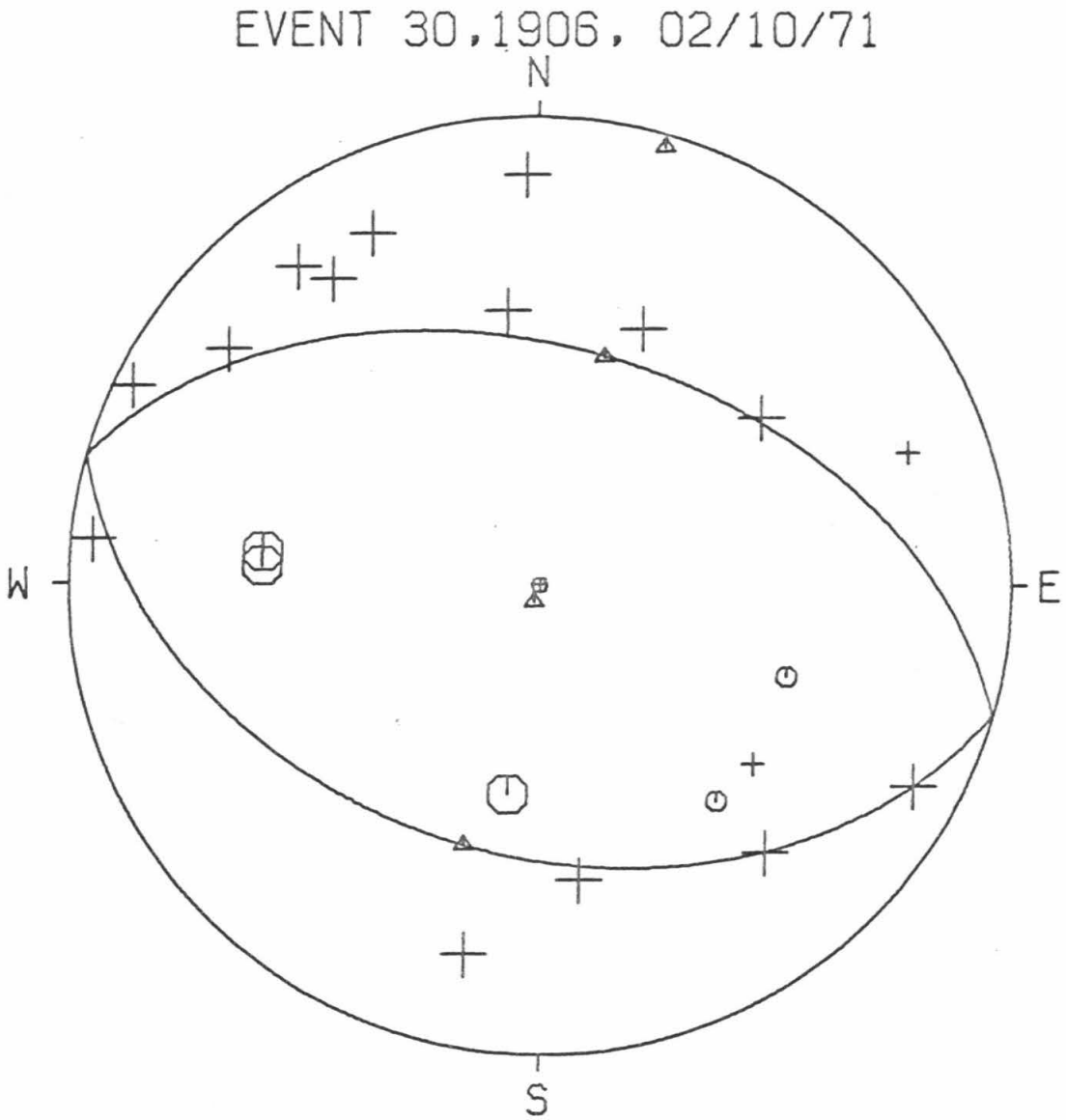
EVENT 30,1906, 02/10/71
N
W
E
S

EVENT DATA

31,2342 0 02/10/71 23 42 0.0

8.1 34.000 23.14 -118.000 21.41 3.5

STA	DIR	QUAL	DIST	EVAZ	TOA	X	Y
CLC	C	2	1.558	23.364	49.400	0.586	1.356
CSP	D	2	0.832	96.100	92.977	-2.420	0.259
GSC	C	2	1.570	53.957	49.400	1.195	0.869
ISA	D	2	1.129	355.552	89.261	-0.193	2.476
MWC	C	2	0.296	123.341	99.733	-1.904	1.253
PAS	C	2	0.283	147.165	99.904	-1.233	1.911
PLM	D	2	1.615	129.213	49.400	1.145	-0.934
PYR	C	2	0.367	300.052	98.790	1.992	-1.152
SYP	C	2	1.347	276.524	49.400	-1.468	0.168
RVR	D	2	0.904	115.462	92.091	-2.216	1.055
USC	D	2	0.376	171.367	98.671	-0.346	2.278
BRWN	D	2	0.217	243.528	104.259	1.943	0.967
IRON	C	2	0.040	301.188	149.887	0.786	-0.476
NAGM	D	2	0.115	14.710	118.416	-0.460	-1.751
NMLM	D	2	0.230	84.843	102.975	-2.193	-0.198
NRTM	D	2	0.232	23.108	102.810	-0.866	-2.029
NWSM	D	2	0.278	323.353	99.978	1.357	-1.824
ENGN	C	-2	0.333	137.678	99.244	-1.542	1.693
LGOR	C	1	0.539	317.390	96.593	1.592	-1.731
NSCF	C	1	0.082	43.930	128.474	-1.066	-1.107
NSGM	D	2	0.059	231.938	138.228	0.992	0.777
RCTR	C	2	0.250	138.597	100.985	-1.488	1.687

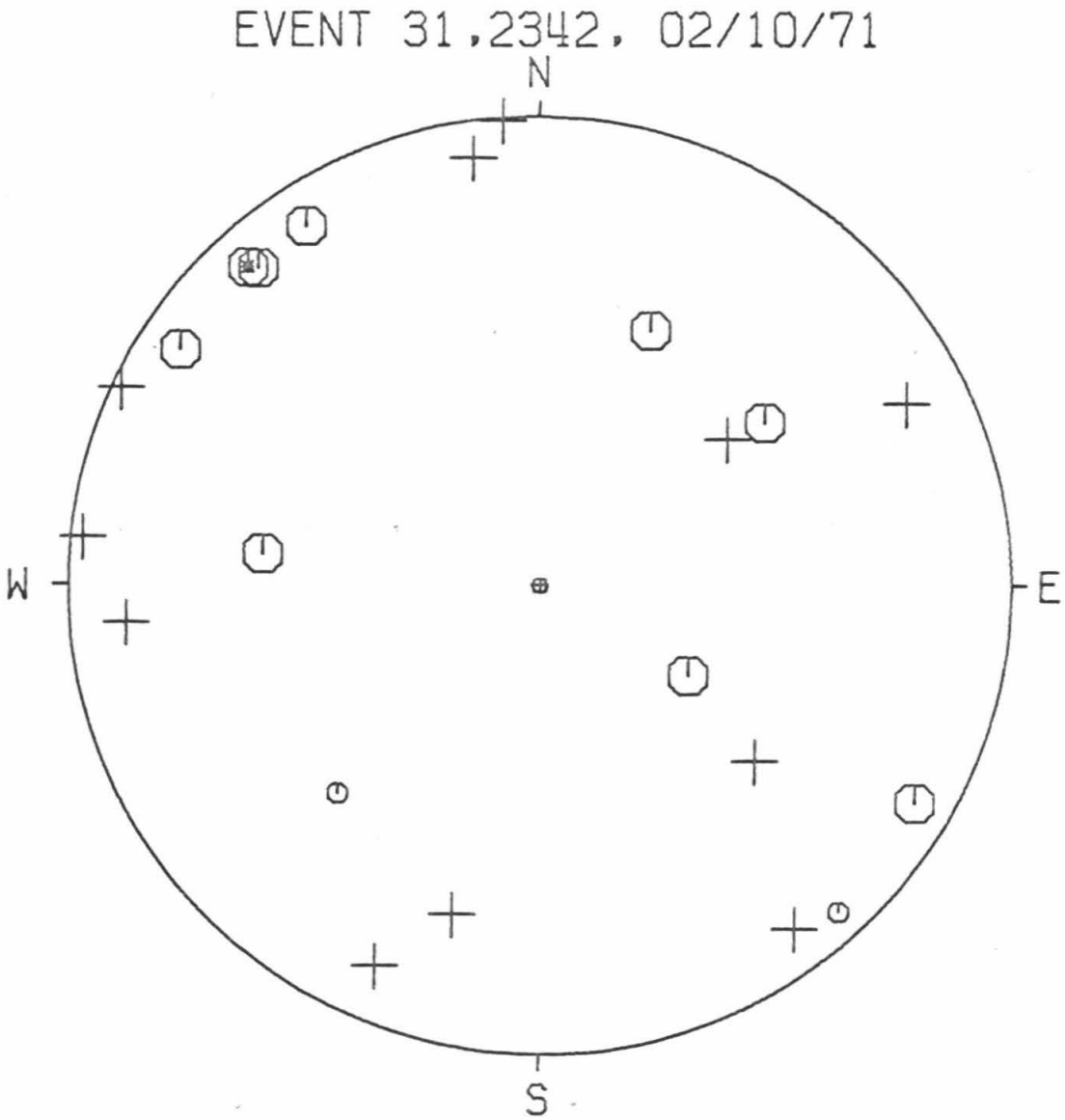
EVENT 31,2342, 02/10/71
N
W
E
S

EVENT DATA

32,0030 0 02/11/71 0 30 0.0

5.0 34.000 24.50 -118.000 16.63 3.5

AZ1= 300.000
DIP1= 20.000
AZ2= 100.000
DIP2= 71.118

SLIP VECTORS= 10.000 71.118 210.000 20.000

PRIN AXES = 359.395 26.711 195.272 64.175

STA	DIR	QUAL	DIST	EVAZ	TOA	X	Y
BAR	D	2	2.184	141.682	48.650	0.903	-1.143
CLC	C	2	1.512	21.458	48.650	0.533	1.355
CSP	C	-2	0.769	98.184	86.524	2.398	-0.345
CWC	C	2	2.033	4.531	48.650	0.115	1.452
GSC	C	2	1.504	53.224	48.650	1.166	0.872
ISA	C	2	1.113	352.488	82.988	-0.306	2.322
MWC	D	2	0.261	135.980	91.743	-1.711	1.770
PAS	D	2	0.276	161.483	91.594	-0.783	2.337
PLM	D	2	1.580	131.402	48.650	1.092	-0.963
PYR	C	2	0.416	292.979	90.147	2.299	-0.975
SBC	D	1	1.355	272.593	48.650	-1.455	0.066
SYP	C	2	1.410	275.401	48.650	-1.450	0.137
RVR	D	2	0.855	118.755	85.640	2.107	-1.156
USC	D	2	0.395	181.417	90.370	0.062	2.491
BOUQ	D	2	0.170	307.298	89.874	-1.987	1.513
BRWN	C	-2	0.285	245.966	91.500	2.253	1.005
IRON	D	2	0.105	252.314	98.175	2.206	0.703
NAGM	D	2	0.095	337.365	99.707	0.877	-2.104
NMLM	D	2	0.166	99.920	89.918	2.461	-0.430
NRTM	D	2	0.192	7.536	89.666	0.327	2.471
NWSM	C	2	0.306	310.958	91.276	1.867	-1.620
ENGN	D	2	0.312	149.527	91.224	-1.254	2.132
NSGM	D	2	0.120	249.368	95.729	2.220	0.836
RCTR	D	2	0.232	154.661	92.579	-1.046	2.208

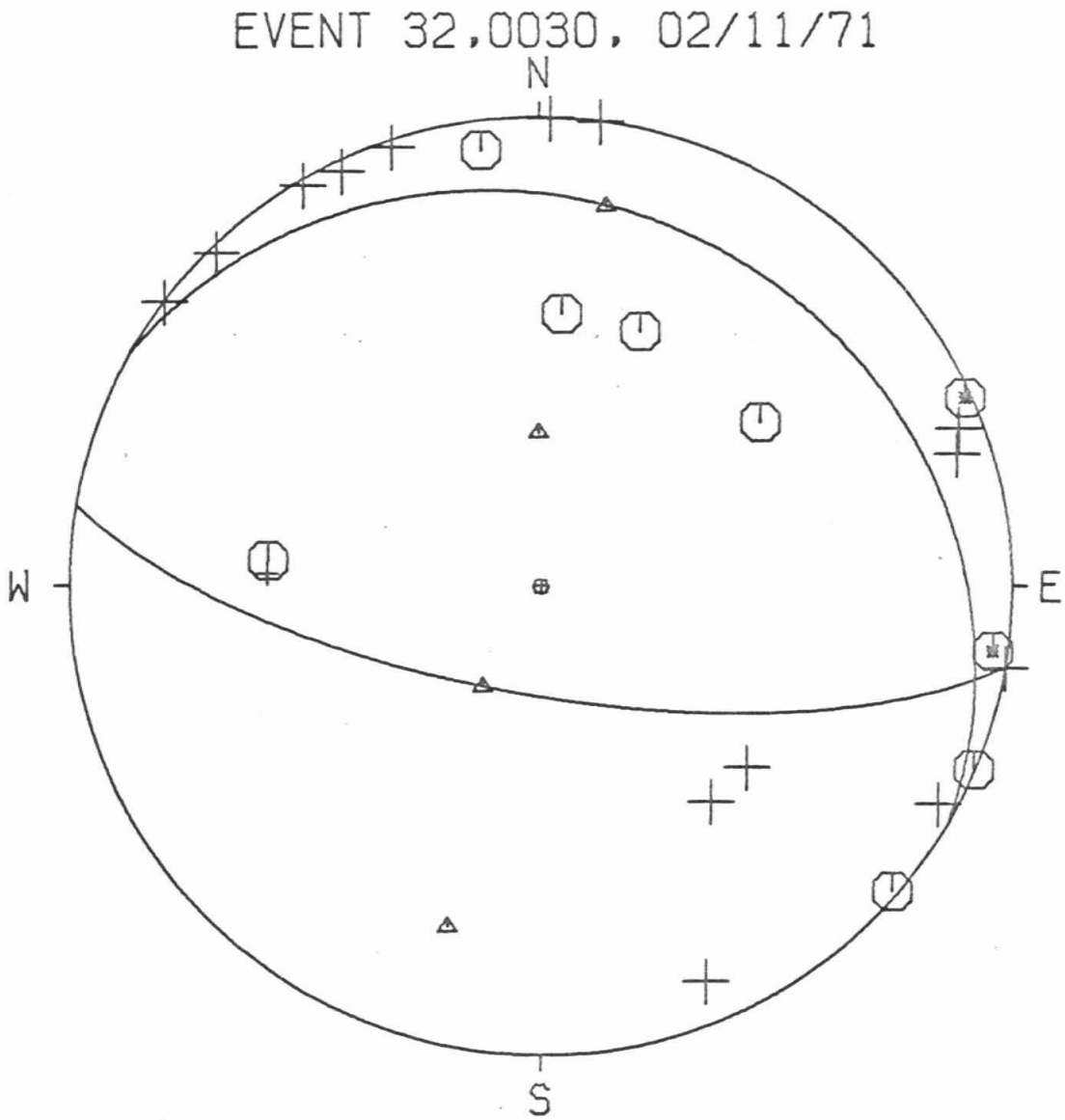
EVENT 32,0030, 02/11/71
N
W
E
S

EVENT DATA

33,0343 0 02/11/71 3 43 0.0

8.0 34.000 25.05 -118.000 26.32 3.2

AZ1= 222.000
DIP1= 60.000
AZ2= 117.000
DIP2= 65.854

SLIP VECTORS= 27.000 65.854 132.000 60.000

PRIN AXES = 77.545 49.999 170.649 86.313

STA	DIR	QUAL	DIST	EVAZ	TCA	X	Y
CLC	C	1	1.557	26.069	49.400	0.649	1.327
GSC	C	2	1.608	56.241	49.400	1.228	0.821
ISA	D	2	1.094	358.551	89.693	-0.063	2.492
MWC	D	2	0.371	121.747	98.611	-1.960	1.213
PAS	D	2	0.349	140.594	98.879	-1.459	1.776
PLM	D	1	1.688	128.546	49.400	1.155	-0.921
PYR	D	2	0.293	301.340	99.571	1.950	-1.187
SBC	C	1	1.221	272.275	49.400	-1.476	0.059
SYP	D	2	1.276	275.431	49.400	-1.471	0.140
RVR	C	2	0.978	115.381	91.119	-2.237	1.061
USC	D	1	0.422	162.872	97.972	-0.683	2.217
BOUQ	D	2	0.095	358.800	123.709	0.035	-1.667
BRWN	C	2	0.180	224.453	107.551	1.463	1.491
IRON	C	2	0.048	135.694	144.090	-0.761	0.780
GOOK	C	2	0.056	213.035	139.546	0.666	1.025
SCLE	C	2	0.069	58.088	133.558	-1.183	-0.737
NAGM	C	2	0.125	50.759	116.099	-1.449	-1.184
NMLM	C	2	0.299	96.792	99.498	-2.268	0.270
NRTM	D	2	0.241	40.993	101.604	-1.466	-1.687
NWSM	D	2	0.215	332.804	104.185	0.993	-1.932
ENGN	D	2	0.403	133.503	98.218	-1.679	1.593
LGOR	C	1	0.471	320.803	97.378	1.475	-1.809
NSCF	D	2	0.130	73.284	115.159	-1.815	-0.545
NSGM	D	2	0.048	154.359	144.090	-0.472	0.983
RCTR	D	2	0.320	133.223	99.233	-1.669	1.569

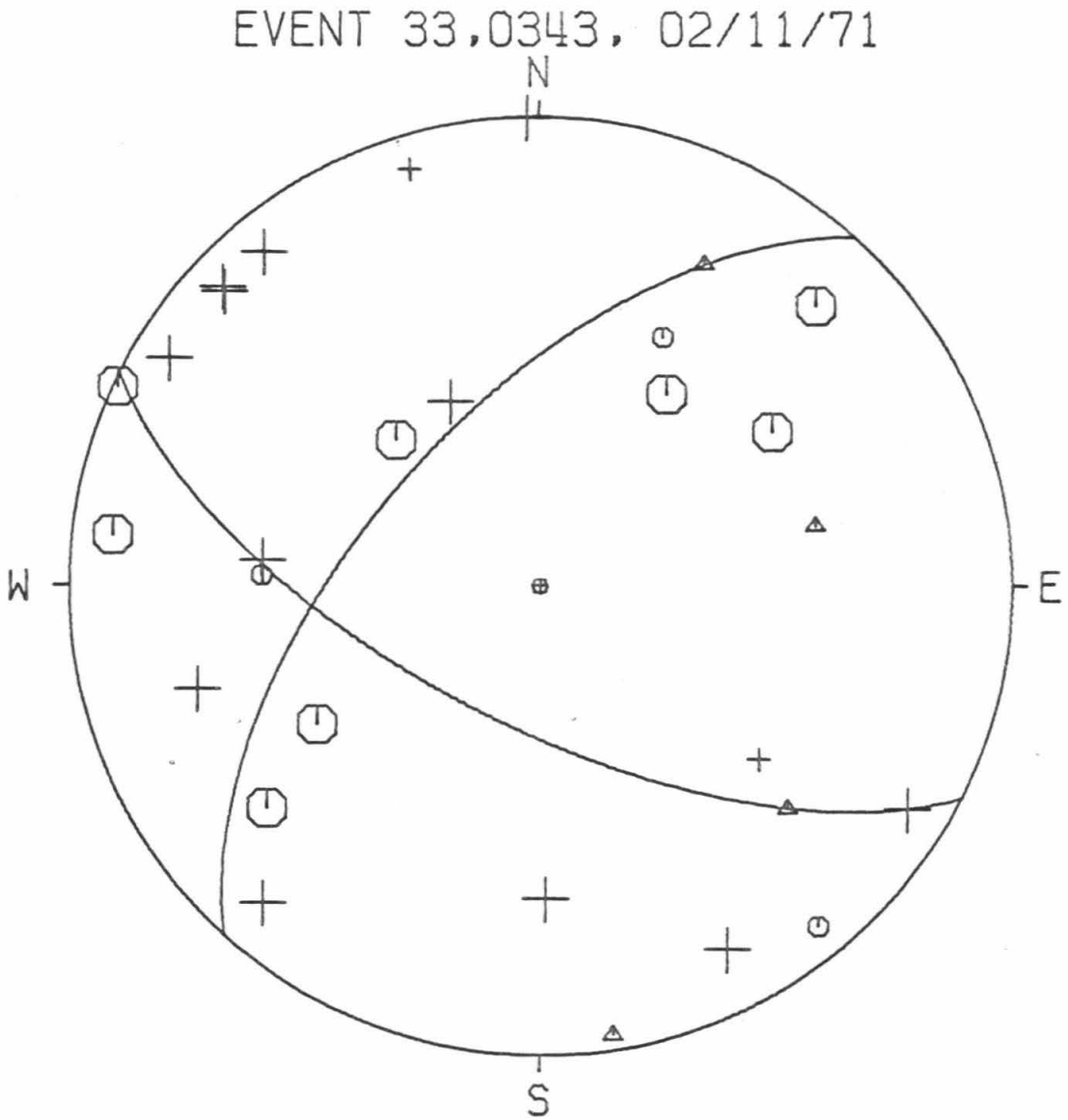
EVENT 33,0343, 02/11/71
N
W
E
S

EVENT DATA

34,0407 0 02/11/71 4 7 0.0

11.3 34.000 18.39 -118.000 32.13 3.4

AZ1= 255.000
DIP1= 70.000
AZ2= 165.000
DIP2= 90.000

SLIP VECTORS= 75.000 90.000 165.000 70.000

PRIN AXES = 118.220 76.005 211.780 76.005

STA	DIR	QUAL	DIST	EVAZ	TOA	X	Y
CLC	D	1	1.692	26.802	49.400	0.666	1.319
ISA	D	2	1.205	2.058	49.400	0.053	1.476
MWC	C	2	0.404	102.146	101.366	-2.190	0.471
PAS	C	2	0.342	118.095	104.153	-1.917	1.023
PLM	C	2	1.687	123.855	49.400	1.227	-0.823
PYR	C	2	0.312	326.974	105.490	1.167	-1.794
SBC	C	2	1.151	278.327	50.967	-1.505	0.220
SYP	C	2	1.213	280.965	49.400	-1.450	0.281
TIN	C	1	2.754	5.122	49.400	0.132	1.471
RVR	C	2	1.012	107.715	92.370	-2.332	0.745
USC	C	1	0.358	145.068	103.454	-1.254	1.795
BOUQ	D	2	0.218	20.998	112.156	-0.707	-1.842
IRON	D	1	0.141	53.743	123.162	-1.357	-0.995
GOCK	D	2	0.099	30.079	133.538	-0.699	-1.207
NAGM	D	2	0.259	43.137	107.879	-1.423	-1.519
NMLM	D	2	0.387	76.966	102.162	-2.164	-0.501
NRTM	D	2	0.376	39.276	102.620	-1.399	-1.711
NWSM	D	2	0.302	356.517	105.945	0.129	-2.125
ENGN	C	2	0.408	114.104	101.215	-2.048	0.916
LGCR	C	2	0.523	335.398	98.593	0.960	-2.096
NSCF	D	1	0.245	56.593	109.003	-1.714	-1.130
RCTR	C	2	0.333	109.561	104.568	-2.038	0.724

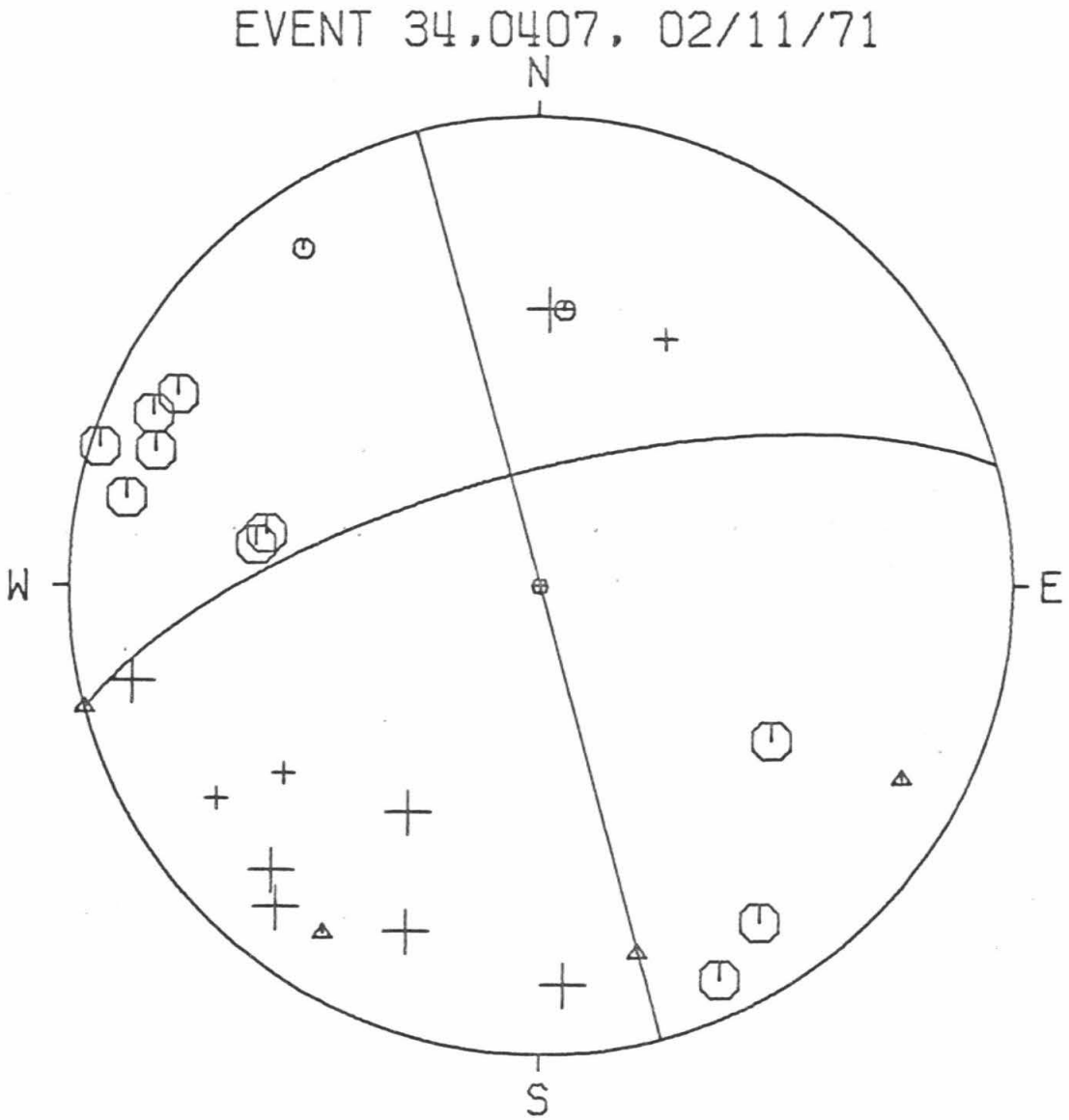
EVENT 34,0407, 02/11/71
N
W
E
S

EVENT DATA

35,0733 0 02/11/71 7 33 0.0

12.4 34.000 27.41 -118.000 26.50 3.3

AZ1= 132.000
DIP1= 64.000
AZ2= 252.000
DIP2= 44.288

SLIP VECTORS= 162.000 44.288 42.000 64.000

PRIN AXES = 89.481 35.300 196.146 78.685

STA	DIR	QUAL	DIST	EVAZ	TOA	X	Y
BAR	C	2	2.308	139.687	49.420	0.956	-1.127
CLC	D	2	1.524	26.795	49.420	0.666	1.319
CSP	C	2	0.911	99.880	94.376	-2.367	0.412
GSC	C	-2	1.588	57.464	49.420	1.246	0.795
ISA	D	2	1.054	358.621	92.183	0.059	-2.451
MWC	D	2	0.395	126.399	103.181	-1.768	1.303
PAS	D	2	0.382	144.058	103.819	-1.280	1.766
PLM	C	2	1.714	129.520	49.420	1.140	-0.940
PYR	C	2	0.273	294.788	109.581	1.851	-0.855
SBC	D	2	1.218	268.185	49.420	-1.477	-0.047
SYP	D	2	1.271	273.929	49.420	-1.474	0.101
BOUQ	D	2	0.059	0.479	150.592	-0.008	-0.897
BRWN	C	-2	0.207	216.803	116.049	1.122	1.499
IRON	C	2	0.082	153.549	142.144	-0.511	1.027
NAGM	D	2	0.110	64.462	133.483	-1.260	-0.602
NMLM	D	2	0.308	103.613	107.660	-2.028	0.491
NRTM	D	2	0.216	48.202	114.905	-1.418	-1.268
NWSM	D	2	0.180	327.915	119.294	0.949	-1.514
ENGN		-1	0.432	137.038	101.359	-1.527	1.639
LGOR	D	2	0.440	317.920	100.965	1.508	-1.670
NSCF	D	1	0.133	107.266	128.054	-1.479	0.460
NSGM	D	2	0.082	163.289	142.144	-0.330	1.098

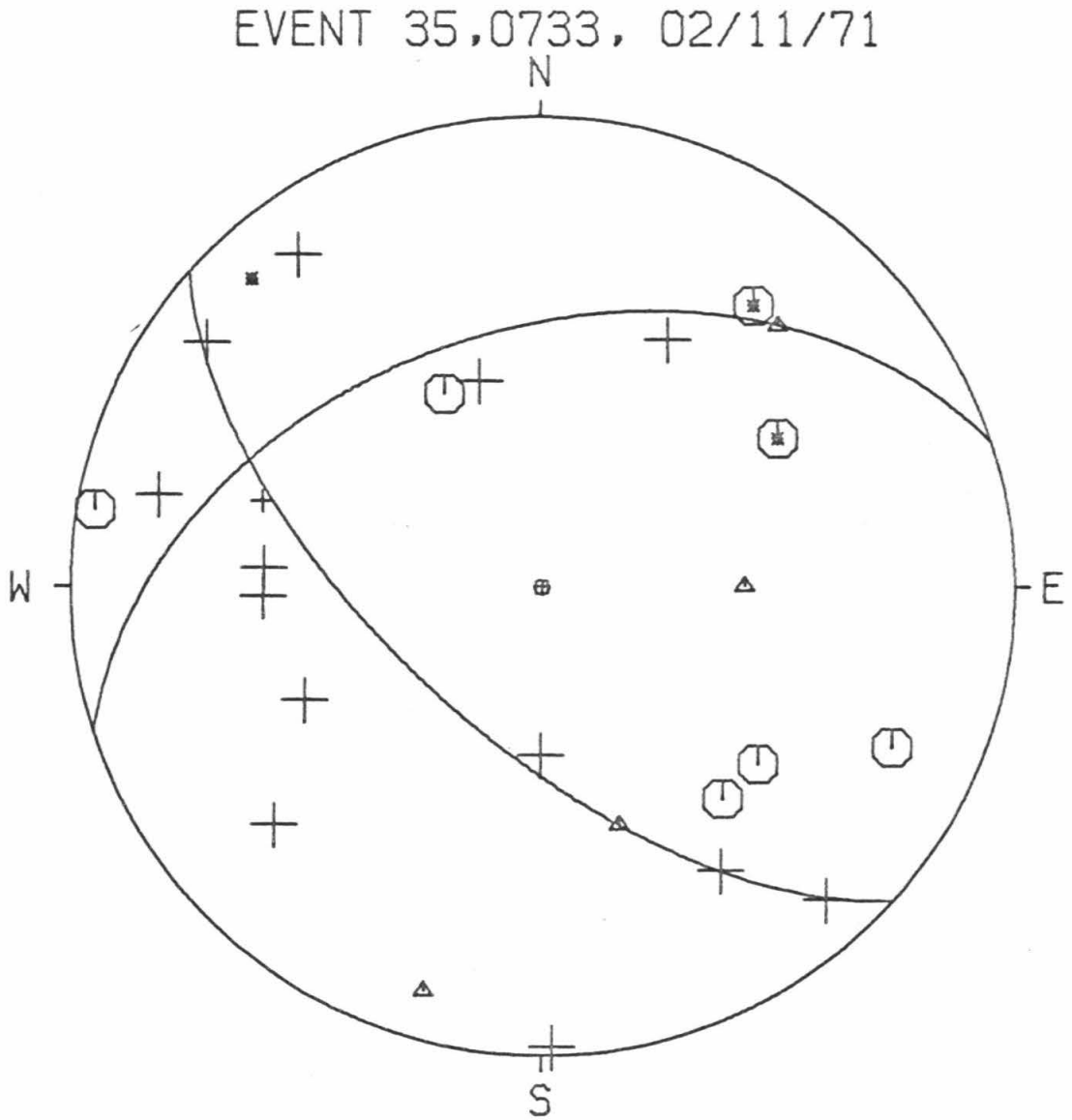
EVENT 35,0733, 02/11/71
N
W
E
S

EVENT DATA

36,0924 0 02/11/71 9 24 0.0

5.0 34.000 24.91 -118.000 20.34 3.3

AZ1= 51.500
DIP1= 20.000
AZ2= 288.000
DIP2= 78.641

SLIP VECTORS= 198.000 78.641 321.499 20.000

PRIN AXES = 217.811 36.513 4.291 58.319

STA	DIR	QUAL	DIST	EVAZ	TOA	X	Y
BAR	C	1	2.221	140.723	48.650	0.922	-1.127
CLC	D	2	1.525	23.303	48.650	0.576	1.338
GSC	D	2	1.541	54.531	48.650	1.186	0.845
ISA	D	2	1.101	354.773	83.115	-0.214	2.336
MWC	D	2	0.303	129.772	91.315	-1.899	1.581
PAS	D	2	0.301	152.570	91.329	-1.138	2.193
PLM	C	2	1.623	130.355	48.650	1.110	-0.943
PYR	D	2	0.367	295.091	90.655	2.251	-1.054
SBC	C	2	1.304	272.173	48.650	-1.455	0.055
SYP	C	2	1.359	275.265	48.650	-1.450	0.134
RVR	D	2	0.903	117.538	85.144	2.121	-1.106
USC	D	2	0.403	174.079	90.279	-0.257	2.481
BOUQ	D	2	0.128	318.891	94.499	1.578	-1.808
BRWN	D	1	0.243	239.167	92.243	2.104	1.256
IRON	D	1	0.059	234.938	112.737	1.603	1.125
GOOK	C	2	0.120	249.799	95.729	2.226	0.819
INDN	D	1	0.063	63.836	110.849	-1.801	-0.885
NAGM	C	2	0.082	10.296	103.943	-0.389	-2.143
NMLM	C	2	0.217	98.739	89.428	2.459	-0.378
NRTM	D	2	0.198	22.649	89.609	0.959	2.299
NWSM	D	2	0.265	317.024	91.705	1.679	-1.802
ENGN	D	2	0.346	142.785	90.869	-1.501	1.976
LGOR	C	1	0.529	314.161	88.990	-1.778	1.726
NSCF	D	1	0.056	48.436	114.734	-1.427	-1.265
NSGM	D	2	0.077	233.336	105.649	1.714	1.276
RCTR	D	2	0.264	145.175	91.713	-1.406	2.021

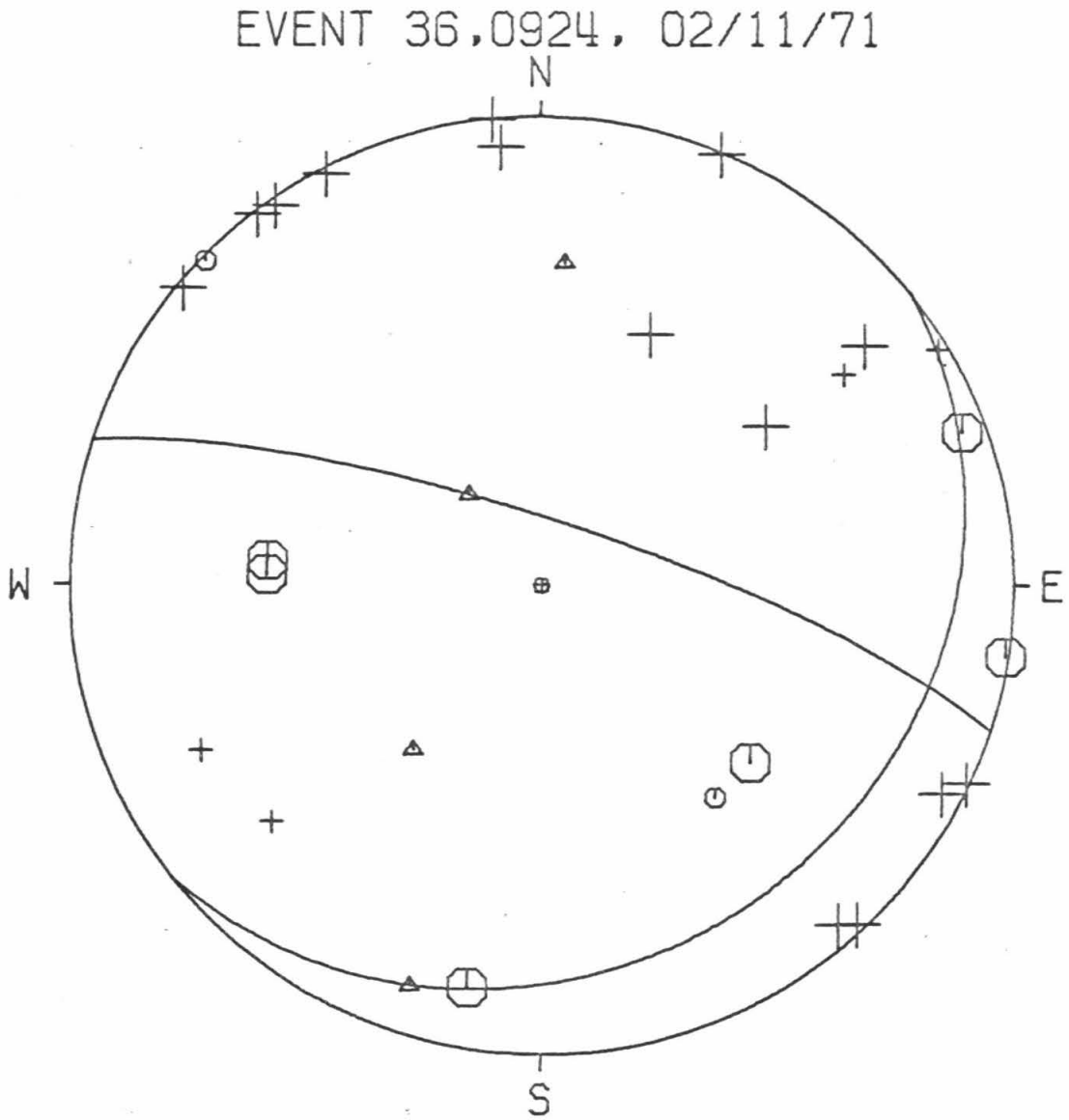
EVENT 36,0924, 02/11/71
N
W
E
S

EVENT DATA

37.1132 0 02/11/71 11 32 0.0

3.0 34.000 20.20 -118.000 18.83 3.5

AZ1= 140.500
DIP1= 80.000
AZ2= 320.500
DIP2= 10.000

SLIP VECTORS= 230.500 10.000 50.500 80.000

PRIN AXES = 50.498 35.001 230.499 55.000

STA	DIR	QUAL	DIST	EVAZ	TOA	X	Y
BAR	C	2	2.148	139.844	44.933	0.871	-1.033
CLC	C	2	1.590	21.513	44.933	0.495	1.257
CSP	D	2	0.793	92.933	83.907	2.360	-0.121
GSC	C	2	1.571	51.772	44.933	1.061	0.836
ISA	C	2	1.181	354.192	80.185	-0.230	2.265
MWC	D	2	0.241	118.393	89.198	2.184	-1.180
PAS	C	1	0.224	148.207	89.359	1.310	-2.113
PLM	C	2	1.557	128.667	44.933	1.055	-0.844
PYR	C	2	0.422	303.300	87.455	-2.043	1.342
SBC	D	2	1.329	275.679	44.933	-1.344	0.134
RVR	D	2	0.851	113.546	83.347	2.155	-0.939
USC	D	2	0.323	176.329	88.406	0.158	-2.460
BOUQ	C	2	0.203	328.771	89.562	-1.291	2.130
BRWN	D	-2	0.236	256.887	89.245	-2.419	-0.563
IRON	C	2	0.088	308.320	100.128	1.781	-1.407
GOOK	C	2	0.144	291.753	92.379	2.273	-0.907
INDN	C	1	0.095	21.859	98.730	-0.857	-2.137
NAGM	D	2	0.157	357.726	90.701	0.099	-2.483
NMLM	D	2	0.203	72.529	89.562	2.376	0.748
NRTM	D	2	0.266	12.014	88.954	0.516	2.423
NWSM	C	2	0.338	323.473	88.264	-1.465	1.978
ENGN	C	2	0.273	136.298	88.891	1.710	-1.790
LGOR	D	2	0.599	318.081	85.762	-1.607	1.790
NSCF	D	1	0.107	11.394	97.224	-0.462	-2.291
NSGM	D	2	0.101	305.332	97.955	1.893	-1.342
RCTR	C	2	0.190	136.818	86.627	1.660	-1.769

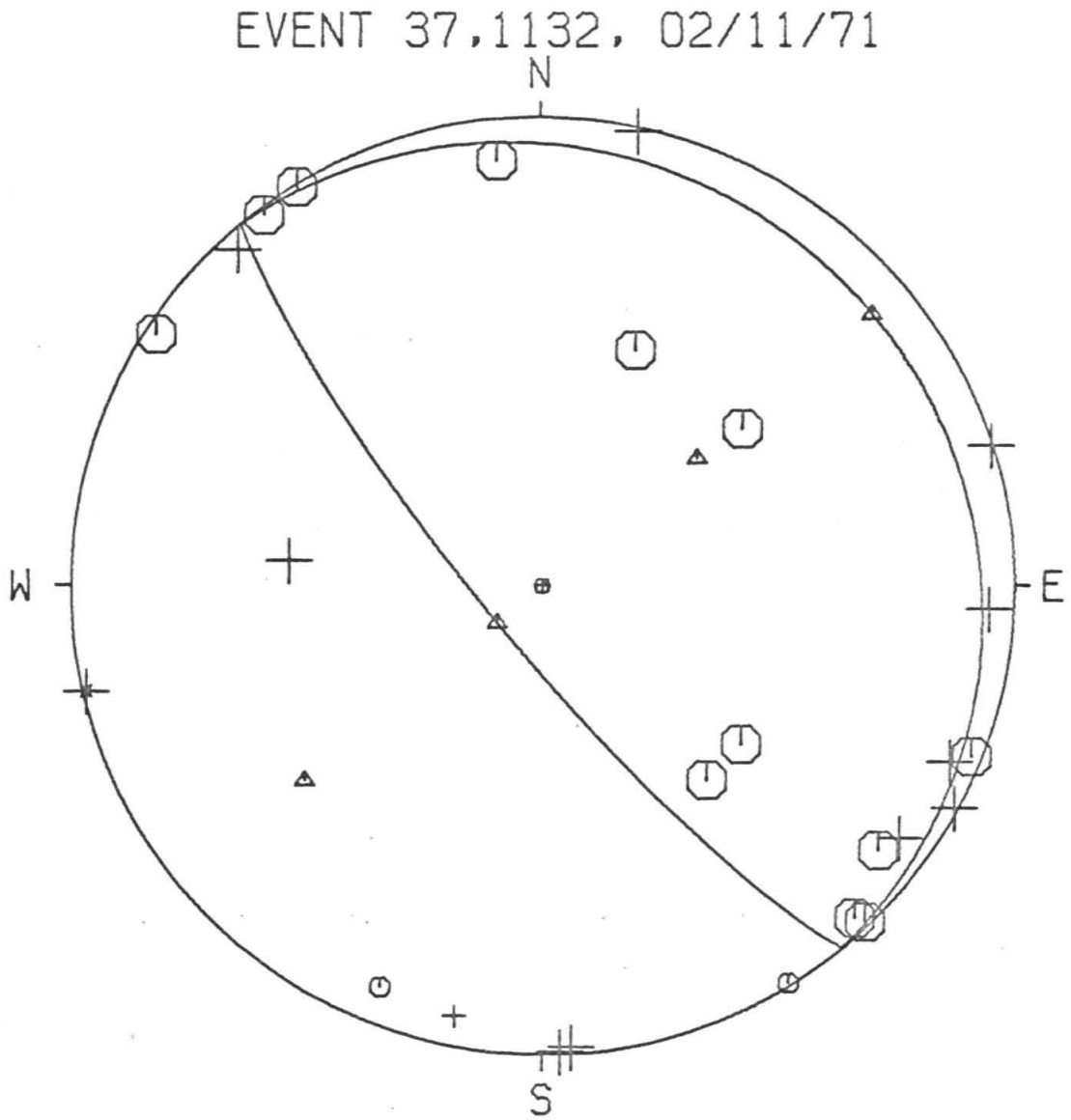
EVENT 37,1132, 02/11/71
N
W
E
S

EVENT DATA

38,1421 0 02/11/71 14 21 0.0

3.0 34.000 17.78 -118.000 19.28 3.5

AZ1= 110.000
DIP1= 40.000
AZ2= 290.000
DIP2= 50.000

SLIP VECTORS= 200.000 50.000 20.000 40.000

PRIN AXES = 199.972 5.007 20.000 85.000

STA	DIR	QUAL	DIST	EVAZ	TCA	X	Y
BAR	C	-2	2.121	139.012	44.933	0.886	-1.020
CLC	D	2	1.629	21.194	44.933	0.488	1.260
CSP	D	2	0.798	87.972	83.852	2.361	0.084
GSC	D	2	1.601	50.776	44.933	1.047	0.854
ISA	D	2	1.220	354.622	50.439	-0.141	1.500
MWC	C	-2	0.232	109.757	89.285	2.338	-0.840
PAS	D	2	0.196	140.668	85.122	1.516	-1.850
PLM	C	2	1.537	127.355	44.933	1.074	-0.820
PYR	D	2	0.441	308.206	87.273	-1.917	1.509
SBC	C	2	1.328	277.666	44.933	-1.339	0.180
SYP	C	2	1.389	280.050	44.933	-1.330	0.236
RVR	C	2	0.841	110.859	83.438	2.199	-0.838
USC	D	2	0.284	174.560	88.783	0.234	-2.462
BOUQ	D	2	0.235	335.097	89.253	-1.046	2.253
BRWN	C	-2	0.226	262.057	89.343	-2.462	-0.343
IRON	D	2	0.114	326.199	96.305	1.312	-1.960
GOOK	D	2	0.158	306.284	90.662	2.004	-1.471
NAGM	D	2	0.198	359.986	89.609	-0.001	2.491
NMLM	D	2	0.221	64.452	89.385	2.243	1.072
NRTM	D	2	0.308	11.542	88.555	0.494	2.418
NWSM	D	2	0.367	327.890	87.987	-1.305	2.080
ENGN	D	2	0.250	128.948	89.106	1.929	-1.559
SWM	D	1	0.473	332.832	86.973	-1.111	2.165
LSWM	C	1	0.442	336.543	87.264	-0.971	2.238
NSGM	C	1	0.120	320.770	95.440	1.504	-1.842
RCTR	D	2	0.168	125.855	90.360	-2.020	1.460

EVENT 38,1421, 02/11/71

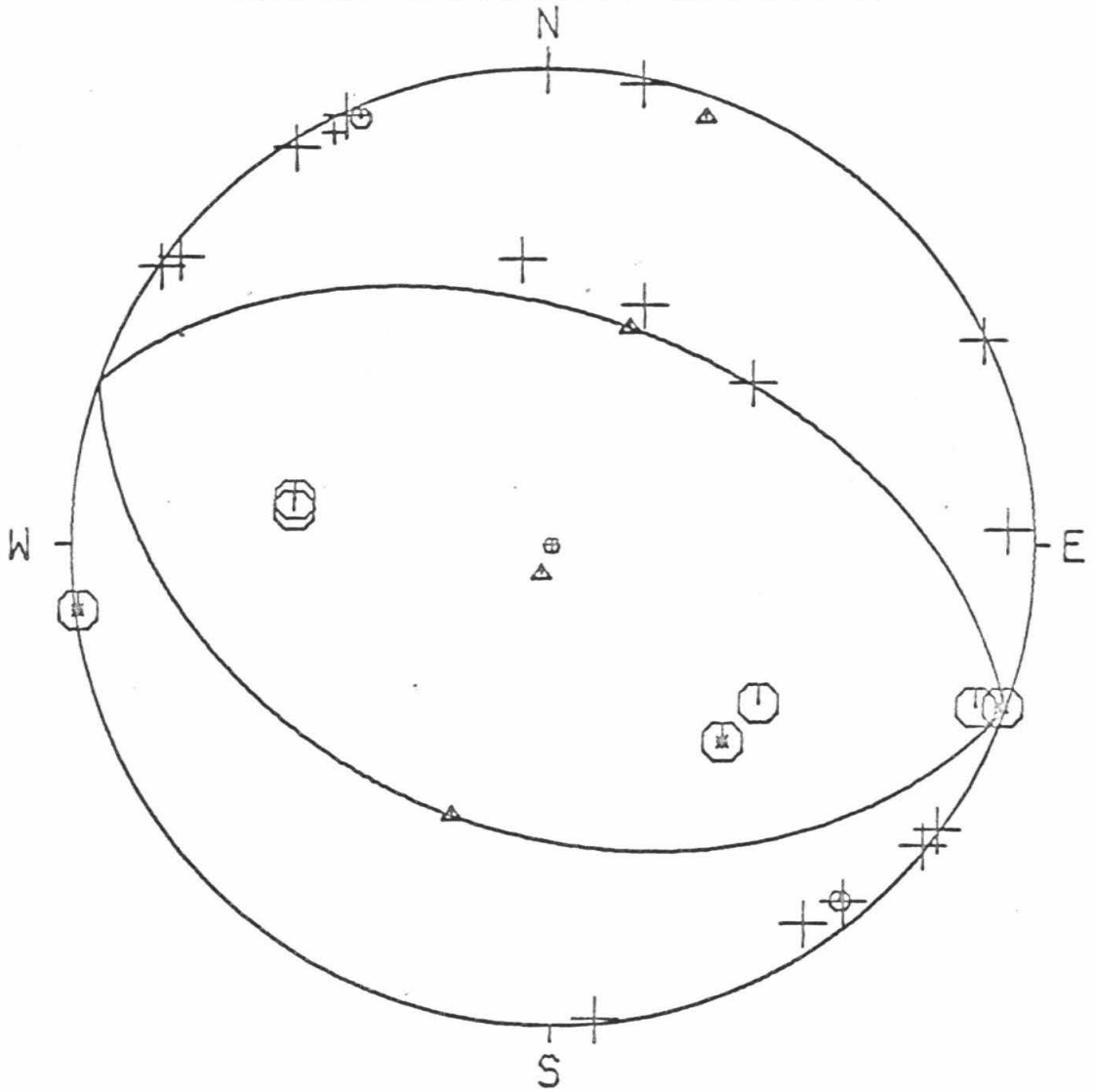

EVENT DATA

39,1643 0 02/11/71 16 43 0.0

3.0 34.000 22.70 -118.000 27.70 3.6

AZ1= 175.000
DIP1= 20.000
AZ2= 355.000
DIP2= 70.000

SLIP VECTORS= 265.000 70.000 85.000 20.000

PRIN AXES = 264.963 25.001 84.992 65.000

STA	DIR	QUAL	DIST	EVAZ	TCA	X	Y
BAR	C	2	2.259	138.073	44.933	0.903	-1.005
CLC	C	2	1.601	26.050	44.933	0.593	1.214
CSP	C	2	0.917	95.071	82.709	2.327	-0.206
GSC	C	2	1.645	55.460	44.933	1.113	0.766
ISA	D	2	1.132	359.446	80.648	-0.022	2.288
MWC	C	2	0.370	115.259	87.962	2.220	-1.048
PAS	C	2	0.333	133.820	88.309	1.777	-1.705
PLM	C	2	1.679	127.095	44.933	1.078	-0.815
PYR	D	2	0.301	309.783	88.623	-1.898	1.580
SBC	D	2	1.204	274.077	50.441	-1.503	0.107
SYP	D	2	1.262	277.354	44.933	-1.340	0.173
RVR	C	2	0.980	112.853	82.111	2.140	-0.902
BOUQ	C	-2	0.134	7.284	93.652	-0.307	-2.400
IRON	C	2	0.059	62.983	108.307	-1.845	-0.941
GOCK	C	2	0.034	340.427	130.818	0.493	-1.386
NAGM	C	2	0.167	44.052	90.397	-1.732	-1.791
NMLM	C	2	0.317	84.423	88.465	2.455	0.240
NRTM	C	2	0.283	38.773	88.790	1.549	1.928
NWSM	D	2	0.244	341.041	89.167	-0.806	2.347
ENGN	C	2	0.392	127.522	87.745	1.943	-1.492
SWM	C	1	0.354	343.552	88.112	-0.696	2.358
NSGM	D	2	0.052	49.829	116.859	-1.414	-1.194
RCTR	C	2	0.310	125.564	88.530	2.007	-1.435

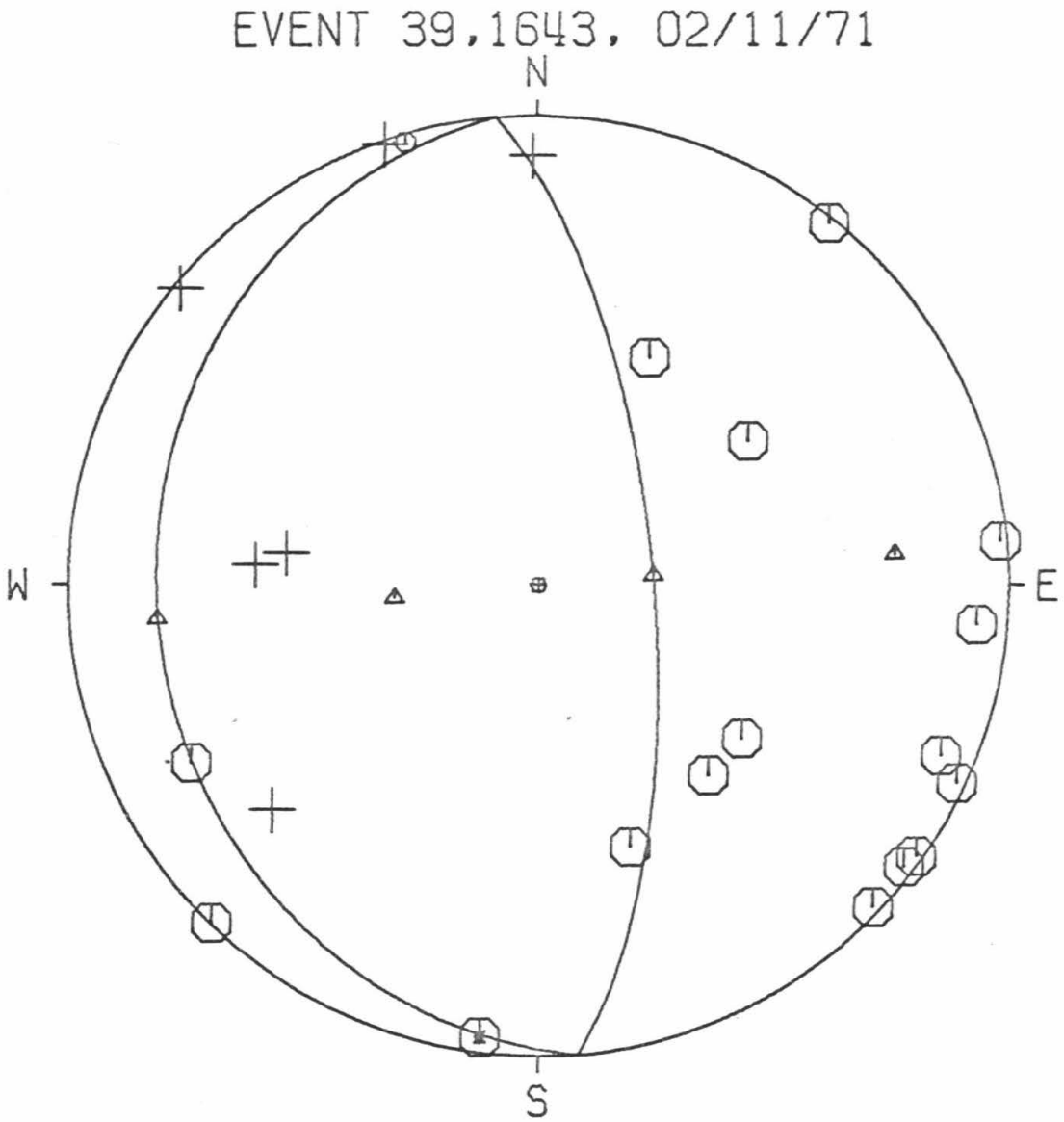
EVENT 39,1643, 02/11/71
N
W
E
S

EVENT DATA

40,1935 0 02/11/71 19 35 0.0

6.4 34.000 24.00 -118.000 26.87 3.7

AZ1= 134.000
DIP1= 60.000
AZ2= 249.000
DIP2= 53.796

SLIP VECTORS= 159.000 53.796 44.000 60.000

PRIN AXES = 98.335 39.537 192.789 86.324

STA	DIR	QUAL	DIST	EVAZ	TOA	X	Y
BAR	C	2	2.268	138.660	49.000	0.968	-1.101
CLC	D	2	1.577	26.031	49.000	0.643	1.317
CSP	C	1	0.908	96.367	88.310	2.448	-0.273
CWC	D	2	2.057	8.337	49.000	0.213	1.451
GSC	C	2	1.624	55.869	49.000	1.214	0.823
HFD	C	1	2.435	105.730	49.000	1.411	-0.397
ISA	D	2	1.111	358.917	86.029	-0.046	2.411
MWC	C	2	0.369	118.997	94.365	-2.102	1.165
PAS	D	-2	0.341	137.871	94.675	-1.607	1.777
PLM	C	2	1.683	127.919	49.000	1.157	-0.901
PYR	D	2	0.297	305.205	95.177	1.948	-1.375
SBC	D	2	1.214	273.094	49.000	-1.464	0.079
SYP	D	2	1.271	276.341	49.000	-1.457	0.162
RVR	C	2	0.978	114.266	87.526	2.229	-1.005
BOUQ	D	2	0.112	2.866	118.795	-0.090	-1.798
BRWN	D	2	0.163	226.646	109.211	1.489	1.406
IRON	D	2	0.052	127.654	141.663	-0.919	0.709
GOOK	C	2	0.040	215.386	149.647	0.536	0.755
NAGM	D	2	0.144	46.509	112.241	-1.430	-1.356
NRTM	D	2	0.259	39.910	95.605	-1.524	-1.822
NWSM	D	2	0.228	336.591	97.466	0.926	-2.140
ENGN	C	2	0.397	130.950	94.055	-1.820	1.580
SWM	D	2	0.336	340.621	94.733	0.795	-2.259
LGOR	C	1	0.480	322.858	93.117	1.468	-1.938
NSCF	D	2	0.141	68.928	112.801	-1.826	-0.703
NSGM	C	2	0.048	143.886	144.090	-0.642	0.880

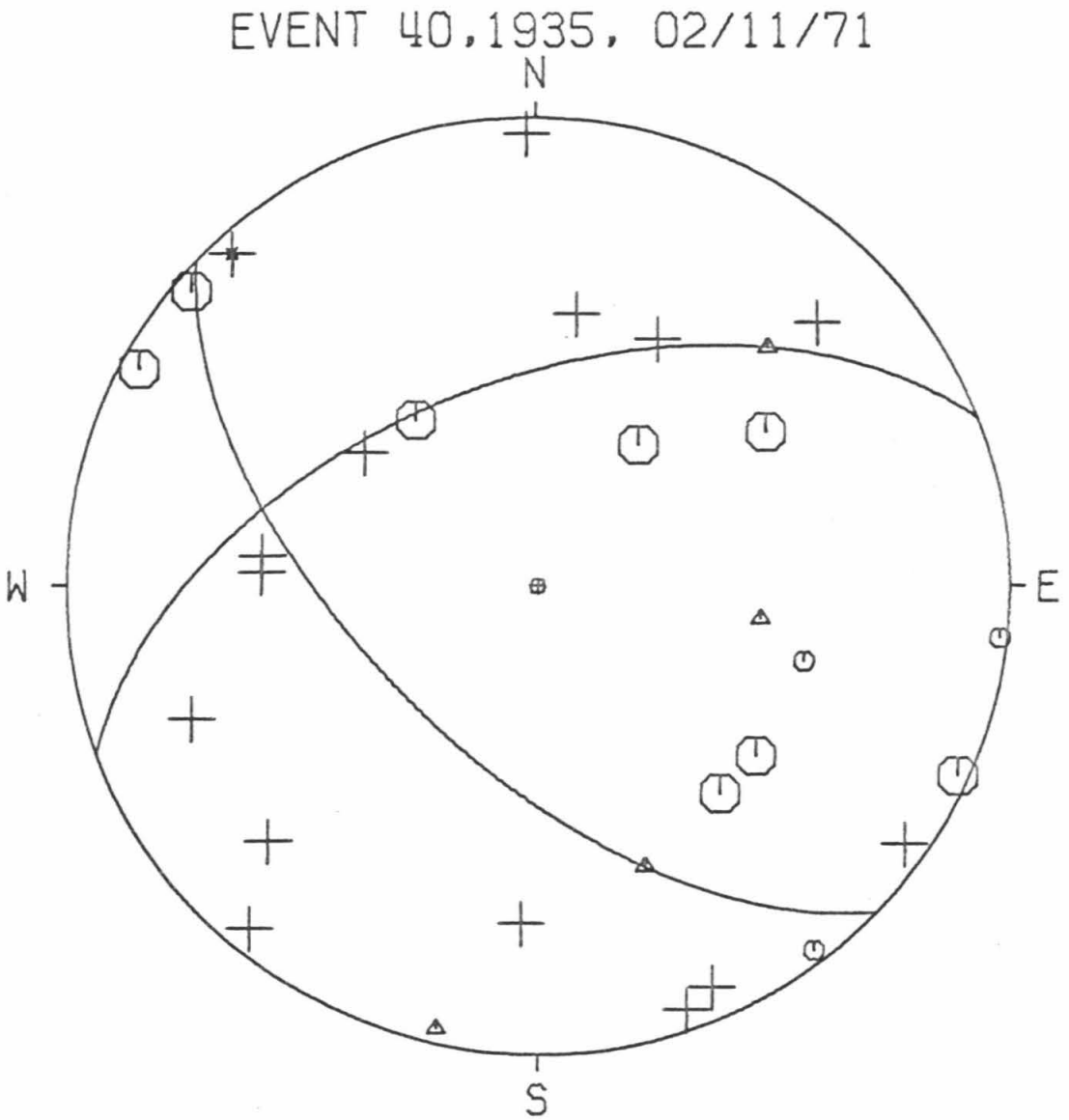
EVENT 40,1935, 02/11/71
N
W
E
S

EVENT DATA

41,2335 C 02/11/71 23 35 0.0

4.6 34.000 21.11 -118.000 20.21 3.7

AZ1= 42.000
DIP1= 32.000
AZ2= 252.000
DIP2= 61.580

SLIP VECTORS= 162.000 61.580 311.999 32.000

PRIN AXES = 194.210 20.579 330.802 74.745

STA	DIR	QUAL	DIST	EVAZ	TOA	X	Y
BAR	C	-2	2.172	139.704	48.550	0.940	-1.109
CLC	D	2	1.583	22.341	48.550	0.553	1.344
CSP	D	2	0.813	94.244	85.130	2.385	-0.177
CWC	D	2	2.094	5.722	48.550	0.145	1.446
GSC	D	1	1.577	52.615	48.550	1.155	0.883
ISA	D	2	1.164	354.949	80.346	-0.201	2.272
MWC	D	2	0.266	119.876	90.595	-2.156	1.239
PAS	D	2	0.246	146.205	90.943	-1.379	2.060
PLM	C	2	1.581	128.657	48.550	1.135	-0.908
PYR	D	2	0.399	303.055	89.271	-2.082	1.355
SBC	C	1	1.309	275.091	48.550	-1.448	0.129
SYP	C	2	1.368	277.897	48.550	-1.440	0.200
BOUQ	D	2	0.180	331.463	89.777	-1.192	2.192
BRWN	D	-2	0.222	251.468	91.493	2.339	0.784
IRON	D	2	0.069	312.671	108.439	1.520	-1.401
GOOK	D	2	0.124	291.760	95.228	2.214	-0.884
NAGM	D	2	0.144	5.038	92.028	-0.218	-2.446
NMLM	D	2	0.217	78.536	89.428	2.438	0.494
NRTM	D	2	0.257	16.811	90.696	-0.719	-2.379
NWSM	D	2	0.315	324.611	90.110	1.446	-2.036
ENGN	D	2	0.297	135.637	90.290	-1.744	1.783
SWM	D	1	0.418	330.956	89.075	-1.204	2.168
LSWM	D	1	0.387	335.018	89.391	-1.050	2.254
NSCF	C	2	0.101	23.399	98.770	-0.914	-2.112
NSGM	C	2	0.077	304.335	105.649	1.764	-1.205

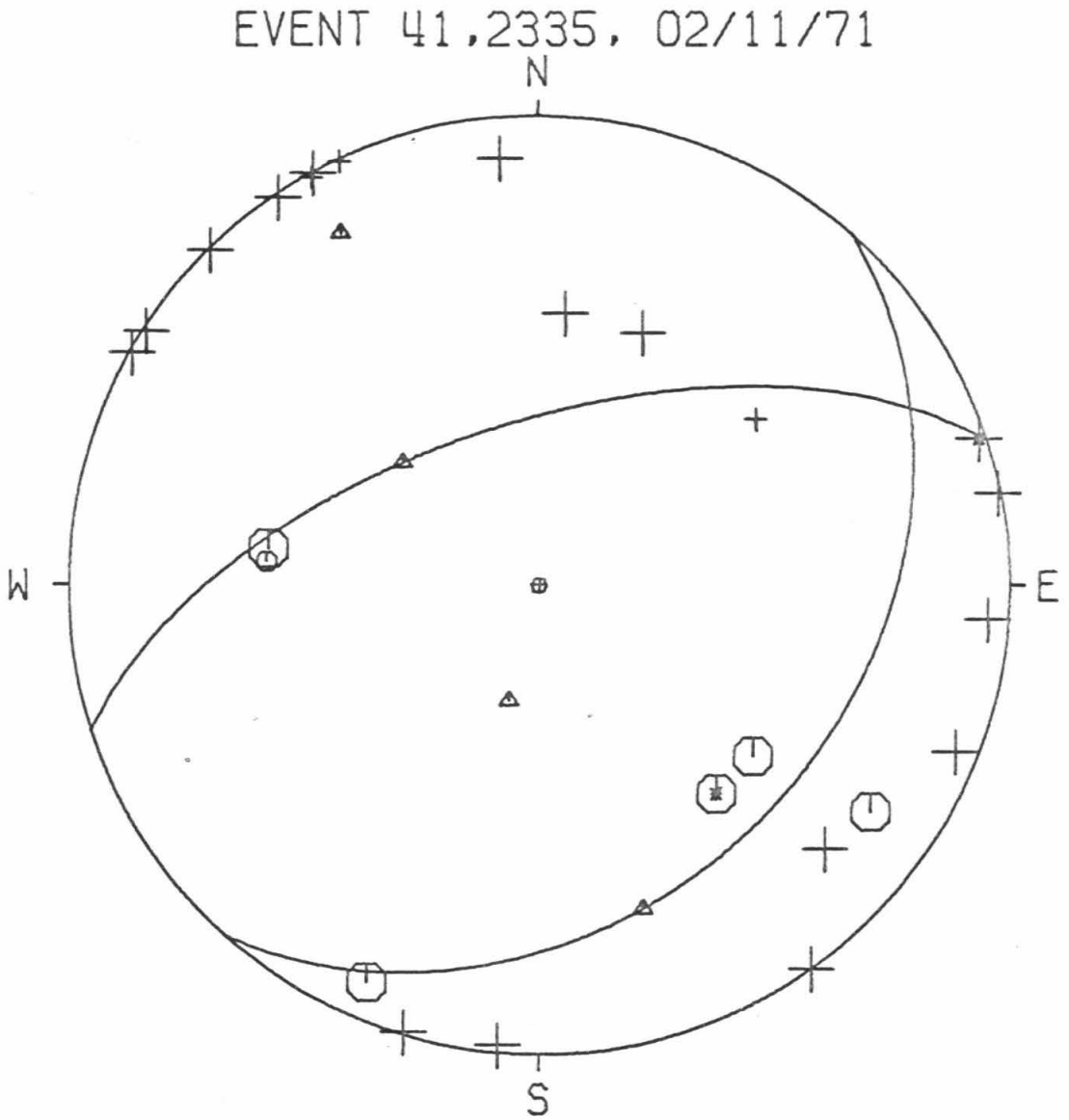
EVENT 41,2335, 02/11/71
N
W
E
S

EVENT DATA

42,0809 0 02/12/71 8 9 0.0

3.0 34.000 21.56 -118.000 21.28 3.2

AZ1= 159.000
DIP1= 80.000
AZ2= 69.000
DIP2= 90.000

SLIP VECTORS= 338.999 90.000 69.000 80.000

PRIN AXES = 23.561 82.947 114.439 82.947

STA	DIR	QUAL	DIST	EVAZ	TOA	X	Y
BAR	C	2	2.187	139.528	44.933	0.877	-1.028
CLC	D	2	1.582	22.928	44.933	0.526	1.244
CSP	C	2	0.828	94.423	83.569	2.349	-0.182
GSC	D	2	1.584	53.149	44.933	1.081	0.810
ISA	D	2	1.155	355.566	80.429	-0.176	2.276
MWC	C	2	0.282	119.390	88.803	2.155	-1.214
PAS	C	2	0.261	144.425	89.003	1.442	-2.016
PLM	C	2	1.597	128.527	44.933	1.057	-0.842
PYR	C	2	0.383	303.412	87.837	-2.047	1.350
SBC	C	2	1.294	274.885	44.933	-1.346	0.115
SYP	C	1	1.352	277.696	44.933	-1.339	0.181
BOUQ	C	-2	0.167	334.659	90.397	1.066	-2.252
IRON	C	2	0.052	317.129	116.859	1.259	-1.357
GOOK	C	2	0.108	292.698	96.988	2.162	-0.904
SOLE	D	2	0.082	352.074	101.888	0.307	-2.206
INDN	D	2	0.097	45.490	98.467	-1.646	-1.618
NAGM	D	2	0.140	11.351	92.914	-0.479	-2.388
NMLM	C	2	0.231	79.946	89.293	2.446	0.434
NRTM	D	2	0.254	20.530	89.069	0.870	2.322
NWSM	D	2	0.300	326.064	88.629	-1.379	2.049
ENGN	C	2	0.313	134.708	88.506	1.753	-1.736
LSWM	C	2	0.374	336.579	87.922	-0.976	2.252
NSCF	C	2	0.101	32.924	97.955	-1.261	-1.948
NSGM	C	1	0.063	309.184	106.968	1.631	-1.329

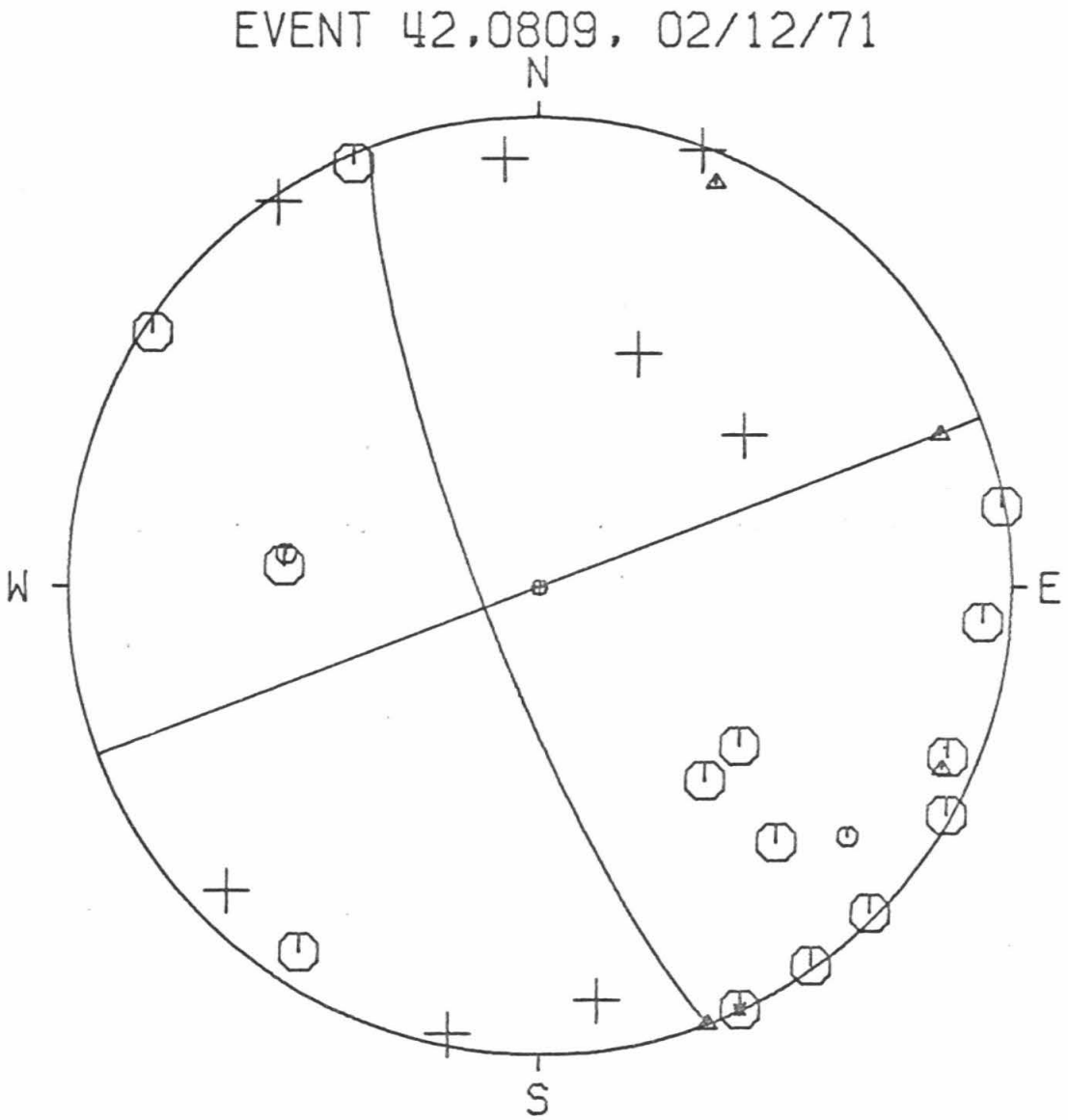
EVENT 42,0809, 02/12/71
N
W
E
S

EVENT DATA

43,0920 0 02/12/71 9 20 0.0

8.1 34.000 25.56 -118.000 25.73 3.3

AZ1= 241.000
DIP1= 25.000
AZ2= 355.000
DIP2= 79.260

SLIP VECTORS= 265.000 79.260 151.000 25.000

PRIN AXES = 239.529 39.411 103.495 59.397

STA	DIR	QUAL	DIST	EVAZ	TOA	X	Y
BAR	D	1	2.277	139.399	49.400	0.961	-1.122
CSP	D	2	0.896	98.216	92.185	-2.427	0.350
GSC	D	2	1.596	56.332	49.400	1.230	0.819
ISA	C	-2	1.086	358.164	89.844	-0.080	2.495
MWC	D	2	0.369	123.700	98.762	-1.915	1.277
PAS	D	2	0.351	142.589	99.000	-1.395	1.824
PLM	D	2	1.687	128.958	49.400	1.149	-0.929
PYR	D	2	0.297	299.544	99.724	1.983	-1.124
SBC	C	2	1.229	272.276	49.400	-1.476	0.059
SYP	C	2	1.284	275.184	49.400	-1.471	0.133
RVR	D	2	0.975	116.071	91.212	-2.222	1.087
BOUQ	C	-2	0.088	353.439	126.172	0.183	-1.590
BRWN	D	2	0.192	224.469	106.692	1.479	1.506
IRON	C	2	0.056	152.643	139.844	-0.558	1.078
GOOK	D	2	0.066	216.078	135.260	0.792	1.088
SOLE	C	2	0.063	53.123	136.707	-1.043	-0.783
INDN	C	2	0.137	107.919	113.976	-1.833	0.593
NAGM	C	2	0.115	50.320	118.416	-1.393	-1.156
NMLM	D	2	0.292	99.013	99.786	-2.250	0.357
NRTM	C	2	0.230	40.832	102.975	-1.439	-1.666
NWSM	D	2	0.212	329.921	104.705	1.082	-1.869
ENGN	D	2	0.403	135.302	98.303	-1.627	1.644
LGCR	D	2	0.470	319.476	97.440	1.516	-1.773
LSWM	D	2	0.291	342.490	99.804	0.685	-2.172
NSCF	C	2	0.122	72.203	117.062	-1.757	-0.564
NSHC	C	2	0.103	31.759	121.412	-0.911	-1.471
NSGM	C	1	0.056	166.740	139.844	-0.278	1.181

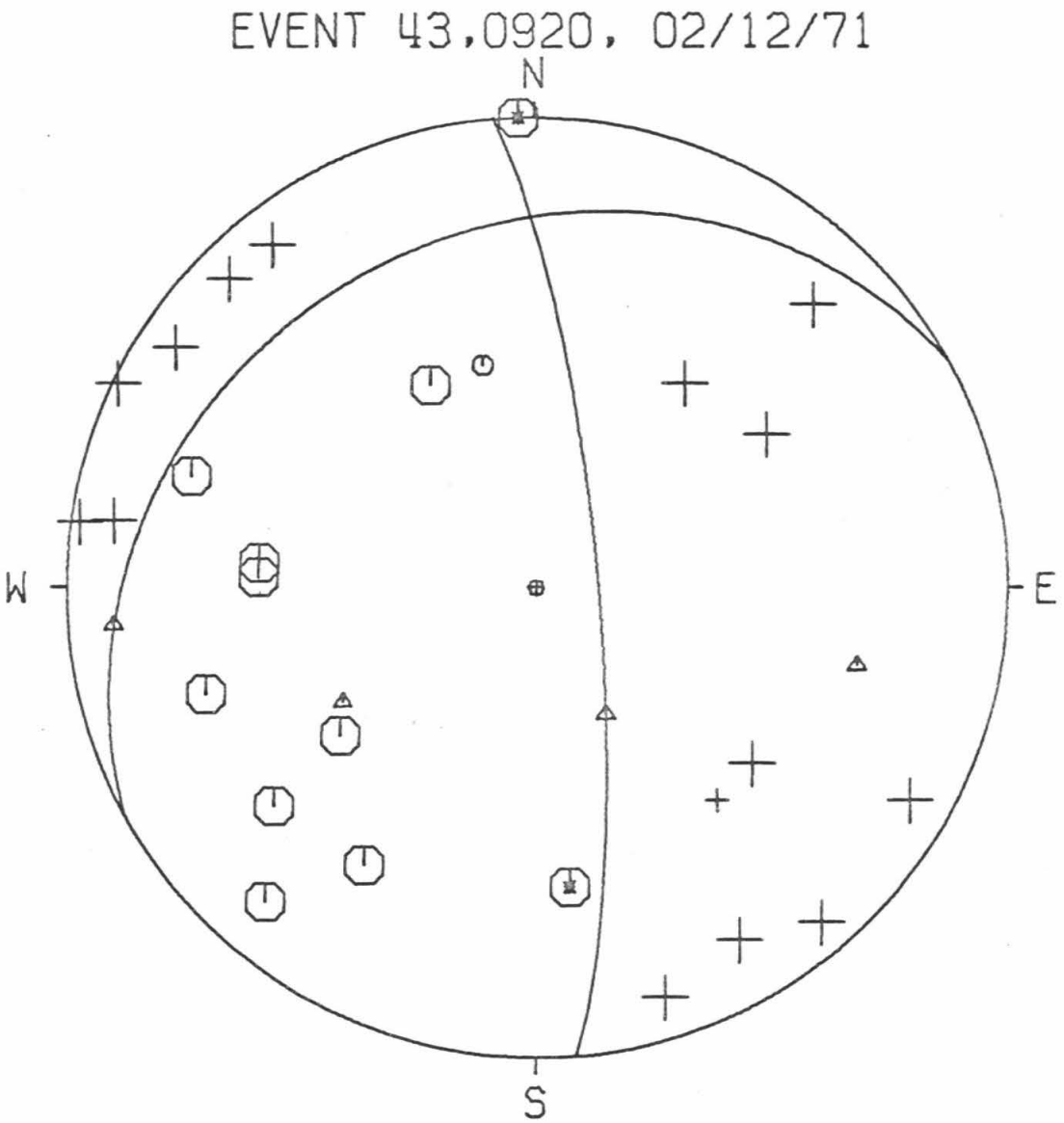
EVENT 43,0920, 02/12/71
N
W
E
S

EVENT DATA

44,0952 0 02/12/71 9 52 0.0

3.0 34.000 21.55 -118.000 27.18 3.4

AZ1= 354.000
DIP1= 80.000
AZ2= 90.000
DIP2= 59.340

SLIP VECTORS= 359.999 59.340 264.000 80.000

PRIN AXES = 307.711 61.094 45.479 76.243

STA	DIR	QUAL	DIST	EVAZ	TOA	X	Y
BAR	C	2	2.240	137.888	44.933	0.906	-1.002
CLC	C	2	1.615	25.530	44.933	0.582	1.219
CSP	C	2	0.909	93.998	82.791	2.332	-0.163
GSC	C	2	1.650	54.791	44.933	1.104	0.779
ISA	D	-2	1.152	359.138	80.464	-0.034	2.283
MWC	D	2	0.355	112.889	88.102	2.265	-0.956
PAS	D	-2	0.315	132.261	88.482	1.826	-1.659
PLM	C	2	1.662	126.719	44.933	1.083	-0.808
PYR	D	2	0.317	311.308	88.465	-1.853	1.628
SBC	D	2	1.213	275.068	50.440	-1.501	0.133
SYP	D	2	1.272	278.131	44.933	-1.338	0.191
RVR	C	2	0.966	111.927	82.248	2.157	-0.868
BOUQ	C	2	0.151	3.744	91.521	-0.161	-2.461
BRWN	D	1	0.134	238.471	93.652	2.062	1.265
IRON	C	2	0.059	50.336	108.307	-1.594	-1.322
GOOK	D	2	0.044	335.044	122.304	0.720	-1.547
SOLE	C	2	0.107	41.080	97.224	-1.536	-1.762
INDN	C	2	0.166	65.304	90.434	-2.263	-1.041
NAGM	C	2	0.175	38.485	90.145	-1.554	-1.954
NMLM	C	2	0.311	82.795	88.524	2.448	0.309
NRTM	C	2	0.293	35.550	88.698	1.437	2.011
NWSM	D	2	0.264	340.890	88.975	-0.811	2.341
ENGN	D	-2	0.375	125.846	87.912	1.989	-1.437
LGOR	D	2	0.511	325.977	86.611	-1.357	2.010
LSWM	D	1	0.349	348.849	88.155	-0.476	2.413
NSGM	C	2	0.052	38.817	116.859	-1.160	-1.442

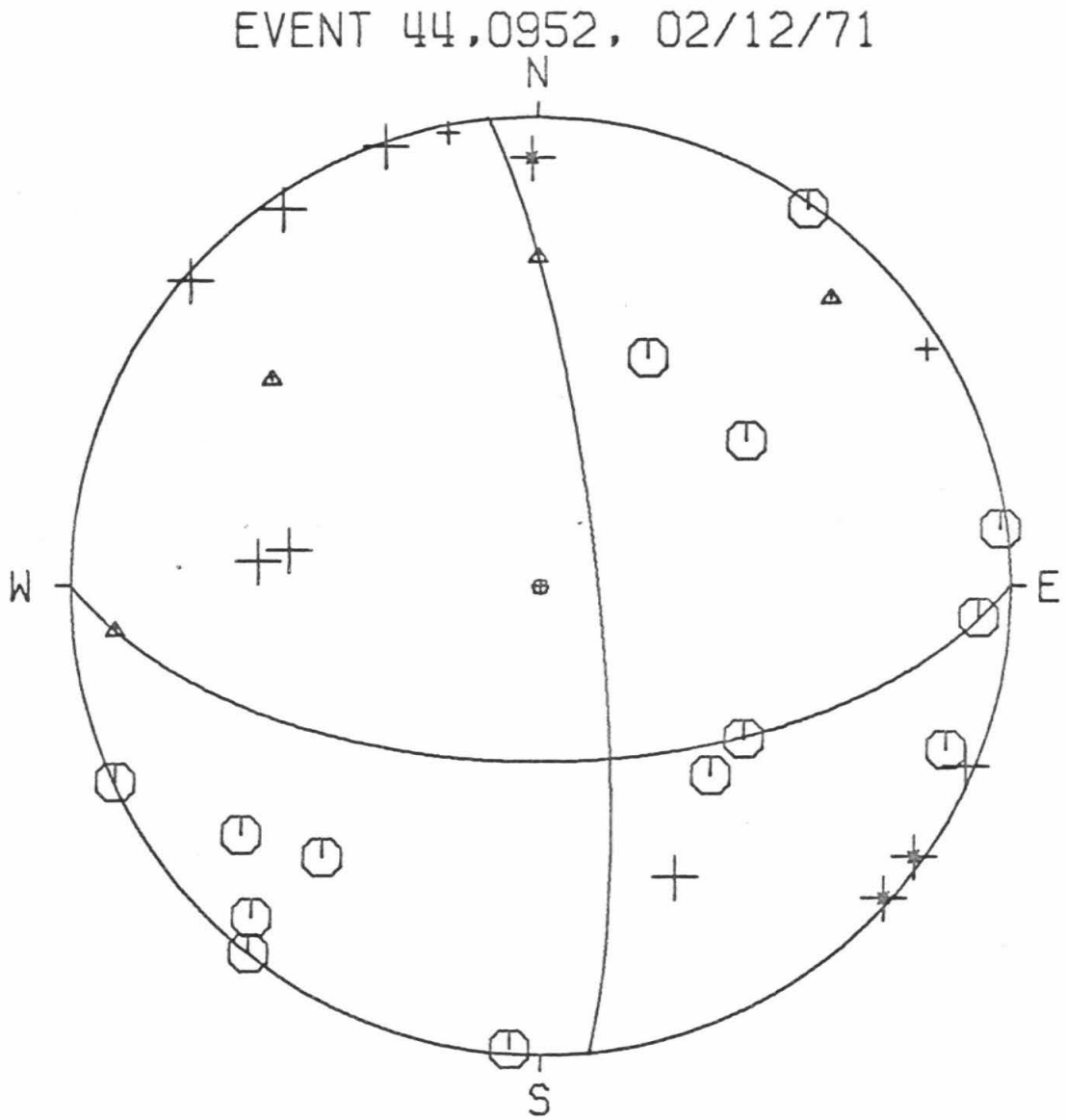
EVENT 44,0952, 02/12/71
N
W
E
S

EVENT DATA

45,1502 0 02/12/71 15 2 0.0

9.5 34.000 24.41 -118.000 25.86 3.4

AZ1= 96.000
DIP1= 35.000
AZ2= 264.500
DIP2= 55.544

SLIP VECTORS= 174.500 55.544 6.000 35.000

PRIN AXES = 150.968 11.684 359.214 79.679

STA	DIR	QUAL	DIST	EVAZ	TCA	X	Y
CLC	D	2	1.564	25.692	49.400	0.641	1.331
CSP	D	2	0.895	97.030	92.922	-2.417	0.298
GSC	C	1	1.608	55.804	49.400	1.222	0.830
ISA	D	2	1.105	358.274	89.559	-0.075	2.489
MWC	D	2	0.360	121.042	100.825	-1.930	1.162
PAS	D	2	0.337	140.316	101.463	-1.429	1.722
PLM	C	2	1.676	128.408	49.400	1.158	-0.918
PYR	D	2	0.305	302.675	102.337	1.866	-1.197
SBC		-1	1.228	272.691	49.400	-1.476	0.069
SYP	C	1	1.284	275.945	49.400	-1.469	0.153
RVR	C	2	0.968	115.002	92.010	-2.226	1.038
BOUQ	D	2	0.107	355.530	125.057	0.127	-1.626
BRWN	D	-2	0.178	228.115	111.853	1.475	1.322
IRON	C	2	0.044	141.528	150.592	-0.558	0.703
GOOK	C	2	0.056	221.165	144.011	0.719	0.822
SOLE	C	2	0.069	49.165	138.350	-0.951	-0.822
INDN	C	-2	0.138	72.704	118.086	-1.736	-0.541
NRTM	D	2	0.245	38.429	104.797	-1.341	-1.690
NWSM	D	2	0.227	332.621	106.640	0.971	-1.875
ENGN	D	2	0.391	133.101	99.995	-1.659	1.553
SWM	D	2	0.336	338.057	101.494	0.836	-2.075
LGOR	D	2	0.484	321.107	98.069	1.455	-1.804
LSWM	D	2	0.308	343.869	102.233	0.617	-2.132
NSHC	C	2	0.120	27.686	121.818	-0.799	-1.522
NSGM	D	2	0.040	158.280	153.250	-0.303	0.760

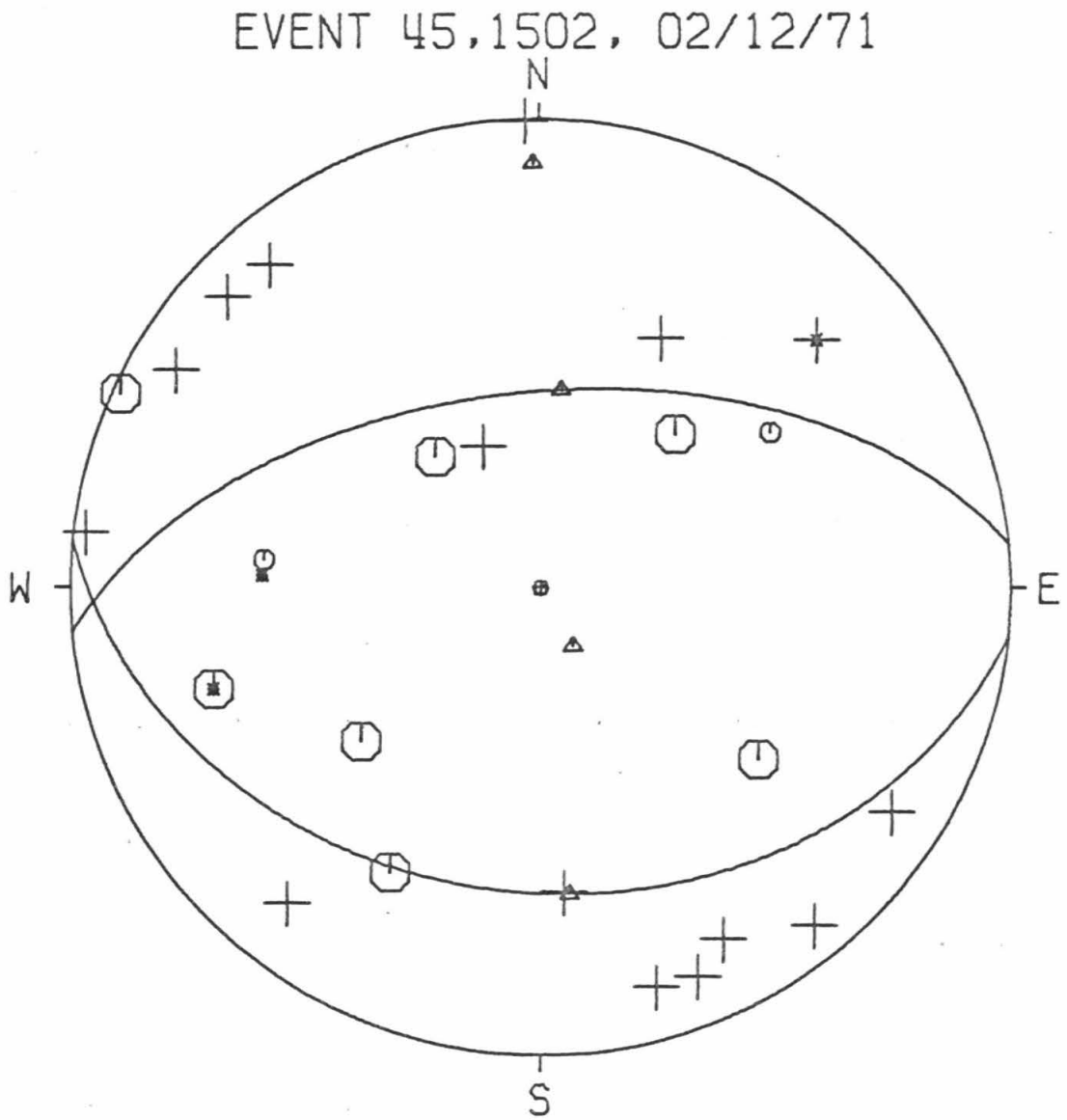
EVENT 45,1502, 02/12/71
N
W
E
S

EVENT DATA

46,1622 0 02/12/71 16 22 0.0

9.2 34.000 24.77 -118.000 25.50 3.9

AZ1= 108.000
DIP1= 50.000
AZ2= 288.000
DIP2= 40.000

SLIP VECTORS= 198.000 40.000 18.000 50.000

PRIN AXES = 17.975 5.007 197.999 85.000

STA	DIR	QUAL	DIST	EVAZ	TOA	X	Y
BAR	C	2	2.265	139.245	49.400	0.964	-1.119
CLC	D	2	1.557	25.628	49.400	0.639	1.332
CWC	C	2	2.042	7.878	49.400	0.202	1.463
GSC	C	2	1.601	55.883	49.400	1.223	0.829
HFD	C	2	2.420	106.166	49.400	1.419	-0.411
ISA	D	2	1.099	358.038	90.227	0.085	-2.494
MWC	D	2	0.359	122.134	100.447	-1.915	1.203
PAS	D	2	0.339	141.643	100.934	-1.397	1.765
PLM	C	2	1.676	128.674	49.400	1.153	-0.923
PYR	D	2	0.305	301.104	101.739	1.910	-1.153
SBC	C	2	1.233	272.467	49.400	-1.476	0.064
SYP	C	2	1.288	275.625	49.400	-1.470	0.145
RVR	C	2	0.966	115.442	91.882	-2.220	1.056
BOUQ	D	2	0.099	352.292	126.426	0.214	-1.579
BRWN	D	2	0.185	228.187	110.361	1.505	1.346
IRON	C	2	0.040	145.255	152.529	-0.478	0.690
GOOK	C	2	0.059	224.776	141.511	0.821	0.827
SOLE	C	2	0.063	48.538	140.070	-0.905	-0.799
INDN	C	2	0.133	73.510	118.329	-1.738	-0.514
NRTM	D	2	0.237	38.300	104.857	-1.336	-1.692
NWSM	D	2	0.225	330.839	106.179	1.035	-1.854
ENGN	D	2	0.392	134.235	99.655	-1.634	1.591
SWM	C	1	0.332	336.844	101.102	0.883	-2.065
PACP	C	2	0.379	193.926	99.949	0.547	2.207
NSCF	C	2	0.120	69.826	120.869	-1.637	-0.602
NSGM	C	-1	0.044	167.372	149.819	-0.201	0.898

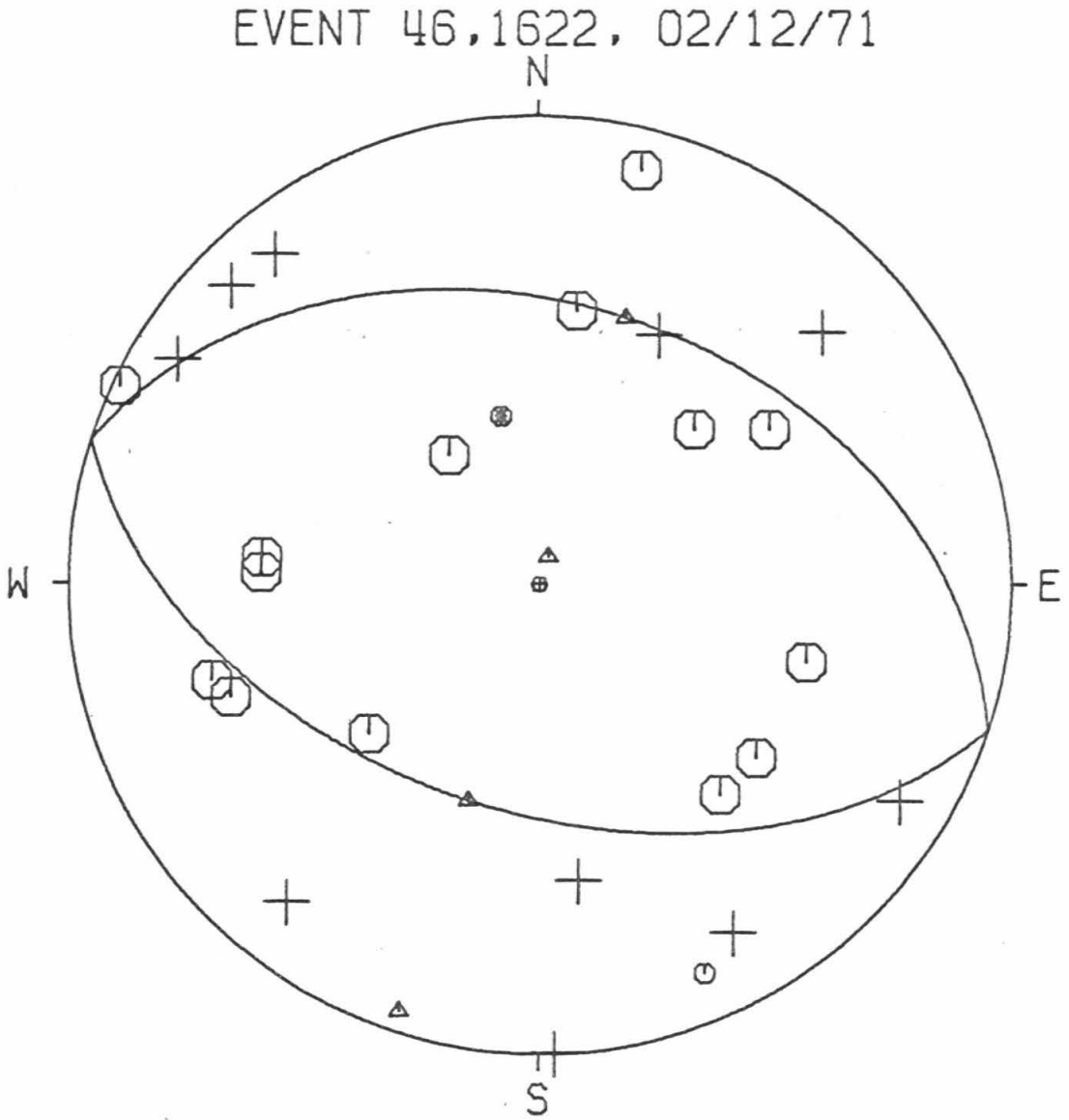
EVENT 46,1622, 02/12/71
N
W
E
S

EVENT DATA

47,0644 C 02/13/71 6 44 54.8

3.0 34.000 19.64 -118.000 32.80 3.2

AZ1= 301.000
DIP1= 51.000
AZ2= 121.000
DIP2= 39.000

SLIP VECTORS= 31.000 39.000 211.000 51.000

PRIN AXES = 210.968 6.005 30.999 84.000

STA	DIR	QUAL	DIST	EVAZ	TCA	X	Y
BAR	C	2	2.270	135.846	44.933	0.941	-0.969
CLC	D	2	1.678	27.396	44.933	0.622	1.200
CSP	C	2	0.985	92.200	82.062	2.319	-0.089
GSC	C	2	1.732	55.354	44.933	1.112	0.768
HFD	C	2	2.496	103.572	44.933	1.313	-0.317
ISA	D	2	1.184	2.486	80.149	0.099	2.274
MWC	C	2	0.419	104.900	87.491	2.362	-0.629
PAS	C	2	0.360	120.217	88.055	2.123	-1.237
PLM	C	2	1.706	124.254	44.933	1.117	-0.760
SBC	C	2	1.139	277.253	80.585	-2.268	0.289
SYP	C	2	1.200	280.038	80.001	-2.238	0.396
BOUQ	D	2	0.203	25.472	89.562	1.071	2.248
BRWN	D	2	0.063	216.061	106.968	1.238	1.701
IRON	D	2	0.140	61.679	92.914	-2.144	-1.156
GOOK	D	2	0.088	41.648	100.128	-1.508	-1.696
SOLE	D	2	0.185	53.027	89.836	1.994	1.501
INDN	D	-2	0.248	66.781	89.129	2.280	0.978
NAGM	D	2	0.250	48.043	89.106	1.845	1.658
NMLM	D	2	0.392	80.152	87.750	2.414	0.419
NRTM	D	2	0.367	42.413	87.987	1.656	1.813
NWSM	D	2	0.280	358.130	88.816	-0.081	2.473
ENGN	C	2	0.425	116.077	87.433	2.195	-1.074
PACP	D	2	0.283	178.044	88.790	0.084	-2.472
INGL	C	2	0.366	152.426	87.993	1.137	-2.177
LGOR	D	2	0.500	335.350	86.711	-1.012	2.206
LSWM	D	2	0.374	1.468	87.917	0.063	2.453
LMER	D	2	0.452	67.659	87.168	2.254	0.927
NSGM	D	2	0.128	59.324	94.423	-2.066	-1.225

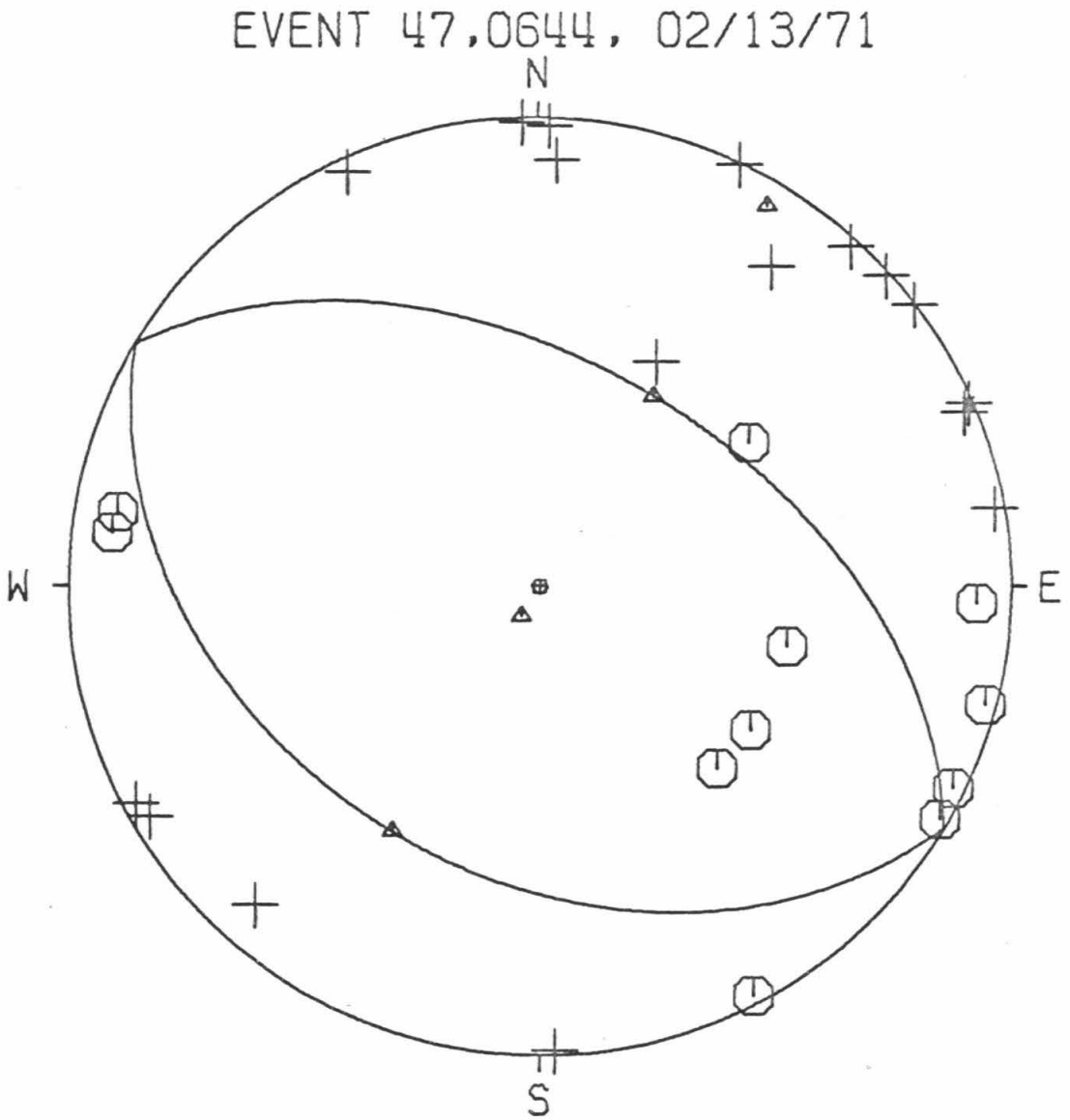
EVENT 47,0644, 02/13/71
N
W
E
S

EVENT DATA

48,0338 0 02/14/71 3 38 0.0

9.4 34.000 23.86 -118.000 23.03 3.3

AZ1= 150.000
DIP1= 50.000
AZ2= 271.000
DIP2= 58.458

SLIP VECTORS= 181.000 58.458 60.000 50.000

PRIN AXES = 125.881 34.471 28.773 85.146

STA	DIR	QUAL	DIST	EVAZ	TOA	X	Y
CLC	D	1	1.556	24.277	49.400	0.607	1.347
CSP	D	2	0.855	96.803	93.367	-2.408	0.287
GSC	C	2	1.582	54.755	49.400	1.207	0.853
ISA	C	2	1.115	356.518	89.427	-0.151	2.483
MWC	D	2	0.322	123.120	101.687	-1.870	1.220
PAS	D	2	0.306	144.874	102.109	-1.279	1.818
PYR	D	2	0.343	300.473	101.150	1.935	-1.139
RVR	D	2	0.929	115.510	92.451	-2.208	1.053
SBC	C	2	1.268	273.284	49.400	-1.475	0.085
SYP	C	2	1.324	276.185	49.400	-1.469	0.159
BOUQ	C	2	0.124	337.493	120.842	0.668	-1.612
BRWN	C	2	0.204	237.427	108.882	1.733	1.107
IRON	C	2	0.028	204.323	160.213	0.250	0.554
GOOK	C	2	0.082	248.470	132.757	1.318	0.520
SOLE	C	2	0.048	15.349	147.915	-0.259	-0.942
NAGM	C	2	0.114	26.997	123.038	-0.765	-1.502
NMLM	D	2	0.253	95.864	103.797	-2.170	0.223
NRTM	C	2	0.232	29.251	105.948	-1.040	-1.858
NWSM	D	2	0.256	325.862	103.547	1.228	-1.811
ENGN	D	2	0.357	136.370	100.771	-1.555	1.632
NSCF	C	2	0.095	56.265	128.395	-1.280	-0.855
NSHC	C	2	0.115	8.436	122.635	-0.249	-1.679
NSGM	C	2	0.048	210.238	147.915	0.492	0.844

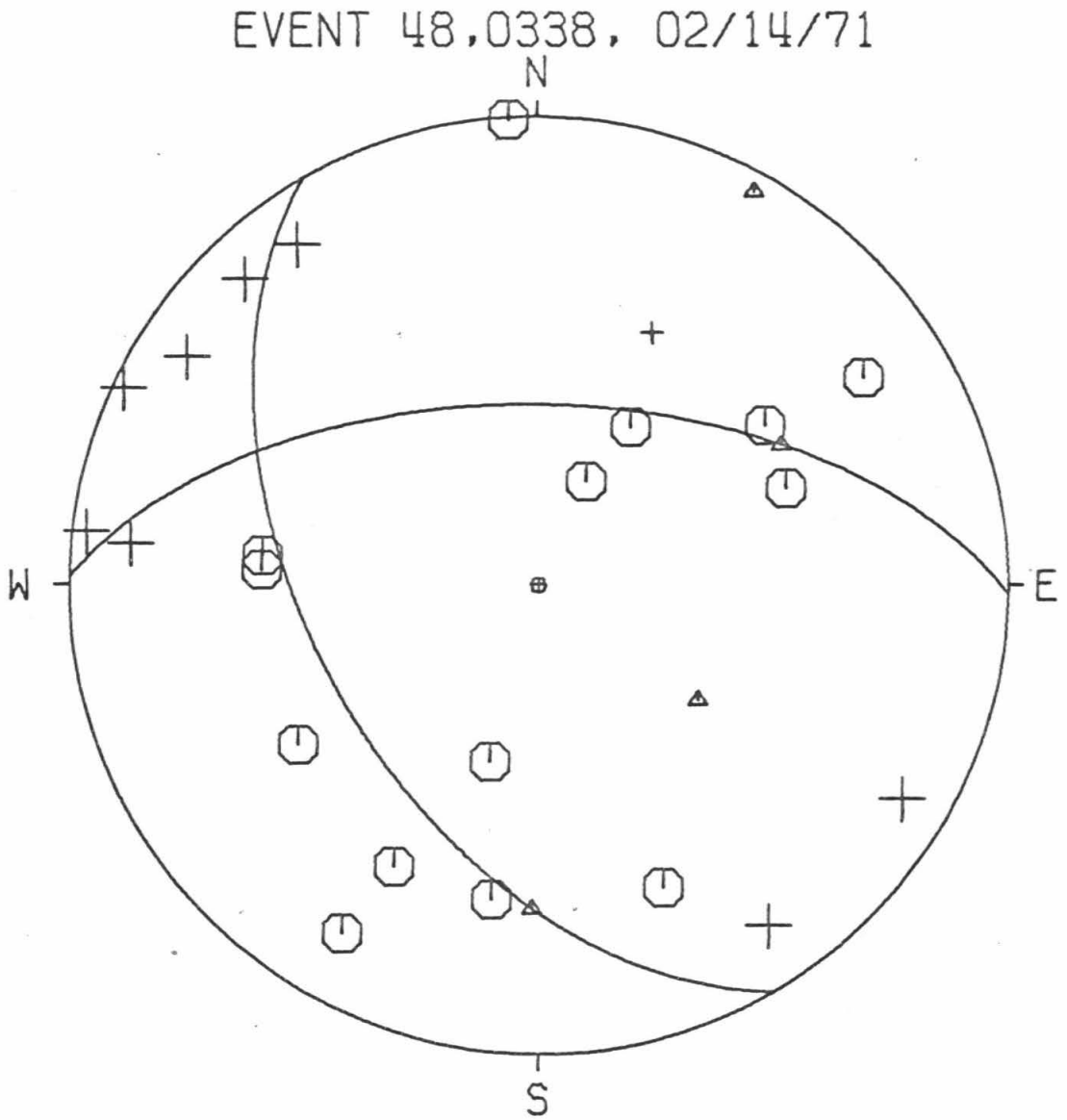
EVENT 48,0338, 02/14/71
N
W
E
S

EVENT DATA

49,1344 C 02/14/71 13 44 0.C

3.0 34.000 17.97 -118.000 30.67 3.8

AZ1= 202.000
DIP1= 62.000
AZ2= 292.000
DIP2= 90.000

SLIP VECTORS= 202.000 90.000 112.000 62.000

PRIN AXES = 160.557 70.612 63.441 70.612

STA	DIR	QUAL	DIST	EVAZ	TCA	X	Y
BAR	D	2	2.230	135.913	44.933	0.940	-0.970
CLC	C	2	1.690	26.101	44.933	0.594	1.213
CSP	C	2	0.956	87.907	82.344	2.326	0.085
CWC	C	2	2.164	9.289	44.933	0.218	1.333
GSC	C	2	1.724	54.056	44.933	1.094	0.793
HFD	C	1	2.461	103.130	44.933	1.316	-0.307
ISA	C	2	1.211	1.202	50.440	0.032	1.506
MWC	C	2	0.385	102.668	87.818	2.392	-0.538
PAS	D	2	0.321	118.628	88.429	2.164	-1.181
PLM	D	2	1.667	124.063	44.933	1.119	-0.757
PYR	D	2	0.330	324.784	88.343	-1.421	2.013
SBC	C	2	1.172	278.687	80.268	-2.253	0.344
SYP	C	2	1.234	281.123	50.436	-1.478	0.291
BOUQ	D	-2	0.219	15.300	89.402	0.656	2.399
BRWN	C	1	0.077	239.750	103.149	1.898	1.107
IRON	C	-2	0.131	45.636	94.033	-1.723	-1.685
GOOK	D	2	0.099	17.330	98.208	-0.689	-2.210
SOLE	C	-2	0.182	40.357	89.903	1.618	1.903
NAGM	C	2	0.251	38.656	89.099	1.549	1.937
NMLM	C	2	0.370	74.763	87.962	2.369	0.645
NRTM	C	2	0.370	36.130	87.957	1.448	1.983
NWSM	D	2	0.311	352.905	88.524	-0.305	2.449
FNGN	D	-2	0.387	114.569	87.793	2.229	-1.019
PACP	D	2	0.257	184.411	89.040	-0.191	-2.472
INGL	D	2	0.329	154.810	88.349	1.049	-2.229
LGOR	D	2	0.538	333.781	86.346	-1.069	2.170
LSWM	D	2	0.403	357.208	87.641	-0.119	2.445
LMER	C	2	0.438	62.709	87.307	2.169	1.119
NSHC	C	2	0.244	30.043	89.167	1.243	2.148
NSGM	C	2	0.124	40.930	95.026	-1.564	-1.804

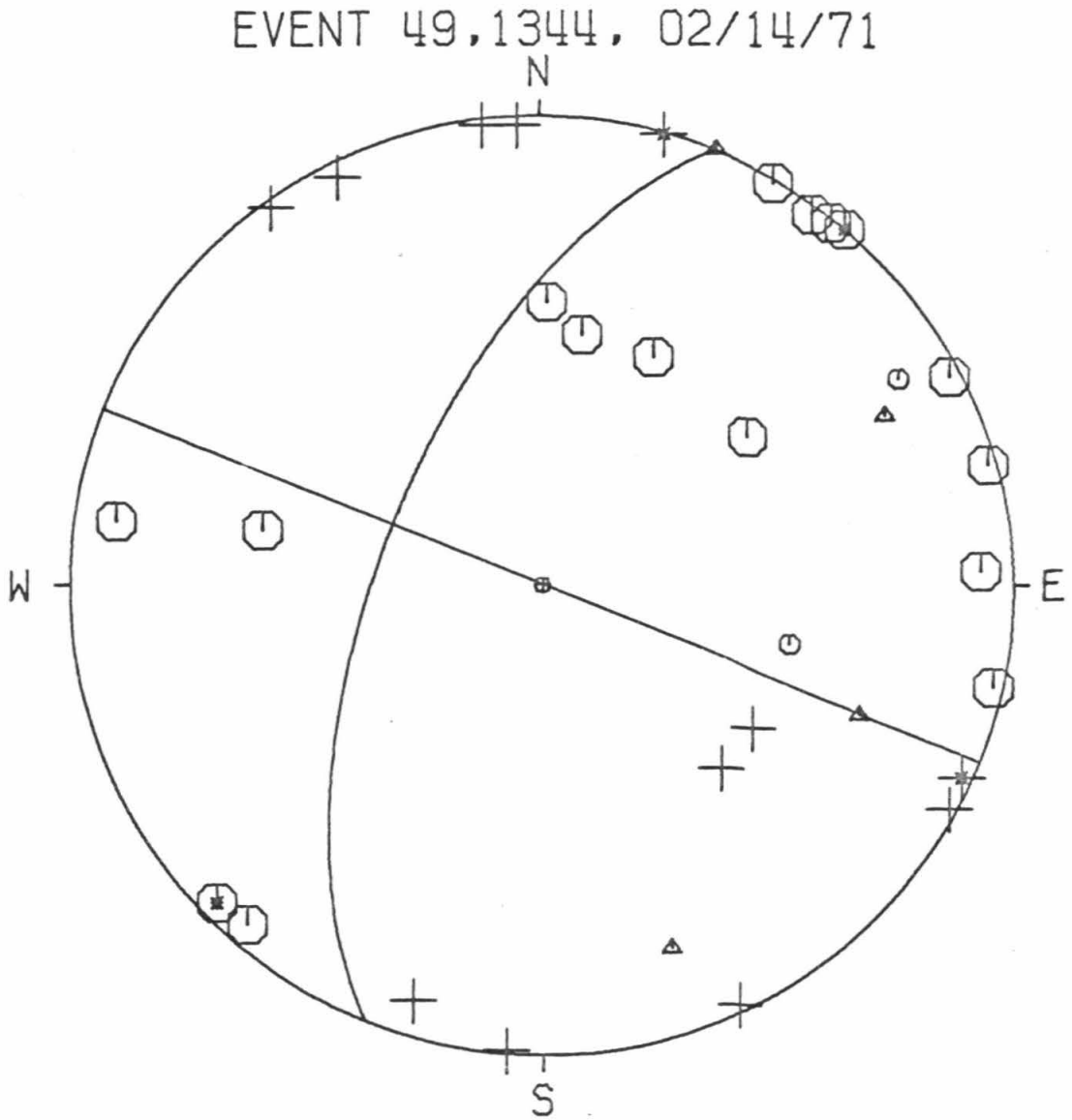
EVENT 49,1344, 02/14/71
N
W
E
S

EVENT DATA

50,0804 0 02/15/71 8 4 0.0

12.9 34.000 28.27 -118.000 24.63 3.9

AZ1= 82.000
DIP1= 40.000
AZ2= 279.500
DIP2= 51.331

SLIP VECTORS= 189.500 51.331 351.999 40.000

PRIN AXES = 238.521 10.429 1.604 84.269

STA	DIR	QUAL	DIST.	EVAZ	TCA	X	Y
BAR	D	2	2.302	140.424	49.445	0.942	-1.140
CLC	D	2	1.499	26.180	49.445	0.652	1.327
CSP	D	-2	0.888	101.061	95.139	-2.341	0.458
CWC	D	2	1.982	7.773	49.445	0.200	1.465
GSC	D	2	1.559	57.411	49.445	1.246	0.796
ISA	D	2	1.041	357.362	92.985	0.112	-2.431
MWC	D	2	0.384	130.472	104.477	-1.647	1.405
PAS	D	2	0.379	148.488	104.686	-1.129	1.841
PLM	C	2	1.704	130.461	49.445	1.125	-0.960
PYR	D	2	0.291	290.305	109.416	1.916	-0.709
SBC	C	2	1.245	267.730	49.445	-1.477	-0.059
SYP	C	2	1.296	273.247	49.445	-1.476	0.084
TIN	C	1	2.583	3.236	49.445	0.083	1.476
USC	D	2	0.468	167.542	101.382	-0.483	2.187
BOUQ	C	2	0.052	331.131	154.604	0.375	-0.681
BRWN	D	-2	0.234	219.714	113.642	1.236	1.488
IRON	C	2	0.086	172.986	141.569	-0.142	1.155
GOOK	C	2	0.105	210.941	136.178	0.678	1.132
SCLE	C	1	0.059	144.020	151.499	-0.511	0.704
NAGM	C	2	0.084	61.290	142.317	-1.001	-0.548
NMLM	C	2	0.286	107.136	109.735	-1.944	0.599
NRTM	C	2	0.187	46.395	119.590	-1.288	-1.227
NWSM	C	2	0.185	318.830	119.858	1.166	-1.334
ENGN	D	2	0.426	140.880	102.576	-1.395	1.715
NSCF	D	2	0.108	111.321	135.104	-1.258	0.491
NSHC	C	2	0.059	41.009	151.499	-0.571	-0.657
NSGM	C	2	0.093	181.451	139.653	0.031	1.219

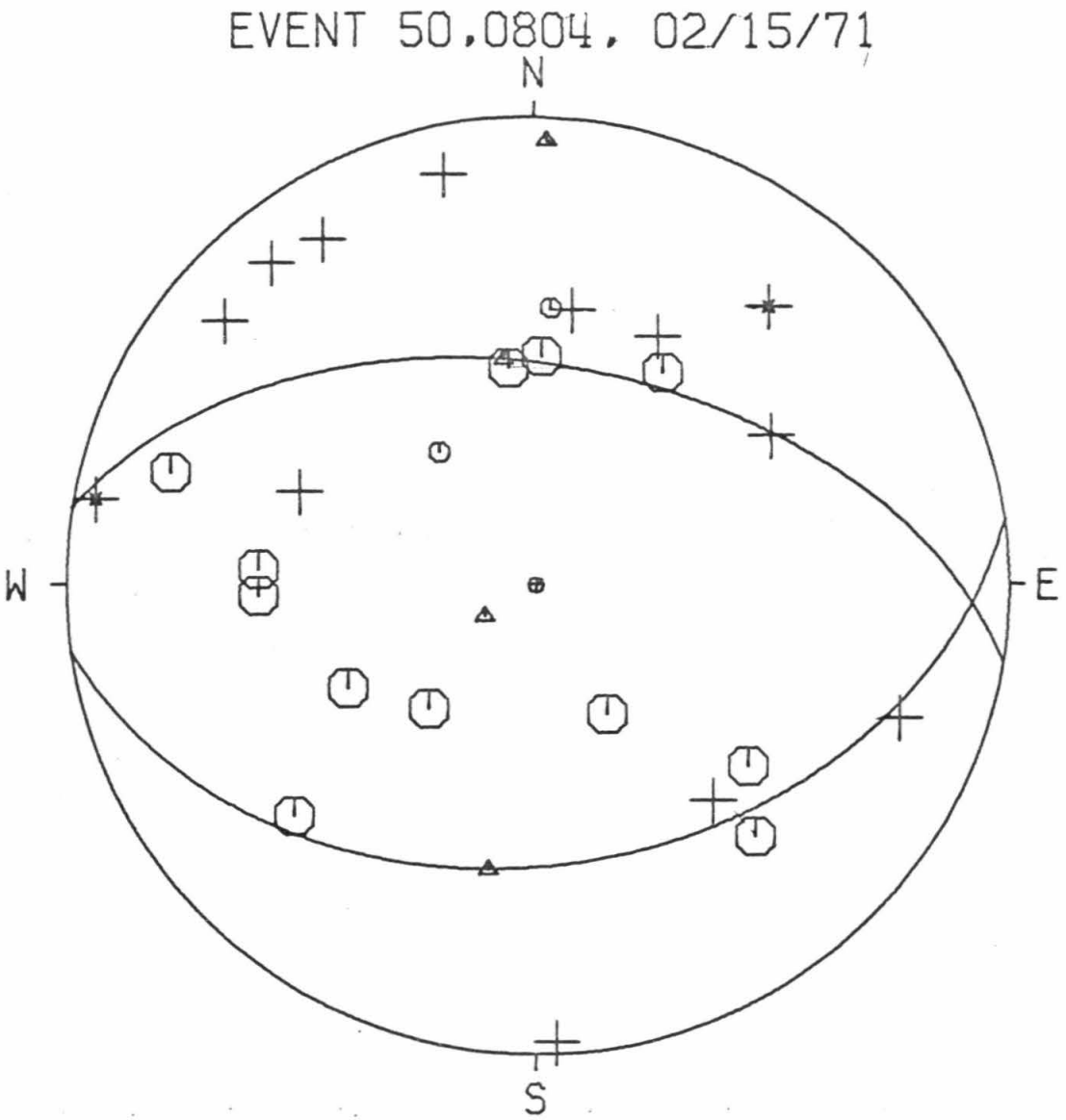
EVENT 50.0804, 02/15/71
N
W
E
S

EVENT DATA

51,0846 0 02/15/71 8 46 0.0

7.9 34.000 24.42 -118.000 26.48 3.4

AZ1= 134.500
DIP1= 73.000
AZ2= 227.000
DIP2= 81.880

SLIP VECTORS= 137.000 81.880 44.500 73.000

PRIN AXES = 91.805 72.145 359.801 83.866

STA	DIR	QUAL	DIST	FVAZ	TCA	X	Y
CLC	D	2	1.568	25.969	49.375	0.647	1.328
CSP	C	2	0.904	96.849	91.810	-2.443	0.293
GSC	C	1	1.615	55.976	49.375	1.224	0.826
ISA	D	2	1.104	358.665	89.349	-0.058	2.485
MWC	C	2	0.367	120.256	98.384	-1.996	1.164
PAS	D	1	0.342	139.163	98.695	-1.506	1.743
PLM	C	2	1.683	128.224	49.375	1.160	-0.914
PYR	C	2	0.297	303.365	99.251	1.913	-1.260
SYP	C	2	1.275	275.948	49.375	-1.469	0.153
USC	D	2	0.413	162.147	97.824	-0.712	2.212
BCUQ	D	2	0.105	0.123	120.441	-0.004	-1.756
BRWN	C	-2	0.171	226.368	108.416	1.497	1.427
IRON	D	2	0.044	125.392	146.728	-0.825	0.586
GOOK	C	2	0.044	219.756	146.728	0.647	0.778
SOLE	C	2	0.071	57.842	132.226	-1.212	-0.762
INDN	C	2	0.145	75.519	111.965	-1.915	-0.495
NMLM	C	2	0.300	95.105	99.211	-2.282	0.204
NRTM	D	2	0.249	40.080	100.538	-1.455	-1.729
NWSM	D	2	0.224	334.599	102.970	0.944	-1.989
ENGN	C	2	0.398	132.282	98.014	-1.716	1.560
NSCF	D	2	0.134	70.472	114.251	-1.809	-0.641
NSHC	D	2	0.124	31.439	116.420	-0.971	-1.589
NSGM	D	2	0.044	148.393	146.728	-0.530	0.862

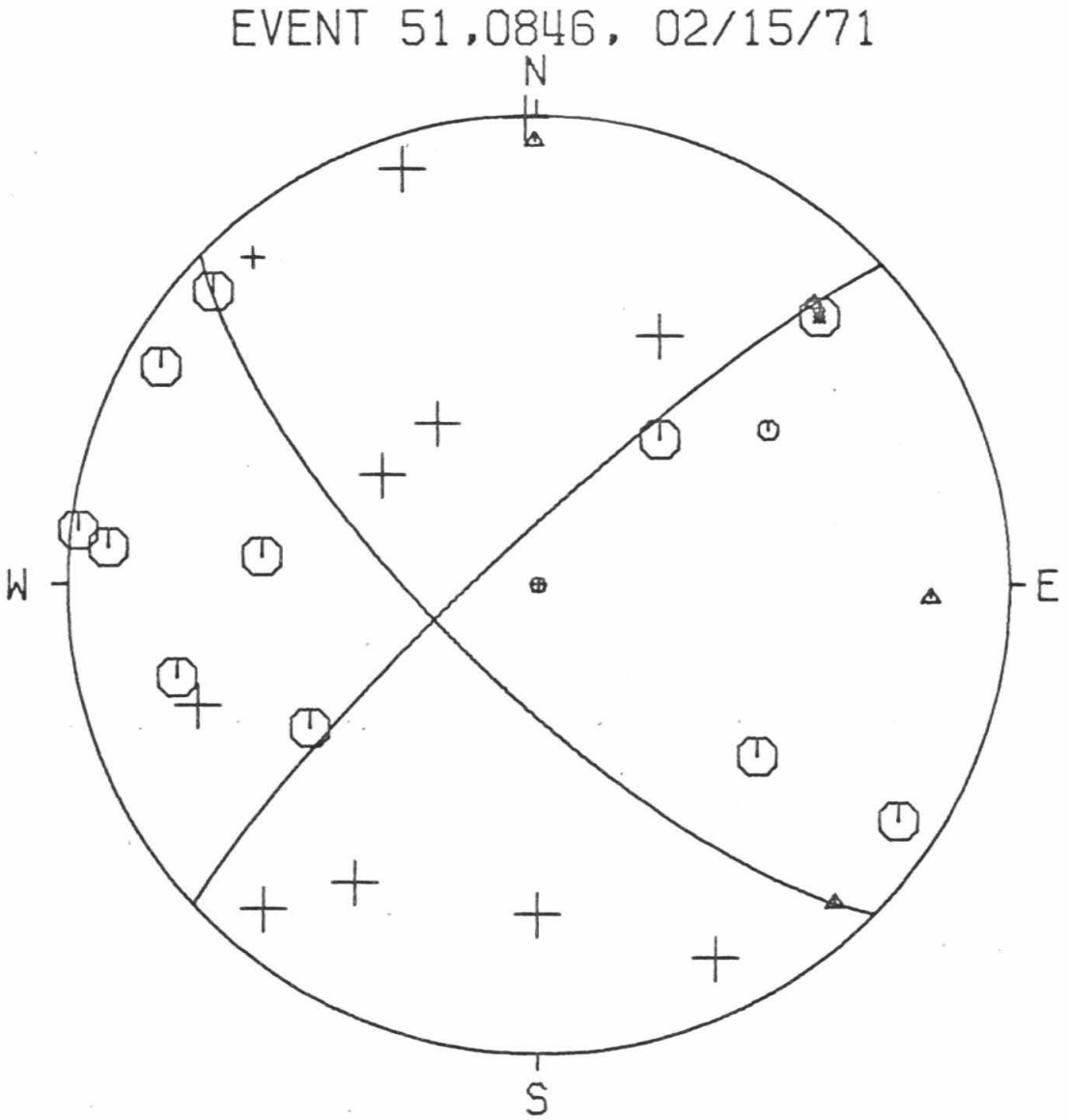
EVENT 51,0846, 02/15/71
N
W
E
S

EVENT DATA

52,1303 0 02/15/71 13 3 0.0

9.7 34.000 25.65 -118.000 26.12 3.4

AZ1= 86.500
DIP1= 46.000
AZ2= 246.500
DIP2= 45.782

SLIP VECTORS= 156.500 45.782 356.499 46.000

PRIN AXES = 75.826 10.159 166.518 89.889

STA	DIR	QUAL	DIST	EVAZ	TCA	X	Y
CLC	D	1	1.547	26.140	49.400	0.651	1.326
CSP	D	-2	0.901	98.218	92.949	-2.410	0.348
GSC	C	2	1.599	56.498	49.400	1.232	0.815
ISA	D	2	1.084	358.411	90.664	0.069	-2.485
MWC	D	2	0.374	123.299	100.717	-1.885	1.238
PAS	D	2	0.354	141.900	101.278	-1.384	1.764
PLM	C	2	1.692	128.874	49.400	1.150	-0.927
PYR	D	2	0.290	299.369	103.145	1.915	-1.078
SBC	D	1	1.224	271.740	49.400	-1.477	0.045
SYP	C	1	1.278	275.053	49.400	-1.472	0.130
BOUQ	D	2	0.084	356.763	132.905	0.080	-1.410
BRWN	C	2	0.188	223.412	111.368	1.370	1.448
IRON	C	2	0.056	146.245	144.606	-0.597	0.894
GOOK	C	2	0.059	214.085	143.003	0.629	0.929
SOLE	C	2	0.063	62.355	141.599	-1.030	-0.540
INDN	C	2	0.138	101.318	118.715	-1.767	0.354
NAGM	C	2	0.119	52.485	122.799	-1.342	-1.031
NMLM	D	2	0.297	98.849	102.932	-2.176	0.339
NWSM	D	2	0.207	330.736	109.349	0.999	-1.783
ENGN	D	2	0.407	134.701	99.758	-1.619	1.603
NSCF	C	1	0.125	76.165	121.466	-1.678	-0.413
NSHC	C	2	0.103	35.351	126.891	-0.914	-1.289

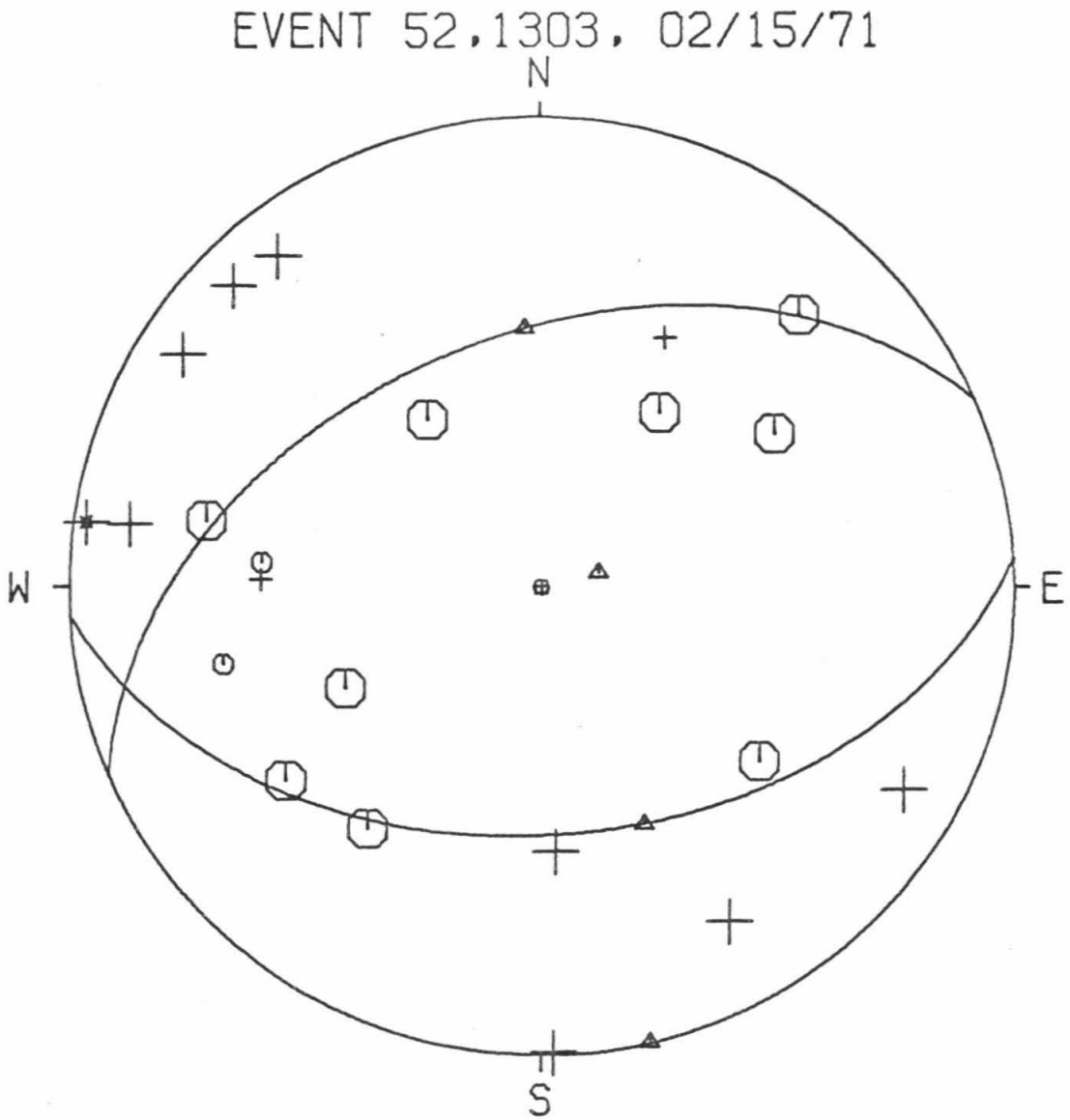
EVENT 52.1303, 02/15/71
N
W
E
S

EVENT DATA

53,0437 0 02/16/71 4 37 0.0

3.0 34.000 17.25 -118.000 32.61 3.5

AZ1= 121.000
DIP1= 65.000
AZ2= 234.000
DIP2= 50.039

SLIP VECTORS= 144.000 50.039 31.000 65.000

PRIN AXES = 80.295 41.151 180.666 81.065

STA	DIR	QUAL	DIST	EVAZ	TOA	X	Y
CLC	C	2	1.712	26.711	44.933	0.607	1.207
CSP	C	2	0.982	87.741	82.086	2.320	0.092
GSC	C	2	1.753	54.238	44.933	1.096	0.790
ISA	C	1	1.224	2.304	50.438	0.061	1.505
MWC	C	2	0.408	100.074	87.591	2.409	-0.428
PAS	C	2	0.340	114.824	88.248	2.234	-1.033
PLM	C	2	1.682	123.193	44.933	1.131	-0.740
PYR	D	2	0.326	329.853	88.383	-1.238	2.131
SBC	C	2	1.147	279.477	80.506	-2.253	0.376
SYP	C	1	1.210	281.894	50.440	-1.474	0.310
RVR	C	2	1.013	106.585	81.793	2.218	-0.661
BOUQ	D	2	0.237	20.868	89.229	0.885	2.320
BRWN	C	2	0.052	311.087	116.859	1.395	-1.216
IRON	D	2	0.159	49.081	90.623	-1.879	-1.629
GOOK	D	2	0.117	28.682	95.867	-1.137	-2.078
SOLE	D	-2	0.208	44.005	89.507	1.729	1.790
INDN	C	2	0.264	58.558	88.975	2.114	1.292
NAGM	D	2	0.277	41.486	88.850	1.639	1.854
NMLM	C	2	0.398	74.311	87.688	2.358	0.662
NRTM	D	2	0.396	38.234	87.712	1.516	1.924
NWSM	D	2	0.320	357.894	88.435	-0.091	2.464
ENGN	C	2	0.407	111.546	87.600	2.276	-0.899
NSCF	D	2	0.261	53.906	89.003	2.002	1.460
NSHC	D	1	0.268	33.775	88.939	1.377	2.059
NSGM	D	2	0.149	46.115	91.690	-1.775	-1.707

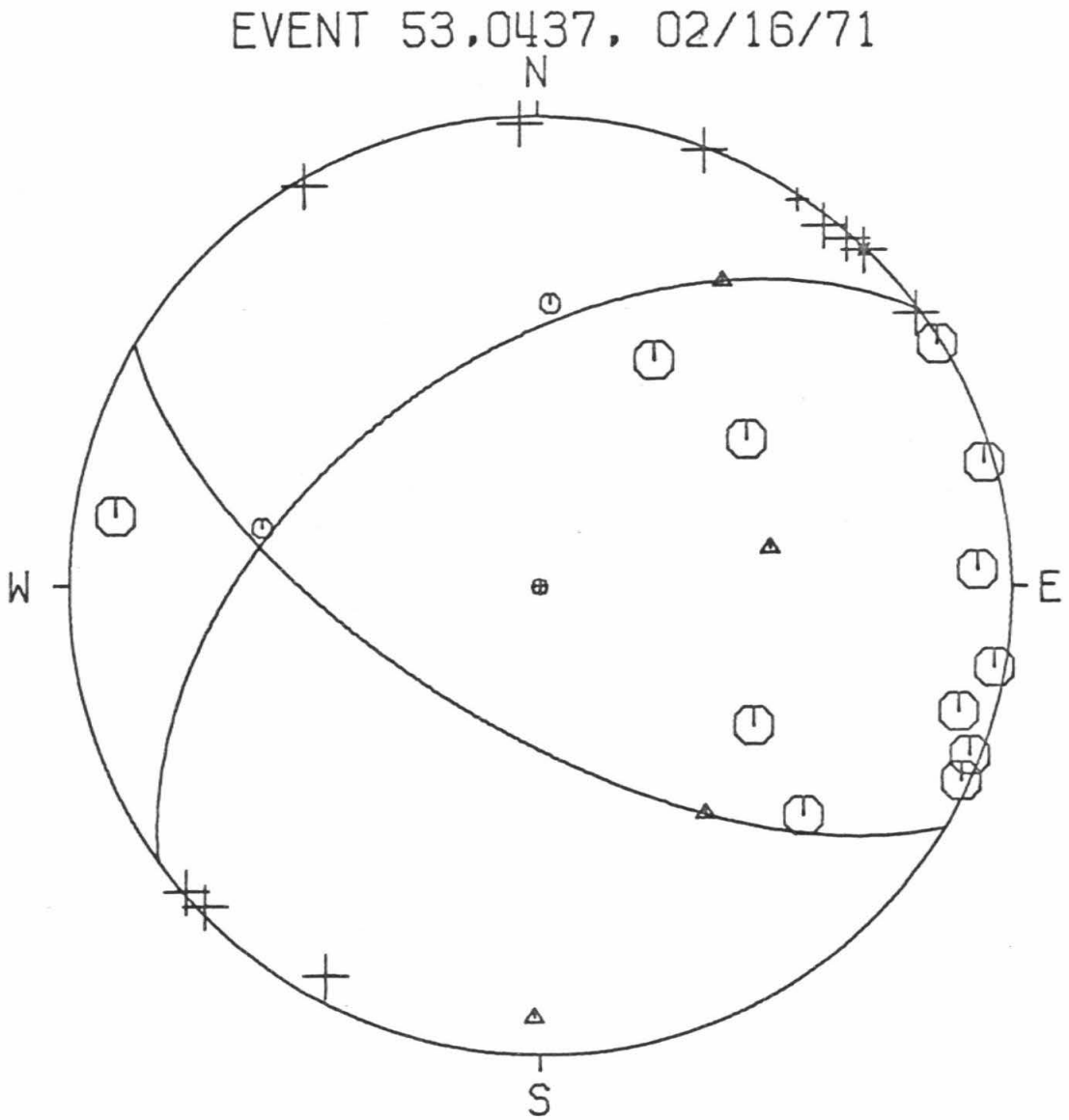
EVENT 53.0437, 02/16/71
N
W
E
S

EVENT DATA

54,0708 0 02/16/71 7 8 26.5

9.3 34.000 24.40 -118.000 26.86 3.3

AZ1= 104.000
DIP1= 45.000
AZ2= 295.000
DIP2= 45.531

SLIP VECTORS= 205.000 45.531 14.000 45.000

PRIN AXES = 286.972 5.538 19.525 89.733

STA	DIR	QUAL	DIST	EVAZ	TOA	X	Y
CLC	D	1	1.571	26.132	49.400	0.651	1.326
CSP	D	1	0.909	96.795	92.650	-2.424	0.289
GSC	C	2	1.620	56.056	49.400	1.226	0.825
ISA	D	2	1.104	358.905	89.561	-0.048	2.490
MWC	C	2	0.372	119.907	100.252	-1.965	1.130
PAS	D	2	0.346	138.579	100.908	-1.489	1.688
PLM	C	2	1.687	128.103	49.400	1.163	-0.912
PYR	D	2	0.293	304.037	102.245	1.839	-1.242
RVR	C	2	0.980	114.620	91.755	-2.238	1.025
SBC	D	2	1.214	272.748	49.400	-1.476	0.071
SYP	D	2	1.270	275.962	49.400	-1.469	0.153
BOUQ	D	2	0.105	2.990	124.916	-0.085	-1.633
BRWN	D	2	0.167	225.432	112.505	1.399	1.378
IRON	C	2	0.056	132.425	143.415	-0.819	0.749
GOOK	C	2	0.044	211.400	150.077	0.476	0.779
NMLM	C	2	0.305	94.913	101.933	-2.218	0.191
NRTM	D	2	0.254	40.739	103.436	-1.429	-1.660
NWSM	D	2	0.222	335.871	106.700	0.863	-1.926
ENGN	D	1	0.401	131.701	99.529	-1.705	1.519
NSCF	C	2	0.137	73.916	117.749	-1.756	-0.506
NSHC	D	1	0.127	33.369	119.883	-0.974	-1.479
NSGM	C	2	0.052	147.106	145.403	-0.571	0.883

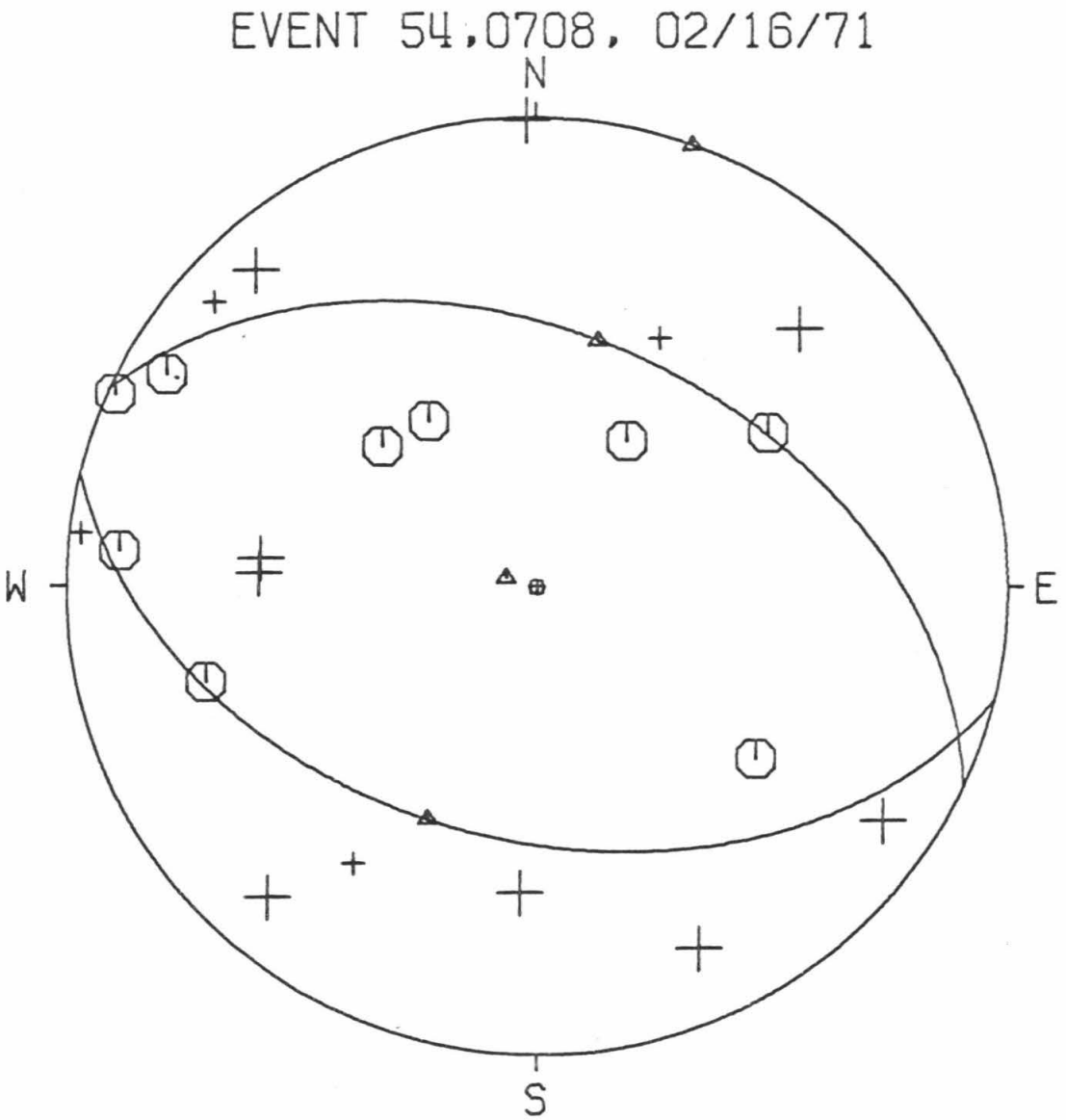
EVENT 54,0708, 02/16/71
N
W
E
S

EVENT DATA

55,1439 0 02/16/71 14 39 0.0

10.0 34.000 20.07 -118.000 17.87 3.1

AZ1= 108.000
DIP1= 40.000
AZ2= 288.000
DIP2= 50.000

SLIP VECTORS= 198.000 50.000 18.000 40.000

PRIN AXES = 197.976 5.007 18.000 85.000

STA	DIR	QUAL	DIST	EVAZ	TCA	X	Y
CLC	D	2	1.587	21.049	49.400	0.531	1.379
CSP	D	2	0.779	93.040	94.638	-2.393	0.127
GSC	D	2	1.562	51.422	49.400	1.155	0.921
ISA	D	2	1.184	353.636	49.400	-0.164	1.468
MWC	D	2	0.229	119.935	107.673	-1.808	1.041
PAS	D	2	0.215	150.861	109.208	-0.997	1.789
PLM	C	2	1.545	128.929	49.400	1.149	-0.928
PYR	D	2	0.435	302.688	99.134	1.930	-1.238
RVR	C	2	0.838	113.785	93.902	-2.208	0.973
BOUQ	D	2	0.211	325.933	109.607	1.142	-1.688
BRWN	D	2	0.248	258.438	105.620	2.094	0.428
IRON	C	2	0.101	304.978	128.521	1.258	-0.880
GOOK	C	2	0.157	290.574	115.942	1.755	-0.659
SOLE	C	2	0.120	331.041	123.399	0.812	-1.467
INDN	D	1	0.093	13.772	131.057	-0.349	-1.422
NAGM	D	2	0.161	353.048	115.378	0.229	-1.876
NMLM	D	2	0.190	71.669	111.943	-1.878	-0.622
NRTM	D	2	0.267	9.096	104.510	-0.342	-2.137
NWSM	D	2	0.348	321.934	101.928	1.373	-1.753
ENGN		-1	0.262	137.997	104.676	-1.446	1.605
NSCF	C	2	0.107	4.206	126.779	-0.116	-1.579
NSHC	D	1	0.182	342.743	112.744	0.581	-1.870
NSGM	D	-2	0.112	301.385	125.441	1.383	-0.844

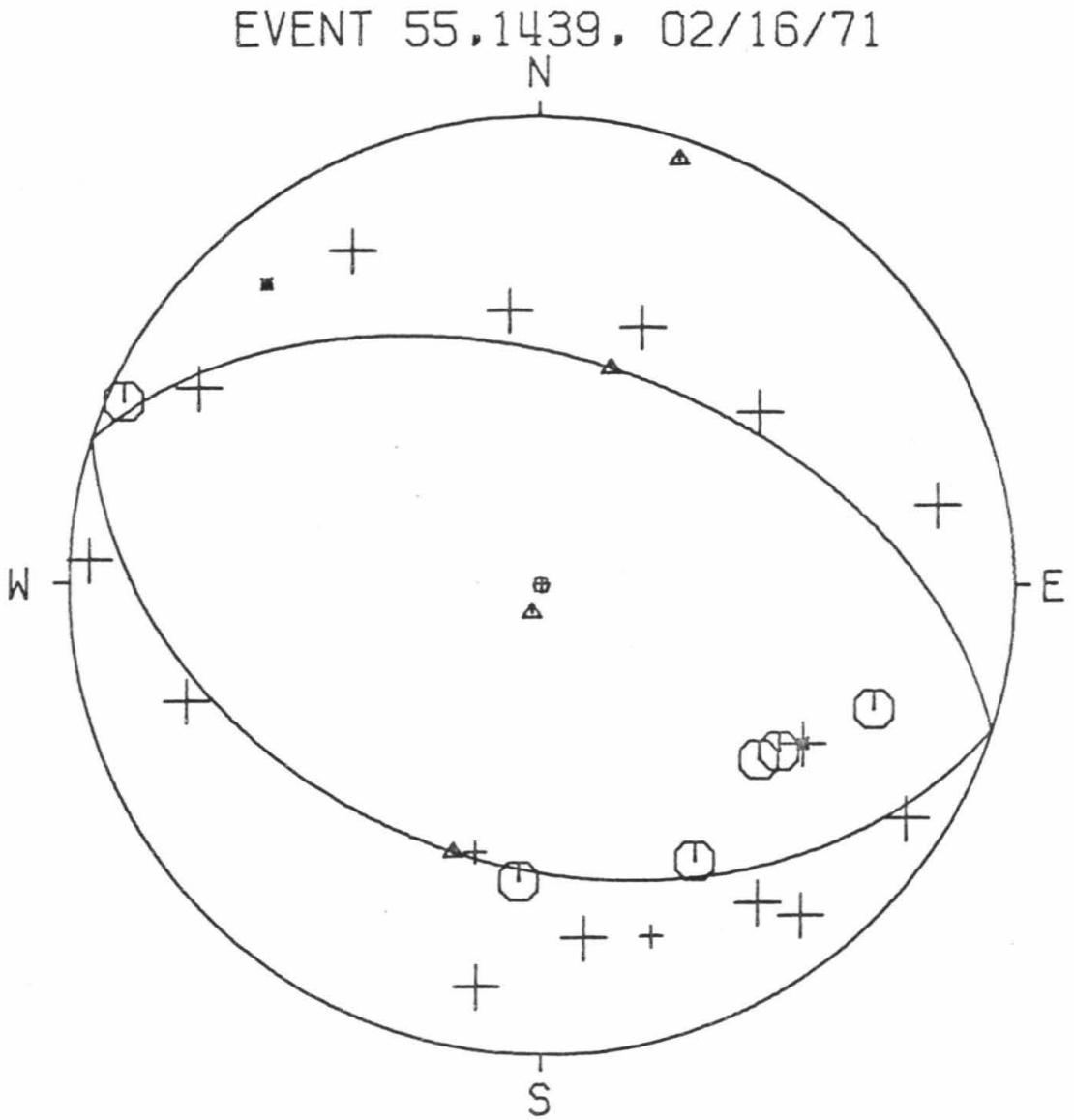
EVENT 55.1439, 02/16/71
N
W
E
S

EVENT DATA

56,1015 0 02/17/71 10 15 0.0

5.3 34.000 21.46 -118.000 18.38 3.5

AZ1= 96.000
DIP1= 85.000
AZ2= 276.000
DIP2= 5.000

SLIP VECTORS= 186.000 5.000 6.000 85.000

PRIN AXES = 6.000 40.001 186.000 50.000

STA	DIR	QUAL	DIST	EVAZ	TOA	X	Y
CLC	C	2	1.568	21.588	48.725	0.537	1.356
CSP	D	1	0.788	94.593	87.044	2.427	-0.195
GSC	C	2	1.554	52.242	48.725	1.153	0.893
ISA	D	-1	1.160	353.828	80.379	-0.245	2.268
MWC	C	2	0.247	123.721	93.012	-2.024	1.351
PAS	C	2	0.239	152.139	93.318	-1.134	2.145
PLM	D	2	1.565	129.418	48.725	1.127	-0.926
PYR	C	2	0.418	300.694	90.922	2.132	-1.266
RVR	C	2	0.854	115.008	86.352	2.192	-1.023
SYP	C	2	1.392	277.545	48.725	-1.446	0.191
BOUQ	D	2	0.190	324.094	89.686	-1.462	2.019
BRWN	D	2	0.246	253.207	93.042	2.329	0.703
IRON	D	2	0.084	295.741	103.128	1.980	-0.955
GOOK	D	2	0.145	285.690	91.817	2.368	-0.665
SCLE	D	2	0.097	328.097	99.389	1.209	-1.942
NAGM	D	2	0.137	354.804	93.116	0.220	-2.421
NMLM	D	2	0.192	77.385	89.666	2.433	0.544
NRTM	D	2	0.245	11.567	93.072	-0.488	-2.383
ENGN	C	2	0.285	140.199	92.317	-1.568	1.881
NSHC	D	2	0.161	342.971	89.964	-0.732	2.390

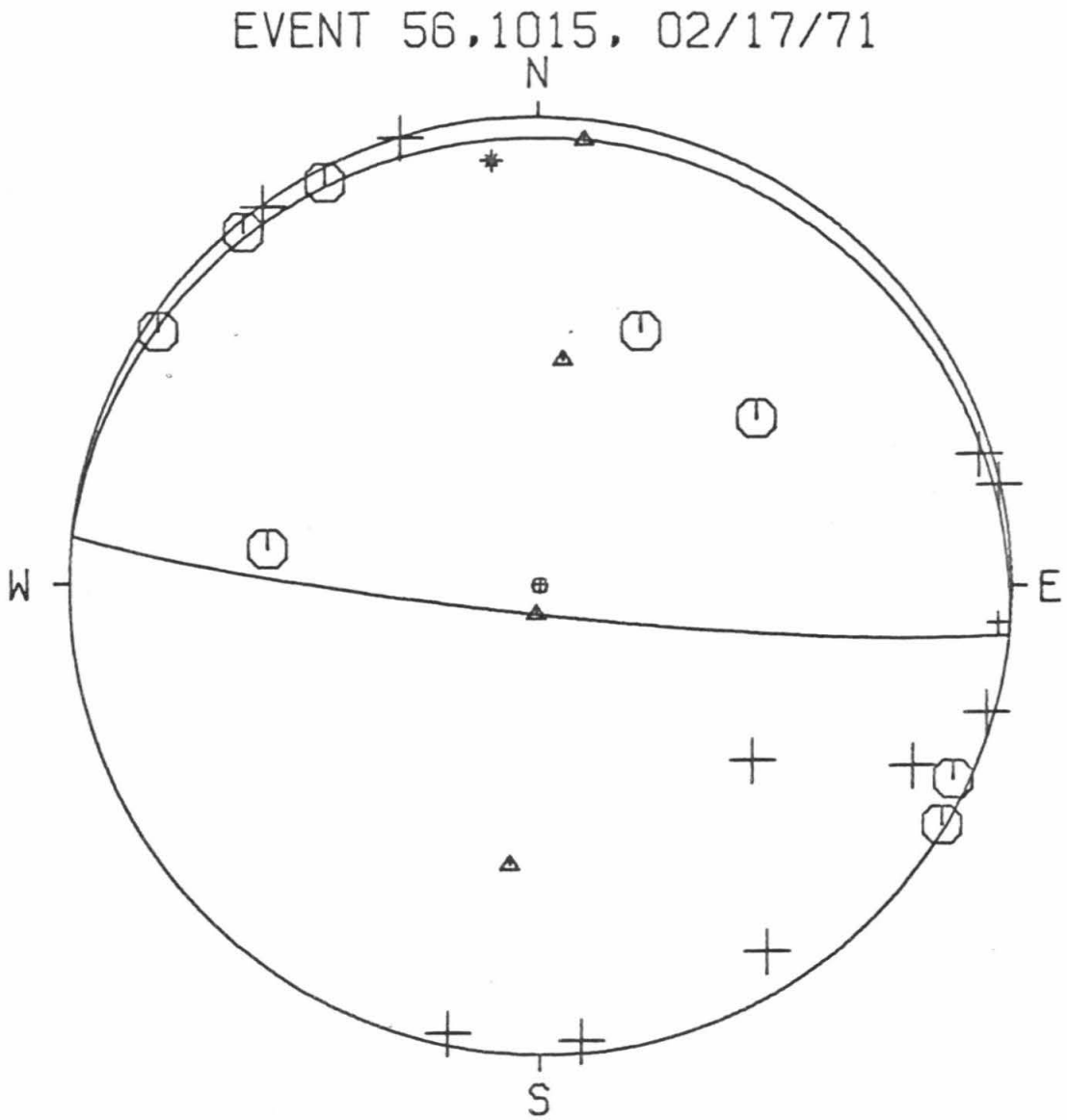
EVENT 56,1015, 02/17/71
N
W
E
S

EVENT DATA

57,2209 0 02/18/71 22 9 0.0

4.4 34.000 23.18 -118.000 25.85 3.2

AZ1= 125.000
DIP1= 70.000
AZ2= 218.000
DIP2= 81.817

SLIP VECTORS= 128.000 81.817 35.000 70.000

PRIN AXES = 83.063 69.971 350.087 81.883

STA	DIR	QUAL	DIST	EVAZ	TCA	X	Y
GSC	C	2	1.620	55.200	48.500	1.192	0.829
ISA	D	2	1.125	358.296	81.577	-0.069	2.309
MWC	C	2	0.350	118.113	89.221	2.190	-1.170
PAS	D	2	0.322	138.120	89.497	1.662	-1.853
PLM	D	1	1.664	127.858	48.500	1.146	-0.891
PYR	D	2	0.315	305.559	89.564	-2.026	1.448
RVR	C	2	0.959	113.880	83.211	2.147	-0.950
SYP	C	2	1.286	276.858	48.500	-1.442	0.173
BOUQ	D	2	0.125	356.132	94.982	0.161	-2.384
BRWN	C	2	0.166	233.290	89.918	-2.003	-1.493
IRON	C	2	0.040	43.799	126.196	-1.107	-1.155
GOOK	C	2	0.048	229.716	119.143	1.366	1.158
SOLE	D	2	0.079	40.807	104.783	-1.410	-1.633
NMLM	C	2	0.291	84.662	89.799	2.485	0.232
NRTM	D	2	0.261	35.613	90.099	-1.455	-2.031
NWSM	D	2	0.245	334.766	90.358	1.062	-2.254
ENGN		-1	0.377	130.854	88.951	1.874	-1.620

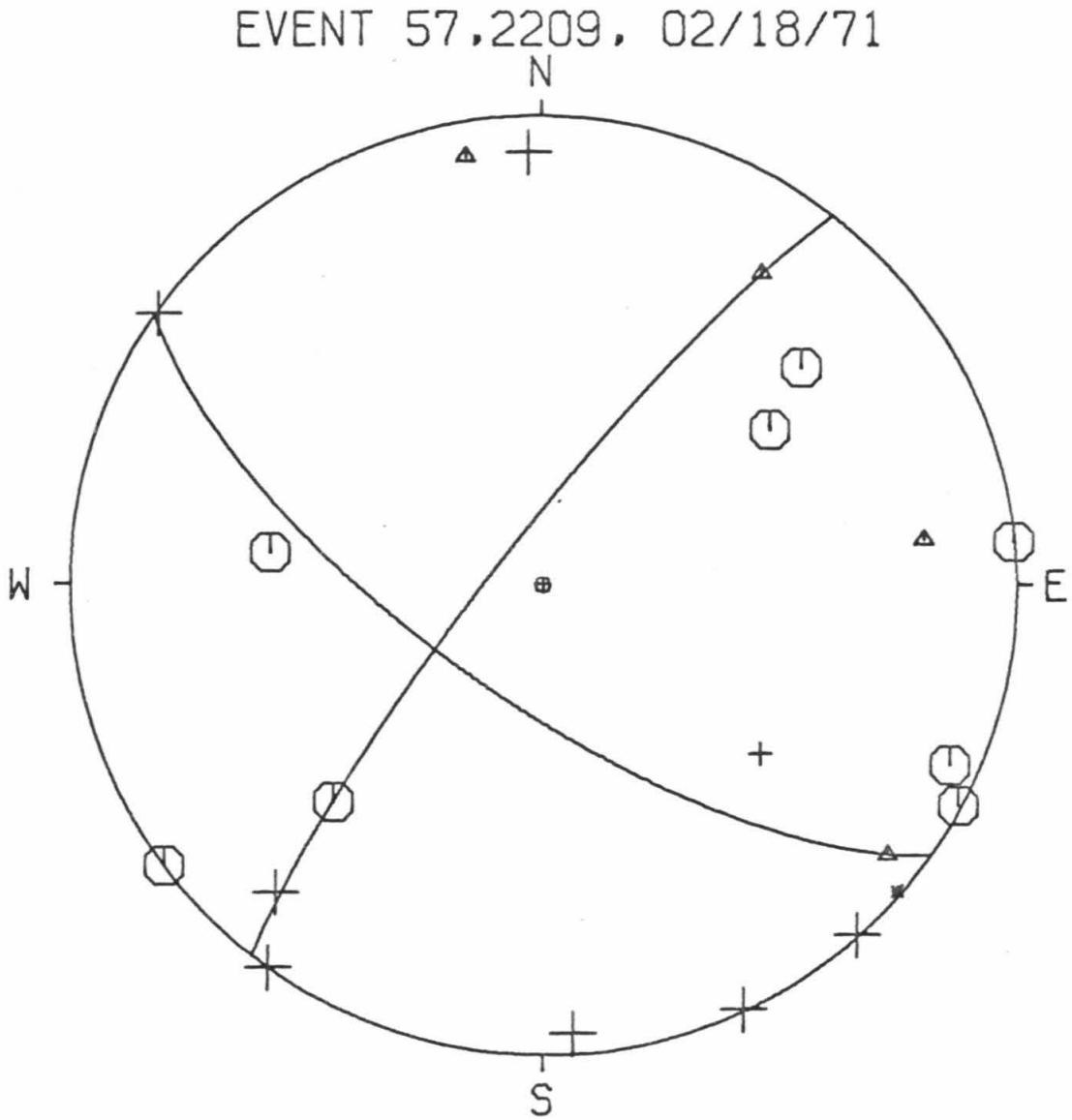
EVENT 57,2209, 02/18/71
N
W
E
S

EVENT DATA

58,0245 0 02/19/71 2 45 11.6

3.0 34.000 21.45 -118.000 27.58 3.5

AZ1= 147.000
DIP1= 56.000
AZ2= 54.000
DIP2= 85.563

SLIP VECTORS= 323.999 85.563 57.000 56.000

PRIN AXES = 4.963 63.250 105.490 70.080

STA	DIR	QUAL	DIST	EVAZ	TOA	X	Y
BAR	C	2	2.243	137.752	44.933	0.908	-1.000
CLC	D	2	1.619	25.677	44.933	0.585	1.218
CSP	C	2	0.914	93.846	82.739	2.331	-0.157
GSC	D	2	1.656	54.845	44.933	1.105	0.778
ISA	D	2	1.153	359.381	80.449	-0.025	2.283
MWC	C	2	0.360	112.482	88.055	2.270	-0.940
PAS	C	2	0.318	131.260	88.459	1.854	-1.626
PLM	C	2	1.665	126.560	44.933	1.085	-0.805
PYR	D	2	0.315	312.426	88.482	-1.821	1.664
RVR	C	2	0.971	111.792	82.200	2.158	-0.863
SBC	C	2	1.208	275.349	50.441	-1.500	0.140
SYP	D	2	1.266	278.183	44.933	-1.337	0.192
BOUQ	D	2	0.153	5.746	91.189	-0.248	-2.462
BRWN	C	2	0.131	236.045	94.033	1.999	1.346
IRON	D	2	0.066	51.292	105.955	-1.661	-1.331
GOOK	D	2	0.040	340.587	126.196	0.532	-1.509
SOLE	D	2	0.114	41.643	96.305	-1.567	-1.763
NAGM	D	2	0.179	39.619	90.005	-1.594	-1.926
NMLM	C	2	0.317	81.888	88.465	2.442	0.348
NRTM	D	2	0.298	36.123	88.648	1.456	1.995
NWSM	D	2	0.264	342.149	88.975	-0.759	2.358
ENGN	C	2	0.378	125.173	87.877	2.005	-1.413

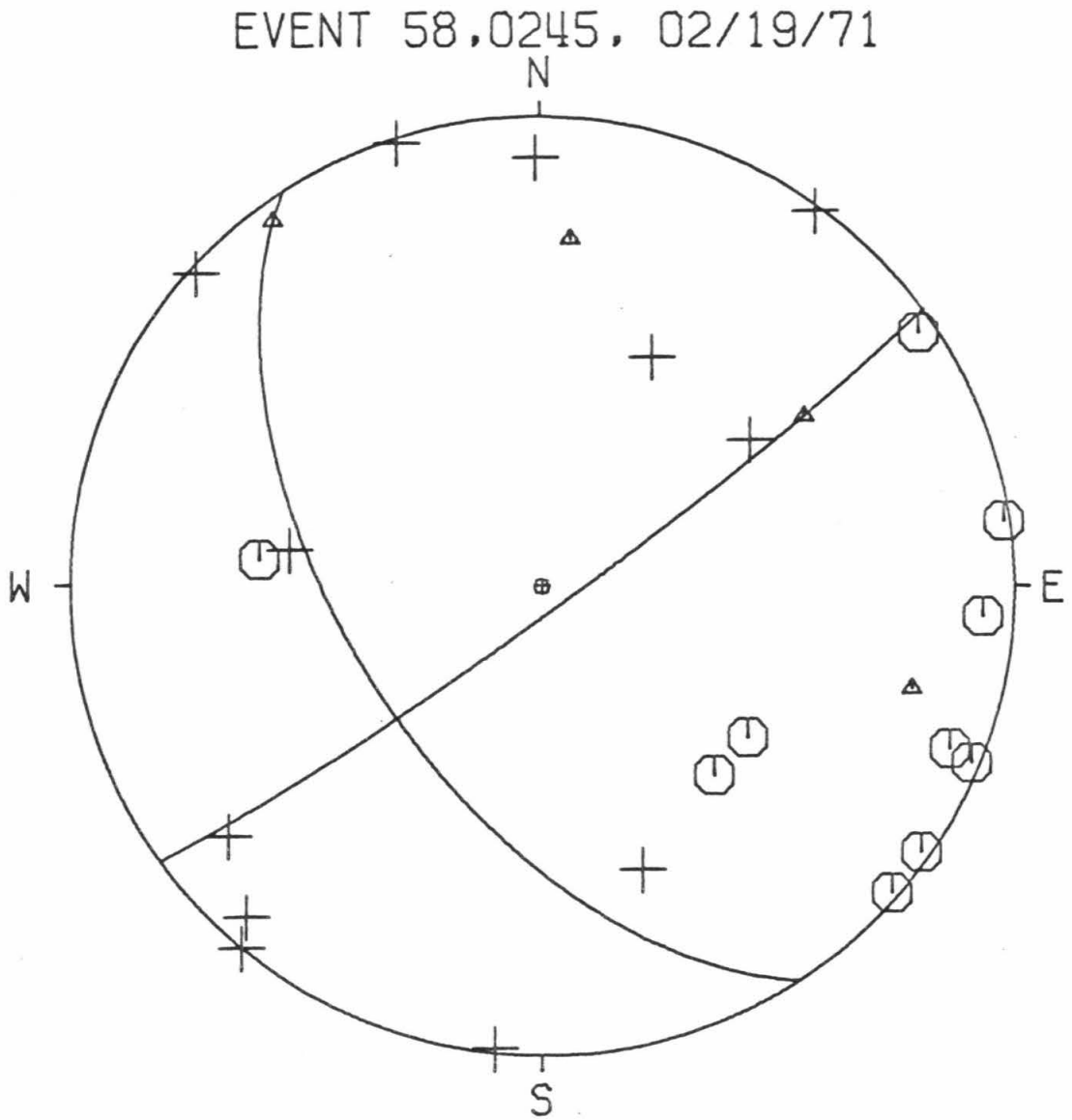
EVENT 58,0245, 02/19/71
N
W
E
S

EVENT DATA

59,0809 0 02/20/71 8 9 0.0

15.2 34.000 27.24 -118.000 24.38 3.6

AZ1= 120.000
DIP1= 60.000
AZ2= 222.000
DIP2= 70.195

SLIP VECTORS= 132.000 70.195 30.000 60.000

PRIN AXES = 83.919 53.621 349.079 83.456

STA	DIR	QUAL	DIST	EVAZ	TCA	X	Y
CLC	C	1	1.513	25.782	49.560	0.645	1.334
CSP	C	2	0.882	100.128	97.352	-2.298	0.411
GSC	C	2	1.565	56.820	49.560	1.240	0.811
ISA	D	2	1.058	357.237	49.600	-0.071	1.481
MWC	D	2	0.370	128.815	108.351	-1.612	1.297
PAS	D	2	0.363	147.537	108.567	-1.108	1.741
PLM	C	2	1.690	130.101	49.560	1.133	-0.955
PYR	C	2	0.301	293.016	112.660	1.804	-0.766
SBC	C	2	1.248	268.263	49.560	-1.481	-0.045
SYP	D	1	1.300	273.907	49.560	-1.478	0.101
BOUQ	C	-2	0.071	336.274	151.445	0.351	-0.798
BRWN	C	2	0.224	223.126	119.251	1.222	1.305
IRON	C	2	0.071	174.291	151.445	-0.087	0.868
GOOK	C	2	0.097	216.213	143.433	0.655	0.895
SOLE	C	2	0.052	143.088	158.265	-0.400	0.533
INDN	C	1	0.122	113.541	136.695	-1.196	0.521
NAGM	D	2	0.088	52.494	145.860	-0.823	-0.632
NMLM	D	2	0.278	104.198	114.389	-1.857	0.470
NRTM	C	2	0.197	42.003	123.122	-1.127	-1.251
NWSM	C	2	0.200	321.309	122.697	1.060	-1.323
ENGN	D	2	0.411	139.792	107.177	-1.355	1.603

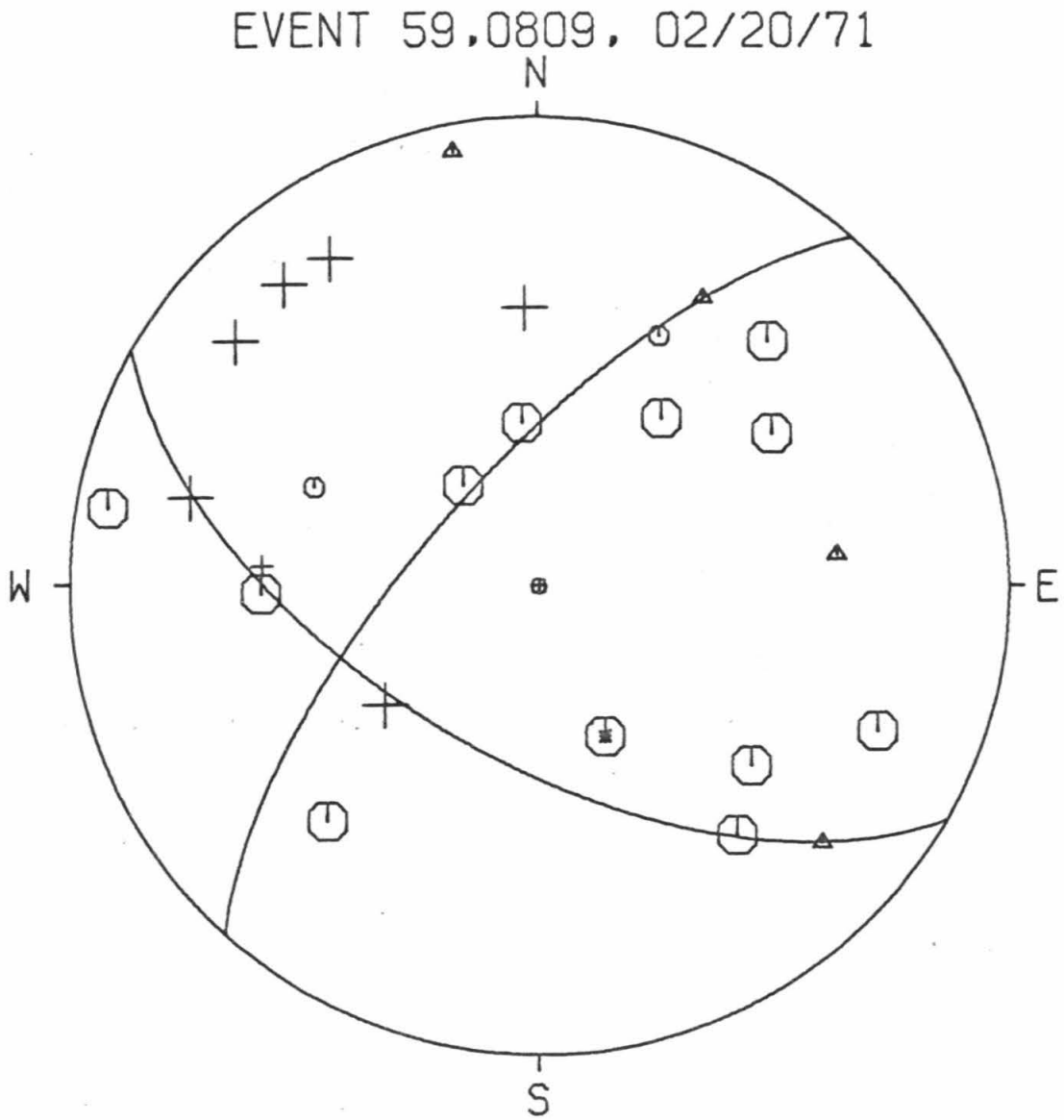
EVENT 59.0809, 02/20/71
N
W
E
S

EVENT DATA

60,0242 0 02/21/71 2 42 0.0

6.8 34.000 17.69 -118.000 31.86 3.6

AZ1= 135.000
DIP1= 39.000
AZ2= 266.500
DIP2= 61.783

SLIP VECTORS= 176.500 61.783 45.000 39.000

PRIN AXES = 131.063 27.890 16.454 77.573

STA	DIR	QUAL	DIST	EVAZ	TOA	X	Y
CLC	D	2	1.701	26.519	49.100	0.656	1.314
CSP	C	2	0.972	88.233	88.495	2.466	0.076
GSC	D	2	1.740	54.238	49.100	1.192	0.858
ISA	D	2	1.216	1.885	49.100	0.048	1.468
MWC	C	2	0.399	101.057	95.086	-2.342	0.458
PAS	C	2	0.333	116.415	95.849	-2.122	1.054
PLM	C	-1	1.677	123.598	49.100	1.224	-0.813
PYR	D	2	0.324	327.604	95.945	1.268	-1.999
RVR	C	2	1.005	107.158	88.110	2.349	-0.725
SBC	C	2	1.156	279.016	49.400	-1.459	0.232
SYP	C	2	1.219	281.446	49.100	-1.440	0.292
BOUQ	D	2	0.226	19.150	98.947	-0.754	-2.170
IRON	D	2	0.147	48.698	111.692	-1.491	-1.310
GOOK	D	2	0.103	26.501	121.069	-0.776	-1.556
SOLE	D	-2	0.196	43.376	106.035	-1.461	-1.546
INDN	D	2	0.250	59.173	97.260	-2.007	-1.197
NAGM	D	2	0.264	41.006	96.641	-1.543	-1.774
NRTM	D	2	0.383	37.759	95.270	-1.459	-1.884
NWSM	D	2	0.313	355.959	96.079	0.167	-2.358
ENGN	C	2	0.400	112.898	95.074	-2.199	0.929

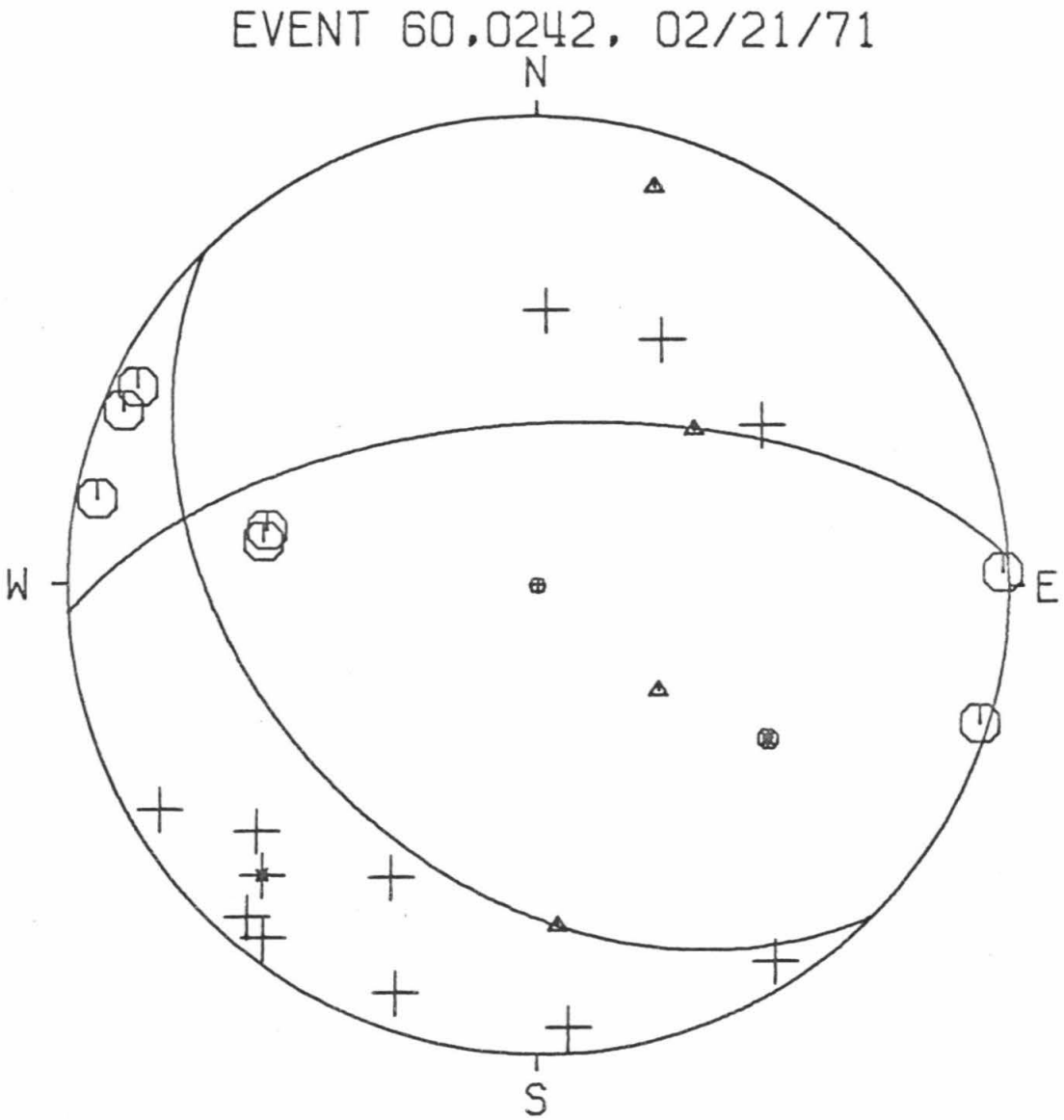
EVENT 60,0242, 02/21/71
N
W
E
S

EVENT DATA
61,0550 0 02/21/71 5 50 0.0
6.9 34.000 23.85 -118.000 26.32 4.7

AZ1= 59.000
DIP1= 46.000
AZ2= 239.000
DIP2= 44.000

SLIP VECTORS= 149.000 44.000 328.999 46.000

PRIN AXES = 330.058 1.032 149.000 89.000

STA	DIR	QUAL	DIST	EVAZ	TCA	X	Y
BAR	D	1	2.261	138.768	49.125	0.969	-1.105
CLC	C	2	1.575	25.749	49.125	0.638	1.324
CSP	D	2	0.900	96.284	89.548	2.475	-0.273
CWC	C	1	2.059	8.123	49.125	0.208	1.455
GLA	C	1	3.296	113.032	49.125	1.353	-0.575
GSC	C	2	1.619	55.655	49.125	1.213	0.829
HFD	C	1	2.427	105.728	49.125	1.415	-0.398
ISA	D	2	1.114	358.574	87.076	-0.061	2.435
MWC	D	2	0.361	119.184	95.791	-2.070	1.156
PAS	D	2	0.334	138.461	96.104	-1.567	1.769
PLM	D	2	1.675	128.014	49.125	1.158	-0.905
PYR	D	2	0.304	304.638	96.452	1.938	-1.339
RVR	D	2	0.970	114.336	88.741	2.253	-1.019
SBC	C	2	1.222	272.939	49.125	-1.468	0.075
SYP	C	2	1.279	276.362	49.125	-1.461	0.163
BOUQ	D	-2	0.114	358.999	118.441	0.032	-1.809
BRWN	C	2	0.167	229.218	108.865	1.557	1.343
IRON	C	2	0.040	121.189	149.647	-0.792	0.479
GOOK	C	2	0.044	223.596	146.728	0.698	0.733
SOLE	C	2	0.077	49.398	129.794	-1.139	-0.976
INDN	C	2	0.144	74.145	112.241	-1.896	-0.538
NAGM	C	2	0.138	44.408	113.372	-1.359	-1.387
NMLM	D	2	0.297	94.160	96.528	-2.347	0.171
NRTM	D	2	0.256	38.153	97.100	-1.446	-1.840
NWSM	D	2	0.233	335.096	98.792	0.969	-2.087
ENGN	D	2	0.389	131.307	95.471	-1.786	1.570
SWM	D	2	0.341	339.580	96.017	0.825	-2.217

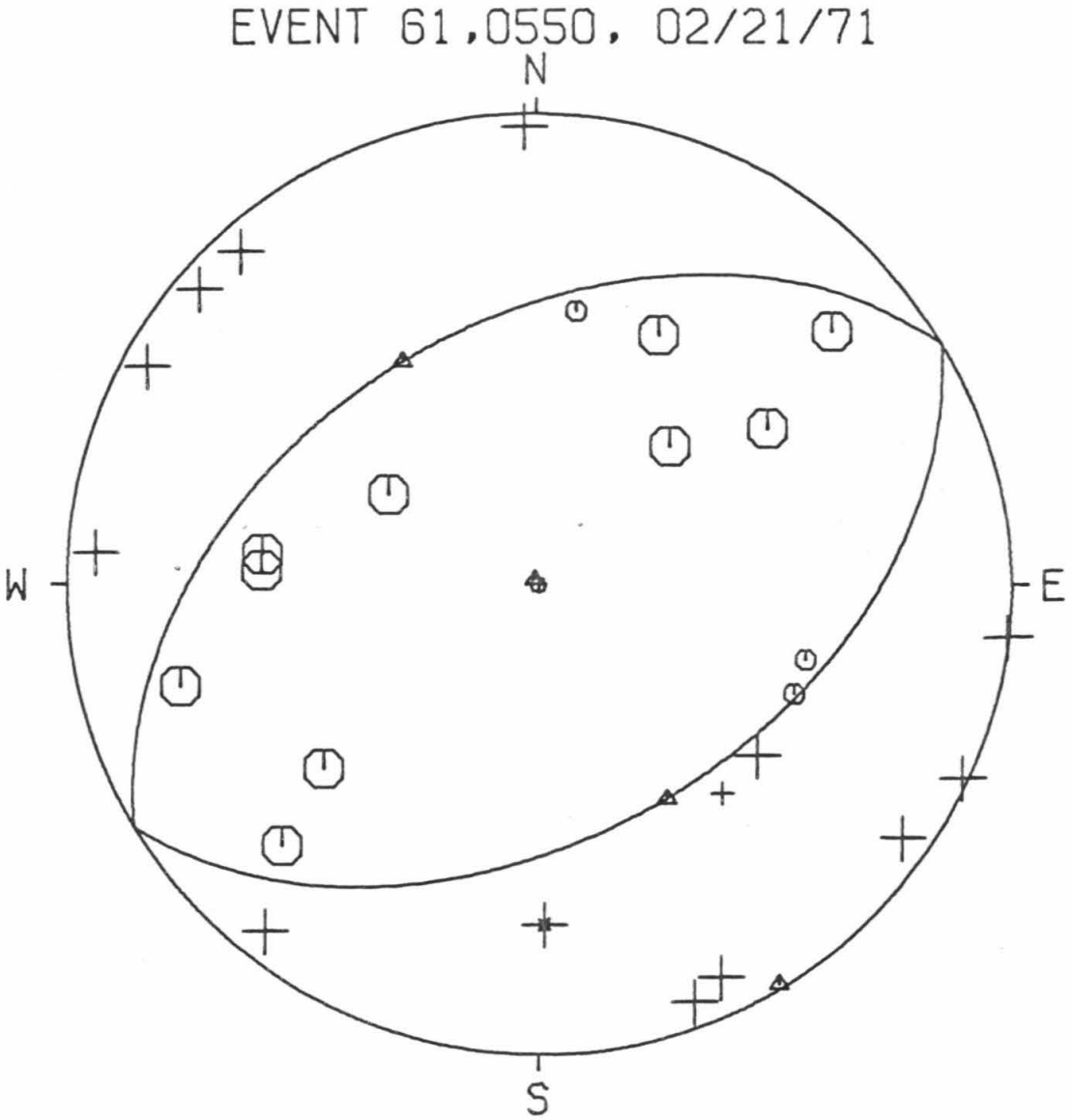
EVENT 61,0550, 02/21/71
N
W
E
S

EVENT DATA

62,0715 0 02/21/71 7 15 0.0

7.2 34.000 23.52 -118.000 25.65 4.5

AZ1= 96.000
DIP1= 52.000
AZ2= 202.000
DIP2= 70.567

SLIP VECTORS= 112.000 70.567 6.000 52.000

PRIN AXES = 65.775 47.887 325.139 78.458

STA	DIR	QUAL	DIST	EVAZ	TOA	X	Y
BAR	D	2	2.251	138.859	49.200	0.968	-1.108
CLC	C	2	1.576	25.367	49.200	0.631	1.330
CSP	C	2	0.891	96.115	90.352	-2.478	0.266
CWC	D	1	2.063	7.853	49.200	0.201	1.458
GSC	C	2	1.614	55.319	49.200	1.210	0.837
ISA	D	2	1.119	358.162	87.656	-0.079	2.447
MWC	D	2	0.350	119.073	96.722	-2.053	1.141
PAS	D	2	0.324	139.069	97.030	-1.534	1.769
PLM	C	2	1.665	128.068	49.200	1.159	-0.907
PYR	D	2	0.314	304.346	97.146	1.931	-1.320
RVR	D	2	0.959	114.265	89.544	2.270	-1.023
SBC	D	2	1.231	273.270	49.200	-1.469	0.084
SYP	D	2	1.288	276.599	49.200	-1.462	0.169
TIN	C	1	2.662	3.433	49.200	0.088	1.469
BOUQ	D	2	0.119	354.568	117.409	0.174	-1.828
BRWN	C	2	0.170	232.768	108.527	1.644	1.249
IRON	C	2	0.034	134.156	153.383	-0.584	0.567
GOOK	C	2	0.048	235.152	144.090	0.894	0.623
SOLE	C	2	0.071	43.295	132.226	-0.982	-1.042
INDN	D	2	0.137	70.605	113.662	-1.825	-0.642
NAGM	C	2	0.137	39.755	113.662	-1.237	-1.487
NMLM	D	2	0.289	95.578	97.444	-2.321	0.227
NRTM	C	2	0.254	35.943	98.116	-1.360	-1.876
NWSM	D	2	0.242	333.673	99.057	1.018	-2.057
ENGN	D	2	0.379	131.766	96.381	-1.758	1.570
SWM	D	2	0.351	338.517	96.716	0.860	-2.186

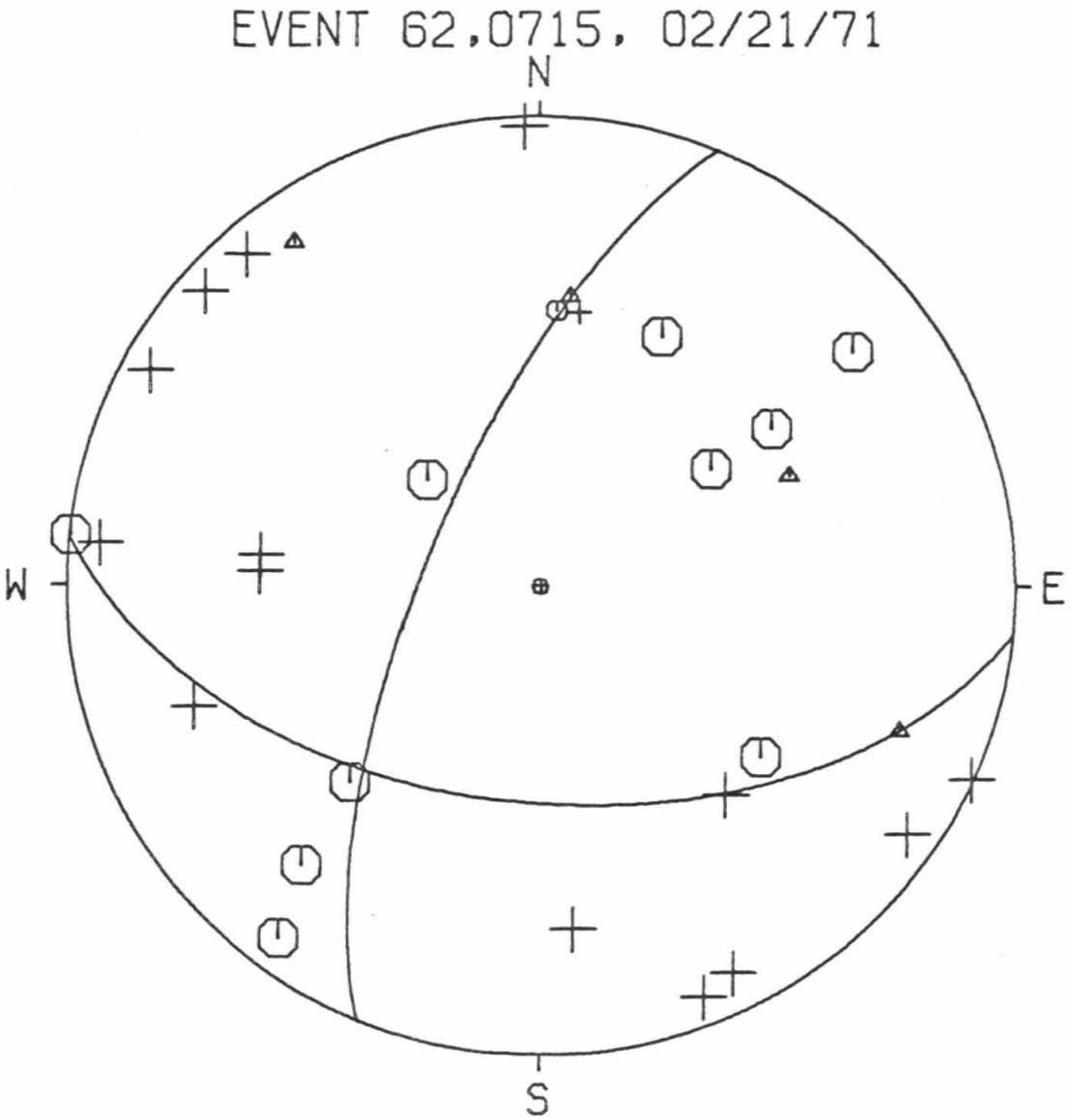
EVENT 62,0715, 02/21/71
N
W
E
S

EVENT DATA

63,0743 0 02/21/71 7 43 0.0

4.9 34.000 23.87 -118.000 25.58 3.5

AZ1= 223.000
DIP1= 37.000
AZ2= 114.000
DIP2= 76.216

SLIP VECTORS= 24.000 76.216 133.000 37.000

PRIN AXES = 60.275 42.845 178.008 66.657

STA	DIR	QUAL	DIST	EVAZ	TOA	X	Y
CLC	D	1	1.571	25.426	48.625	0.625	1.315
CSP	C	2	0.890	96.291	85.050	2.375	-0.262
GSC	D	1	1.610	55.473	48.625	1.199	0.825
ISA	D	2	1.114	358.111	82.768	-0.077	2.336
MWC	D	2	0.352	120.029	90.538	-2.154	1.245
PAS	D	2	0.327	139.832	90.791	-1.601	1.897
PLM	C	-1	1.668	128.245	48.625	1.143	-0.901
PYR	D	2	0.312	303.526	90.947	2.067	-1.369
RVR	C	2	0.961	114.616	84.327	2.158	-C.989
SBC	D	2	1.232	273.241	48.625	-1.453	0.082
SYP	C	2	1.289	276.283	48.625	-1.447	0.159
BRWN	C	2	0.175	231.347	89.830	-1.949	-1.559
IRON	C	2	0.040	143.320	126.196	-0.956	1.283
GOOK	C	2	0.052	231.071	116.859	1.440	1.163
INDN	C	2	0.133	75.249	93.796	-2.336	-0.615
NAGM	D	2	0.133	40.793	93.796	-1.578	-1.829
NMLM	C	2	0.288	96.112	91.193	-2.460	0.263
NRTM	D	2	0.249	36.587	91.773	-1.467	-1.976
NWSM	D	2	0.237	332.830	92.103	1.120	-2.183
ENGN	D	2	0.382	132.410	90.239	-1.842	1.683
SWM	D	2	0.344	337.941	90.618	0.934	-2.304

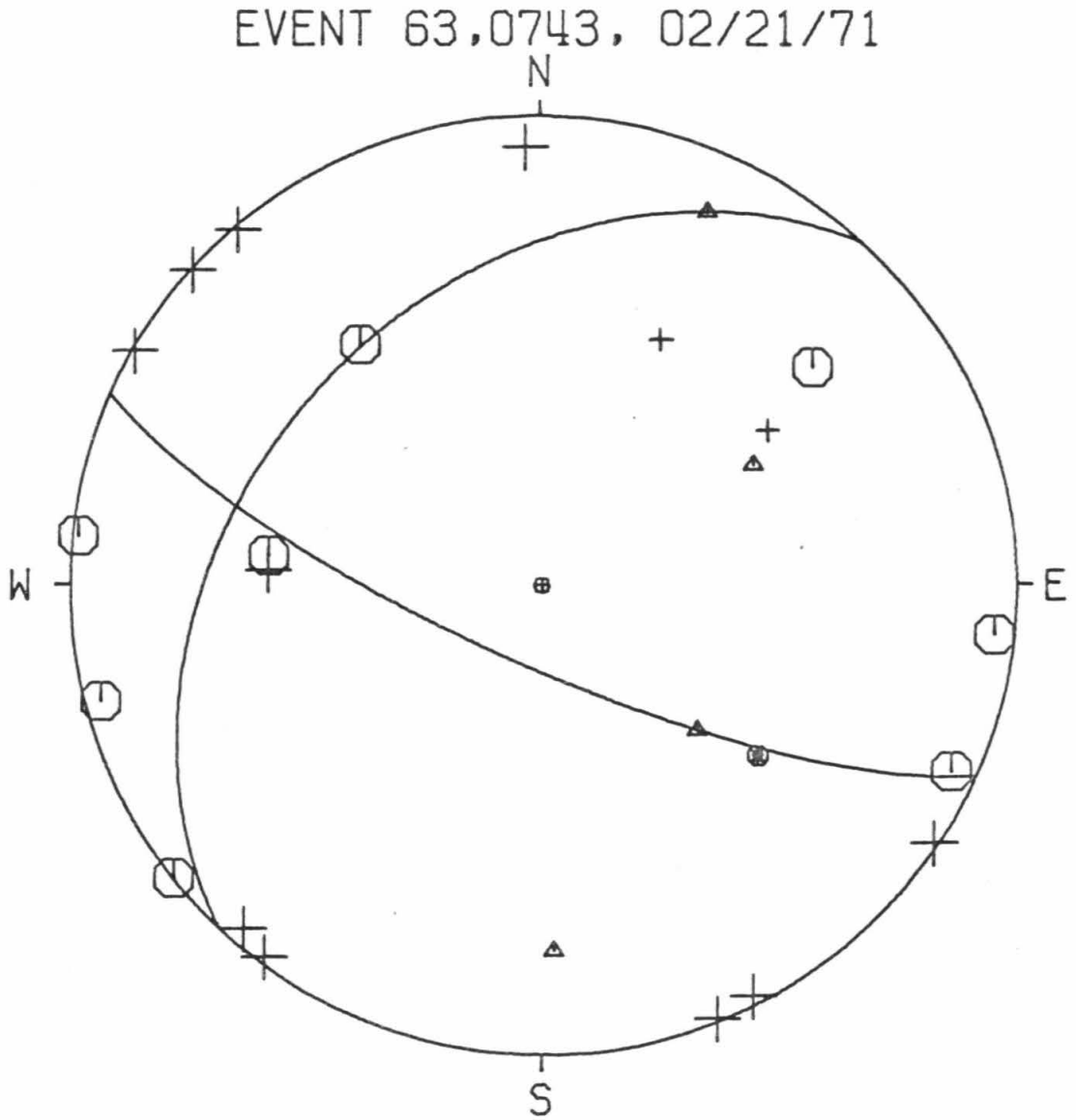
EVENT 63,0743, 02/21/71
N
W
E
S

EVENT DATA

64,1406 0 02/21/71 14 6 0.0

6.2 34.000 23.89 -118.000 26.70 3.5

AZ1= 228.000
DIP1= 85.000
AZ2= 138.000
DIP2= 90.000

SLIP VECTORS= 48.000 90.000 138.000 85.000

PRIN AXES = 92.902 86.467 183.109 86.467

STA	DIR	QUAL	DIST	EVAZ	TCA	X	Y
CLC	D	2	1.577	25.929	48.950	0.640	1.317
CSP	C	2	0.905	96.240	87.879	2.439	-0.267
GSC	C	2	1.623	55.773	48.950	1.211	0.824
ISA	D	2	1.113	358.811	85.578	-0.050	2.401
MWC	C	2	0.366	118.854	93.868	-2.114	1.165
PAS	C	2	0.338	137.880	94.176	-1.615	1.786
PLM	C	2	1.680	127.918	48.950	1.156	-0.900
PYR	D	-2	0.299	304.960	94.613	1.965	-1.374
RVR	C	2	0.975	114.212	87.110	2.222	-0.999
SYP	C	-1	1.273	276.320	48.950	-1.456	0.161
BOUQ	D	2	0.112	1.664	118.795	-0.052	-1.799
BRWN	C	-2	0.162	228.337	109.328	1.528	1.359
IRON	C	2	0.048	126.229	144.090	-0.879	0.644
GOOK	C	2	0.040	219.678	149.647	0.591	0.712
SOLE	C	2	0.082	51.025	128.145	-1.202	-0.972
INDN	C	2	0.148	76.223	111.421	-1.935	-0.474
NMLM	C	2	0.303	95.519	94.562	-2.387	0.231
NRTM	D	2	0.259	39.237	95.057	-1.510	-1.849
ENGN	C	2	0.393	130.892	93.564	-1.830	1.585

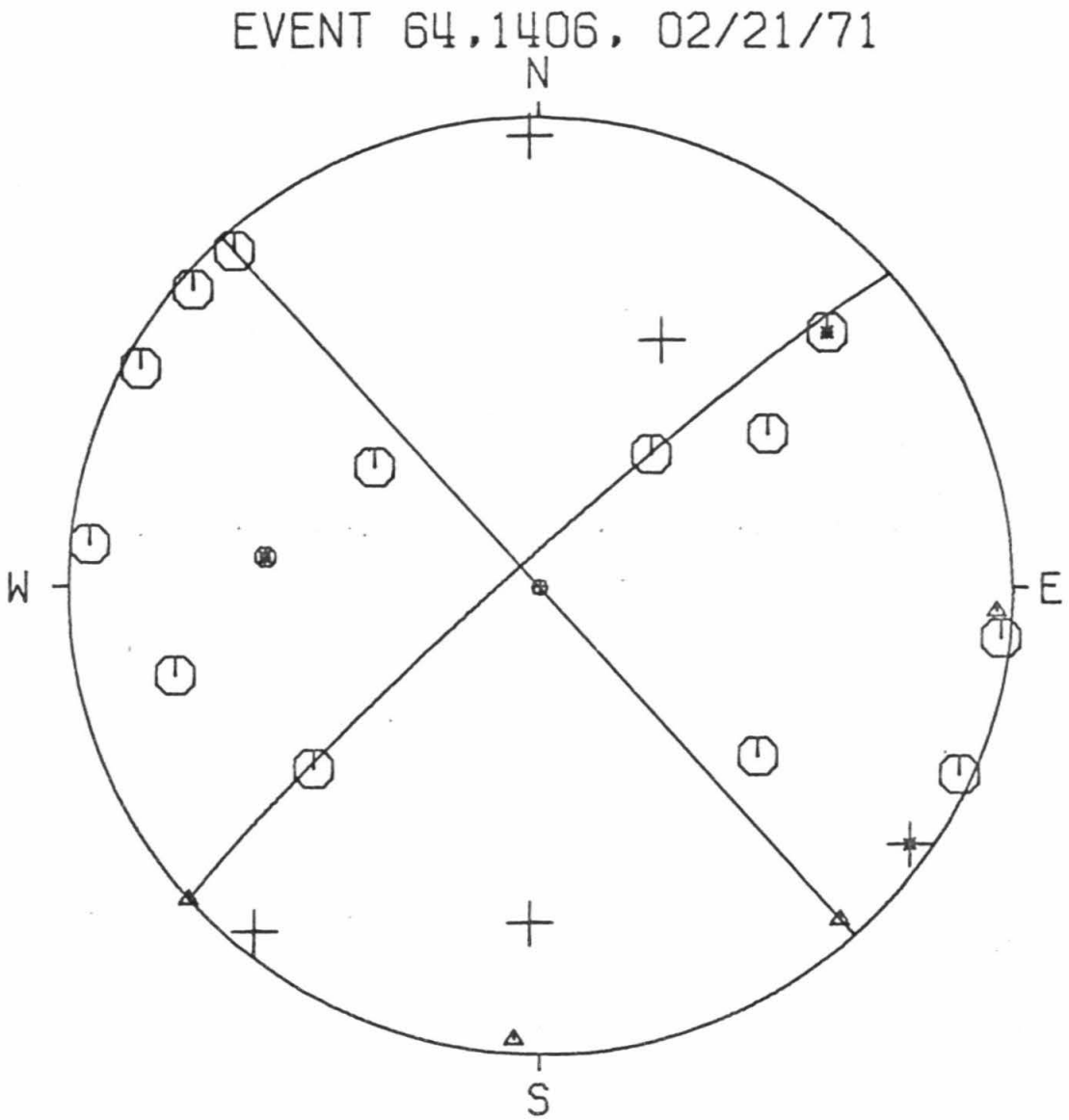
EVENT 64,1406, 02/21/71
N
W
E
S

EVENT DATA

65,1604 0 02/24/71 16 4 0.0

10.8 34.000 26.48 -118.000 24.64 3.7

AZ1= 104.000
DIP1= 60.000
AZ2= 208.000
DIP2= 67.265

SLIP VECTORS= 118.000 67.265 14.000 60.000

PRIN AXES = 68.304 51.184 334.591 85.395

STA	DIR	QUAL	DIST	EVAZ	TOA	X	Y
CLC	C	2	1.526	25.693	49.400	0.641	1.331
CSP	C	2	0.883	99.167	93.754	-2.386	0.385
GSC	C	2	1.575	56.508	49.400	1.232	0.815
ISA	D	2	1.071	357.433	91.376	0.111	-2.467
MWC	D	2	0.365	126.948	102.443	-1.770	1.331
PAS	D	2	0.354	145.936	102.897	-1.234	1.825
PLM	C	2	1.685	129.688	49.400	1.137	-0.943
PYR	D	2	0.303	295.484	104.937	1.944	-0.927
RVR	D	2	0.968	117.254	92.677	-2.170	1.118
SBC	D	2	1.244	271.630	49.400	-1.477	0.042
SYP	D	2	1.298	274.342	49.400	-1.473	0.112
TIN	D	1	2.612	3.202	49.400	0.083	1.475
BRWN	C	2	0.212	224.778	111.528	1.401	1.412
IRON	C	2	0.059	169.648	146.286	-0.184	1.009
GOOK	C	2	0.082	221.162	137.368	0.846	0.968
NAGM	C	2	0.095	51.016	133.080	-1.094	-0.885
NMLM	D	2	0.280	102.217	105.845	-2.083	0.451
NRTM	C	2	0.207	40.692	112.058	-1.288	-1.498
NWSM	D	2	0.207	324.211	112.058	1.155	-1.603
ENGN	D	2	0.403	138.243	100.924	-1.499	1.679
SWM	D	2	0.311	332.774	104.607	0.989	-1.922

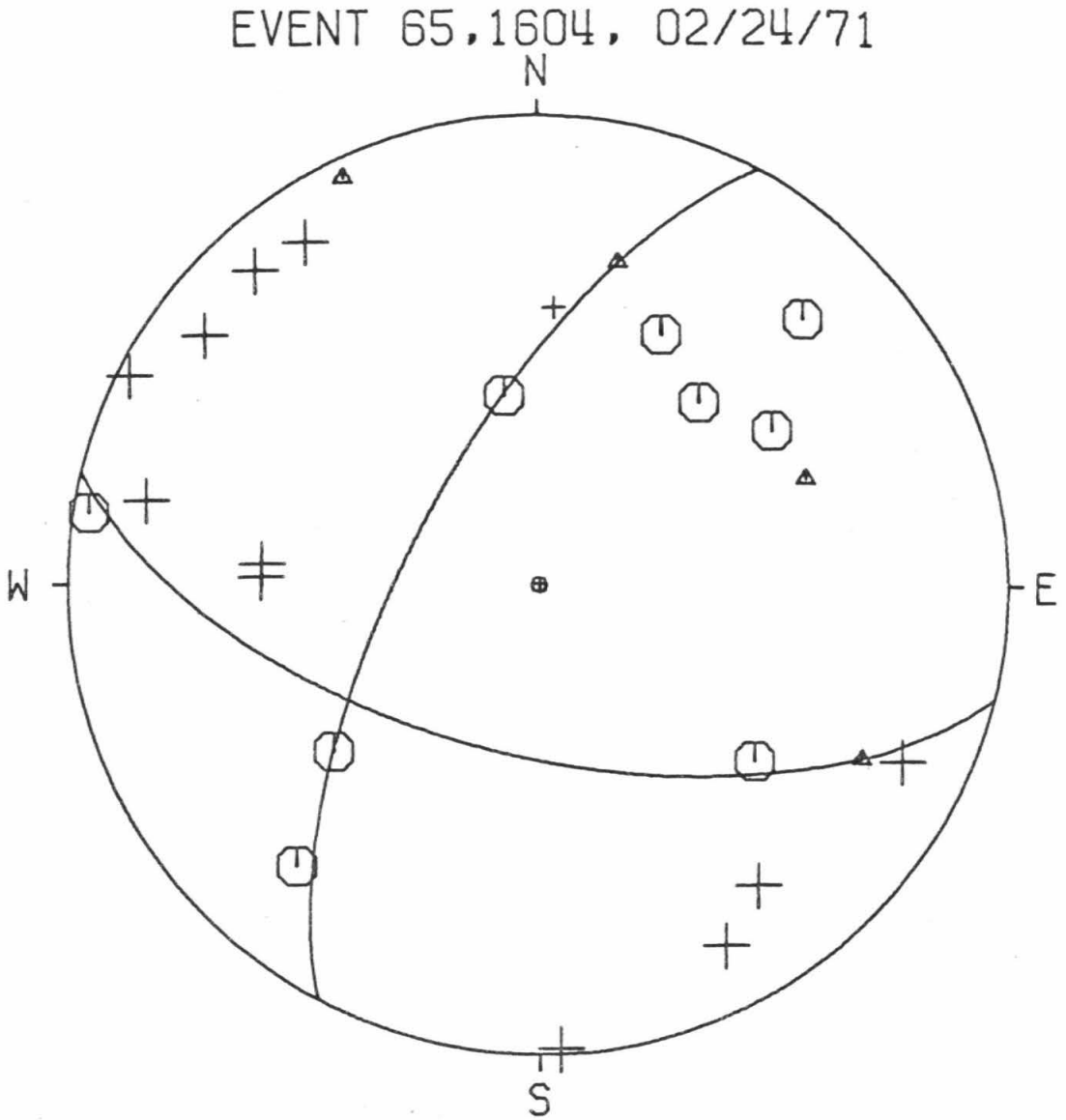
EVENT 65,1604, 02/24/71
N
W
E
S

EVENT DATA

66,1127 0 02/25/71 11 27 32.9

7.5 34.000 25.23 -118.000 26.51 3.2

AZ1= 58.000
DIP1= 42.000
AZ2= 224.000
DIP2= 48.858

SLIP VECTORS= 134.000 48.858 327.999 42.000

PRIN AXES = 76.543 7.820 320.584 86.546

STA	DIR	QUAL	DIST	EVAZ	TCA	X	Y
GSC	C	2	1.608	56.375	49.275	1.227	0.816
ISA	D	2	1.091	358.669	88.645	-0.057	2.470
MWC	D	2	0.374	121.893	97.235	-1.984	1.235
PAS	D	2	0.353	140.637	97.486	-1.479	1.803
PLM	C	1	1.692	128.574	49.275	1.152	-0.919
PYR	D	2	0.289	301.243	98.253	1.978	-1.200
SYP	D	2	1.274	275.367	49.275	-1.467	0.138
BOUQ	D	2	0.093	0.390	124.404	-0.011	-1.649
BRWN	C	-2	0.179	223.625	107.657	1.440	1.510
IRON	C	2	0.052	135.833	141.663	-0.809	0.833
GOOK	C	2	0.056	209.888	139.546	0.609	1.060
SOLE	C	2	0.066	67.900	134.947	-1.255	-0.510
INDN	D	2	0.145	76.175	111.965	-1.921	-0.473
NMLM	D	2	0.302	97.715	98.102	-2.296	0.311
NOMM	C	2	0.162	233.919	109.328	1.653	1.204
NWSM	D	2	0.212	333.216	104.452	0.976	-1.933
ENGN	D	2	0.407	133.611	96.844	-1.699	1.618

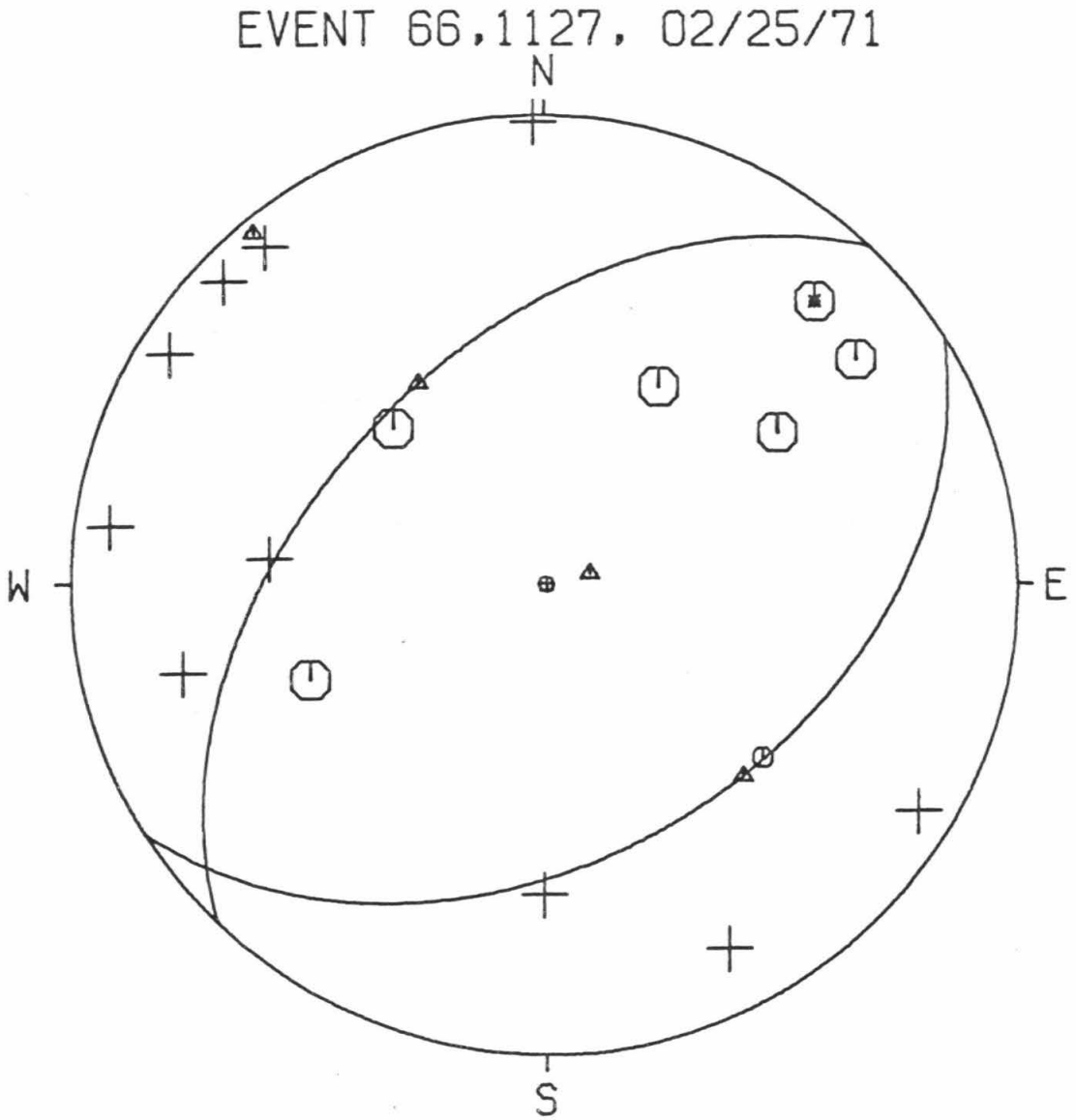
EVENT 66,1127, 02/25/71
N
W
E
S

EVENT DATA

67,2027 0 02/25/71 20 27 0.0

3.0 34.000 20.17 -118.000 21.79 3.5

AZ1= 65.000
DIP1= 46.000
AZ2= 284.000
DIP2= 51.174

SLIP VECTORS= 194.000 51.174 334.999 46.000

PRIN AXES = 258.057 20.851 355.308 87.256

STA	DIR	QUAL	DIST	EVAZ	TCA	X	Y
CLC	D	2	1.606	22.833	44.933	0.524	1.245
CSP	C	2	0.834	93.253	83.512	2.351	-0.134
GSC	D	2	1.604	52.634	44.933	1.074	0.820
ISA	D	2	1.178	355.946	80.213	-0.161	2.272
MWC	D	2	0.279	115.155	88.830	2.240	-1.052
PAS	D	2	0.247	139.996	89.136	1.595	-1.901
PLM	D	2	1.589	127.714	44.933	1.069	-0.826
PYR	D	1	0.390	306.816	87.764	-1.962	1.469
RVR	D	1	0.888	112.431	82.989	2.165	-0.894
SYP	C	2	1.348	278.669	44.933	-1.336	0.204
BRWN	C	2	0.196	254.526	85.122	-2.305	-0.638
IRON	D	2	0.069	335.328	105.211	0.896	-1.951
GOOK	D	2	0.108	300.918	96.988	2.010	-1.204
SOLE	D	2	0.105	357.675	97.463	0.095	-2.330
INDN	D	2	0.119	39.885	95.652	-1.522	-1.821
NAGM	D	2	0.163	12.219	90.509	-0.527	-2.432
NMLM	C	2	0.241	75.863	89.190	2.407	0.606
NOMM	C	2	0.199	260.324	89.599	-2.456	-0.419
NWSM	D	2	0.316	329.464	88.477	-1.253	2.124
ENGN	D	2	0.302	130.586	88.610	1.875	-1.607

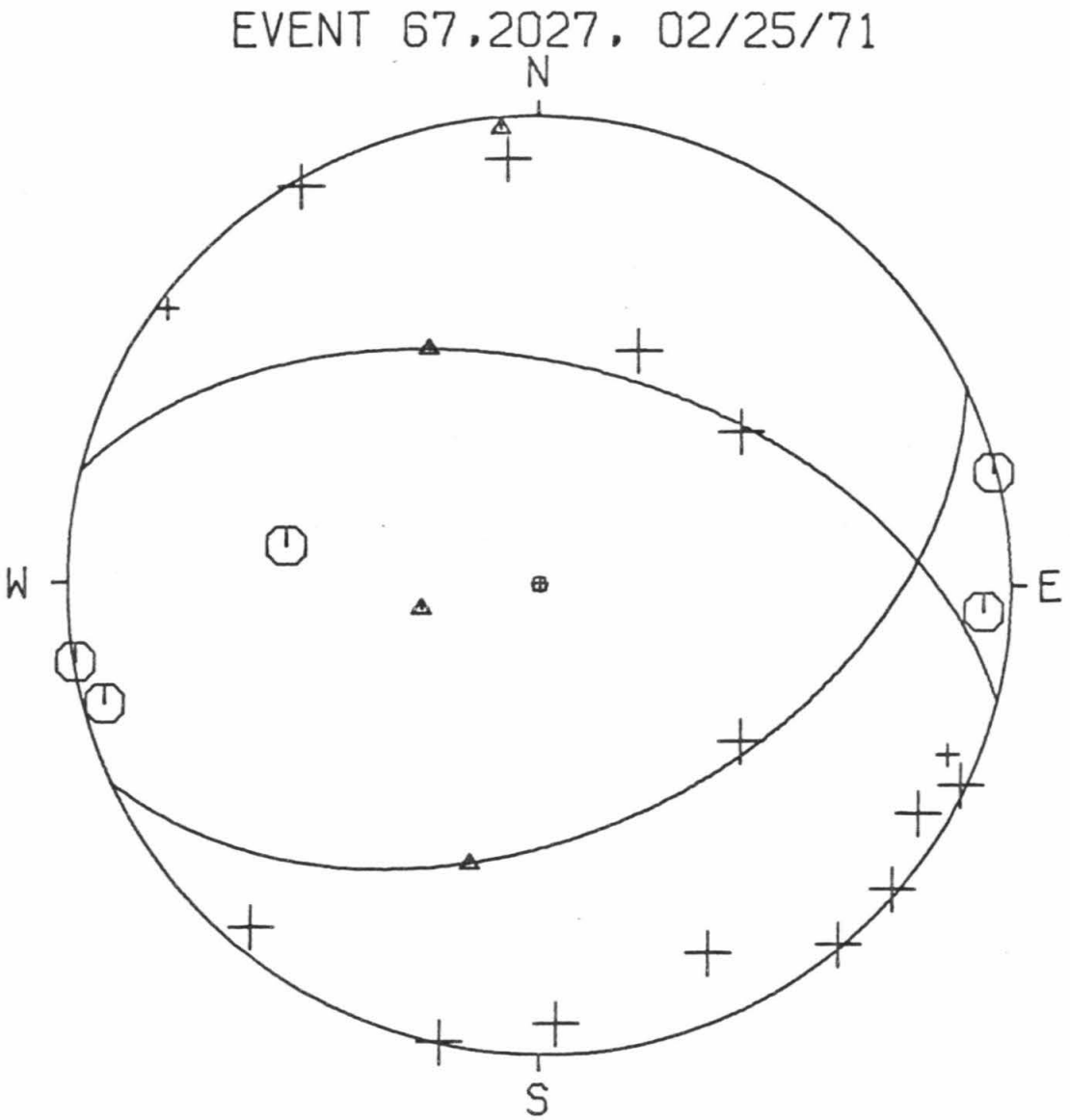
EVENT 67,2027, 02/25/71
N
W
E
S

EVENT DATA

68,0333 0 02/26/71 3 33 0.0

7.5 34.000 25.13 -118.000 22.95 3.5

AZ1= 98.000
DIP1= 36.000
AZ2= 315.000
DIP2= 59.876

SLIP VECTORS= 225.000 59.876 8.000 36.000

PRIN AXES = 266.736 22.039 30.152 77.457

STA	DIR	QUAL	DIST.	EVAZ	TOA	X	Y
CLC	D	2	1.537	24.564	49.275	0.613	1.340
CSP	C	2	0.857	98.067	91.450	-2.444	0.346
GSC	D	2	1.568	55.373	49.275	1.213	0.838
ISA	D	2	1.094	356.408	88.603	-0.155	2.464
MWC	C	2	0.333	126.177	97.732	-1.877	1.373
PAS	D	2	0.323	147.179	97.854	-1.259	1.952
PLM	C	2	1.653	129.620	49.275	1.135	-0.940
PYR	D	1	0.333	297.048	97.732	2.071	-1.058
RVR	C	2	0.937	116.713	90.487	-2.224	1.119
SBC	C	2	1.268	272.079	49.275	-1.473	0.053
SYP	C	2	1.322	275.198	49.275	-1.468	0.134
BOUQ	D	2	0.105	332.476	120.441	0.811	-1.557
BRWN	D	2	0.215	233.491	104.185	1.746	1.292
IRON	C	2	0.040	198.581	149.647	0.295	0.877
GOOK	D	2	0.091	238.095	125.115	1.383	0.861
SOLE	C	2	0.034	20.042	153.383	-0.279	-0.765
INDN	C	1	0.097	71.872	123.029	-1.603	-0.525
NAGM	C	2	0.095	32.163	123.709	-0.888	-1.412
NMLM	C	2	0.253	99.087	99.031	-2.267	0.363
ENGN	C	2	0.371	138.544	97.279	-1.547	1.751

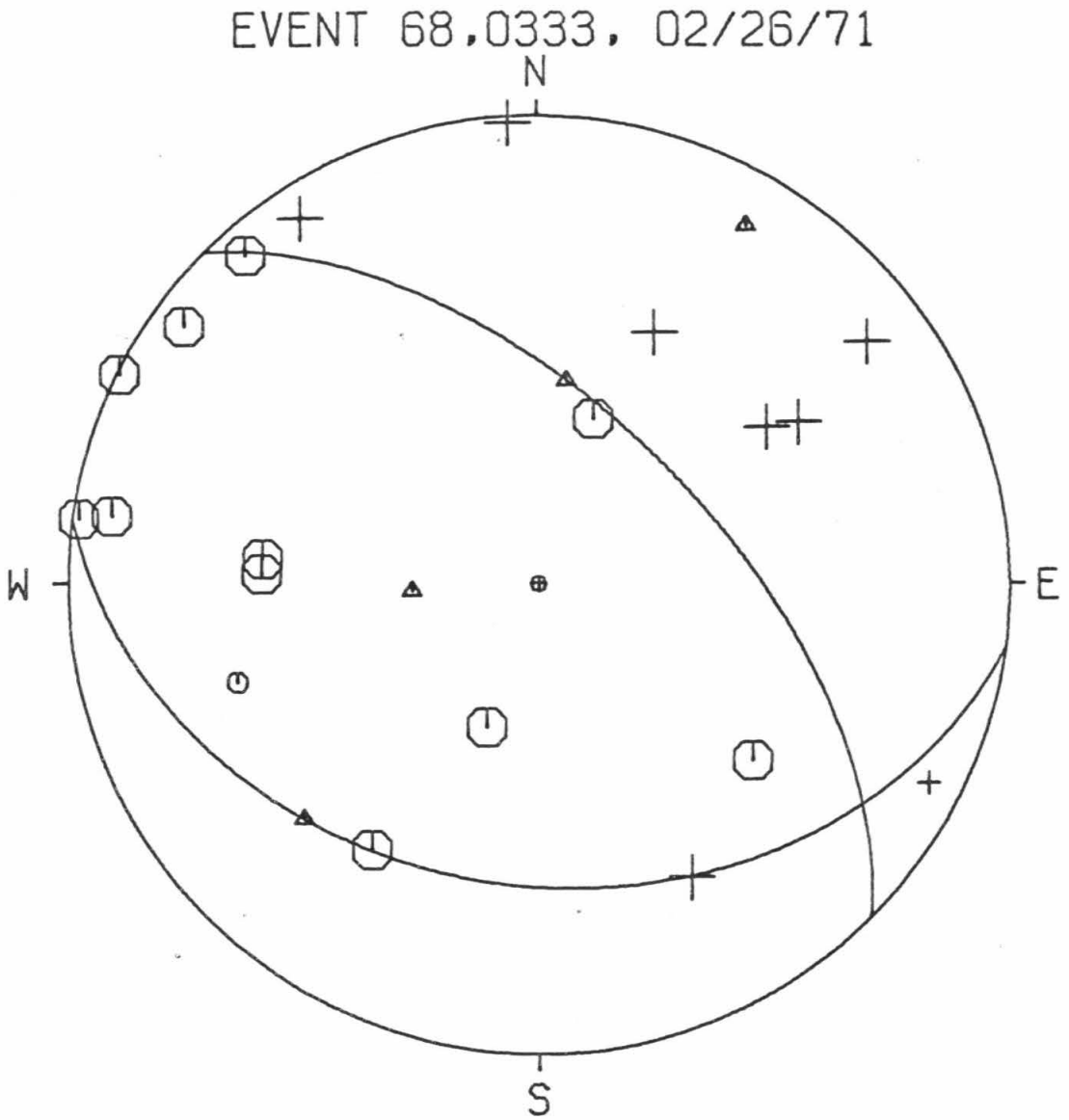
EVENT 68,0333, 02/26/71
N
W
E
S

EVENT DATA

69,2122 0 02/26/71 21 22 33.9

10.0 34.000 27.25 -118.000 27.21 3.3

STA	DIR	QUAL	DIST	EVAZ	TOA	X	Y
GSC		-1	1.598	57.570	49.400	1.247	0.792
ISA	D	2	1.057	359.088	91.149	0.039	-2.474
MWC	D	2	0.401	125.268	100.225	-1.851	1.309
PAS	D	2	0.385	142.632	100.734	-1.369	1.792
PLM	D	2	1.720	129.237	49.400	1.144	-0.934
PYR	D	2	0.265	296.357	104.557	1.938	-0.960
RVR	D	2	1.005	116.948	91.799	-2.193	1.115
SYP	D	1	1.261	273.846	49.400	-1.474	0.099
BOUQ	D	2	0.059	9.939	143.898	-0.189	-1.079
BRWN	C	-2	0.199	214.973	110.957	1.148	1.642
IRON	C	2	0.084	146.689	133.884	-0.760	1.157
GOOK	C	2	0.077	193.785	136.509	0.312	1.272
SOLE	C	2	0.079	117.151	135.607	-1.188	0.609
INDN	C	1	0.158	107.685	115.752	-1.791	0.571
NAGM	C	2	0.120	65.083	123.399	-1.520	-0.706
NMLM	D	2	0.316	102.121	102.945	-2.153	0.462
NWSM	D	2	0.177	330.920	113.336	0.944	-1.698
ENGN	D	2	0.437	135.878	99.076	-1.597	1.647

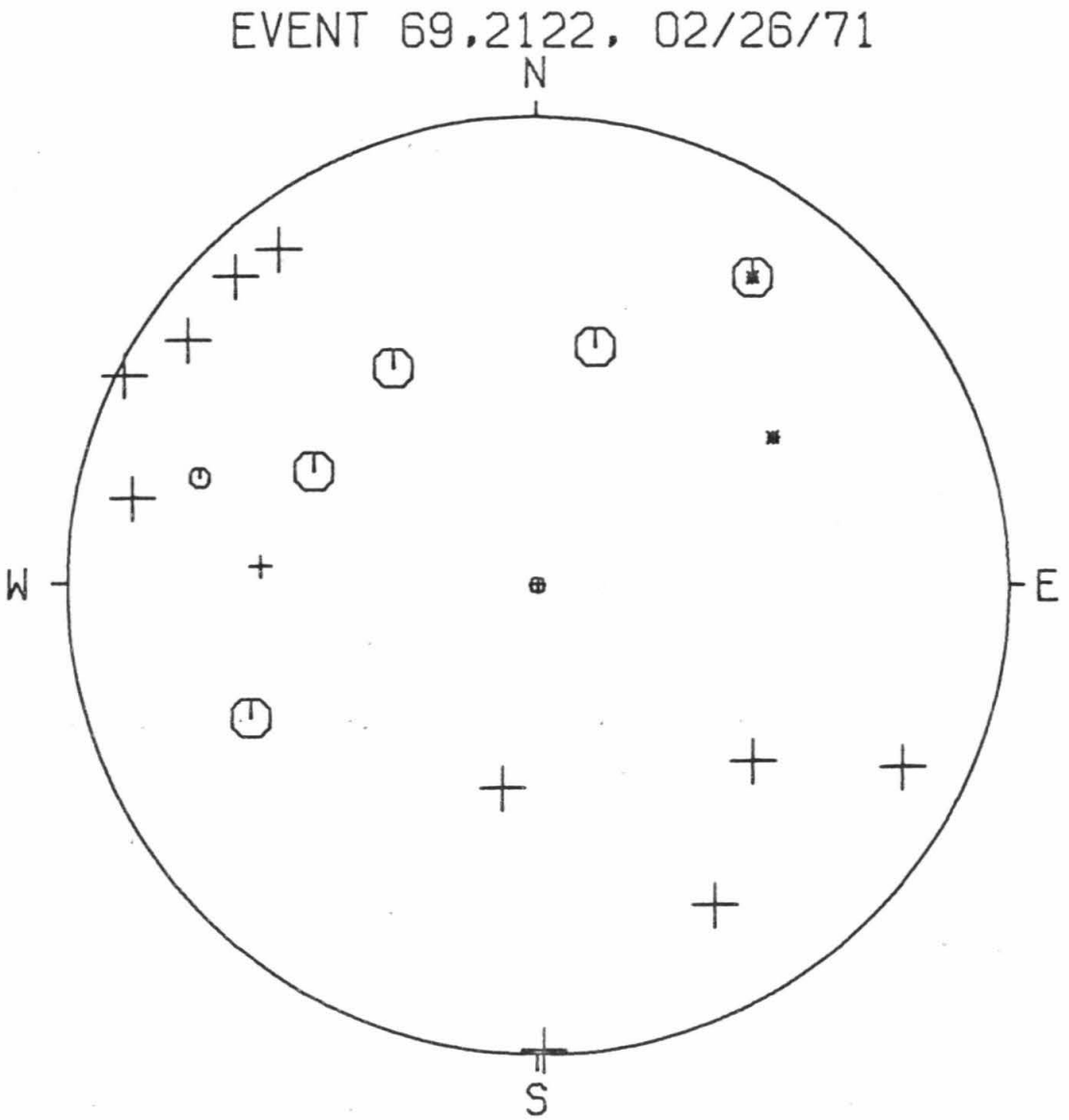
EVENT 69,2122, 02/26/71
N
W
E
S

EVENT DATA

70,0428 0 03/01/71 4 28 0.0

4.4 34.000 24.05 -118.000 26.00 3.4

STA	DIR	QUAL	DIST	EVAZ	TOA	X	Y
CLC	D	2	1.570	25.660	48.500	0.629	1.309
GSC	C	2	1.613	55.662	48.500	1.199	0.819
ISA	D	2	1.110	358.369	81.723	-0.066	2.312
MWC	C	2	0.359	120.004	89.134	2.149	-1.241
PAS	C	-2	0.333	139.385	89.385	1.619	-1.888
PLM	C	2	1.674	128.201	48.500	1.141	-0.898
PYR	D	2	0.306	303.693	89.657	-2.074	1.383
RVR	C	2	0.967	114.630	83.133	2.132	-0.978
SBC	C	2	1.226	272.952	48.500	-1.450	0.075
SYP	D	1	1.283	276.231	48.500	-1.444	0.158
BOUQ	D	2	0.110	356.664	97.321	0.136	-2.331
BRWN	C	2	0.172	229.251	89.852	-1.891	-1.630
IRON	C	-2	0.044	138.315	122.304	-1.134	1.274
GOOK	C	2	0.044	232.157	122.304	1.347	1.047
SCLE	D	2	0.069	51.653	108.439	-1.621	-1.283
INDN	D	2	0.138	75.577	92.894	-2.359	-0.607
ENGN	C	2	0.388	132.208	88.845	1.833	-1.663
SWM	D	1	0.340	338.675	89.322	-0.904	2.315
BHR	D	2	0.397	171.422	88.756	0.369	-2.445

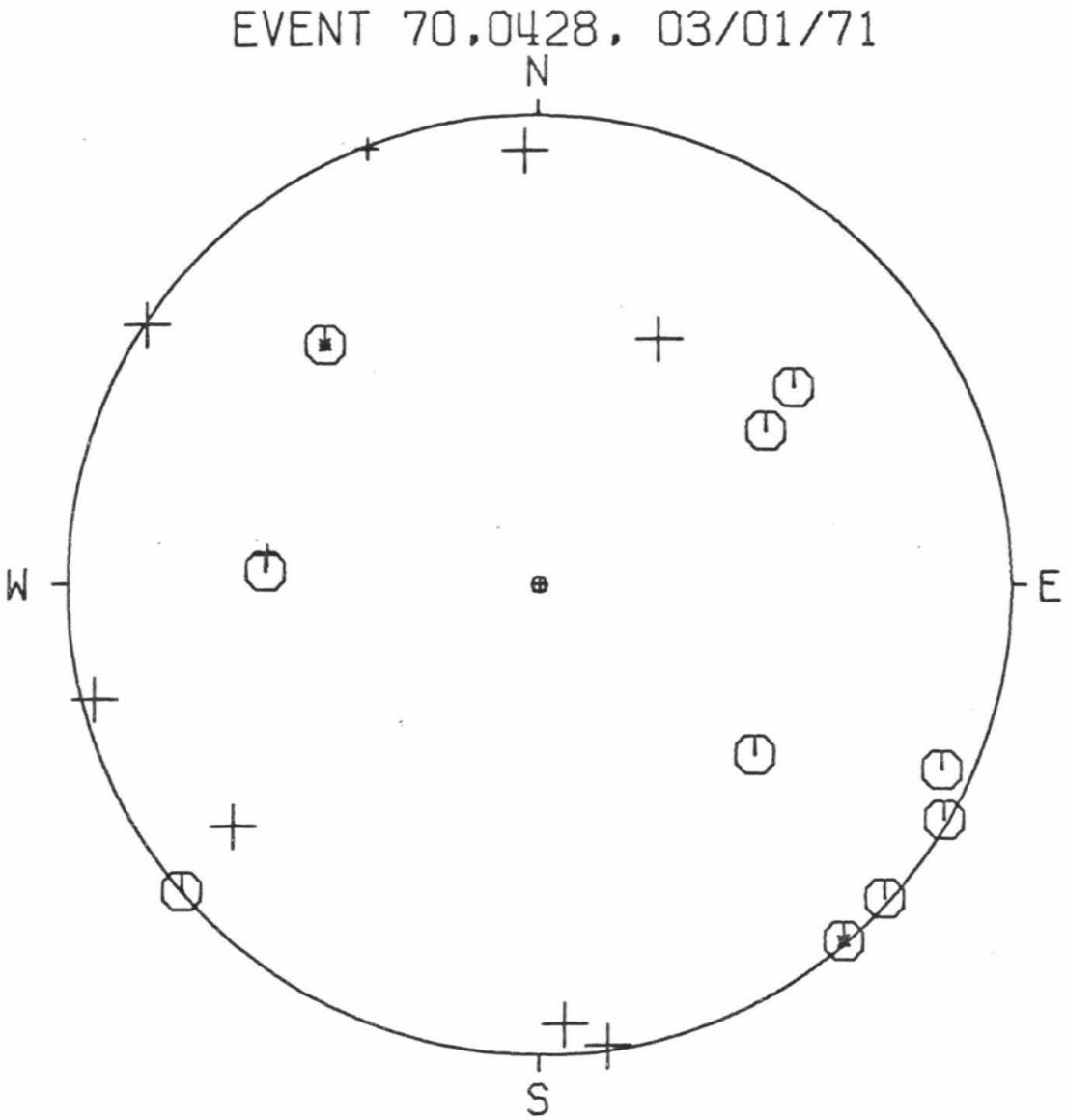
EVENT 70,0428, 03/01/71
N
W
E
S

EVENT DATA

71,0133 0 03/07/71 1 33 0.0

3.2 34.000 21.19 -118.000 27.35 4.5

AZ1= 121.500
DIP1= 67.000
AZ2= 216.000
DIP2= 79.527

SLIP VECTORS= 126.000 79.527 31.500 67.000

PRIN AXES = 80.790 66.120 347.002 81.503

STA	DIR	QUAL	DIST	EVAZ	TOA	X	Y
BAR	C	2	2.238	137.740	45.627	0.922	-1.015
CLC	C	2	1.622	25.510	45.627	0.590	1.237
CSP	C	2	0.911	93.807	82.770	2.332	-0.155
CWC	C	1	2.104	8.326	45.627	0.199	1.356
GLA	C	1	3.292	112.216	45.627	1.269	-0.518
GSC	C	2	1.656	54.658	45.627	1.118	0.793
HFD	D	1	2.429	104.622	45.627	1.326	-0.346
ISA	D	2	1.158	359.245	80.407	-0.030	2.282
MWC	C	2	0.355	111.891	88.102	2.281	-0.917
PAS	C	2	0.313	131.234	88.500	1.855	-1.626
PLM	C	2	1.660	126.505	45.627	1.102	-0.815
PYR	D	2	0.320	312.553	88.435	-1.816	1.667
RVR	C	2	0.966	111.579	82.246	2.162	-0.855
SBC	D	2	1.211	275.468	50.032	-1.488	0.142
SYP	D	2	1.270	278.342	45.627	-1.356	0.199
TIN	C	1	2.702	3.864	45.627	0.092	1.368
BOUQ	D	2	0.157	4.450	90.561	-0.193	-2.480
BRWN	C	2	0.131	238.606	94.032	2.058	1.256
IRON	C	2	0.066	47.065	106.653	-1.546	-1.438
GOOK	D	2	0.044	338.358	122.304	0.629	-1.586
SOLE	D	2	0.112	40.282	96.633	-1.520	-1.794
INDN	C	2	0.170	63.824	90.205	-2.240	-1.101
NAGM	D	2	0.181	37.779	89.903	1.530	1.974
NMLM	C	2	0.314	81.767	88.494	2.442	0.353
NOMM	C	2	0.127	250.346	94.645	2.257	0.806
NRTM	C	2	0.299	35.198	88.635	1.424	2.018
NWSM	D	2	0.268	341.744	88.932	-0.776	2.352
ENGN	C	2	0.373	124.883	87.927	2.013	-1.404
SWM	D	2	0.378	343.890	87.877	-0.681	2.357
IPC	D	2	0.395	165.820	87.721	0.600	-2.375
HCC	D	2	0.365	170.493	88.008	0.406	-2.422
BHR	D	2	0.354	167.297	88.107	0.541	-2.398
BLNY	D	2	0.110	175.474	96.870	-0.185	2.338

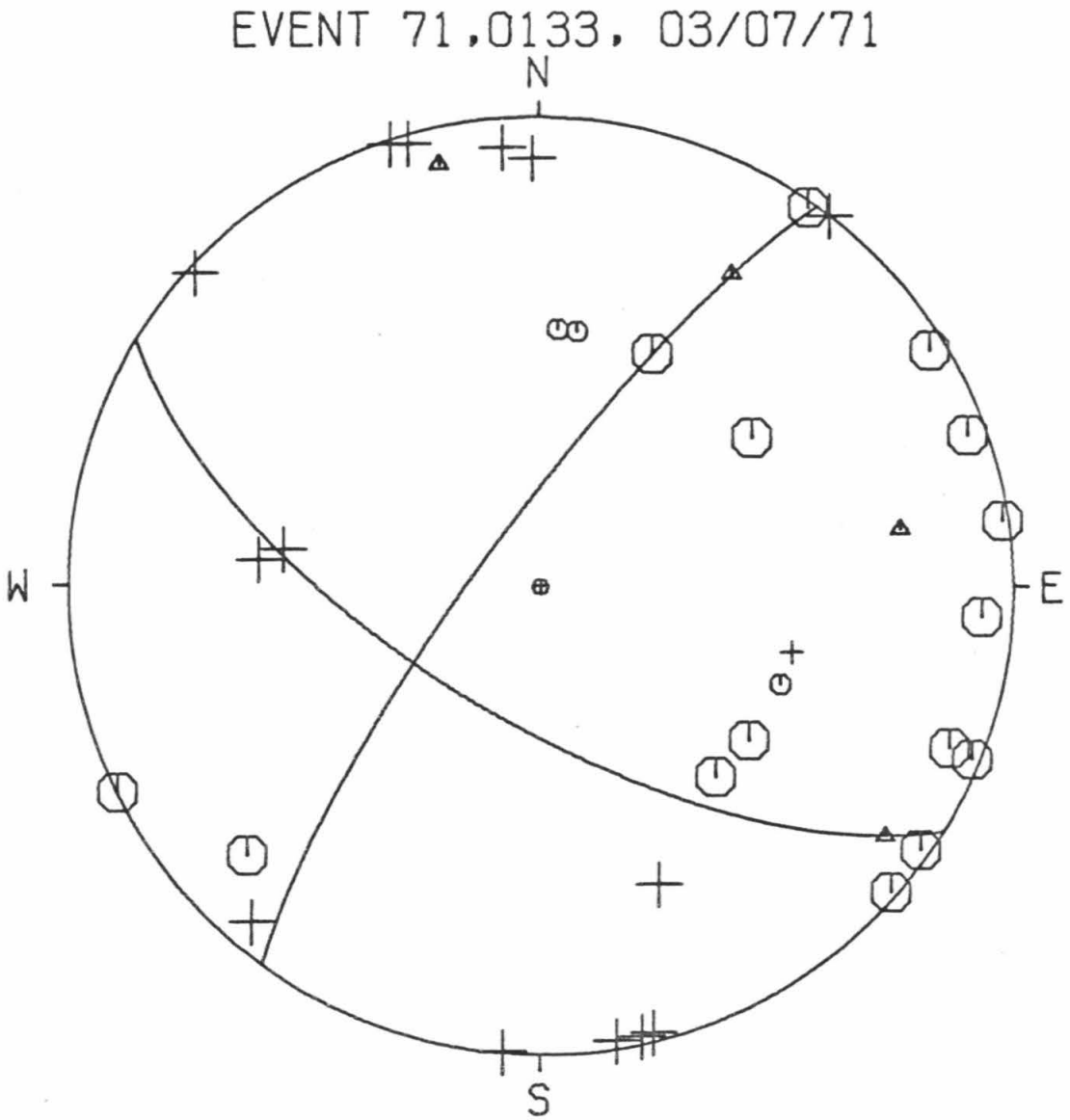
EVENT 71,0133, 03/07/71
N
W
E
S

EVENT DATA

72,0656 0 03/07/71 6 56 0.0

4.9 34.000 22.59 -118.000 26.00 3.9

STA	DIR	QUAL	DIST	EVAZ	TCA	X	Y
BAR	C	2	2.242	138.502	48.625	0.964	-1.090
CLC	D	1	1.592	25.283	48.625	0.622	1.316
CSP	C	2	0.894	95.085	85.010	2.379	-0.212
GSC	C	2	1.627	54.959	48.625	1.192	0.836
HFD	C	1	2.417	105.282	48.625	1.404	-0.384
ISA	D	2	1.135	358.400	82.554	-0.065	2.331
MWC	D	2	0.348	116.674	90.584	-2.223	1.117
PAS	D	2	0.315	136.501	90.915	-1.707	1.799
PLM	C	2	1.659	127.542	48.625	1.154	-0.887
PYR	D	2	0.319	307.087	90.877	1.979	-1.496
RVR	C	1	0.957	113.267	84.364	2.181	-0.938
SBC	D	2	1.228	274.224	48.625	-1.452	0.107
SYP	D	2	1.285	277.212	48.625	-1.444	0.183
BCUQ	D	2	0.133	357.232	93.796	0.117	-2.413
BRWN	C	2	0.158	235.644	89.988	-2.064	-1.411
GOOK	C	2	0.044	307.843	122.304	1.347	-1.047
SOLE	C	2	0.084	39.818	103.128	-1.407	-1.688
INDN	D	2	0.144	68.626	92.028	-2.286	-0.895
NAGM	C	2	0.152	37.488	90.789	-1.511	-1.970
NOMM	C	2	0.148	248.694	91.400	2.301	0.897
NWSM	D	2	0.253	336.102	91.636	0.998	-2.253
ENGN	D	2	0.373	129.522	90.329	-1.923	1.586
SWM	D	2	0.362	340.046	90.437	0.850	-2.341
IPC	C	2	0.413	169.119	89.917	0.472	-2.453
HCC	C	2	0.386	173.816	90.197	-0.269	2.481
BHR	D	1	0.373	170.855	90.329	-0.396	2.461
BLNY	D	2	0.133	184.303	93.796	0.181	2.409

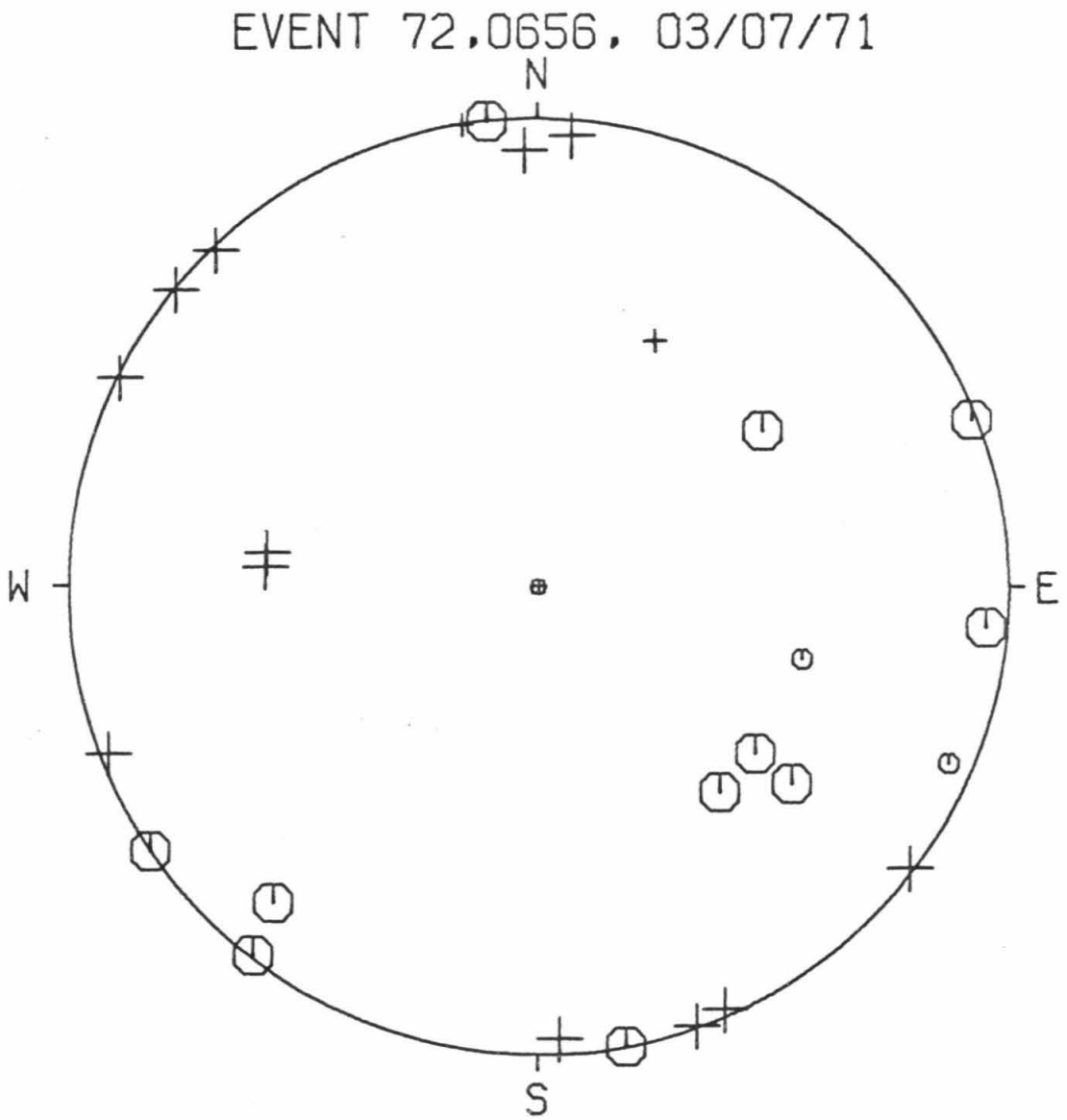
EVENT 72,0656, 03/07/71
N
W
E
S

EVENT DATA

73,0711 0 03/07/71 7 11 0.0

3.0 34.000 22.65 -118.000 26.22 3.3

AZ1= 70.000
DIP1= 44.000
AZ2= 215.000
DIP2= 51.654

SLIP VECTORS= 125.000 51.654 339.999 44.000

PRIN AXES = 63.368 18.678 321.405 85.988

STA	DIR	QUAL	DIST	EVAZ	TCA	X	Y
CLC	C	2	1.593	25.395	44.933	0.579	1.221
CSP	C	1	0.897	95.097	82.905	2.331	-0.208
GSC	C	2	1.629	55.046	44.933	1.107	0.774
ISA	D	-2	1.134	358.534	80.636	-0.059	2.287
MWC	D	2	0.351	116.481	88.144	2.201	-1.097
PAS	D	2	0.318	136.168	88.459	1.708	-1.779
PLM	C	1	1.662	127.506	44.933	1.072	-0.823
PYR	D	2	0.317	307.403	88.471	-1.959	1.498
SBC	D	2	1.224	274.004	50.438	-1.503	0.105
SYP	D	2	1.282	277.157	44.933	-1.341	0.168
BOUQ	D	-2	0.133	358.538	93.842	0.062	-2.414
BRWN	C	-2	0.156	235.014	90.861	2.033	1.423
GOOK	C	2	0.044	313.842	122.304	1.230	-1.182
SCLE	D	2	0.086	41.176	100.699	-1.485	-1.698
INDN	D	2	0.147	69.189	92.032	-2.295	-0.872
NMLM	D	2	0.297	84.187	88.660	2.458	0.250
NOMM	C	2	0.144	249.492	92.379	2.292	0.857
NRTM	C	2	0.271	35.477	88.912	1.437	2.016
NWSM	D	2	0.252	336.696	89.091	-0.981	2.278
ENGN	D	2	0.375	129.277	87.907	1.900	-1.554
SWM	D	2	0.360	340.462	88.049	-0.822	2.316
BHR	D	1	0.374	170.422	87.917	0.408	-2.420
BLNY	D	2	0.134	182.958	93.652	0.125	2.416

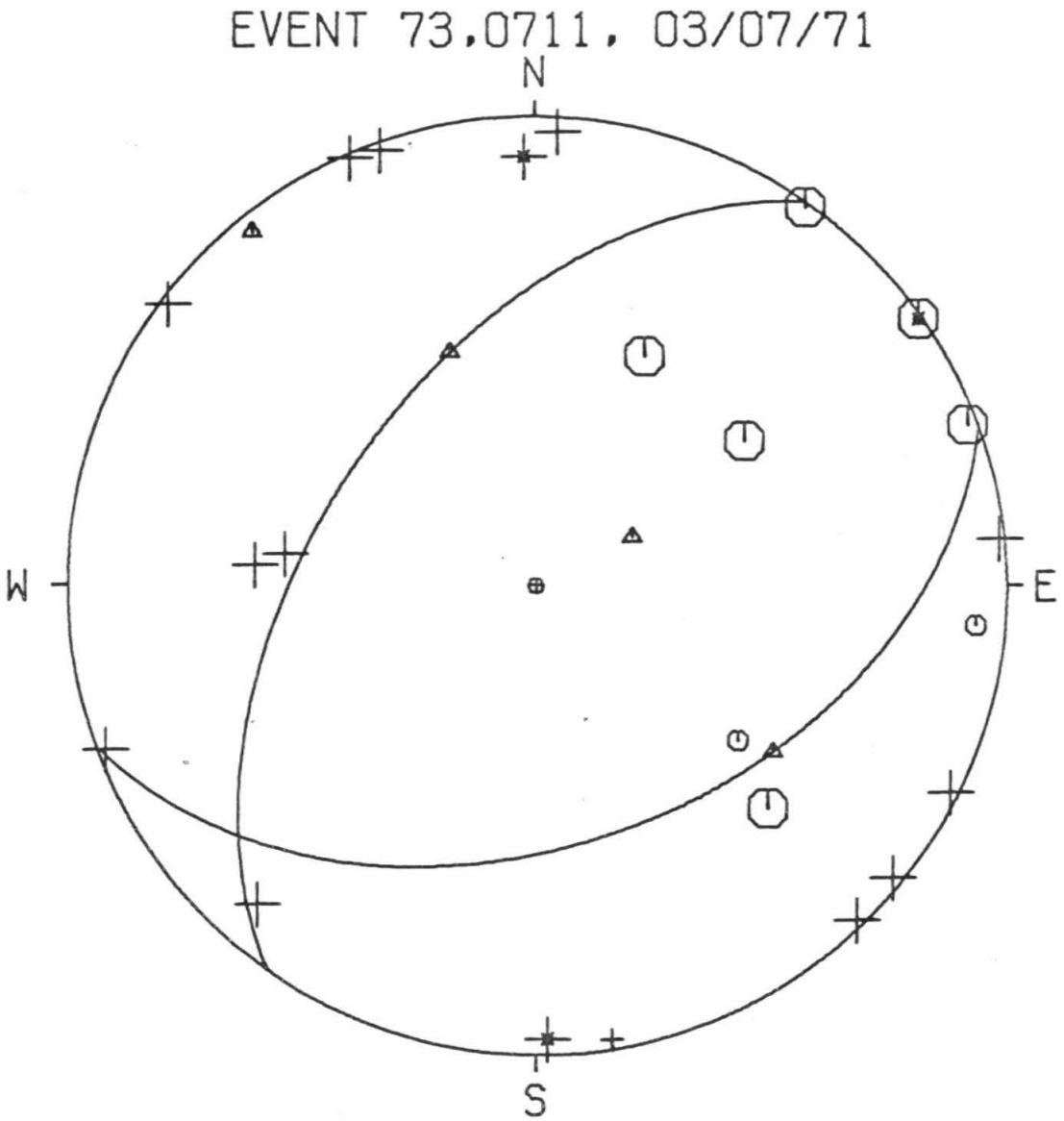
EVENT 73.0711, 03/07/71
N
W
E
S

EVENT DATA

74,2136 0 03/07/71 21 36 0.0

3.8 34.000 24.83 -118.000 22.85 3.3

AZ1= 42.000
DIP1= 70.000
AZ2= 240.000
DIP2= 20.942

SLIP VECTORS= 150.000 20.942 311.999 70.000

PRIN AXES = 301.569 25.547 136.933 65.257

STA	DIR	QUAL	DIST	EVAZ	TCA	X	Y
CLC	C	2	1.540	24.443	47.707	0.592	1.302
CSP	C	1	0.855	97.758	83.310	2.328	-0.317
GSC	C	2	1.570	55.185	47.707	1.174	0.816
ISA	D	2	1.099	356.359	80.965	-0.146	2.291
MWC	D	2	0.329	125.601	88.354	2.003	-1.434
PAS	D	2	0.318	146.911	88.459	1.346	-2.066
PLM	D	2	1.648	129.513	47.707	1.103	-0.910
PYR	D	2	0.336	297.688	88.281	-2.180	1.144
RVR	D	2	0.933	116.444	82.557	2.088	-1.039
SYP	C	2	1.324	275.439	47.707	-1.423	0.136
BOUQ	D	2	0.110	333.135	97.208	1.056	-2.086
BRWN	C	2	0.214	234.464	89.454	-2.025	-1.446
COOK	D	2	0.086	245.331	102.008	2.022	0.929
SOLE	D	2	0.034	17.569	130.818	-0.444	-1.403
INDN	C	2	0.095	72.950	99.512	-2.184	-0.670
NAGM	D	2	0.099	29.765	98.903	-1.141	-1.995
NMLM	D	2	0.251	97.682	89.099	2.458	-0.332
NOMM	D	2	0.202	244.034	89.571	-2.239	-1.090
NRTM	C	2	0.215	30.995	89.445	1.281	2.133
ENGN	D	2	0.367	138.324	87.987	1.633	-1.834
SWM	D	2	0.346	331.180	88.187	-1.186	2.155
IPC	D	2	0.444	175.566	87.247	0.189	-2.432
HCC	D	2	0.420	180.285	87.477	-0.012	-2.444
BHR	D	2	0.405	177.792	87.618	0.094	-2.446
BLNY	C	2	0.176	197.699	89.877	-0.759	-2.379

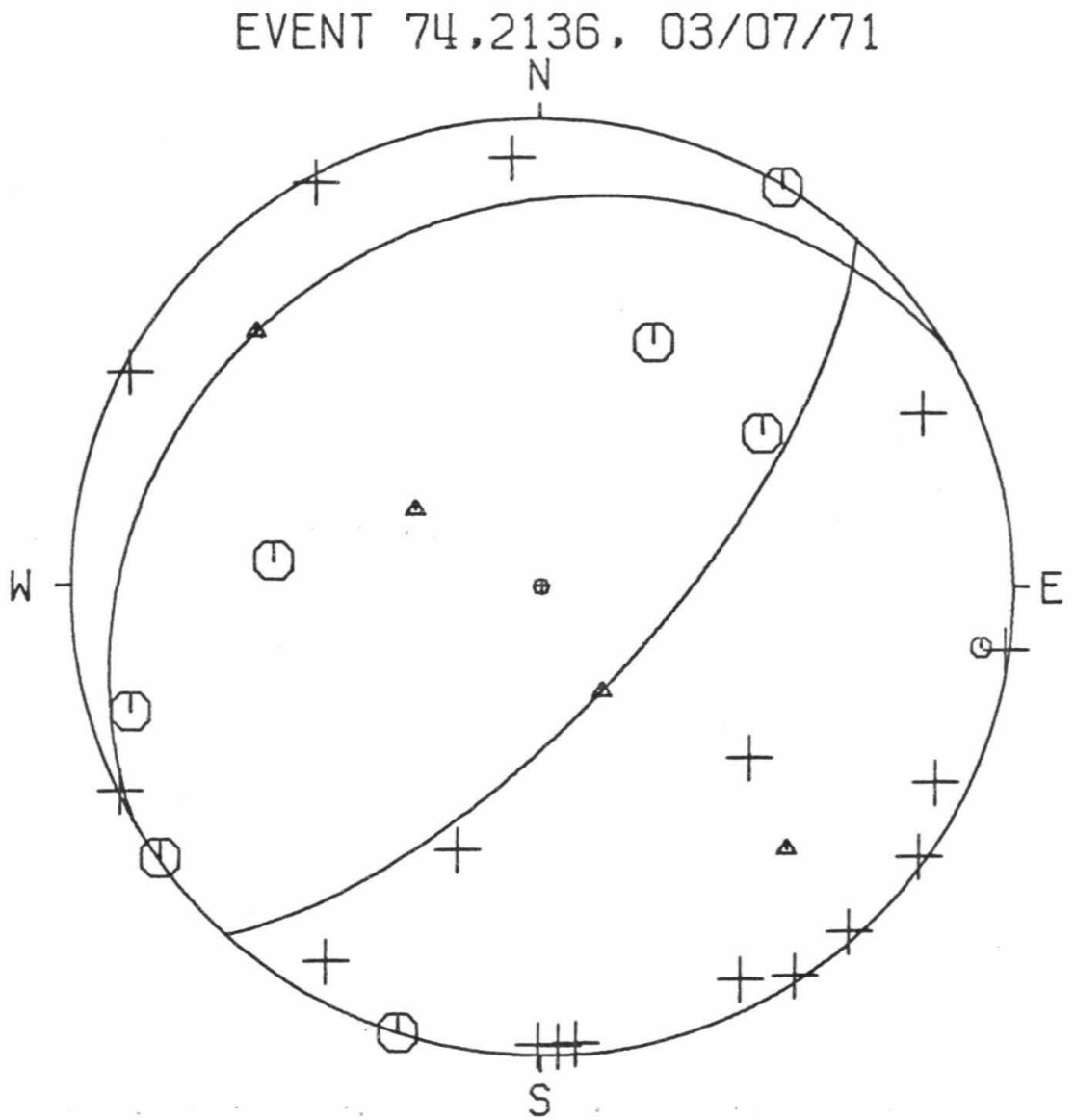
EVENT 74,2136, 03/07/71
N
W
E
S

EVENT DATA

75,2254 0 03/25/71 22 54 0.0

4.6 34.000 21.38 -118.000 28.47 4.2

AZ1= 228.000
DIP1= 50.000
AZ2= 131.000
DIP2= 81.736

SLIP VECTORS= 41.000 81.736 138.000 50.000

PRIN AXES = 81.304 56.210 185.928 69.336

STA	DIR	QUAL	DIST	EVAZ	TCA	X	Y
BAR	D	1	2.250	137.491	48.550	0.982	-1.071
CLC	C	2	1.625	26.040	48.550	0.638	1.306
CSP	C	1	0.927	93.887	83.991	2.360	-0.160
CWC	C	2	2.103	8.744	48.550	0.221	1.437
GSC	C	2	1.666	55.046	48.550	1.191	0.833
HFD	D	1	2.445	104.587	48.550	1.407	-0.366
ISA	D	2	1.154	359.920	80.439	-0.003	2.283
MWC	C	2	0.370	111.295	89.556	2.320	-0.904
PAS	C	-2	0.326	129.667	89.994	1.924	-1.596
PYR	D	2	0.306	313.987	90.192	1.796	-1.733
RVR	C	2	0.981	111.406	83.445	2.191	-0.859
SBC	C	2	1.195	275.115	80.049	-2.265	0.203
SYP	C	-2	1.254	278.258	48.550	-1.438	0.209
TIN	C	1	2.700	4.184	48.550	0.106	1.450
BOUQ	D	2	0.156	10.195	90.193	-0.442	-2.456
BRWN	C	2	0.119	234.462	95.985	1.925	1.375
IRON	D	2	0.077	55.902	105.649	-1.769	-1.198
GOOK	D	2	0.034	358.488	130.818	0.039	-1.471
SCLE	D	2	0.120	46.824	95.729	-1.730	-1.623
NAGM	D	2	0.188	42.365	89.706	1.680	1.842
NMLM	C	2	0.329	83.012	89.970	2.481	0.304
NWSM	D	2	0.261	344.738	90.647	0.654	-2.398
ENGN	C	2	0.387	123.820	89.385	2.066	-1.384
NANM	D	2	0.103	343.409	98.470	0.659	-2.212
IPC	D	2	0.401	163.759	89.246	0.695	-2.384
HCC	D	2	0.371	168.210	89.551	0.509	-2.438
BHR	D	2	0.360	164.956	89.658	0.647	-2.407
BLNY	D	2	0.115	167.927	96.508	-0.492	2.302

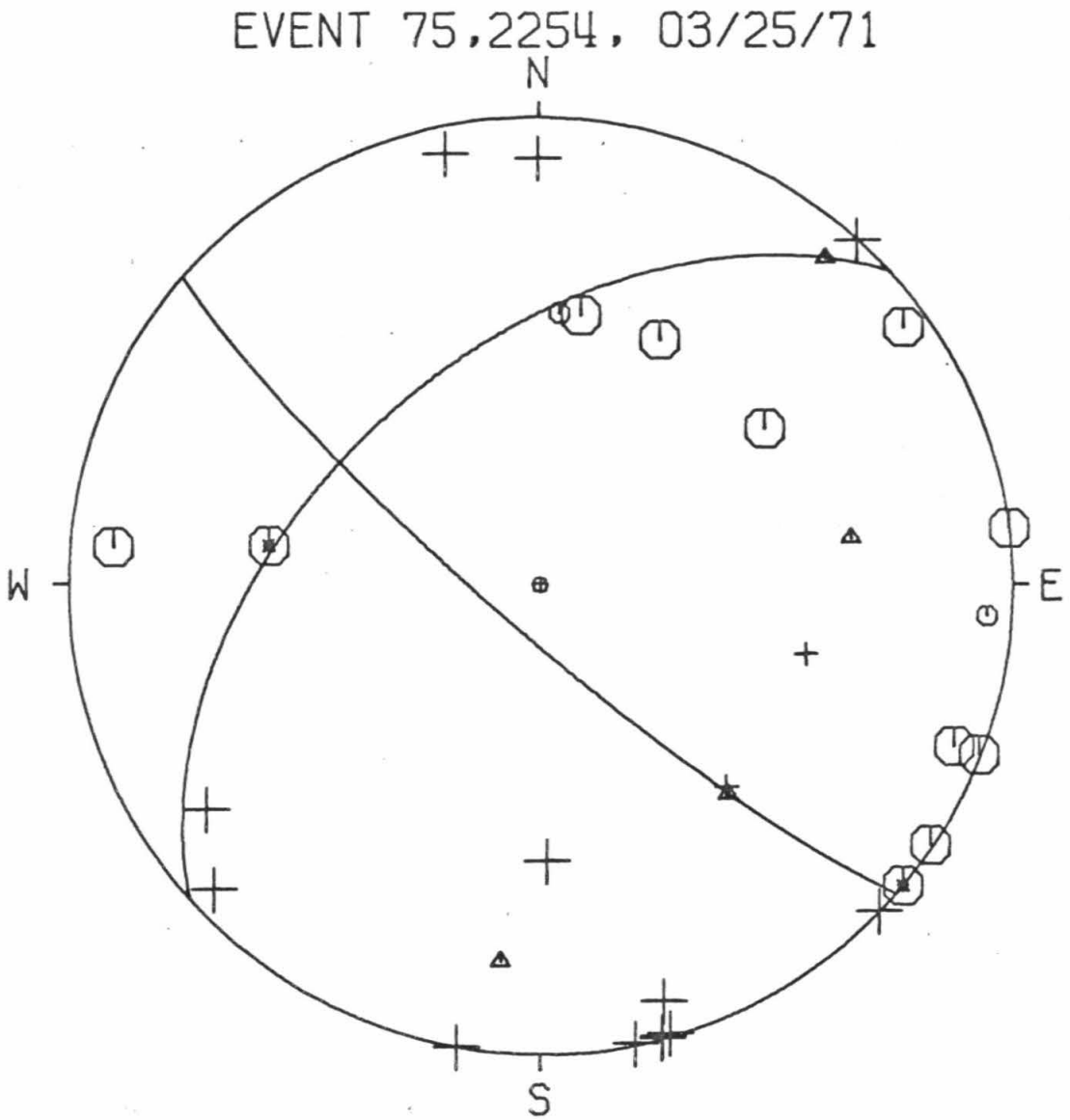
EVENT 75,2254, 03/25/71
N
W
E
S

EVENT DATA

76,2055 0 03/26/71 20 55 0.0

11.3 34.000 28.09 -118.000 27.68 3.3

AZ1= 93.500
DIP1= 48.000
AZ2= 258.000
DIP2= 43.057

SLIP VECTORS= 168.000 43.057 3.500 48.000

PRIN AXES = 68.385 8.191 176.080 87.506

STA	DIR	QUAL	DIST	EVAZ	TOA	X	Y
GSC	C	-2	1.596	58.105	49.400	1.254	0.781
ISA	D	2	1.043	359.388	91.980	0.026	-2.456
MWC	D	-2	0.414	126.242	100.938	-1.815	1.330
PAS	D	2	0.400	143.098	101.561	-1.342	1.788
PLM	C	2	1.734	129.463	49.400	1.141	-0.939
PYR	D	2	0.253	294.037	108.187	1.894	-0.845
SBC	C	2	1.202	268.366	49.400	-1.477	-0.042
SYP	C	2	1.254	273.463	49.400	-1.475	0.089
BRWN		-1	0.207	211.202	113.335	1.006	1.662
IRCN	C	2	0.099	147.905	133.538	-0.741	1.181
GOOK	C	2	0.088	187.661	136.681	0.174	1.293
SOLE	C	2	0.091	122.012	136.023	-1.122	0.702
INDN	C	1	0.167	109.385	118.105	-1.715	0.603
ENGN	D	2	0.452	136.518	99.503	-1.572	1.657
SWM	D	2	0.269	338.064	107.415	0.782	-1.941
IPC	D	2	0.507	168.494	98.791	-0.459	2.255
HCC	D	2	0.478	172.218	99.160	-0.310	2.271
BHR	D	2	0.467	169.834	99.302	-0.404	2.253
BLNY	D	2	0.223	176.601	111.536	-0.118	1.985

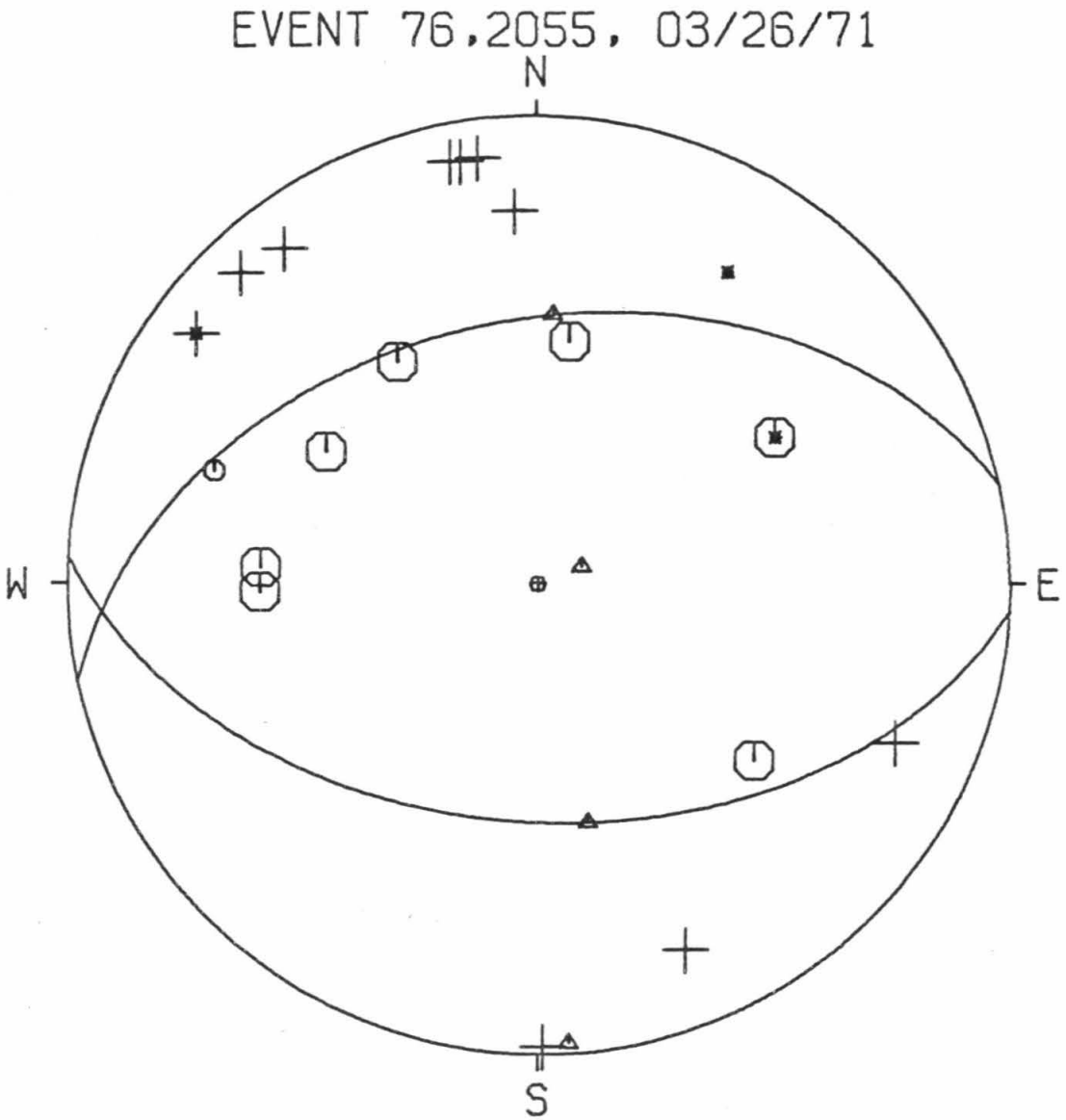
EVENT 76,2055, 03/26/71
N
W
E
S

EVENT DATA

77,1716 0 03/28/71 17 16 0.0

5.7 34.000 21.28 -118.000 28.39 3.7

AZ1= 132.000
DIP1= 75.000
AZ2= 225.000
DIP2= 78.947

SLIP VECTORS= 135.000 78.947 42.000 75.000

PRIN AXES = 88.946 71.424 358.066 87.280

STA	DIR	QUAL	DIST	EVAZ	TOA	X	Y
BAR	C	2	2.248	137.485	48.825	0.987	-1.077
CLC	D	2	1.626	25.980	48.825	0.640	1.314
CSP	D	1	0.925	93.292	86.521	2.419	-0.139
GSC	C	2	1.666	54.981	48.825	1.197	0.839
ISA	D	2	1.156	359.873	80.423	-0.005	2.283
MWC	C	2	0.369	111.125	92.505	-2.280	0.881
PAS	C	2	0.325	129.712	92.972	-1.873	1.555
PLM	C	2	1.672	126.245	48.825	1.178	-0.864
PYR	D	2	0.308	314.065	93.151	1.746	-1.690
RVR	C	2	0.979	111.312	85.935	2.245	-0.876
SBC	C	2	1.196	275.264	80.036	-2.264	0.209
SYP	C	2	1.256	278.403	48.825	-1.446	0.214
BOUQ	D	2	0.157	9.712	90.000	0.422	2.464
BRWN	C	2	0.117	236.569	96.245	1.970	1.300
IRON	C	2	0.077	54.481	105.649	-1.739	-1.241
GOOK	D	2	0.044	357.423	122.304	0.077	-1.704
SOLE	D	2	0.124	44.551	95.228	-1.672	-1.698
INDN	C	2	0.182	66.330	89.757	2.285	1.002
NAGM	D	2	0.188	41.919	89.706	1.666	1.855
NMLM	C	2	0.328	82.337	92.940	-2.413	-0.325
NOMM	C	2	0.112	249.699	97.046	2.196	0.812
NWSM	D	2	0.262	344.582	93.645	0.643	-2.332
ENGN	C	2	0.386	123.773	92.321	-2.036	1.361
NANM	D	2	0.105	343.097	98.175	0.673	-2.215
IPC	D	2	0.399	163.840	92.176	-0.682	2.355
HCC	D	2	0.369	168.314	92.505	-0.495	2.394
BHR	D	2	0.358	165.066	92.615	-0.629	2.360
BLNY	D	2	0.112	168.119	97.046	-0.482	2.291

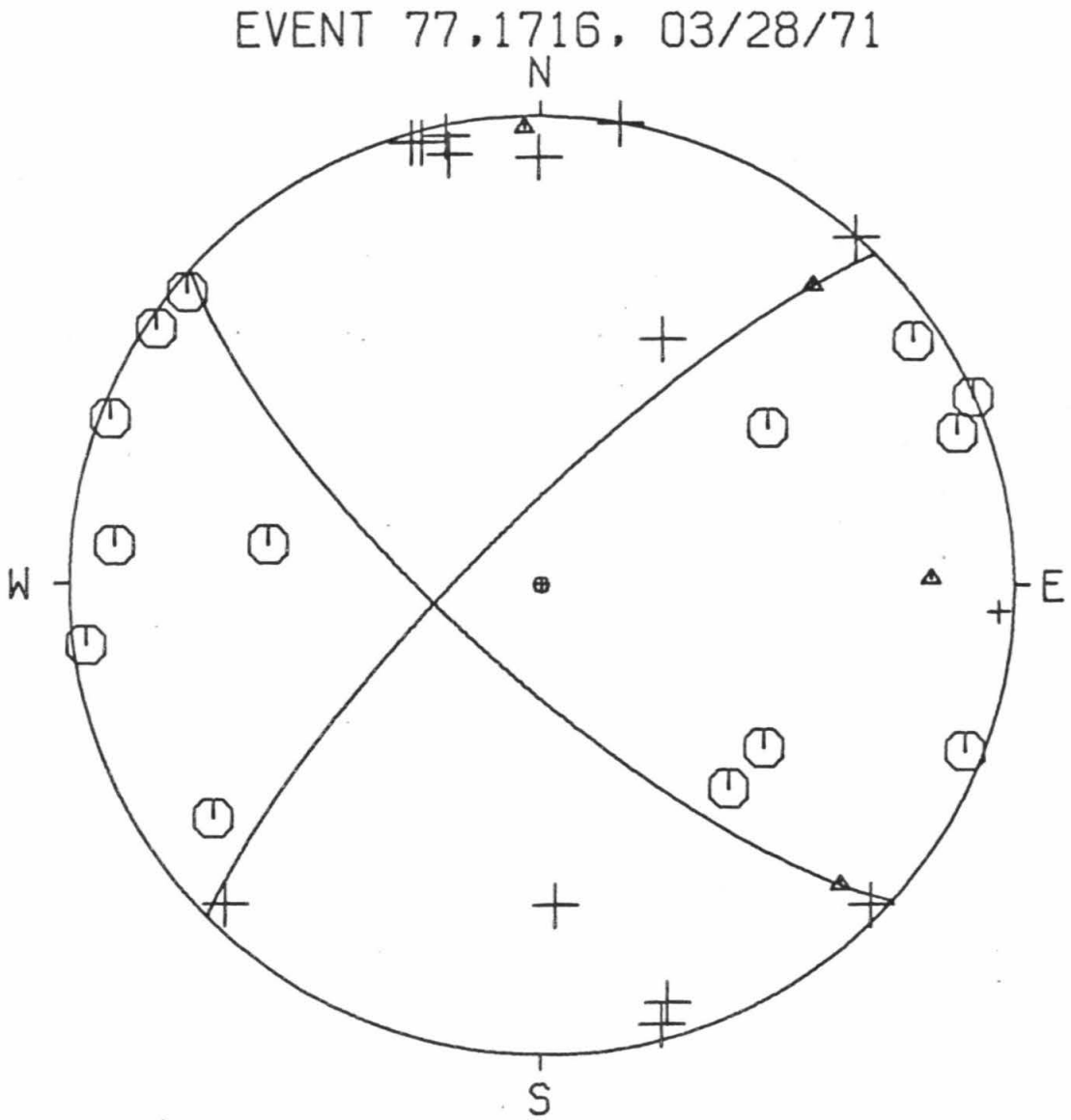
EVENT 77,1716, 03/28/71
N
W
E
S

EVENT DATA

78,0854 0 03/30/71 8 54 0.0

3.0 34.000 17.74 -118.000 27.84 4.1

AZ1= 40.000
DIP1= 43.000
AZ2= 235.000
DIP2= 47.989

SLIP VECTORS= 145.000 47.989 309.999 43.000

PRIN AXES = 209.465 7.954 317.823 87.484

STA	DIR	QUAL	DIST	EVAZ	TOA	X	Y
BAR	D	2	2.200	136.601	44.933	0.928	-0.982
CLC	C	2	1.676	24.870	44.933	0.568	1.226
CSP	D	1	0.916	87.885	82.719	2.335	0.086
CWC	C	2	2.162	8.278	44.933	0.195	1.337
GSC	C	2	1.695	53.202	44.933	1.082	0.809
ISA	D	-2	1.215	359.560	50.439	-0.012	1.506
MWC	D	2	0.345	103.362	88.193	2.394	-0.569
PAS	D	2	0.285	121.814	88.770	2.101	-1.304
PLM	D	2	1.632	124.741	44.933	1.110	-0.770
PYR	D	1	0.357	320.016	88.086	-1.579	1.883
RVR	D	2	0.953	108.240	82.372	2.211	-0.729
SBC	C	2	1.211	278.504	50.440	-1.490	0.223
SYP	C	2	1.273	280.963	44.933	-1.326	0.257
TIN	C	1	2.760	3.918	44.933	0.092	1.348
BOUQ	D	-2	0.215	5.048	89.445	0.219	2.478
BRWN	D	-2	0.112	250.171	96.529	2.214	0.798
IRON	D	2	0.110	29.818	96.757	-1.168	-2.037
GOOK	D	2	0.095	354.204	98.730	0.233	-2.291
SOLE	D	2	0.163	28.998	90.509	-1.207	-2.177
INDN	C	-2	0.207	50.538	89.525	1.922	1.582
NAGM	D	2	0.230	30.830	89.302	1.273	2.134
NWSM	D	2	0.322	346.103	88.418	-0.592	2.393
ENGN	D	2	0.350	116.601	88.150	2.199	-1.101
SWM	D	2	0.433	346.862	87.359	-0.555	2.378
NANM	D	2	0.163	346.522	90.509	0.580	-2.420
HCC	D	2	0.310	167.528	88.530	0.533	-2.409
IPC	D	2	0.341	162.336	88.237	0.747	-2.345
BHR	D	2	0.300	163.601	88.629	0.697	-2.369
BLNY	D	2	0.059	164.925	108.307	-0.538	1.999

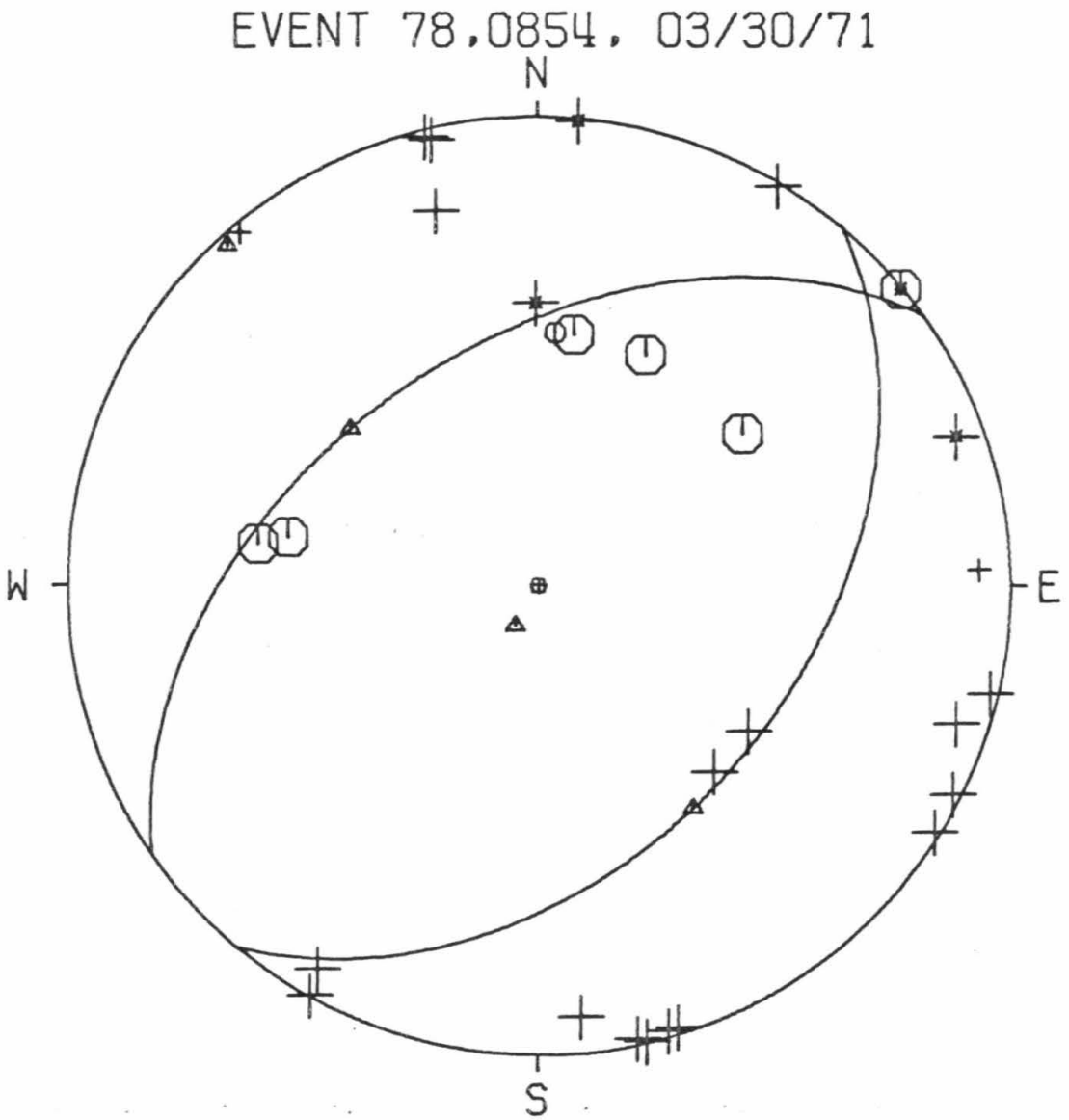
EVENT 78,0854, 03/30/71
N
W
E
S

EVENT DATA

79,1452 0 03/31/71 14 52 0.0

3.0 34.000 17.15 -118.000 30.89 4.6

AZ1= 231.000
DIP1= 50.000
AZ2= 136.000
DIP2= 84.070

SLIP VECTORS= 46.000 84.070 141.000 50.000

PRIN AXES = 85.425 58.159 190.284 67.576

STA	DIR	QUAL	DIST	EVAZ	TOA	X	Y
BAR	D	2	2.222	135.611	44.933	0.945	-0.965
CLC	C	2	1.703	25.990	44.933	0.592	1.214
CWC	C	2	2.178	9.309	44.933	0.219	1.333
GLA	D	1	3.313	110.791	44.933	1.263	-0.480
GSC	C	2	1.734	53.752	44.933	1.090	0.799
HFD	D	1	2.461	102.789	44.933	1.318	-0.299
ISA	D	2	1.225	1.316	50.438	0.035	1.506
MWC	C	2	0.384	99.987	87.823	2.415	-0.425
PAS	C	2	0.317	115.939	88.471	2.218	-1.079
PLM	C	2	1.661	123.608	44.933	1.125	-0.748
PYR	D	2	0.339	326.507	88.253	-1.358	2.053
RVR	C	2	0.990	106.887	82.016	2.220	-0.674
SBC	D	-2	1.171	279.434	80.278	-2.248	0.374
SYP	D	2	1.234	281.758	50.436	-1.475	0.307
BOUQ	D	-2	0.231	15.311	89.293	0.656	2.396
BRWN	C	2	0.069	292.842	105.211	1.979	-0.834
IRON	D	2	0.143	42.753	92.556	-1.659	-1.794
GOOK	D	2	0.108	17.450	96.988	-0.703	-2.235
SOLE	D	-2	0.193	38.919	85.812	1.512	1.873
INDN	C	2	0.245	55.437	89.159	2.044	1.408
NAGM	D	2	0.262	37.514	88.989	1.509	1.965
NMLM	C	2	0.375	73.347	87.907	2.351	0.703
NWSM	D	2	0.323	353.716	88.406	-0.270	2.450
ENGN	C	2	0.385	112.580	87.818	2.264	-0.941
SWM	D	1	0.434	352.530	87.346	-0.317	2.421
NANM	D	2	0.168	1.372	90.360	-0.060	-2.491
IPC	D	-2	0.347	155.182	88.177	1.033	-2.233
HCC	D	2	0.313	159.552	88.506	0.862	-2.312
BHR	D	2	0.305	155.417	88.579	1.027	-2.245
BLNY	C	2	0.077	131.281	103.149	-1.651	1.450

EVENT 79.1452, 03/31/71

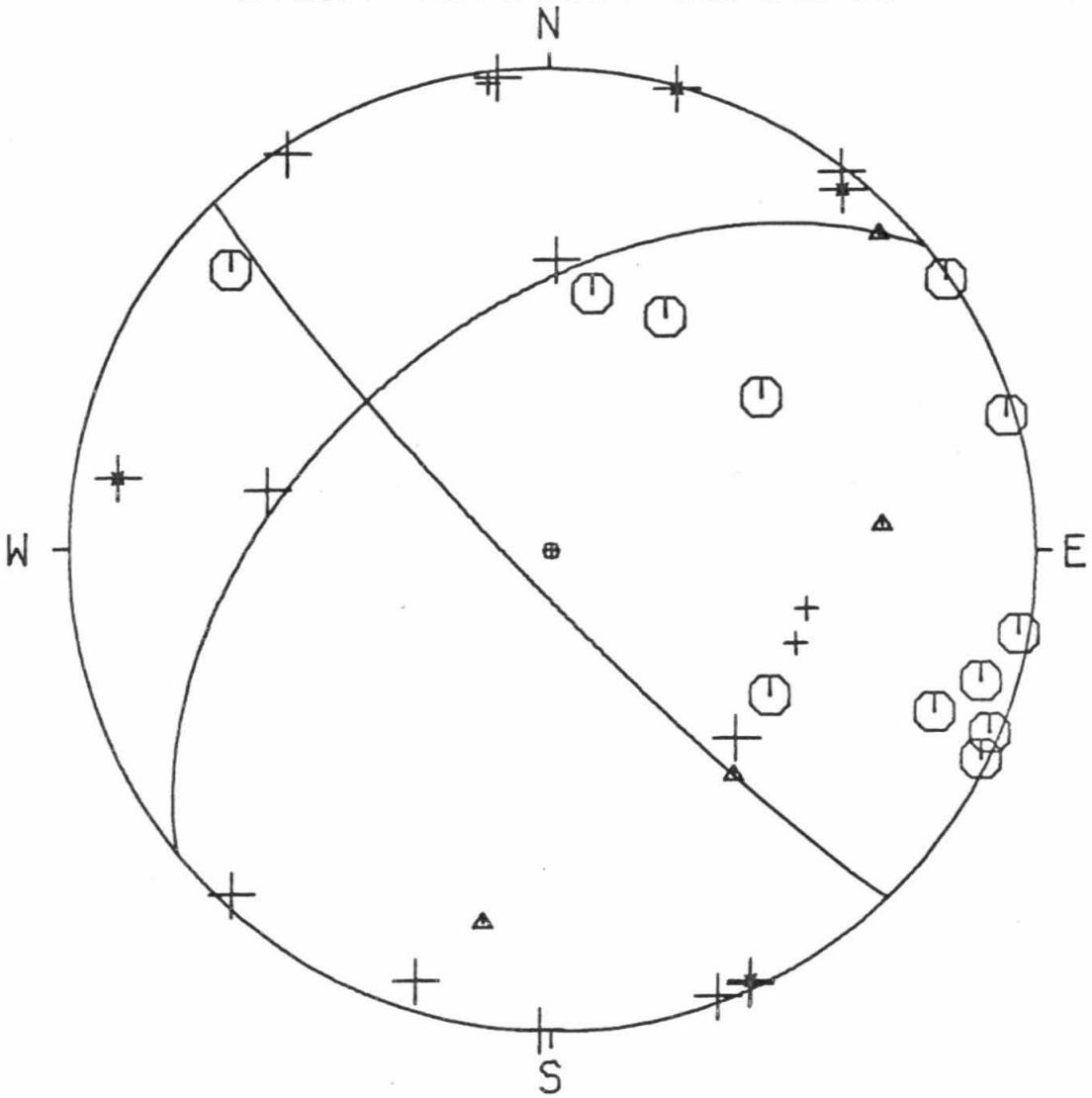

EVENT DATA

80,0154 0 04/01/71 1 54 36.1

6.3 34.000 15.94 -118.000 35.34 3.4

AZ1= 126.000
DIP1= 46.000
AZ2= 267.000
DIP2= 51.174

SLIP VECTORS= 177.000 51.174 36.000 46.000

PRIN AXES = 112.932 20.851 15.691 87.256

STA	DIR	QUAL	DIST	EVAZ	TOA	X	Y
CLC	C	1	1.749	27.466	48.975	0.676	1.300
CSP	C	2	1.020	87.236	86.825	2.427	0.117
GSC	C	1	1.796	54.351	48.975	1.191	0.854
MWC	C	2	0.443	96.747	93.275	-2.411	0.285
PAS	C	2	0.366	109.138	94.128	-2.275	0.790
PLM	C	2	1.702	121.857	48.975	1.245	-0.773
PYR	D	2	0.328	337.415	94.556	0.921	-2.215
RVR	C	2	1.043	104.835	86.569	2.343	-0.621
SBC	D	1	1.114	281.155	85.780	-2.361	0.466
SYP	C	2	1.178	283.266	49.400	-1.438	0.339
BRWN	C	2	0.040	357.444	149.647	0.041	-0.925
IRON	D	2	0.202	51.626	105.462	-1.678	-1.329
GOOK	D	2	0.155	37.387	110.101	-1.230	-1.609
SOLE	C	2	0.250	46.802	95.804	-1.728	-1.622
INDN	D	2	0.306	59.040	94.797	-2.052	-1.231
NOMM	C	2	0.071	352.678	132.226	0.182	-1.420
ENGN	C	2	0.436	106.998	93.355	-2.320	0.709
SWM	D	2	0.451	0.595	93.182	-0.025	-2.429
NANM	D	2	0.199	19.173	105.747	-0.701	-2.016
IPC	D	2	0.361	144.944	94.188	-1.383	1.970
HCC	C	1	0.322	147.952	94.623	-1.272	2.032
BHR	C	1	0.320	143.924	94.644	-1.411	1.937
BLNY	C	2	0.124	105.584	116.420	-1.794	0.500

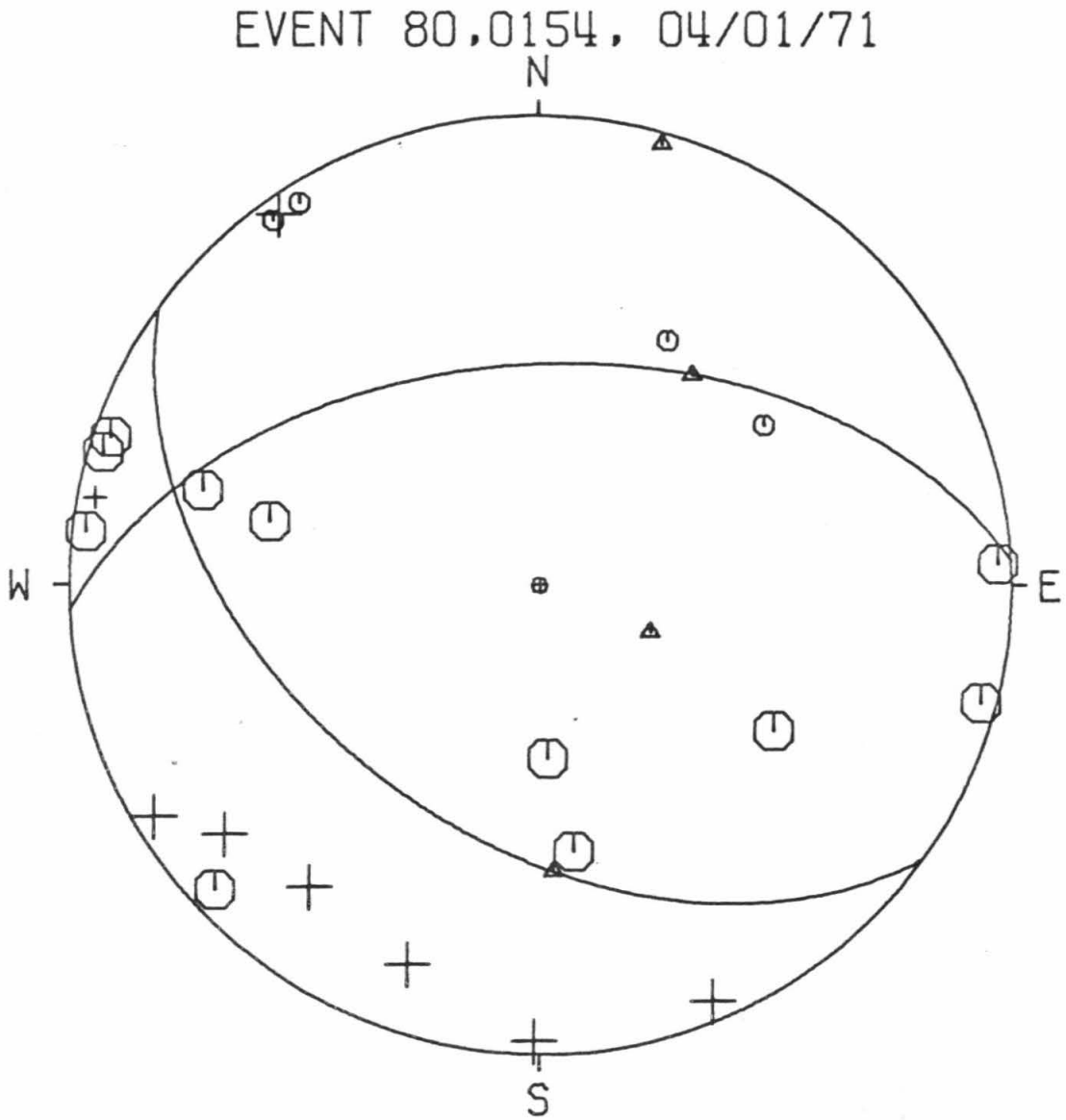
EVENT 80.0154, 04/01/71
N
W
E
S

EVENT DATA

81,1503 0 04/01/71 15 3 0.0

7.1 34.000 24.72 -118.000 25.19 4.2

AZ1= 117.500
DIP1= 68.000
AZ2= 216.000
DIP2= 69.905

SLIP VECTORS= 126.000 69.905 27.500 68.000

PRIN AXES = 77.172 59.481 346.434 88.743

STA	DIR	QUAL	DIST	EVAZ	TCA	X	Y
BAR	C	2	2.262	139.318	49.175	0.959	-1.116
CLC	D	2	1.556	25.472	49.175	0.633	1.328
CSP	C	2	0.886	97.316	90.170	-2.476	0.318
CWC	D	2	2.042	7.759	49.175	0.199	1.458
GSC	C	2	1.598	55.773	49.175	1.216	0.827
HFD	D	1	2.416	106.177	49.175	1.413	-0.410
ISA	D	2	1.100	357.843	87.670	-0.092	2.447
MWC	D	2	0.355	122.452	96.396	-1.989	1.265
PAS	D	2	0.335	142.109	96.629	-1.444	1.856
PLM	C	2	1.672	128.747	49.175	1.147	-0.921
PYR	D	2	0.310	300.936	96.927	2.011	-1.205
RVR	C	2	0.962	115.481	89.289	2.243	-1.069
SBC	C	2	1.237	272.593	49.175	-1.470	0.067
SYP	C	2	1.293	275.666	49.175	-1.464	0.145
TIN	D	1	2.642	3.326	49.175	0.085	1.469
BCUQ	D	2	0.103	350.167	121.069	0.297	-1.714
BRWN	C	-2	0.188	229.087	106.828	1.592	1.380
IRON	C	2	0.040	152.521	149.647	-0.427	0.821
GOOK	C	2	0.059	230.957	137.930	0.986	0.799
SOLE	C	2	0.059	45.859	137.930	-0.911	-0.884
INDN	C	2	0.128	73.547	115.469	-1.810	-0.535
NAGM	D	2	0.119	43.251	117.409	-1.258	-1.338
NOMM	C	2	0.174	239.189	108.195	1.781	1.062
NWSM	D	2	0.227	329.965	99.910	1.139	-1.969
ENGN	D	2	0.388	134.537	96.013	-1.686	1.659
SWM	D	2	0.334	336.217	96.642	0.948	-2.151
NANM	C	2	0.088	302.632	125.844	1.355	-0.868
IPC	D	2	0.446	171.389	95.331	-0.356	2.354
HCC	D	2	0.420	175.860	95.633	-0.171	2.368
BHR	D	2	0.406	173.213	95.794	-0.280	2.354
BLNY	D	2	0.169	187.184	108.639	0.258	2.046

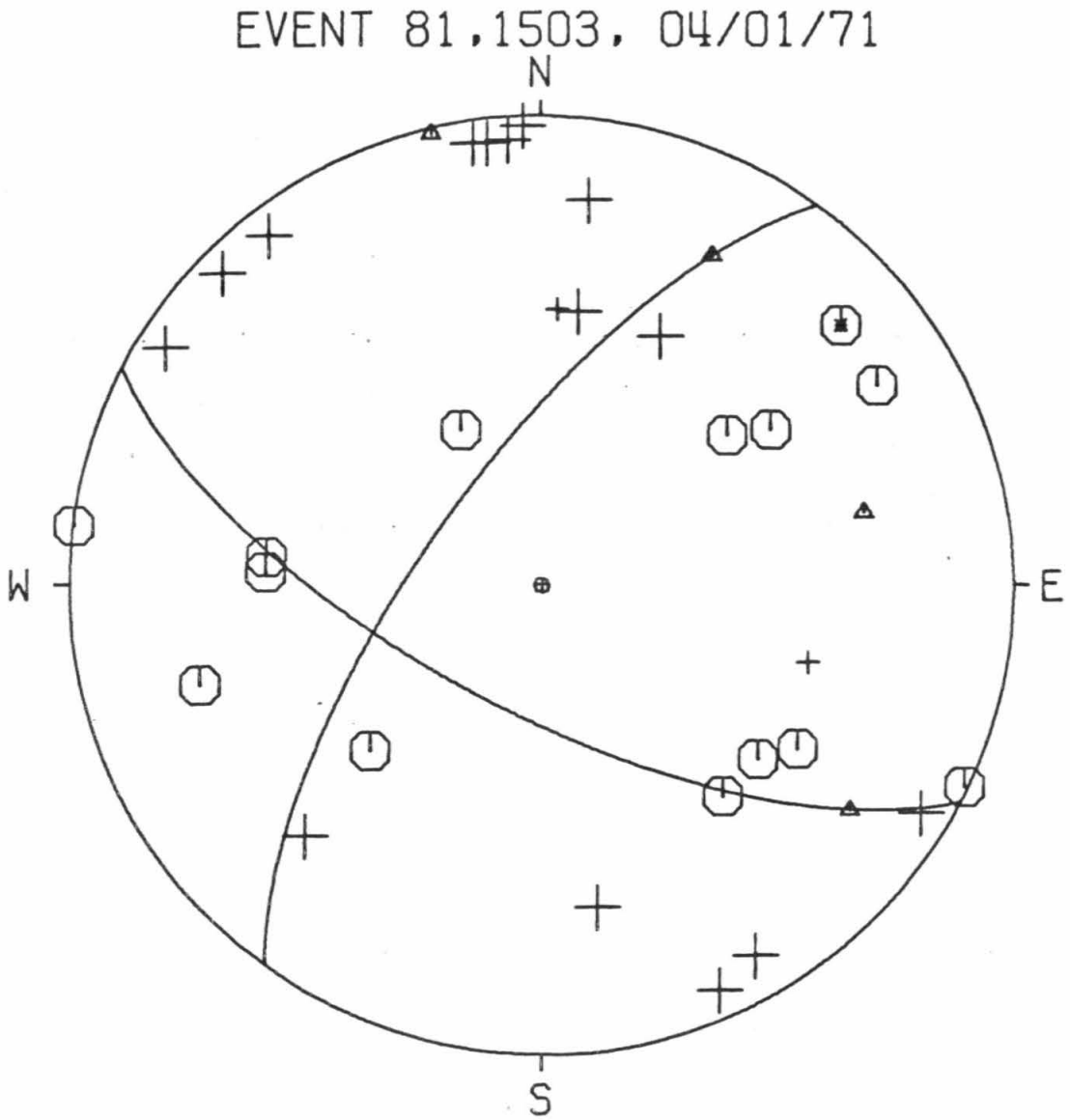
EVENT 81,1503, 04/01/71
N
W
E
S

EVENT DATA

82,2115 0 04/01/71 21 15 0.0

7.9 34.000 24.32 -118.000 25.85 3.2

AZ1= 240.000
DIP1= 44.000
AZ2= 88.000
DIP2= 49.547

SLIP VECTORS= 357.999 49.547 150.000 44.000

PRIN AXES = 63.631 14.664 164.650 87.142

STA	DIR	QUAL	DIST	EVAZ	TOA	X	Y
GSC	C	2	1.609	55.751	49.375	1.221	0.831
ISA	D	2	1.106	358.271	89.324	-0.075	2.484
MWC	D	2	0.359	120.795	98.483	-1.983	1.182
PAS	D	2	0.336	140.181	98.773	-1.474	1.768
PLM	C	1	1.675	128.370	49.375	1.158	-0.917
PYR	D	2	0.305	302.815	99.147	1.927	-1.242
RVR	D	2	0.967	114.893	91.030	-2.247	1.043
SYP	C	1	1.284	276.016	49.375	-1.469	0.155
BRWN	C	2	0.177	228.581	107.870	1.561	1.377
IRON	C	2	0.044	141.752	146.728	-0.627	0.795
GOOK	C	2	0.056	221.349	139.546	0.808	0.918
SCLE	C	2	0.069	48.992	133.558	-1.052	-0.915
NAGM	D	2	0.131	43.572	114.853	-1.312	-1.379
NOMM	C	2	0.162	239.805	109.328	1.767	1.028
NWSM	D	2	0.229	332.805	102.478	1.012	-1.969
ENGN	D	2	0.390	132.973	98.105	-1.695	1.579
SWM	D	2	0.337	338.112	98.758	0.858	-2.136
NANM	D	2	0.086	310.690	126.590	1.205	-1.036
IPC	C	2	0.441	170.096	97.476	-0.401	2.297
BHR	D	2	0.402	171.811	97.966	-0.331	2.297
BLNY	D	2	0.162	184.248	109.328	0.151	2.039

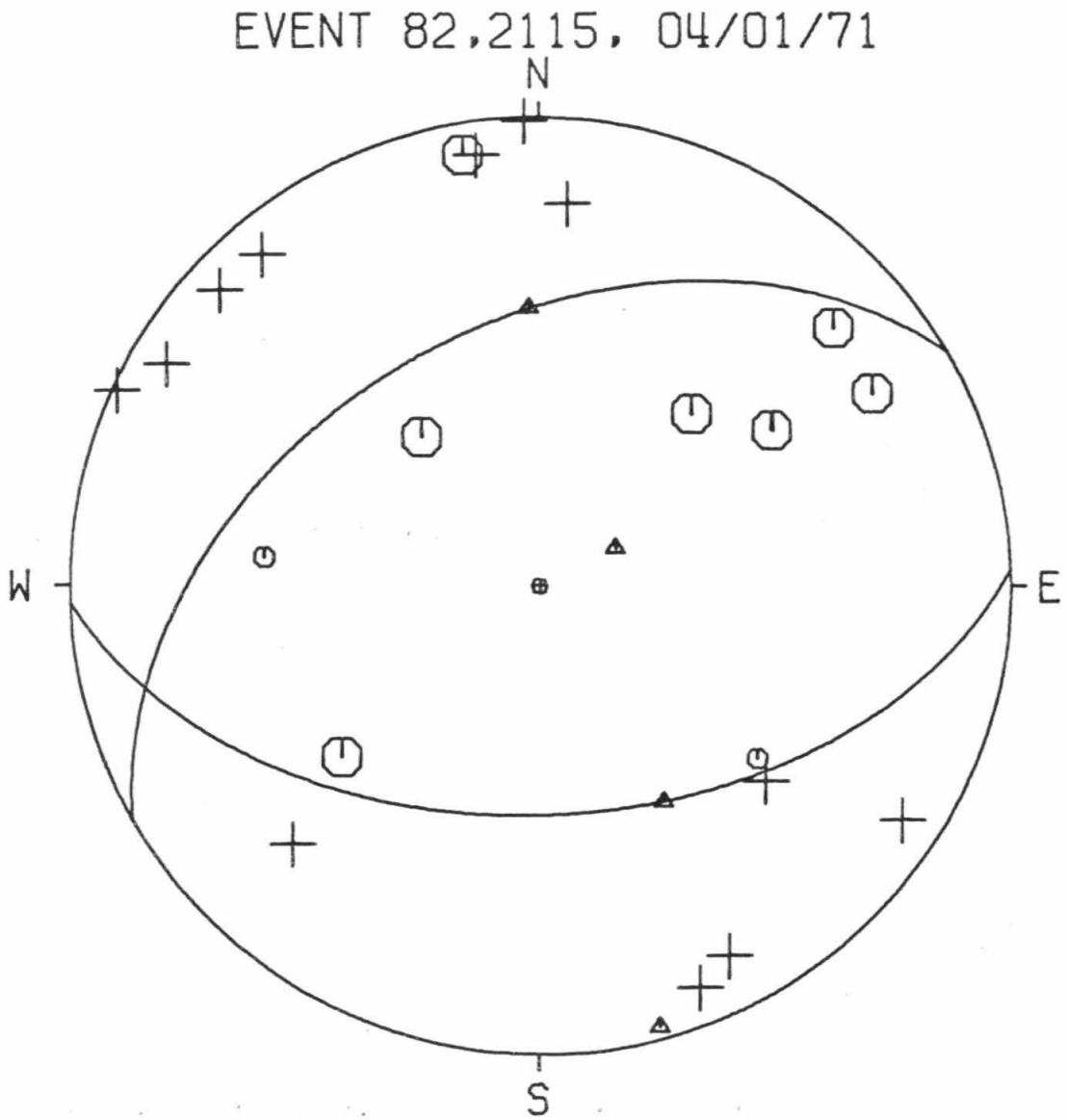
EVENT 82,2115, 04/01/71
N
W
E
S

EVENT DATA

83,2118 0 04/01/71 21 18 35.6

7.3 34.000 23.73 -118.000 25.73 3.5

AZ1= 61.500
DIP1= 30.000
AZ2= 241.500
DIP2= 60.000

SLIP VECTORS= 151.500 60.000 331.499 30.000

PRIN AXES = 151.505 15.002 331.500 75.000

STA	DIR	QUAL	DIST	EVAZ	TOA	X	Y
BAR	D	1	2.254	138.897	49.225	0.968	-1.110
CLC	D	1	1.574	25.457	49.225	0.633	1.330
CSP	D	2	0.892	96.350	90.564	-2.472	0.275
GSC	C	2	1.613	55.438	49.225	1.213	0.835
ISA	D	2	1.116	358.208	87.914	-0.077	2.453
MWC	D	2	0.353	119.505	96.957	-2.040	1.154
PAS	D	2	0.327	139.353	97.257	-1.522	1.773
PLM	C	2	1.668	128.149	49.225	1.158	-0.910
PYR	D	2	0.312	304.209	97.439	1.929	-1.311
RVR	D	2	0.962	114.423	89.741	2.271	-1.031
SBC	D	2	1.230	273.296	49.225	-1.470	0.085
SYP	D	1	1.287	276.509	49.225	-1.463	0.167
BRWN	D	2	0.172	231.177	108.305	1.613	1.298
IRON	C	2	0.040	139.467	149.647	-0.602	0.703
GOOK	C	2	0.052	227.579	141.663	0.857	0.783
SOLE	C	2	0.074	42.537	130.943	-0.992	-1.082
INDN	C	2	0.137	72.081	113.662	-1.840	-0.595
NAGM	C	2	0.134	41.427	114.251	-1.270	-1.439
NMLM	D	2	0.289	94.555	97.708	-2.319	0.185
NOMM	C	2	0.158	243.497	109.684	1.822	0.908
NWSM	D	2	0.238	333.490	99.699	1.018	-2.040
ENGN	D	2	0.383	132.114	96.604	-1.745	1.577
SWM	D	2	0.346	338.424	97.037	0.861	-2.178
NANM	C	2	0.091	312.297	125.115	1.205	-1.097
IPC	C	2	0.432	170.094	96.023	-0.407	2.330
HCC	D	2	0.404	174.628	96.351	-0.221	2.347
BHR	D	2	0.391	171.841	96.502	-0.334	2.330
BLNY	D	2	0.152	185.161	110.622	0.181	2.004

EVENT 83.2118. 04/01/71

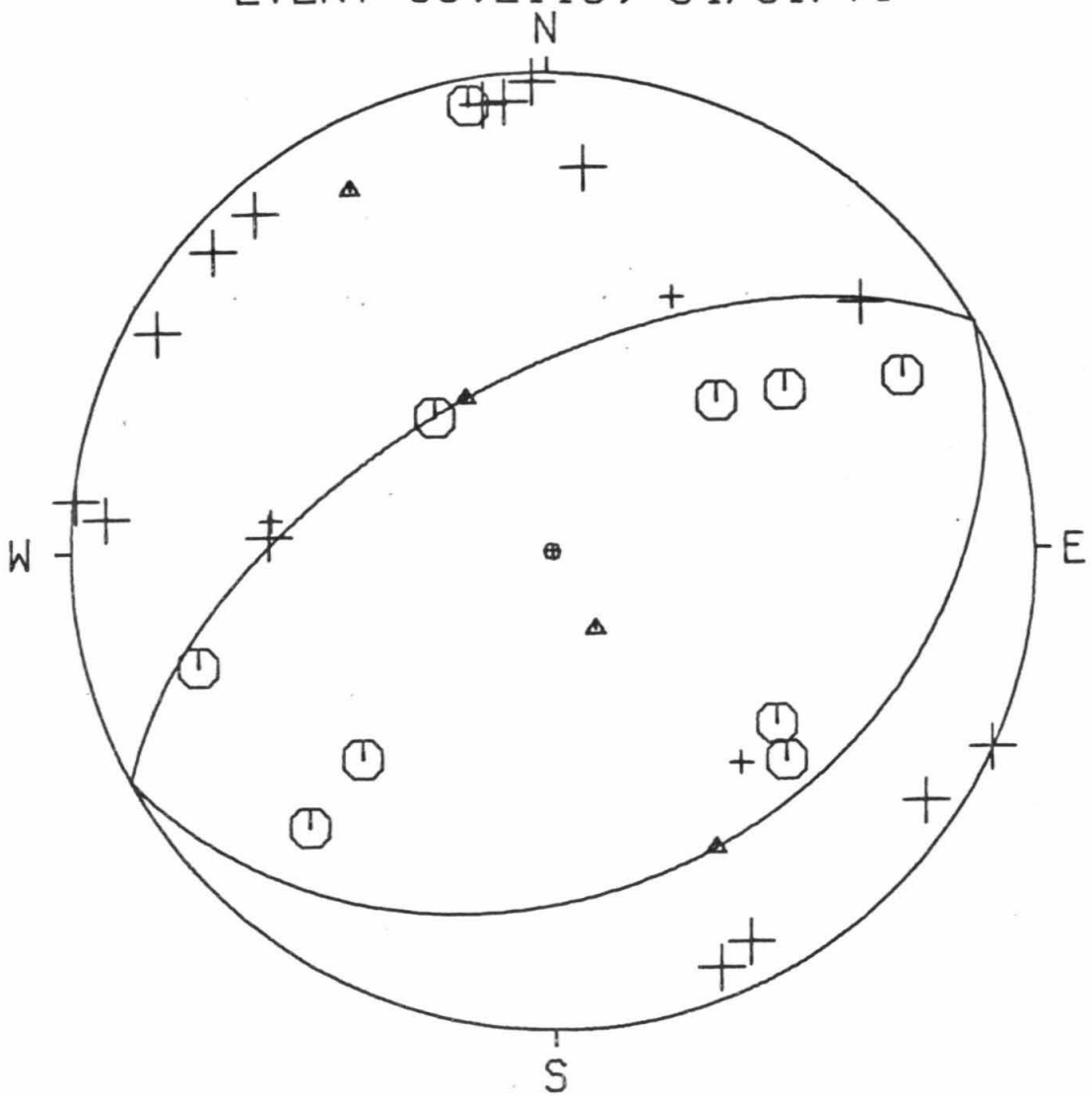

EVENT DATA

84,0540 C 04/02/71 5 40 0.0

3.0 34.000 17.03 -118.000 31.70 4.0

AZ1= 225.500
DIP1= 54.000
AZ2= 129.000
DIP2= 81.144

SLIP VECTORS= 39.000 81.144 135.500 54.000

PRIN AXES = 80.875 58.367 182.332 72.136

STA	DIR	QUAL	DIST	EVAZ	TCA	X	Y
BAR	D	1	2.229	135.364	44.933	0.949	-0.961
CLC	C	2	1.710	26.288	44.933	0.598	1.211
CSP	C	2	0.970	87.881	82.208	2.323	0.086
CWC	C	2	2.182	9.582	44.933	0.225	1.332
GSC	C	2	1.745	53.906	44.933	1.092	0.796
ISA	D	-2	1.227	1.778	50.437	0.047	1.506
MWC	C	2	0.396	100.140	87.712	2.411	-0.431
PAS	C	2	0.327	115.169	88.371	2.230	-1.048
PLM	C	2	1.670	123.331	44.933	1.129	-0.742
PYR	D	2	0.336	328.374	88.286	-1.291	2.097
RVR	C	2	1.000	106.603	81.918	2.221	-0.662
SBC	C	2	1.160	279.616	80.381	-2.250	0.381
SYP	C	2	1.223	281.951	50.438	-1.474	0.312
TIN	D	1	2.776	4.962	44.933	0.117	1.346
BRWN	C	2	0.063	303.807	106.968	1.748	-1.171
IRON	D	2	0.153	44.814	91.189	-1.744	-1.755
GOOK	D	2	0.115	22.237	96.084	-0.895	-2.188
SOLE	D	-2	0.203	40.737	89.562	1.625	1.887
INDN	C	-2	0.255	56.551	89.062	2.069	1.367
NAGM	D	2	0.271	39.072	88.905	1.561	1.922
NMLM	C	2	0.387	73.522	87.798	2.351	0.695
NOMM	D	2	0.082	313.379	101.888	1.619	-1.530
NWSM	D	2	0.325	355.721	88.389	-0.184	2.458
ENGN	C	2	0.394	111.662	87.726	2.277	-0.904
SWM	D	2	0.435	354.027	87.333	-0.254	2.428
NANM	D	2	0.170	5.115	90.287	-0.222	-2.484
IPC	C	1	0.351	153.403	88.144	1.101	-2.199
BHR	D	2	0.310	153.498	88.536	1.101	-2.209
HCC	D	2	0.315	157.532	88.482	0.943	-2.279
BLNY	C	2	0.084	124.994	101.285	-1.837	1.286

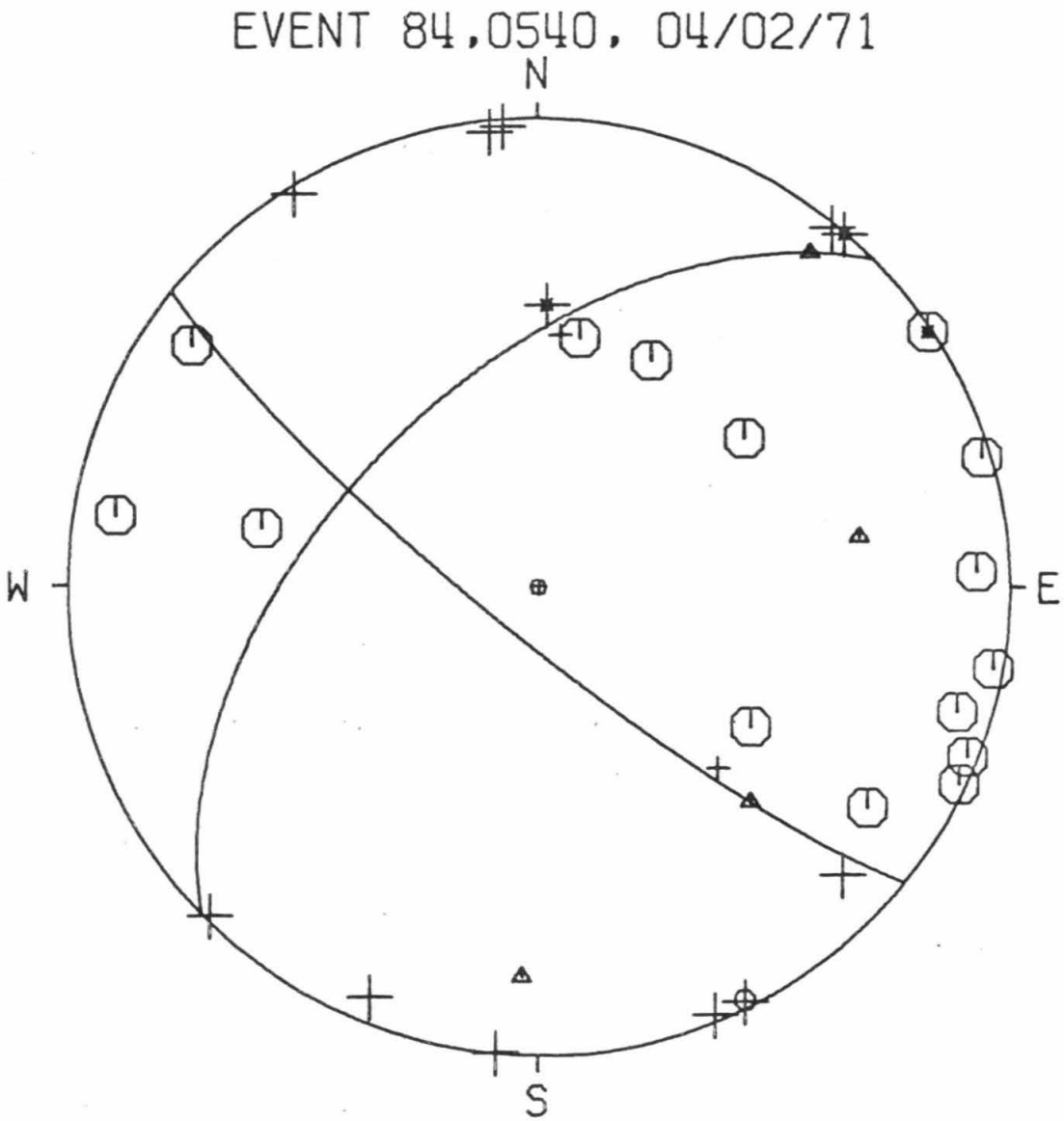
EVENT 84,0540, 04/02/71
N
W
E
S

EVENT DATA

85,1114 0 04/15/71 11 14 0.0

4.2 34.000 15.88 -118.000 34.62 4.2

AZ1= 113.000
DIP1= 56.000
AZ2= 239.500
DIP2= 48.592

SLIP VECTORS= 149.500 48.592 23.000 56.000

PRIN AXES = 80.566 30.335 177.695 85.855

STA	DIR	QUAL	DIST	EVAZ	TCA	X	Y
ENGN	C	2	0.426	107.165	87.949	2.346	-0.725
GSC	C	2	1.789	54.145	48.450	1.176	0.850
ISA	D	2	1.248	3.401	48.450	0.086	1.448
MWC	C	2	0.433	96.916	87.879	2.435	-0.295
PLM	C	2	1.693	122.015	48.450	1.230	-0.769
SYP	C	2	1.188	283.220	80.116	-2.215	0.520
BAR	C	2	2.244	134.260	48.450	1.039	-1.012
CLC	C	2	1.745	27.170	48.450	0.662	1.291
CWC	C	2	2.208	10.504	48.450	0.264	1.426
RVR	C	2	1.034	104.936	82.037	2.242	-0.598
SBC	C	2	1.124	281.090	81.159	-2.257	0.442
TIN	C	1	2.799	5.723	48.450	0.145	1.443
PAS	C	2	0.356	109.236	88.626	2.332	-0.814
SWM	D	2	0.452	359.343	87.694	-0.028	2.449
BOUQ	D	-2	0.270	24.590	89.465	1.035	2.263
BRWN	D	2	0.044	344.700	122.304	0.450	-1.645
IRON	D	2	0.196	49.208	89.628	1.887	1.628
GOOK	D	2	0.149	34.185	91.195	-1.390	-2.046
SOLE	D	-2	0.244	45.022	89.777	1.765	1.764
INON	D	1	0.299	57.654	89.178	2.097	1.328
NOMM	D	2	0.074	345.132	106.545	0.543	-2.043
NANM	D	2	0.198	16.264	89.609	0.698	2.392
NWSM	D	2	0.343	2.661	88.757	0.115	2.470
NMLM	C	2	0.431	72.426	87.896	2.339	0.741
IPC	D	2	0.355	146.214	88.637	1.374	-2.053
HCC	D	2	0.317	149.438	89.011	1.260	-2.134
BHR	D	2	0.314	145.336	89.035	1.410	-2.039
BLNY	D	2	0.115	108.968	96.508	-2.226	0.765

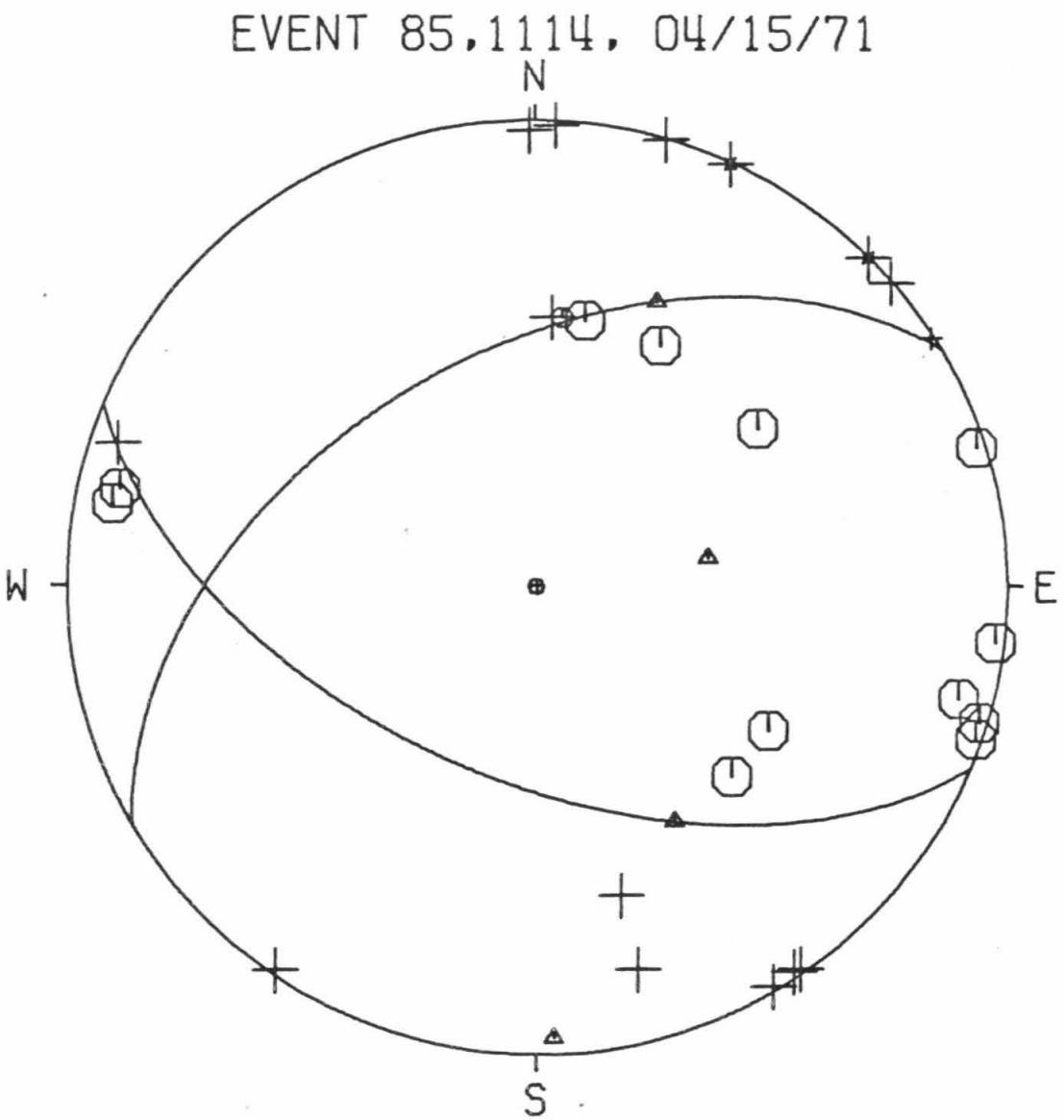
EVENT 85.1114, 04/15/71
N
W
E
S

EVENT DATA

86,1448 0 04/25/71 14 48 0.0

3.0 34.000 22.09 -118.000 18.86 4.0

AZ1= 114.000
DIP1= 66.000
AZ2= 223.000
DIP2= 53.824

SLIP VECTORS= 133.000 53.824 24.000 66.000

PRIN AXES = 73.544 45.172 171.024 82.543

STA	DIR	QUAL	DIST	EVAZ	TCA	X	Y
ENGN	D	2	0.297	140.485	88.660	1.572	-1.906
CSP	C	2	0.795	95.255	83.881	2.353	-0.216
GSC	C	-2	1.552	52.692	44.933	1.075	0.819
ISA	D	1	1.149	354.067	80.484	-0.236	2.272
MWC	D	2	0.259	124.916	89.025	2.032	-1.419
PLM	D	2	1.577	129.547	44.933	1.042	-0.860
PYR	D	-2	0.406	299.793	87.609	-2.124	1.216
SYP	C	2	1.384	277.143	44.933	-1.341	0.168
BAR	D	2	2.172	140.370	44.933	0.862	-1.041
CLC	C	2	1.561	21.948	44.933	0.505	1.253
CWC	C	2	2.075	5.268	44.933	0.124	1.345
RVR	D	2	0.864	115.453	83.218	2.120	-1.009
SBC	D	2	1.326	274.177	44.933	-1.347	0.098
TIN	D	2	2.682	1.471	44.933	0.035	1.351
PAS	D	2	0.251	151.876	89.099	1.169	-2.187
IRON	C	2	0.074	291.214	103.812	2.033	-0.789
GOOK	C	2	0.137	283.344	93.279	2.362	-0.560
IPC	D	2	0.398	183.014	87.688	-0.129	-2.446
HCC	D	2	0.379	188.702	87.872	-0.371	-2.425
BLNY	D	2	0.164	221.341	90.471	1.645	1.869

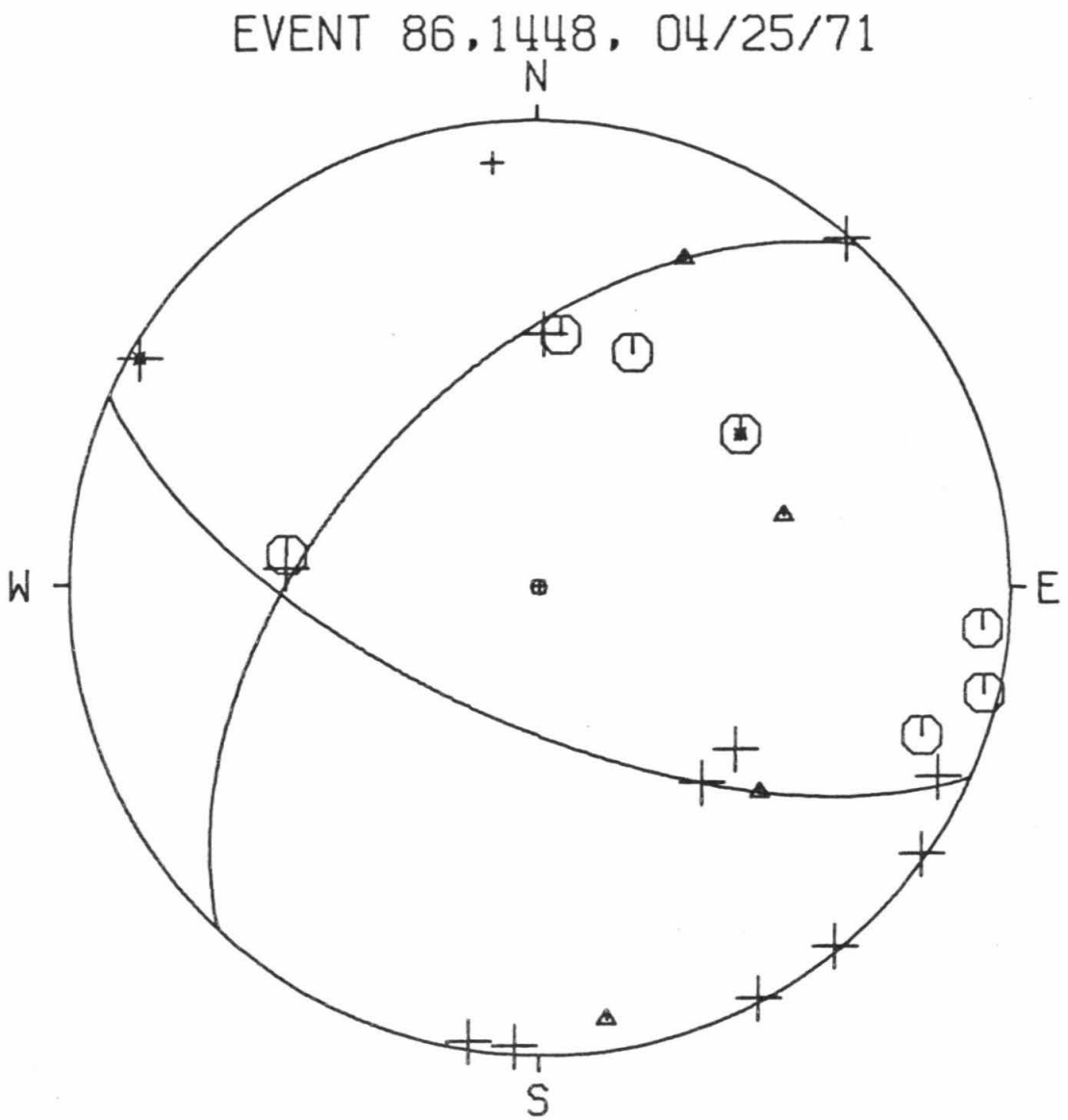
EVENT 86,1448, 04/25/71
N
W
E
S

EVENT DATA

87,0425 0 05/01/71 4 25 0.0

4.8 34.000 26.00 -118.000 24.15 3.6

AZ1= 90.500
DIP1= 55.000
AZ2= 200.000
DIP2= 64.511

SLIP VECTORS= 110.000 64.511 0.500 55.000

PRIN AXES = 59.174 44.776 323.286 84.187

STA	DIR	QUAL	DIST	EVAZ	TOA	X	Y
ENGN	D	2	0.393	138.220	89.855	1.664	-1.862
CSP	C	2	0.875	98.862	84.967	2.359	-0.368
GSC	C	2	1.574	56.132	48.600	1.208	0.811
ISA	D	2	1.079	357.136	82.903	-0.117	2.338
MWC	D	2	0.354	126.422	90.248	-2.007	1.481
PLM	D	-2	1.675	129.631	48.600	1.121	-0.928
PYR	D	2	0.312	296.049	90.683	2.233	-1.091
SYP	D	2	1.305	274.691	48.600	-1.450	0.119
BAR	C	2	2.269	139.949	48.600	0.936	-1.114
CLC	C	2	1.530	25.340	48.600	0.623	1.315
CWC	C	2	2.019	7.447	48.600	0.189	1.443
RVR	C	1	0.958	117.028	84.126	2.110	-1.076
PAS	D	2	0.344	146.219	90.350	-1.386	2.072
SWM	D	2	0.321	332.336	90.589	1.155	-2.203
BOUQ	D	1	0.086	338.318	102.335	0.819	-2.060
IRON	C	2	0.052	175.692	116.859	-0.139	1.846
GOOK	C	2	0.082	227.795	103.943	1.613	1.463
SOLE	C	2	0.044	39.728	122.304	-1.090	-1.312
IPC	D	2	0.465	173.537	89.125	0.279	-2.465
HCC	D	2	0.440	177.923	89.384	0.090	-2.485
BHR	D	2	0.426	175.473	89.521	0.197	-2.482
BLNY	D	2	0.191	190.720	89.676	-0.464	-2.449

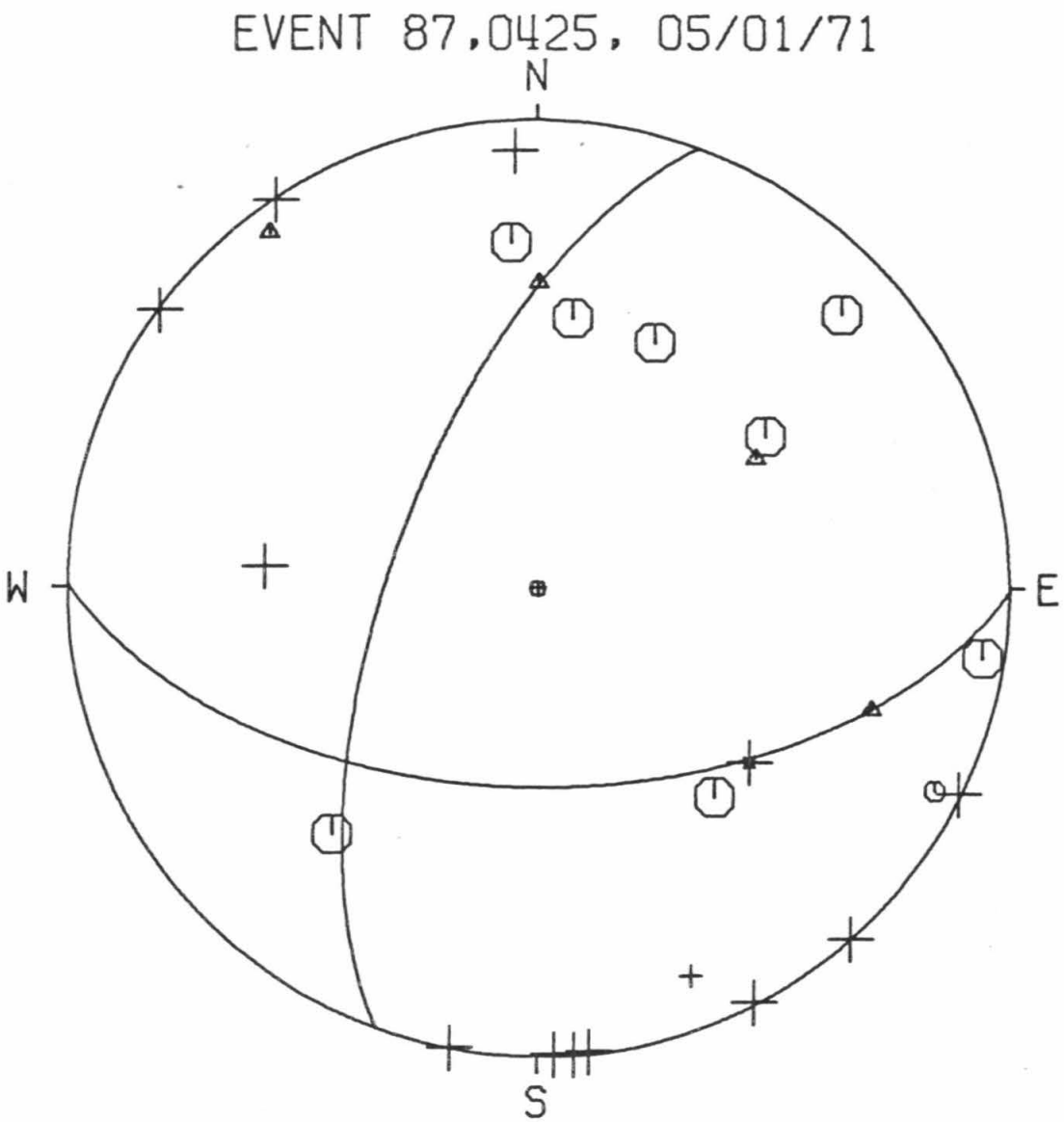
EVENT 87,0425, 05/01/71
N
W
E
S